CHARACTERIZING MODERN MICROBIALITES AND THE GEOBIOLOGICAL PROCESSES UNDERLYING THEIR FORMATION

EDITED BY: Jamie S. Foster, Pieter T. Visscher, Ruth Pamela Reid and Christophe Dupraz

PUBLISHED IN: Frontiers in Microbiology

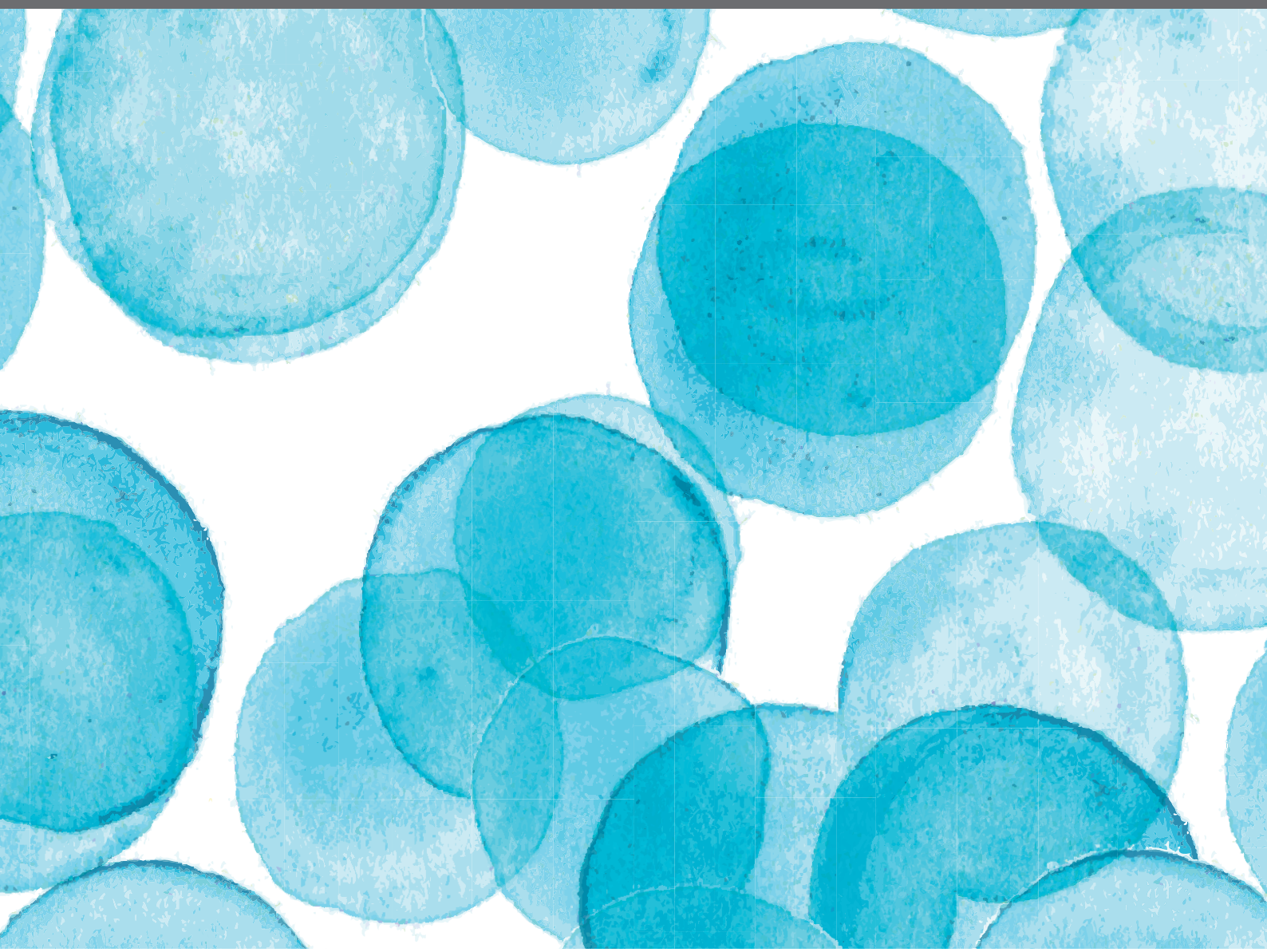

frontiers Research Topics

frontiers

ISSN 1664-8714
ISBN 978-2-88963-252-7
DOI 10.3389/978-2-88963-252-7

About Frontiers

Frontiers is more than just an open-access publisher of scholarly articles: it is a pioneering approach to the world of academia, radically improving the way scholarly research is managed. The grand vision of Frontiers is a world where all people have an equal opportunity to seek, share and generate knowledge. Frontiers provides immediate and permanent online open access to all its publications, but this alone is not enough to realize our grand goals.

Frontiers Journal Series

The Frontiers Journal Series is a multi-tier and interdisciplinary set of open-access, online journals, promising a paradigm shift from the current review, selection and dissemination processes in academic publishing. All Frontiers journals are driven by researchers for researchers; therefore, they constitute a service to the scholarly community. At the same time, the Frontiers Journal Series operates on a revolutionary invention, the tiered publishing system, initially addressing specific communities of scholars, and gradually climbing up to broader public understanding, thus serving the interests of the lay society, too.

Dedication to Quality

Each Frontiers article is a landmark of the highest quality, thanks to genuinely collaborative interactions between authors and review editors, who include some of the world's best academicians. Research must be certified by peers before entering a stream of knowledge that may eventually reach the public - and shape society; therefore, Frontiers only applies the most rigorous and unbiased reviews.
Frontiers revolutionizes research publishing by freely delivering the most outstanding research, evaluated with no bias from both the academic and social point of view. By applying the most advanced information technologies, Frontiers is catapulting scholarly publishing into a new generation.

What are Frontiers Research Topics?

Frontiers Research Topics are very popular trademarks of the Frontiers Journals Series: they are collections of at least ten articles, all centered on a particular subject. With their unique mix of varied contributions from Original Research to Review Articles, Frontiers Research Topics unify the most influential researchers, the latest key findings and historical advances in a hot research area! Find out more on how to host your own Frontiers Research Topic or contribute to one as an author by contacting the Frontiers Editorial Office: researchtopics@frontiersin.org

CHARACTERIZING MODERN MICROBIALITES AND THE GEOBIOLOGICAL PROCESSES UNDERLYING THEIR FORMATION

Topic Editors:
Jamie S. Foster, University of Florida, United States
Pieter T. Visscher, University of Connecticut, United States
Ruth Pamela Reid, University of Miami, United States
Christophe Dupraz, Stockholm University, Sweden

Citation: Foster, J. S., Visscher, P. T., Reid, R. P., Dupraz, C., eds. (2019). Characterizing Modern Microbialites and The Geobiological Processes Underlying Their Formation. Lausanne: Frontiers Media SA. doi: 10.3389/978-2-88963-252-7

Table of Contents

frontiers in Microbiology

EDITORIAL
published: 09 October 2019
doi: 10.3389/fmicb.2019.02299

Editorial: Characterizing Modern Microbialites and the Geobiological Processes Underlying Their Formation

Jamie S. Foster[1], R. Pamela Reid[2], Pieter T. Visscher[3] and Christophe Dupraz[4]*

[1] Department of Microbiology and Cell Science, Space Life Science Laboratory, University of Florida, Merritt Island, FL, United States, [2] Rosenstiel School of Marine and Atmospheric Science, University of Miami, Miami, FL, United States, [3] Department of Geosciences, University of Connecticut, Groton, CT, United States, [4] Department of Geological Sciences, Stockholm University, Stockholm, Sweden

Keywords: microbialites, microbiome, geobiology, meta-omics approaches, microbiology

Editorial on the Research Topic

Characterizing Modern Microbialites and the Geobiological Processes Underlying Their Formation

Microbialites represent one of the oldest known ecosystems on Earth, with a fossil record dating back over 3.5 billion years. These long-lived communities form sedimentary structures as a result of the synergy between microbial metabolisms and the environment. Although once global on the ancient Earth, modern microbialites are found mainly in restricted habitats with sparse eukaryotic populations. Living microbialites offer an opportunity to examine how these ancient ecosystems interface and respond to changes in their environment. Even today, microbialites are bellwethers for an ever-changing Earth and are becoming increasingly exposed to effects of global climate change, such as rising sea levels, ocean acidification, and warmer temperatures. Investigations into extant microbialites represent a unique opportunity to understand the feedbacks that occur between microbialite communities and their environment.

In this collection of research articles, experts investigate and discuss the formation of modern microbialites and the interactions between microbes and the environment. These research contributions target communities from a diverse range of freshwater, marine, and hypersaline environments. Key questions addressed by the papers include (Q1) what are the taxa and metabolic processes that influence microbialite formation? (Q2) How do microbes network and coordinate their activities to form lithified structures? (Q3) How do environmental conditions influence microbialite ecosystems both in the past and present? And (Q4) how are modern microbialite systems likely to respond to ongoing climate change?

Questions 1 and 2 are highly integrative and most papers in the collection touched upon these key areas of research. For example, Wilmeth et al. use novel tracer experiments to quantify mat biomass addition as well as assess the deposition of calcium carbonate within hot spring microbial mats. Their analysis of the rates of carbon fixation and biogenic carbonate precipitation suggests that metabolic processes other than autotrophy may play critical roles in the preservation of mats as microbialites. Additionally, Kraus et al. looked at the formation of minerals in microbialites to help improve our understanding of biosignature in hot springs. Their results reveal that abiotic mineralization of calcite can be subsequently modified by microbial activities, suggesting that biosignature formation is a complex, multi-stage process.

Also addressing Q1 and Q2, the role of certain phototrophic taxa in the formation of mineral precipitates was examined in diverse hypersaline environments including Laguna Negra in Argentina (Mlewski et al.) and Lake Dziani Dzaha on Mayotee Island (Gérard et al.), revealing

OPEN ACCESS

Edited by:
Lasse Riemann, University of Copenhagen, Denmark

Reviewed by:
Matthias Labrenz, Leibniz Institute for Baltic Sea Research (LG), Germany

****Correspondence:***
Jamie S. Foster
jfoster@ufl.edu

Specialty section:
This article was submitted to Aquatic Microbiology, a section of the journal Frontiers in Microbiology

Received: *14 August 2019*
Accepted: *20 September 2019*
Published: *09 October 2019*

Citation:
Foster JS, Reid RP, Visscher PT and Dupraz C (2019) Editorial: Characterizing Modern Microbialites and the Geobiological Processes Underlying Their Formation. Front. Microbiol. 10:2299. doi: 10.3389/fmicb.2019.02299

a multifaceted role of phototrophs in microbialite precipitation. Additionally, several of the articles begin to characterize and close the genomes of some of the more abundant taxa within freshwater microbialites derived from Pavilion Lake in British Columbia (White et al.; White et al.), including novel species of the *Exiguobacterium* and *Agrococcus* genera. These efforts have helped expand the genome databases of taxa associated with the formation and growth of modern microbialites.

Although most studies on microbialites typically focus role of bacteria and archaea in the molecular and biochemical processes associated with element cycling and carbonate precipitation in microbialites, such as the study of Valdespino-Castillo et al., two studies within this collection also addressed Question 1 by targeting organisms that are typically overlooked—algae and viruses. In Frommlet et al., *in vitro* experiments using the alga *Symbiodinium* and its naturally associated microbial consortia revealed that bacterial-algal associations can affect the physicochemical macroenvironment in culture and that the structural integrity of the bacterial-algal biofilms in the microenvironment influences and can facilitate calcification. Alternatively, the role of viruses within microbialite-forming communities was explored by White et al. Their analysis revealed a diverse assemblage of single-stranded DNA viruses within the microbialites, which may be important in element cycling and perhaps modulating microbial diversity of microbialite communities.

In addition to examining microbialite formation, other authors explored Question 3 regarding the impact of the environment on microbialite-forming communities. In the paper by De Anda et al., the authors used metagenomic techniques to examine the specific interactions between taxa in response to environmental perturbations in the freshwater microbialites of Cuatros Ciénegas in Mexico. Their results show that water availability impacts the balance between competition and cooperation interactions. Similarly in the hypersaline system of Hamelin Pool in Western Australia, Babilonia et al. used comparative metagenomics to reveal different metabolic strategies for microbialite formation that was highly dependent on environment, in particular water depth.

Together, this collection of articles has provided new insight into the processes by which microbialites form and how these dynamic ecosystems potentially adapt to and alter their surrounding environment. These articles also reveal several universal processes associated with mineral precipitation across different habitats and help elucidate dynamic feedbacks that occur between microbialites and their environment. Although several of the manuscripts in this collection touch upon how modern microbialite systems are affected by ongoing changes in the climate, this last key question (Q4) represents an important frontier for microbialite research. As microbialites have persisted on Earth for most of evolutionary history, the mechanisms and pathways in which they have caused, responded and adapted to climate change represent a valuable resource to more fully explore the feedbacks and constraints underlying the continued habitability of our planet.

AUTHOR CONTRIBUTIONS

All authors listed have made a substantial, direct and intellectual contribution to the work, and approved it for publication.

FUNDING

This work was supported in part by the NASA Exobiology and Evolutionary Biology program awards NNX12AD64G and NNX14AK14G.

Conflict of Interest: The authors declare that the research was conducted in the absence of any commercial or financial relationships that could be construed as a potential conflict of interest.

frontiers in Microbiology

ORIGINAL RESEARCH
published: 03 April 2018
doi: 10.3389/fmicb.2018.00510

Exploring Biogeochemistry and Microbial Diversity of Extant Microbialites in Mexico and Cuba

*Patricia M. Valdespino-Castillo[1], Ping Hu[1], Martín Merino-Ibarra[2], Luz M. López-Gómez[2], Daniel Cerqueda-García[3], Roberto González-De Zayas[4], Teresa Pi-Puig[5,6], Julio A. Lestayo[4], Hoi-Ying Holman[1,7] and Luisa I. Falcón[3]**

[1] Climate and Ecosystem Sciences Division, Lawrence Berkeley National Laboratory, University of California, Berkeley, Berkeley, CA, United States, [2] Unidad Académica de Ecología y Biodiversidad Acuática, Instituto de Ciencias del Mar y Limnología, Universidad Nacional Autónoma de México, Mexico City, Mexico, [3] Laboratorio de Ecología Bacteriana, Instituto de Ecología, Universidad Nacional Autónoma de México, Mexico City, Mexico, [4] Centro de Investigaciones de Ecosistemas Costeros, Cayo Coco, Cuba, [5] Instituto de Geología, Universidad Nacional Autónoma de México, Mexico City, Mexico, [6] Laboratorio Nacional de Geoquímica y Mineralogía, Universidad Nacional Autónoma de México, Mexico City, Mexico, [7] Molecular Biophysics and Integrated Bioimaging Division, Lawrence Berkeley National Laboratory, University of California, Berkeley, Berkeley, CA, United States

OPEN ACCESS

Edited by:
Jamie S. Foster, University of Florida, United States

Reviewed by:
Jennifer Mobberley, University of California, Santa Barbara, United States
Lukasz Drewniak, University of Warsaw, Poland

***Correspondence:**
Luisa I. Falcón
falcon@ecologia.unam.mx

Specialty section:
This article was submitted to Aquatic Microbiology, a section of the journal Frontiers in Microbiology

Received: *30 November 2017*
Accepted: *06 March 2018*
Published: *03 April 2018*

Citation:
Valdespino-Castillo PM, Hu P, Merino-Ibarra M, López-Gómez LM, Cerqueda-García D, González-De Zayas R, Pi-Puig T, Lestayo JA, Holman H-Y and Falcón LI (2018) Exploring Biogeochemistry and Microbial Diversity of Extant Microbialites in Mexico and Cuba. Front. Microbiol. 9:510. doi: 10.3389/fmicb.2018.00510

Microbialites are modern analogs of ancient microbial consortia that date as far back as the Archaean Eon. Microbialites have contributed to the geochemical history of our planet through their diverse metabolic capacities that mediate mineral precipitation. These mineral-forming microbial assemblages accumulate major ions, trace elements and biomass from their ambient aquatic environments; their role in the resulting chemical structure of these lithifications needs clarification. We studied the biogeochemistry and microbial structure of microbialites collected from diverse locations in Mexico and in a previously undescribed microbialite in Cuba. We examined their structure, chemistry and mineralogy at different scales using an array of nested methods including 16S rRNA gene high-throughput sequencing, elemental analysis, X-Ray fluorescence (XRF), X-Ray diffraction (XRD), Scanning Electron Microscopy-Energy Dispersive Spectroscopy (SEM-EDS), Fourier Transformed Infrared (FTIR) spectroscopy and Synchrotron Radiation-based Fourier Transformed Infrared (SR-FTIR) spectromicroscopy. The resulting data revealed high biological and chemical diversity among microbialites and specific microbe to chemical correlations. Regardless of the sampling site, Proteobacteria had the most significant correlations with biogeochemical parameters such as organic carbon (C_{org}), nitrogen and C_{org}:Ca ratio. Biogeochemically relevant bacterial groups (dominant phototrophs and heterotrophs) showed significant correlations with major ion composition, mineral type and transition element content, such as cadmium, cobalt, chromium, copper and nickel. Microbial-chemical relationships were discussed in reference to microbialite formation, microbial metabolic capacities and the role of transition elements as enzyme cofactors. This paper provides an analytical baseline to drive our understanding of the links between microbial diversity with the chemistry of their lithified precipitations.

Keywords: mineral diversity, organic C, biomineralization, biogeochemical interactions, microbe lithification chemistry, bioactive transition elements, Mexico, Cuba

INTRODUCTION

Extant microbialites are modern analogs of stromatolite deposits left by ancient microbial consortia as early as ∼3,500 Ma ago (Krumbein, 1983; Schopf, 2006). Modern microbialites comprise massive mineral structures with a growing surface layer where diverse microbial communities reside. Modern microbialites are often found in low-nutrient (oligotrophic) aquatic environments, extremely cold or hot environments (Coman et al., 2015; White et al., 2015), marine (Myshrall et al., 2010) and athalassohaline (whose ionic composition differs from that of seawater) environments (Dupraz et al., 2004; Centeno et al., 2012). The diverse metabolic capacities of microbes induce and mediate a variety of mineral precipitations (Dupraz et al., 2009) and have thereby contributed to the geochemical history of the Earth (see Des Marais, 1995, 2000; Dupraz et al., 2009).

Mineral-forming microbial assemblages accumulate biomass as well as major ions and trace elements in their growing layer. Through microbial specific metabolisms, biorelevant trace elements may be concentrated and preserved in microbialites (Webb and Kamber, 2000). In recent years, different studies have focused on the microbial communities within microbialites (microbial structure and metabolic potential) using 16S rRNA gene sequencing and metagenomics. These studies have found that microbialites harbor a highly diverse microbial community fundamentally driven by environmental factors such as pH, conductivity and availability of nitrate (Centeno et al., 2012). Genomic surveys for some microbialites have revealed a broad potential for photoautotrophy and heterotrophic pathways involved in biogeochemical C, S, N, and P cycling (Beltrán et al., 2012; Valdespino-Castillo et al., 2014, 2017; Cerqueda-García and Falcón, 2016; Saghaï et al., 2016; Alcántara-Hernández et al., 2017); and synthesis of enzyme cofactors, amino acids, production and degradation of extracellular polymeric substances (EPS) (Breitbart et al., 2009; Myshrall et al., 2010; Mobberley et al., 2013; White et al., 2015; Cerqueda-García and Falcón, 2016). Microbialite extracellular polymeric substances provide an adequate environment for binding transition metals to organic ligands (Geesey et al., 1988; Sforna et al., 2017) that may be microbe-dependent (Micheletti et al., 2008) and needs further exploration. These transition elements (Period 4 in the periodic table, from V to Zn) and heavier elements such as Cd and Mo are essential trace nutrients for organisms, present as cofactors for enzymes (i.e., Co and Ni) or structural elements in proteins (i.e., Fe and Mn) (Ledin, 2000; Rosen, 2002; Cavet et al., 2003; Silver and Phung, 2005) although some are toxic for microorganisms (Tebo and Obraztsova, 1998; Ledin, 2000; Williams and Da Silva, 2000; Silver and Phung, 2005). Besides being redox reagents, metals are used in a variety of metabolic pathways (see Webb and Kamber, 2000). Examples include: Co in cobalamin (vitamin B12) and carbonic anhydrase, Ni in [NiFe]-hydrogenase and as a cofactor in methyl-CoM reductase, Cu in thylakoidal plastocyanin and Cd in carbonic anhydrase (Ankel-Fuchs and Thauer, 1988; Lee and Morel, 1995; Butler, 1998; Williams and Da Silva, 2000; Cavet et al., 2003; Morel and Price, 2003; Giordano et al., 2005).

The chemistry and mineralogy of microbialites in relation to particular microbes needs clarification since different groups of microbes, both prokaryote and eukaryote, utilize trace elements in different ways and in different fundamental ratios (Quigg et al., 2003). It has been proposed that an accumulation of elements out of equilibrium with the surrounding environment may provide a biosignature (Webb and Kamber, 2000) of life processes. Illuminating relations between microbe type and microbialite chemistry will likely facilitate understanding of the processes that create these organo-sedimentary structures. Interdisciplinary efforts will be needed to address these questions.

Some studies, focused on the elemental chemistry of microbialites and lithifying mats have incorporated the microbial component structure and metabolic potential (see Webb and Kamber, 2011; Gérard et al., 2013; Wong et al., 2015; Paul et al., 2016; Zeyen et al., 2017) providing relevant clues to the understanding of microbialite formation and the role of microbes in geochemical signatures and mineral diversity. Here we studied microbialites collected from low nutrient aquatic environments, from four locations in Mexico and one previously undescribed microbialite in Cuba (Northern Keys, Sabinal System), using a cross-system comparison approach. Their contrasting hydro-geochemical features and the ionic composition of microbialite ambient waters are summarized in **Table 1**. Sampling locations include a soda lake (Lake Alchichica) and karstic (calcium carbonate) environments. Karstic locations include an inland system (PAI = Cuatro Ciénegas, México) and lagoons near the coast. Karst coastal systems characteristics include a salinity gradient from oligosaline (BAC = Bacalar and MU = Muyil, Mexico) and a hypersaline sytem (CU = Sabinal, Cuba). In order to uncover the microbial communities' compositions and their relationship with the microstructure and chemical signature of microbialites, we performed an array of nested methods including 16S rRNA gene high-throughput sequencing, XRF and elemental analysis, XRD, SEM-EDS, Fourier transform infrared (FTIR) spectroscopy and Synchrotron Radiation-based Fourier transform infrared (SR-FTIR) spectromicroscopy. We intend that this cross-system approach will be useful to explore microbial taxa relationships with chemical composition descriptors, and to gain insight on the links between microbial community structure, chemical composition, microstructure and mineral diversity.

MATERIALS AND METHODS

Study Area

Microbialites collected for this study were sampled in five different tropical locations. The geographical location, altitude, landscape type and main water physicochemical conditions for each of the locations are described in **Figure 1** and **Table 1**. Photographs and environmental data show that these systems are clear-water, low-nutrient (oligotrophic) environments, with characteristic ionic compositions ranging from low conductivity to hypersaline. Human activity occurs to some extent (mostly associated with tourism) near these microbialites. This study is the first report on the microbialites from Cayo Sabinal, Cuba, a hypersaline (hypersalinity >40‰; Battaglia, 1959)

TABLE 1 | Microbialite sample locations, physicochemical and geochemical aquatic environment.

Aquatic ecosystem	Temp (°C)	pH	Conductivity (mS/cm)	Salinity (psu)	Altitude (masl)	Major cations in water	Ca^{+2}	Mg^{+2}	Na^{+}	K^{+}	Cl^{-}	SO_4^{-2}	$HCO3^{-}$	Mg:Ca	References
							mg/L								
Soda inland (athalassohaline)															
AS, AC Alchichica lake, Mexico	18.7	9.3	13.0	7.5	2,350	$Na^{+} > Mg^{+2} > K^{+} > Ca^{+2}$	11	431	2,349	232	3,195	978	966	39.182	3, 4, 7
Karst inland (oligosaline)															
PAI Pozas Azules, Mexico	28.8	7.4	2.7	1.5[c]	0–700	$Ca^{+2} > Na^{+} > Mg^{+2}$	385	114	165	10	121	1,441	189	0.30	1, 2
Karst inland-coastal (oligosaline)															
BAC Bacalar Lagoon, Mexico	29	7.8	2.2	1.2[c]-9	0–20	$Ca^{+2} > Mg^{+2} > Na^{+}$	320	78	61	5	70	1,112	171	0.24	5
MU Muyil Lagoon, Mexico	25.5	7.7	1.7	0.7	0–20	$Na^{+} > Mg^{+2} > Ca^{+2} > K^{+}$	48	37	147	4	277	38	201	0.76	2, 6
Karst coastal *(hypersaline)*															
CU Sabinal (Sabana-Camagüey System), Cuba	29	8.9	97.2	58.8	0–20	$Na^{+} > Mg^{+2} > K^{+} > Ca^{+2}$	750	2,689	21,046	807	43,330	5,529	–	3.59	This study

[1]*Johannesson et al., 2014 (mean Cuatro Cienegas);* [2]*Centeno et al., 2012;* [3]*Arnienta et al., 2008;* [4]*Caballero et al., 2003;* [5]*Gischler et al., 2008;* [6]*Lagomasino et al., 2015;* [7]*Kaźmierczak et al., 2011;* [c]*calculated from conductivity.*

lagoon system in the Northern Cuban Keys (Sabana-Camagüey System; **Table 1**). High microbial diversity has been previously documented for some of the microbialites from Mexico. Environmental factors, such as pH, conductivity and nitrate content are relevant drivers of the microbial structure of these microbialites (Centeno et al., 2012). A metagenomic exploration over two locations of Cuatro Ciénegas Basin (same pond of our PAI microbialite) showed microbialites were enriched in genes for phosphorus metabolism, establishment and development of biofilms and heterotrophic respiration (Breitbart et al., 2009). A vast genetic diversity for nitrogen (N) and phosphorus (P) cycling has been described for the microbialites from Alchichica soda lake (Beltrán et al., 2012; Valdespino-Castillo et al., 2014, 2017; Alcántara-Hernández et al., 2017), where microbialites actively fix nitrogen (Beltrán et al., 2012). The geochemical characteristics (major cations) of microbialite ambient waters (**Table 1**) were compiled from different reference studies.

Sample Collection and Post-treatment

Approximately 12 grams of microbialites were collected in each of five locations that include Cuatro Ciénegas, North of Mexico, Mexican highlands, Mexican Caribbean, and Cuban coast, Cayo Sabinal. All microbialites were found and collected at the surface (∼less than 0.4 m depth). The general physico- and geochemical features of each sampling site are detailed in **Figure 1** and **Table 1**. Physicochemical characterization of microbialite ambient waters included temperature, dissolved oxygen (DO) and pH. Samples used for chemical determinations (XRD, XRF, elemental analysis, SEM and DNA surveys were frozen at −20°C and sectioned in the laboratory (before drying) in order to control elemental content per area units (∼1 cm^2) and to avoid aquarium effects. Fresh samples for Infrared spectromiscroscopy were collected (1–2 weeks before the analyses) and preserved (during this period) in an aquarium with lake water in similar physicochemical conditions (DO, temperature and diel light cycle).

Microbialite Chemical Characterization

Pulverized Microbialites

Each microbialite surface sample (three per site) was divided into three fractions: (A) 5 g of each microbialite were cold-dried (10°C) for mineral and chemical composition determinations, samples were pulverized in agate mortars. Each pulverized sample was used for the next analyses: X-Ray Diffraction (XRD), X-Ray Fluorescence (XRF), elemental analysis (EA), and Fourier Transform Infrared FTIR Spectroscopy. (B) Approximately 5 g were kept frozen (−20°C) until DNA extraction and amplification and (C) approximately a cubic cm from the undisturbed microbialite surface was preserved for Scanning Electron Microscopy (SEM) coupled to an Energy-dispersive micro spectroscopy (SEM-EDS) and for SR-FTIR spectromicroscopy examinations.

X-Ray Diffraction (XRD)

For XRD analyses, samples were cold dried (10°C), ground and homogenized using a pestle and agate mortar (<75 μm) and mounted using double-side aluminum holders as non-oriented

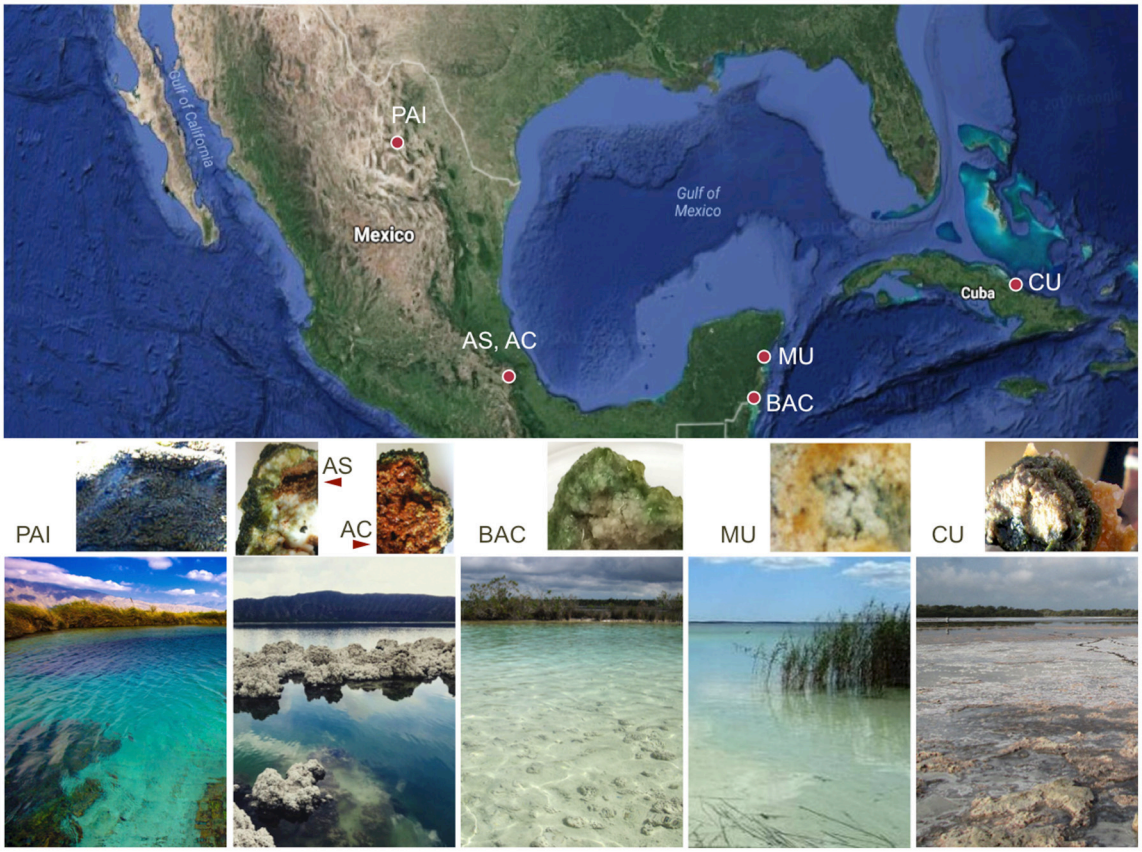

FIGURE 1 | Geographical location, landscape view and cross-sections of extant microbialites. Five sampling locations include six microbialites: PAI, Pozas Azules I, Cuatro Ciénegas Basin, karstic inland, freshwater system; AS and AC, Alchichica crater lake, Mexican highlands, soda lake, athalassohaline; BAC, Bacalar Lagoon, karstic coastal, freshwater system; MU, Muyil Lagoon, Quintana Roo, karstic coastal, freshwater system; and CU, Cayo Sabinal, Northern Cuban Keys, Sabana-Camagüey System, karstic coastal, hypersaline system.

fractions. Measurements were performed in triplicates in an angular range 2θ from 5° to 70° in step scanning of 0.003° (2 Theta) and 40 s of integration time per step. Diffractograms were obtained using an EMPYREAN diffractometer equipped with a Ni filter, cooper tube and a PIXcel3D detector. The diffraction patterns were analyzed with the HighScore version 4.5 software with reference patterns from the ICDD PDF-2 and ICSD databases.

Elemental Analysis (EA)

For organic elemental analysis, about 20 mg of the microbialite powder was used for the determination of elemental C and N (PerkinElmer 2400 Elemental Analyzer) in five replicates. Additionally, one gram subsamples of pulverized microbialite samples followed inorganic carbon removal of each sample (incubation in HCl 10%) to analyze organic carbon (C_{org}) through elemental analysis; all elemental N in this fraction was assumed to be part of biomass. Total N and P were determined using this (incubated) fraction through a high temperature persulfate oxidation (Valderrama, 1981). P fractions were determined after alkaline and acid extractions as reported by López-Gómez (2003).

X-Ray Fluorescence (XRF)

Elemental composition of major elements (mg/g content in microbialites) and trace element (μg/g) was determined in triplicates by X-ray fluorescence (XRF) system (Spectro^{TM} Xepos) under Helium atmosphere. Here pulverized microbialite samples were compressed manually with a Teflon roller prior to the measurements. In this the subsequent analysis, we organized the data into three groups: the main biogeochemical elements (C, N, P, S, Si,), the major ions in aquatic systems (Na, Mg, K, Ca, Cl), and the trace elements (i.e., Cr, As, Co, Cu, Fe, Cd, Mo, Mn, Ag, Se).

Fourier Transform Infrared (FTIR) Spectroscopy and Spectromicroscopy

To verify and enrich the results from XRD analysis, we also used transmission FTIR spectroscopy to characterize carbonate minerals, sulfate-bearing minerals, and silicate minerals in the microbialite powder prepared from all six microbialites. Our previous experience has shown that silicate minerals are readily detected by FTIR, but uncertain from XRD. Here, a drop of aqueous microbialite powder suspension was micropipetted onto a 1-mm thick ZnSe disc and allowed to dehydrate under a stream

of dry nitrogen gas to dryness at room temperature. Normal incidence transmission spectra of the microbialite powder films and the microbialite-free ZnSe disc were recorded using a Nicolet Nic-Plan IR microscope which was coupled to a Nicolet Magna 760 FTIR bench (Thermo Scientific Inc., MA, USA), a thermal emission mid infrared light source (thermal globar) and a single-element MCT (mercury-cadmium-telluride) detector. All transmission spectra were collected in the mid-infrared region (∼2.5 to ∼15.5 μm wavelength, or ∼4,000 to ∼650 wavenumber in cm^{-1}) at a spectral resolution of 4 cm^{-1} with 8 co-added scans and a peak position accuracy of 1/100 cm^{-1}. All data pre- and post-processing were conducted using Thermo Electron's Omnic version 7.3. Spectral absorption peaks were compared to those in our in-house library and in published database to derive mineral information (see **Table 2**).

To supplement information on the relative abundance and distributions of biomolecules and minerals, SR-FTIR spectromicrosopy was also performed on fresh thin layers of intact microbialites. By using a bright synchrotron as an infrared light source, this SR-FTIR approach offers a signal-to-noise ratio that is 100–1,000 times better than the thermal global FTIR approaches (Holman et al., 2010). SR-FTIR has enabled a variety of studies in biogeochemical processes (Holman et al., 1999, 2002; Baelum et al., 2012; Probst et al., 2013, 2014), in cyanobacterial silicification (Benning et al., 2004), in cyanobacteria bicarbonate transporters (Kamennaya et al., 2015), and even in microbial metabolic functions at terrestrial interface of extreme fluctuations (Holman et al., 2009, 2010). Here, intact and fresh microbialites were placed onto an infrared transparent ZnSe disc and free-flowing lake water was removed carefully without disturbing the structure of the microbialites prior to imaging. For each SR-FTIR imaging measurement, the entire view-field of the intact microbialite was divided into equal-sized 5 × 5-μm squares before scanning. Background spectra were acquired from

TABLE 2 | Band assignments of the diagnostic vibrational modes used in FTIR spectroscopy (**Figure 3**) of microbialite pulverized samples.

Minerals	Peak position (cm^{-1})	Assignment	References
Carbonates	∼1,780, ∼1,470, ∼875, ∼712, ∼699	Aragonite structure; coupling among CO_3^{2-} groups in the presence of Ca	White, 1975; Dubrawski et al., 1989; Jones and Jackson, 1993
	∼1,775, ∼1,460, ∼857, ∼706	Aragonite structure; coupling among CO_3^{2-} groups in the presence of Sr^{2+}	
	∼2,515, ∼1,798, ∼1,740, ∼1,430, ∼1,162, ∼870, ∼712	Calcite structure; coupling among CO_3^{2-} groups in the presence of Ca^{2+}	
	∼1,480, ∼1,425, ∼884, ∼854, ∼790	Hydromagnesite structure; coupling among CO_3^{2-} groups in the presence of Mg^{2+}	
	∼3,650, ∼3,510, ∼3,445	Hydromagnesite structure; coupling among O–H…O groups in the presence of Mg carbonates.	
	∼1,422, ∼865, ∼735	Siderite structure; coupling among CO_3^{2-} groups in the presence of Fe^{2+}	
Silicates	∼3,740, ∼3,500—∼3,300	Layer silicates (kaolinite) structure; O–H vibration associated with Si; replacement of Si by Al; the band broadened leads to peak broadenin	Farmer, 1975; Nash and Salisbury, 1991; Ritz et al., 2010; Müller et al., 2011; Djomgoue and Njopwouo, 2013; Kuang et al., 2016
	∼1,117, ∼1,100, ∼1,033, ∼1,011	Layer silicates (kaolinite) structure; Si–O–Si and Si–O–Al stretching vibration	
	∼1,540, ∼1,625	Vibration of heterocylic organic compounds H-bonded to layer silicates (kaolinite)	
	∼2,970, ∼2,930, ∼2,875	Vibration of CH of organic compounds bonded to layer silicates (kaolinite)	
	∼1,303, ∼1,245, ∼1,149, ∼1,098, ∼1,030, ∼1,010	Plagioclase structure; stretching and bending vibrations of the Si–O and Al–O bonds.	
	∼1,150, ∼1,080, ∼1,050	Quartz (α-, β-); SiO_4 stretching and Si–O–Si bending transition.	
Sulfate-containing minerals	∼1,010, ∼676	Gypsum; stretch and bending vibration modes of $(SO_4)^{2-}$ in the presence of Ca^{2+}	Ross, 1975; Lane, 2007
	∼3,500, ∼3,400, ∼3,250	Gypsum; Combination modes of $(SO_4)^{2}$- and O–H (of H_2O) vibrations in the presence of Ca^{2+}	
	∼1,250, ∼1,124, ∼676	Hexahidrite; stretch and bending vibration modes of $(SO_4)^{2-}$ in the presence of $6H_2O$ and Mg^{2+}	
Water as inclusion or structurally bonded molecules	1,640–1,620	O–H bending modes of the H_2O molecules	Henning, 1975; Aines and Rossman, 1984; Kronenberg and Wolf, 1990
	3,600–3,000	O–H stretching vibrations of the H_2O molecules	

locations without any microbialite material and were used as reference spectra. A data cube of position-associated infrared spectra was obtained following each SR-FTIR data acquisition experiment. This data cube was then subjected to an array of data processing calculations using Thermo Electron's Omnic version 7.3.

Scanning Electron Microscopy Coupled to Energy-Dispersive Detector

Intact surface (∼0.1 cm^3) microbialite dry samples were analyzed using a JEOL35C scanning electron microscope (SEM) with a dispersive X-ray spectrometer (EDS). Operating conditions were set at 15 kV accelerating voltage and 100 s measuring time.

Nucleic Acids Extraction and Total DNA 16S rRNA Gene Amplification

Approximately 2 g of each microbialite (corresponding to a cubic cm of the surface layer; in triplicates) were ground in mortars adding liquid nitrogen and a buffer solution buffer solution composed by 100 mM Tris-HCl, 20 20 mM NaCl, 100 mM EDTA (pH 8), and cetyl trimethylammonium bromide (CTAB) 0.06 of volume. Mixtures were then incubated with lysozyme (30 mg ml^{-1}) (Sigma Aldrich, USA) for 30 min at 37°C. An incubation adding proteinase K (10 mg ml^{-1}, Sigma Aldrich, USA) and 0.1 V of sodium dodecyl sulfate (SDS) followed (at 55°C, overnight). The aqueous phase was carefully separated (centrifuged 20 min, 1,800 g) and extracted twice with a 25:24:1 solution of phenol:chloroform:isoamyl alcohol and with 24:1 chloroform:isoamyl alcohol. DNA precipitation was conducted (at −20°C, adding 0.1 volume of sodium acetate (3M), 2 sample volumes of 2-propanol, and 2 μL of GlycoBlue (Ambion Inc., USA). Precipitated DNA was washed with ethanol twice (90–80%) and resuspended in molecular grade water. For DNA purification, Mini Spin columns (DNeasy Blood & Tissue, QIAGEN, Alameda, CA) were used following the instructions of the manufacturer. Purified DNA was stored at −20°C until analysis.

The V4 hypervariable region of prokaryote 16S rRNA gene was amplified from total DNA (in triplicates per sample site) by PCR using primers 515F/806R (Caporaso et al., 2010, 2012); PCR reactions contained a specific Golay reverse primer (Caporaso et al., 2010). Every PCR reaction plus negative controls were prepared with nuclease free-water and 2 ng/μl of total DNA per mat studied. Every PCR mix of a final volume of 25 μl contained 2.5 μl Takara ExTaq PCR 10X buffer (TaKaRa Corp., Shiga, Japan), 0.7 μl bovine serum albumin (20 mg ml-1, Roche), forward and reverse primers (10 ſM final concentration), 2 μl of Takara dNTP mix (2.5 mM), and 0.625 U Takara Ex Taq DNA Polymerase. Amplification program included a (95°C, 3 min) initial denaturalization step followed by 35 cycles of 95°C (30 s) - 52°C (40 s) - 72°C (90 s); and a final (72°C, 12 min) extension. When no amplicons were detected in negative controls, three PCR products (length ∼250 bp) were purified and pooled for each microbialite location (∼20 ng per sample) using SPRI platform (Beckman Coulter, Brea, CA, USA). Amplicons were sequenced on the Illumina MiSeq platform (Yale Center for Genome Analysis, CT, USA). Sequences derived from this study (16S rRNA gene) are available in GenBank under BioProject PRJNA418176.

Bioinformatic Analyses

16S rRNA gene sequences were obtained in paired end reads (V4 PE reads, 2 x 250 bp), which were merged with FLASH (Magoč and Salzberg, 2011), and analyzed in the QIIME pipeline (Caporaso et al., 2010; Bokulich et al., 2013). Quality filtering and demultiplexing were performed *sensu* (Caporaso et al., 2012; Bokulich et al., 2013) using parameters $r = 1$; $p = 0.75$; $q = 20$; $n = 0$. Operational taxonomic units (OTU) clustering and chimeric sequences detection and removal were performed with USEARCH (Edgar et al., 2011) grouping sequences at 97% of similarity. Taxonomic assignation was performed using the RDP classifier (Wang et al., 2007) and Greengenes database 13.5 in QIIME 1.9. Singletons were removed ($n = 1$) and counts were normalized by rarefaction to a maximum value of 10,000 sequences. Alpha and Beta diversity analysis were performed using unifrac distance metrics (in QIIME platform) to compare the community structure and diversity of microbialite samples. We used Mantel tests based on distance dissimilarity matrices (permutations = 999) in R vegan package, and adonis (multivariate ANOVA based on dissimilarities, QIIME; permutations = 999) to determine the analysis of variance using unifrac distance matrices in order to statistically test differences in the community structure (composition and relative abundance of different taxa) with environmental parameters (microbialite chemistry). Analyses were performed with the overall community and with the most abundant bacterial groups; 75 variables were tested including Geography, Category (an indication of beta diversity clustering), biogeochemical, mineral, elemental composition and stoichiometrical ratios. Spearman tests (rho coefficient) were used to clarify significant correlations with chemical parameters at OTU level.

A taxonomic exploration of cyanobacterial phylotypes (OTUs shared in at least in four microbialites) was performed using refseq Database, NCBI. Phylogenetic affiliations are shown in Figure S2, in a phylogenetic reconstruction (GTR evolution model, Maximum likelihood, 1,000 bootstrap) that included microbialite phylotypes and their best hits.

RESULTS

Chemical Composition of Microbialites: Mineral Content and Major Ions

Determinations of mineral composition by XRD [relative abundance, as percentage calculated using the Reference Intensity Method (RIR)] per site, are shown in **Figure 2**. XRD exam showed a total of 10 different mineral species (mineral content >1% of the bulk sample). The most abundant minerals were calcite, aragonite and hydromagnesite, these carbonates correspond to primary minerals (non diagenetically altered) *sensu* (Müller et al., 1972); iron carbonate (siderite) contributed to <1% when present. Sulfur minerals contributing >10% of microbialites were hexahidrite (hydrated magnesium sulfate), gypsum (calcium sulfate dihydrate) and pyrite (iron sulfide). Other minerals detected in low proportion by XRD were non

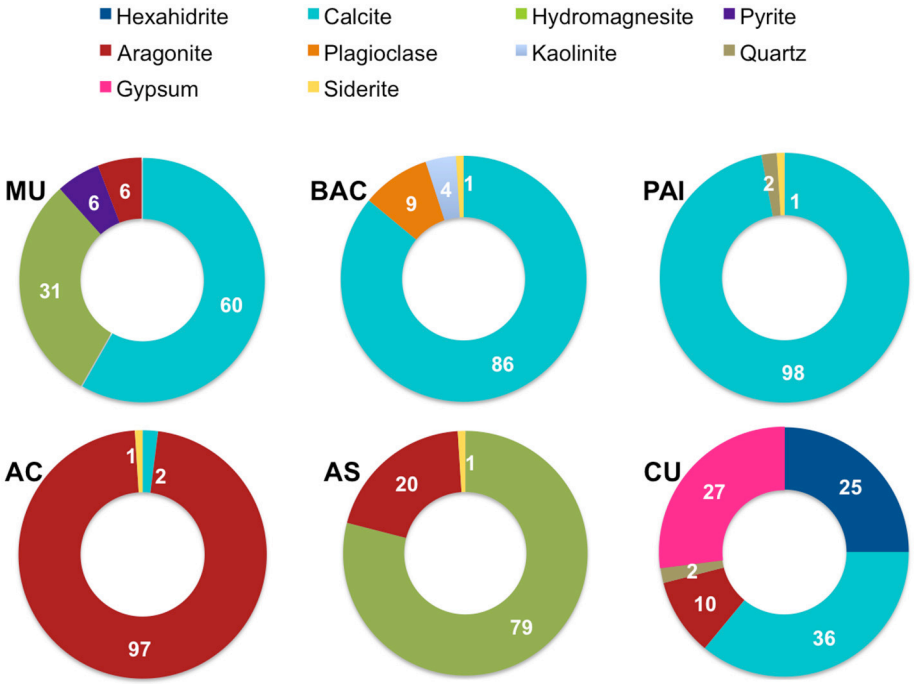

FIGURE 2 | Mineral composition (as percentage) of microbialites from PAI (Pozas Azules I, Cuatro Ciénegas Basin); AS and AC (Alchichica crater lake); BAC (Bacalar Lagoon); MU (Muyil Lagoon, Quintana Roo), and CU (Cayo Sabinal, Northern Keys, Cuba).

biogenic detrital silicates such as quartz, plagioclase and kaolinite, a clay mineral derived from the weathering of alumino-silicate minerals.

The mid-infrared spectra of pulverized microbialite samples (**Figure 3**) highlight absorption peaks of the fundamental vibrational modes assigned to carbonate minerals, complex silicate minerals, and sulfate minerals. Our assignments for all peaks, as summarized in **Table 2**, are consistent with those in previous literature Farmer, 1975; Hu, 1980; Nash and Salisbury, 1991; Smith and Seshadri, 1999; Lane, 2007; Djomgoue and Njopwouo, 2013; Müller et al., 2014). A comparative analysis of FTIR spectra shows spectra from all six microbialites (AS, AC, PAI, MU, BAC, and CU) have strong absorption bands in the 900–700 cm^{-1} and the 1,500–1,400 cm^{-1} regions exhibited strong spectral features characteristics of carbonate minerals containing metal ions Ca^{2+}, Mg^{2+}, and Sr^{2+}. Spectra from all but samples from AS and AC showed spectral signatures of silicates in the region of 1,030–1,150 cm^{-1} (Si-O and Al-O bonds of plagioclase structure and quartz), water inclusions or bonded water molecules in the region of 3,300–3,500 cm^{-1} (O-H vibration associated with water molecules in silicates); and signatures of organic molecules at ∼1,540 cm^{-1} and ∼2,900 cm^{-1} (heterocyclic organic compounds -H and -CH bonded to layer silicates). Only spectra of CU microbialites exhibit sulfate signatures typical of gypsum (∼1,010, ∼676 cm^{-1}) and of hexahydrite (∼1,250, ∼1,124, stretch and bending vibration modes of sulfate in the presence of $6H_2O$ and Mg^{2+})(see **Table 2** and **Figure 3** for details).

The sequence of major ions content in the microbialites was Ca<Mg<Na in general (**Figure 4**). The exception was CU (coastal hypersaline system), where microbialite Na content was two orders of magnitude higher, compared to the rest of microbialites. Ca and Mg were interestingly different between the microbialite morphotypes of lake Alchichica. Mg content was the maximum in AS, the microbialite with the highest content in hydromagnesite, and contrastingly low in the Alchichica columnar morphotype (AC). Ca content showed the opposite pattern between these microbialites. Mg showed an inverse trend with aragonite among microbialites (**Figure 4**) and direct with arsenic, particularly for AC and AS (**Figure 5**). Although Mg:Ca ratio is useful to predict the type of mineral (particularly for carbonates, Müller et al., 1972), major ion ratios were not sufficient to reconstruct accurately microbialite mineral diversity or microbialite chemistry because carbonate mineral precipitation is not commonly that which would be predicted via straightforward equilibrium thermodynamic considerations, but is formed as a result of complex reaction kinetics (e.g., Morse and Casey, 1988).

Elemental Composition and Main Biogeochemical Parameters

Main biogeochemical elements (C, N, P, S, and Si) as well as major ions (Na, Mg, K, Ca, Cl) together with aluminum contributed to concentrations in the range of mg/g in each microbialite, (**Figure 4**). Elemental analyses of microbialite surface samples (∼1 cm^3) showed that organic carbon concentration was similar among systems, being BAC the system with the highest C_{org}

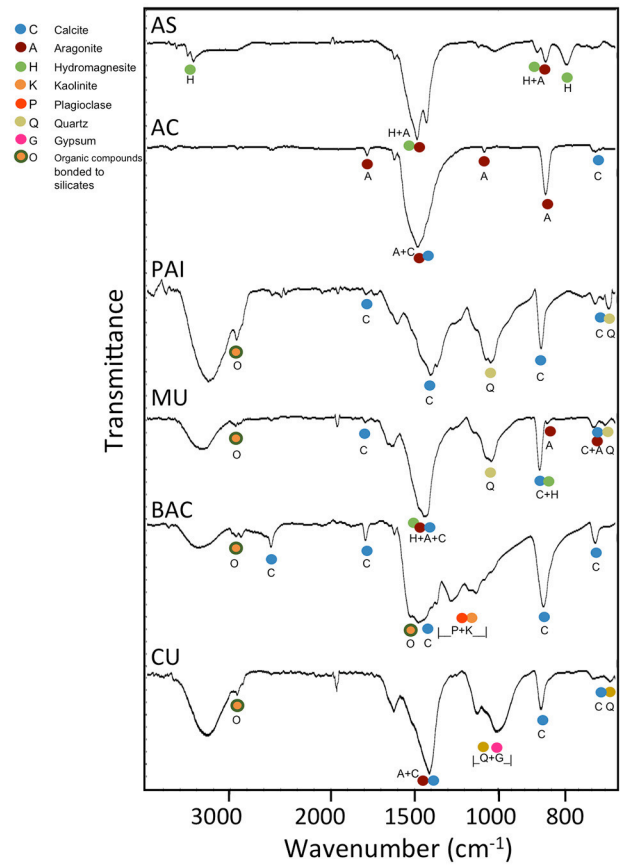

FIGURE 3 | Typical FTIR transmittance spectra of pulverized microbialite samples from Alchichica soda lake (AC and AS morphotypes), Pozas Azules I (PAI, karst inland), Muyil and Bacalar (MU and BAC, karst coastal, oligosaline lagoons) in Mexico and Sabinal (CU, karst coastal, hypersaline system) in Cuba. The mineral markers are color coded for easier comparison against the FTIR band assignments of the fundamental vibrational modes in carbonate minerals (aragonite, calcite, hydromagnesite, siderite), silicate minerals (kaolinite, plagioclase, quartz), and sulfate minerals (gypsum, hexahidrite) (see **Table 2**). The band depths centered around the regions of 1,640–1,620 cm^{-1} and 3,600–3,000 cm^{-1} in the PAI, MU, BAC, and CU samples are from the bending and stretching vibrations of mineral water (as inclusion or structurally bonded molecules). Additional fine spectral features in the 3,000–2,850 cm^{-1} region detected are likely from the CH vibrations of organics bonded to silicate minerals.

content (**Figure 4**). Elements (i.e., transition elements) exhibiting lower concentrations (in the range of μg/g) in the microbialites are included in **Figure 5**. Both, major and trace elements are more concentrated in microbialites relatively to their ambient waters. Natural systems exhibit concentration of major ions in the range of mg/L (e.g., **Table 1**), and trace elements in the range of μg/L (Calabrese et al., 1985). Replicates and standard deviation of microbialite chemical determinations may be consulted in Table S9.

Chromium (sensitive to aerobic manganese cycling, *sensu* Hardisty, 2016) and vanadium exhibited and elevated concentration in the microbialites studied ranging from 5.7 to 13 μg/mg overall (**Figure 5**). These two elements were relatively higher in the systems with higher Mg:Ca ratios and interestingly their concentration in Alchichica lake morphotypes was different and inverse. Holocene reef microbialites from Australian Great Barrier Reef also have elevated Cr and V concentrations relative to associated skeletal carbonates (Webb and Kamber, 2011), such as scleractinian -corals, mollusks and coralline red algae, and in ratios that do not reflect their abundances in seawater.

In addition to geography and nitrogen content (**Table 3** and Table S5), notoriously, differences in microbialite community structure were also associated to the concentration of some metals (**Table 3**). Cadmium showed the strongest correlation, but the overall communities correlations to cobalt, chromium, copper and nickel also showed high scores (adonis results, **Table 3**). Specific microbial associations to these elements will be discussed in section The Role of Bioreactive Transition Elements Within Microbialites From Mexico and Cuba (Tables S6–S8).

Microbialite Microstructure

SEM microscopic observations of organic "trabeculae" provided a suggestion that EPS may be contributing to C_{org} in BAC, the microbialite with the highest content of $C_{org.}$(**Figure 4**). Accordingly, BAC also exhibited the highest C:N and C:P and N:P ratios. Additionally, FTIR spectroscopy of BAC pulverized samples indicate the presence of organic compounds bonded to layer silicates (**Figure 3**, **Table 2**) in the mineral matrix. SR-FTIR spectromicroscopy of fresh BAC microbialite reveal the lowest transmittance (i.e., the strongest absorptions) at ∼1,000 cm^{-1} that are associated with carbohydrates (Hazen et al., 2010) (**Figure 8A**). The distribution of calcite (embedded in a carbohydrates layer) spatially converges with sites rich in lipids and protein amides II (**Figure 8B**).

SEM microscopy- EDS spectroscopy observations were useful to visualize different microbialite surface microstructures, intra and inter-site heterogeneity and the micro-features of mineral precipitations. Most of the observations showed amorphous shaped precipitations ranging in size from round (∼2 μm) to tabular/laminar (up to ∼20 μm) (**Figures 6–8**). SEM-EDS results were consistent with the results from XRD analysis, showing the presence of major cations (calcium and magnesium), Si in all microbialites, and sulfur rich-microlocations in microbialites MU and CU (**Figure 6**). Alchichica columnar (AC) SEM exploration showed it was the most crystalline-structured microbialite (**Figure 7**), a mineral matrix organized as a regular (honey bee type) network builds this mineral architecture (the main component of this, as explored by the XRD, is aragonite exhibiting pentagonal-hexagonal conducts whose diameter is ∼25–30 μm). Diatoms comprised a relevant feature of the macro-architecture of microbialites including AS, MU and PAI (**Figure 6**). SEM-EDS analysis was useful to identify iron signals in the mineral matrix of AS.

Microbial Community Structure and Diversity

The total number of sequences was 1.42 million (rarefaction was performed to a depth of 10,000 per sample). Sequences clustered in 8,843 total OTUs. Four dominating microbial phyla contributed to the main differences in microbial structure.

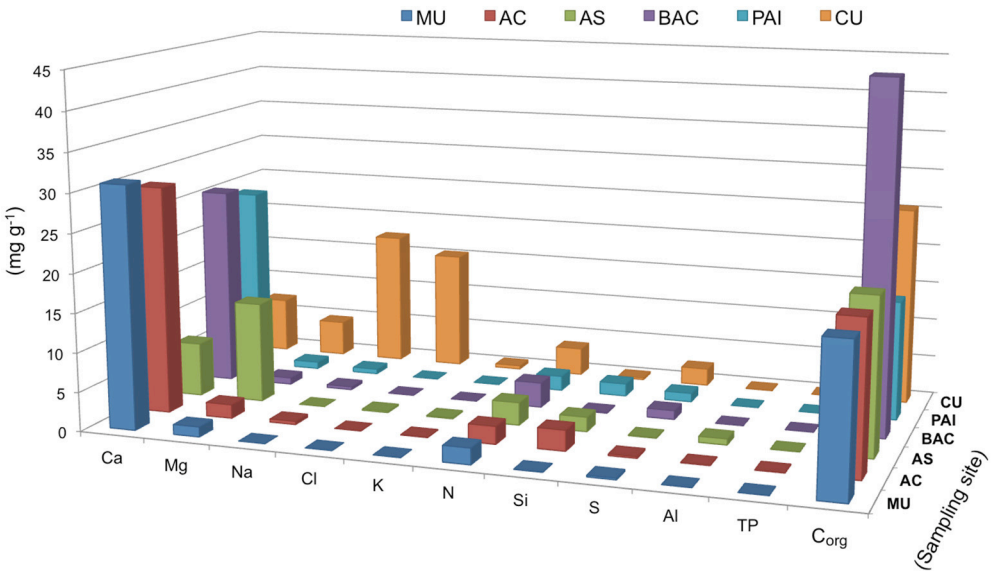

FIGURE 4 | Biogeochemical parameters and major ions in six microbialites studied, bars show concentrations in mg/g of microbialites from. Parameters are organized in the x axis to allow better visualization. PAI (Pozas Azules I, Cuatro Ciénegas Basin); AS and AC (Alchichica crater lake); BAC (Bacalar Lagoon); MU (Muyil Lagoon, Quintana Roo) and CU (Cayo Sabinal, Northern Keys, Cuba).

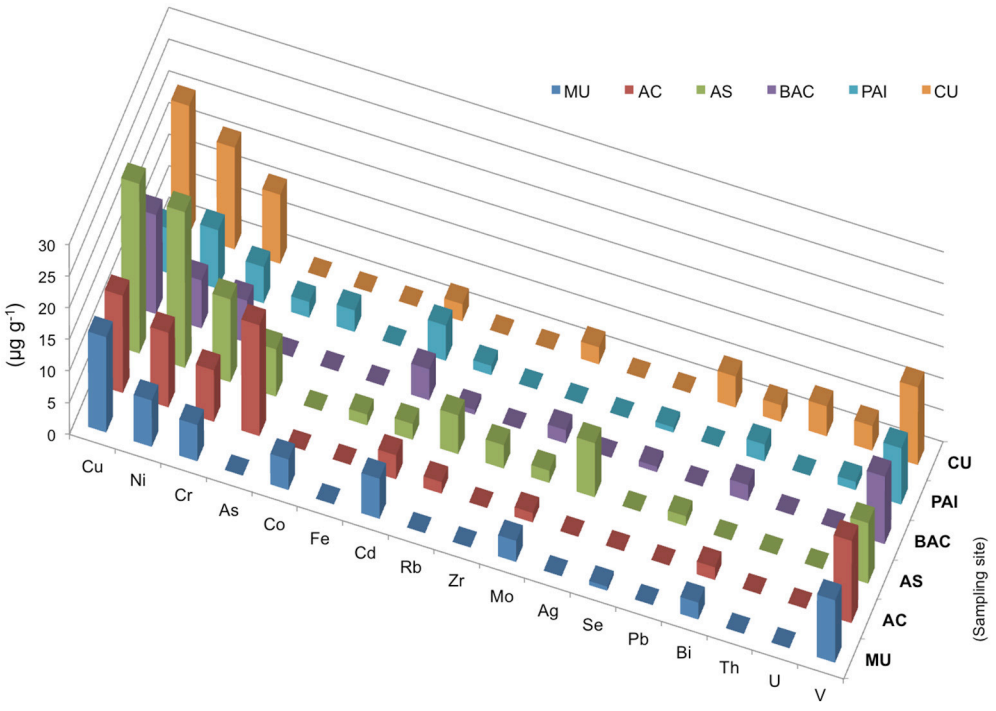

FIGURE 5 | Elemental chemistry (XRF) of microbialites. Bars show concentration in µg/mg of microbialites from PAI (Pozas Azules I, Cuatro Ciénegas Basin); AS and AC (Alchichica crater lake); BAC (Bacalar Lagoon); MU (Muyil Lagoon, Quintana Roo), and CU (Cayo Sabinal, Northern Keys, Cuba).

Cyanobacteria (accounting for 22–70% of abundance in Alchichica and BAC, was more abundant than in the rest of microbialites (in which they accounted for 1.6–2.5%). Proteobacteria, contributing 45–50% of abundance in the low cyanobacterial-microbialites, accounted for 7.8–33% in BAC and Alchichica microbialites (Figure S1). Firmicutes, contributing 25.5–27.6% in MU and PAI accounted for ≤0.5% in the rest of the samples. Bacteroidetes exhibited an overall variation

TABLE 3 | Adonis tests significant correlations between environmental and chemical data and overall microbial community structure (unifrac distance).

Parameter	Adonis (R^2)
Category	0.3539
Cd	0.3320
N	0.3136
Geography	0.3043
Co	0.3764
Cr	0.2896
C_{org}:Ca	0.2835
Cu	0.2804
N:Ca	0.2655
Ca:Mg	0.2627
Pyrite	0.2469
Calcite	0.2457
P_{XRF}	0.2446
Ni	0.2380
C_{org}	0.2257
C_{org}:S	0.2251
N:Mg	0.1953
C_{org}:Mg	0.1851

Significant (adonis $p < 0.05$) are shown in red while results corresponding to (adonis $> 0.05 < 0.1$ are shown in blue color). Non-significant relationships ($p > 0.05$) with $R^2 > 0.1851$ are colorless. Geography groups are karst inland, coastal and soda systems, and Category is an indication of beta diversity clustering.

from 3.2 to 19.6% throughout the samples. Cyanobacteria and Deltaproteobacteria distribution are shown as examples of OTU distribution among microbialites. Although Alchichica lake morphotypes share a number of cyanobacterial phylotypes, at OTU level, most of Cyanobacteria are unique for each system (Figure S1), actually only four phylotypes are shared among the five microbialite types: OTUs 818188, 164038, and 763271 (Pseudanabaenaceae) and 208315 (Phormidiaceae). A deeper taxonomic exploration of these phylotypes can be consulted in Supplementary Material (Figure S2).

Mantel tests showed that β-diversity was positively correlated with category, geography, nitrogen and cadmium ($r = 0.632$, $p = 0.05$).

Minerals, Major Ions and Microbes

Overall, differences in community structure were related to C_{org}:Ca ratio (**Table 3**, Table S1), although stoichiometrical ratios N:Ca and Ca:Mg exhibited also high correlation with community structure (high adonis scores) (**Table 3**, Tables S2, S4). Microbial correlations with these parameters will be discussed below. Spearman test revealed that at OTU level, a number of Bacteroidetes showed positive correlation coefficients (mostly from Flavobacteriia, Cytophagia), as well as some Rhodobacterales and Burkholderiales (Alpha and Betaproteobacteria) and Pseudanabaenales (Cyanobacteria) OTUs. A number of OTUs related to these previous groups showed also strong (inverse) correlations with Ca:Mg this was supported by a high adonis R^2 correlation (**Table 3**). Among

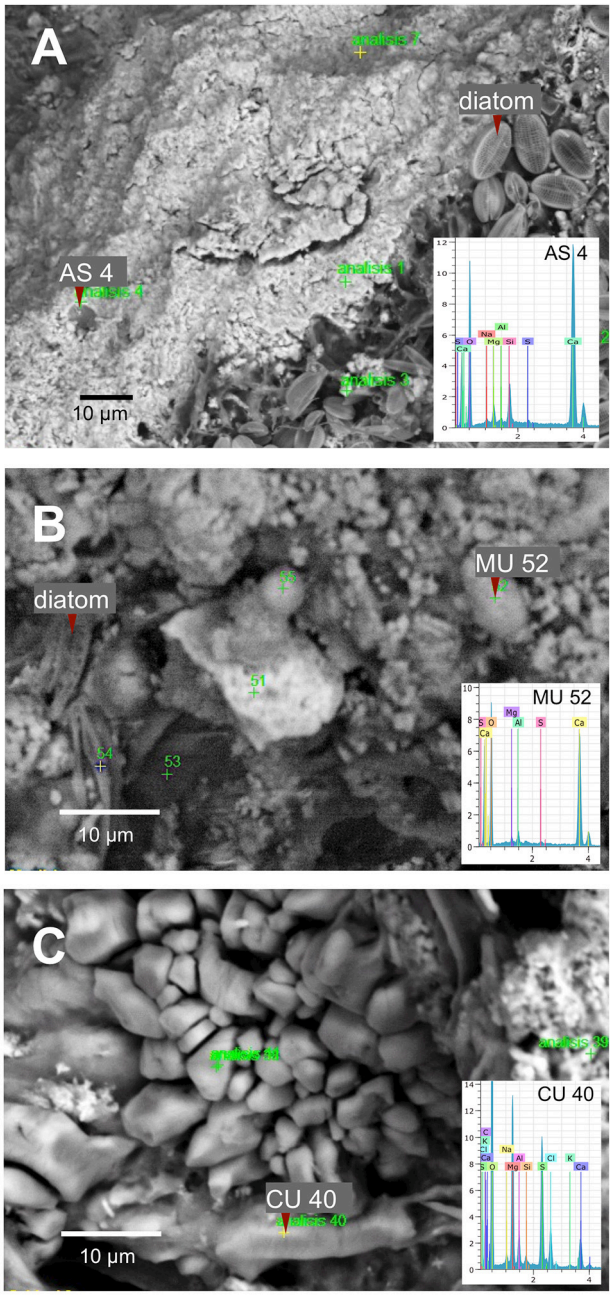

FIGURE 6 | SEM-EDS spectromicroscopy exploration of microbialite surface microstructure of **(A)** AS (Alchichica spongy), **(B)** MU (Muyil), and **(C)** CU (Sabinal).

these, Alphaproteobacteria showed a significant correlation with Ca:Mg ratio, Spearman test revealed that OTUS comprised in families Sphingomonadaceae and Rhodobacteraceae exhibited significant, inverse rho > 0.90, $p < 0.02$, Table S2). Besides their correlation to C_{org}:Ca ratio, N:Ca ratio was significantly correlated to Bacteroidetes (mostly Cytophagales and Saprospirales, Alpha and Betaproteobacteria (at OTU level, Table S4). Significant correlations with mineral content

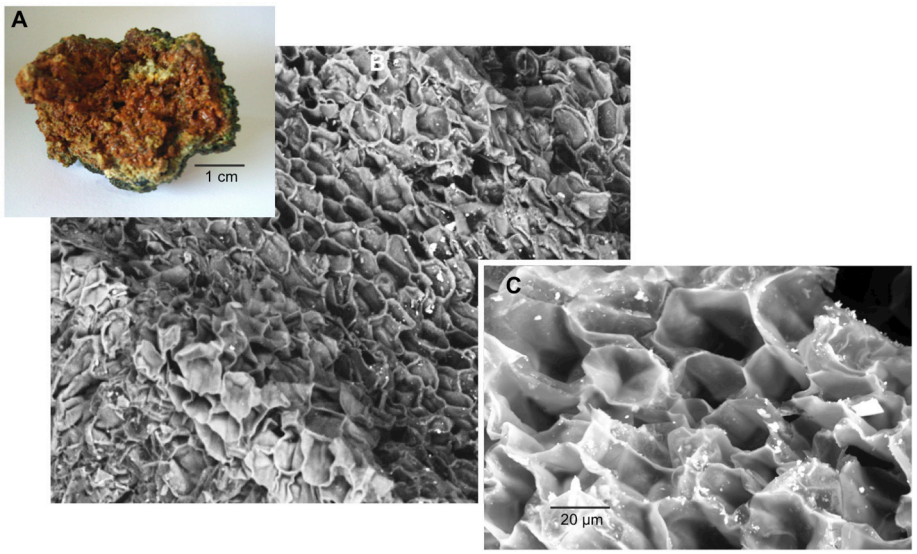

FIGURE 7 | AC (Alchichica columnar) microbialite **(A)** cross section, SEM observation **(B)** 200X and **(C)** 1,000X, aragonite honey-comb shaped microstructure.

(adonis $R^2 < 0.24$, **Table 3**) were found in Oscillatoriales (Cyanobacteria), Xanthomonadales (Gammaproteobacteria), and Betaproteobacteria, groups that overall showed a significant correlation with pyrite. Planctomycetes was correlated with calcite and with ratios C_{org}:Mg and N:Mg, in particular through OTUs assigned to the Pirellulaceae family (Table S3). The Spearman test over Oceanospirillales (Gammaproteobacteria), particularly *Halomonas* OTUs showed significant (positive rho > 0.80, $p < 0.04$) relationship.

Specific OTU Correlations With Microbialite N Content

Overall microbial distribution showed a significant correlation with N (adonis $R^2 = 0.31358$, $p < 0.05$) (**Table 3**). **Figure 9** shows individual OTUs who exhibited a specific significant correlation to microbialite N content (cutoff: Spearman rho > 0.08, $p < 0.05$; OTUs shared in at least three of the six systems, named here N*OTUs). The identity of these N*OTUs was comprised into seven bacterial groups: Cyanobacteria, Proteobacteria (Alpha and Gamma), Bacteroidetes, Firmicutes, Actinobacteria, Chloroflexi, and Fusobacteria; the distribution was heterogeneous among systems (**Figure 9**). The abundance of these bacterial OTUs among the systems is shown in **Figure 9**. Relevant OTUs among the filtered 15 OTUs are *Pseudanabaena* (241071) and Gammaproteobacteria, Pasteurellaceae (823745), Deltaproteobacteria, Myxococcales (873518), Bacteroidetes, *Flavobacterium* (1117222), Firmicutes: Staphylococcus (1084865), *Anaerococcus* (495084). At genus level, five of the most prevalent N*OTUs were the Clostridiales genus *Anaerococcus* (Firmicutes) and the Bacillales *Staphylococcus* and OTU 823745 (Pasteurellaceae family, Gammaproteobacteria). Two more N*OTUs were the genera *Pseudanabaena* (Cyanobacteria) and OTU 1088120 from the Sphingobacteriaceae family (Bacteroidetes, Sphingobacteriales).

DISCUSSION

Specific Relationships Among Major Ions, Minerals and Geography

The concentration of major cations including Na^+, Ca^{+2}, and K^+ in the water environment provided a good approximation to their content in the microbialites where a higher concentration in water corresponded to higher Na^+, Ca^{+2}, and K^+ in the microbialite, although Mg^{+2} showed a more complex pattern (see **Table 1** and **Figure 4**), being overall higher in Alchichica AS microbialite. Our results, in general, agree with those of Müller et al. (1972) who concluded that aquatic system's Mg:Ca drives the carbonate-type formation (higher Mg:Ca ratios result on the formation of high Mg carbonates, such as hydromagnesite, and aragonite compared to low Mg calcite that forms in environmental lower Mg:Ca ratio). Intriguingly, the two microbialite morphotypes of lake Alchichica (Mg:Ca = 39) have a different mineral composition, dominated by hydromagnesite in AS and by aragonite in AC (**Figures 2**, **7**). Since both minerals are considered primary (non-diagenetic) carbonates, we hypothesize that different particularities may be contributing to this result: i.e., (1) cation exchange among minerals (see Putnis, 2002), (2) both microbialites may have significantly different microbial communities resulting in different physiology, (3) a physicochemical process modifying the thermodynamics of mineral formation (e.g., a Mg^{+2} or Ca^{+2} local source different than the rest of the lake) or the influence of a particular physicochemical process (e.g., high energy input through waves) since AC microbialites are segregated to the area of the lake were wave-breaking occurs (see location of AS and AC in Valdespino-Castillo et al., 2014).

Besides Alchichica's microbialites, CU exhibited a relatively high content of Mg. The influence of ocean water (rich in Mg^{+2} and SO_4^{-2}), may be certainly contributing to this result. Among

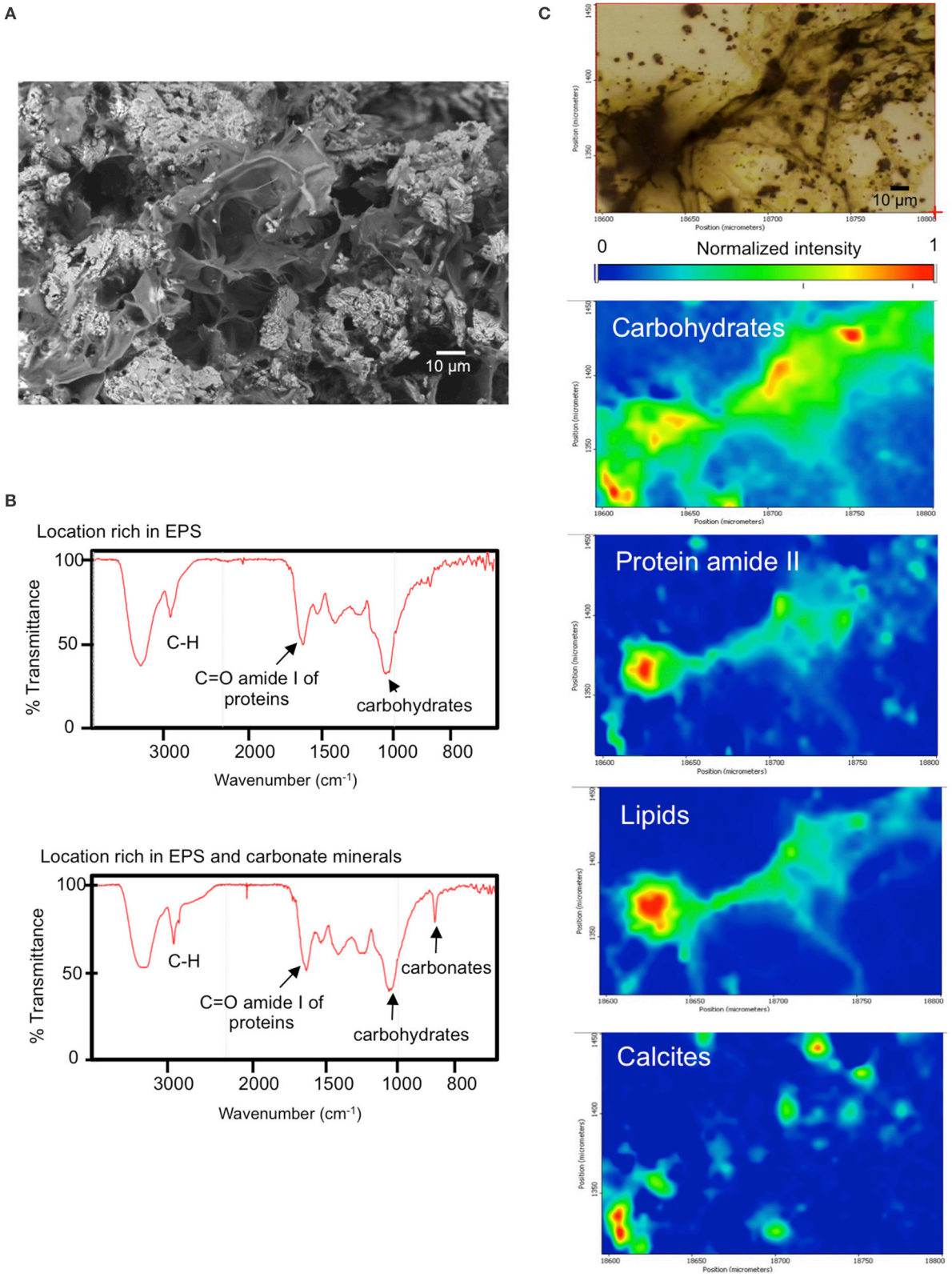

FIGURE 8 | (A) BAC (Bacalar microbialite) mineral inclusions and embedding organic matter (top, scanning electron micrograph), **(B)** SR-FTIR spectra of surface locations rich in EPS and EPS plus minerals of fresh BAC microbialite, **(C)** SR-FTIR spectromicroscopy images (200 μm by 150 μm) showing the distribution of microbes and minerals in a living BAC microbialite. Distribution heat maps of the protein amide II vibration modes at ~1,542 cm^{-1}, the carbohydrates vibration modes at ~1,000 cm^{-1}, calcite at ~870 cm^{-1}, and lipid is base on the CH vibration modes near 2,900 cm^{-1}. Scale bars: 10 μm. Transmittance is given in % units.

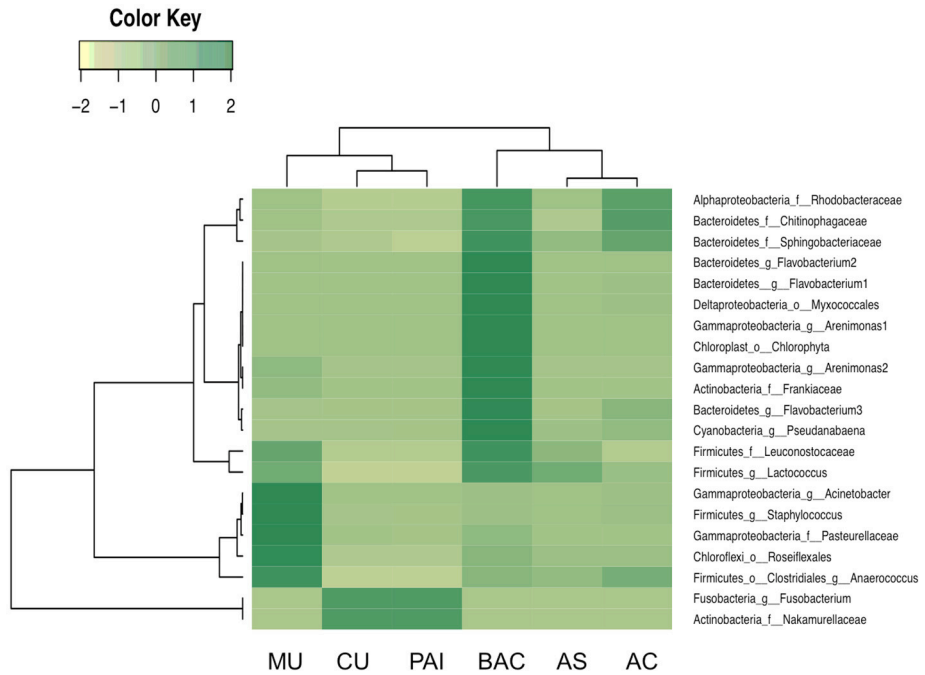

FIGURE 9 | Distribution of N*OTUs, phylotypes who exhibited specific significant correlation to microbialite N content (cutoff: Spearman rho > 0.08, $p < 0.05$; shared in at least three of the six systems).

microbialites, CU (rich in Mg and NaCl) had the highest content of sulfur and one of the lowest of Ca (**Figure 4**). CU was the only microbialite containing gypsum ($CaSO_4{\cdot}2H_2O$, hydrous calcium sulfate) and hexahidrite ($MgSO_4{\cdot}6H_2O$, hydrous magnesium sulfate), the last, a mineral that has been detected in the sediments of Mars (Vaniman et al., 2004). Hydrated sulfates (i.e., bloedite, epsomite, and gypsum) have been also found in Guerrero Negro, Mexico (associated to biofilms related to gypsum precipitations; Vogel et al., 2009) and in biolaminated crusts (microbialites) living in modern magnesium sulfate lakes (Del Buey et al., 2016); here, most hydrated sulfates were associated with microbial activity since geochemical modeling was able to explain only the presence of mirabilite (Cabestrero et al., 2016). Mineral forms of the $MgSO_4$.nH2O series have many hydration states; these are salts that retain a higher content of water than other cation's salts formed in extreme temperature and pressure conditions. Further studies are needed to explore if this feature may be related to life potential in extreme environments.

Besides Mg, the segregation of other elements is affected by mineral formation because carbonates are seldom pure and aragonite minerals show preferential substitution with large cations such as Sr (Milliman et al., 2012). Alchichica's microbialite morphotypes are a good example, our results showed a Sr content close to three times higher in morphotype AC compared to AS.

S and Si content in the microbialites were explained in general by the geography of the aquatic systems, which influences the microbialite geochemistry in agreement with Chagas et al. (2016), where water Si concentration and salinity exhibited strong relationships with mineral type. Si content was higher in the inland systems (microbialites AS, AC, and PAI), which have volcanic basements, than in the coastal karstic environments, various studies actually use Si as a useful tracer for ground water in karstic systems (Smith et al., 1999; Hernández-Terrones et al., 2011). Microbialite sulfur content followed the distribution of SO_4^{-2} in the water (**Table 1**). The lowest sulfur content corresponded to microbialites from lake Alchichica and MU. Sulfur concentration (higher in the systems in proximity with marine water, such as CU) was interestingly relatively high in PAI (an inland location). It is interesting that in lithifying marine mats (i.e., in Shark Bay marine water), sulfur content is not among the most abundant elements (calcium, sodium, magnesium and potassium; Wong et al., 2015) suggesting that even in high sulfur cycling systems, sulfur is not highly accumulated; their accumulation was therefore more related to hydrated sulfates (as discussed above).

Minerals Contributing to Microbialite Microstructure Preservation

No evident signals of diagenetic recrystallization were found for carbonates since most of the mineral composition among microbialites corresponds to primary minerals (as explained in the Results section), from recent (living) surface microbialite subsections. Silicon components of microbialites may have their origin in pre-existing substrates or from erosion processes; they were particularly abundant within BAC microbialite mineralogy (**Figure 2**) but were found in association with organic compounds also in PAI, MU and CU microbialites (**Figure 3**).

In the complex structure of surface microbialites, diatoms and some cyanobacteria (such as filamentous morphotypes) may structure cavities (crypts) that contribute to microenvironment

architecture but overall, to a complex depositional environment, which includes trapped particles or shells (in the range of tens of micrometers). The growth of a microbialite, incorporating geochemical as well as biologically induced (or influenced) precipitation, requires a continual influx of ambient water into the microenvironment to provide adequate ions for mineral growth (Webb and Kamber, 2011). The surface crypts allow the formation of micro-niches (with different oxygen, light and nutrient availability) favorable for the settlement and development of average size bacteria (∼2 μm); it is in these micro-sites where diverse metabolic processes mediate or influence mineral precipitations (see physicochemical models in Riding, 1991, 2000; Reid et al., 2000; Dupraz and Visscher, 2005; Dupraz et al., 2009; Martinez et al., 2016). Additionally, polymeric biogenic silica has been shown to act as a buffer for carbonic anhydrase in diatoms conducting the CO_2 system to carbonates in the surface of diatoms (Milligan and Morel, 2002). SR-FTIRs analyses showed silicate signatures in the microbialites of PAI, MU, and BAC. In each case, signatures of heterocyclic H-bonded and CH of organic compounds bonded to layer silicates were evidenced (**Figure 3**, **Table 2**). Silicification of microbes has been studied in mats of Lake Bogoria, described as a mechanism that involves impregnation of organic biomass by amorphous silica (and silica spheroids), which contributes to the microbial microstructure preservation (Renaut et al., 1998).

Organic Carbon Content, Potential for Oxygenic Phototrophy and Sulfate-Reduction

BAC was the microbialite with the highest content of C_{org}. Relative to the rest of microbialites, BAC showed also the highest Se content and the second highest in N and S content. Although kaolinite ($Al_2Si_2O_5(OH)_4$) and plagioclase ($CaAl_2Si_2O_8$) were minerals only present in BAC, the microbialite chemistry provides no evidence of a significant accumulation of Al or Si (from detritic minerals), suggesting a higher dynamics of these elements through biotic compartments or erosive processes affecting microbialites. SEM shows BAC posses a "low" horizontally layered macrostructure compared to other microbialites. BAC phylotypes are mostly unique and the cyanobacterial community is large among microbialites (see Figure S1).

CU has the second largest C_{org} content. The abundance of sodium chloride and magnesium sulfate in a hypersaline environment (such as CU) suggests that microbes present there may be specialized to hypersaline conditions, and while halophilic archaea abundance was low, other microbial groups such as Acidobacteria distinguish CU microbial community from the rest of the microbialites studied (details are described below). All microbialite C:N, C:P, and N:P ratios were higher than Redfield ratios suggesting N and P limitation, a condition that is consistent with low nutrient concentration reported for the systems studied (Centeno et al., 2012).

Planctomycetes, particularly OTUs from Pirellulaceae family were correlated to C_{org}:Mg and N:Mg ratios (Table S3). Planctomycetes are generally aerobic chemo-organoheterotrophs with complex membrane systems; their compartmentalization allows different electrochemical ion gradients linked to anammox efficiency and ATP synthesis. Their relationship with Mg may be related to the presence of volutin (or metachromatic granules) rich in phosphorus, magnesium, potassium and calcium (van Niftrik et al., 2004). Anammox microbes have the potential to assimilate ammonium without the addition of organic carbon (van Niftrik et al., 2004), therefore, Planctomycetes has been correlated to low C_{org} content and increasing C:N in soils (Hermans et al., 2017). Their direct Spearman correlations with C_{org}:Mg and N:Mg in microbialites suggest the relationship of this group to low C_{org} and N sources.

Alphaproteobacterial phylotypes showed interesting relationships with major cations content. Particularly significant (and inverse) Spearman coefficients with Ca:Mg ratio found in Sphingomonadaceae and Rhodobacteraceae (Table S2), as well as an inverse correlation of OTUs to N:Ca ratio for most alphaproteobacterial families (Table S4) revealing a particular sensitivity to the proportion of these cations. Although this relationship needs further clarification; these strong correlations with major cations may suggest the relevant role of Mg in metabolic pathways (as relevant as the synthesis of bacteriochlorophyll; Boldareva-Nuianzina et al., 2013). The contrasting N:Ca correlation of OTUs, mostly positive for Bacteroidetes but negative for Proteobacteria (Table S4), may be an indication of profound differences between these groups such as in reproductive strategies, resource utilization (Taylor et al., 2013), diazotrophic potential (Alcántara-Hernández et al., 2017) and overall niche specialization. Actually, in some cases, synergistic associations have been proposed for these microbes (particularly between Flavobacterales and Rhodobacterales in phytoplankton blooms; Buchan et al., 2014).

Halomonas (Oceanospirillales, Gammaproteobacteria), correlated to Ca:Mg ratio, has been described as a moderately halophilic bacterial genus, mostly marine but also found in soda systems (see Valenzuela-Encinas et al., 2009) and considered part of the beneficial microbes in holobionts such as coral because of their sulfur metabolism (catabolism of dimethylsulfoniopropionate) that potentially generates sulfur-based antimicrobial compounds (Peixoto et al., 2017). Our results suggest a relationship of the halophilic condition of these bacteria, but if these bacteria mediate or bioinduce carbonates (e.g., in corals), will need further exploration.

Both oxygenic and anoxygenic photosynthetic OTUs found, indicated a broad potential for phototrophic metabolisms across the microbialite samples (Figure S1). Cyanobacteria (oxygenic photosynthetic), purple non-sulfur and purple sulfur bacteria found belong to groups Rhodobacterales, Rhodospirillales; families Acetobacteraceae, Rhodospirillaceae, Bradyrhizobiaceae, Rhodobacteraceae, Rhodobiaceae, Erythrobacteraceae (Alphaproteobacteria); families Rhodocyclaceae and Comamonadaceae (Betaproteobacteria); Chromatiaceae (Gammaproteobacteria) and chlorophototrophic bacteria (Chlorobi, Chloroflexus, and Chloracidobacteria) but no Heliobacteria (Firmicutes). Proteobacteria are dominant autotrophs across microbialite systems (Figure S1), which exhibited specific correlations to major ions (Tables S2, S4).

These correlations probably suggest the marine diversification of this group, since major ions Mg^{+2}, Ca^{+2}, K^{-}, and SO_4^{-2} (and therefore Mg:Ca) of Precambrian seawater exhibited secular variations (Hardie, 1996, 2003). Species from these groups have been described to harbor carbon fixation pathways such as reductive pentose phosphate cycle, reductive citric acid cycle, reductive Acetyl-CoA pathway and 3-hydroxypropionate cycle that are likely to be present (see Canfield et al., 2005). The frequency of transcripts in oxic zones revealed that Cyanobacteria and Proteobacteria are dominant functional participants of thrombolytic mats (Mobberley et al., 2015). Further studies are needed to clarify if rhodopsin-coupled metabolic strategies are present and therefore some organisms may exhibit chlorophyll-independent photosynthetic pathways (see Bryant and Frigaard, 2006).

BAC is the microbialite with the highest content of C_{org} among samples (**Figure 4**). Although Cyanobacteria comprises the most abundant phototrophic composition of BAC microbialite (Figure S1), and are probably dominant in biomass, SEM and FTIR analyses revealed the contribution of EPS chemistry and organic matter bonded to silicates (**Figure 3**) to C_{org}; the high content of carbohydrates to proteins in BAC EPS helped to understand the highest C:N ratio of BAC microbialite (**Figure 8**).

The abundance of potential sulfate reducing deltaproteobacteria (e.g., Desulfobacterales, Desulfovibrionales, Desulfuromonadales, Syntrophobacterales OTUs) accounted for less than 0.01 percent, even in the CU microbialite, abundant in SO_4^{-} and NaCl, compounds required for sulfate reducing bacteria development. Consistent with this, in a metagenomic study of Alchichica's microbialites, sulfate reduction genes were also found to be negligible (Saghaï et al., 2016). Other Deltaproteobacteria such as Myxococcales, Bdellovibrionales, Spirobacillales, PB19, MIZ46 showed higher abundance. These results suggest that despite sulfate reduction has been linked to the precipitation of carbonates in modern stromatolites (Visscher et al., 1998, 2000; Reid et al., 2000; Andres et al., 2006), and to other minerals precipitation *in-vitro* (Wolicka and Borkowski, 2011) their contribution to biomineralization may be rather low in these systems, or other participants may be involved in sulfur metabolism. Acidobacteria abundance may provide a hint in this sense since Chloracidobacteria, more specifically *Chloracidobacterium thermophilum* has been used as a model to understand different pathways of sulfur metabolism including assimilatory and dissimilatory sulfate reduction and oxidation genes (cysteine and methionine metabolisms, KEGG database). The higher abundance of Acidobacteria (Chloracidobacteria Ellin6075) was a relevant feature distinguishing CU from the rest of the microbialites.

Lactic Acid Bacteria (LAB) Potential Contribution to EPS Formation and Heterotrophy (Fermentation)

Discarding unclassified sequences, microbial structures of MU and PAI were considerably similar (Figure S1). Both are located over karstic basement systems and showed higher abundance of Firmicutes groups (Lactobacillales, Clostridiales, and Erysipelotrichales), Gammaproteobacteria (Xanthomonadales, Oceanospirillales) and Bacteroidetes (Bacteroidales and Cytophagales). Their community structure differed clearly from the karstic systems with higher (CU) and lower (BAC) salinity. PAI and MU microbialites share some chemical features such as the highest cobalt and cadmium concentration among samples, relatively low nickel concentration (**Figure 5**) and the indication of organic compounds bonded to layered silicates (**Figure 3**); specific OTU relationships with these parameters needs clarification, although results broadly suggest the sensitivity of microbialite lactic acid bacteria (LAB) to heavy metals. Lactobacilliales have been referenced as exopolysaccharide producing LAB, their highest abundance in microbialites MU and PAI, referred by the presence of e.g., Carnobacteriaceae, genera *Dezemzia* and *Leuconostoc* (heterofermentative metabolism) points to similarities in bacterial metabolic functionality within these systems. LAB exopolysaccharides have been reported to participate in both, biofilm formation or anti-formation (Ruas-Madiedo et al., 2002). Other known LAB bacteria, such as *Bifidobacterium* (Actinobacteria) were present exclusively in these two systems. Roughly, higher fermenter LAB bacteria abundance may be an indication of high heterotrophy; in addition, C_{org} content of PAI and MU were the lowest among microbialites studied. Moreover, Firmicutes and Actinobacteria were the groups that exhibited the highest proportion of the total respiration transcripts recovered in thrombolites (Mobberley et al., 2015), together with Cyanobacteria, Alpha- and Gamma-proteobacteria. The physiological influence of fermenters (and LAB bacteria) in microbialite formation needs further exploration.

Bacterial Phylotypes Related to Nitrogen Patterns

Different studies have shown that nitrogen availability has significant effects on microbial structural assembly (particularly bacteria; see Centeno et al., 2012; Zhao et al., 2012). While Centeno et al. (2012) showed a significant relationship of microbialite community structure and environmental nitrate, our results showed that regardless of the microbialite type (sample location), microbial phylotypes belonging to Gamma and Alphaproteobacteria (Rhodobacterales), Archaea and Acidobacteria show a significant statistical relationship with microbialite N content (**Figure 9**, Table 5S). Elemental C and N correlations with Cyanobacteria and Proteobacteria may be referred to their well-known machineries for (oxygenic) photosynthesis and nitrogen fixation. Interestingly, the groups with the highest correlations with organic carbon show also a high C_{org}:S correlation (Synechococcales, Cyanobacteria, as well as Alpha, Beta, and Gammaproteobacteria) probably because sulfur is an abundant element in the nitrogenase architecture or because cellular sulfur (previously reduced) may be efficiently recycled during protein turnover, contributing to higher C:S ratios (see Cuhel et al., 1984).

Cyanobacterial OTUs in general showed a very heterogeneous distribution among microbialites (Figure S1), but it is

interesting that three Synechococcales OTUs (two assigned to Pseudanabaenaceae) were present in most microbialites (Figure S2). *Pseudanabaena* (OTUs 241071, 225125) were the cyanobacteria that exhibited significant association to N composition (Table S5). Interestingly, *Pseudanabaena* has been observed to exhibit a particular control of nitrogen acquisition compared to other cyanobacteria. *Pseudanabaena* sp. PCC 6903 encodes only one type of glutamine synthetase (GS) type III, different to most cyanobacterial GS (type I). GS plays a major role in fixing ammonium to form glutamine and GS type III is only present in N limited environments (Crespo et al., 1998), such as the ones included in this study. *Pseudanabaena glnN* gene expression and GS type III activity showed upregulation under nitrogen starvation or using nitrate as a nitrogen source. GS catalyzes the synthesis of glutamine from glutamic acid and ammonium in the presence of divalent cations (Mg^{+2} or Mn^{+2}) and using the energy of ATP hydrolysis (Muro-Pastor et al., 2005). Cyanobacterial genera *Leptolyngbya*, *Pseudanabaena*, *Acaryochloris*, and *Microcoleus* were found to be dominant photosynthetic participants of other microbialites (as in Pavilion Lake: Chan et al., 2014; Russell et al., 2014) and in tufa biofilms from karstic waters (*Pseudanabaena* and *Phormidium*: Arp et al., 2001, 2010). An exploration to insight the taxonomic resolution of the shared cyanobacterial OTUs can be consulted in Figure S2.

Other OTUs significantly related to N content comprise genera such as *Flavobacterium* (Bacteroidetes) and *Clostridium* (Firmicutes). *Flavobacterium* is one of the genera that Repert et al. (2014) found to explain differences in N-processing rates (in lake sediments). Furthermore Firmicutes and Bacteroidetes have shown a potential participation in the N cycle, harboring periplasmic pentahaem nitrite reductase (*nrfA*) genes, NADH-dependent nitrite reductase *(nirB*) in Bacilliales and in Bacteroidetes such as *Flavobacterium* (Moir, 2011). Some metalloenzymes such as copper nitrite reductase have been characterized in Flavobacteriales, who also exhibit nitric oxide reductases with homologs in Chitinophagaceae and Staphylococcus (Bacilli) (Moir, 2011).

The role of Cyanobacteria (such as *Pseudanabaena*) and Clostridiales as diazotrophs has been confirmed by the presence of nitrogenase *nifH* and more particularly, Mo-Fe-type nitrogenases in the case of Clostridiales (Moir, 2011). Also clostridial genera have been reported to harbor a NADH-dependent *nirB* type nitrite reductase. Cyanobacterial *nifH* assigned to Nostocales and Oscillatoriales cyanobacteria as well as Alpha and Gammaproteobacteria (from different microbialite locations including Alchichica, Cuatro Ciénegas and Muyil) are described in Beltrán et al. (2012) as well as Clostridiales and Deltaproteobacteria phylotypes (Alcántara-Hernández et al., 2017) in Alchichica microbialites.

The Role of Bioreactive Transition Elements Within Microbialites From Mexico and Cuba

Interestingly, certain transition elements showed significant associations with bacterial taxa (**Table 3**). These are elements accumulated in microbialite precipitations (relative to their water environments), such as Co, Cu, Fe, and Ni, besides Cd and Zn (elements usually included in the transition elements group). Together these results outline a first analytic baseline in the search for the bonds between microbial diversity and the chemical environment. At taxonomic level Order, Alphaproteobacteria seems to be the group with the strongest relationships with the concentrations of transition elements; Alphaproteobacteria showed significant relations with Cd, Co, Cu, Fe, and Ni (following adonis and Spearman tests), statistical results for the whole community are shown in **Table 3**. Previous research following a metagenomic approach has also suggested a series of metabolic adaptations of microbialites to heavy metals (White et al., 2015; Warden et al., 2016).

Copper and Chromium

Cu and Cr correlations with microbial community structure were high (adonis $R^2 > 0.28$; **Table 3**), positive Spearman coefficients indicated a direct relationship with Alphaproteobacterial OTUs (rho > 0.8, $p < 0.05$; Table S6). Comparatively, more OTUs showed statistically significant (Spearman) relationships with Cr than with Cu. Alphaproteobacterial families Sphingomonadacea and Rhodobacteraceae (particularly *Rubellimicrobium* for Cr) grouped the OTUs more strongly and positively correlated to Cr (Table S6). The microbial response to chromium depends on the oxidation state of chromium, since $Cr^{(IV)}$ is highly toxic while $Cr^{(III)}$ is less toxic and bioavailable. Some Proteobacteria, Bacillales, and Clostridiales, aerobic and anaerobic, have chromate reduction abilities, acting as mediators in the reduction process of $Cr^{(VI)}$ to $Cr^{(III)}$, which facilitate biosorption by other organisms and therefore environmental remediation of oxidized chromium pollutants (Tandukar et al., 2009). Trivalent chromium is an essential nutrient involved in glucose utilization, lipid metabolism and possibly in the stabilization of nucleic acids (Huff et al., 1964; Mertz, 1993). Although chromium toxicity is microbe-specific, *Micrococcus, Bacillus, Pseudomona*s strains and other EPS producers exhibit remarkable high tolerance to environmental chromium. A concentration as high as 51–100 mg $Cr^{(VI)}$ / L was reported by Srinath et al. (2002) as the minimal inhibitory concentration (at which growth doesn't occur), but some microbes have been found capable of surviving concentrations of up to 8,000 mg/L (Congeevaram et al., 2007). Chromium concentrations in the microbialites studied are lower ($\leq$13.1 μg/g of the microbialite lithification; in the same order or magnitude if parts per million are considered) than these thresholds, but the microbialite living layer is likely to provide a locally complex (potentially more concentrated, related to their microstructure) chromium microenvironment (i.e., $Cr^{(VI)}$ is present as dichromate in acidic environments or as chromate in alkaline environments).

Copper is an active metal for redox metabolism, it is potentially toxic and apparently carefully regulated by microbes (Prohaska, 2008). Proteobacteria harbor by themselves more than half of the proteins annotated for copper homeostasis (Protein database, NCBI) and more than 80% of the proteins associated with copper resistance. Copper homeostasis genes (e.g., copper homeostasis protein *cutC*, copper transporter *cupA*) have been recently identified in

freshwater microbialites of Lake Pavilion (White et al., 2015). Alphaproteobacteria harbor 10.7 and 40% (respectively) of the total annotated bacterial *cutC* and *cupA* genes (NCBI, gene database).

Cadmium and Cobalt

Cd is a toxic element for organisms (Trevors et al., 1986) and cadmium resistance has been found in Gram-positive and Gram-negative bacteria (Trajanovska et al., 1997). Our results suggest that among metals, Cd and Co may be key elements involved in microbialite microbial composition since these heavy metals showed the strongest correlation with the distribution of different bacterial groups. Cadmium and cobalt were significantly related to the distribution of dominant microbialite organisms such as Alpha, Beta, Deltaproteobacteria, and Cyanobacteria (Oscillatoriales and Synechococcales), Bacteroidetes and Acidobacteria (overall community results are shown in **Table 3** and inverse significant phylotype correlations in Table S8). These bacterial groups lead redox microbialite chemistry and metabolic pathways closely linked to mineral formation (phototrophy and sulfate reduction; see Visscher and Stolz, 2005; Mobberley et al., 2013).

Compared to Spearman Co results, more OTUs were significantly (inversely) correlated to Cd (meaning a higher number of OTUs with higher rho coefficients) strengthening the hypothesis of widespread toxicity by Cd (significant inverse Spearman coefficient). Actually, Co Spearman showed positive and inverse significant relationships with different OTUs, but the strongest correlations were inverse, including OTUs assigned to Cyanobacteria (*Synechococcales)*, Bacteroidetes (Cytophagales and Flavobacteriales), Alphaproteobacteria (Rhodobacterales, Rhizobiales, and Sphingomonadales), Gammaproteobacteria (Pasteurellales, Aeromonadales, and Enterobacteriales), Firmicutes (Lactobacillales and Clostridiales) (Table S7).

Alphaproteobacteria was one of the microbial groups with the highest representation of cobaltochelatase (*cobN* genes) in thrombolites from Australia, together with Cyanobacteria, Gammaproteobacteria, Bacteroidetes and Actinobacteria (Warden et al., 2016). Consistently, in the microbialites studied here, OTUs from these groups, besides Beta- and Delta-proteobacteria showed significant relationships with Co content. Presumably *cobN* is participating in the oxygen dependent synthetic pathway of cobalamin (vitamin B12). Although vitamin B_{12} acts as a coenzyme in a wide spectrum of metabolic pathways, the actual number of known B_{12}-dependent enzymes is relatively small and most organisms require cobalamin in small amounts (Raux et al., 2000). Accordingly, Spearman tests shown direct and inverse relationships within bacterial groups (e.g., Spearman coefficients were positive for many Comamonadacea, Xanthomonadaceae, and Chitinophagaceae OTUs and Beta-, Gamma-proteobacteria and Bacteroidetes families respectively), Cobalt is a relevant regulator of microbial composition among sampled microbialites from Mexico and Cuba. Saito et al. (2003) findings have been useful to explain the Cu and Co toxicity to cyanobacteria, a relevant fact probably because the concentration of metals such as Cu and Co is higher in the present biosphere compared to that of early oceans (Saito et al., 2003), overall in evaporation inland and coastal systems.

There is a broad consensus that the signatures of some transition metals remain in time, and are useful to reconstruct ancient seawater chemistry (see Riding et al., 2014). However, their signature may be disrupted by diagenetic mobilization, fractionation during secondary mineral precipitation (such as hematite and siderite), or contamination with metals derived from exogenous sources (see Petrash et al., 2016).

The concentrations of transition elements in the microbialites reported here are in the range of those reported by Petrash et al. (2016) for ancient stromatolites (chromium was marginally higher in AS and iron was overall lower.) Microbialites of this study show in general higher concentrations of trace elements compared to other microbial carbonates (Kamber and Webb, 2007).

CONCLUSIONS

Our results revealed a high genetic and chemical (elemental and mineral) diversity among microbialites, comprising a gradient of major ions and metallic elements. Besides geography and nitrogen content, cadmium content was significantly correlated to microbial structure in the cross-system microbialite comparison. Micrometric SR-FTIR analysis showed relatively low-N polysaccharides are a major component of the EPS embedding the microbialites' surface layer. Carbonate IR signals spatially converged with nitrogen-rich (protein amide II) and lipid-rich microsites of the microbialite living layer. SR-FTIRs was essential to reveal organic compounds bonded to layer silicates in the mineral matrix, likely contributing to microbialite total organic carbon content. Cyanobacterial phylotypes differed between microbialites. Pseudanabaenaceae with metabolic abilities for life in low N environments comprised most of the cyanobacterial phylotypes shared among microbialites, and some phylotypes were significantly correlated with N content. The abundance and distribution of Synechococcales (Cyanobacteria), Rhodobacterales and Ricketsiales (Alphaproteobacteria), and Burkholderiales (Betaproteobacteria) was correlated with microbialite C_{org} content, C_{org}:Ca and Ca:Mg ratios; the major cations calcium, magnesium and sodium evidently influenced both mineralogy and microbial community composition. Cyanobacteria and Planctomycetes correlated most significantly with mineral content (pyrite, calcite), C_{org}:Mg and N:Mg ratios. Magnesium and calcium contents correlated with the distributions of alphaproteobacterial microbes, particularly those involved in phototrophy and N_2 fixation. Interestingly, the dominant groups of Proteobacteria and Bacteroidetes showed the strongest correlations with trace elements, mainly Cd, Co, Cu, and Ni. These biogeochemical relationships with microbial metabolic capacities and with specific transition elements (metals) are part of the analytical baseline established here to target the search for the bonds between microbial diversity and the geochemistry of microbialites.

AUTHOR CONTRIBUTIONS

PV-C: manuscript design. LF, H-YH, and MM-I: contributed to the drafting of the manuscript. LF, H-YH, MM-I, DC-G, LL-G, TP-P, PH, RG-DZ, and JL: contributed with analyses and expertise. all authors approved the final version. LF, H-YH, and MM-I: obtained funding for this research.

FUNDING

Funding for this project was granted to LF through SEP-CONACyT No. 254962 and PAPIIT-UNAM No. IT202016-3, to MM-I through CFE-GEIC/UNAM-ICML/004-2016 and PAPIIT-UNAM No. IT201314-3, and to H-YH through DOE/BER No. KP1605010. UC MEXUS-CONACYT (University of California Institute for Mexico and the United States-Consejo Nacional de Ciencia y Tecnología) awarded PV-C with a postdoctoral fellowship and funding through grant No. UCMEXUS CN16-111 (LF and H-YH).

ACKNOWLEDGMENTS

We acknowledge F. Sergio Castillo of the Aquatic Biogeochemistry Laboratory (ICMyL, UNAM) for the accomplishment of chemical analyses. Additionally Osiris Gaona provided technical and laboratory assistance. XRF analyses were performed at the Laboratory of Isotopic Geochemistry and Geochronology, ICML, UNAM- U. Mazatlán. We acknowledge M. Reyes-Salas and S. Angeles-García for SEM-EDS microspectroscopy analyses at the Electronic Microscopy and Microanalysis Lab., I. Geology, UNAM; XRD analyses were carried out by TP-P (X-Ray Diffraction Lab., I. Geology, UNAM). Infrared spectromicroscopy was conducted at the Berkeley Synchrotron Infrared Structural Biology (BSISB) imaging program infrared beamlines at the Advanced Light Source under its US Department of Energy contract DE-AC02-05CH11231. Sampling was done under collector permit No. PPF/DGOPA.033/2013 (LF), Cuban samples were collected under the Institutional collaboration agreement UNAM-CIEC 2015 (MM-I and RG-D). We thank Dr. William Holman for editing the manuscript.

SUPPLEMENTARY MATERIAL

The Supplementary Material for this article can be found online at: https://www.frontiersin.org/articles/10.3389/fmicb.2018.00510/full#supplementary-material

REFERENCES

Aines, R. D., and Rossman, G. R. (1984). Water in minerals - a peak in the infrared. *J. Geophys. Res.* 89, 4059–4071. doi: 10.1029/JB089iB06p04059

Alcántara-Hernández, R. J., Valdespino-Castillo, P. M., Centeno, C. M., Alcocer, J., Merino-Ibarra, M., and Falcón, L. I. (2017). Genetic diversity associated with N-cycle pathways in microbialites from Lake Alchichica, Mexico. *Aquat. Microb. Ecol.* 78, 121–133. doi: 10.3354/ame01806

Andres, M. S., Sumner, D. Y., Reid, R. P., and Swart, P. K. (2006). Isotopic fingerprints of microbial respiration in aragonite from Bahamian stromatolites. *Geology* 34, 973–976. doi: 10.1130/G22859A.1

Ankel-Fuchs, D., and Thauer, R. K. (1988). "Nickel in biology: nickel as an essential trace element," in *The Bioinorganic Chemistry Of Nickel*, eds R. Cammack, V. M. Fernandez, K. Schneider, and J. R. Lancaster (New York, NY: VCH Publishers), 93–110.

Armienta, M. A., Vilaclara, G., De la Cruz-Reyna, S., Ramos, S., Ceniceros, N., Cruz, O. et al. (2008). Water chemistry of lakes related to active and inactive Mexican volcanoes. *J. Volcanol. Geotherm. Res.* 178, 249–258. doi: 10.1016/j.jvolgeores.2008.06.019

Arp, G., Bissett, A., Brinkmann, N., Cousin, S., De Beer, D., Friedl, T., et al. (2010). Tufa-forming biofilms of German karstwater streams: microorganisms, exopolymers, hydrochemistry and calcification. *Geol. Soc. Spec. Publ.* 336, 83–118. doi: 10.1144/SP336.6

Arp, G., Wedemeyer, N., and Reitner, J. (2001). Fluvival tufa formation in a hard-water creek (Deinschwanger Bach, Franconian Alb, Germany). *Facies* 44, 1–22. doi: 10.1007/BF02668163

Baelum, J., Borglin, S., Chakraborty, R., Fortney, J. L., Lamendella, R., Mason, O. U. et al. (2012). Deep-sea bacteria enriched by oil and dispersant from the Deepwater Horizon spill. *Environ. Microbiol.* 14, 2405–2416. doi: 10.1111/j.1462-2920.2012.02780.x

Battaglia, B. (1959). Final resolution of the symposium on the classification of brackish waters. *Archo. Oceanogr. Limnol.* 11, 243–248.

Beltrán, Y., Centeno, C. M., García-Oliva, F., Legendre, P., and Falcón, L. I. (2012). N2 fixation rates and associated diversity (nifH) of microbialite and mat-forming consortia from different aquatic environments in Mexico. *Aquat. Microb. Ecol.* 67, 15–24. doi: 10.3354/ame01572

Benning, L. G., Phoenix, V. R., Yee, N., and Tobin, M. J. (2004). Molecular characterization of cyanobacterial silicification using synchrotron infrared micro-spectroscopy. *Geochim. Cosmochim. Ac.* 68, 729–741. doi: 10.1016/S0016-7037(03)00489-7

Bokulich, N. A., Subramanian, S., Faith, J. J., Gevers, D., Gordon, J. I., Knight, R., et al. (2013). Quality-filtering vastly improves diversity estimates from Illumina amplicon sequencing. *Nat. Methods* 10, 57–59. doi: 10.1038/nmeth.2276

Boldareva-Nuianzina, E. N., Bláhová, Z., Sobotka, R., and KoblíŽek, M. (2013). Distribution and origin of oxygen-dependent and oxygen-independent forms of Mg-protoporphyrin monomethylester cyclase among phototrophic proteobacteria. *Appl. Environ. Microbiol.* 79, 2596–2604. doi: 10.1128/AEM.00104-13

Breitbart, M., Hoare, A., Nitti, A., Siefert, J., Haynes, M., Dinsdale, E., et al. (2009). Metagenomic and stable isotopic analyses of modern freshwater microbialites in Cuatro Ciénegas, Mexico. *Environ. Microbiol.* 11, 16–34. doi: 10.1111/j.1462-2920.2008.01725.x

Bryant, D. A., and Frigaard, N. U. (2006). Prokaryotic photosynthesis and phototrophy illuminated. *Trends Microbiol.* 14, 488–496. doi: 10.1016/j.tim.2006.09.001

Buchan, A., LeCleir, G. R., Gulvik, C. A., and González, J. M. (2014). Master recyclers: features and functions of bacteria associated with phytoplankton blooms. *Nat. Rev. Microbiol.* 12, 686–698. doi: 10.1038/nrmicro3326

Butler, A. (1998). Acquisition and utilization of transition metal ions by marine organisms. *Science* 281, 207–209. doi: 10.1126/science.281.5374.207

Caballero, M., Vilaclara, G., Rodríguez, A., and Juárez, D. (2003). Short-term climatic change in lake sediments from lake Alchichica, Oriental, Mexico. *Geofis. Int.* 42, 529–537.

Cabestrero, Ó., Del Buey, P., and Montero, E. S. (2016). Geochemical modeling of the precipitation process in SO4-Mg/Na microbialites. *Macla Rev. Soc. Española Mineral.* 21, 20–21. Available online at: http://www.ehu.eus/sem/macla_pdf/macla21/Macla21_020.pdf

Calabrese, E. J., Canada, A. T., and Sacco, C. (1985). Trace elements and public health. *Annu. Rev. Public Health* 6, 131–146. doi: 10.1146/annurev.pu.06.050185.001023

Canfield, D. E., Kristensen, E., and Thamdrup, B. (2005). Carbon fixation and phototrophy. *Adv. Mar. Biol.* 48, 95–127. doi: 10.1016/S0065-2881(05)48004-9

Caporaso, J. G., Kuczynski, J., Stombaugh, J., Bittinger, K., Bushman, F. D., Costello, E. K., et al. (2010). QIIME allows analysis of high-throughput community sequencing data. *Nat. Methods* 7, 335–336. doi: 10.1038/nmeth.f.303

Caporaso, J. G., Lauber, C. L., Walters, W. A., Berg-Lyons, D., Huntley, J., Fierer, N., et al. (2012). Ultra-high-throughput microbial community analysis on the Illumina HiSeq and MiSeq platforms. *ISME J.* 6, 1621–1624. doi: 10.1038/ismej.2012.8

Cavet, J. S., Borrelly, G. P., and Robinson, N. J. (2003). Zn, Cu and Co in cyanobacteria: selective control of metal availability. *FEMS Microbiol. Rev.* 27, 165–181. doi: 10.1016/S0168-6445(03)00050-0

Centeno, C. M., Legendre, P., Beltrán, Y., Alcántara-Hernández, R. J., Lidström, U. E., Ashby, M. N., et al. (2012). Microbialite genetic diversity and composition relate to environmental variables. *FEMS Microbiol. Ecol.* 82, 724–735. doi: 10.1111/j.1574-6941.2012.01447.x

Cerqueda-García, D., and Falcón, L. I. (2016). Metabolic potential of microbial mats and microbialites: autotrophic capabilities described by an *in silico* stoichiometric approach from shared genomic resources. *J. Bioinf. Comput. Biol.* 14:16500207. doi: 10.1142/S0219720016500207

Chagas, A. A., Webb, G. E., Burne, R. V., and Southam, G. (2016). Modern lacustrine microbialites: towards a synthesis of aqueous and carbonate geochemistry and mineralogy. *Earth Sci. Rev.* 162, 338–363. doi: 10.1016/j.earscirev.2016.09.012

Chan, O. W., Bugler-Lacap, D. C., Biddle, J. F., Lim, D. S. S., McKay, C. P., and Pointing, S. B. (2014). Phylogenetic diversity of a microbialite reef in a cold alkaline freshwater lake. *Can. J. Microbiol.* 6, 391–398. doi: 10.1139/cjm-2014-0024

Coman, C., Chiriac, C. M., Robeson, M. S., Ionescu, C., Dragos, N., Barbu-Tudoran, L., et al. (2015). Structure, mineralogy, and microbial diversity of geothermal spring microbialites associated with a deep oil drilling in Romania. *Front. Microbiol.* 6:253. doi: 10.3389/fmicb.2015.00253

Congeevaram, S., Dhanarani, S., Park, J., Dexilin, M., and Thamaraiselvi, K. (2007). Biosorption of chromium and nickel by heavy metal resistant fungal and bacterial isolates. *J. Hazard. Mater.* 146, 270–277. doi: 10.1016/j.jhazmat.2006.12.017

Crespo, J. L., García-Domínguez, M., and Florencio, F. J. (1998). Nitrogen control of the glnN gene that codes for GS type III, the only glutamine synthetase in the cyanobacterium Pseudanabaena sp. PCC 6903. *Mol. Microbiol.* 30, 1101–1112. doi: 10.1046/j.1365-2958.1998.01143.x

Cuhel, R. L., Ortner, P. B., and Lean, D. R. (1984). Night synthesis of protein by algae. *Limnol. Oceanogr.* 29, 731–744. doi: 10.4319/lo.1984.29.4.0731

Del Buey, P., Cabestrero, Ó., and Montero, E. S. (2016). New insights into the bioinduced precipitation of hydrated sulfates in hypersaline microbialites. *Macla Rev. Soc. Española Mineral.* 21, 25–26. Available online at: http://www.ehu.eus/sem/macla_pdf/macla21/Macla21_025.pdf

Des Marais, D. J. (1995). "The biogeochemistry of hypersaline microbial mats," in *Advances In Microbial Ecology*, ed. J. G. Jones (Boston, MA: Springer), 251–274.

Des Marais, D. J. (2000). When did photosynthesis emerge on Earth? *Science* 289, 1703–1705. doi: 10.1126/science.289.5485.1703

Djomgoue, P., and Njopwouo, D. (2013). FTIR spectroscopy applied for surface clays characterization. *J. Surf. Eng. Mat. Adv. Tech.* 3, 275–282. doi: 10.4236/jsemat.2013.34037

Dubrawski, J. V., Channon, A. L., and Warne, S. S. (1989). Examination of the siderite-magnesite mineral series by fourier-transform infrared-spectroscopy. *Am. Mineral.* 74, 187–190.

Dupraz, C., Reid, R. P., Braissant, O., Decho, A. W., Norman, R. S., and Visscher, P. T. (2009). Processes of carbonate precipitation in modern microbial mats. *Earth Sci. Rev.* 96, 141–162. doi: 10.1016/j.earscirev.2008.10.005

Dupraz, C., and Visscher, P. T. (2005). Microbial lithification in marine stromatolites and hypersaline mats. *Trends Microbiol.* 13, 429–438. doi: 10.1016/j.tim.2005.07.008

Dupraz, C., Visscher, P. T., Baumgartner, L. K., and Reid, R. P. (2004). Microbe–mineral interactions: early carbonate precipitation in a hypersaline lake (Eleuthera Island, Bahamas). *Sedimentology* 51, 745–765. doi: 10.1111/j.1365-3091.2004.00649.x

Edgar, R. C., Haas, B. J., Clemente, J. C., Quince, C., and Knight, R. (2011). UCHIME improves sensitivity and speed of chimera detection. *Bioinformatics* 27, 2194–2200. doi: 10.1093/bioinformatics/btr381

Farmer, V. C. (1975). "The layer silicates," in *The Infrared Spectra of Minerals*, ed V. C. Farmer (London: Mineral Society), 331–363.

Geesey, G. G., Jang, L., Jolley, J. G., Hankins, M. R., Iwaoka, T., and Griffiths, P. R. (1988). Binding of metal ions by extracellular polymers of biofilm bacteria. *Water Sci. Technol.* 20, 161–165.

Gérard, E., Ménez, B., Couradeau, E., Moreira, D., Benzerara, K., Tavera, R., et al. (2013). Specific carbonate–microbe interactions in the modern microbialites of Lake Alchichica (Mexico). *ISME J.* 7, 1997–2009. doi: 10.1038/ismej.2013.81

Giordano, M., Beardall, J., and Raven, J. A. (2005). CO 2 concentrating mechanisms in algae: mechanisms, environmental modulation, and evolution. *Annu. Rev. Plant Biol.* 56, 99–131. doi: 10.1146/annurev.arplant.56.032604.144052

Gischler, E., Gibson, M. A., and Oschmann, W. (2008). Giant holocene freshwater microbialites, Laguna Bacalar, Quintana Roo, Mexico. *Sedimentology* 55, 1293–1309. doi: 10.1111/j.1365-3091.2007.00946.x

Hardie, L. A. (1996). Secular variation in seawater chemistry: an explanation for the coupled secular variation in the mineralogies of marine limestones and potash evaporites over the past 600 my. *Geology* 24, 279–283.

Hardie, L. A. (2003). Secular variations in Precambrian seawater chemistry and the timing of Precambrian aragonite seas and calcite seas. *Geology* 31, 785–788. doi: 10.1130/G19657.1

Hardisty, D. S. (2016). *Intermediate and Vacillating Redox in Ancient Marine Settings and their Biological Implications*. Riverside, CA: University of California.

Hazen, T. C., Dubinsky, E. A., DeSantis, T. Z., Andersen, G. L., Piceno, Y. M., Singh, N., et al. (2010). Deep-sea oil plume enriches indigenous oil-degrading bacteria. *Science* 330, 204–208. doi: 10.1126/science.1195979

Henning, O. (1975). "Cements; The hydrated silicates and aluminates," in *The Infrared Spectra of Minerals*, ed V. C. Farmer (London: Mineral Society), 445–464.

Hermans, S. M., Buckley, H. L., Case, B. S., Curran-Cournane, F., Taylor, M., and Lear, G. (2017). Bacteria as emerging indicators of soil condition. *Appl. Environ. Microbiol.* 83, e02826–e02816. doi: 10.1128/AEM.02826-16

Hernández-Terrones, L., Rebolledo-Vieyra, M., Merino-Ibarra, M., Soto, M., Le-Cossec, A., and Monroy-Ríos, E. (2011). Groundwater pollution in a karstic region (NE Yucatan): baseline nutrient content and flux to coastal ecosystems. *Water. Air. Soil Poll.* 218, 517–528. doi: 10.1007/s11270-010-0664-x

Holman, H. Y. N., Bechtel, H. A., Hao, Z., and Martin, M. C. (2010). Synchrotron IR spectromicroscopy: chemistry of living cells. *Anal. Chem.* 82, 8757–8765. doi: 10.1021/ac100991d

Holman, H. Y. N., Nieman, K., Sorensen, D. L., Miller, C. D., Martin, M. C., Borch, T., et al. (2002). Catalysis of PAH biodegradation by humic acid shown in synchrotron infrared studies. *Environ. Sci. Technol.* 36, 1276–1280. doi: 10.1021/es0157200

Holman, H. Y. N., Perrym, D. L., Martin, M. C., Lamble, G. M., McKinney, W. R., and Hunter-Cevera, J. C. (1999). Real-time characterization of biogeochemical reduction of Cr(VI) on basalt surfaces by SR-FTIR imaging. *Geomicrobiol. J.* 16, 307–324. doi: 10.1080/014904599270569

Holman, H. Y. N., Wozei, E., Lin, Z., Comolli, L. R., Ball, D. A., Borglin, S., et al. (2009). Real-time molecular monitoring of chemical environment in obligate anaerobes during oxygen adaptive response. *Proc. Natl. Acad. Sci. U.S.A.* 106, 12599–12604. doi: 10.1073/pnas.0902070106

Hu, S. M. (1980). Infrared absorption spectra of SiO2 precipitates of various shapes in silicon: calculated and experimental. *J. Appl. Phys.* 51, 5945–5948. doi: 10.1063/1.327512

Huff, J. W., Sastry, K. S., Gordon, M. P., and Wacker, W. E. (1964). The action of metal ions on tobacco mosaic virus ribonucleic acid. *Biochemistry* 3, 501–506. doi: 10.1021/bi00892a006

Johannesson, K. H., Telfeyan, K., Chevis, D. A., Rosenheim, B. E., and Leybourne, M. I. (2014). "Rare earth elements in stromatolites-1. Evidence that modern terrestrial stromatolites fractionate rare earth elements during incorporation

from ambient waters," in *Evolution of Archean Crust and Early Life*, eds Y. Dilek and H. Furnes (Dordrecht: Springer), 385–411.

Jones, G. C., and Jackson, B. (1993). *Infrared Transmission Spectra of Carbonate Minerals*. London: Chapman and Hall.

Kamber, B. S., and Webb, G. E. (2007). Transition metal abundances in microbial carbonate: a pilot study based on *in situ* LA-ICP-MS analysis. *Geobiology* 5, 375–389. doi: 10.1111/j.1472-4669.2007.00129.x

Kamennaya, N. A., Ahn, S., Park, H., Bartal, R., Sasaki, K. A., Holman, H. Y., et al. (2015). Installing extra bicarbonate transporters in the cyanobacterium *Synechocystis* sp. PCC6803 enhances biomass production. *Metab. Eng.* 29, 76–85. doi: 10.1016/j.ymben.2015.03.002

Kaźmierczak, J., Kempe, S., Kremer, B., López-García, P., Moreira, D., and Tavera, R. (2011). Hydrochemistry and microbialites of the alkaline crater lake Alchichica, Mexico. *Facies* 57, 543–570. doi: 10.1007/s10347-010-0255-8

Kronenberg, A. K., and Wolf, G. H. (1990). Fourier-transform infrared-spectroscopy determinations of intragranular water-content in quartz-bearing rocks - implications for hydrolytic weakening in the laboratory and within the earth. *Tectonophysics* 172, 255–271. doi: 10.1016/0040-1951(90)90034-6

Krumbein, W. E. (1983). Stromatolites—the challenge of a term in space and time. *Precambrian Res*. 20, 493–531. doi: 10.1016/0301-9268(83)90087-6

Kuang, X., Shao, J., Chen, A., Luo, S., Peng, L., Wu, G., et al. (2016). Effects of bloom-forming cyanobacterial extracellular polymeric substances on the adsorption of cadmium onto kaolinite: behaviors and possible mechanisms. *SpringerPlus* 5, 542. doi: 10.1186/s40064-016-2191-8

Lagomasino, D., Price, R. M., Herrera-Silveira, J., Miralles-Wilhelm, F., Merediz-Alonso, G., and Gómez-Hernández, Y. (2015). Connecting groundwater and surface water sources in groundwater dependent coastal wetlands and estuaries: sian Ka'an Biosphere Reserve, Quintana Roo, Mexico. *Estuar. Coast*. 38, 1744–1763.

Lane, M. D. (2007). Mid-infrared emission spectroscopy of sulfate and sulfate-bearing minerals. *Am. Mineral.* 92, 1–18. doi: 10.2138/am.2007.2170

Ledin, M. (2000). Accumulation of metals by microorganisms—processes and importance for soil systems. *Earth Sci. Rev.* 51, 1–31. doi: 10.1016/S0012-8252(00)00008-8

Lee, J. G., and Morel, F. M. (1995). Replacement of zinc by cadmium in marine phytoplankton. *Mar. Ecol. Prog. Ser*. 305–309. doi: 10.3354/meps127305

López-Gómez, L. M. R. (2003). *El Contenido de Fosforo en Esqueletos de Corales: Revisión de la Metodología y Evaluación de Patrones en el coral Montastrea Annularis en Arrecifes del Atlantico Mexicano*. [dissertation/master's thesis], Mexico City, Universidad Nacional Autónoma de México.

Magoč, T., and Salzberg, S. L. (2011). FLASH: fast length adjustment of short reads to improve genome assemblies. *Bioinformatics* 27, 2957–2963. doi: 10.1093/bioinformatics/btr507

Martinez, R. E., Weber, S., and Grimm, C. (2016). Effects of freshwater *Synechococcus* sp. cyanobacteria pH buffering on $CaCO_3$ precipitation: implications for CO_2 sequestration. *Appl. Geochem.* 75, 76–89. doi: 10.1016/j.apgeochem.2016.10.017

Mertz, W. (1993). Chromium in human nutrition: a review. *J. Nutr*. 123, 626–633. doi: 10.1093/jn/123.4.626

Micheletti, E., Colica, G., Viti, C., Tamagnini, P., and De Philippis, R. (2008). Selectivity in the heavy metal removal by exopolysaccharide-producing cyanobacteria. *J. Appl. Microbiol.* 105, 88–94. doi: 10.1111/j.1365-2672.2008.03728.x

Milligan, A. J., and Morel, F. M. (2002). A proton buffering role for silica in diatoms. *Science* 297, 1848–1850. doi: 10.1126/science.1074958

Milliman, J., Müller, G., and Förstner, F. (2012). *Recent Sedimentary Carbonates: Part 1 Marine Carbonates*. Berlin, Heidelberg, New York: Springer-Verlag.

Mobberley, J. M., Khodadad, C. L., and Foster, J. S. (2013). Metabolic potential of lithifying cyanobacteria-dominated thrombolitic mats. *Photosynth. Res*. 118, 125–140. doi: 10.1007/s11120-013-9890-6

Mobberley, J. M., Khodadad, C. L. M., Visscher, P. T., Reid, R. P., Hagan, P., and Foster, J. S. (2015). Inner workings of thrombolites: spatial gradients of metabolic activity as revealed by metatranscriptome profiling. *Sci. Rep*. 5:12601. doi: 10.1038/srep12601

Moir, J. W. (2011). "Bacterial nitrogen cycling in the human body. nitrogen cycling in bacteria: molecular analysis," in *Nitrogen Cycling in Bacteria: Molecular Analysis*, ed J. W. Moir (Norfolk: Caister Academic Press), 233.

Morel, F. M. M., and Price, N. M. (2003). The biogeochemical cycles of trace metals in the oceans. *Science* 300, 944–947. doi: 10.1126/science.1083545

Morse, J. W., and Casey, W. H. (1988). Ostwald processes and mineral paragenesis in sediments. *Am. J. Sci*. 288, 537–560. doi: 10.2475/ajs.288.6.537

Müller, C. M., Molinelli, A., Karlowatz, M., Aleksandrov, A., Orlando, T., and Mizaikoff, B. (2011). Infrared attenuated total reflection spectroscopy of quartz and silica micro- and nanoparticulate films. *J. Phys. Chem. C* 116, 37–43. doi: 10.1021/jp205137b

Müller, C. M., Pejcic, B., Esteban, L., Delle Piane, C., Raven, M., and Mizaikoff, B. (2014). Infrared attenuated total reflectance spectroscopy: an innovative strategy for analyzing mineral components in energy relevant systems. *Sci. Rep*. 4:6764. doi: 10.1038/srep06764

Müller, G., Irion, G., and Förstner, U. (1972). Formation and diagenesis of inorganic Ca– Mg carbonates in the lacustrine environment. *Naturwissenschaften* 59, 158–164. doi: 10.1007/BF00637354

Muro-Pastor, M. I., Reyes, J. C., and Florencio, F. J. (2005). Ammonium assimilation in cyanobacteria. *Photosynth. Res*. 83, 135–150. doi: 10.1007/s11120-004-2082-7

Myshrall, K. L., Mobberley, J. M., Green, S. J., Visscher, P. T., Havemann, S. A., Reid, R. P., et al. (2010). Biogeochemical cycling and microbial diversity in the thrombolitic microbialites of Highborne Cay, Bahamas. *Geobiology* 8, 337–354. doi: 10.1111/j.1472-4669.2010.00245.x

Nash, D. B., and Salisbury, J. W. (1991). Infrared reflectance spectra (2.2-15-Mu-M) of plagioclase feldspars. *Geophys. Res. Lett*. 18, 1151–1154. doi: 10.1029/91GL01008

Paul, V. G., Wronkiewicz, D. J., Mormile, M. R., and Foster, J. S. (2016). Mineralogy and microbial diversity of the microbialites in the hypersaline storr's Lake, the bahamas. *Astrobiology* 16, 282–300. doi: 10.1089/ast.2015.1326

Peixoto, R. S., Rosado, P. M., de Assis Leite, D. C., Rosado, A. S., and Bourne, D. G. (2017). Beneficial Microorganisms for Corals (BMC): proposed mechanisms for coral health and resilience. *Front. Microbiol*. 8:341. doi: 10.3389/fmicb.2017.00341

Petrash, D. A., Robbins, L. J., Shapiro, R. S., Mojzsis, S. J., and Konhauser, K. O. (2016). Chemical and textural overprinting of ancient stromatolites: Timing, processes, and implications for their use as paleoenvironmental proxies. *Precambrian Res*. 278, 145–160. doi: 10.1016/j.precamres.2016.03.010

Probst, A. J., Birarda, G., Holman, H. Y. N., DeSantis, T. Z., Wanner, G., Andersen, G. L., et al. (2014). Coupling genetic and chemical microbiome profiling reveals heterogeneity of archaeome and bacteriome in subsurface biofilms that are dominated by the same archaeal species. *PLoS ONE* 9:e99801. doi: 10.1371/journal.pone.0099801

Probst, A. J., Holman, H. Y. N., DeSantis, T. Z., Andersen, G. L., Birarda, G., Bechtel, H. A., et al. (2013). Tackling the minority: sulfate-reducing bacteria in an archaea-dominated subsurface biofilm. *ISME J.* 7, 635–651. doi: 10.1038/ismej.2012.133

Prohaska, J. R. (2008). Role of copper transporters in copper homeostasis. *Am. J. Clin. Nutr.* 88, 826S—829S. doi: 10.1093/ajcn/88.3.826S

Putnis, A. (2002). Mineral replacement reactions: from macroscopic observations to microscopic mechanisms. *Mineral. Mag.* 66, 689–708. doi: 10.1180/0026461026650056

Quigg, A., Finkel, Z. V., Irwin, A. J., Rosenthal, Y., Ho, T. Y., Reinfelder, J. R., et al. (2003). The evolutionary inheritance of elemental stoichiometry in marine phytoplankton. *Nature* 425, 291–294. doi: 10.1038/nature01953

Raux, E., Schubert, H. L., and Warren, M. J. (2000). Biosynthesis of cobalamin (vitamin B12): a bacterial conundrum. *Cell. Mol. Life Sci*. 57, 1880–1893. doi: 10.1007/PL00000670

Reid, R. P., Visscher, P. T., Decho, A. W., Stolz, J. F., Bebout, B. M., Dupraz, C., et al. (2000). The role of microbes in accretion, lamination and early lithification of modern marine stromatolites. *Nature* 406, 989–992. doi: 10.1038/35023158

Renaut, R. W., Jones, B., and Tiercelin, J. J. (1998). Rapid *in situ* silicification of microbes at loburu hot springs, lake bogoria, kenya rift valley. *Sedimentology* 45, 1083–1103. doi: 10.1046/j.1365-3091.1998.00194.x

Repert, D. A., Underwood, J. C., Smith, R. L., and Song, B. (2014). Nitrogen cycling processes and microbial community composition in bed sediments in the Yukon River at Pilot Station. *J. Geophys. Res. Biogeo*. 119, 2328–2344. doi: 10.1002/2014JG002707

Riding, R. (1991). "Classification of microbial carbonates," in *Calcareous algae and Stromatolites*, ed R. Riding (Springer: Science and Business Media), 21–51.

Riding, R. (2000). Microbial carbonates: the geological record of calcified bacterial–algal mats and biofilms. *Sedimentology* 47, 179–214. doi: 10.1046/j.1365-3091.2000.00003.x

Riding, R., Fralick, P., and Liang, L. (2014). Identification of an Archean marine oxygen oasis. *Precambrian Res.* 251, 232–237. doi: 10.1016/j.precamres.2014.06.017

Ritz, M., Vaculikova, L., and Plevova, E. (2010). Identification of clay minerals by infrared spectroscopy and discriminant analysis. *Appl. Spectrosc.* 64, 1379–1387. doi: 10.1366/000370210793561592

Rosen, B. P. (2002). Transport and detoxification systems for transition metals, heavy metals and metalloids in eukaryotic and prokaryotic microbes. *Comp. Biochem. Phys. A* 133, 689–693. doi: 10.1016/S1095-6433(02)00201-5

Ross, S. D. (1975). "Sulphates and other oxy-anions of Group VI," in *The Infrared Spectra of Minerals*, ed V. C. Farmer (London: Mineral Society), 423–444.

Ruas-Madiedo, P., Hugenholtz, J., and Zoon, P. (2002). An overview of the functionality of exopolysaccharides produced by lactic acid bacteria. *Int. Dairy J.* 12, 163–171. doi: 10.1016/S0958-6946(01)00160-1

Russell, J. A., Brady, A. L., Cardman, Z., Slater, G. F., Lim, D. S. S., and Biddle, J. F. (2014). Prokaryote populations of extant microbialites along a depth gradient in Pavilion Lake, British Columbia, Canada. *Geobiology* 12, 250–264. doi: 10.1111/gbi.12082.

Saghaï, A., Zivanovic, Y., Moreira, D., Benzerara, K., Bertolino, P., Ragon, M., et al. (2016). Comparative metagenomics unveils functions and genome features of microbialite-associated communities along a depth gradient. *Environ. Microbiol.* 18, 4990–5004. doi: 10.1111/1462-2920.13456

Saito, M. A., Sigman, D. M., and Morel, F. M. (2003). The bioinorganic chemistry of the ancient ocean: the co-evolution of cyanobacterial metal requirements and biogeochemical cycles at the Archean–Proterozoic boundary?. *Inorg. Chim. Acta* 356, 308–318. doi: 10.1016/S0020-1693(03)00442-0

Schopf, J. W. (2006). Fossil evidence of Archaean life. *Philos. T. Roy. Soc. B* 361, 869–885. doi: 10.1098/rstb.2006.1834

Sforna, M. C., Daye, M., Philippot, P., Somogyi, A., Zuilen, M. A., Medjoubi, K., et al. (2017). Patterns of metal distribution in hypersaline microbialites during early diagenesis: implications for the fossil record. *Geobiology* 15, 259–279. doi: 10.1111/gbi.12218

Silver, S., and Phung, L. T. (2005). A bacterial view of the periodic table: genes and proteins for toxic inorganic ions. *J. Ind. Microbiol. Biot.* 32, 587–605. doi: 10.1007/s10295-005-0019-6

Smith, D. H., and Seshadri, K. S. (1999). Infrared spectra of Mg 2 $Ca(SO_4)_3$, $MgSO_4$, hexagonal $CaSO_4$, and orthorhombic $CaSO_4$. *Spectrochim. Acta A* 55, 795–805. doi: 10.1016/S1386-1425(98)00206-6

Smith, S. V., Camacho Ibar, V., Herrera Silveira, J., Valdés, D., David, L., Merino, M., et al. (1999). "Estimating groundwater flow using multiple conservative tracers," in *Mexican and Central American Coastal Lagoon Systems: Carbon, Nitrogen and Phosphorus Fluxes Regional Workshop, I. I., LOICZ Reports & Studies No. 13*, eds S. V. Smith, J. I. Marshall Crossland, and C. J. Crossland (Texel: LOICZ IPO), 96–105.

Srinath, T., Verma, T., Ramteke, P. W., and Garg, S. K. (2002). Chromium (VI) biosorption and bioaccumulation by chromate resistant bacteria. *Chemosphere* 48, 427–435. doi: 10.1016/S0045-6535(02)00089-9

Tandukar, M., Huber, S. J., Onodera, T., and Pavlostathis, S. G. (2009). Biological chromium (VI) reduction in the cathode of a microbial fuel cell. *Environ. Sci. Technol.* 43, 8159–8165. doi: 10.1021/es9014184

Taylor, M. H., Losch, M., and Bracher, A. (2013). On the drivers of phytoplankton blooms in the Antarctic marginal ice zone: a modeling approach. *J. Geophys. Res. Oceans* 118, 63–75. doi: 10.1029/2012JC008418

Tebo, B. M., and Obraztsova, A. Y. (1998). Sulfate-reducing bacterium grows with Cr (VI), U (VI), Mn(IV), and Fe (III) as electron acceptors. *FEMS Microbiol. Lett.* 162, 193–199. doi: 10.1111/j.1574-6968.1998.tb12998.x

Trajanovska, S., Britz, M. L., and Bhave, M. (1997). Detection of heavy metal ion resistance genes in Gram-positive and Gram-negative bacteria isolated from a lead-contaminated site. *Biodegradation* 8, 113–124. doi: 10.1023/A:1008212614677

Trevors, J. T., Stratton, G. W., and Gadd, G. M. (1986). Cadmium transport, resistance, and toxicity in bacteria, algae, and fungi. *Can. J. Microbiol.* 32, 447–464. doi: 10.1139/m86-085

Valderrama, J. C. (1981). The simultaneous analysis of total nitrogen and total phosphorus in natural waters. *Mar. Chem.* 10, 109–122. doi: 10.1016/0304-4203(81)90027-X

Valdespino-Castillo, P. M., Alcántara-Hernández, R. J., Alcocer, J., Merino-Ibarra, M., Macek, M., and Falcón, L. I. (2014). Alkaline phosphatases in microbialites and bacterioplankton from Alchichica soda lake, Mexico. *FEMS Microbiol. Ecol.* 90, 504–519. doi: 10.1111/1574-6941.12411

Valdespino-Castillo, P. M., Alcántara-Hernández, R. J., Merino-Ibarra, M., Alcocer, J., Macek, M., Moreno-Guillén, O. A., et al. (2017). Phylotype dynamics of bacterial P utilization genes in microbialites and bacterioplankton of a monomictic endorheic lake. *Microb. Ecol.* 73, 296–309. doi: 10.1007/s00248-016-0862-1

Valenzuela-Encinas, C., Neria-González, I., Alcántara-Hernández, R. J., Estrada-Alvarado, I., Dendooven, L., and Marsch, R. (2009). Changes in the bacterial populations of the highly alkaline saline soil of the former lake Texcoco (Mexico) following flooding. *Extremophiles* 13, 609–621. doi: 10.1007/s00792-009-0244-4

Vaniman, D. T., Bish, D. L., Chipera, S. J., Fialips, C. I., Carey, J. W., and Feldman, W. C. (2004). Magnesium sulphate salts and the history of water on Mars. *Nature* 431, 663–665. doi: 10.1038/nature02973

van Niftrik, L. A., Fuerst, J. A., Damsté, J. S. S., Kuenen, J. G., Jetten, M. S., and Strous, M. (2004). The anammoxosome: an intracytoplasmic compartment in anammox bacteria. *FEMS Microbiol. Lett.* 233, 7–13. doi: 10.1016/j.femsle.2004.01.044

Visscher, P. T., Reid, R. P., and Bebout, B. M. (2000). Microscale observations of sulfate reduction: correlation of microbial activity with lithified micritic laminae in modern marine stromatolites. *Geology* 28, 919–922. doi: 10.1130/0091-7613(2000)28<919:MOOSRC>2.0.CO;2

Visscher, P. T., Reid, R. P., Bebout, B. M., Hoeft, S. E., Macintyre, I. G., and Thompson, J. A. (1998). Formation of lithified micritic laminae in modern marine stromatolites (Bahamas): the role of sulfur cycling. *Am. Mineral.* 83, 1482–1493. doi: 10.1007/s12237-014-9892-4

Visscher, P. T., and Stolz, J. F. (2005). Microbial mats as bioreactors: populations, processes, and products. *Palaeogr. Palaeocl.* 219, 87–100. doi: 10.1016/j.palaeo.2004.10.016

Vogel, M. B., Des Marais, D. J., Turk, K. A., Parenteau, M. N., Jahnke, L. L., and Kubo, M. D. (2009). The role of biofilms in the sedimentology of actively forming gypsum deposits at Guerrero Negro, Mexico. *Astrobiology* 9, 875–893. doi: 10.1089/ast.2008.0325

Wang, Q., Garrity, G. M., Tiedje, J. M., and Cole, J. R. (2007). Naive Bayesian classifier for rapid assignment of rRNA sequences into the new bacterial taxonomy. *Appl. Environ. Microb.* 73, 5261–5267. doi: 10.1128/AEM.00062-07

Warden, J. G., Casaburi, G., Omelon, C. R., Bennett, P. C., Breecker, D. O., and Foster, J. S. (2016). Characterization of microbial mat microbiomes in the modern thrombolite ecosystem of Lake Clifton, Western Australia using shotgun metagenomics. *Front. Microbiol.* 7:1064. doi: 10.3389/fmicb.2016.01064

Webb, G. E., and Kamber, B. S. (2000). Rare earth elements in Holocene reefal microbialites: a new shallow seawater proxy. *Geochim. Cosmochim. Ac.* 64, 1557–1565. doi: 10.1016/S0016-7037(99)00400-7

Webb, G. E., and Kamber, B. S. (2011). "Trace element Geochemistry as a tool for interpreting microbialites," in *Earliest Life on Earth: Habitats, Environments and Methods of Detection*, eds S. D. Golding and M. Glikson (Springer), 127–170.

White, R. A. III., Chan, A. M., Gavelis, G. S., Leander, B. S., and Brady, A. L., Slater, G. F., et. al. (2015). Metagenomic analysis suggests modern freshwater microbialites harbor a distinct core microbial community. *Front. Microbiol.* 6:1531. doi: 10.3389/fmicb.2015.01531

White, W. B. (1975). "The carbonate minerals," in *The Infrared Spectra of Minerals*, ed V. C. Farmer (London: Mineral Society), 227–284.

Williams, R. J. P., and Da Silva, J. F. (2000). The distribution of elements in cells. *Coordin. Chem. Rev.* 200, 247–348. doi: 10.1016/S0010-8545(00)00324-6

Wolicka, D., and Borkowski, A. (2011). "Precipitation of $CaCO_3$ under sulphate-reduction conditions," in *Advances in Stromatolite Geobiology*, eds J. Reitner, N. V. Quéric, and G. Arp (Berlin; Heidelberg: Springer), 151–160.

Wong, H. L., Smith, D. L., Visscher, P. T., and Burns, B. P. (2015). Niche differentiation of bacterial communities at a millimeter scale in Shark Bay microbial mats. *Sci. Rep*. 5:15607. doi: 10.1038/srep 15607

Zeyen, N., Daval, D., Lopez-Garcia, P., Moreira, D., Gaillardet, J., and Benzerara, K. (2017). Geochemical conditions allowing the formation of modern lacustrine microbialites. *Procedia Earth Planet. Sci.* 17, 380–383. doi: 10.1016/j.proeps.2016.12.096

Zhao, D., Huang, R., Zeng, J., Yan, W., Wang, J., Ma, T., et al. (2012). Diversity analysis of bacterial community compositions in sediments of urban lakes by terminal restriction fragment length polymorphism (T-RFLP). *World J. Microb. Biot*. 28, 3159–3170. doi: 10.1007/s11274-012-1126-y

Conflict of Interest Statement: The authors declare that the research was conducted in the absence of any commercial or financial relationships that could be construed as a potential conflict of interest.

frontiers in Microbiology

ORIGINAL RESEARCH
published: 17 May 2018
doi: 10.3389/fmicb.2018.00998

Symbiodinium-Induced Formation of Microbialites: Mechanistic Insights From *in Vitro* Experiments and the Prospect of Its Occurrence in Nature

Jörg C. Frommlet[1†], Daniel Wangpraseurt[2,3†], Maria L. Sousa[1‡], Bárbara Guimarães[1‡], Mariana Medeiros da Silva[4], Michael Kühl[2,5] and João Serôdio[1]*

[1] Department of Biology and Centre for Environmental and Marine Studies (CESAM), University of Aveiro, Aveiro, Portugal, [2] Marine Biological Section, Department of Biology, University of Copenhagen, Helsingør, Denmark, [3] Department of Chemistry, University of Cambridge, Cambridge, United Kingdom, [4] Coral Reef and Global Changes Research Group (RECOR), Department of Oceanography, Institute of Geosciences, Federal University of Bahia (UFBA), Salvador, Brazil, [5] Climate Change Cluster, University of Technology Sydney, Sydney, NSW, Australia

OPEN ACCESS

Edited by:
Christophe Dupraz,
Stockholm University, Sweden

Reviewed by:
Dirk De Beer,
Max-Planck-Gesellschaft (MPG), Germany
Ilana Kolodkin-Gal,
Weizmann Institute of Science, Israel

***Correspondence:**
Jörg C. Frommlet
jfrommlet@ua.pt

[†] These authors have contributed equally to this work.

[‡]Present Address:
Maria L. Sousa,
Interdisciplinary Centre of Marine and Environmental Research, Faculty of Sciences, University of Porto, Porto, Portugal
Bárbara Guimarães,
Xanthella Ltd., Oban, United Kingdom

Specialty section:
This article was submitted to Aquatic Microbiology, a section of the journal Frontiers in Microbiology

Received: 01 December 2017
Accepted: 27 April 2018
Published: 17 May 2018

Citation:
Frommlet JC, Wangpraseurt D, Sousa ML, Guimarães B, Medeiros da Silva M, Kühl M and Serôdio J (2018) Symbiodinium-Induced Formation of Microbialites: Mechanistic Insights From in Vitro Experiments and the Prospect of Its Occurrence in Nature. Front. Microbiol. 9:998. doi: 10.3389/fmicb.2018.00998

Dinoflagellates in the genus *Symbiodinium* exhibit a variety of life styles, ranging from mutualistic endosymbioses with animal and protist hosts to free-living life styles. In culture, *Symbiodinium* spp. and naturally associated bacteria are known to form calcifying biofilms that produce so-called symbiolites, i.e., aragonitic microbialites that incorporate *Symbiodinium* as endolithic cells. In this study, we investigated (i) how algal growth and the combined physiological activity of these bacterial-algal associations affect the physicochemical macroenvironment in culture and the microenvironment within bacterial-algal biofilms, and (ii) how these interactions induce the formation of symbiolites. In batch culture, calcification typically commenced when *Symbiodinium* spp. growth approached stationary phase and when photosynthetic activity and its influence on pH and the carbonate system of the culture medium had already subsided, indicating that symbiolite formation is not simply a function of photosynthetic activity in the bulk medium. Physical disturbance of bacteria-algal biofilms, via repeated detaching and dispersing of the developing biofilm, generally impeded symbiolite formation, suggesting that the structural integrity of biofilms plays an important role in generating conditions conducive to calcification. Microsensor measurements of pH and O_2 revealed a biofilm microenvironment characterized by high photosynthetic rates and by dynamic changes in photosynthesis and respiration with light intensity and culture age. Ca^{2+} microsensor measurements confirmed the significance of the biofilm microenvironment in inducing calcification, as photosynthesis within the biofilm induced calcification without the influence of batch culture medium and under environmentally relevant flow conditions. Furthermore, first quantitative data on calcification from 26 calcifying cultures enabled a first broad comparison of *Symbiodinium*-induced bacterial-algal calcification with other calcification processes. Our findings support the idea that symbiolite formation is a typical, photosynthesis-induced, bacterial-algal calcification process that is likely to occur under natural conditions.

Keywords: *Symbiodinium*, coral endosymbiont, free-living life style, bacterial-algal calcification, photosynthesis-induced calcification, microbialite, endolithic algae

INTRODUCTION

Dinoflagellates in the genus *Symbiodinium* are important primary producers that engage in trophic endosymbioses with corals and various other animal, and protist hosts (Trench, 1993; Stat et al., 2006). These mutualistic symbioses are of critical importance for tropical coral reef ecosystems, where symbiotic *Symbiodinium* spp., also known as zooxanthellae, provide their hosts with photosynthates in exchange for inorganic nutrients (e.g., Yellowlees et al., 2008). In doing so, they contribute significantly to the coral reef food web (reviewed in Silveira et al., 2017) and they enhance coral calcification (reviewed in Tambutté et al., 2011), demonstrating that *Symbiodinium* spp. both lay the trophic foundation of coral reef ecosystems and play an important role in the formation of the physical reef structure.

Members of the *Symbiodinium* genus, despite their distinctive endosymbiotic life histories, also exhibit temporarily, and probably also exclusively free-living life styles (e.g., Coffroth et al., 2006; Thornhill et al., 2017). The existence of temporarily free-living *Symbiodinium* populations has long been inferred, as the majority of coral species rely on symbiont acquisition from the environment (reviewed in Baird et al., 2009). Besides, the numerous symbiotic strains that were brought into culture over the years demonstrate that at least certain *Symbiodinium* phylotypes do not rely on their hosts as obligate partners (e.g., Schoenberg and Trench, 1980; Trench, 1981; Santos et al., 2001). Field-based studies repeatedly discovered and characterized free-living *Symbiodinium* communities in planktonic, epiphytic, and benthic habitats (e.g., Koike et al., 2007; Venera-Ponton et al., 2010; Granados-Cifuentes et al., 2015). Especially reef sediments appear to be hotspots for the occurrence of free-living *Symbiodinium* spp. (e.g., Littman et al., 2008; Takabayashi et al., 2012; Yamashita and Koike, 2013), and experimental data suggest that reef sediments play an important role as recruitment reservoir for the establishment of host-symbiont associations (Adams et al., 2009; Nitschke et al., 2016). Moreover, environmental *Symbiodinium* populations are increasingly being recognized for their potential to influence the resilience of coral reef ecosystems to stress and their adaptability to environmental change and yet, the life histories of free-living *Symbiodinium* spp. and their ecological niche(s) in the environment remain practically unexplored (Pochon et al., 2014; Boulotte et al., 2016; Suggett et al., 2017; Thornhill et al., 2017).

Sediment-associated *Symbiodinium* populations are presumed to behave much like *Symbiodinium* in culture: diurnally switching between nonmotile and motile stages (Manning and Gates, 2008). A first indication that benthic *Symbiodinium* life histories could be more complex was recently provided by the discovery that a diverse range of cultured *Symbiodinium* strains and their inherent bacterial communities commonly form calcifying bacterial-algal communities (Frommlet et al., 2015a,b). Jointly, these novel calcifying associations produce aragonitic microbialites, termed symbiolites, which encase adjacent *Symbiodinium* as endolithic cells. Symbiolite formation is an autoendolithic process because cells become endolithic as a result of mineral precipitation (Marlow et al., 2015). In the course of symbiolite formation/calcification (the two terms are used synonymously in this study) thin ducts, starting from the endolithic cells and reaching to the symbiolite surface, remain un-calcified (Frommlet et al., 2015a). Probably assisted by these residual connections to the outside environment, endolithic *Symbiodinium* cells remain alive and photosynthetically active for days to weeks, and upon medium exchange they can return to a free-living state by vacating the symbiolite through the described ducts (Frommlet et al., 2015a). Because of this reversibility of the autoendolithic process, symbiolite formation does not appear to be a dead end for endolithic cells but instead points toward a transient endolithic phase in the life history of benthic *Symbiodinium* populations.

Mineralized structures, ranging from simple sheaths and microbialites to complex shells and skeletons, form an integral part of many lifeforms (Riding, 2000; Knoll, 2003). Their formation can be influenced, induced, or strictly controlled by biological activity (Mann, 2001; Weiner and Dove, 2003; Dupraz et al., 2009). Biologically induced mineralization refers to processes that depend on metabolic activity to induce conditions for mineral precipitation. Often, these conditions are induced by the collective physiological activity of a microbial community, then also referred to as "microbially induced mineralization" (Arp et al., 2001; Aloisi, 2008; Gallagher et al., 2012). One of the most prominent microbially induced mineralization processes throughout much of Earth's history is carbonate precipitation. Modern examples include calcifying microbial mats, ooids, oncoids, stromatolite biofilms, and coral reef sediments (e.g., Garcia-Pichel et al., 2004; Ludwig et al., 2005; Werner et al., 2008; Arp et al., 2010). Calcification in these communities is induced by processes such as ammonium oxidation, sulfate reduction, and especially oxygenic photosynthesis, which all have the potential to increase the calcium carbonate saturation state (Ω) to a point where carbonate precipitation occurs from solution (Visscher and Stolz, 2005; Dupraz et al., 2009; Shiraishi, 2012). This influence of microbial activity on Ω and calcification is known as the "intrinsic alkalinity engine" (Dupraz et al., 2009; Gallagher et al., 2012). In its simplest form, oxygenic photosynthesis induces calcification by increasing pH in the surrounding medium through the assimilation of CO_2 and HCO_3^- and the release of OH^- from carbon concentrating mechanisms, which shifts the carbonate equilibrium toward CO_3^{2-} and in turn increases Ω and leads to what is called "*Cis*"-calcification or "photosynthesis-induced carbonate precipitation" (PCP) (McConnaughey and Whelan, 1997; Riding, 2006; Shiraishi, 2012). Besides alkalinity engines such as PCP, microbially induced calcification also crucially depends on the chemical composition and structure of extracellular polymeric substances (EPS), which (i) form a protective and adhesive organic matrix around the cells (Flemming and Wingender, 2010), (ii) create a diffusion-controlled microenvironment, which is strongly influenced by microbial metabolisms, and (iii) provide nucleation points for mineral precipitation (Kawaguchi and Decho, 2002; Dupraz et al., 2009; Decho, 2010).

PCP is attributed predominantly to cyanobacteria and in some cases to diatoms, green and red algae (Awramik and

Riding, 1988; Reid et al., 2000; Saghaï et al., 2015). The presence of dinoflagellates in calcifying reef sediments has previously been inferred from marker pigments (Werner et al., 2008; Schoon et al., 2010) but only the discovery of symbiolites provided first direct evidence for PCP by a dinoflagellate (Frommlet et al., 2015a). The latter study showed that symbiolite growth is light dependent, indicating that the underlying calcification process is induced by the photosynthetic activity of *Symbiodinium*, and that bacteria are essential for the process because (i) symbiolite formation was fully inhibited by antibiotics, and (ii) symbiolite formation could be reinitiated by inoculating previously antibiotics-treated *Symbiodinium* cultures with bacteria from a calcifying *Symbiodinium* culture. The study also demonstrated co-localization of symbiolites with acidic polysaccharides, a group of polysaccharides with important Ca^{2+}-binding properties (Dupraz et al., 2009) and antibiotics led to a qualitative weakening of biofilms. Thus, symbiolite formation is based on two typical components of microbially induced calcification, (i) the alkalinity engine, in this case photosynthesis, and (ii) bacteria, which support calcification most likely by producing, degrading and modifying EPS components (Dupraz et al., 2009; Decho, 2010; Arp et al., 2012). And yet, symbiolite formation is to our knowledge the only microbial calcifying process that was discovered *in vitro*, i.e., without knowledge of a natural analog.

The ensuing question of whether *Symbiodinium*-induced PCP could in principle also occur in nature, was the primary motivation for the present study. Calcifying microbial communities in nature are subject to dynamic changes in photosynthesis and respiration and thus an ever-shifting balance between precipitation and dissolution of minerals (Visscher and Stolz, 2005; Gallagher et al., 2012; Shiraishi, 2012). In closed systems such as batch cultures, these dynamics can be amplified, creating conditions the cultured organisms would not experience in nature (Brewer and Goldman, 1976; Wanner and Egli, 1990). Consequently, symbiolite formation cannot simply be assumed to occur in natural environments. Another point to consider when asking the question of whether symbiolite formation could occur naturally concerns the critical influence of EPS properties on microbial calcification processes (Dupraz et al., 2009; Decho, 2010; Arp et al., 2012). EPS functional groups are typically not distributed homogeneously but are organized in microdomains on the nm to μm scale, giving biofilm matrices a microspatial structure that strongly influences their properties (e.g., Kawaguchi and Decho, 2002; Lawrence et al., 2007). These properties include both calcification-inhibiting, and -enhancing microdomains, but which of these domains dominate is in part determined by how the domains are structured on a microspatial scale (Dupraz et al., 2009; Decho, 2010) and how they are changed during dynamic processes of EPS production, degradation and modification (Arp et al., 2012). Resistance of the structural component of EPS to hydromechanical shear stress varies widely in naturally occurring biofilms (reviewed in Flemming and Wingender, 2010; Gerbersdorf and Wieprecht, 2015). For example, biofilms in dynamic systems with high levels of hydrodynamic shear stress are generally more resistant to this type of disturbance than biofilms grown under stagnant conditions (e.g., Jaeger-Zuern and Gruberg, 2000). Thus, the fact that the *Symbiodinium* cultures studied by Frommlet et al. (2015a) were not aerated nor agitated because of the well-known sensitivity of dinoflagellates to hydromechanical shear stress (reviewed in Peters and Marrasé, 2000), raises the questions of how naturally relevant flow conditions and disturbance of biofilm integrity would affect symbiolite formation.

Here, we studied symbiolite formation in batch culture, i.e., the *in vitro* condition under which symbiolites were first discovered in Frommlet et al. (2015a), and for the first time in natural seawater under laminar flow, in order to determine how algal growth dynamics, the physicochemical macroenvironment in cultures, and the microenvironment of *Symbiodinium*-bacterial biofilms influence the underlying calcification process. Together, these different lines of experimental studies provide insights into some of the processes that govern these novel calcifying communities and allow a first evaluation of how likely symbiolite formation is under natural conditions.

MATERIALS AND METHODS

Symbiodinium Strains and Culturing Conditions

A total of 46 non-axenic *Symbiodinium* strains were used in this study (**Table 1**). Strains lacking published references, were identified to clade level based on partial ribosomal gene and internal transcribed spacer sequences, amplified according to Lajeunesse and Trench (2000) and Santos et al. (2001) (for details, see Supplementary Information). Stock cultures were routinely maintained in f/2 medium (Guillard, 1975) at 26°C and 130–150 μmol photons m^{-2} s^{-1} under a 12:12-h light:dark cycle and were subcultured monthly at a 1:40 ratio of culture to f/2 medium (for details, see Supplementary Information). Depending on the required volumes, experimental cultures were grown either in 24-well plates for suspended cell cultures (Sarstedt, Nürnbrecht, Germany), sealed with parafilm to prevent evaporation, or in 75 cm^2 tissue culture flasks for suspended cell cultures with vented caps (Sarstedt, Nürnbrecht, Germany). Customized culturing flasks were used for microsensor measurements (see Supplementary Figure 1).

Assessment of Growth Curves and Onset of Calcification in Batch Culture

Symbiodinium growth curves were determined for five strains under standard light and temperature conditions (see above). For this, triplicate cultures of each strain were inoculated with 25,000–50,000 cells mL^{-1} in f/2 medium and their growth was monitored until cultures reached stationary phase by performing manual cell counts of Lugol-preserved samples in a Nageotte counting chamber (for details, see Supplementary Information). To determine the onset of calcification under standard batch culture conditions, 45 calcifying *Symbiodinium* strains (Supplementary Table 1) were inoculated at a ratio of 1:40 of culture to f/2 medium and monitored microscopically for the appearance of symbiolites (for details, see Supplementary Information).

TABLE 1 | *Symbiodinium* strains used in this study.

Culture (NCMA no.)	Species (*)	Clade or ITS type (Ref.)	GenBank accession no	Host species	Geographic origin
61 (2464)	*S. microadriaticum* Freudenthal 1962	A1 (1)		*Cassiopeia xamachana*	Florida
362 (2458)	*S. microadriaticum* Freudenthal 1962	A1 (1)		*Cassiopeia andromeda*	Gulf of Aqaba
370 (2467)	*S. microadriaticum* Freudenthal 1962	A1 (1)		*Stylophora pistillata*	Gulf of Aqaba
23		A2 (1)		*Bartholomea annulata*	Barbados
89		A2 (1)		*Gorgonia ventalina*	Bermuda
97		A2 (1)		*Gorgonia ventalina*	Puerto Rico
104		A2 (1)		*Heliopora* sp.	Enewetak
130		A2 (1)		*Meandrina meandrites*	Jamaica
185 (2461)	*S. pilosum* Trench and Blank 1987	A2 (1)		*Zoanthus sociatus*	Jamaica
PHMS TD1e		A3a (2)		*Tridacna* sp.	Philippines
292 (2465)		A3 (1)		*Tridacna maxima*	Palau
379 (2456)		A4 (1)		*Plexaura homomalla*	Bahamas
Culture X		A12 (2)		Unknown	Aquarium tank
80 (2469)	*S. necroappetens* LaJeunesse et al. 2015	A13 (1)		*Condylactis gigantea*	Jamaica
PTA1		A13 (2)		*Porites asteroides*	Caribbean, Florida
m. mirabilis		A14 (2)		*Madracis mirabilis*	Florida
FLAp1		A (3)		*Aiptasia* sp.	Florida Keys
Pk708		A (4)		*Plexaura kuna*	San Blas
AV32		A (this study)	MF616331	*Galaxea fascicularis*	Red Sea
99		A (this study)	MF616332	*Gorgonia ventalina*	Puerto Rico
105		A (this study)	MF616333	*Heliopora* sp.	Enewetak
107		A (this study)	MF616334	*Heliopora* sp.	Enewetak
108		A (this study)	MF616335	*Heliopora* sp.	Enewetak
154		A (this study)	MF616336	*Discoma sanctithomae*	Jamaica
2 (2460)	*S. minutum* LaJeunesse et al., 2012	B1 (1)		*Aiptasia pallida*	Florida
12 (2463)		B1 (1)		*Aiptasia tagetes*	Puerto Rico
13		B1 (1)		*Aiptasia tagetes*	Bermuda
64		B1 (1)		*Cassiopeia xamachana*	Jamaica
74		B1 (1)		*Cassiopeia xamachana*	Jamaica
Pk704		B1 (3)		*Plexaura kuna*	San Blas
Pk706		B1 (3)		*Plexaura kuna*	San Blas
146 (3450)	*S. pseudominutum* Parkinson et al., 2015	B1 (1)		*Oculina diffusa*	Bermuda
147 (2470)		B1 (1)		*Pseudoterogorgia bipinnata*	Jamaica
M. capitata		B1 (1)		*Montipora capitata*	Hawaii
351		B1 (1)		*Pocillopora damicornis*	Hawaii
Pk702		B2 (3)		*Plexaura kuna*	San Blas
141 (3320)	*S. psygmophilum* LaJeunesse et al., 2012	B2.1 (1)		*Oculina diffusa*	Bermuda
385 (2462)		B3 (2)		*Dichotomia* sp.	Caribbean
FLAp2		B (3)		*Aiptasia pallida*	Florida
203		C2 (1)		*Hippopus hippopus*	Palau
HHC1B		C2 (2)		*Hippopus hippopus*	Philippines
401		D (5)		Unknown	Unknown
Ap31		D (4)		Unknown anemone	Okinawa
383 (3420)	*S. voratum* Jeong et al., 2014	E1 (1)		*Anthopleura elegantissima*	California
135 (2468)	*S. kawagutii* Trench and Blank, 1987	F1 (2)		*Montipora verrucosa*	Hawaii
133 (2455)		F2 (1)		Meandrina meandrites	Jamaica

*NCMA, National Center for Marine Algae and Microbiota. *Species names are provided for cultures that are deposited in a collection and are either identified to species level by the collection or could be matched with the holotype in the respective species description. (1) LaJeunesse, 2001; (2) LaJeunesse et al., 2005; (3) Santos et al., 2001; (4) Santos et al., 2002; (5) Thornhill and Lord, 2010.*

Carbonate System, pH, and Onset of Calcification in Undisturbed and Disturbed Batch Culture

Duplicate batch cultures of four *Symbiodinium* strains were grown under standard batch culture conditions (see above) in 75 cm^2 tissue culture flasks for suspended cell cultures with vented caps (Sarstedt). For each strain, one flask was kept undisturbed, while the other flask was disturbed several times a week to disrupt the microstructure of the developing biofilm (see results for specific days). Due to the experimental design, which included laborious microscopic screenings of the entire culture flask surface and manual titrations that were too time consuming to guarantee that DIC and related parameters would not change during the storage of experimental replicates (see below), the four *Symbiodinium* strains were studied without experimental replication and in two separate experiments. The first experiment was conducted with strains (clade/ITS type) AV32(A) and PK702(B1), the second with 74(B1) and 203(C2). During the second experiment, a sterile f/2 medium control was kept in the incubator, alongside cultures 74 and 203, as a control for abiotic changes in medium chemistry. Due to natural variability, the batch of seawater for the second experiment had slightly higher initial TA, pH, DIC, and Ω_{arag}.

Disruption of developing biofilms was achieved by detaching cells and the biofilm from the culture flask's surfaces using a cell scraper (Orange Scientific, Braine-l'Alleud, Belgium), followed by repeated pipetting with a 10-mL micropipette to further disperse algal cells and break up the developing bacterial-algal biofilm into a fine suspension. Throughout culture growth, pH, total alkalinity (TA), total dissolved inorganic carbon (DIC), and the aragonite saturation state (Ω_{arag}) were monitored in undisturbed and disturbed batch cultures, while microscopically screening for the appearance of symbiolites (for details, see Supplementary Information). Culture pH was measured using a WTW pH meter (Weilheim, Germany), followed by manual volumetric titrations to determine TA, using a Gran function plot method (Gran, 1950, 1952) in the online version of the Alkalinity Calculator software (U.S. Geological Survey; Rounds, 2012). Based on measured variables pH, TA, salinity and temperature (for details, see Supplementary Information), DIC and Ω_{arag} were calculated, using the Microsoft Excel macro CO2SYS (CO2Sys_v2.1, Pierrot et al., 2006).

Assessment of Symbiolite Growth-Limitation Using Image Analysis

Symbiodinium strain 105 was grown in 12 × 2 mL of f/2 medium (Guillard, 1975) on a 24-well tissue culture plate for suspended cell cultures (Sarstedt) under standard batch culture conditions (see above). All cultures were screened daily by microscopy for calcification, i.e., the formation of symbiolites. As soon as calcification was evident in all cultures, symbiolite growth was monitored using image analysis according to Frommlet et al. (2015a). Once symbiolites had stopped growing in all cultures, all cultures were resupplied with vitamins and trace elements according to the f/2 medium recipe (control). In addition, three cultures each received as experiential treatment either (i) nitrogen ($NaNO_3$) and phosphorus (NaH_2PO_4) according to the f/2 medium recipe, (ii) 10.87 mM calcium in form of $CaCl_2$ (calcium concentration of modern seawater; Tyrrell and Zeebe, 2004), or (iii) a combination of the macronutrient and calcium treatment. To determine the effect of these treatments, monitoring of symbiolite growth by image analysis was continued and results were expressed relative to symbiolite size at the time of medium replenishment.

Microsensor Measurements in Batch Culture Medium and in Flowing Natural Seawater

Symbiodinium batch cultures for microsensor measurements were grown in f/2 medium under standard batch culture conditions (see above) using 75 cm^2 tissue culture flasks for suspended cell cultures that were cut-open to provide physical access of microsensors (Sarstedt; for details, see Supplementary Information). Microsensor measurements in batch culture were performed directly in these modified flasks. For measurements in natural, flowing seawater, the growth medium was decanted, a self-built laminar flow chamber was introduced into the modified flasks, and the flasks were filled carefully with natural, sterile-filtered seawater without disturbing the biofilm (for details, see Supplementary Figure 1). Liquid ion-exchange (LIX) glass microsensors for pH and Ca^{2+} with a tip size of 10–25 μm were constructed as described previously (Ammann et al., 1987; de Beer et al., 1997, 2000). Electrochemical Clark type O_2 microsensors were obtained from Unisense A/S (Aarhus, Denmark; Revsbech, 1989). Oxygen and pH dynamics were measured on the biofilm/symbiolite surface over several light-dark cycles. Depth profiles of O_2, pH and Ca^{2+} were measured from the biofilm/symbiolite surface through the diffusive boundary layer into the overlying water column. Using dichlorophenyl dimethylurea (DCMU), a specific inhibitor of photosystem II (Bishop, 1958), we tested whether calcification could be suppressed by inhibiting photosynthesis. DCMU was dissolved in ethanol and added to seawater to a final concentration of 1 μM (Al-Horani et al., 2003). For such measurements, we increased the ambient flow to ensure effective mixing of DCMU in the experimental flow chamber. Calcium concentration profiles were measured before and 10 min after DCMU addition. For further technical details and for calculations of parameters, see Supplementary Information.

Quantification of Precipitated $CaCO_3$ Using LIX Ca^{2+} Microsensors

For the determination of culture-specific, maximum amounts of precipitated $CaCO_3$, 32 *Symbiodinium* strains, covering a wide range of phylotypes, were cultivated in 24-well tissue culture plates for suspended cell cultures (Sarstedt) under standard batch culture conditions (see above) for 56 days. Based on previous results (Frommlet et al., 2015a) and the data presented in the present study, this culturing period generally ensures that calcifying cultures reach a post-calcifying stage. To quantify the precipitated $CaCO_3$, in these cultures, we established a protocol that involved the removal of growth medium, followed

by the dissolution of the precipitated $CaCO_3$ in HCl and the determination of the calcium concentration in solution using Ca^{2+} microsensors (for details, see Supplementary Figures 2, 3).

Statistical Analysis

One-way ANOVA was used to test for differences in the maximum amount of precipitated $CaCO_3$ between different clades and to test for differences between calcification endpoints of symbiolite growth limitation experiments. When statistical differences were observed ($P < 0.05$), Tukey's HSD post-hoc comparisons were applied to determine which of the groups and experimental treatments were significantly different (see Supplementary Information).

RESULTS

Calcification in Relation to *Symbiodinium* Growth, Carbonate System Dynamics, and Culture Disturbance

Symbiolite formation in undisturbed *Symbiodinium* batch cultures started on average after 14.5 days (95% confidence interval [11.8–17.2]; $n = 45$) (**Figure 1A**; Supplementary Table 1). A comparison to growth curves of 5 of the 45 investigated *Symbiodinium* strains showed that the average onset of calcification corresponded to the late log- to early stationary growth phase (**Figure 1B**).

How the onset of calcification in undisturbed and disturbed batch cultures of *Symbiodinium* strains (clade/ITS2-type) AV32 (A) and Pk702 (B1) related to their pH and carbonate system dynamics is shown in **Figure 2**. In the undisturbed culture of strain AV32 ($AV32_{undist}$), pH increased within the first 8 days from pH 7.98 to a maximum of pH 9.87, while total alkalinity (TA) decreased from 1795 μEq Kg^{-1} to a minimum of 1024 μEq Kg^{-1} (**Figure 2A**). By day 24 to 29, pH and TA had returned to values similar to those at the beginning of culture growth and those of a sterile f/2 medium control. Total DIC dynamics were similar to those of TA, decreasing from 1.61 mmol Kg^{-1} to a minimum of 0.11 mmol Kg^{-1} by day 8, before rising again to 1.74 mmol Kg^{-1} by day 29 (**Figure 2B**). Microscopic examinations showed that calcification started between day 21 and 23, when pH, TA, and DIC had already passed through their most extreme states and when the aragonite saturation state approached a maximum of $\Omega_{arag} = 6.32$ on day 24 (**Figures 2A,B**). The calcifying phase was accompanied by a second, less pronounced increase of pH and Ω_{arag}, which peaked on day 35 at pH 8.71 and 4.72, respectively, and a second decrease of TA to 1,249 μEq Kg^{-1} and of DIC to 0.86 mmol Kg^{-1} on day 43. Thereafter, all four parameters returned to values close to those of the medium control, indicating the end of the calcification phase.

In the disturbed culture of strain AV32 ($AV32_{dist}$), pH increased to pH 9.88 on day 16 and TA decreased to ~800 μEq Kg^{-1} between day 8 and 24, before returning to values similar to the medium control around days 35–43 (**Figure 2C**). Changes in DIC mirrored the TA dynamics with a drop from 1.60 to 0.014 mmol Kg^{-1} on day 16 before returning to 1.69 mmol Kg^{-1} by day 35 (**Figure 2D**). After an initial drop 0.19 on day 16, Ω_{arag} increased to a maximum of 6.11 on day 35 and dropped again to ~2 by day 43 (**Figure 2D**). First symbiolites were evident in $AV32_{dist}$ on day 42 (**Figures 2C,D**). Thus, calcification had commenced between day 35 and 42. Like in $AV32_{undist}$, calcification coincided with a peak in Ω_{arag} but was accompanied by only a small decrease of TA and DIC until day 60, followed by a recovery toward the end of the 66-day experiment. Consistent with the small changes in carbonate chemistry, only few symbiolites formed in protected corners of the culturing flask that could not be disturbed as thoroughly as the rest of the culture.

Both undisturbed and disturbed cultures of Pk702 displayed pH and carbonate chemistry dynamics during the pre-calcifying phase that were similar to those in AV32. For instance, a temporary increase of pH and a temporary decrease of TA, DIC and Ω_{arag} was evident (**Figures 2E–H**). The time periods during which these initial changes, especially of pH, persisted were several days longer than in the AV32 cultures. Yet, as in both AV32 cultures, calcification only commenced when pH and

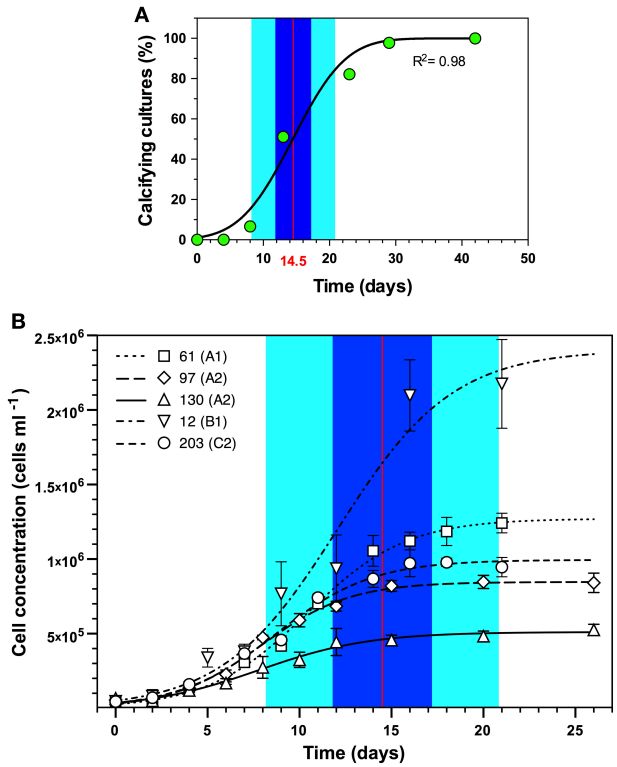

FIGURE 1 | Onset of symbiolite formation in relation to *Symbiodinium* spp. growth dynamics. **(A)** *Symbiodinium* spp. cultures, inoculated 1:40 (~25,000–50,000 cells mL^{-1}) in f/2 medium on average started to calcify after 14.5 days (red vertical line) with a 95% confidence interval from 11.8 to 17.2 days (Blue area) and a standard deviation of 6.3 days (light cyan area) ($n = 45$). **(B)** Projection of calcification dynamics in **(A)** onto growth curves of five of the 45 *Symbiodinium* strains (61, 97, 130, 12, and 203; ITS2-type designations in brackets) inoculated with 25,000–50,000 cells mL^{-1}. Data are means ± s.d. ($n = 3$). Logistic functions were fitted to growth curves using the software Plot (version 1.997, http://plot1.micw.org).

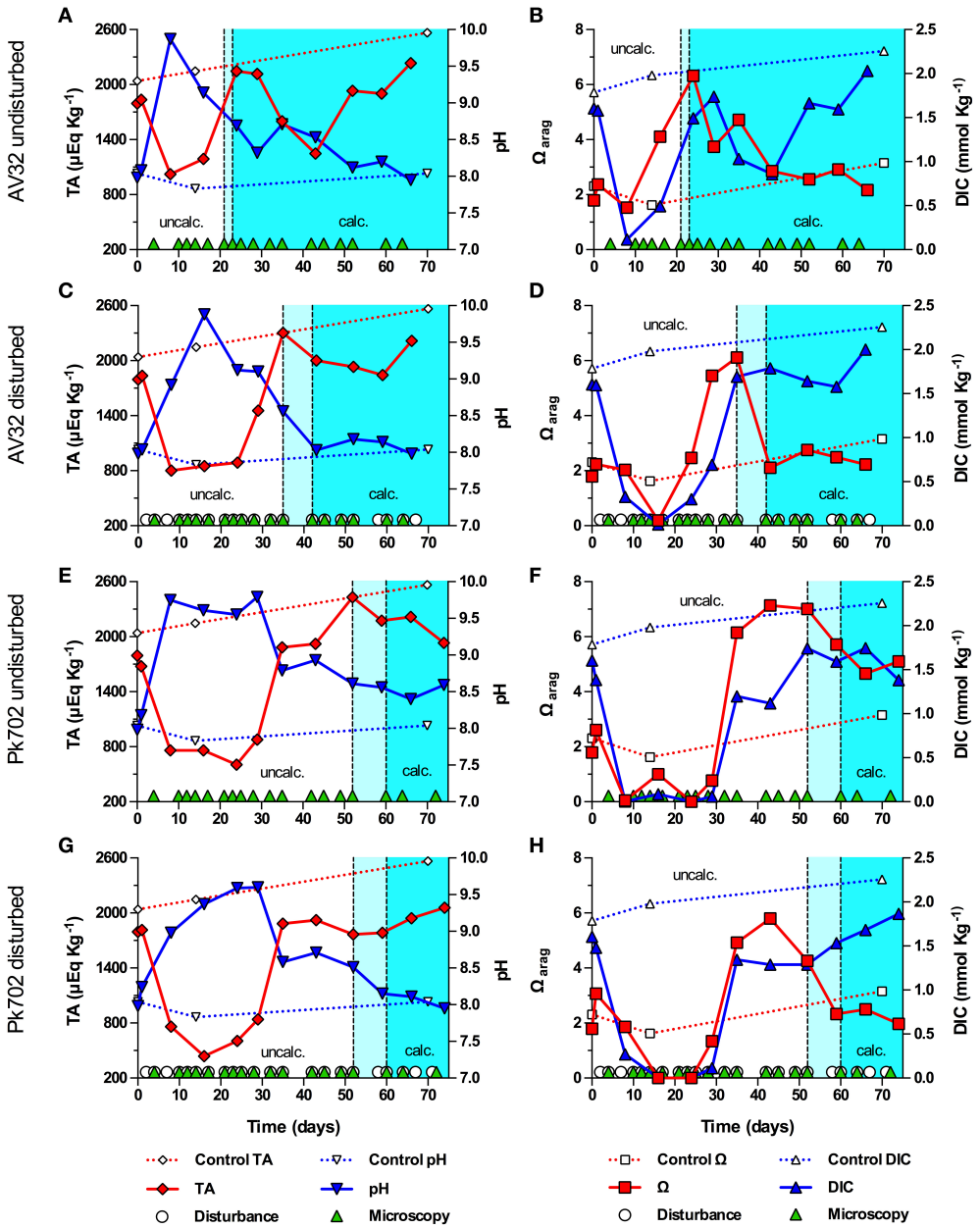

FIGURE 2 | Onset of symbiolite formation in strains AV32 and Pk702 relative to carbonate system and culture disturbance. Total alkalinity (TA), pH, aragonite saturation state (Ω_{arag}) and total dissolved inorganic carbon (DIC) in batch cultures of AV32 undisturbed **(A,B)**, AV32 disturbed **(C,D)**, Pk702 undisturbed **(E,F)**, and Pk702 disturbed **(G,H)**. A sterile f/2 medium control (dashed data lines) was kept under standard culturing conditions as described in section Material and Methods. Light cyan areas between vertical, dashed lines mark time windows during which cultures started to form symbiolites, i.e., transition from an un-calcified stage (uncalc., white background) to a calcified stage (calc., cyan background). Green triangles on the x-axis mark days on which cultures were screened microscopically for calcification (i.e., appearance and development of symbiolites). White circles on the x-axis in **(C,D,G,H)** mark days on which cultures were physically disturbed.

the carbonate system had passed through their most extreme phases. When first symbiolites appeared, Ω_{arag} in $Pk702_{undist}$ was still close to its maximum of 7.14 on day 43 and in $Pk702_{dist}$ was still elevated at 4.26 (**Figures 2E,F**). The main difference to $AV32_{undist}$ was that $Pk702_{undist}$ calcified much later (between days 52 and 60) and produced only few and small symbiolites. The lower production of symbiolites, was reflected in the modest decline in TA and DIC. However, TA and DIC dynamics also indicated that calcification was still ongoing by the end of the experiment as both parameters had not yet started to recover from the calcification-associated decline. In $Pk702_{dist}$, calcification commenced between days 52 and 60 but was minor and, as in $AV32_{dist}$, restricted to corners of the culturing flask, causing no decrease in DIC and TA (**Figures 2G,H**).

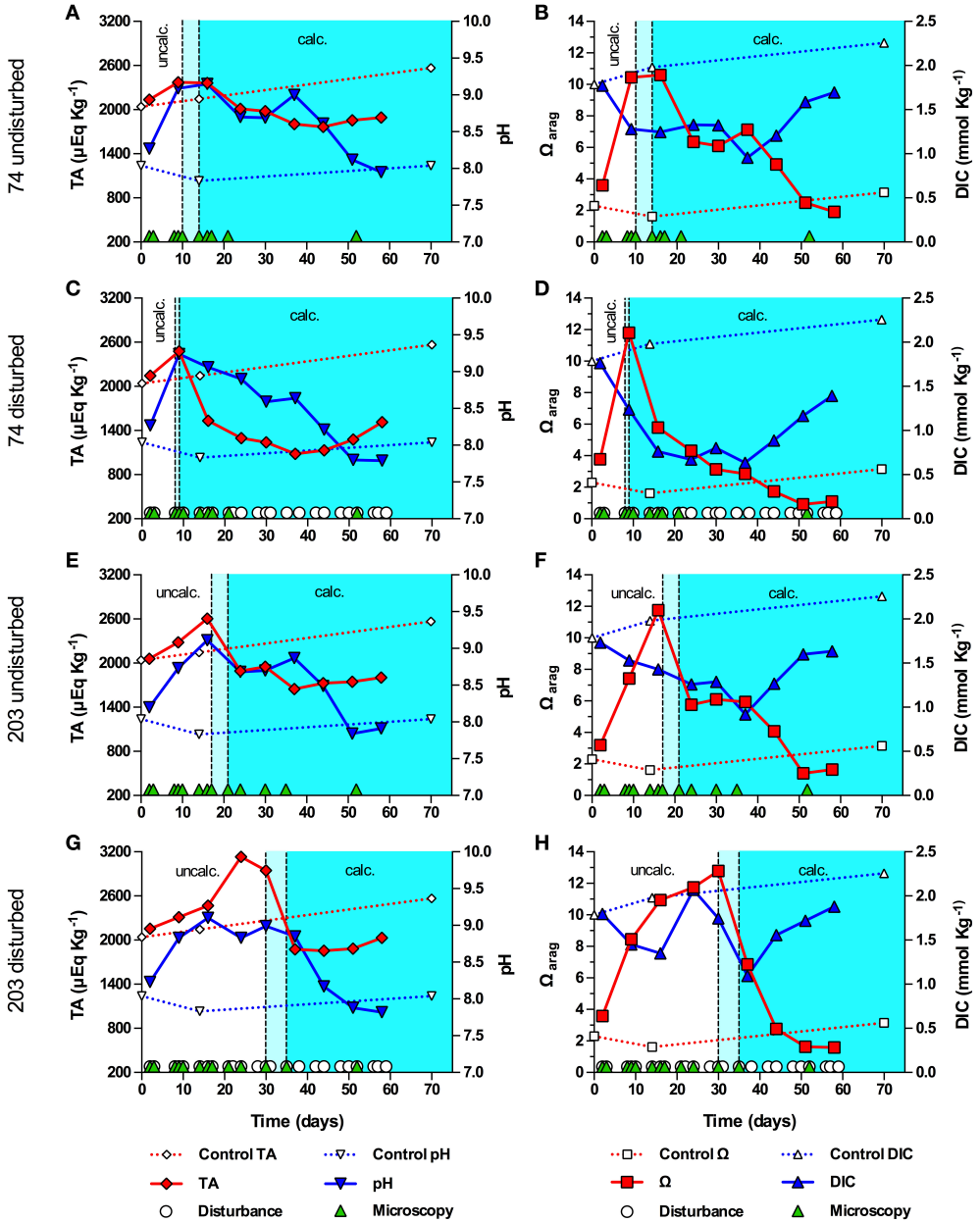

FIGURE 3 | Onset of symbiolite formation in strains 74 and 203 relative to carbonate system and culture disturbance. Total alkalinity (TA), pH, aragonite saturation state (Ω_{arag}) and total dissolved inorganic carbon (DIC) in batch cultures of 74 undisturbed **(A,B)**, 74 disturbed **(C,D)**, 203 undisturbed **(E,F)**, and 203 disturbed **(G,H)**. A sterile f/2 medium control (dashed data lines) was kept under standard culturing conditions. Light cyan areas between vertical, dashed lines mark time windows during which cultures started to form symbiolites, i.e., transition from a un-calcified stage (uncalc./white background area) to a calcified stage (calc., cyan background). Green triangles on the x-axis mark days on which cultures were visually screened for calcification on a microscope (i.e., appearance and development of symbiolites). White circles on the x-axis in **(C,D,G,H)** mark days on which cultures were physically disturbed.

A second experiment, conducted with strains (ITS type) 74 (B1) and 203 (C2), revealed that the pH in 74 and 203 were less strong than during the first experiment, with none of the cultures reaching a pH above 9.24 (**Figure 3**). In contrast to the first experiment, TA increased in all cultures during the pre-calcifying phase, decreased during the calcifying phase, and showed a recovery trend toward the end of the experiment (**Figures 3A,C,E,G**). All cultures showed a modest decline of DIC during the pre-calcifying phase with values remaining between 1 and 1.5 mmol Kg^{-1}. With the exception of culture 203_{dist}, DIC did not recover prior to calcification, kept decreasing during calcification, and recovered toward the end of the experiment (**Figures 3B,D,F,H**). In 203_{dist}, DIC recovered during the pre-calcifying phase, then dropped associated with

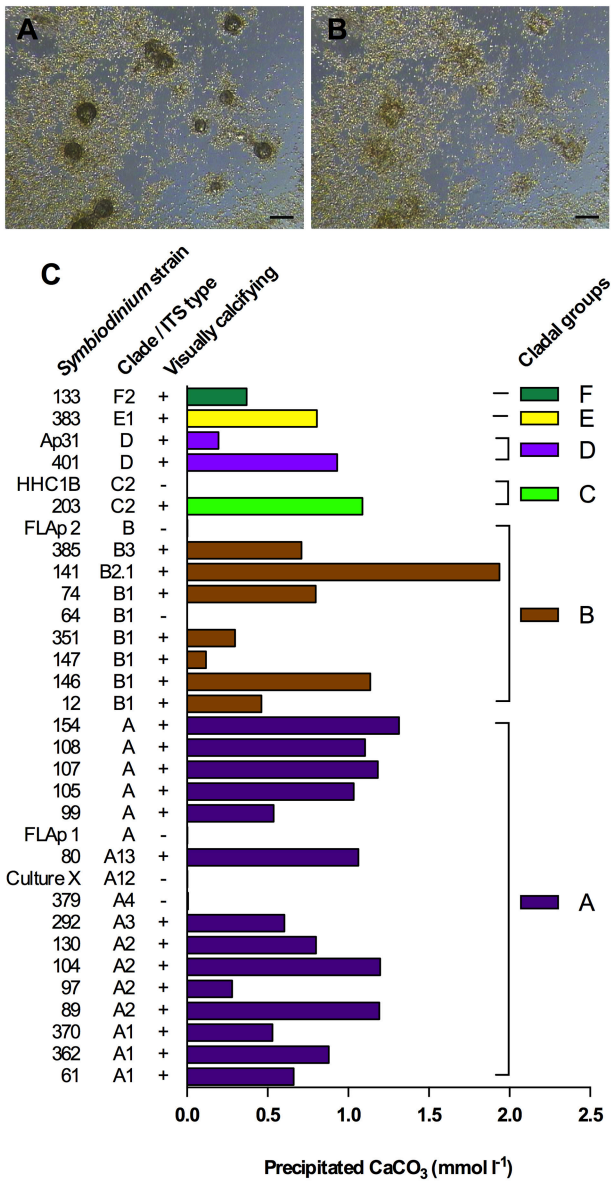

FIGURE 4 | *Symbiodinium*-driven $CaCO_3$ precipitation in batch culture. **(A,B)** Dissolution of symbiolites in a *S. minutum* culture (strain 12) using HCl (25 mM), to prepare the culture for Ca measurements. **(A)** 9 min after acidification, symbiolites are partially digested. **(B)** Same spot as in **(A)** after 35 min. Symbiolites are fully digested. Scale bar = 100 μm. **(C)** Final amounts of precipitated $CaCO_3$ in 26 calcifying and 6 non-calcifying *Symbiodinium* strains after 56 days of batch culture growth. On day 56 of batch culture growth, prior to acid digestions, cultures were screened for symbiolite formation by microscopy (visually calcifying; ±).

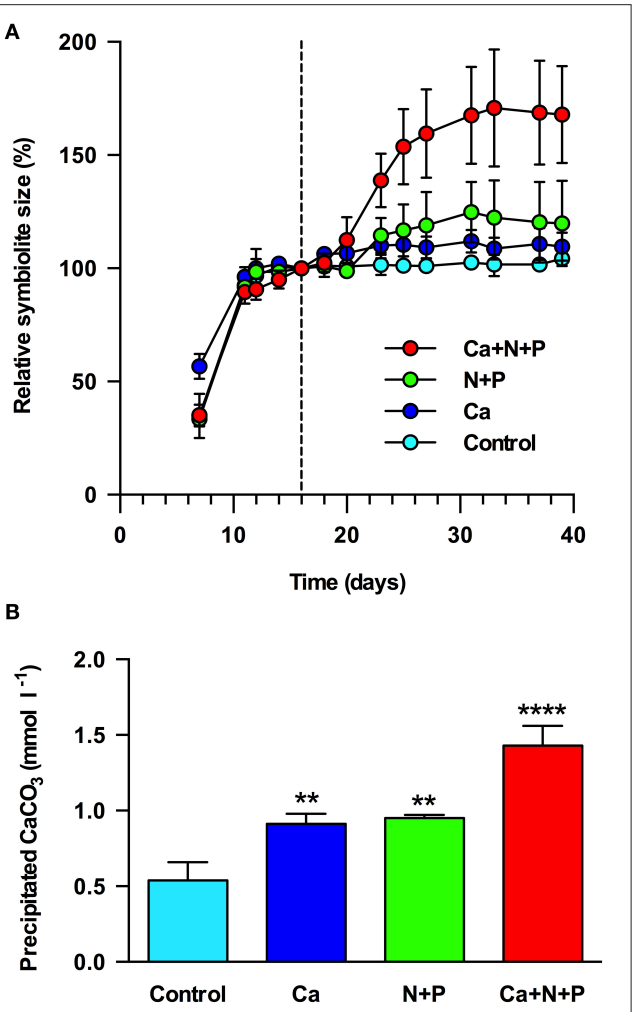

FIGURE 5 | Limitation of symbiolite growth in batch culture. **(A)** Relative symbiolite size in batch cultures of *Symbiodinium* strain 105 before and after the medium was replenished on day 16 (marked by black, dashed line). Medium was replenished only with f/2 vitamins and trace elements (control) or in addition with calcium (Ca), nitrogen and phosphorus (N+P) or a combination of calcium, nitrogen and phosphorus (Ca+N+P). **(B)** Final amounts of precipitated $CaCO_3$ at the end of the experiment (day 39) shown in **(A)**, measured by LIX Ca^{2+} microsensor. Asterisks indicate results from ANOVA where amounts of precipitated $CaCO_3$ in treatments were significantly different from controls at $^{**}P < 0.01$, $^{****}P < 0.001$. Data are expressed as mean ± *sd*. ($n = 3$).

calcification and recovered toward the end of the experiment (**Figure 3H**); exhibiting dynamics comparable to those during the first experiment. Together, these differences resulted in a higher Ω_{arag}, which peaked between 10.44 and 12.79 and, except for 203_{dist}, were synchronized with the initial rise in pH and the onset of calcification. Culture 203_{dist} reached a peak in Ω_{arag} and began to calcify after the initial pH peak and DIC had recovered from its initial decrease (>9 days later than 203_{undist}). Unlike in all other strains, disturbance promoted calcification in strain 74, as symbiolites appeared 1 and 7 days earlier in the disturbed culture than in the undisturbed culture.

Throughout experiments, the sterile f/2-medium control did not calcify and TA and DIC increased steadily from 2039 to 2566 μEq Kg^{-1} and from 1.79 to 2.26 mmol Kg^{-1}, respectively, while pH and Ω_{arag} first decreased from pH 8.04 to 7.83 and from 2.31 to 1.62, respectively, and then rose to pH 8.04 and 3.15.

Total $CaCO_3$ Precipitation in Batch Culture

Using a novel Ca^{2+} microsensor-based approach (Supplementary Figures 2, 3), we measured the total amount of precipitated

$CaCO_3$ in 26 visually calcifying and 6 visually non-calcifying *Symbiodinium* strains, representing 6 different clades and 12 different ITS2-types (**Figures 4A–C**). Excluding the non-calcifying cultures, total precipitated $CaCO_3$ ranged from 0.12–1.94 mmol L^{-1} and averaged at 0.82 ± 0.42 mmol L^{-1} (mean ± *sd*). Amounts of precipitated $CaCO_3$ in cladal groups with at least two strains (clades A, B, C and D) were not significantly different (ANOVA, $F = 0.5460$, $P = 0.6663$).

Symbiolite Growth Limitation in Batch Culture

The replenishment of post-calcifying cultures with vitamins and trace elements did not stimulate additional symbiolite growth (**Figures 5**). Calcium caused a rapid but moderate increase in symbiolite size, evident 2 days after medium supplementation and leading to an increase of symbiolites by ∼10%. Macronutrients led to an increase in symbiolite size by ∼20%, which was evident after 7 days. The combined supplementation of calcium and macronutrients increased symbiolite size by ∼70%. At the end of the experiment, quantitative measurements of calcification showed that the imaging-based approach had provided conservative estimates of the effects and that all treatments significantly increased growth relative to the control (**Figure 5B**; ANOVA; $P = 0.001$).

Biofilm Microenvironment in Batch Culture vs. Flowing Natural Seawater for Different Irradiance Regimes

pH microprofiles in a 10-day old, pre-calcifying batch culture (i.e., no flow and batch medium) of strain AV32 displayed an elevated medium pH of 8.8, typical for log phase batch cultures (compare to **Figure 2**) and a further rise of pH toward the biofilm microenvironment (pH = 8.9). Replacing the culture medium with a flow of natural seawater (0.5 cm s^{-1}) reduced the pH in the bulk phase of the flow system to a regular seawater pH of ∼8.1, while local photosynthesis within the biofilm microenvironment of this pre-calcifying culture elevated pH to ∼8.4 (**Figure 6A**).

The O_2 and pH microenvironment of actively calcifying biofilms of strain AV32 responded rapidly (within <1 s) to changes in incident irradiance (**Figures 6B–D**). Under an ambient flow velocity of 0.5 cm s^{-1}, the biofilm O_2 concentration dropped to ∼85% air saturation in darkness (178 ± 9.0 μmol O_2 L^{-1}; mean ± s.e.) and reached values of ∼230% air saturation (475 ± 10.5 μmol O_2 L^{-1}; mean ± s.e.) at PAR levels >120 μmol photons m^{-2} s^{-1} (**Figure 6C**). These light-dependent changes in O_2 concentration were accompanied by simultaneous changes in the pH microenvironment (**Figure 6B**). In darkness, the symbiolite surface pH was 0.09 pH units lower than that of ambient seawater (**Figure 6D**). Under PAR levels of >120 μmol photons m^{-2} s^{-1}, pH-values at the symbiolite surface were 0.53 ± 0.07 pH units (mean ± s.e.) higher than the ambient seawater (**Figure 6D**). The thickness of the diffusive boundary layer (DBL) for both O_2 and pH was ∼1 mm at a flow velocity of 0.5 cm s^{-1} (**Figure 6C–D**).

Photosynthetic Activity and Photosynthesis-Dependent Calcium Precipitation

Calcifying cultures were actively photosynthesizing (**Figures 7A–D**). Volumetric gross photosynthetic rates measured at the symbiolite surface under increasing levels of incident irradiance reached a maximum photosynthesis rate (P_{max}) of 14.1 nmol O_2 cm^{-3} s^{-1} with a light use efficiency factor $\alpha = 0.22$ and an onset of photosynthesis saturation, E_k at ∼75 μmol photons m^{-2} s^{-1} (**Figure 7A**). Net photosynthesis (P_N) amounted to 22% and 54% of total gross photosynthesis (P_G) at PAR levels of 60 and 120 μmol photons m^{-2} s^{-1}, respectively (**Figure 7B**). Thus, calcifying biofilms respired about 78% and 46% of P_G at low to moderate light levels. At higher photon irradiance (>120 μmol photons m^{-2} s^{-1}), light respiration decreased in proportion to P_N, and P_N was about 80–85% of P_G (**Figure 7B**). Calcium microsensor measurements at the surface of symbiolites revealed active calcium precipitation in light (**Figure 7C**), which was inhibited ∼5 min after the addition of the photosystem II inhibitor DCMU (**Figure 7D**).

Microenvironments in Calcifying vs. Post-calcifying Biofilms

O_2 and pH dynamics in the biofilm microenvironment of actively calcifying and post-calcifying cultures of strain Pk702 are shown in **Figure 8**. Actively calcifying cultures reached up to 190% air saturation (390 μmol O_2 L^{-1}), while post-calcifying cultures showed only moderate changes in O_2, reaching maximal values of 120% air saturation (250 μmol O_2 L^{-1}; compare **Figures 8A,D**). Likewise, the biofilm pH of calcifying cultures ranged from pH 7.92 to 8.57 in darkness and light, respectively (**Figure 8B**), while pH in post-calcifying cultures ranged from pH 7.93 in darkness to pH 8.34 at 200 μmol photons m^{-2} s^{-1} and then decreased at a photon irradiance of 400 μmol photons m^{-2} s^{-1} to lower values than observed under 100 μmol photons m^{-2} s^{-1} (**Figure 8E**). This apparent inhibition effect was not pronounced for pH measurements performed on young cultures (**Figure 8B**). Repeated light-dark cycles showed maximal pH changes of 0.61 pH units vs. 0.17 pH units for calcifying and post-calcifying cultures, respectively (**Figure 8C,F**).

DISCUSSION

Symbiolite Formation Relative to Batch Culture Growth Phase

One objective of the present study was to establish in which growth phase batch cultures become calcifying. However, culture dispersion, which is required to attain accurate cell counts for growth curves, influences the onset of calcification (see disturbance experiments). Thus, studying the onset of calcification in a culture relative to this culture's growth dynamics is practically impossible based on cell counts. Future studies may address this issue by using non-intrusive methods, e.g., optical density- or chlorophyll fluorescence measurements to estimate culture growth. Here we resorted to (i) determine the average time for undisturbed cultures to become calcifying

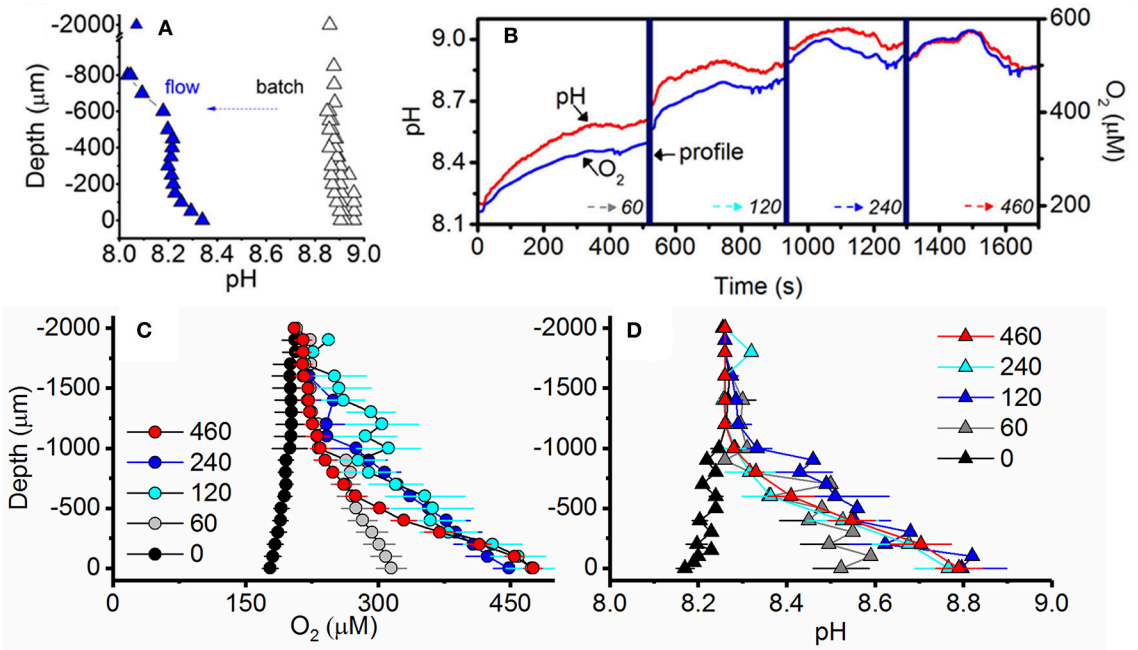

FIGURE 6 | Irradiance and flow dependent changes of the O_2 and pH microenvironment of symbiolites. **(A)** Comparison of pH under quasi-stagnant batch culture conditions (black) and under flow conditions (blue) measured consecutively in the same culture of strain AV32. Measurements were performed at an incident photon irradiance of 120 µmol photons m^{-2} s^{-1} under an ambient flow velocity of 0.5 cm s^{-1} (flow, $n = 1$) and under batch (quasi-stagnant) conditions ($n = 3$). **(B)** Example of simultaneous measurements of pH (red line) and O_2 (blue line) dynamics at the surface of two adjacent calcifying symbiolites (separated by 200–700 µm distance) in a culture of AV32. Surface dynamics were measured in darkness (time = 0) and as a function of increasing photon irradiance (60, 120, 240, and 460 µmol photons m^{-2} s^{-1}; indicated by dotted arrows). Microsensor depth profiles (time period shown as thick vertical blue line) were performed before irradiance was increased to a subsequent higher value. **(C)** O_2 concentration and **(D)** pH profiles measured from the symbiolite surface (depth = 0 µm) into the overlying water column (negative values). Measurements were performed at increasing levels of incident downwelling photon irradiance (numbers denote µmol photons m^{-2} s^{-1}). Data points with error bars represent means ± s.e. ($n = 4$–8 symbiolites).

based on microscopic screenings of all 45 calcifying strains used in this study, and (ii) to separately acquire growth curves from a phylogenetically diverse subset of these strains. Comparing the average time for calcification to commence (14.5 days) with the separately obtained growth curves showed that calcification typically commenced when cultures reached late log- to early stationary phase (**Figure 1**). Directly comparable data from the literature do not exist because few other studies on calcifying microbial communities have worked with experimentally grown biofilms, and these studies reported only very broadly on the growth stage of cultures or biofilms when calcification commenced (Hartley et al., 1996; Brehm et al., 2006). Constitutively biomineralizing microalgae such as coccolithophores calcify at the highest rate during log-phase, when growth rates and metabolic activities are typically highest (de Bodt et al., 2008). Considering that PCP is induced by photosynthesis (Arp et al., 2001; Dupraz et al., 2009; Shiraishi, 2012), one may thus expect that *Symbiodinium*-induced calcification would also commence during log-phase and not only toward stationary phase. However, as symbiolite formation is a bacterial-algal calcification process, the activity of the phototroph is but one of several factors driving calcification. Other important factors are the growth, the relative composition and the physiological activity of bacterial communities, as well as their production, modification, and degradation of EPS, and the structural development of the bacterial-algal biofilm (Dupraz et al., 2009; Decho, 2010; Arp et al., 2012). As shown by Frommlet et al. (2015a), bacteria are essential for symbiolite formation and are thought to be the main EPS producers. Because bacterial growth depends on photosynthates produced by *Symbiodinium*, a certain time lag between algal growth and the development of the bacterial community and their production and modification of EPS is likely, which could explain the late onset of calcification. Regarding the development of the bacterial-algal biofilm, it is also important to point out that under nutrient limitation and associated with the resulting reduction in cell division rates (Gunnersen et al., 1988; Rodríguez-Román and Iglesias-Prieto, 2005), an increasing number of *Symbiodinium* cells remain in the non-motile, coccoid stage during the photoperiod (Fitt and Trench, 1983). This change from motile zoospores to non-motile coccoid cells could be a key event in the development of the bacterial-algal biofilm and a decisive factor in initiating calcification, as it represents a major relocation of photosynthetic activity from the planktonic phase in the bulk medium into the surface-associated biofilm microenvironment. Under nutrient limitation, i.e., in a state of unbalanced growth, *Symbiodinium* may also excrete larger amounts of photosynthates (Davy et al., 2012), fueling bacterial growth and EPS production

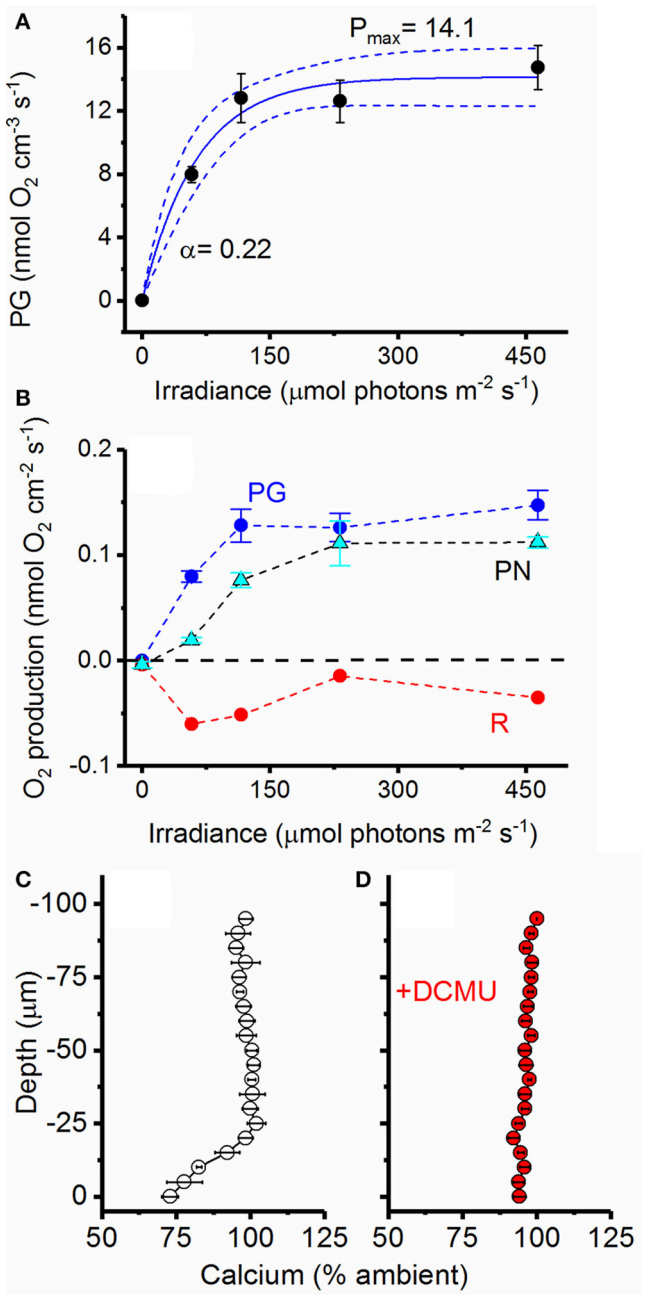

FIGURE 7 | Photosynthetic activity and photosystem II dependent calcium uptake**. (A)** Volumetric gross photosynthetic rates (PG; black circles) measured at the surface of symbiolites (symbols with error bars represent means ± s.e.; $n = 4$). Data was fit to an exponential function (Webb et al., 1974, see section Materials and Methods) and the best fit (blue line, $R^2 = 0.74$) and 95% confidence intervals (dotted blue lines) are shown. **(B)** Areal rates of gross photosynthesis (P_G; blue), net photosynthesis (P_N; cyan) and Respiration (R; red) (Symbols with error bars represent means ± s.e.; $n = 4$). The dotted black line marks the border between a net photosynthetic and net respiring system. **(C)** Active Ca^{2+} uptake measured at the surface of symbiolites with Ca^{2+} liquid-ion-exchange membrane microsensors under a photon irradiance of 460 µmol photons m^{-2} s^{-1}. **(D)** The addition of DCMU (dichlorophenyl dimethyl urea), a strong inhibitor of photosystem II, led to the inhibition of calcium uptake (symbols with error bars represent means ± s.e.; $n = 3$).

more efficiently during late stages of growth. Precisely how the bacterial communities and their metabolic activity develop in relation to *Symbiodinium* growth and how specific bacterial-algal interactions influence symbiolite formation are the focus of ongoing work.

Symbiolite Formation Relative to the Physicochemical Conditions in Batch Culture

In general, batch cultures are not representative of the natural environment of a cultivated organism, as nutrients are initially available at unnaturally high concentrations, followed by their near-complete removal during growth. This leads to dense populations that strongly influence their physicochemical environment before they enter starvation (Wanner and Egli, 1990). Calcification-relevant factors, such as pH and the carbonate system are particularly affected by respiration and oxygenic photosynthesis (e.g., Brewer and Goldman, 1976). The two main objectives of this part of the study were therefore (i) to assess how culture growth affects the physicochemical conditions in batch culture and how these macroenvironmental conditions in the bulk medium relate to the initiation of symbiolite formation, and (ii), based on these data, to evaluate if symbiolite formation could also occur under natural conditions.

In strains AV32 and Pk702, maxima in pH and minima in DIC marked the time of highest photosynthetic activity, yet these cultures only became calcifying when both parameters had already relaxed substantially (**Figure 2**). The pH and carbonate system dynamics of these cultures thus confirmed that calcification typically sets in during late stages of growth, after cultures exerted their strongest influence on calcification-relevant parameters. To understand why the highest photosynthetic activity did not induce PCP, it is important to consider that photosynthesis-driven changes in pH and DIC have opposing effects on TA and Ω. More specifically, a photosynthesis-driven rise in pH shifts the DIC system toward CO_3^{2-} and increases TA and Ω, while the accompanying CO_2 assimilation decreases DIC and lowers TA and Ω (McConnaughey and Whelan, 1997; Riding, 2006; Shiraishi, 2012). It is this ambivalent effect of photosynthesis on Ω that explains why the strong rise of pH in AV32 and Pk702, indicative of logarithmic growth, did not lead to a high Ω_{arag} and calcification. Essentially, AV32 and Pk702 had depleted DIC to such an extent that even the strong rise in pH could not cause a high Ω_{arag}. Only when pH-values indicated that cultures had passed through late log-phase, i.e., when bacterial respiration and/or diffusion of CO_2 from the atmosphere into the medium caught up with CO_2-assimilation, did DIC and TA recover sufficiently for Ω_{arag} to rise and for calcification to commence.

In experiments with strains 74 and 203, the drop in DIC was far less pronounced, TA remained high, pH did not become as alkaline, and Ω_{arag} reached higher values compared to AV32 and Pk702 and co-varied with the pH dynamics. Ultimately, these differences caused calcification to start earlier and at a time when, based on pH and carbonate system dynamics, cultures were still in log-phase. Independent of what caused these differences (see

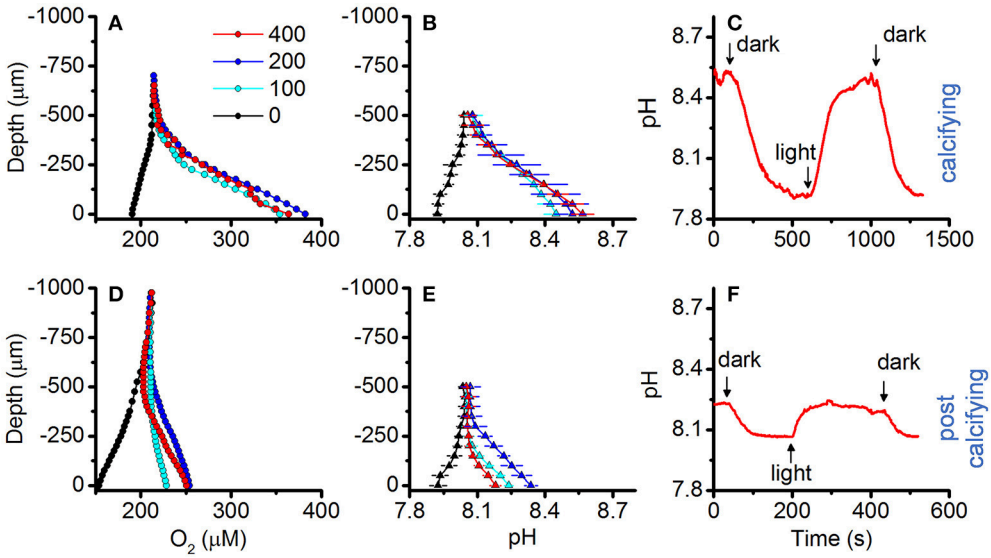

FIGURE 8 | Effect of symbiolite age on O_2 and pH microenvironmental dynamics. O_2 and pH microsensor measurements were performed on actively calcifying symbiolites (days = 19; upper panel, **(A–C)** and post-calcifying symbiolites (days = 37, lower panel, **(D–F)** of *Symbiodinium* culture Pk702. **(A,D)** O_2 and **(B,E)** pH microsensor measurements performed from the symbiolite surface (depth = 0 µm) into the overlying water column (negative values). Measurements were performed at increasing levels of incident downwelling irradiance (colors, in µmol photons m^{-2} s^{-1}), Data points with error bars represent means ± s.e. ($n = 2$). **(C,F)** Example data of repeated light (100 µmol photons m^{-2} s^{-1}) to dark cycles.

Supplementary Information for an extended discussion), these experiments showed that, given a large enough DIC pool, peaks in photosynthetic activity could induce calcification in batch cultures. Considering both cases: (i) onset of calcification not coinciding with highest photosynthetic activity and pronounced DIC depletion, combined with high maximum pH, and (ii) calcification coinciding with highest photosynthetic activity but under less extreme DIC and pH conditions, it can be concluded that *Symbiodinium*-driven calcification in batch culture is not the result of the most extreme conditions and that symbiolite formation is not merely an artifact of batch culture conditions.

Effects of Disturbance on Physicochemical Conditions in Batch Culture and Symbiolite Formation

Repeated physical disturbance influenced the onset of calcification in all four studied strains (**Figures 2**, **3**). Considering that the properties of EPS and the biofilm matrix have important functional roles in bacterial-algal calcification and that these properties depend strongly on the microspatial structure of biofilms (Riding, 2000; Kawaguchi and Decho, 2002; Dupraz et al., 2009; Decho, 2010), it is likely that the inhibitory effect of biofilm disturbance on calcification in cultures AV32, Pk702 and 203 was caused by a disruption of the microspatial structure of the biofilm. However, in culture 74 disturbance actually promoted calcification, suggesting not only that this culture had a more resistant biofilm but that disturbance also had calcification promoting effects. Resistance of biofilms to hydromechanical shear stress is known to vary widely (reviewed in Flemming and Wingender, 2010; Gerbersdorf and Wieprecht, 2015), and thus it is not implausible that certain combinations of *Symbiodinium* strains and bacterial communities could form biofilms that are more resistant to physical disturbance than others and several other calcification-promoting and -inhibiting effects of disturbance are possible. A detailed assessment of these potential effects was beyond the scope of this study but see Supplementary Information for an extended discussion of possible effects. However, independent of the potentially complex effects, our results showed that physical biofilm disturbance generally had a negative effect on calcification but also that even severe physical biofilm disturbance by repeatedly dispersing the developing bacterial-algal biofilm into a fine suspension could not completely prevent calcification. Hence, the absence of significant hydromechanical shear stress, characteristic for batch cultures, does not appear to be an essential requirement for symbiolite formation, which increases the probability for this process to also occur in dynamic, natural environments.

Quantitative Assessment of Calcification in Batch Culture

Previous data suggested that the genus *Symbiodinium* has broad potential to establish calcifying bacterial-algal communities and showed no correlation between *Symbiodinium* phylotypes and their potential to form symbiolites (Frommlet et al., 2015a). In this previous study, the calcification potential was assessed qualitatively by classifying strains as calcifying if they were at least once observed to form symbiolites. A Ca^{2+} microsensor-based approach (see Supplementary Information) now enabled the first quantitative assessment of *Symbiodinium*-induced microbial calcification (**Figure 4**). On average, calcifying cultures

precipitated a total of 0.82 ± 0.42 mmoles $CaCO_3$ L^{-1}; equivalent to ∼8% of the Ca^{2+} concentration in seawater (Tyrrell and Zeebe, 2004). Calcification varied widely between cultures but was not significantly correlated with *Symbiodinium* phylotypes, confirming on one hand a broad calcification potential of this genus but on the other hand indicating that calcification potential also depends on other factors, most likely functional differences in culture-associated bacterial communities. Five strains, previously reported as calcifiers, did not calcify during our experiments (e.g., FLAp 1 and HHC1B; compare to Frommlet et al., 2015a). This inconsistency in reaching a calcifying stage appears to be a feature of some of the weakly calcifying strains. Considering that microbial calcification is not tightly biologically controlled and that the process depends on several components, such as the physiological activity of heterotrophic and autotrophic partners and EPS dynamics, which in turn are all influenced by culture history prior to experimentation and slight variations in medium composition and light levels, such variations in calcification from one experiment to another are to be expected due to the complex nature of bacterial-algal calcification processes (e.g., Dupraz et al., 2009). It is therefore important to point out that the calcification amounts reported here only broadly define the calcification potential of *Symbiodinium*-bacterial associations.

Nevertheless, considering that (i) stationary phase *Symbiodinium* cultures typically reach $\sim 10^6$ cells mL^{-1} (see **Figure 1**), (ii) the calcification phase lasts about 5–10 days (Frommlet et al., 2015a), and assuming cautiously that (iii) the entire algal population contributes to calcification, the average amount of total precipitated $CaCO_3$ of 0.82 mmol L^{-1} corresponds to an average calcification rate of 0.082–0.164 pmol $CaCO_3$ *Symbiodinium* $cell^{-1}$ day^{-1}, equivalent to 8.2–16.4 pg $CaCO_3$ or 0.98–1.96 pg C *Symbiodinium* $cell^{-1}$ day^{-1}. Interestingly, these rates are not that dissimilar from those of strong calcifiers such as coccolithophores (1 pg C cell−1 d−1 in Trimborn et al., 2007; 7–22 pg C cell−1 d−1 in Zondervan et al., 2001). However, how important *Symbiodinium*-driven bacterial-algal calcification could be in terms of global calcification budgets, for example, compared to other microbial calcification processes (e.g., Heldal et al., 2012), can only be addressed if direct evidence for symbiolite formation is found in nature.

Limitation of Symbiolite Growth in Batch Culture

Previous results showed that post-calcifying *Symbiodinium* cultures reacted to the replacement of their growth medium with additional symbiolite growth, suggesting that calcification was limited by a medium component (Frommlet et al., 2015a). In the present study, instead of replacing the medium entirely, we resupplied the original growth medium with specific medium components. This experimental design revealed that both calcium and macronutrient addition induced further symbiolite growth, and that their joint provision had a synergistic effect. However, at the time of these experiments we did not yet have the knowledge that batch cultures on average "only" remove ∼8% of the total calcium from solution (**Figure 4**; Tyrrell and Zeebe, 2004). Consequently, replenishment of post-calcifying cultures with calcium, assuming that calcium had been substantially removed, overcompensated the actual calcium drawdown and must have resulted in ∼20 mM calcium; a concentration the oceans have last seen tens of millions of years ago (Tyrrell and Zeebe, 2004). Therefore, the observed effect of the calcium treatment is interesting as it suggests increased symbiolite formation under calcium concentrations present in Earth's geological past. However, a near doubling of modern day calcium concentrations instantly increases the calcium ion activity $\{Ca^{2+}\}$, which increases Ω and provides the potential for the observed fast re-initiation of calcification, without being a biologically meaningful indicator of whether calcification prior to the calcium addition was actually limited by calcium. In contrast, the calcification-promoting effect of macronutrients, explained by the necessity of macronutrients for algal photophysiology and the resulting effect on Ω (e.g., Shiraishi, 2012), must have been genuine because all presented data indicate that post-calcifying cultures were in stationary phase and thus medium replenishment did not overcompensate but only reinstated the original macronutrient status. Thus, symbiolite formation in batch culture is ultimately limited by the availability of macronutrients. The dynamics of nutrient availability in the nutrient poor surface waters of tropical coral reefs and the effects of these dynamics on the potential for symbiolite formation in nature will have to be addressed in future studies. However, the fact that coral reef sediments support high rates of organic matter mineralization and high primary productivity (Rasheed et al., 2004) and are known to calcify due to photosynthesis-driven microbial processes (Werner et al., 2008; Schoon et al., 2010; Cyronak and Eyre, 2016) show that in principle *Symbiodinium*-bacterial calcification should also be possible under natural nutrient conditions in reef habitats.

Photosynthesis-Induced Calcification in Unconditioned Natural Seawater

A comparison between pH profiles of a pre-calcifying culture of AV32 under batch culture conditions with the same culture once the medium had been replaced with flowing natural seawater, illustrates that the bulk medium (macroenvironment) of batch cultures strongly affects the biofilm microenvironment (**Figure 6A**). Yet, even in a young, pre-calcifying culture, photosynthesis in the biofilm alone, i.e., with the influence of the batch medium removed, was strong enough to cause a pronounced local increase in pH (**Figure 6A**). When reaching a calcifying stage, the same strain (AV32) displayed even more pronounced microenvironmental pH dynamics, reaching pH-values in the biofilm that were almost as high as those of the bulk medium during the pre-calcifying stage (compare **Figures 5A,B,D)**. This increase of photosynthetic activity in the biofilm indicates that cultures, as they mature, develop a larger biofilm-associated algal population that eventually induces pH changes that are high enough to induce calcification. However, the fact that the highest pH measured in the calcifying culture was still lower than the bulk pH of the younger, pre-calcifying culture also confirms the idea that symbiolite formation is not simply a function of culture pH, and that other factors, related to the development of the bacterial-algal biofilm, are required to initiate calcification. Once these factors are in place, calcification does not

require the extreme pH-values that are sometimes recorded in batch cultures (**Figure 2**).

Photosynthesis within the microenvironment of the bacterial-algal biofilm was very high, reaching a P_{max} of about 14 nmol O_2 cm^{-3} s^{-1} (**Figure 7A**). Such high volumetric gross photosynthetic rates are similar to values obtained from corals (Kühl et al., 1995; Brodersen et al., 2014), and benthic foraminifera (Köhler-Rink and Kühl, 2000, 2001). Importantly, calcium profiles showed that these biofilms were actively calcifying without being influenced by macroenvironmental batch culture conditions. This proves that symbiolite formation can occur in unconditioned natural seawater and that moderate flow rates, indicative of coral reef lagoons (e.g., Jimenez et al., 2011), do not interfere with biofilm functionality in terms of its calcification potential. The fact that the photosynthesis inhibitor DCMU inhibited calcification provided further evidence that *Symbiodinium*-bacterial calcification is induced by the photosynthetic activity of *Symbiodinium* (**Figure 7C,D**). The thin Ca^{2+} boundary layer of ∼25 μm in this experiment is explained by the fact that we increased the ambient flow to ensure effective mixing of DCMU in the flow chamber, leading to an erosion of the diffusive boundary layer. Finally, O_2 and pH dynamics in actively calcifying *vs.* post-calcifying biofilms showed that with increasing age photosynthesis in *Symbiodinium*-bacterial biofilms decreases, while respiration increases (**Figure 8**), suggesting that arrest of calcification is related to the diminishing photophysiological activity in older cultures.

CONCLUSIONS AND PERSPECTIVES

The experimental evidence presented here strengthens the notion that symbiolite formation is a typical bacterial-algal calcification process that is induced by photosynthesis of *Symbiodinium* spp. in the microenvironment of a bacterial-algal biofilm. Moreover, our data suggest that symbiolite formation is not merely an *in vitro* phenomenon but that this process should also occur under natural conditions. Whether *Symbiodinium* spp. actually drive bacterial-algal calcification and produce endolithic stages in natural habitats remains to be explored, but field studies that showed that (i) free-living *Symbiodinium* spp. occupy benthic reef habitat, especially reef sediments (e.g., Littman et al., 2008; Takabayashi et al., 2012), and (ii) that reef sediments calcify due to photosynthesis-driven calcification (Werner et al., 2008; Schoon et al., 2010; Cyronak and Eyre, 2016) provide first circumstantial evidence to support the novel concept of benthic *Symbiodinium* forming an endolithic life-stage by inducing the formation of microbialites. The prospect of a transient autoendolithic phase provides new perspectives on the biology and ecology of *Symbiodinium* and adds an entirely new ecological niche to be explored for *Symbiodinium* but also for dinoflagellates as a phylum. As outlined before by Frommlet et al. (2015a), an endolithic niche could be of important ecological relevance for free-living *Symbiodinium*, as it could act as a refuge from grazers and UV radiation, while still permitting photosynthesis (Friedmann, 1982; Shashar et al., 1997; Jeong et al., 2014). Finally, as *Symbiodinium* spp. are the first dinoflagellates known to drive a microbially induced mineralization process, symbiolite formation represents a valuable new model for the study of microbial calcification processes and the formation of microbialites. Current efforts in the study of symbiolites are directed at describing the bacterial communities and their role in biofilm formation and calcification, the assessment of potential functions of an endolithic stage for *Symbiodinium*, and the exploration of natural reef habitats for direct evidence of symbiolite formation and endolithic *Symbiodinium* populations.

AUTHOR CONTRIBUTIONS

JF, DW, and JS designed and planned the study. JF, DW, MS, BG, and MM performed the research and analyzed the results. JF, DW, MK, and JS interpreted the data and wrote the manuscript. All authors approved the final version of the manuscript.

ACKNOWLEDGMENTS

This work was funded by the Portuguese Foundation for Science and Technology (FCT) through project SeReZoox (PTDC/MAR/113962/2009) and by national funds from FCT/MCTES and co-financed by FEDER within PT2020, and Compete 2020 through project Symbiolite (PTDC/MAR-EST/3726/2014 - POCI-01-0145-FEDER-016748), and CESAM (UID/AMB/50017 - POCI-01-0145-FEDER-007638). Further financial support was provided by EU FP7 (Marie Curie Actions – People; Grant number PIRSES-GA-2011-295191). JF was supported by a FCT-funded postdoctoral fellowship (SFRH/BPD/111685/2015). MK was supported by a Sapere-Aude Advanced grant from the Danish Council for Independent Research|Natural Sciences. DW was supported by a grant from the Carlsberg Foundation.

SUPPLEMENTARY MATERIAL

The Supplementary Material for this article can be found online at: https://www.frontiersin.org/articles/10.3389/fmicb.2018.00998/full#supplementary-material

REFERENCES

Adams, L. M., Cumbo, V. R., and Takabayashi, M. (2009). Exposure to sediment enhances primary acquisition of *Symbiodinium* by asymbiotic coral larvae. *Mar. Ecol. Prog. Ser.* 377, 149–156. doi: 10.3354/meps07834

Al-Horani, F. A., Al-Moghrabi, S. M., and de Beer, D. (2003). The mechanism of calcification and its relation to photosynthesis and respiration in the scleractinian coral *Galaxea fascicularis*. *Mar. Biol.* 142, 419–426. doi: 10.1007/s00227-002-0981-8

Aloisi, G. (2008). The calcium carbonate saturation state in cyanobacterial mats throughout Earth's history. *Geochim. Cosmochim. Acta* 72, 6037–6060. doi: 10.1016/j.gca.2008.10.007

Ammann, D., Bührer, T., Schefer, U., Müller, M., and Simon, W. (1987). Intracellular neutral carrier-based Ca^{2+} microelectrode with subnanomolar

detection limit. *Pflugers Arch.* 409, 223–228. doi: 10.1007/BF00583469

Arp, G., Bissett, A., Brinkmann, N., Cousin, S., de Beer, D., Friedl, T., et al. (2010). Tufa-forming biofilms of German karstwater streams: microorganisms, exopolymers, hydrochemistry and calcification. *Geol. Soc. London Spec. Publ.* 336, 83–118. doi: 10.1144/SP336.6

Arp, G., Helms, G., Karlinska, K., Schumann, G., Reimer, A., Reitner, J., et al. (2012). Photosynthesis versus exopolymer degradation in the formation of microbialites on the Atoll of Kiritimati, Republic of Kiribati, Central Pacific. *Geomicrobiol. J.* 29, 29–65. doi: 10.1080/01490451.2010.521436

Arp, G., Reimer, A., and Reitner, J. (2001). Photosynthesis-induced biofilm calcification and calcium concentrations in Phanerozoic oceans. *Science* 292, 1701–1704. doi: 10.1126/science.1057204

Awramik, S. M., and Riding, R. (1988). Role of algal eukaryotes in subtidal columnar stromatolite formation. *Proc. Natl. Acad. Sci. U.S.A.* 85, 1327–1329. doi: 10.1073/pnas.85.5.1327

Baird, A. H., Guest, J. R., and Willis, B. L. (2009). Systematic and biogeographical patterns in the reproductive biology of scleractinian corals. *Annu. Rev. Ecol. Evol. Syst.* 40, 551–571. doi: 10.1146/annurev.ecolsys.110308.120220

Bishop, N. I. (1958). The influence of the herbicide, DCMU, on the oxygen-evolving system of photosynthesis. *Biochim. Biophys. Acta* 27, 205–206. doi: 10.,1016/0006-3002(58)90313-5

Boulotte, N. M., Dalton, S. J., Carroll, A. G., Harrison, P. L., Putnam, H. M., Peplow, L. M., et al. (2016). Exploring the *Symbiodinium* rare biosphere provides evidence for symbiont switching in reef-building corals. *ISME J.* 10, 2693–2701. doi: 10.1038/ismej.2016.54

Brehm, U., Krumbein, W. E., and Palinska, K. A. (2006). Biomicrospheres generate ooids in the laboratory. *Geomicrobiol. J.* 23, 545–550. doi: 10.1080/01490450600897302

Brewer, P. G., and Goldman, J. C. (1976). Alkalinity changes generated by phytoplankton growth. *Limnol. Oceanogr.* 21, 108–117. doi: 10.4319/lo.1976.21.1.0108

Brodersen, K. E., Lichtenberg, M., Ralph, P. J., Kühl, M., and Wangpraseurt, D. (2014). Radiative energy budget reveals high photosynthetic efficiency in symbiont-bearing corals. *J. R. Soc. Interface* 11:20130997. doi: 10.1098/rsif.2013.0997

Coffroth, M. A., Lewis, C. F., Santos, S. R., and Weaver, J. L. (2006). Environmental populations of symbiotic dinoflagellates in the genus *Symbiodinium* can initiate symbioses with reef cnidarians. *Curr. Biol.* 16, R985–R987. doi: 10.1016/j.cub.2006.10.049

Cyronak, T., and Eyre, B. D. (2016). The synergistic effects of ocean acidification and organic metabolism on calcium carbonate (CaCO3) dissolution in coral reef sediments. *Mar. Chem.* 183, 1–12. doi: 10.1016/j.marchem.2016.05.001

Davy, S. K., Allemand, D., and Weis, V. M. (2012). Cell biology of cnidarian-dinoflagellate symbiosis. *Microbiol. Mol. Biol. Rev.* 76, 229–261. doi: 10.1128/MMBR.05014-11

de Beer, D., Glud, A., Epping, E., and Kühl, M. (1997). A fast-responding CO_2 microelectrode for profiling sediments, microbial mats, and biofilms. *Limnol. Oceangr.* 42, 1590–1600. doi: 10.4319/lo.1997.42.7.1590

de Beer, D., Kühl, M., Stambler, N., and Vaki, L. (2000). A microsensor study of light enhanced Ca^{2+} uptake and photosynthesis in the reef-building hermatypic coral Favia sp. *Mar. Ecol. Prog. Ser.* 194, 75–85. doi: 10.3354/meps194075

de Bodt, C., Harlay, J., and Chou, L. (2008). Biocalcification by Emiliania huxleyi in batch culture experiments. *Mineral. Mag.* 72, 251–256. doi: 10.1180/minmag.2008.072.1.251

Decho, A. W. (2010). Overview of biopolymer-induced mineralization: what goes on in biofilms? *Ecol. Eng.*. 36, 137–144. doi: 10.1016/j.ecoleng.2009.01.003

Dupraz, C., Reid, R. P., Braissant, O., Decho, A. W., Norman, R. S., and Visscher, P. T. (2009). Processes of carbonate precipitation in modern microbial mats. *Earth Sci. Rev.* 96, 141–162. doi: 10.1016/j.earscirev.2008.10.005

Fitt, W. K., and Trench, R. K. (1983). The relation of diel patterns of cell division to diel patterns of motility in the symbiotic dinoflagellate *Symbiodinium* microadriaticum Freudenthal in culture. *New Phytol.*. 94, 421–432. doi: 10.1111/j.1469-8137.1983.tb03456.x

Flemming, H.-C., and Wingender, J. (2010). The biofilm matrix. *Nat. Rev. Microbiol.* 8, 623–633. doi: 10.1038/nrmicro2415

Friedmann, E. I. (1982). Endolithic microorganisms in the Antarctic cold desert. *Science* 215, 1045–1053. doi: 10.1126/science.215.4536.1045

Frommlet, J. C., Sousa, M. L., Alves, A., Vieira, S. I., Suggett, D. J., and Serôdio, J. (2015a). Coral symbiotic algae calcify ex hospite in partnership with bacteria. *Proc. Natl. Acad. Sci. U.S.A.* 112, 6158–6163. doi: 10.1073/pnas.1420991112

Frommlet, J., Guimaraes, B., Sousa, L., Serôdio, J., and Alves, A. (2015b). Neptunomonas phycophila sp. nov. isolated from a culture of *Symbiodinium* sp., a dinoflagellate symbiont of the sea anemone Aiptasia tagetes. *Int. J. Syst. Evol. Microbiol.* 65, 915–919. doi: 10.1099/ijs.0.000039

Gallagher, K. L., Kading, T. J., Braissant, O., Dupraz, C., and Visscher, P. T. (2012). Inside the alkalinity engine: the role of electron donors in the organomineralization potential of sulfate-reducing bacteria. *Geobiology* 10, 518–530. doi: 10.1111/j.1472-4669.2012.00342.x

Garcia-Pichel, F., Al-Horani, F. A., Farmer, J. D., Ludwig, R., and Wade, B. D. (2004). Balance between microbial calcification and metazoan bioerosion in modern stromatolitic oncolites. *Geobiology* 2, 49–57. doi: 10.1111/j.1472-4669.2004.00017.x

Gerbersdorf, S. U., and Wieprecht, S. (2015). Biostabilization of cohesive sediments: revisiting the role of abiotic conditions, physiology and diversity of microbes, polymeric secretion, and biofilm architecture. *Geobiology* 13, 68–97. doi: 10.1111/gbi.12115

Gran, G. (1950). Determination of the equivalent point in potentiometric titrations. *Acta Chem. Scand.* 4, 559–577. doi: 10.3891/acta.chem.scand.04-0559

Gran, G. (1952). Determination of the equivalence point in potentiometric titrations. Part II. *Analyst* 77, 661–671. doi: 10.1039/an9527700661

Granados-Cifuentes, C., Neigel, J., Leberg, P., and Rodriguez-Lanetty, M. (2015). Genetic diversity of free-living *Symbiodinium* in the Caribbean: the importance of habitats and seasons. *Coral Reefs* 34, 927–939. doi: 10.1007/s00338-015-1291-1

Guillard, R. R. L. (1975). "Culture of phytoplankton for feeding marine invertebrates," in *Culture of Marine Invertebrate Animals,* eds W. L. Smith and M. H. Chanley (New York, NY: Plenum Press), 26–60.

Gunnersen, J., Yellowlees, D., and Miller, D. J. (1988). The ammonium methylammonium uptake system of *Symbiodinium* microadriaticum. *Mar. Biol.* 97, 593–596. doi: 10.1007/BF00391057

Hartley, A. M., House, W. A., Leadbeater, B. S. C., and Callow, M. E. (1996). The use of microelectrodes to study the precipitation of calcite upon algal biofilms. *J. Colloid. Interf. Sci.* 183, 498–505. doi: 10.1006/jcis.1996.0573

Heldal, M., Norland, S., Erichsen, E. S., Thingstad, T. F., and Bratbak, G. (2012). An unaccounted fraction of marine biogenic $CaCO_3$ particles. *PLoS ONE* 7:e47887. doi: 10.1371/journal.pone.0047887

Jaeger-Zuern, I., and Gruberg, M. (2000). Podostemaceae depend on sticky biofilms with respect to attachment to rocks in waterfalls. *Int. J. Plant Sci.* 161, 599–607. doi: 10.1086/314292

Jeong, H. J., Lim, A. S., Yoo, Y. D., Lee, M. J., Lee, K., and Jang, T. Y. (2014). Feeding by heterotrophic dinoflagellates and ciliates on the free-living dinoflagellate *Symbiodinium* sp. *(Clade E). J. Eukaryot. Microbiol.* 61, 27–41. doi: 10.1111/jeu.12083

Jimenez, I. M., Kühl, M., Larkum, A. W., and Ralph, P. J. (2011). Effects of flow and colony morphology on the thermal boundary layer of corals. *J. R. Soc. Interface* 8, 1785–1795. doi: 10.1098/rsif.2011.0144

Kawaguchi, T., and Decho, A. W. (2002). A laboratory investigation of cyanobacterial extracellular polymeric secretions (EPS) in influencing $CaCO_3$ polymorphism. *J. Crystal Growth* 240, 230–235. doi: 10.1016/S0022-0248(02)00918-1

Knoll, A. H. (2003). Biomineralization and evolutionary history. *Rev. Mineral. Geochem.* 54, 329–356. doi: 10.2113/0540329

Köhler-Rink, S., and Kühl, M. (2000). Microsensor analysis of photosynthesis and respiration in larger symbiotic foraminifera. I The physico-chemical microenvironment of *Amphistegina lobifera, Amphisorus hemprichii* and *Marginopora vertrebralis. Mar. Biol.* 137, 473–486. doi: 10.1007/s002270000335

Köhler-Rink, S., and Kühl, M. (2001). Microsensor studies of photosynthesis and respiration in the larger foraminifera Amphistegina lobifera and Amphisorus hemprichii. *Ophelia* 55, 111–122. doi: 10.1080/00785236.2001.10409478

Koike, K. Y., Yamashita, H., Oh-Uchi, A., Tamaki, M., and Hayashibara, T. (2007). A quantitative real-time PCR method for monitoring *Symbiodinium* in the water column. *Galaxea.* 9, 1–12. doi: 10.3755/jcrs.9.1

Kühl, M., Cohen, Y., Dalsgaard, T., Jørgensen, B. B., and Revsbech, N. P. (1995). The microenvironment and photosynthesis of zooxanthellae in scleractinian corals studied with microsensors for O_2, pH and light. *Mar. Ecol. Progr. Ser.* 117, 159–172. doi: 10.3354/meps117159

LaJeunesse, T. C. (2001). Investigating the biodiversity, ecology, and phylogeny of endosymbiotic dinoflagellates in the genus *Symbiodinium* using the internal transcribed spacer region: in search of a "species" level marker. *J. Phycol.* 37, 866–880. doi: 10.1046/j.1529-8817.2001.01031.x

LaJeunesse, T. C., Lambert, G., Andersen, R. A., Coffroth, M.-A., and Galbraith, D. W. (2005). *Symbiodinium* (Pyrrhophyta) genome sizes (DNA content) are smallest among dinoflagellates. *J. Phycol.* 41, 880–886. doi: 10.1111/j.0022-3646.2005.04231.x

Lajeunesse, T. C., and Trench, R. K. (2000). The biogeography of two species of *Symbiodinium* (Freudenthal) inhabiting the intertidal anemone, *Anthopleura elegantissima* (Brandt). *Biol. Bull.* 199, 126–134. doi: 10.2307/1542872

Lawrence, J. R., Swerhone, G. D., Kuhlicke, U., and Neu, T. R. (2007). In situ evidence for microdomains in the polymer matrix of bacterial microcolonies. *Can. J. Microbiol.* 53, 450–458. doi: 10.1139/W06-146

Littman, R. A., van Oppen, M. J. H., and Willis, B. L. (2008). Methods for sampling free-living *Symbiodinium* (zooxanthellae) and their distribution and abundance at Lizard Island (Great Barrier Reef). *J. Exp. Mar. Biol. Ecol.* 364, 48–53. doi: 10.1016/j.jembe.2008.06.034

Ludwig, R., Al-Horani, F. A., de Beer, D., and Jonkers, H. M. (2005). Photosynthesis-controlled calcification in a hypersaline microbial mat. *Limnol. Oceanogr.* 50, 1836–1843. doi: 10.4319/lo.2005.50.6.1836

Mann, S. (2001). *Biomineralization: Principles and Concepts in Bioinorganic Materials Chemistry*. New York, NY: Oxford University Press.

Manning, M. M., and Gates, R. D. (2008). Diversity in populations of free-living *Symbiodinium* from a Caribbean and Pacific reef. *Limnol. Oceanogr.* 53, 1853–1861. doi: 10.4319/lo.2008.53.5.1853

Marlow, J., Peckmann, J., and Orphan, V. (2015). Autoendoliths: a distinct type of rock-hosted microbial life. *Geobiology* 13, 303–307. doi: 10.1111/gbi.12131

McConnaughey, T. A., and Whelan, J. F. (1997). Calcification generates protons for nutrient and bicarbonate uptake. *Earth Sci. Rev.* 42, 95–117. doi: 10.1016/S0012-8252(96)00036-0

Nitschke, M. R., Davy, S. K., and Ward, S. (2016). Horizontal transmission of *Symbiodinium* cells between adult and juvenile corals is aided by benthic sediment. *Coral Reefs* 35, 335–344. doi: 10.1007/s00338-015-1349-0

Peters, F., and Marrasé, C. (2000). Effects of turbulence on plankton: an overview of experimental evidence and some theoretical consideration. *Mar. Ecol. Prog. Ser.* 205, 291–306. doi: 10.3354/meps205291

Pierrot, D., Lewis, E., and Wallace, D. W. R. (2006). *Program developed for CO2 System calculations, Tech. Rep., Carbon dioxide Information Analysis Center*. Oak Ridge National Laboratory, US Department of Energy, Oak Ridge, TN.

Pochon, X., Putnam, H. M., and Gates, R. D. (2014). Multi-gene analysis of *Symbiodinium* dinoflagellates: a perspective on rarity, symbiosis, and evolution. *PeerJ.* 2:e394. doi: 10.7717/peerj.394

Rasheed, M., Wild, C., Franke, U., and Huettel, M. (2004). Benthic photosynthesis and oxygen consumption in permeable carbonate sediments at Heron Island, Great Barrier Reef, Australia. *Estuar. Coast. Shelf Sci.* 59, 139–150. doi: 10.1016/j.ecss.2003.08.013

Reid, R. P., Visscher, P. T., Decho, A. W., Stolz, J. F., Bebout, B. M., Dupraz, C., et al. (2000). The role of microbes in accretion, lamination and early lithification of modern marine stromatolites. *Nature* 406, 989–992. doi: 10.1038/35023158

Revsbech, N. P. (1989). An oxygen microsensor with a guard cathode. *Limnol. Oceangr.* 34, 474–478. doi: 10.4319/lo.1989.34.2.0474

Riding, R. (2000). Microbial carbonates: the geological record of calcified bacterial-algal mats and biofilms. *Sedimentology* 47, 179–214. doi: 10.1046/j.1365-3091.2000.00003.x

Riding, R. (2006). Cyanobacterial calcification, carbon dioxide concentrating mechanisms, and Proterozoic-Cambrian changes in atmospheric composition. *Geobiology* 4, 299–316. doi: 10.1111/j.1472-4669.2006.00087.x

Rodríguez-Román, A., and Iglesias-Prieto, R. (2005). Regulation of photochemical activity in cultured symbiotic dinoflagellates under nitrate limitation and deprivation. *Mar. Biol.* 146, 1063–1073. doi: 10.1007/s00227-004-1529-x

Rounds, S. A. (2012). "Chapter A6: Alkalinity and acid neutralizing capacity (version 4.0)," in *National Field Manual for the Collection of Water-Quality Data*, Chapter A6, eds F. D. Wilde and D. B. Radtke (Reston: Geological Survey Techniques of Water-Resources Investigations), 45.

Saghaï, A., Zivanovic, Y., Zeyen, N., Moreira, D., Benzerara, K., and , Deschamps, P., et al. (2015). Metagenome-based diversity analyses suggest a significant contribution of non-cyanobacterial lineages to carbonate precipitation in modern microbialites. *Front. Microbiol.* 6:797. doi: 10.3389/fmicb.2015.00797

Santos, S. R., Taylor, D. J., and Coffroth, M. A. (2001). Genetic comparisons of freshly isolated versus cultured symbiotic dinoflagellates: implications for extrapolating to the intact symbiosis. *J. Phycol.* 37, 900–912. doi: 10.1046/j.1529-8817.2001.00194.x

Santos, S. R., Taylor, D. J., Kinzie, R. A. III, Hidaka, M., Sakai, K., and Coffroth, M. A. (2002). Molecular phylogeny of symbiotic dinoflagellates inferred from partial chloroplast large subunit (23S)-rDNA sequences. *Mol. Phylogenet. Evol.* 23, 97–111. doi: 10.1016/S1055-7903(02)00010-6

Schoenberg, D. A., and Trench, R. K. (1980). Genetic variation in *Symbiodinium* (Gymnodinium) microadriaticum Freudenthal, and specificity in its symbiosis with marine invertebrates. I. Isoenzyme and soluble protein patterns of axenic cultures of *S. microadriaticum*. *Proc. R. Soc. B* 207, 405–427. doi: 10.1098/rspb.1980.0031

Schoon, R., Bissett, A., and de Beer, D. (2010). Resilience of pore-water chemistry and calcification in photosynthetic zones of calcifying sediments. *Limnol. Oceanogr.* 55, 377–385. doi: 10.4319/lo.2010.55.1.0377

Shashar, N., Banaszak, A. T., Lesser, M. P., and Amrami, D. (1997). Coral endolithic algae: life in a protected environment. *Pac. Sci.* 51, 167–173.

Shiraishi, F. (2012). Chemical conditions favoring photosynthesis-induced CaCO3 precipitation and implications for microbial carbonate formation in the ancient ocean. *Geochim. Cosmochim. Ac.* 77, 157–174. doi: 10.1016/j.gca.2011.11.004

Silveira, C. B., Cavalcanti, G. S., Walter, J. M., Silva-Lima, A. W., Dinsdale, E. A., Bourne, et al. (2017). Microbial processes driving coral reef organic carbon flow. *FEMS Microbiol. Rev.* 41, 575–595. doi: 10.1093/femsre/fux018

Stat, M., Carter, D., and Hoegh-Guldberg, O. (2006). The evolutionary history of *Symbiodinium* and scleractinian hosts – Symbiosis, diversity, and the effect of climate change. *Perspect. Plant. Ecol. Evol. Syst.* 8, 23–43. doi: 10.1016/j.ppees.2006.04.001

Suggett, D. J., Warner, M. E., and Leggat, W. (2017). Symbiotic dinoflagellate functional diversity mediates corals survival under ecological crisis. *Trends Ecol. Evol.* 32, 735–745. doi: 10.1016/j.tree.2017.07.013

Takabayashi, M., Adams, L. M., Pochon, X., and Gates, R. D. (2012). Genetic diversity of free-living *Symbiodinium* in surface water and sediment of Hawai'i and Florida. *Coral Reefs* 31, 157–167. doi: 10.1007/s00338-011-0832-5

Tambutté, S., Holcomb, M., Ferrier-Pagès, C., Reynaud, S., Tambutté, E., Zoccola, D., et al. (2011). Coral biomineralization: from the gene to the environment. *J. Exp. Mar. Biol. Ecol.* 408, 58–78. doi: 10.1016/j.jembe.2011.07.026

Thornhill, D. J., Howells, E. J., Wham, D. C., Steury, T. D., and Santos, S. R. (2017). Population genetics of reef coral endosymbionts (*Symbiodinium*, Dinophyceae). *Mol. Ecol.* 26, 2640–2659. doi: 10.1111/mec.14055

Thornhill, D. J., and Lord, J. B. (2010). Secondary structure models for the internal transcribed spacer (ITS) region 1 from symbiotic dinoflagellates. *Protist* 161, 434–451. doi: 10.1016/j.protis.2009.11.004

Trench, R. K. (1981). Cellular and molecular interactions in symbioses between dinoflagellates and marine invertebrates. *Pure Appl. Chem.* 53, 819–835. doi: 10.1351/pac198153040819

Trench, R. K. (1993). Microalgal-invertebrate symbioses: a review. Endocyto. *Cell Res.* 9, 135–175.

Trimborn, S., Langer, G., and Rost, B. (2007). Effect of calcium concentration and irradiance on calcification and photosynthesis in the coccolithophore *Emiliania huxleyi*. *Limnol. Oceanogr.* 52, 2285–2293. doi: 10.4319/lo.2007.52.5.2285

Tyrrell, T., and Zeebe, R. E. (2004). History of carbonate ion concentration over the last 100 million years. *Geochim. Cosmochim. Acta* 68, 3521–3530. doi: 10.1016/j.gca.2004.02.018

Venera-Ponton, D. E., Diaz-Pulido, G., Rodriguez-Lanetty, M., and Hoegh-Guldberg, O. (2010). Presence of *Symbiodinium* spp. in macroalgal microhabitats from the southern Great Barrier Reef. *Coral Reefs* 29, 1049–1060. doi: 10.1007/s00338-010-0666-6

Visscher, P. T., and Stolz, J. F. (2005). Microbial mats as bioreactors: populations, processes, and products. *Palaeogeogr. Palaeocl.* 219, 87–100. doi: 10.1016/j.palaeo.2004.10.016

Wanner, U., and Egli, T. (1990). Dynamics of microbial growth and cell composition in batch culture. *FEMS Microbiol. Rev.* 6, 19–43. doi: 10.1111/j.1574-6968.1990.tb04084.x

Webb, W. L., Newton, M., and Starr, D. (1974). Carbon dioxide exchange of *Alnus rubra*. *Oecologia* 17, 281–291. doi: 10.1007/BF00345747

Weiner, S., and Dove, P. M. (2003). "An overview of biomineralization processes and the problem of vital effect," in *Biomineralization,* eds P. M. Dove, J. J. De Yoreo, and S. Weiner (Washington, DC: Reviews in Mineralogy and Geochemistry, Mineralogical Society of America and Geochemical Society), 1–29.

Werner, U., Blazejak, A., Bird, P., Eickert, G., Schoon, R., Abed, R. M. M., et al. (2008). Microbial photosynthesis in coral reef sediments (Heron Reef, Australia). *Estuar. Coast. Shelf S.* 76, 876–888. doi: 10.1016/j.ecss.2007.08.015

Yamashita, H., and Koike, K. (2013). Genetic identity of free-living *Symbiodinium* obtained over a broad latitudinal range in the Japanese coast. *Phycol. Res.* 61, 68–80. doi: 10.1111/pre.12004

Yellowlees, D., Rees, T. A., and Leggat, W. (2008). Metabolic interactions between algal symbionts and invertebrate hosts. *Plant Cell Environ.* 31, 679–694. doi: 10.1111/j.1365-3040.2008.01802.x

Zondervan, I., Zeebe, R. E., Rost, B., and Riebesell, U. (2001). Decreasing marine biogenic calcification: a negative feedback on rising atmospheric pCO_2. *Glob. Biogeochem. Cycles* 15, 507–516. doi: 10.1029/2000GB001321

Conflict of Interest Statement: The authors declare that the research was conducted in the absence of any commercial or financial relationships that could be construed as a potential conflict of interest.

frontiers in Microbiology

ORIGINAL RESEARCH
published: 22 May 2018
doi: 10.3389/fmicb.2018.00796

Key Role of Alphaproteobacteria and Cyanobacteria in the Formation of Stromatolites of Lake Dziani Dzaha (Mayotte, Western Indian Ocean)

Emmanuelle Gérard[1], Siham De Goeyse[1], Mylène Hugoni[2], Hélène Agogué[3], Laurent Richard[4], Vincent Milesi[1], François Guyot[5], Léna Lecourt[1], Stephan Borensztajn[1], Marie-Béatrice Joseph[1], Thomas Leclerc[1], Gérard Sarazin[1], Didier Jézéquel[1], Christophe Leboulanger[6] and Magali Ader[1]*

[1] UMR CNRS 7154 Institut de Physique du Globe de Paris, Sorbonne Paris Cité, Université Paris Diderot, Centre National de la Recherche Scientifique, Paris, France, [2] Université Lyon 1, UMR CNRS 5557 / INRA 1418, Ecologie Microbienne, Villeurbanne, France, [3] UMR 7266 CNRS-Université de la Rochelle, LIttoral ENvironnement Et Sociétés, La Rochelle, France, [4] School of Mining and Geosciences, Nazarbayev University, Astana, Kazakhstan, [5] Museum National d'Histoire Naturelle, Institut de Minéralogie, de Physique des Matériaux et de Cosmochimie, UMR 7590 CNRS Sorbonne Universités, Université Pierre et Marie Curie, Institut de Recherche pour le Développement UMR 206, Paris, France, [6] UMR MARBEC, IRD, Ifremer, CNRS, Université de Montpellier, Sète, France

OPEN ACCESS

Edited by:
Christophe Dupraz, Stockholm University, Sweden

Reviewed by:
Trinity L. Hamilton, University of Minnesota Twin Cities, United States
Virginia Helena Albarracín, Center for Electron Microscopy (CIME), Argentina

***Correspondence:**
Emmanuelle Gérard
emgerard@ipgp.fr

Specialty section:
This article was submitted to Aquatic Microbiology, a section of the journal Frontiers in Microbiology

Received: *06 January 2018*
Accepted: *09 April 2018*
Published: *22 May 2018*

Citation:
Gérard E, De Goeyse S, Hugoni M, Agogué H, Richard L, Milesi V, Guyot F, Lecourt L, Borensztajn S, Joseph M-B, Leclerc T, Sarazin G, Jézéquel D, Leboulanger C and Ader M (2018) Key Role of Alphaproteobacteria and Cyanobacteria in the Formation of Stromatolites of Lake Dziani Dzaha (Mayotte, Western Indian Ocean). Front. Microbiol. 9:796. doi: 10.3389/fmicb.2018.00796

Lake Dziani Dzaha is a thalassohaline tropical crater lake located on the "Petite Terre" Island of Mayotte (Comoros archipelago, Western Indian Ocean). Stromatolites are actively growing in the shallow waters of the lake shores. These stromatolites are mainly composed of aragonite with lesser proportions of hydromagnesite, calcite, dolomite, and phyllosilicates. They are morphologically and texturally diverse ranging from tabular covered by a cauliflower-like crust to columnar ones with a smooth surface. High-throughput sequencing of bacterial and archaeal 16S rRNA genes combined with confocal laser scanning microscopy (CLSM) analysis revealed that the microbial composition of the mats associated with the stromatolites was clearly distinct from that of the *Arthrospira*-dominated lake water. Unicellular-colonial Cyanobacteria belonging to the *Xenococcus* genus of the Pleurocapsales order were detected in the cauliflower crust mats, whereas filamentous Cyanobacteria belonging to the *Leptolyngbya* genus were found in the smooth surface mats. Observations using CLSM, scanning electron microscopy (SEM) and Raman spectroscopy indicated that the cauliflower texture consists of laminations of aragonite, magnesium-silicate phase and hydromagnesite. The associated microbial mat, as confirmed by laser microdissection and whole-genome amplification (WGA), is composed of Pleurocapsales coated by abundant filamentous and coccoid Alphaproteobacteria. These phototrophic Alphaproteobacteria promote the precipitation of aragonite in which they become incrusted. In contrast, the Pleurocapsales are not calcifying but instead accumulate silicon and magnesium in their sheaths, which may be responsible for the formation of the Mg-silicate phase found in the cauliflower crust. We therefore propose that Pleurocapsales and

Alphaproteobacteria are involved in the formation of two distinct mineral phases present in the cauliflower texture: Mg-silicate and aragonite, respectively. These results point out the role of phototrophic Alphaproteobacteria in the formation of stromatolites, which may open new perspective for the analysis of the fossil record.

Keywords: stromatolites, alkaline lake, Pleurocapsales, Mg-silicate, Alphaproteobacteria, anoxygenic phototrophic bacteria, aragonite, hydromagnesite

INTRODUCTION

Microbialites are sedimentary structures which construction is microbially mediated, and may show stromatolitic (laminated) or thrombolytic (clotted) fabrics (Burne and Moore, 1987). Fossil microbialites, and in particular fossil stromatolites, can be traced back to 3700 Myr ago (Nutman et al., 2016) and are thus considered among the oldest fossil records of life on Earth (Allwood et al., 2006; Nutman et al., 2016). They were particularly abundant during the Proterozoic Eon, especially around 1250 Myr ago (Riding, 2006; Peters et al., 2017). By analogy with modern stromatolites developing today, it has been proposed that fossil stromatolites were formed by microbial mats dominated by Cyanobacteria (Altermann et al., 2006; Bosak et al., 2009). However, Precambrian and Cambrian stromatolites rarely contain observable fossils of microorganisms. Presumed microfossils constituted of organic globules associated with aragonite were found in 2724-Myr-old stromatolites from the Tumbiana Formation (Fortescue Group, Australia) (Lepot et al., 2008). The oldest potential filamentous carbonate-encrusted cells identified in the Transvaal Supergroup in South Africa have been dated at 2,500–2,300 Myr (Klein et al., 1987). However, the earliest undisputed occurrence of fossil filamentous Cyanobacteria (*Girvanella* genus) is much less ancient, dated at 750–700 Myr (Riding, 1982). The lack of microfossils in ancient stromatolites has resulted in the proposition of other hypotheses for their formation, including formation by anoxygenic photosynthesis (Bosak et al., 2007) or purely abiotic processes (Lowe, 1994; Grotzinger and Rothman, 1996; McLoughlin et al., 2008). Although environmental conditions undoubtedly changed through geological time, detailed biological and mineralogical studies of modern microbialites developing in marine or lacustrine environments offer a unique opportunity to obtain new information which will help in the interpretation of the fossil record.

Cyanobacteria play a key role in the formation of microbialites, being usually the main primary producers in the microbial mats associated with modern stromatolites. They have been shown to influence the shape of growing stromatolites in different ways. First, filamentous Cyanobacteria can trap and bind sedimentary particles and depending on the length of filaments, the size of the trapped sedimentary particles is variable (Franz et al., 2015). Consequently, it has been postulated that the grain size distributions observed in fossil stromatolites were determined by the size of Cyanobacteria or other filamentous microorganisms (Franz et al., 2015). Second, the conical shape of certain modern stromatolites has indeed been attributed to thin filamentous Cyanobacteria forming small cones in response to light, even in the absence of lithification (Walter et al., 1976; Bosak et al., 2009). Finally, the oxygen produced by Cyanobacteria at the tip of lithifying cones induces the formation of contorted laminations, in which oxygen bubbles can be trapped (Bosak et al., 2009). Such contorted laminations with supposed fossil oxygen bubbles were traced back in 2700-Myr-old stromatolites from the Meentheena Member of the Tumbiana Formation in Australia but not in older formations (Bosak et al., 2009).

Furthermore, the metabolism of Cyanobacteria can favor the formation of carbonate minerals. Photosynthetic activity is indeed an alkalinizing process that may promote carbonate precipitation in the vicinity of Cyanobacteria (Dupraz and Visscher, 2005; Visscher and Stolz, 2005; Dupraz et al., 2009). During photosynthesis, Cyanobacteria assimilate CO_2 mainly through the active import of bicarbonate ions and less through the passive diffusion of CO_2 into their cells (Jansson and Northen, 2010). Within the cell, carbonic anhydrase catalyzes the conversion of bicarbonate ions to CO_2 and produces OH^-. It is hypothesized that both CO_2 uptake and OH^- release may induce a rise of pH and an increase of the activity of the CO_3^{2-} ion and therefore the possible precipitation of Mg or Ca carbonate depending on cation availability (Merz, 1992; Riding, 2006; Jansson and Northen, 2010). The nature of the precipitating carbonate can be influenced by some Cyanobacteria as those belonging to the Pleurocapsales and Chroococcales orders. In the microbialites from the hyperalkaline Lake Alchichica in Mexico, Pleurocapsales induce the formation of aragonite, in which they become encrusted, at the expense of hydromagnesite which is the major component of the microbialites (Couradeau et al., 2013; Gerard et al., 2013; Saghai et al., 2015). This may be due to the properties of the sheaths of the Pleurocapsales in which cations can be accumulated.

The mechanism of lamination formation in growing stromatolites is still an open question and seems to involve different species of Cyanobacteria and heterotrophic bacteria. A model for the formation of biologically induced laminations was proposed for the Bahamian stromatolites. It involves the temporal succession of three different microbial mats dominated by filamentous Cyanobacteria trapping and binding carbonate sand grains, subsequently by heterotrophic bacteria forming thin crusts of microcrystalline aragonite, and finally by coccoid endolithic Cyanobacteria favoring cementation of the grains (Reid et al., 2000). It has been shown that heterotrophic degradation of extracellular polymeric substances (EPS) by

sulfate reducing bacteria (SRB) was a major factor controlling mineral precipitation and micritization in microbial mats associated with stromatolites [for reviews (Decho, 2010; Dupraz and Visscher, 2005)]. Recently, it has been observed that the highest degrees of lamination were related to the presence of coccoid Cyanobacteria and pervasive aragonite precipitation in the microbial mats rather than to the presence of filamentous Cyanobacteria trapping and binding carbonate sand grains (Suosaari et al., 2016).

Comparatively to Cyanobacteria, less attention has been paid to the calcifying role of the phototrophic purple bacteria which are abundant in stromatolitic mats (e.g., Papineau et al., 2005; Saghai et al., 2015). Yet, the Earth atmosphere and ocean were probably largely anoxic before 2,500 Myr and anoxygenic phototrophy most likely predated oxygenic photosynthesis (Blankenship, 2010; Xiong et al., 2000). Phototrophic bacteria may thus have been important stromatolite builders prior to the appearance of oxygenic photosynthesis. It that sense, it has been shown experimentally that both anoxygenic photosynthetic and photoheterotrophic purple bacteria are able to promote carbonate precipitation (Bosak et al., 2007; Bundeleva et al., 2012). However, experimental evidence suggests also that they should be far less efficient in promoting carbonate precipitation than oxygenic photosynthetic Cyanobacteria in natural environments (Bundeleva et al., 2012). The potential role of phototrophic bacteria in the formation of stromatolites remains thus unclear and, so far, evidences based on the study of modern microbialites indicating that their formation may occur through anoxygenic photosynthesis are still lacking.

We describe for the first time the microbialites developing in Lake Dziani Dzaha, a tropical crater lake located on Mayotte Island (Comoros archipelago, Western Indian Ocean). Dziani Dzaha is a shallow and turbid lake located in close proximity to the ocean (Leboulanger et al., 2017). The lake water has a salinity 1.5 times that of sea water, a high level of dissolved organic matter (average DOC $= 7186 \pm 843$ μmol L^{-1}) and an extremely high alkalinity (100 times seawater) (Leboulanger et al., 2017). The green color of the lake is due to a permanent bloom of filamentous Cyanobacteria belonging to the *Arthrospira* genus (Leboulanger et al., 2017). Stromatolites with variable degrees of laminations and different surface morphologies are developing on the shores of the lake. Most of the dome-shaped or small columnar stromatolites are covered by a hard cauliflower-like crust, whereas the large columnar stromatolites are characterized by friable, smooth to granular surfaces. The purpose of the present study was: (i) to determine if the different types of stromatolites were associated with different types of microbial mats, (ii) to identify particular microbial lineages responsible for the building of stromatolites by trapping, binding or precipitating minerals, (iii) to discriminate among the mineral phases of the stromatolites those for which the formation may have been bioinduced. Toward this aim, the microbial diversity of the different mats was analyzed using Illumina high-throughput 16S rRNA gene amplicon sequencing. The bulk mineralogy of the stromatolites was determined using X-ray powder diffraction and the geochemistry of the lake water was interpreted in terms of mineral-solution equilibria. Detailed observations using confocal laser scanning microscopy (CLSM), Raman spectroscopy, scanning electron microscopy (SEM), and laser microdissection permitted us to explore the relations between the formation of mineral phases and the different microbial lineages at the microscale.

MATERIALS AND METHODS

Sample Collection and Fixation

Lake Dziani Dzaha is located on the island of "Petite Terre" (12°46′15.6″S; 45° 17′19.2″E), belonging to the island complex of Mayotte (Leboulanger et al., 2017). The field campaign of October 2014 was conducted at the end of the dry season, when the lake water was at its lowest level. The water column was not stratified, except for dissolved oxygen which decreased with depth (55.5, 0.3, and 0 μM at surface, 1 and 2.5 m below the surface, respectively). A number of stromatolites were emerged from the lake, while others were still immerged. All stromatolite samples presented in this study were taken from the oxic zone between 0 and 1 m water depth in October 2014. The annual drawdown of the lake is about 70 cm, the highest water level being reached during the rainy season from December to March. Consequently, the stromatolites sampled above 30 cm depth in October 2014 were probably located at the transition between the oxic and the anoxic zones when the lake was at its highest level. The dissolved oxygen concentrations recorded in April 2014 were 405, 88.8, and 0 μM, at surface, 1 and 2.5 m below the surface, respectively. Stromatolites were sampled all around the lake (**Figure 1** and Supplementary Table S1). On the west shore, only scarce flat crusts were found and were not analyzed in this study.

Three stromatolites covered by a cauliflower crust (one flat and two small columnar of about 20 cm high) and the top of three columnar stromatolites of about 1 m high without cauliflower crust (two granular and one smooth) were chosen (**Figure 1**, Supplementary Figures S2, S3, and Supplementary Table S1) and prepared in three different ways for CLSM. Samples were fixed immediately on the field in RNAlater® (Thermo Fisher Scientific, Waltham, MA, United States), 50% ethanol in phosphate buffered saline or formalin neutral buffered 10% (Merck KGa, Darmstadt, Germany) solutions and preserved on ice (for a maximum period of 2 h) before being transferred in a freezer at −20°C. Samples for DNA extractions were not fixed; they were kept at 4°C (for a maximum period of 2 h) and transferred at −20°C as soon as possible. Samples were fixed in RNAlater® to preserve the pigmentation of Cyanobacteria and Purple Bacteria. Otherwise, samples were fixed in formaldehyde 4% and ethanol 50%, and then embedded in LR-white resin (Polysciences, Warrington, PA, United States) to analyze correlations between microorganisms and mineral phases by concomitant CLSM/Raman and SEM analysis as previously described in Couradeau et al. (2013), Gerard et al. (2013). Formaldehyde/ethanol fixed samples were dried by the CO_2 critical-point method using Emcpd300 (Leica Microsystems GmbH, Wetzlar, Germany) at Institut de Biologie Paris-Seine (IBPS, Paris, France) for SEM analysis. Finally, unfixed stromatolites were also included in epoxy resin for SEM analysis.

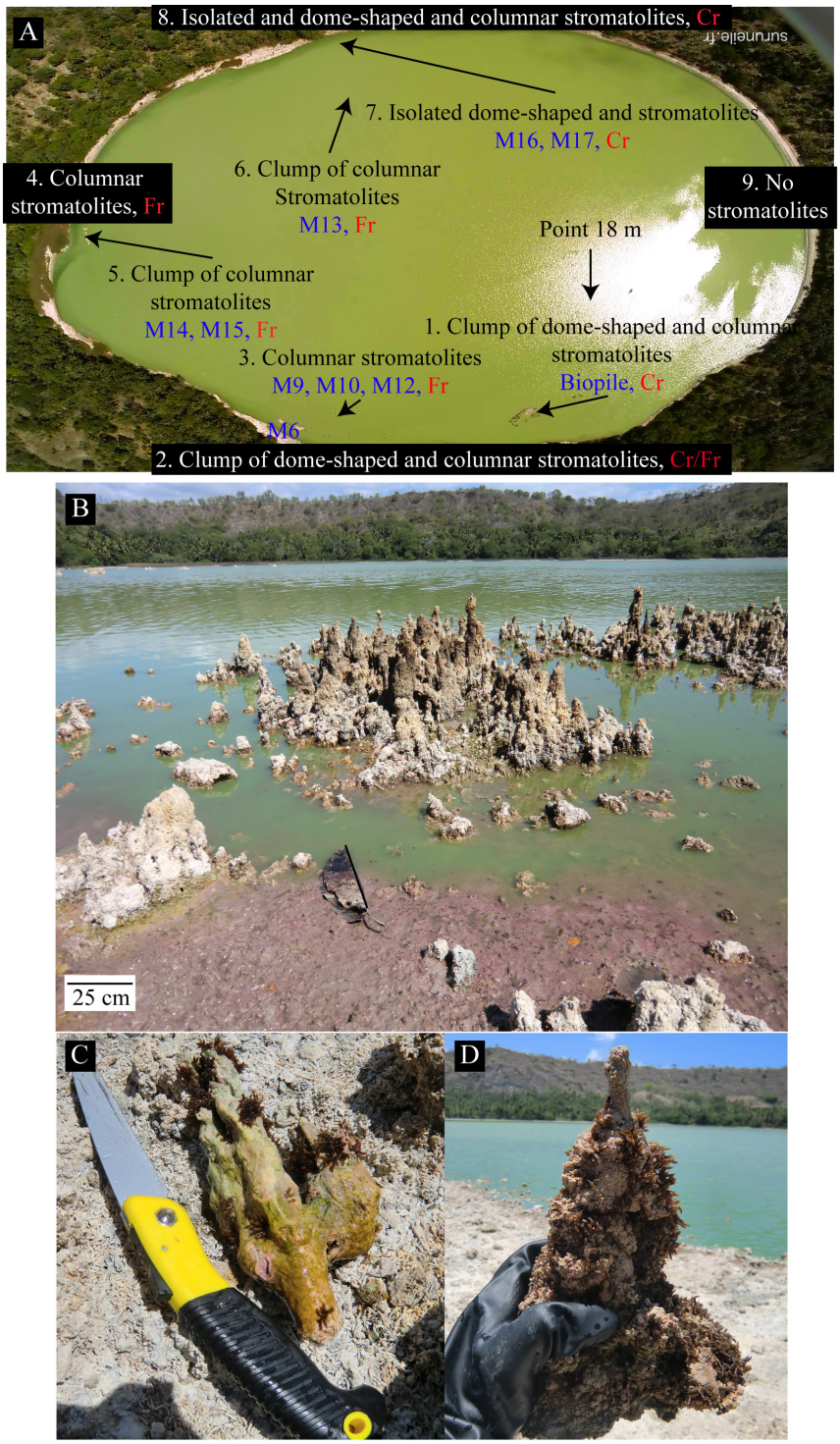

FIGURE 1 | (A) Aerial view of the Dziani Dzaha Lake in October 2014 showing the positions of the sampled stromatolites (M6–M19) and the points where water was collected (point 18 m) for the chemical analysis. A general description of the types of the different stromatolites found on the North (8), South (2), West (4), and East (9) shores is indicated in the red boxes. No stromatolites or only scarce friable flat crusts were found on the East shore. Cr and Fr describe the surface of stromatolites, Cr: crust, Fr: friable. **(B)** Global view of the lake with clumps of emerged columnar stromatolites on the south part of the lake. The green color of the water is due to the high abundance of Cyanobacteria. The purple color visible on the shore may be related to purple bacteria. **(C)** A columnar stromatolite (M6) collected 30 cm under the water surface covered by a greenish to purple microbial mat. **(D)** A columnar stromatolite (M16), collected 20 cm under the water surface with a cauliflower-like texture covered by a purple to green thin biofilm. Note that both stromatolites are partly covered by fly pupae except the top few centimeters of the M16 stromatolite that was probably formed after the last fly laying.

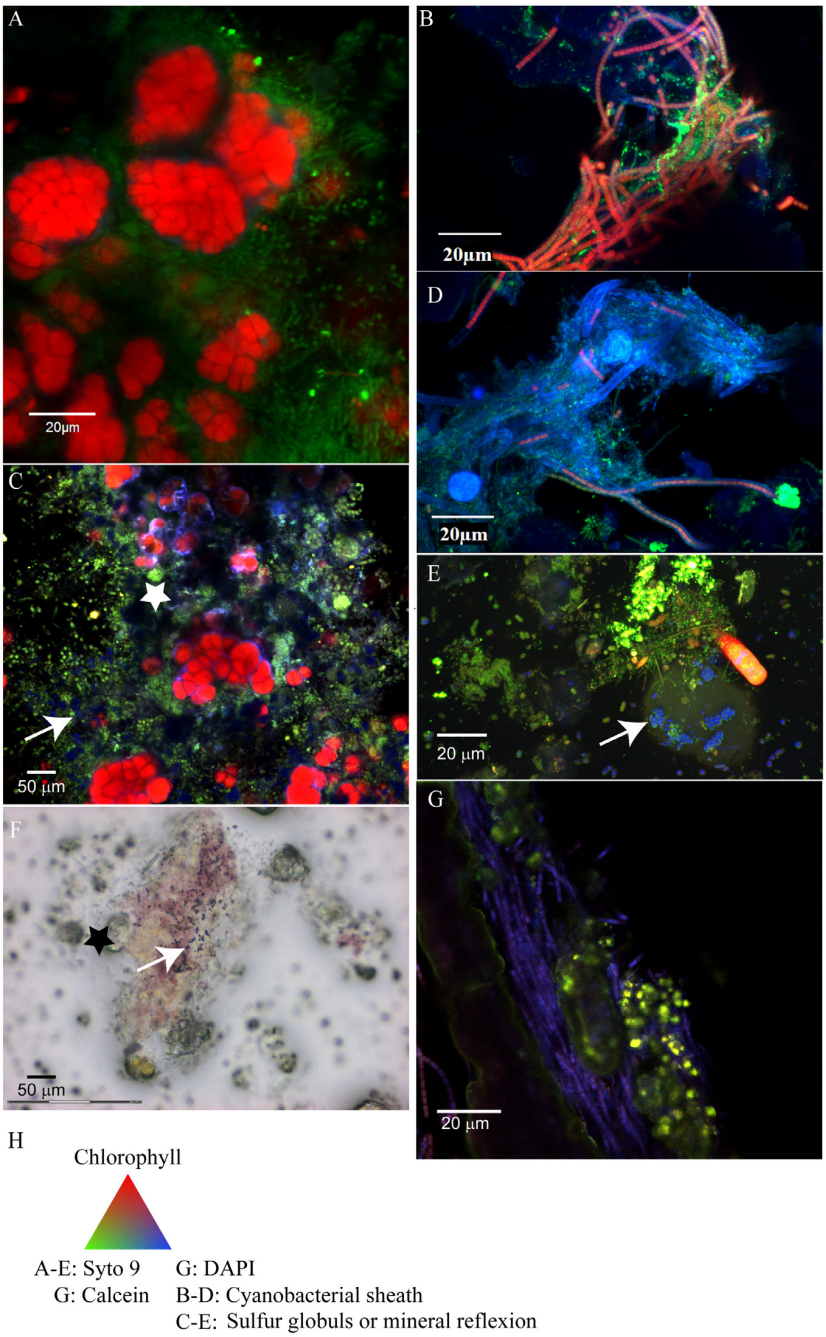

FIGURE 2 | Confocal laser scanning microscopy (CLSM) and optical images of the microbial mats associated with the cauliflower-like crust **(A,C,F)** or columnar stromatolites with friable surfaces **(B,D,E,G)**. **(A)** Pleurocapsales (red) coated by filamentous microorganisms (green) located at the surface of the microbial mat associated with M17 fixed with formaldehyde and ethanol and stained with Syto9® (green) observed with CLSM. **(B)** Filamentous Cyanobacteria (red) with persistent sheath (blue) detected by CLSM in the microbial mat associated with M12 fixed with formaldehyde and ethanol and stained with Syto9® (the Cyanobacteria detected in M15 had the same morphology as in M12). **(C)** Microbial mat associated with M17 fixed with RNAlater®, stained with Syto9® and observed with CLSM where micrometric coccoid microorganisms are visible in the empty sheath of Pleurocapsales (white star) and in association with refractive dots (blue, white arrow) which are probably elemental sulfur globules produced by the coccoid microorganisms. **(D)** Filamentous Cyanobacteria detected in the smooth surface of M10 which arbor shorter trichomes than Cyanobacteria detected on M12 and M15. **(F)** Microbial mat associated with M17 fixed with RNAlater and observed with optical microscopy in which elemental sulfur grains (black arrow) associated with the purple bacteria located around the Pleurocapsales cells (black star) are visible. **(E)** Red microbial mat associated with M15 fixed with RNA later and stained with Syto9® in which refractive grains (blue, white arrow) in rod shaped bacteria probably corresponding to elemental sulfur globules are visible. **(G)** Transversal cutting of M10 stained with DAPI (blue) and calcein (green), included in LR white resin and observed with CLSM where aragonite grains stained by calcein (white arrow) trapped by filamentous Cyanobacteria stained with DAPI are visible. **(H)** Colors associated with the CLSM images.

X-Ray Powder Diffraction (XRPD)

The bulk mineralogy of microbialites was determined by XRPD. About 1 g of each sample was ground in an agate mortar. The powder was deposited on a single crystal silicon sample holder. Measurements were performed with an Empyrean Panalytical diffractometer using Cu-Kα radiation. Data were recorded between 4 and 90° (2 θ) with a step of 0.013° and a total counting time of half an hour. The PANalytical Highscore Plus software (Degen et al., 2014) was used for background subtraction, peak identification and matching with XRD patterns of reference compounds from the International Crystal Structure Database (ICSD, FIZ Karlsruhe, Germany; US Institute of Standards and Technology, United States).

Physicochemical Parameters of the Lake Dziani Dzaha Water

The following physicochemical parameters of the lake water have been measured during five different campaigns (2012–2015): pH, temperature, concentrations of dissolved O_2, major anionic and cationic species, conductivity and alkalinity. All the methods used are described in Leboulanger et al. (2017). Vertical profiles were taken using either a MPP350 probe connected to a Multi 350i data logger (WTW GmbH) or an YSI 600XLM probe (YSI) to measure pH, dissolved O_2, temperature and conductivity. The total alkalinity was determined by titration with 0.01 M HCl after 100 times dilution. Major cations were analyzed to ±5% by inductively coupled plasma atomic emission spectroscopy (ICP-AES iCAP6200 Thermo Fisher). Sulfate was measured to ±3% using 20-fold diluted samples by ionic chromatography (ICS 1100 Thermo Fisher). Chloride was titrated using a standard $AgNO_3$ solution (0.5 M), after acidification with analytical grade HNO_3 (to prevent Ag_2CO_3 precipitation). Dissolved silicate and soluble reactive phosphorus were measured using classical methods of spectrometry developed for seawater analysis (Amino and Kérouel, 2004). Dissolved organic carbon (DOC) was measured using a TOC analyzer (Shimadzu, TOC V CHS/CHN) after acidification with 1% H_3PO_4 and 1/10 dilution. The concentration of aqueous hydrogen sulfide [$\Sigma H_2Saq = H_2Saq + HS^- + S_2^-$ (trace) + RS(-II) ion complexes, clusters, nanoparticles, and colloids] was determined by a colorimetric method described in Reese et al. (2011). In this method, hydrogen sulfide reacts with N,N′-dimethyl-1,4-phenylene-diamine in $H_2N\text{-}SO_3H$ (at 120 g/l). Leucomethylene blue complex is formed and oxidized by ferric ions to methylene blue having a maximum absorbance at 664 nm.

Thermodynamic Analysis

The saturation state of the surface waters with respect to selected mineral phases was evaluated from the relation:

$$\Omega = \log\frac{Q}{K}$$

where **Ω** is the saturation index, Q is the reaction quotient or ion activity product, and K is the equilibrium constant for the reaction of dissolution of the mineral under consideration. The reaction quotient is defined by:

$$Q = \prod_i a_i^{n_i}$$

where a_i is the activity of the subscripted aqueous species and n_i is the stoichiometric coefficient of that species in the reaction. Values of a_i were computed with the PHREEQC computer program (Parkhurst and Appelo, 1999) using an extended Debye–Hückel model for the activity coefficients. Mineral stability diagrams were constructed using equilibrium constants calculated with the SUPCRT92 program (Johnson et al., 1992).

DNA Extraction and High-Throughput Sequencing

DNA extractions were performed using the Powersoil DNA kit (Mo Bio, Carlsbad, CA, United States). The biofilms associated with the stromatolites were discriminated according to their color (green or red) using a sterile scalpel only when this was possible. For the stromatolites M10, M12, and M15 a distinct green or red area of a few centimeters was distinguished (Supplementary Figures S3D,G). The mats were dissected in accordance to the colors observed (M10, M12, and M15). It was not possible to separate the different colors from the cauliflower crust for DNA extraction because the green and purple/pink colors were overlapping (M16 and M17).

Amplification of the V3–V5 region of the 16S rRNA genes was performed for both Bacteria and Archaea, using the primers 357F (Schuurman et al., 2004) and 926R (Walters et al., 2016) and 519F and 915R (Hugoni et al., 2015), respectively. High-throughput sequencing was achieved after a multiplexing step, using a HiSeq Rapid Run 300bp PE technology on an Illumina HiSeq 2500 system (GATC Biotech, Konstanz, Germany).

Bioinformatic Analysis and Sequence Processing

Bacterial and archaeal 16S rRNA paired-end reads were merged with a maximum of 10% mismatches in the overlap region using FLASH (Magoc and Salzberg, 2011). Denoising procedures consisted in discarding reads with no expected length (i.e., expected size between 450 and 580 bp, 370 and 580 bp, for bacterial and archaeal 16S rRNA genes, respectively) and the ones containing ambiguous bases (N). After dereplication, the clusterisation tool ran with SWARM (Mahe et al., 2014). In the present work, aggregation distance was equal to 3. Chimeras were then removed using VSEARCH (Rognes et al., 2016) and low abundance sequences were filtered at 0.005% [i.e., to keep OTUs accounting for at least 0.005% of all sequences (Bokulich et al., 2013), in order to remove singletons from the datasets]. Taxonomic affiliation was performed with both RDP Classifier (Wang et al., 2007) and Blastn+ (Camacho et al., 2009) against the 128 SILVA database (Pruesse et al., 2007). This procedure was automated in the FROGS pipeline (Escudie et al., 2017).

To compare samples, a normalization procedure was applied to randomly resample down to 51,730 and 21,673 sequences for bacterial and archaeal 16S rRNA genes, respectively.

Differences in bacterial community structure were visualized using non-metric multidimensional scaling (NMDS) ordinations on abundance-based (Bray–Curtis) dissimilarity matrices. Using non-parametric permutation-based multivariate analysis of variance (PERMANOVA, function adonis in R package vegan, (Anderson, 2001) on abundance-based (Bray–Curtis) dissimilarity matrices, we tested for significant differences in community structure. These analyses were performed with the VEGAN package[1] in R.

The Illumina sequence data generated in this study were deposited here: http://www.ebi.ac.uk/ena/data/view/PRJEB25249. The GenBank accession numbers for the Sanger sequence data are MH036348 for T12-5C and MH036349 for M17-60.

Scanning Electron Microscopy (SEM)

Samples for SEM were divided into three groups: the first group was dried using the CO_2 critical-point method; the second embedded in LR-white resin and cut in 1–2 mm thick slices, and the third embedded in epoxy, cut and mounted on microscopy slides, and all samples were coated with a 15 nm carbon layer.

The SEM was performed at the Service Commun de Microscopie Electronique à Balayage (UPMC, Paris, France) using a Zeiss SUPRA 55 VP Field Emission Scanning Electron Microscope. Images were collected using secondary electron detectors (Everhart-Thornley for high voltage mode, VPSE for variable pressure mode and InLens for low voltage mode) and a backscattered electron detector (AsB). Accelerating voltage ranged from 3 to 15 kV at variable pressures and high current (up to 1 nA) or was fixed at 3 kV under high vacuum and low current (down to 10 pA). Alternatively, a Zeiss EVO MA 10 microscope equipped with both a back-scattered electron (BSE) detector and a secondary electron (SE2) detector, as well as a Zeiss Auriga FEG-FIB microscope were used (Plateforme de Microscopie Electronique, IPGP, Paris, France). Elemental microanalyses and mapping were performed using Energy Dispersive X-ray (EDX) spectrometers (PGT Sahara and Bruker Quanta 200).

Combined CLSM and Raman Spectrometry Imaging

Confocal laser scanning microscopy and Raman analyses were performed as previously described in Gerard et al. (2013) using an Olympus FluoView FV1000 confocal microscope (Olympus Tokyo, Japan) combined with an Invia Raman Spectrometer (Renishaw, Wotton-under-Edge, United Kingdom). Samples fixed with RNAlater® or formaldehyde, unstained or stained were observed using an oil immersion objective (Olympus UPSLAPO X60). DNA staining of microorganisms were performed either with DAPI (4′,6-diamidino-2-phenylindole) at 1 to 10 $\mu g.ml^{-1}$ or Syto9® Green Fluorescent Nucleic Acid Stain at 10 μM (Thermo Fisher Scientific, Waltham, MA, United States) for 10 min at room temperature in the dark, followed by two washings with sterile Milli-Q water. For concomitant CSLM/Raman image acquisitions on samples embedded in LR-white resin, a water immersion LUMPLFL 60×W objective (Olympus; 60× magnification) was used. Fluorescence image stacks were obtained with concomitant excitation at wavelengths of 405, 488, and 543 nm by collecting the emitted fluorescence between 425–475, 500–530, and 560–660 nm, respectively. For Raman analyses we used a 785 nm laser source and proceeded as described in Gerard et al. (2013). Briefly, dynamic line–scanning Raman mapping (Renishaw Streamline) was performed in the range 387–1538 cm^{-1} by scanning the sample over selected areas (20 s pt^{-1}) by using a motorized PRIORTM stage. Laser intensity was set at 300 mW. Light was 1200 grooves per millimeter and the signal was analyzed with a RECAM charge-coupled device detector. Compositional maps representing the intensity distributions of characteristic peaks were determined using the software Wire 3.2.

Laser Microdissection, Whole Genome Amplification (WGA) and Cloning-Sequencing of 16S RNA Genes

Small individual Pleurocapsales colonies and associated coccoid and filamentous cells were isolated using a Zeiss PALM MicroBeam apparatus installed in a clean room. We then used the REPLI-g Single Cell Kit (Qiagen, Hilden, Germany) to amplify whole genomic DNA of the microdissected cells. Bacterial 16S rRNA genes were then amplified by PCR using the bacterial specific primer 27F (5′-AGAGTTTGATCCTGGCTCAG-3′) and with the universal prokaryotic reverse primer 1492R (5′-GGTTACCTTGTTACGACTT-3′). One microliter of 1/10 diluted amplified genomic DNA was used in a reaction buffer volume of 25 μL containing dNTPs (10 nmol each), 20 pmol of each primer and 1 U of GoTaq polymerase (Promega, France). PCR was performed under the following conditions: 35 cycles (denaturation at 94°C for 15 s, annealing at 55°C for 30 s, extension at 72°C for 2 min) preceded by 2 min denaturation at 94°C, and followed by 7 min extension at 72°C. Cloning was done using the Topo TA Cloning system (Thermo Fisher Scientific, Waltham, MA, United States) following the instructions provided by the manufacturer. After plating, positive transformants were screened by PCR amplification of inserts using flanking vector primers and the PCR products were partially sequenced (≈700 bp) by GATC Biotech (Konstanz, Germany) using flanking vector primer T7 (5′-TAATACGACTCACTATAGGG-3′). At least one representative clone per phylotype or Operational Taxonomic Unit (OTU, group of sequences sharing >97% identity) was fully sequenced using flanking vector primer M13R (5′-CAGGAAACAGCTATGAC -3′) for detailed phylogenetic analysis.

Phylogenetic Analyses

Taxonomic affiliations at the phylum level were first obtained by comparing several portions of partial 16S rRNA gene sequences with sequences of the GenBank database using BLAST [Basic Local Alignment Search Tool (Altschul et al.,

[1]http://cran.r-project.org/web/packages/vegan/index.html

1997)]. Representative clones of the dominant phyla were then fully sequenced and analyzed with the ARB software (Ludwig et al., 2004) by using the 123 SILVA database (Pruesse et al., 2007; Quast et al., 2013; Yilmaz et al., 2014). The sequences were first aligned with the SINA online aligner (Pruesse et al., 2012) and then added in the ARB guide tree using the ARB parsimony tool. The phylogenetic tree was constructed by adding to the aligned sequences, sequences of the closest cultivated bacteria and environmental clones in the RAxML (Randomized Accelerated Maximum Likelihood) program (Stamatakis et al., 2008) by using the GTRCAT substitution model. The bootstrap values were calculated from 1,000 replicates.

RESULTS

Lake Chemistry

The water chemistry of the lake, previously described in Leboulanger et al. (2017), is characterized by high levels of Na^+, K^+, Mg^{2+}, and Cl^-, and low levels of Ca^{2+} (**Table 1**). It is noticeable that the concentration of Ca^{2+} in the lake water increased during the rainy season (Leboulanger et al., 2017) whereas the concentrations of Mg^{2+} stayed relatively constant.

Although values reported in the literature for the solubility product K_{sp} of hydromagnesite at 25°C appear to disagree by as much as 10 log units (Gautier et al., 2014), a van't Hoff interpolation of experimental K_{sp} values recently reported by these authors at 25 and 50°C yields $\log K_{sp} = -37.5 \pm 0.5$ at 30°C for the reaction

$$Mg_5(CO_3)_4(OH)_2{\cdot}4H_2O = 5Mg^{2+} + 4CO_3^{2-} + 2OH^- + 4H_2O$$

Values calculated in the present study for the logarithm of the ion activity product range between $\log Q = -35.74$ and $\log Q = -37.50$, the corresponding saturation index ranging between $\Omega = 0$ and $\Omega = 1.73$ and suggesting that the lake waters are at equilibrium or slightly supersaturated with respect to hydromagnesite. The solubility product of aragonite at 30°C is $\log K_{sp} = -8.37$ (Plummer and Busenberg, 1982). The calculated ion activity products range between $\log Q = -7.03$ and $\log Q = -8.01$, corresponding to saturation index values ranging between $\Omega = 0.36$ and $\Omega = 1.34$. Hence, the lake waters also appear to be close to equilibrium with or slightly supersaturated with respect to aragonite. Although the uncertainties on the solubility product of hydromagnesite do not allow to draw a definitive conclusion, it is possible that the lower concentrations of Ca^{2+} observed toward the end of the dry season would displace the equilibrium

$$4CaCO_3 + 5Mg^{2+} + 6H_2O = Mg_5(CO_3)_4(OH)_2{\cdot}4H_2O + 4Ca^{2+} + 2H^+ \quad (1)$$

toward the right, favoring the replacement of aragonite by hydromagnesite (Supplementary Figure S1A).

The lake waters are highly supersaturated with respect to talc and sepiolite (Supplementary Figure S1B), but these phases may not be representative of the material formed in the stromatolites.

Stromatolite Morphologies and Textures

Stromatolites were detected in abundance all around the lake near the shores except on the East shore (**Figure 1**). Numerous distinct structures were detected and classified in two main categories: stromatolites with a hard cauliflower-like surface that we named cauliflower crust (**Figure 1**, Supplementary Figure S2, and Supplementary Table S1) and stromatolites with friable surfaces (**Figure 1**, Supplementary Figure S3, and Supplementary Table S1).

The Cauliflower Texture Is Specifically Associated With the Presence of Alphaproteobacteria and Pleurocapsales

The Cyanobacteria associated with the cauliflower crust exhibited characteristic shape of Cyanobacteria belonging to the Pleurocapsales order in the three samples observed (M16, M17, and biopile), i.e., colonies of coalescent globular cells with thick sheath mother cells and smaller daughter cells called baeocytes (**Figure 2**). The Pleurocapsales colonies were closely associated with 20 μm long filamentous microorganisms growing on their sheaths (**Figure 2**) in which electron transparent inclusions were detected, usually interpreted as poly-β-hydroxybutyrate deposits (D'Amelio et al., 1987; Tian et al., 2005) (Supplementary Figure S4). In areas where empty Pleurocapsales sheaths were present, due to Pleurocapsales cells degradation or the release of baeocytes, numerous morphologically different cells were also detected by Syto9® staining (**Figure 2**). Most of them were small pink to purple cocci or rods able to form short chains growing in close association with the Pleurocapsales colonies and some invading the empty Pleurocapsales sheaths. These small pink cocci were sometimes associated with highly reflective particles, which are most probably composed of elemental sulfur globules (**Figures 2C,F**) that could be formed through the oxidation of sulfide by purple bacteria (Dahl and Prange, 2006). These highly reflective particles were detected only in samples fixed with RNAlater®, not in samples fixed with ethanol. Elemental sulfur globules indeed dissolve during ethanol dehydration and are

TABLE 1 | Dissolved anions, cations, silicon, and alkalinity in μM for October 2014 in Dziani Dzaha water.

T°C	pH	Alkalinity	Na^+	K^+	Cl^-	Mg^2	$SO_4{}^{2-}$	Si	Ca^{2+} *	H_2S
31	9.18	258865	1016177	38608	892153	4724	2615	228	54	31

**Data missing for October 2014; this value is estimated with the average Ca concentration at the end of dry season in 2010, 2011, and 2015.*

often destroyed during usual EDS analyses (Dahl and Prange, 2006), we were thus unable to analyze them using EDS.

The microbial community composition analyses based on 16S rRNA genes Illumina sequencing confirmed the observations made by CLSM. The rarefaction curves for the number of bacterial and archaeal OTUs detected in each sample indicated that a complete coverage of microbial composition was reached or nearly so (Supplementary Figure S5). Cyanobacteria affiliated to the Pleurocapsales order and to the *Xenococcus* genus were systematically and exclusively detected in cauliflower crusts of both stromatolites analyzed. They account for 99% and almost 100% of all the Cyanobacteria recovered in the DNA extract from the cauliflower crusts of the M16 and M17 stromatolites, respectively. Filamentous Cyanobacteria belonging to the *Leptolyngbya* genus were largely dominant in other stromatolites (M10, M12, and M15, **Figure 3**). However, filamentous Cyanobacteria belonging to the *Arthrospira* genus, dominant in the lake water, were not abundant in stromatolites. The maximal proportion of *Arthrospira* was retrieved in M15, in which they accounted for 24% of Cyanobacterial sequences.

The non-metric multidimensional scaling (NMDS) ordination of bacterial community including Cyanobacteria showed that M16 and M17 had similar bacterial community composition, distinct from those of the other stromatolites and of the lake water (Supplementary Figure S6). Alphaproteobacteria were largely dominant in M16 and M17 (around 60% of the bacterial sequences) and more abundant than Cyanobacteria (only 11 and 12% in M16 and M17, respectively). Alphaproteobacteria were also three times more abundant in M16 and M17 than in the other stromatolites. The most abundant Alphaproteobacteria detected in M16 and M17 belonged to the Rhodobacterales order and to the Rhodobacteraceae family (71 and 76% of the Alphaproteobacteria in M16 and M17, respectively) and mostly to several unknown genus (87 and 90% of Rhodobacterales, **Figure 3**). The second most abundant alphaproteobacterial family detected in M16 and M17 is Rhodospirillales *incertae sedis*, with bacteria belonging to the *Candidatus Alysiosphaera* genus (18 and 25% of all Alphaproteobacteria in M16 and M17, respectively). This genus comprises filamentous-flock-forming bacteria described from wastewater treatment plants, which are known to accumulate polyhydroxyalkanoate granules (Kragelund et al., 2006).

Alphaproteobacteria were also abundantly detected in stromatolites with friable surfaces (up to 27% of all bacterial 16S sequences detected in M15 green). They belonged mainly to the same unknown genus of the Rhodobacteraceae family as in M16 and M17, but they were also more diverse and encompassed species affiliated to *Roseibaca* (21–22% of the Rhodobacteraceae) which members produce bacteriochlorophyll a (Labrenz et al., 2009). Firmicutes belonging to the Clostridiales order were also detected in large amounts (up to 29% of all bacterial 16S sequences detected in M15 red), as well as Bacteroidetes (up to 22% of all bacterial 16S sequences detected in M12 red). Notably, filamentous Cyanobacteria stayed dominant in all the green parts of these stromatolites (92%, 45 and 30% in M10, M12 green and M15 green, respectively).

As observed for bacteria, archaeal communities detected in stromatolites were different depending on the presence or absence of the cauliflower crust. Archaea were detected in M17 but not in M16 samples. Haloalkaliphilic Archaea belonging to the Halobacteriales order and the *Natronococcus* genus constituted 98% of the archaeal sequences in M17. We recovered nine different classes of Archaea in M10, M12, and M15 (Supplementary Figure S7). This phylogenetic variety of Archaea was not detected previously in the microbialites of Alchichica Lake which represent a similar environment (Couradeau et al., 2011; Saghai et al., 2015).

Regarding eukaryotes, the presence of diatoms and green algae belonging to the *Picocystis* genus (data not shown) sometimes abundantly entombed was reported in all types of stromatolite using CLSM and SEM. Furthermore, patches of fly pupae were present (probably belonging to the Ephydridae family, common in brine waters) and their entombment contributes significantly to the stromatolites construction (Supplementary Figures S2, S3). For this study, only the surfaces of stromatolites devoid of fly pupae were analyzed.

Mineral Composition of Stromatolites

The bulk analysis of six different stromatolites by XRPD revealed that they were dominated by aragonite together with small amounts of hydromagnesite, halite, calcite, Mg-calcite and dolomite (Supplementary Figure S8). Hydromagnesite was only present in the cauliflower crusts where the consortia of Pleurocapsales and Alphaproteobacteria were found. In one occurrence 27% of albite was also detected, which we interpret as a detrital input incrusted in the stromatolite. Halite most probably results from the drying of the pore water since stromatolites were not rinsed in distilled water prior to XRPD analyses.

Minerals/Microorganisms Interactions

In the Cauliflower Crust

Using CLSM, Raman and SEM, three distinct mineral phases were observed in the cauliflower crust: aragonite, hydromagnesite and a magnesium silicate phase probably poorly crystallized, since it was not detected by XRPD.

This millimetric cauliflower crust was always associated with an endolithic intermixed green and purple microbial mat (Supplementary Figure S2F). This microbial mat developed also above the crust (Supplementary Figures S2E,F). Below the water surface, the crust was pink pigmented. In some zones, the green biofilm developed above the pink crust, while in some others, the pink crust developed above the green mat and fly pupae (Supplementary Figure S2E). This suggests that the green mat and the pink crust grew up alternatively (Supplementary Figure S2E). In this pink crust, aragonite was the main mineral phase detected, with spikes of hydromagnesite growing on it (**Figure 4**). Relics of micrometric coccoid cells which have been used as nucleation sites for aragonite precipitation were detected in the center of aragonite grains (**Figure 4A**). No relics of Pleurocapsales were found

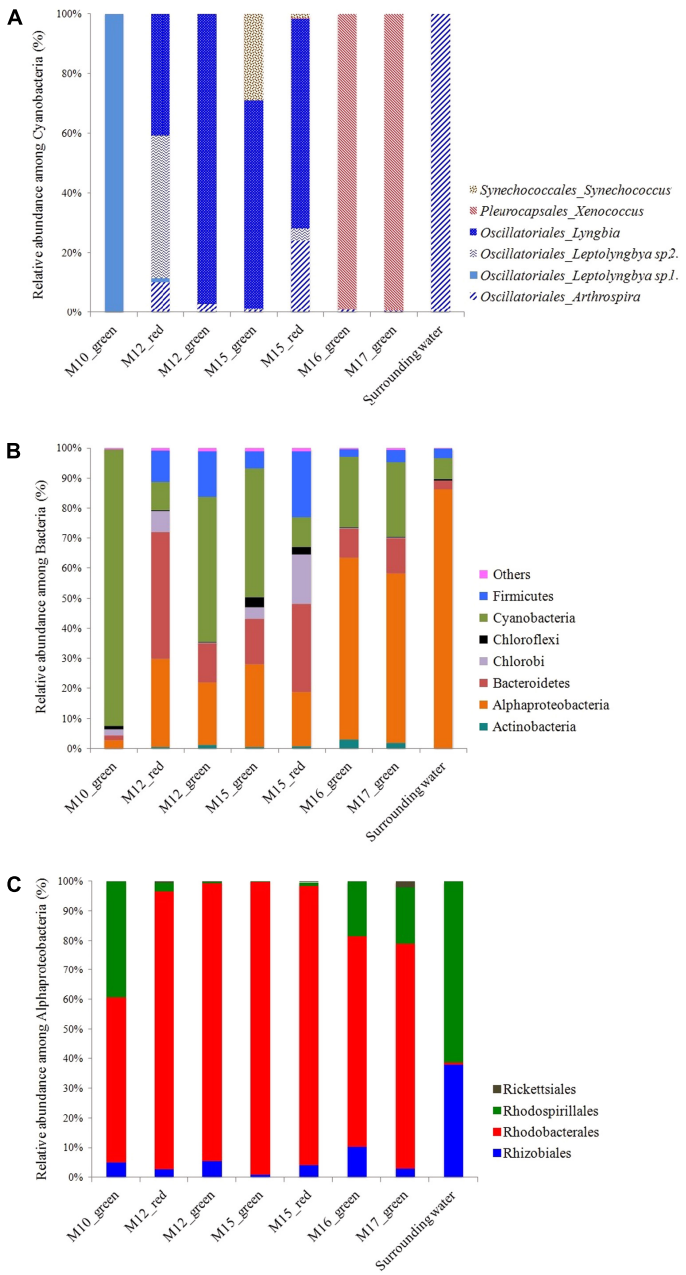

FIGURE 3 | (A) Relative abundance of the different cyanobacterial classes inferred from 16S rRNA gene sequences in Dziani Dzaha stromatolites. **(B)** Proportion of sequences affiliated with major bacterial phyla (defined as >0.2% of total sequence number). **(C)** Relative abundance of the different alphaproteobacterial orders inferred from 16S rRNA genes sequences in Dziani Dzaha stromatolites.

in the pink crust, this suggests that the pink aragonite crust grew only in association with the pink pigmented Alphaproteobacteria. Indeed, Alphaproteobacteria are the most abundant microorganisms detected in the 16S RNA gene sequences retrieved from the cauliflower crusts. Below the green microbial mat (Supplementary Figures S2E,F), where Pleurocapsales were detected, aragonite laminations of a few microns were identified in the first hundreds of microns of the upper crust, alternating with hydromagnesite mixed with a silicon rich phase (**Figures 5**–**7** and Supplementary Figures S9, S12). In this phase, embedded relics of Pleurocapsales colonies were observed (**Figures 5**, **6** and Supplementary Figure S12). The EDS analyses of this phase indicated a Mg-silicate phase (Supplementary Figure S10) with a Mg/Si average ratio of 0.90. The repartition of silicon and magnesium in the chemical maps of stromatolites showed that this phase, abundant in the cauliflower crust (**Figure 6** and Supplementary Figures S9, S12), was related to the presence of the Pleurocapsales colonies. Silicon

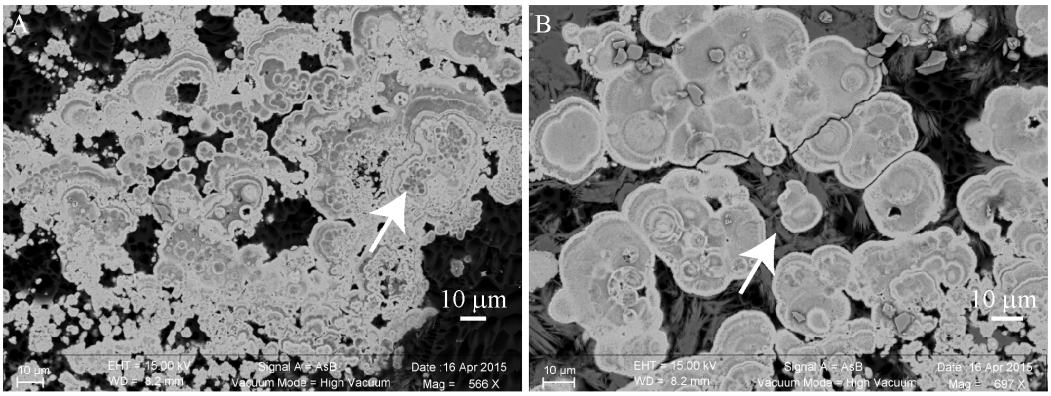

FIGURE 4 | Scanning electron microscopy (SEM) images of a transversal cutting of the cauliflower-like crust from a pink colored area of M17, embedded in LR white resin, showing the mineral distribution in the microbial mat. **(A)** Relics of micrometric cells (white arrow) that seemingly served as nucleation points for aragonite (bright gray) precipitation. **(B)** Hydromagnesite needles (dark gray, white arrow) growing on aragonite grains.

accumulation was evidenced in the sheaths of Pleurocapsales, correlated with magnesium in several occurrences (**Figure 6** and Supplementary Figure S12). This accumulation increased from the top to the bottom of the mat seemingly coinciding with the decay of the mat. Preserved Pleurocapsales sheaths with the silicate phase were identified in M16 below 200 µm layers of aragonite and hydromagnesite, but the sheaths were empty without any photosynthetic pigment detectable (**Figure 6**). Using SEM, formation of submicrometric magnesium-and-silicon rich beads around the sheaths of Pleurocapsales were furthermore identified (**Figure 5** and Supplementary Figure S11).

The SEM-EDS maps showed that calcium was negatively correlated with silicon and magnesium (**Figure 6** and Supplementary Figures S9, S12). At the top of the mat, aragonite particles were detected by SEM and Raman spectroscopy around Pleurocapsales colonies, where coccoid microorganisms were also detected by CLSM (**Figure 7**). Scarce aragonite particles were also detected in some Pleurocapsales cells that were probably decaying. The precipitation of aragonite thus seems to be favored by coccoid microorganisms which may also be at the origin of the micrometric organic globules detected in the pink aragonite crust (**Figure 4**).

Raman and CLSM analyses showed in addition that some aragonite particles were clustered around the filamentous Alphaproteobacteria at the top of the mat (**Figure 7**). It is noticeable that these filamentous bacteria were strongly stained with calcein, revealing the presence of calcium or magnesium (**Figure 7**). Raman cartography showed that they were also associated with hydromagnesite (**Figure 7**).

More generally, SEM and Raman spectroscopy measurements were consistent with the growth of hydromagnesite needles on aragonite particles at the top of the green mat or in the pink crust (**Figures 4**, **7**). Underneath the cauliflower crust, in the deepest part of stromatolites, aragonite was the only mineral detected in friable laminations (Supplementary Figures S2F, S9); both hydromagnesite and the Mg-Si phase were absent.

In the Columnar Stromatolites With Smooth and Granular Friable Surfaces

Aragonite grains were mainly trapped by filamentous Cyanobacteria (**Figure 2**), or massive aragonite precipitation and entombment of the whole biofilms were observed in areas devoid of Cyanobacteria (**Figure 8**). This resulted in purple and green laminations of aragonite of variable densities and coloration (Supplementary Figure S3F). The transversal cutting of the aragonite grains at the surface of stromatolites showed that their center was sometimes enriched in magnesium in M10, M12, and M15 (**Figure 8**). This magnesium enrichment in the center of the aragonite grains was also detected in the deepest parts of M17 and M16 under the cauliflower crusts (not shown), suggesting that they could have been formed previously by the same type of community as observed at the surface of M10, M12, or M15. The only mineral phases containing magnesium detected in the friable stromatolites surfaces were magnesian calcite and dolomite, both in small amounts (Supplementary Figure S8). A morphological correlation can be done between the whole biofilm embedded in aragonite and the center of the aragonite grains rich in magnesium (**Figure 8**), suggesting that the magnesium accumulation could be linked to the presence of the entombed microorganisms. No magnesium silicate phase was detected by SEM.

Microdissection and Whole Genome Amplification

In order to gain more information on the phylogeny and metabolic capabilities of the microorganisms associated with the cauliflower crusts, laser microdissection was used to isolate consortia of Pleurocapsales with closely associated coccoid microorganisms (Supplementary Figure S13). The coccoid microorganisms were pink to purple pigmented (**Figure 2**). After whole genome amplification and 16S RNA gene analysis, one species of Pleurocapsales (in five different amplifications) and one species of Rhodobacteraceae (in two different amplifications) were identified.

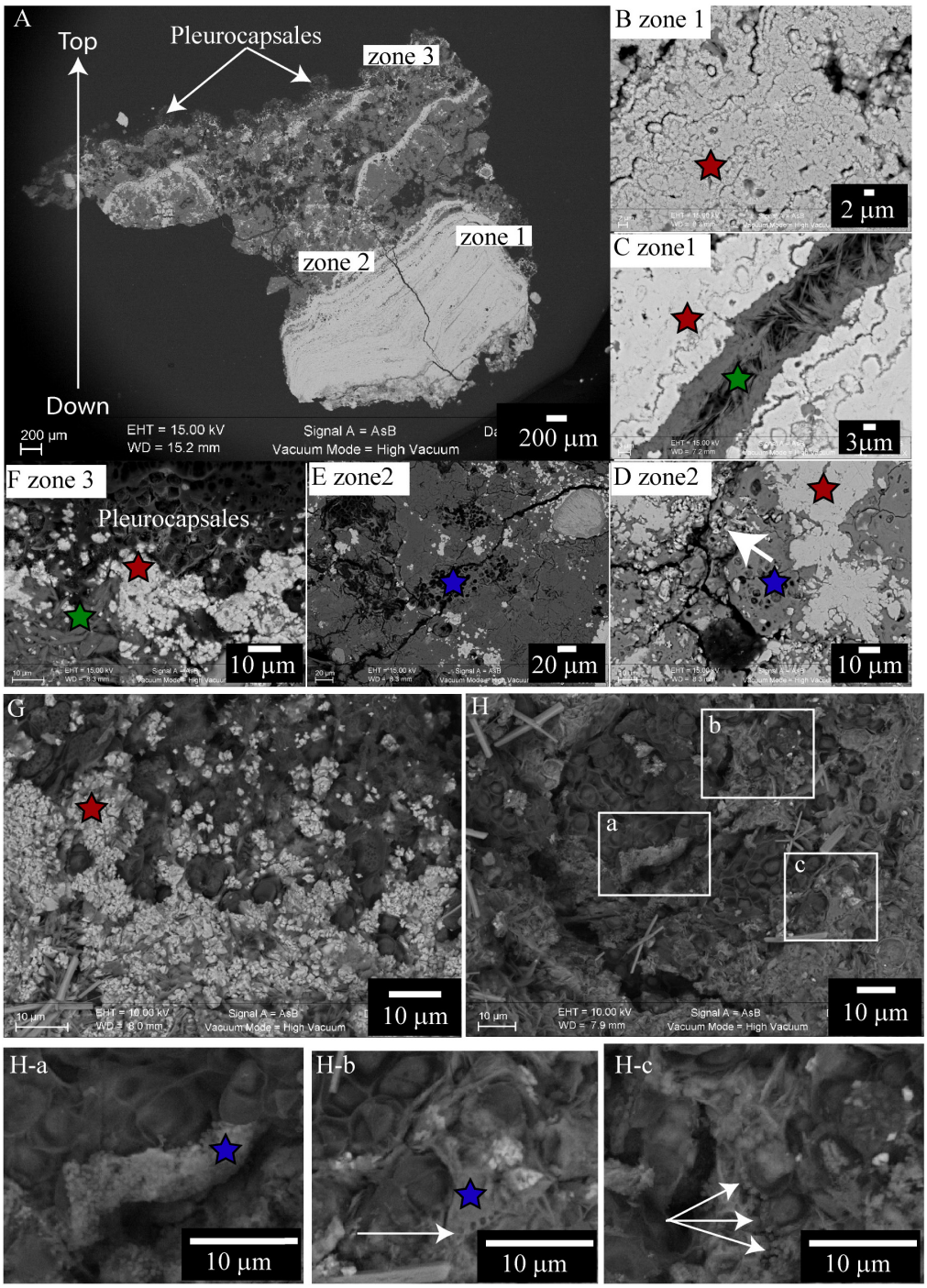

FIGURE 5 | Scanning electron microscopy images of a transversal cutting of the cauliflower-like crust from a green/pink colored area of M17, embedded in LR white resin **(A–F)**, or top of the microbial mat of M17 desiccated to the critical point **(G,H)**, showing the mineral distribution in the microbial mat. In all the images red stars correspond to aragonite; green stars correspond to hydromagnesite; blue stars to magnesium silicate. **(A)** Global view of the globular crust (at 15 KV, AsB detector), bright gray indicates the Ca rich phases and dark gray the Mg rich phases. Colonies of Pleurocapsales are visible on the top of the transversal cutting. **(B–F)** Enlargement of the transversal cutting shown in **(A)**. **(B)** Aragonite zone at the bottom of the transversal cutting with relics of micrometric cells (at 15 KV, AsB detector). **(C)** Hydromagnesite needles grown on aragonite (at 15 KV, AsB detector). **(D)** Aragonite grown on relics of Pleurocapsales cells embedded in a magnesium silicate phase (at 15 KV, AsB detector). **(E)** Relics of Pleurocapsales colonies embedded in a magnesium silicate phase (at 15 KV, AsB detector). **(F)** Aragonite precipitated at the bottom of Pleurocapsales colonies and hydromagnesite needles on aragonite (at 15 KV, AsB detector). **(G)** Aragonite precipitated around Pleurocapsales cells at the surface of the microbial mat (at 10 KV, AsB detector). **(H)** Pleurocapsales embedded in a magnesium silicate phase (at 10 KV, AsB detector). **(H-a – H-c)** Enlargements of the SEM image shown in **(H)** highlighting Mg-Si beads around the Pleurocapsales cells. White arrow in **(H-b)** indicates holes in the silicate magnesium phase. White arrows in **(H-c)** indicate silicate beads around Pleurocapsales cells.

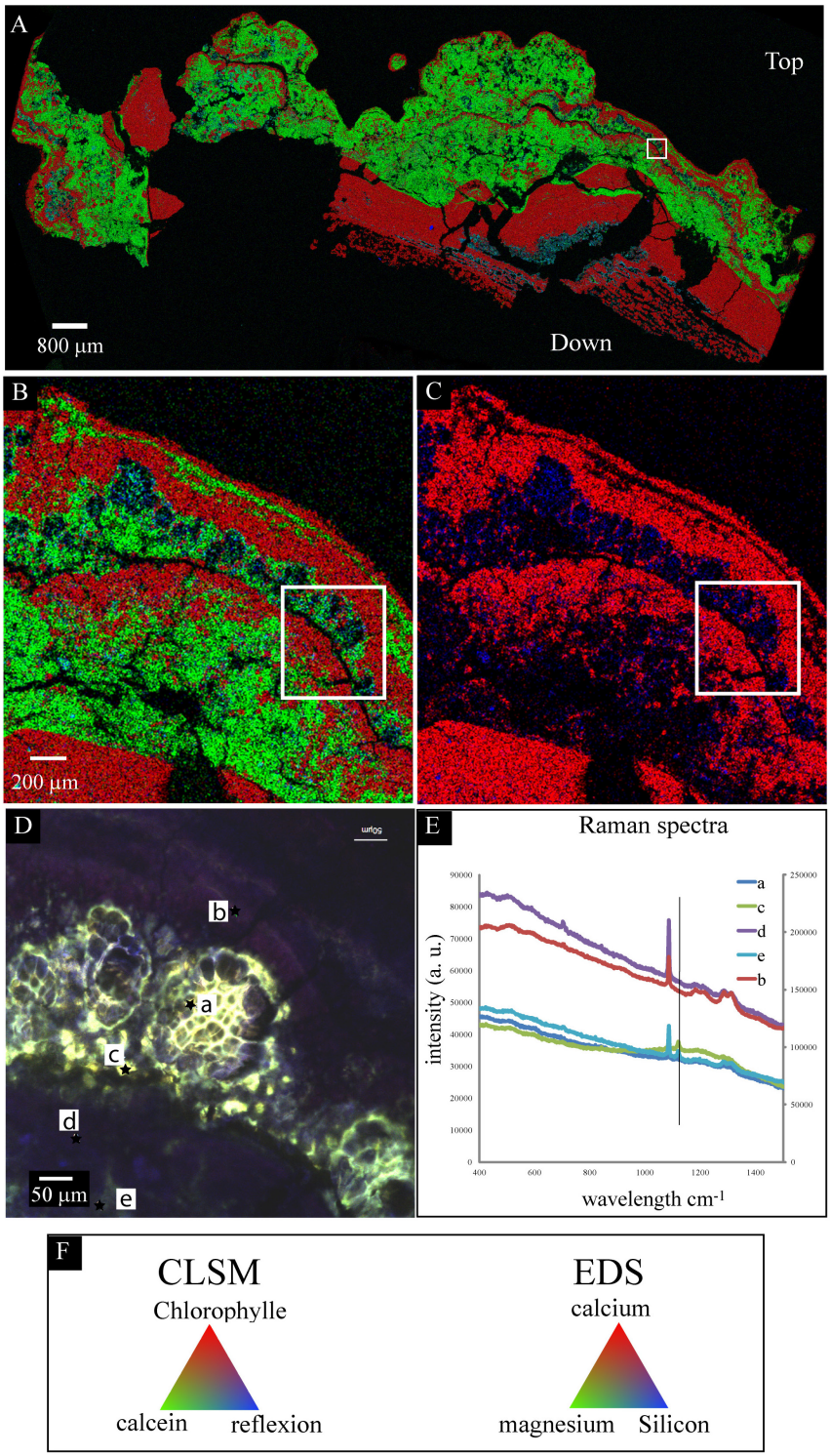

FIGURE 6 | Scanning electron microscopy-EDS/CLSM/Raman on the same transversal cutting of the globular crust of M16 embedded in LR white resin, showing the accumulation of silicon in the sheaths of Pleurocapsales. **(A,B)** SEM-EDS mappings of calcium, magnesium, and silicon. **(C)** SEM-EDS mapping of calcium and silicon in the same area as in **(A,B)**. **(B,C)** Are enlargement of the mapping shown in **(A)**. The white rectangle shows exactly the same zone in the four images **(A–D)**. In **(A–C)**, the EDS mapping shows that calcium and silicon were negatively correlated whereas magnesium and silicon were sometimes positively correlated. **(D)** CLSM image of the same area showing that the silicon accumulated in the empty sheaths of Pleurocapsales. **(E)** Raman spectra of points a, b, c, d, and e highlighted in **(D)**. The vertical line fits the specific peak for hydromagnesite detected at points a, e, and c. The other peaks are specific for aragonite that was detected at all points. **(F)** Colors associated with the CLSM **(D)** and EDS mappings **(A–C)**.

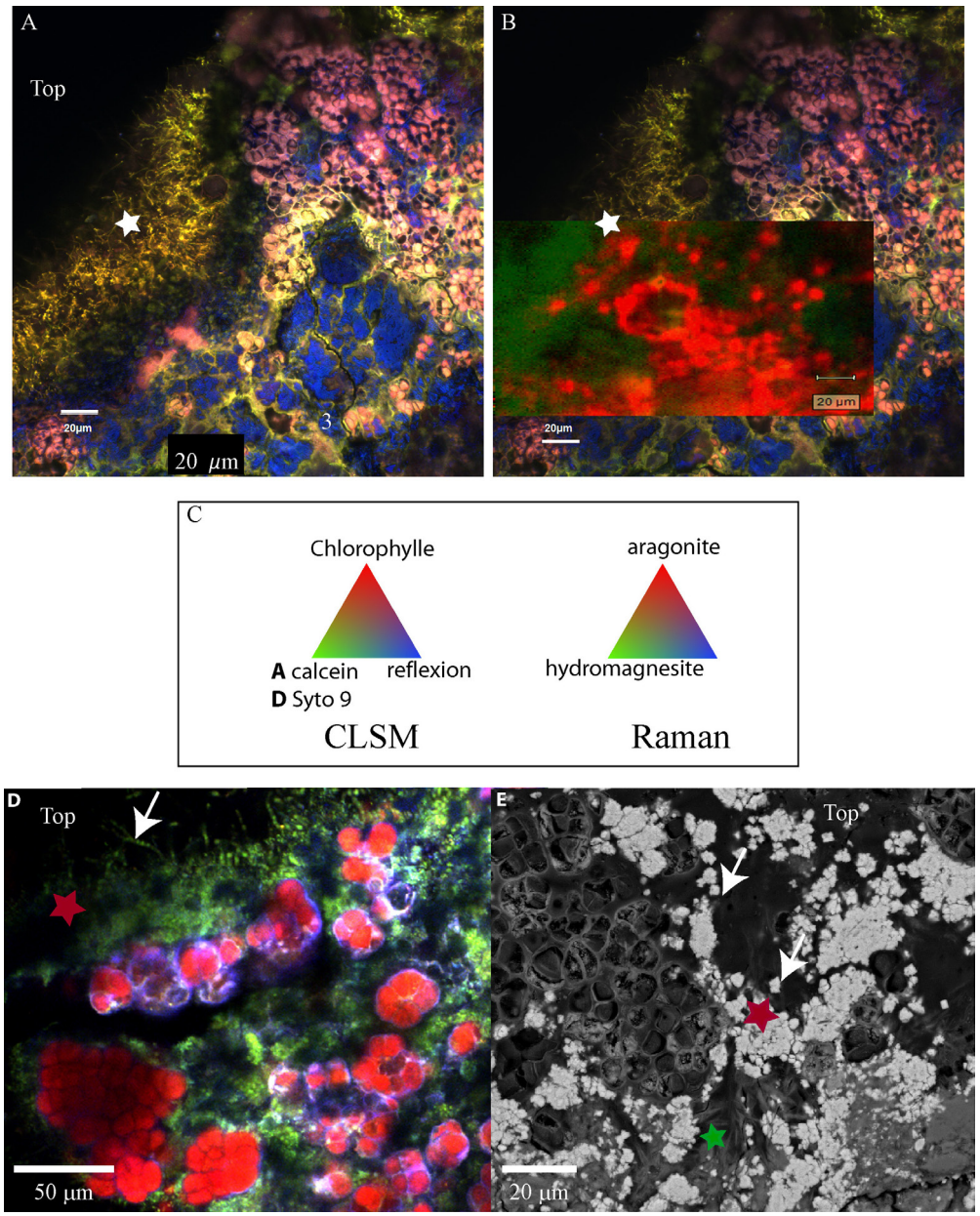

FIGURE 7 | (A) Confocal laser scanning microscopy image of a transversal cutting of the globular crust of M17 embedded in LR white resin, showing the Pleurocapsales colonies (pink/red) topped with grains stained with calcein (green) and filamentous Alphaproteobacteria also strongly stained with calcein (green, white star). **(B)** Raman mapping superimposed on the CLSM image showing the distribution of the aragonite grains around the Pleurocapsales colonies. **(C)** Colors associated with the CLSM and Raman mappings. **(D)** CLSM image of the microbial mat fixed in RNAlater and stained with Syto9 (green) showing the distribution of the Pleurocapsales colonies topped with coccoid microorganisms associated with aragonite grains and filamentous cells on the top. **(E)** SEM image (at 15 KV, AsB detector) on the same transversal cutting shown in **(A,B)**, showing aragonite grains associated with the coccoid and filamentous microorganisms associated with the Pleurocapsales. Red stars correspond to aragonite and the green star to hydromagnesite in all images.

The Pleurocapsales species shares 98% 16S rRNA gene identities with one Pleurocapsales species associated with the microbialites of Alchichica Lake in Mexico (accession number JN825323). However, this Pleurocapsales species was not the main calcifying Pleurocapsales (accession number JN825326) detected in the Alchichica microbialites (Supplementary Figure S13). The Dziani Dzaha Pleurocapsales is also closely related to Pleurocapsales species belonging to the microbial community involved in marble dissolution (accession numbers JQ404416 and JQ404419) (Supplementary Figure S13). The Pleurocapsales detected in Dziani Dzaha stromatolites could thus have the capacity of colonizing and dissolving calcium carbonate. However, we did not detect clear evidence of Pleurocapsales boring activity in the samples collected.

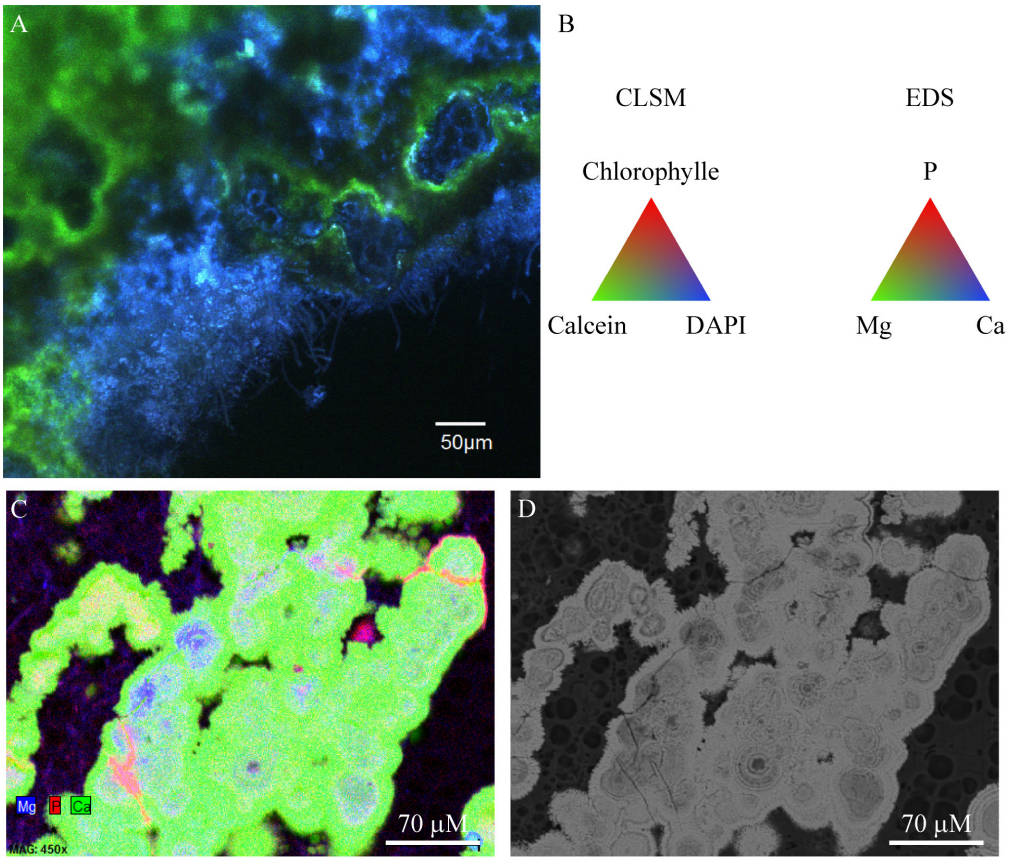

FIGURE 8 | Confocal laser scanning microscopy/Raman/SEM-EDS on the same transversal cutting in red colored zone of M12 microbial mat embedded in LR white showing aragonite precipitating around the microbial mat. **(A)** CLSM image showing coccoid, rod shaped and filamentous microorganisms (blue) being incrusted in aragonite (green). No Cyanobacteria were detected in this zone. **(B)** Colors associated with the CLSM and EDS mappings. **(C)** EDS mapping of the same transversal cutting showing the centers of aragonite grains where magnesium and phosphorus is detected, which could correspond to relics of the encrusted microbial mat. **(D)** SEM image of the same image as in **(C)** (at 15 KV, AsB detector). The LR white resin appears in black and aragonite in bright gray.

Interestingly, we found that the microdissected Rhodobacteraceae is also closely related to bacteria of the same microbialites in Alchichica lake (JN825344) (Supplementary Figure S14), suggesting that this type of Rhodobacteraceae may have an important role in the formation of microbialites not only in lake Dziani Dzaha. The Rhodobacteraceae of Dziani Lake and Alchichica Lake microbialites share 98% identities at the level of their 16S rRNA gene (Couradeau et al., 2011). They are also closely related to Alphaproteobacteria detected in the extreme saline-alkaline soil of the former lake Texcoco (Mexico) (accession numbers JN178563 and JN177885). They are distantly related (94% identities) to known cultivated species such as *Amaricoccus* species isolated from activated sludge system (Falvo et al., 2001) and phototrophic purple non-sulfur bacteria such as *Rhodobacter blasticus* (Eckersley and Dow, 1980).

DISCUSSION

The presence of the three mineral phases (aragonite, hydromagnesite, Mg-silicate) closely associated with microorganisms at the top of the mat in the globular crust is in accordance with geochemical modeling taking into account the chemistry of lake water. This was modeled precisely in the case of aragonite and hydromagnesite (Supplementary Figure S1A). The unknown thermodynamic properties of the precipitated Mg-silicate phase prevent such a modeling; however, the formation of this phase is still consistent with thermodynamic modeling which predicts the formation of talc and sepiolite (Supplementary Figure S1B), the precipitation of which appears to be kinetically hindered in the conditions of precipitation. Instead, a metastable Mg-silicate yet to be characterized is precipitated in local microenvironments provided by some microorganisms of the stromatolites.

Hydromagnesite Precipitation

Hydromagnesite was detected on the aragonite grains suggesting that it precipitated preferentially with respect to aragonite in calcium-depleted microenvironments as shown by the stoichiometry of reaction (1). However, hydromagnesite was only found at the top of the cauliflower crust where the phototrophic pigmented microorganisms were detected and not in the stromatolites having a friable surface, suggesting

that its precipitation could be biologically influenced. Indeed, hydromagnesite was more particularly associated with the filamentous yellow pigmented Alphaproteobacteria at the top of the mat. These bacteria were systematically located at the surface of the microbial mat (**Figure 7** and Supplementary Figure S4), suggesting that their growth may be light-dependent, as could be the accumulation of polyhydroxyalkanoate granules, the location of which has been detected by SEM. The formation of polyhydroxyalkanoate through the phototrophic activity of purple non-sulfur bacteria (PNSB) has been well documented (Liebergesell et al., 1991; Higuchi-Takeuchi et al., 2016). Furthermore, as revealed by calcein staining, these filamentous bacteria accumulated Ca^{2+} and/or Mg^{2+} in their sheaths. This feature could be related to the capacity of this kind of filamentous cells to form flocks where bacteria are strongly bound to each other. Indeed, it has been shown that calcium and to a lesser extent magnesium may be necessary in the process of bacterial cells adhesion (Kragelund et al., 2006). These filamentous cells may thus potentially change the Mg/Ca ratio at the surface of the mat and could have an influence on the balance between aragonite or hydromagnesite precipitation. In addition, the adhesion properties of these bacteria probably played a key role in the trapping and binding of hydromagnesite spikes as well as aragonite particles. It has already been shown that Cyanobacteria isolated from the alkaline lake Salda (SE Turkey) mediate the precipitation of hydromagnesite (Shirokova et al., 2013). However, it is not clear at this stage if the metabolic activity of these potentially photosynthetic filamentous Alphaproteobacteria induced the precipitation hydromagnesite in Dziani stromatolites. Further experiments should be carried out in the laboratory to answer this question, if it is possible to isolate and cultivate these bacteria.

Mg-Silicate Precipitation

The formation of the Mg-silicate seemed to be initiated by the accumulation of Si and Mg in the sheaths of Pleurocapsales where the formation of microbeads of Mg-Si was detected. Similar microbeads were observed in association with the decay of the EPS from Cyanobacteria belonging to the *Synechococcus* genus in the ocean (Tang et al., 2014). The authors suggested that the progressive accumulation of magnesium and silicon in decaying EPS of *Synechococcus* species leads to the formation of these beads that could account for a significant part of the silicate found in the bottom of the ocean (Tang et al., 2014). Similarly, the accumulation of silicon and magnesium in the Pleurocapsales sheaths during their decay may be at the origin of the Mg-Si phase observed in the cauliflower crust of stromatolites. The presence of Mg-Si phases was already reported in several modern lacustrine microbialites: in Mono Lake and Great Salt Lake (United States), in the Crater Lake Satonda (Indonesia), in basaltic caves at Kauai (Hawaii), in the alkaline and hyposaline Lake Clifton in Western Australia, and in several Mexican crater lakes in Mexico (Léveillé et al., 2000a,b, 2002, 2007; Arp et al., 2003; Souza-Egipsy et al., 2005; Burne et al., 2014; Zeyen et al., 2015; Pace et al., 2016). Interestingly, Mg-silicates associated with fossil microbialites have also been reported in the extensive hydrocarbon-bearing Pre-Salt layer offshore of Brazil (Corrêa, 2012) and Angola (Wasson et al., 2012), which were interpreted as the result of lacustrine deposition in highly alkaline lake waters (Wright, 2012). Furthermore, Mg-silicates seem to be important in the formation of microbialites: the modern thrombolites of Lake Clifton, Western Australia, for example, gain their initial structural rigidity from biofilm mineralization with Mg-silicate (Burne et al., 2014). Similarly, Mg-silicate is associated with the most rigid surface texture observed on Dziani stromatolites. However, in modern microbialites, Mg-silicates seem to be unstable and are rapidly replaced by aragonite following the degradation of the associated organic components (Burne et al., 2014; Pace et al., 2016). Although the Mg-silicate was only detected in association with Pleurocapsales sheaths in the cauliflower crust, its replacement by aragonite was not clearly evidenced. Nevertheless, it suggests that the Mg-silicate was dissolved in the deepest part of the stromatolites. An alternative explanation would be that the internal part of the stromatolites building was mediated by another type of microbial consortium, as the one observed in the friable surface stromatolites dominated by filamentous Cyanobacteria, and that the Mg-silicate never formed.

Aragonite Precipitation

In the cauliflower crust, Rhodobacteraceae were associated with the precipitation of aragonite. Given the pink to purple pigmentation of the cells and the pink coloration of the aragonite crust, these Rhodobacteraceae coccoid cells were potentially phototrophic bacteria. Indeed, the Rhodobacteraceae family comprises, among others, purple non-sulfur bacteria (PNSB), which possess an extensive range of metabolic capabilities (Pujalte et al., 2014). PNSB may accumulate sulfur globules outside their cells during anoxygenic photosynthesis based on the oxidation of reduced sulfur compounds (Dahl and Prange, 2006). Probable sulfur globules were detected with CLSM, indicating that some of the Alphaproteobacteria were oxidizing reduced sulfur compounds. This is in accordance with the relatively high level of H_2S (31–100 μM between the surface and 1 m depth) measured in October 2014. Some coccoid cells colonized empty Pleurocapsales sheaths suggesting as well that photoheterotrophic or heterotrophic activities could have induced the formation of aragonite. Anoxygenic photoautotrophic bacteria are supposed to favor precipitation of calcium or magnesium carbonates through alkalization during photosynthesis (Dupraz and Visscher, 2005; Visscher and Stolz, 2005). However, it has also been shown that anoxygenic photosynthesis in which H_2S is oxidized to S° may, in a second step, acidify the medium when S° is ultimately oxidized to sulfate in presence of oxygen (Visscher and Stolz, 2005). Comparatively, photoheterophy may be a more efficient alkalinizing process leading to the precipitation of calcium carbonate in PNSB environment (Bundeleva et al., 2012), depending on the organic substrate used. It is thus not possible to know exactly at this stage which metabolism favored aragonite precipitation.

Other bacterial lineages could have influenced aragonite formation although we did not evidence that using microscopic

or spectrometric methods. Firmicutes belonging to the Clostridiales order were present in all stromatolites and represented an important proportion of the microbial composition associated with M15 and M12 stromatolites. Members of the Clostridiales order encompassed SRB (Castro et al., 2000) and that type of metabolism has been shown to induce aragonite formation as a result of the degradation of Cyanobacteria and extracellular organic matrix (Pace et al., 2016). Furthermore, members of the Chlorobi and Chloroflexi bacterial lineages, that encompass anoxygenic photosynthesizers (Bryant and Frigaard, 2006), were abundantly detected in M15, M12, and M10 stromatolites and could also have participated in the formation of aragonite. Thus, we cannot exclude that SRB, Chlorobi and Chloroflexi could have favored the formation of aragonite and we should continue to investigate this possibility in particular in the stromatolite M15, where they were the most abundantly detected.

Influence of Microorganisms on the Stromatolites Surface Textures

Different types of Cyanobacteria were associated with different stromatolite surface textures. Oscillatoriales, trapping and binding aragonite grains, were associated with friable surfaces, whereas in the hard cauliflower surfaces, we observed the permineralization of Pleurocapsales by Mg-silicate. The difference in surface textures may be linked to the locus of mineral precipitation. Mg-silicate precipitation takes place within the sheaths of Pleurocapsales which form dense colonies, while no evidence of mineral precipitation was detected in the sheaths of Oscillatoriales. The rigidity of the cauliflower crusts may be due to the presence of the Mg-silicate phase as previously noticed in the microbialites of Lake Clifton [Western Australia (Burne et al., 2014)]. The property of Pleurocapsales to favor mineral precipitation in their sheaths has already been highlighted in the microbialites from Lake Alchichica in Mexico (Couradeau et al., 2013) and in several other lacustrine and marine microbialites, such as microbialites from Lake Van, Turkey (Kempe et al., 1991; Lopez-Garcia et al., 2005), Satonda, Indonesia (Arp et al., 2003) and the Bahamas (Mobberley et al., 2012), except that aragonite was precipitated with Pleurocapsales in these cases (Couradeau et al., 2013). This may be due to different sheath properties or different environmental conditions, and in particular to variation of dissolved silica concentrations. Indeed, we detected a calcium accumulation in the sheath of Pleurocapsales in the microbialites of Alchichica Lake (Gerard et al., 2013) but not in the sheath of the Pleurocapsales of Dziani Dzaha stromatolites. However, the concentration of calcium is five time higher in Alchichica Lake water than in Dziani Dzaha Lake water [54 μM in Dziani Dzaha Lake and 275 μM in Alchichica Lake (Armienta et al., 2008)] and the concentration of ortho-silicic acid is less than 160 μM in Alchichica Lake where no magnesium–silicate phase was observed. Nonetheless, it emphasizes the important role of Pleurocapsales in the formation of lacustrine and marine microbialites (Zeyen et al., 2017). In addition, the high abundance of calcifying Alphaproteobacteria in the cauliflower crusts must also have played a role in the stiffening of the structure.

CONCLUSION

Purple non-sulfur bacteria and Cyanobacteria influenced the shape and mineralogy of the Dziani Dzaha stromatolites. The formation of Mg-silicate was biologically mediated by the presence of Pleurocapsales. Purple non-sulfur bacteria were the dominant and the most calcifying microorganisms in the microbial mats associated to stromatolites with a cauliflower shape. They fossilized into aragonite and contributed to the formation of aragonite and hydromagnesite laminations. As stromatolites developed under an anoxic Earth surface before 2,500 Myr, this raises the possibility that the oldest stromatolites were formed by microbial communities dominated by anoxygenic phototrophic bacteria. To test this idea, it will be necessary to analyze the metabolic capacities of the purple non-sulfur bacteria involved in aragonite precipitation through the analysis of their genome after laser microdissection and whole genome amplification to determine if they can be primary producers in these microbial mats. Attempts to isolate them in pure culture should be done to measure their capacity to induce carbonate precipitation without the influence of Cyanobacteria. Furthermore, it would be interesting to follow the evolution of the microbial communities and mineral composition associated with stromatolites according to the lake water level, as some of the stromatolites analyzed may be placed at the oxic/anoxic transition zone when the lake is at its highest level. These conditions may be more representative of the Precambrian conditions with low level or absence of oxygen.

AUTHOR CONTRIBUTIONS

EG, SD, MH, HA, LR, VM, FG, LL, SB, TL, M-BJ, GS, and DJ made the analyses. EG wrote the manuscript. EG, SD, LR, FG, MH, HA, VM, GS, CL and MA discussed the results and revised the manuscript. EG, MA, CL, HA, DJ, and GS performed the Dziani Dzaha sampling expedition and provided the stromatolites. MA and CL obtained funding for the project. All authors read and approved this manuscript.

FUNDING

The research leading to these results has received funding from the French National Research Agency ANR through the DZIANI (ANR-13-BS06-0001) and the Total Corporate Foundation, project DZAHA, grant no. C001493. This is IPGP contribution number 3941.

ACKNOWLEDGMENTS

We wish to thank Omar Boudouma for SEM analyses at University of Paris VI, Institut des Sciences de la Terre de Paris, UMR7193 and Sophie Nowak for XRD analyses at University of

Paris Diderot, Paris VII, UFR de chimie. We wish to thank the Air Austral Airline Company, and Alexandra and Laurent at the Les Couleurs Guest House in Mayotte for their valuable assistance and support. We also thank S. Nicolas N. Villeriot, and A. Dubost for their contributions and discussions on molecular analysis.

SUPPLEMENTARY MATERIAL

The Supplementary Material for this article can be found online at: https://www.frontiersin.org/articles/10.3389/fmicb.2018.00796/full#supplementary-material

REFERENCES

Allwood, A. C., Walter, M. R., Kamber, B. S., Marshall, C. P., and Burch, I. W. (2006). Stromatolite reef from the early archaean era of Australia. *Nature* 441, 714–718. doi: 10.1038/nature04764

Altermann, W., Kazmierczak, J., Oren, A., and Wright, D. (2006). Cyanobacterial calcification and its rock-building potential during 3.5 billion years of Earth history. *Geobiology* 4, 147–166. doi: 10.1111/j.1472-4669.2006.00076.x

Altschul, S. F., Madden, T. L., Schaffer, A. A., Zhang, J., Zhang, Z., Miller, W., et al. (1997). Gapped BLAST and PSI-BLAST: a new generation of protein database search programs. *Nucleic Acids Res.* 25, 3389–3402. doi: 10.1093/nar/25.17.3389

Amino, A., and Kérouel, L. (2004). *Hydrologie des Écosystèmes Marins. Paramètres et Analyses*. Paris: QUAE.

Anderson, M. (2001). A new method for non-parametric multivariate analysis of variance. *Austral Ecol.* 26, 32–46.

Armienta, M. A., Vilaclara, G., De la Cruz-Reyna, S., Ramos, S., Ceniceros, N., Cruz, O., et al. (2008). Water chemistry of lakes related to active and inactive Mexican volcanoes. *J. Volcanol. Geother. Res.* 178, 249–258. doi: 10.1016/j.jvolgeores.2008.06.019

Arp, G., Reimer, A., and Reitner, J. (2003). Microbialite formation in seawater of increased alkalinity, satonda Crater lake, Indonesia. *J. Sediment. Res.* 73, 105–127. doi: 10.1306/071002730105

Blankenship, R. E. (2010). Early evolution of photosynthesis. *Plant Physiol.* 154, 434–438. doi: 10.1104/pp.110.161687

Bokulich, N. A., Subramanian, S., Faith, J. J., Gevers, D., Gordon, J. I., Knight, R., et al. (2013). Quality-filtering vastly improves diversity estimates from Illumina amplicon sequencing. *Nat. Methods* 10, 57–59. doi: 10.1038/nmeth.2276

Bosak, T., Greene, S. E., and Newman, D. K. (2007). A likely role for anoxygenic photosynthetic microbes in the formation of ancient stromatolites. *Geobiology* 5, 119–126. doi: 10.1111/j.1472-4669.2007.00104.x

Bosak, T., Liang, B., Sim, M. S., and Petroff, A. P. (2009). Morphological record of oxygenic photosynthesis in conical stromatolites. *Proc. Natl. Acad. Sci. U.S.A.* 106, 10939–10943. doi: 10.1073/pnas.0900885106

Bryant, D. A., and Frigaard, N. U. (2006). Prokaryotic photosynthesis and phototrophy illuminated. *Trends Microbiol.* 14, 488–496. doi: 10.1016/j.tim.2006.09.001

Bundeleva, I., Shirokova, L. S., Bénézeth, P., Pokrovsky, O. S., Kompantseva, E. I., and Balor, S. (2012). Calcium carbonate precipitation by anoxygenic phototrophic bacteria. *Chem. Geol.* 291, 116–131. doi: 10.1016/j.chemgeo.2011.10.003

Burne, R. V., and Moore, L. S. (1987). Microbialites: organosedimentary deposits of benthic microbial communities. *Palaios* 2, 241–254. doi: 10.2307/3514674

Burne, R. V., Moore, L. S., Christy, A. G., Troitzsch, U., King, P. L., Carnerup, A. M., et al. (2014). Stevensite in the modern thrombolites of Lake Clifton, Western Australia: a missing link in microbialite mineralization. *Geology* 42, 575–578. doi: 10.1130/G35484.1

Camacho, C., Coulouris, G., Avagyan, V., Ma, N., Papadopoulos, J., Bealer, K., et al. (2009). BLAST+: architecture and applications. *BMC Bioinformatics* 10:421. doi: 10.1186/1471-2105-10-421

Castro, H. F., Williams, N. H., and Ogram, A. (2000). Phylogeny of sulfate-reducing bacteria(1). *FEMS Microbiol. Ecol.* 31, 1–9. doi: 10.1016/S0168-6496(99)00071-9

Corrêa, A. C. (2012). Petrobras and the oil and gas industry in Brazil. *Paper Presented at III Brazil-UK Oil and Gas Meeting: Cooperation in Human Resources and Skills Development*, London, 24.

Couradeau, E., Benzerara, K., Gérard, E., Estève, I., Moreira, D., Tavera, R., et al. (2013). Cyanobacterial calcification in modern microbialites at the submicrometer scale. *Biogeosciences* 10, 5255–5266. doi: 10.5194/bg-10-5255-2013

Couradeau, E., Benzerara, K., Moreira, D., Gerard, E., Kazmierczak, J., Tavera, R., et al. (2011). Prokaryotic and eukaryotic community structure in field and cultured microbialites from the alkaline Lake Alchichica (Mexico). *PLoS One* 6:e28767. doi: 10.1371/journal.pone.0028767

Dahl, C., and Prange, A. (2006). "Bacterial sulfur globules: occurrence, structure and metabolism," in *Inclusions in Prokaryotes. Microbiology Monographs*, Vol. 1, ed. J. M. Shively (Berlin, Heidelberg: Springer).

D'Amelio, E. D., Cohen, Y., and Des Marais, D. J. (1987). Association of a new type of gliding, filamentous, purple phototrophic bacterium inside bundles of microcoleus chthonoplastes in hypersaline cyanobacterial mats. *Arch. Microbiol.* 147, 213–220. doi: 10.1007/BF00463477

Decho, A. W. (2010). Overview of biopolymer-induced mineralization: what goes on in biofilms. *Ecol. Eng.* 36, 137–144. doi: 10.1016/j.ecoleng.2009.01.003

Degen, T., Sadki, M., Bron, E., König, U., and Nénert, G. (2014). The highscore suite. *Powder Diffr.* 29, S13–S18. doi: 10.1017/S0885715614000840

Dupraz, C., Reid, R. P., Braissant, O., Decho, A. W., Norman, R. S., and Visscher, P. T. (2009). Processes of carbonate precipitation in modern microbial mats. *Earth Sci. Rev.* 96, 141–152. doi: 10.1016/j.earscirev.2008.10.005

Dupraz, C., and Visscher, P. T. (2005). Microbial lithification in marine stromatolites and hypersaline mats. *Trends Microbiol.* 13, 429–438. doi: 10.1016/j.tim.2005.07.008

Eckersley, K., and Dow, C. S. (1980). *Rhodopseudomonas blastica* sp.nov: a Member of the *Rhodospirillaceae*. *J. Gen. Microbiol.* 119, 465–473. doi: 10.1099/00221287-119-2-465

Escudie, F., Auer, L., Bernard, M., Mariadassou, M., Cauquil, L., Vidal, K., et al. (2017). FROGS: find, rapidly, OTUs with galaxy solution. *Bioinformatics* doi: 10.1093/bioinformatics/btx791 [Epub ahead of print].

Falvo, A., Levantesi, C., Rossetti, S., Seviour, R. J., and Tandoi, V. (2001). Synthesis of intracellular storage polymers by *Amaricoccus kaplicensis*, a tetrad forming bacterium present in activated sludge. *J. Appl. Microbiol.* 91, 299–305. doi: 10.1046/j.1365-2672.2001.01384.x

Franz, C. M., Petryshyn, V. A., and Corsetti, F. A. (2015). Grain trapping by filamentous cyanobacterial and algal mats: implications for stromatolite microfabrics through time. *Geobiology* 13, 409–423. doi: 10.1111/gbi.12145

Gautier, Q., Bénézeth, P., Mavromatis, V., and Schott, J. (2014). Hydromagnesite solubility product and growth kinetics in aqueous solution from 25 to 75°C. *Geochim. Cosmochim. Acta* 138, 1–20. doi: 10.1016/j.gca.2014.03.044

Gerard, E., Menez, B., Couradeau, E., Moreira, D., Benzerara, K., Tavera, R., et al. (2013). Specific carbonate-microbe interactions in the modern microbialites of Lake Alchichica (Mexico). *ISME J.* 7, 1997–2009. doi: 10.1038/ismej.2013.81

Grotzinger, J. P., and Rothman, D. H. (1996). An abiotic model for stromatolite morphogenesis. *Nature* 383, 423–425. doi: 10.1038/383423a0

Higuchi-Takeuchi, M., Morisaki, K., and Numata, K. (2016). A screening method for the isolation of polyhydroxyalkanoate-producing purple non-sulfur photosynthetic bacteria from natural seawater. *Front. Microbiol.* 7:1509. doi: 10.1038/ismej.2013.81

Hugoni, M., Domaizon, I., Taib, N., Biderre-Petit, C., Agogue, H., Galand, P. E., et al. (2015). Temporal dynamics of active *Archaea* in oxygen-depleted zones of two deep lakes. *Environ. Microbiol. Rep.* 7, 321–329. doi: 10.1111/1758-2229.12251

Jansson, C., and Northen, T. (2010). Calcifying cyanobacteria—the potential of biomineralization for carbon capture and storage. *Curr. Opin. Biotechnol.* 21, 365–371. doi: 10.1016/j.copbio.2010.03.017

Johnson, J. W., Oelkers, E. H., and Helgeson, H. C. (1992). SUPCRT92: a software package for calculating the standard molal thermodynamic properties of minerals, gases, aqueous species, and reactions from 1 to 5000 bar and 0 to 1000°C. *Comput. Geosci.* 18, 899–947. doi: 10.1016/0098-3004(92)90029-Q

Kempe, S., Kazmierczak, J., Landmann, G., Konuk, T., Reimer, A., and Lipp, A. (1991). Largest known microbialites discovered in Lake Van. Turkey. *Nature* 349, 605–608. doi: 10.1038/349605a0

Klein, C., Beukes, N. J., and Schopf, J. W. (1987). Filamentous microfossils in the early proterozoic transvaal supergroup: their morphology, significance, and paleoenvironmental setting. *Precam. Res.* 36, 81–94. doi: 10.1016/0301-9268(87)90018-0

Kragelund, C., Kong, Y., van der Waarde, J., Thelen, K., Eikelboom, D., Tandoi, V., et al. (2006). Ecophysiology of different filamentous *Alphaproteobacteria* in industrial wastewater treatment plants. *Microbiology* 152, 3003–3012. doi: 10.1099/mic.0.29249-0

Labrenz, M., Lawson, P. A., Tindall, B. J., and Hirsch, P. (2009). *Roseibaca ekhonensis* gen. nov., sp. nov., an alkalitolerant and aerobic bacteriochlorophyll a-producing alphaproteobacterium from hypersaline Ekho Lake. *Int. J. Syst. Evol. Microbiol.* 59, 1935–1940. doi: 10.1099/ijs.0.016717-0

Leboulanger, C., Agogué, H., Bernard, C., Bouvy, M., Carré, C., Cellamare, M., et al. (2017). Microbial diversity and cyanobacterial production in Dziani Dzaha crater lake, a unique tropical thalassohaline environment. *PLoS One* 12:e0168879. doi: 10.1371/journal.pone.0168879

Lepot, K., Benzerara, K., Brown, G. E. J., and Philippot, P. (2008). Microbially influenced formation of 2,724-million-year-old stromatolites. *Nat. Geosci.* 1, 118–121. doi: 10.1038/ngeo107

Léveillé, R. J., Fyfe, W. S., and Longstaffe, F. J. (2000a). Geomicrobiology of carbonate–silicate microbialites from Hawaiian basaltic sea caves. *Chem. Geol.* 169, 339–355. doi: 10.1016/S0009-2541(00)00213-8

Léveillé, R. J., Fyfe, W. S., and Longstaffe, F. J. (2000b). Unusual secondary Ca-Mg-Carbonate-kerolite deposits in Basaltic Caves, Kauai, Hawaii. *J. Geol.* 108, 613–621. doi: 10.1086/314417

Léveillé, R. J., Longstaffe, F. J., and Fyfe, W. S. (2002). Kerolite in carbonate-rich speleothems and microbial deposits from basaltic caves, Kauai, Hawaii. *Clays Clay Miner.* 50, 514–524. doi: 10.1346/000986002320514235

Léveillé, R. J., Longstaffe, F. J., and Fyfe, W. S. (2007). An isotopic and geochemical study of carbonate-clay mineralization in basaltic caves: abiotic versus microbial processes. *Geobiology* 5, 235–249. doi: 10.1111/j.1472-4669.2007.00109.x

Liebergesell, M., Hustede, E., Timm, A., Steinbüchel, A., Fuller, R. C., Lenz, R. W., et al. (1991). Formation of poly (3-hydroxyalkanoates) by phototrophic and chemolithotrophic bacteria. *Arch. Microbiol.* 155, 415–421. doi: 10.1007/BF00244955

Lopez-Garcia, P., Kazmierczak, J., Benzerara, K., Kempe, S., Guyot, F., and Moreira, D. (2005). Bacterial diversity and carbonate precipitation in the giant microbialites from the highly alkaline Lake Van, Turkey. *Extremophiles* 9, 263–274. doi: 10.1007/s00792-005-0457-0

Lowe, D. R. (1994). Abiological origin of described stromatolites older than 3.2 Ga. *Geology* 22, 387–390. doi: 10.1130/0091-7613(1994)022<0387:AOODSO>2.3.CO;2

Ludwig, W., Strunk, O., Westram, R., Richter, L., Meier, H., and Yadhukumar (2004). ARB: a software environment for sequence data. *Nucleic Acids Res.* 32, 1363–1371. doi: 10.1093/nar/gkh293

Magoc, T., and Salzberg, S. L. (2011). FLASH: fast length adjustment of short reads to improve genome assemblies. *Bioinformatics* 27, 2957–2963. doi: 10.1093/bioinformatics/btr507

Mahe, F., Rognes, T., Quince, C., de Vargas, C., and Dunthorn, M. (2014). Swarm: robust and fast clustering method for amplicon-based studies. *PeerJ* 2:e593. doi: 10.7717/peerj.593

McLoughlin, N., Wilson, L. A., and Brasier, M. D. (2008). Growth of synthetic stromatolites and wrinkle structures in the absence of microbes - implications for the early fossil record. *Geobiology* 6, 95–105. doi: 10.1111/j.1472-4669.2007.00141.x

Merz, M. U. E. (1992). The biology of carbonate precipitation by cyanobacteria. *Facies* 26, 81–101. doi: 10.1007/BF02539795

Mobberley, J. M., Ortega, M. C., and Foster, J. S. (2012). Comparative microbial diversity analyses of modern marine thrombolitic mats by barcoded pyrosequencing. *Environ. Microbiol.* 14, 82–100. doi: 10.1111/j.1462-2920.2011.02509.x

Nutman, A. P., Bennett, V. C., Friend, C. R., Van Kranendonk, M. J., and Chivas, A. R. (2016). Rapid emergence of life shown by discovery of 3,700-million-year-old microbial structures. *Nature* 537, 535–538. doi: 10.1038/nature19355

Pace, A., Bourillot, R., Bouton, A., Vennin, E., Galaup, S., Bundeleva, I., et al. (2016). Microbial and diagenetic steps leading to the mineralisation of Great Salt Lake microbialites. *Sci. Rep.* 6:31495. doi: 10.1038/srep31495

Papineau, D., Walker, J. J., Mojzsis, S. J., and Pace, N. R. (2005). Composition and structure of microbial communities from stromatolites of Hamelin Pool in Shark Bay, Western Australia. *Appl. Environ. Microbiol.* 71, 4822–4832. doi: 10.1128/AEM.71.8.4822-4832.2005

Parkhurst, D. L., and Appelo, C. A. J. (1999). User's guide to PHREEQC (version 2)–A computer program for speciation, batch-reaction, one-dimensional transport, and inverse geochemical calculations. *Geol. Surv. Water Resour. Invest. Rep.* 99:312.

Peters, E. S., Husson, M. J., and Wilcot, J. (2017). The rise and fall of stromatolites in shallow marine environments. *Geology* 45, 487–490. doi: 10.1130/G38931.1

Plummer, L. N., and Busenberg, E. (1982). The solubilities of calcite, aragonite and vaterite in CO2-H2O solutions between 0 and 90°C, and an evaluation of the aqueous model for the system CaCO3-CO2-H2O. *Geochim. Cosmochim. Acta* 46, 1011–1040. doi: 10.1016/0016-7037(82)90056-4

Pruesse, E., Peplies, J., and Glockner, F. O. (2012). SINA: accurate high-throughput multiple sequence alignment of ribosomal RNA genes. *Bioinformatics* 28, 1823–1829. doi: 10.1093/bioinformatics/bts252

Pruesse, E., Quast, C., Knittel, K., Fuchs, B. M., Ludwig, W., Peplies, J., et al. (2007). SILVA: a comprehensive online resource for quality checked and aligned ribosomal RNA sequence data compatible with ARB. *Nucleic Acids Res.* 35, 7188–7196. doi: 10.1093/nar/gkm864

Pujalte, M. J., Lucena, T., Ruvira, M. A., Arahal, D. R., and Macián, M. C. (2014). "The family Rhodobacteraceae," in *The Prokaryotes*, eds E. Rosenberg, E. F. DeLong, S. Lory, E. Stackebrandt, and F. Thompson (Berlin, Heidelberg: Springer).

Quast, C., Pruesse, E., Yilmaz, P., Gerken, J., Schweer, T., Yarza, P., et al. (2013). The SILVA ribosomal RNA gene database project: improved data processing and web-based tools. *Nucleic Acids Res.* 41, D590–D596. doi: 10.1093/nar/gks1219

Reese, B. K., Finneran, D. W., Mills, H. J., Zhu, M. X., and Morse, J. W. (2011). Examination and refinement of the determination of aqueous hydrogen sulfide by the methylene blue method. *Aquat. Geochem.* 17, 567–582. doi: 10.1007/s10498-011-9128-1

Reid, R. P., Visscher, P. T., Decho, A. W., Stolz, J. F., Bebout, B. M., Dupraz, C., et al. (2000). The role of microbes in accretion, lamination and early lithification of modern marine stromatolites. *Nature* 406, 989–992. doi: 10.1038/35023158

Riding, R. (1982). Cyanophyte calcification and changes in ocean chemistry. *Nature* 299, 814–815. doi: 10.1038/299814a0

Riding, R. (2006). Cyanobacterial calcification, carbon dioxide concentrating mechanisms, and Proterozoic–Cambrian changes in atmospheric composition. *Geobiology* 4, 299–316. doi: 10.1111/j.1472-4669.2006.00087.x

Rognes, T., Flouri, T., Nichols, B., Quince, C., and Mahe, F. (2016). VSEARCH: a versatile open source tool for metagenomics. *PeerJ* 4:e2584. doi: 10.7717/peerj.2584

Saghai, A., Zivanovic, Y., Zeyen, N., Moreira, D., Benzerara, K., Deschamps, P., et al. (2015). Metagenome-based diversity analyses suggest a significant contribution of non-cyanobacterial lineages to carbonate precipitation in modern microbialites. *Front. Microbiol.* 6:797. doi: 10.3389/fmicb.2015.00797

Schuurman, T., de Boer, R. F., Kooistra-Smid, A. M., and van Zwet, A. A. (2004). Prospective study of use of PCR amplification and sequencing of 16S ribosomal DNA from cerebrospinal fluid for diagnosis of bacterial meningitis in a clinical setting. *J. Clin. Microbiol.* 42, 734–740. doi: 10.1128/JCM.42.2.734-740.2004

Shirokova, L. S., Mavromatis, V., Bundeleva, I., Pokrosky, O. S., Bénézeth, P., Gérard, E., et al. (2013). Using Mg isotopes to trace cyanobacterially mediated magnesium carbonate precipitation in alkaline lakes. *Aquat. Geochem.* 19, 1–24. doi: 10.1007/s10498-012-9174-3

Souza-Egipsy, V., Wierzchos, J., Ascaso, C., and Nealson, K. H. (2005). Mg-silica precipitation in fossilization mechanisms of sand tufa endolithic microbial community, Mono Lake (California). *Chem. Geol.* 217, 77–87. doi: 10.1016/j.chemgeo.2004.12.004

Stamatakis, A., Hoover, P., and Rougemont, J. (2008). A rapid bootstrap algorithm for the RAxML Web servers. *Syst. Biol.* 57, 758–771. doi: 10.1080/10635150802429642

Suosaari, E. P., Reid, R. P., Playford, P. E., Foster, J. S., Stolz, J. F., Casaburi, G., et al. (2016). New multi-scale perspectives on the stromatolites of Shark Bay, Western Australia. *Sci. Rep.* 6:20557. doi: 10.1038/srep20557

Tang, T., Kisslinger, K., and Lee, C. (2014). Silicate deposition during decomposition of cyanobacteria may promote export of picophytoplankton to the deep ocean. *Nat. Commun.* 5:4143. doi: 10.1038/ncomms5143

Tian, J., Sinskey, A. J., and Stubbe, J. (2005). Kinetic studies of polyhydroxybutyrate granule formation in *Wautersia eutropha* H16 by transmission electron microscopy. *J. Bacteriol.* 187, 3814–3824. doi: 10.1128/JB.187.11.3814-3824.2005

Visscher, P. T., and Stolz, J. F. (2005). Microbial mats as bioreactors: populations, processes, and products. *Palaeogeogr. Palaeoclimatol. Palaeoecol.* 219, 87–100. doi: 10.1016/j.palaeo.2004.10.016

Walter, M. R., Bauld, J., and Brock, T. D. (1976). "Chapter 6.2 Microbiology and morphogenesis of columnar stromatolites (conophyton, vacerrilla) from hot springs in yellowstone national park," in *Developments in Sedimentology*, ed. M. R. Walter (New York, NY: Elsevier), 273–310.

Walters, W., Hyde, E. R., Berg-Lyons, D., Ackermann, G., Humphrey, G., Parada, A., et al. (2016). Improved Bacterial 16S rRNA Gene (V4 and V4-5) and Fungal Internal Transcribed spacer marker gene primers for microbial community surveys. *mSystems* 1:e00009-e15. doi: 10.1128/mSystems.00009-15

Wang, Q., Garrity, G. M., Tiedje, J. M., and Cole, J. R. (2007). Naive Bayesian classifier for rapid assignment of rRNA sequences into the new bacterial taxonomy. *Appl. Environ. Microbiol.* 73, 5261–5267. doi: 10.1128/AEM.00062-07

Wasson, M. S., Saller, A., Andres, M., Self, D., and Lomando, A. (2012). Lacustrine microbial carbonate facies in core from the lower Cretaceous Toca Formation, offshore Angola. *Paper Presented at AAPG Hedberg Conference "Microbial Carbonate Reservoir Characterization*, Houston, TX.

Wright, V. P. (2012). Lacustrine carbonates in rift settings: the interaction of volcanic and microbial processes on carbonate deposition. *Geol. Soc.* 370, 39–47. doi: 10.1144/SP370.2

Xiong, J., Fischer, W. M., Inoue, K., Nakahara, M., and Bauer, C. E. (2000). Molecular evidence for the early evolution of photosynthesis. *Science* 289, 1724–1730. doi: 10.1126/science.289.5485.1724

Yilmaz, P., Parfrey, L. W., Yarza, P., Gerken, J., Pruesse, E., Quast, C., et al. (2014). The SILVA and "all-species living tree project (LTP)" taxonomic frameworks. *Nucleic Acids Res.* 42, D643–D648. doi: 10.1093/nar/gkt1209

Zeyen, N., Benzerara, K., Li, J., Groleau, A., Balan, E., Robert, J. L., et al. (2015). Formation of low-T hydrated silicates in modern microbialites from Mexico and implications for microbial fossilization. *Front. Earth Sci.* 3:64. doi: 10.3389/feart.2015.00064

Zeyen, N., Daval, D., Lopez-Garcia, P., Moreira, D., Gaillardet, J., and Benzerara, K. (2017). Geochemical conditions allowing the formation of modern lacustrine microbialites. *Procedia Earth Planet. Sci.* 17, 380–383. doi: 10.1016/j.proeps.2016.12.096

Conflict of Interest Statement: The authors declare that the research was conducted in the absence of any commercial or financial relationships that could be construed as a potential conflict of interest.

frontiers in Microbiology

ORIGINAL RESEARCH
published: 22 May 2018
doi: 10.3389/fmicb.2018.00996

Characterization of Pustular Mats and Related *Rivularia*-Rich Laminations in Oncoids From the Laguna Negra Lake (Argentina)

Estela C. Mlewski[1†], Céline Pisapia[2,3†], Fernando Gomez[1], Lena Lecourt[2], Eliana Soto Rueda[1], Karim Benzerara[4], Bénédicte Ménez[2], Stephan Borensztajn[2], Frédéric Jamme[3], Matthieu Réfrégiers[3] and Emmanuelle Gérard[2*]*

[1] Centro de Investigaciones en Ciencias de la Tierra (CICTERRA), Cordoba, Argentina, [2] Institut de Physique du Globe de Paris, Sorbonne Paris Cité, Centre National de la Recherche Scientifique, Université Paris Diderot, Paris, France, [3] Synchrotron SOLEIL, DISCO Beamline, Saint Aubin, France, [4] Institut de Minéralogie, de Physique des Matériaux et de Cosmochimie, UMR Centre National de la Recherche Scientifique 7590, Sorbonne Université, Muséum National d'Histoire Naturelle, IRD UMR 206, Paris, France

OPEN ACCESS

Edited by:
Christophe Dupraz,
Stockholm University, Sweden

Reviewed by:
Virginia Helena Albarracín,
Center for Electron Microscopy (CIME), Argentina
John Senko,
University of Akron, United States

***Correspondence:**
Estela C. Mlewski
cmlewski@gmail.com
Emmanuelle Gérard
emgerard@ipgp.fr

[†] These authors have contributed equally to this work.

Specialty section:
This article was submitted to Aquatic Microbiology, a section of the journal Frontiers in Microbiology

Received: 30 January 2018
Accepted: 27 April 2018
Published: 22 May 2018

Citation:
Mlewski EC, Pisapia C, Gomez F, Lecourt L, Soto Rueda E, Benzerara K, Ménez B, Borensztajn S, Jamme F, Réfrégiers M and Gérard E (2018) Characterization of Pustular Mats and Related Rivularia-Rich Laminations in Oncoids From the Laguna Negra Lake (Argentina). Front. Microbiol. 9:996. doi: 10.3389/fmicb.2018.00996

Stromatolites are organo-sedimentary structures that represent some of the oldest records of the early biosphere on Earth. Cyanobacteria are considered as a main component of the microbial mats that are supposed to produce stromatolite-like structures. Understanding the role of cyanobacteria and associated microorganisms on the mineralization processes is critical to better understand what can be preserved in the laminated structure of stromatolites. Laguna Negra (Catamarca, Argentina), a high-altitude hypersaline lake where stromatolites are currently formed, is considered as an analog environment of early Earth. This study aimed at characterizing carbonate precipitation within microbial mats and associated oncoids in Laguna Negra. In particular, we focused on carbonated black pustular mats. By combining Confocal Laser Scanning Microscopy, Scanning Electron Microscopy, Laser Microdissection and Whole Genome Amplification, Cloning and Sanger sequencing, and Focused Ion Beam milling for Transmission Electron Microscopy, we showed that carbonate precipitation did not directly initiate on the sheaths of cyanobacterial *Rivularia*, which dominate in the mat. It occurred via organo-mineralization processes within a large EPS matrix excreted by the diverse microbial consortium associated with *Rivularia* where diatoms and anoxygenic phototrophic bacteria were particularly abundant. By structuring a large microbial consortium, *Rivularia* should then favor the formation of organic-rich laminations of carbonates that can be preserved in stromatolites. By using Fourier Transform Infrared spectroscopy and Synchrotron-based deep UV fluorescence imaging, we compared laminations rich in structures resembling *Rivularia* to putatively chemically-precipitated laminations in oncoids associated with the mats. We showed that they presented a different mineralogy jointly with a higher content in organic remnants, hence providing some criteria of biogenicity to be searched for in the fossil record.

Keywords: *Rivularia*, carbonate precipitation, oncoids, Andean lakes, pustular mats

INTRODUCTION

Microbialites record microbial activities and sedimentary processes under a lithified form (Walter et al., 1972; Burne and Moore, 1987). Stromatolites are laminated microbialites probably produced by lithification of microbial mats (Knoll, 2003; Bosak et al., 2007). Yet, comparable stromatolite-like products can form abiotically, casting doubts on the biological origin of some fossil stromatolites (Buick et al., 1981; Grotzinger and Knoll, 1999). Stromatolites are pervasive in the Precambrian fossil record. They can be traced back to the early Archean, 3.43 billion years (Awramik and Sprinkle, 1999; Allwood et al., 2006) and even 3.7 billion years ago (Nutman et al., 2016). Understanding the mechanisms of stromatolite formation is thus mandatory for the quest of the oldest traces of life on Earth and for documenting the early Earth environment. Notably, it is important to decipher the role played by microbial activity on the lithification processes. Microbial metabolisms known to favor carbonate precipitation (by reaching supersaturation with respect to carbonates through increased alkalinity) include oxygenic and anoxygenic photosynthesis, ureolysis, ammonification, denitrification, sulfate and iron reduction, anaerobic sulfide oxidation, or methane oxidation (Dupraz and Visscher, 2005; Dupraz et al., 2009; Zhu and Dittrich, 2016). In addition, microbial exopolymeric substances (EPS), consisting of a mixture of carbohydrates, proteins and nucleic acids, may promote or inhibit solid carbonate formation (e.g., Benzerara et al., 2006), possibly depending on their divalent-cation binding capacity (Braissant et al., 2007; Glunk et al., 2011). Among other phyla, cyanobacteria are important producers of EPS in microbialites (e.g., Foster et al., 2009) and it has long been suggested that the formation of some ancient stromatolites was mediated by oxygenic photosynthesis performed by cyanobacteria (Arp et al., 2001; Aloisi et al., 2006; Altermann et al., 2006; Riding, 2006). However, several studies have indicated that primary production in stromatolites could be partly performed by other organisms such as diatoms, anoxygenic phototrophs and/or non-phototrophic carbon fixers (Braissant et al., 2003; Bosak et al., 2007; Meister, 2013; Saghaï et al., 2015). The study of modern stromatolites may help to better understand the impact of these different metabolic processes on microbialite formation, some of which may have also played a role in the formation of ancient stromatolites. Furthermore, understanding stromatolites is attractive for petroleum geologists with the recent discovery of oil reservoir associated with stromatolites in the South Oman Salt Basin and the "pre-salt" deposits offshore of Brazil (Bosence et al., 2015). Overall, there is a need to document in a broader range of environments the type of microorganisms which contribute to carbonate precipitation in modern microbialites. Modern microbialites and stromatolites currently develop in restrictive, sometimes extreme environments such as the hypersaline Shark Bay in Australia (Logan, 1961), hot springs (Berelson et al., 2011), alkaline lakes (e.g., Kempe et al., 1991; Chagas et al., 2016) and also high-altitude lakes like Socompa, Brava, and Tebenquiche lakes in the Andes (Farías et al., 2013, 2014; Fernandez et al., 2015).

The Laguna Negra is a high-altitude hypersaline lake in Catamarca, Argentina where extreme environmental conditions (i.e., high UV-radiation and extreme temperature, salinity, and water activity) restrict eukaryotic life. Lithification is controlled by environmental processes (Gomez et al., 2014) along with microbial mats where diatoms and anoxygenic phototrophic bacteria are abundant (Gomez et al., 2018). This latter work focused on the texture, mineralogy and stable isotope geochemistry of subfossil oncoids and related microbialites from the Laguna Negra stromatolite belt. This belt mostly consists of carbonated laminar crusts, stromatolites and oncoids. Different types of carbonate laminations were identified within the oncoids based on their texture (e.g., micritic, sparry, botryoidal, tufted filament-rich palisade fabrics). These different laminations were partly associated with different microbial communities (i.e., stratified pink colored, greenish and black pustular mats; Gomez et al., 2018). Interestingly, laminations with calcified *Rivularia*-like cyanobacterial filaments showing tufted palisade fabrics were found alternating with micritic and botryoidal laminations. Consequently, potential changes in the microbial community could possibly be recorded within the oncoids as different types of laminations.

The main objectives of this study were (i) to investigate at Laguna Negra the potential role of a microbial consortium forming the black pustular mat (BP) on the initiation of carbonate precipitation and lamination formation and (ii) to identify biogenicity criteria for the corresponding laminations in subfossil oncoids. By jointly using Confocal Laser Scanning Microscopy (CLSM), Scanning and Transmission Electron Microscopy (SEM/TEM) associated with Energy Dispersive X-ray Spectrometry (EDXS) and Focused Ion Beam (FIB) milling, as well as phylogenetic analyses on the bulk BP mat and on laser microdissected mat cells, we highlighted the presence of an interesting microbial consortium associated with *Rivularia* filaments that triggers carbonate precipitation in the BP mats. In parallel, we determined the composition of the corresponding fossil laminations on oncoids associated with BP mats in order to identify potential biomarkers. By using Fourier Transform Infrared microspectroscopy (FTIR), powder X-Ray Diffraction (XRD) and Synchrotron-based deep UV fluorescence imaging (S-DUV), we clearly highlighted that these laminations present a different pattern compared to putatively chemically-formed laminations, hence providing for laminations some criteria of biogenicity to be searched for in the fossil record.

MATERIALS AND METHODS

Sample Collection and Fixation

The Laguna Negra is a high altitude lake (4,100 m above sea level) located in the Puna region of the Catamarca Province, Argentina (**Figure 1A**). At the southeastern edge of the Laguna Negra, a stromatolite belt of around 0.3 km^2 is observed. This belt mostly consists of oncoids and associated microbial mats with morphological and textural differences described in Gomez et al. (2014) (**Figures 1B–D**). Samples analyzed in this study were collected during two field trips in 2013 (autumn) and in 2015 (spring). We focused on particular black pustular mats

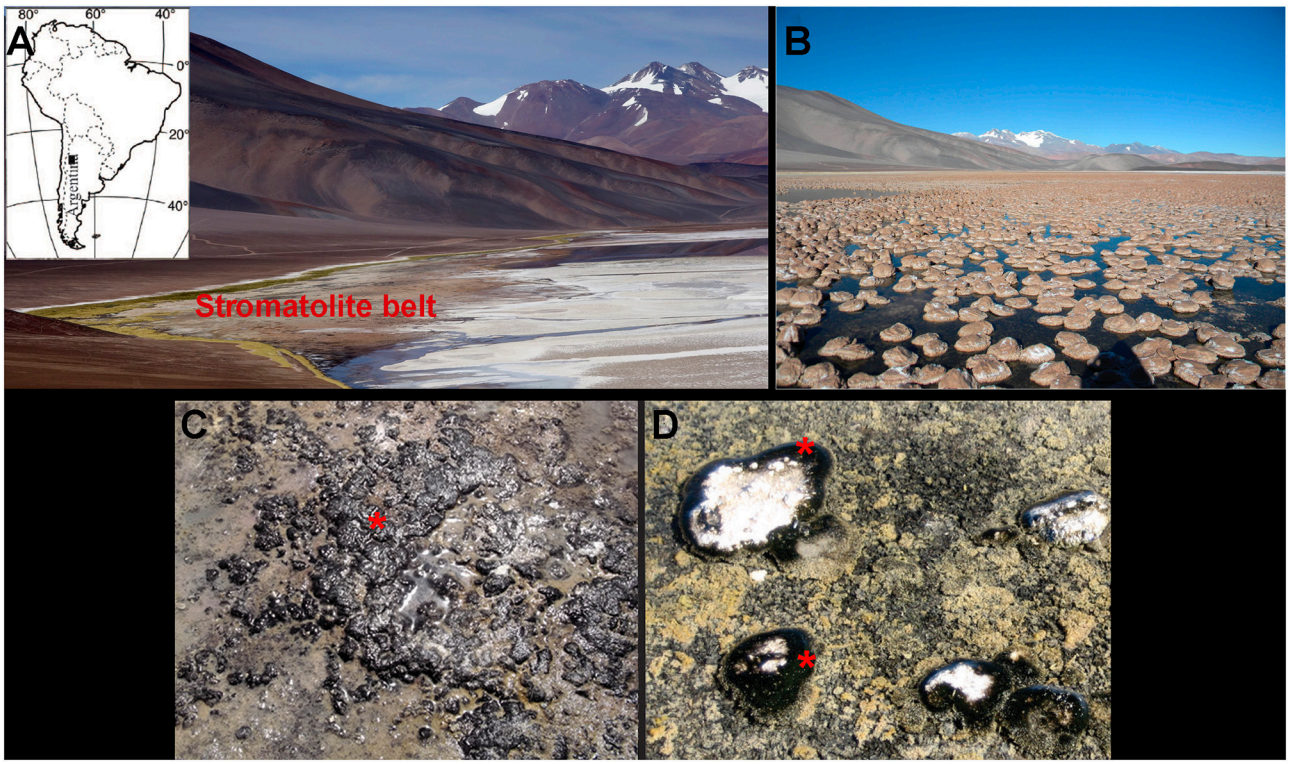

FIGURE 1 | (A) Location map of the Laguna Negra (LN) lake in the Catamarca province, Argentina (indicated by a black square) along with a panoramic view of the lake shore and the stromatolite belt. **(B)** Close view of the subspherical oncoids that compose the stromatolite belt. **(C)** Emerged black pustular (BP) mat and **(D)** BP mat covering the periphery of partly emerged oncoids (red asterisks).

usually found in the shallow shore of the lake (**Figure 1C**), and sometimes covering the periphery of partly emerged oncoids (**Figure 1D**) where the samples were taken. Mats were sampled with sterile instruments and gloves. Samples for DNA analyses were stored in the dark at −20°C until used, or in RNA*later*® (Ambion, Inc.). Samples for SEM-EDXS were fixed in the laboratory with a 2% glutaraldehyde solution and stored in the dark at 4°C for 2 h. After fixation, samples were washed and progressively dehydrated in a gradual series of ethanol and water baths at increasing ethanol concentrations (i.e., 10, 30, 50, 70, and 100%), prior to air drying or critical point drying (CPD7501, Quorum Technologies). Samples for CLSM were fixed in 4% paraformaldehyde solution directly in the field at 4°C, then washed in phosphate buffered saline (PBS) once back in the laboratory and stored in (1/1) ethanol/PBS solution at −20°C until use. Oncoids and microbialites were also collected and stored at 4°C without any chemical fixation.

Calcein Staining and Resin Embedding of BP Microbialites

Calcein (2,4-bis-[N,N′-di(carbomethyl)-aminomethyl]-fluorescein) produces a stable fluorescent complex in the presence of calcium, strontium, barium, and magnesium ions (Diehl and Ellingboe, 1956) and fluoresces (in the green region of visible light) in the presence of these cations at high pH. These stable fluorescent complexes are integrated in growing carbonates and have been used to stain the growth front of calcium carbonate surfaces in tufa-associated biofilms (Zippel and Neu, 2011) and in living microbialites from Alchichica, Mexico (Gérard et al., 2013). Microbialites samples from the BP mats were stained with calcein (0.1 mg/mL; Merck) at 4°C during 48 h. After staining, microbialite fragments were dehydrated in a gradual series of ethanol baths (30, 50, 70, 90, and 100%), and progressively impregnated with hard grade LR-white resin (Polysciences, Inc.). After polymerization, transverse sections were cut with a diamond wire and polished (diamond powder 0.24 μm) to a final thickness of about 500 μm.

Confocal Laser Scanning Microscopy (CLSM)

Fresh BP microbial mat samples were stained with Syto®9 (10 μg/mL; ThermoFisher Scientific), a green fluorescent nucleic acid dye. Syto®9-stained samples and resin-embedded microbial mat samples were examined at the Institut de Physique du Globe de Paris (IPGP, Paris, France) using a FluoView™ FV1000 confocal laser scanning microscope with a spectral resolution of 2 nm and a spatial resolution of 0.2 μm (Olympus). The microscope was equipped with a 405 nm laser diode, and multi-line argon (458, 488, and 515 nm), helium-neon-green (543 nm) and helium-neon-red (633 nm) lasers. Fluorescence images were

obtained with concomitant excitation at wavelengths of 405, 488, and 543 nm by collecting the emitted fluorescence between 425 and 475 nm, 500 and 530 nm, and 560 and 660 nm, respectively. For CSLM image acquisitions on resin-embedded sections, a water immersion LUMPLFL 60XW objective (Olympus; ×60 magnification) with a numerical aperture (N.A.) of 0.9 was used. For fresh biofilms examination, an oil immersion objective UPLSAPO 60XO (Olympus; ×60 magnification, N.A. = 1.35) was used. 3D images were acquired, visualized, and processed using the F10-ASW FLUOVIEW software (Olympus).

Bulk DNA Extraction, PCR Amplification, Cloning, and Sanger Sequencing of 16S rRNA Genes

DNA extractions were performed using the MoBio PowerSoil® DNA kit (MoBio) following the instructions provided by the manufacturer. Bacterial 16S rRNA genes were amplified by polymerase chain reaction (PCR) using the bacterial specific primer 27F (5′-AGAGTTTGATCCTGGCTCAG-3′) combined with the universal prokaryotic reverse primer 1492R (5′-GGTTACCTTGTTACGACTT-3′). Archaeal 16S rRNA genes were amplified using the archaeal specific primer 21F (5′-TTCCGGTTGATCCTGCCGGA-3′) and the prokaryote specific reverse primer 1492R. Cyanobacteria 16S rRNA genes were amplified using the cyanobacterial specific primers Cya-106F (5′-CGGACGGGTGAGTAACGCGTGA-3′) and the cyanobacterial specific reverse primer Cya-1387R (5′-TAACGACTTCGGGCGTGACC-3′). One microliter of the extracted DNA was used in a reaction buffer volume of 25 μL containing dNTPs (10 nmol each), 20 pmol of each primer and 1 U GoTaq polymerase (Promega). PCR reactions were performed under the following conditions: 35 cycles (denaturation at 94°C for 15 s, annealing at 55°C for 30 s, extension at 72°C for 2 min) preceded by 2 min denaturation at 94°C, and followed by 7 min extension at 72°C. Cloning was done using the Topo® TA Cloning® system (ThermoFisher Scientific) following the instructions provided by the manufacturer. After plating, positive clones were screened by PCR amplification of inserts using flanking vector primers and the PCR products were partially sequenced (≈700 bp) by GATC Biotech using flanking vector primer T7 (5′-TAATACGACTCACTATAGGG-3′). At least one representative clone per phylotype or Operational Taxonomic Unit (OTU; group of sequences sharing >97% identity) was fully sequenced for Cyanobacteria using flanking vector primer M13R (5′-CAGGAAACAGCTATGAC-3′) for detailed phylogenetic analysis. The sequences have been deposited at the GenBank database and correspond to the accession numbers MH084957 to MH084967 for cyanobacteria, from MH109330 to 109371 for bacteria, and from MH127632 to MH127645 for archaea.

Laser Microdissection, Whole Genome Amplification (WGA), PCR Amplification, Cloning and Sanger Sequencing of 16S rRNA Genes

Filamentous cyanobacterial cells were isolated using a Zeiss PALM MicroBeam apparatus (Carl Zeiss NTS GmbH) installed in a sterile room at IPGP. We then used the REPLI-g Single Cell Kit (Qiagen) to amplify whole genomic DNA of the microdissected cells. Bacterial 16S rRNA encoding genes were then amplified by PCR using the bacterial specific primer 27F (5′-AGAGTTTGATCCTGGCTCAG-3′) combined with the prokaryote specific reverse primer 1492R (5′-GGTTACCTTGTTACGACTT-3′). One microliter of 1/10 diluted amplified genomic DNA was used in a reaction buffer volume of 25 μL containing dNTPs (10 nmol each), 20 pmol of each primer and 1U of GoTaq polymerase (Promega). PCR reactions were performed under the following conditions: 35 cycles (denaturation at 94°C for 15 s, annealing at 55°C for 30 s, extension at 72°C for 2 min) preceded by 2 min denaturation at 94°C, and followed by 7 min extension at 72°C. Cloning and Sanger sequencing were done as previously described for the 16S rRNA encoding genes retrieved from the bulk DNA extraction. The corresponding sequences have been deposited at the GenBank database and accession numbers range from MH119800 to MH119817.

PCR Amplification, Cloning, and Sanger Sequencing of Partial *pufL* and *pufM* Genes

Partial *pufL* and *pufM* genes coding for subunits of the photosynthetic reaction center of aerobic anoxygenic photosynthetic bacteria (AAnPB; Koblizek, 2015) were amplified by nested PCR. The first amplification was done using the *pufLM-F* primer (5′-CTKTTCGACTTCTGGGTSGG-3′) and the *pufLM-R* primer (5′-CCCATSGTCCAGCGCCAGAA-3′) (Oz et al., 2005). One microliter of the DNA extracted from the bulk sample was used in a reaction buffer volume of 25 μL containing dNTPs (10 nmol each), 20 pmol of each primer and 1 U GoTaq polymerase (Promega). PCR reactions were performed under the following conditions: 40 cycles (denaturation at 94°C for 15 s, annealing at 50°C for 30 s, extension at 72°C for 2 min) preceded by 2 min denaturation at 94°C, and followed by 7 min extension at 72°C. One microliter of the first amplification products was then used for the nested amplification with the primers Mf150f (5′-AGATYGGYCCGATCTAYCT-3′) and M572r (5′-CCAGTCSAGGTGCGGGAA-3′) (Hirose et al., 2012). The PCR conditions of the first amplification were also used for the nested PCR. As previously described for the 16S rRNA encoding genes, the *pufLM* genes were cloned using the Topo® TA Cloning® system (ThermoFisher Scientific) following the instructions provided by the manufacturer and the PCR products were totally sequenced by GATC Biotech using flanking vector primer T7 (5′-TAATACGACTCACTATAGGG-3′) and M13R (5′-CAGGAAACAGCTATGAC-3′). The corresponding sequences have been deposited in the GenBank database and accession numbers range from MH101761 to MH101777.

Phylogenetic Analysis

Taxonomic affiliations were obtained using BLAST (Altschul et al., 1997) on the non-redundant NCBI database, as well as using the Silva Incremental Aligner (SINA) software (Pruesse et al., 2012). For Cyanobacteria, phylogenetic trees were built with the ARB software (Ludwig et al., 2004) and the SILVA 123 database (Quast et al., 2013; Yilmaz et al., 2014). Representative

clones of the dominant phyla were aligned with SINA and then added in the ARB guide tree using the ARB parsimony tool. In addition, the closest environmental 16S rRNA gene sequences retrieved by BLAST were added if they were not present in the SILVA 123 database. Phylogenetic tree was reconstructed using the method of Randomized Accelerated Maximum Likelihood (RAxML) (Stamatakis et al., 2008) with the GTRCAT substitution model. Bootstrap values were calculated from 1,000 replicates.

The phylogenetic tree of partial *pufLM* operons was built using MEGA7 (Tamura et al., 2013), and the Maximum Likelihood method based on the Jukes-Cantor model (Jukes and Cantor, 1969). Initial tree(s) for the heuristic search were obtained automatically by applying Neighbor-Join and BioNJ algorithms to a matrix of pair wise distances estimated using the Maximum Composite Likelihood approach, and then by selecting the topology with the highest log likelihood value. The tree was drawn to scale, with branch lengths measured in the number of substitutions per site. The analysis involved 54 nucleotide sequences. Codon positions included were 1st+2nd+3rd+Noncoding. All positions containing gaps and missing data were eliminated. There were a total of 273 positions in the final dataset.

Scanning Electron Microscopy (SEM)

SEM analyses were performed on gold-coated air-dried samples using a Field Emission Zeiss Sigma Scanning Electron Microscope (Carl Zeiss NTS GmbH) at the X Ray Analysis Laboratory (LAMARX, Universidad Nacional de Córdoba, Argentina). SEM observation on carbon-coated samples dried at the critical point were also performed at the Service Commun de Microscopie Electronique à Balayage (UPMC, Paris, France) using a Zeiss Supra 55VP (Carl Zeiss NTS GmbH) SEM equipped with an EDXS spectrometer (X flash Quad detector, Brucker). Images were collected using secondary electron detectors (Everhart-Thornley for high voltage mode, VPSE for variable pressure mode and InLens for low voltage mode) and a backscattered electron detector (AsB). Accelerating voltage ranged from 3 to 15 kV at variable pressures and high current (up to 1 nA).

Mineralogical Identification

Powder X-ray diffraction (XRD) analyses were conducted on BP microbial mat and lithified BP samples using a Philips PW1800/10 powder diffractometer equipped with a Cu anode and a graphite monochromator (LAMARX). Measurements were performed at 40 kV voltage and 30 mA current, from 10 to 60° (2 θ), with an acquisition time of 2.0 s and an angular step of 0.100° 2θ. Resulting diffractograms were analyzed using Highscore software.

Focused Ion Beam Milling (FIB) and Transmission Electron Microscopy (TEM)

Eight ultrathin electron-transparent sections (∼100 nm in thickness) were prepared by FIB milling on an Auriga® FIB-SEM (Carl Zeiss NTS GmbH) available at IPGP using the FIB "lift out" technique (see Heaney et al., 2001 for details). A 30 kV Ga^+ beam operated at 20 nA was used for the initial steps of the milling. Progressive excavation from both sides of the section area was performed through repeated milling steps. Depth of milling was approximately 7 microns. The final thinning of the section was performed with a less intense Ga^+ beam operated at 100 pA current.

Transmission Electron Microscope (TEM) observations were carried out on all FIB sections using a JEOL 2100F microscope (JEOL Ltd.) operating at 200 kV at the Institut de Minéralogie, de Physique des Matériaux et de Cosmochimie (IMPMC, Paris, France). The TEM is equipped with a field emission gun, a ultrahigh resolution UHR pole piece and a Gatan energy filter. High-angle annular dark-field scanning transmission electron microscopy (HAADF-STEM) was used with a focused electron beam of a few nm for Z-contrast imaging. Energy Dispersive X-ray Spectrometry (EDXS) analyses were performed using a JEOL detector equipped with an ultrathin window that allowed detection of low Z elements.

Fourier Transform Infrared Microspectroscopy (FTIR)

Cross-sections of oncoids associated with the black pustular mats were obtained using a sterilized diamond saw and sterile deionized water. They were prepared as doubly-polished sections of about 100 μm thick and without any resin or glue in order to avoid organic contamination. FTIR hyperspectral images were acquired at IPGP using a Thermo Scientific iN10 MX microscope (Ever-Glo™ conventional Infrared source) with a liquid nitrogen cooled detector. Maps were collected in Attenuated Total Reflection (ATR) mode with a germanium tip. Punctual analyses were performed in the 4,000–700 cm^{-1} range, with a spot size of 20 × 20 μm, a spectral resolution of 8 cm^{-1} and with 64 accumulations per spectrum. Background spectra were acquired between each spectrum under the same analytical conditions. Data were processed using the OMNIC™ software (Thermo Fisher Scientific).

Synchrotron Based Deep UV Fluorescence Microspectroscopy (S-DUV)

Slices from oncoid samples associated with black pustular mats were also investigated using synchrotron-based deep UV fluorescence microspectroscopy (S-DUV) and full-field imaging at the French national synchrotron radiation facility SOLEIL (Saint-Aubin, France) on the DISCO beamline (Giuliani et al., 2009). We focused on *Rivularia*-rich laminations in order to better describe the nature and spatial relationships between mineral phases and organic remnants at the micrometer scale. Both TELEMOS and POLYPHEME end stations available on the beamline were used. Samples were first investigated by full-field luminescence microscopy (TELEMOS end station) using an Axio ObserverZ1 microscope (Carl Zeiss MicroImaging) with a ×40 objective. The excitation wavelength was set at 275 nm with a DM300 dichroic mirror. Fluorescence emission was collected using 3 filters (bandpass at 327–353 nm, 370–410 nm, and 420–480 nm). Acquisition time was set at 30 s for all channels except for the 327–353 nm filter (60 s) and 2D fluorescence images were acquired along a transect, perpendicularly to

the laminations of the oncoid sample. Images obtained with TELEMOS microscope were treated with ImageJ software (Schneider et al., 2012) and allowed localizing areas with the highest fluorescent signals. We then selected specific areas with *Rivularia*-like morphologies on which hyperspectral fluorescence maps were acquired (POLYPHEME end station) on an Olympus IX71 inverted microscope with homemade replacement of the intermediate lenses set to be transparent in the deep UV range (Jamme et al., 2010, 2013; Thoury et al., 2011) and a ×40 objective. Excitation was set at 275 nm and a bypass mode was used in order to increase the intensity of the collected fluorescence signal. The collection range was set from 310 to 600 nm. Spectra were processed using LabSpec software (Horiba Scientific).

RESULTS

Description of the Microbial Mat and Associated Oncoids

The microbial mat was characterized by a bulbous to pustular morphology (**Figure 1C**) and measured 1 to 8 mm in thickness. It had a dark pigmentation (**Figures 1C,D**), possibly due to the abundancy of scytonemin, a photoprotective pigment produced under high UV irradiation (Garcial-Pichel and Castenholz, 1991). No clear lamination was visible beneath the surface layer, although mixed green, pink and black patches along with white carbonated patches were detected (**Figure 2A**). Optical observation of this mat (**Figure 2B**) highlighted the predominance of large filamentous microorganisms resembling cyanobacterial *Rivularia* sp. (as confirmed by Sanger sequencing) and measuring around 12 to 15 μm in diameter.

Irregular laminations with dark brown to yellowish vertically oriented *Rivularia* filaments (15–20 μm in diameter) were observed in petrographic sections of associated oncoids (**Figure 2C**). They alternated with micritic or botryoidal laminations. They presented a tufted paintbrush-like palisade fabric (Reitner et al., 1996). CLSM observations of these petrographic sections carried out at an excitation of 633 nm revealed a strong fluorescence of the *Rivularia* filaments within the paintbrush-like laminations (in red in **Figure 2D**). Some pigments were also observed near the filament sheaths using excitation at 543 nm.

Microbial Associations in BP Mats

Conventional optical microscopy revealed the presence of a strongly mineralized microbial consortium associated with the *Rivularia*-like filaments. This latter included sulfur-bearing bacterial filaments and diatoms (**Figure 3A**). This consortium was also observed by CLSM. Filamentous cyanobacteria were identified based on the auto-fluorescence of their photosynthetic pigments (in red in **Figure 3B**). Numerous cocci (*c1*, *c2,* and *c3*) and filamentous cells were also observed, fluorescing in green after Syto®9 staining. Among them, colonies of cells with a peculiar coccus shape (*c1*) were detected in close association with the *Rivularia* sheaths and the minerals (in light blue in **Figure 3B**). At high magnification, abundant microorganisms were observed in association with the thick sheath of a *Rivularia* filament (in green in **Figure 3C**). *Rivularia* cells were also visible (in red in **Figure 3C**). Consistently with conventional optical microscopy, filamentous sulfur-bearing bacteria were also detected in bright blue (laser reflection on the sulfur grains, **Figure 3D**) close to the *Rivularia* filaments. This was also confirmed by SEM imaging highlighting elemental sulfur grains on these filaments (*SF.* in **Figure 3E**). No precipitated mineral was detected in close relationship with the *Rivularia* sheaths.

Microbial Diversity

In order to characterize the microorganisms forming the consortium associated with the *Rivularia* filaments and to assess their potential role in mineral precipitation, 16S rRNA gene sequences of Bacteria and Archaea were analyzed for the BP mat samples collected in 2013 and 2015. Results obtained from either laser microdissected cyanobacterial filaments collected in 2015 or bulk DNA extractions on all samples are summarized in the following sections.

Laser Microdissection and Whole Genome Amplification of *Rivularia* Filaments and of the Associated Bacterial Consortium

After laser microdissection of large filamentous cyanobacteria, we detected three different representative 16S rRNA gene sequences (3c-25, 3c-38, and 3c-57) of cyanobacteria affiliated to the *Rivularia* genus (**Table 1**). 16 sequences represented by 3c-25 and 3c-57 shared 99% identities with the 16S rRNA gene sequence of *Rivularia* detected in a microbial mat associated with the microbialites of Alchichica Lake (JN825310) and *Rivularia atra* BIR MGR1 (AM230675), a marine species forming black colonies (Guiry and Morrison, 2015) and *Calothrix* sp. XP9A (AM230670). 14 sequences represented by 3c-38 share 100% identities with *Rivularia* sp. PUNA_NP3_PCI185B (KY296608) isolated from Laguna Negra microbial mat. Heterotrophic Bacteroidetes affiliated to *Marivirga* (Pagani et al., 2011), *Maribacter* and *Winogradskyella* genera constituted the most abundant epiphytic bacterial community associated with the *Rivularia* filaments (**Table 1**). No archaeal sequences were detected within the consortium, hence suggesting that archaea were not closely associated with the *Rivularia* filaments.

Bulk DNA Extraction

After bulk DNA extraction, cyanobacteria affiliated to the *Rivularia* genus were detected in both mats collected in 2013 and 2015 using cyanobacterial specific primers (**Figure 4**) but not using universal bacterial primers. The 16S rRNA gene sequences of *Rivularia* species detected in 2015 (BP2015-9*) were identical to the 3c-25 sequences detected after whole genome amplification (**Figure 4**). Yet, the most abundant cyanobacterial 16S rRNA gene sequences detected using cyanobacterial specific primers were affiliated to the *Phormidium* genus for both 2013 and 2015 (**Figure 4**). The clones were notably affiliated to *Phormidium* sp. MBIC10210 LEGE 11384 and *Phormidium lucidum* CY-012 (JQ927355 and KC217548, respectively; 98% to 99% identities). 17 sequences from 2015 were also closely related to sequences detected in microbialites from Alchichica, an alkaline Mexican lake (*Halomicronema* sp., JN825328; 97% identity).

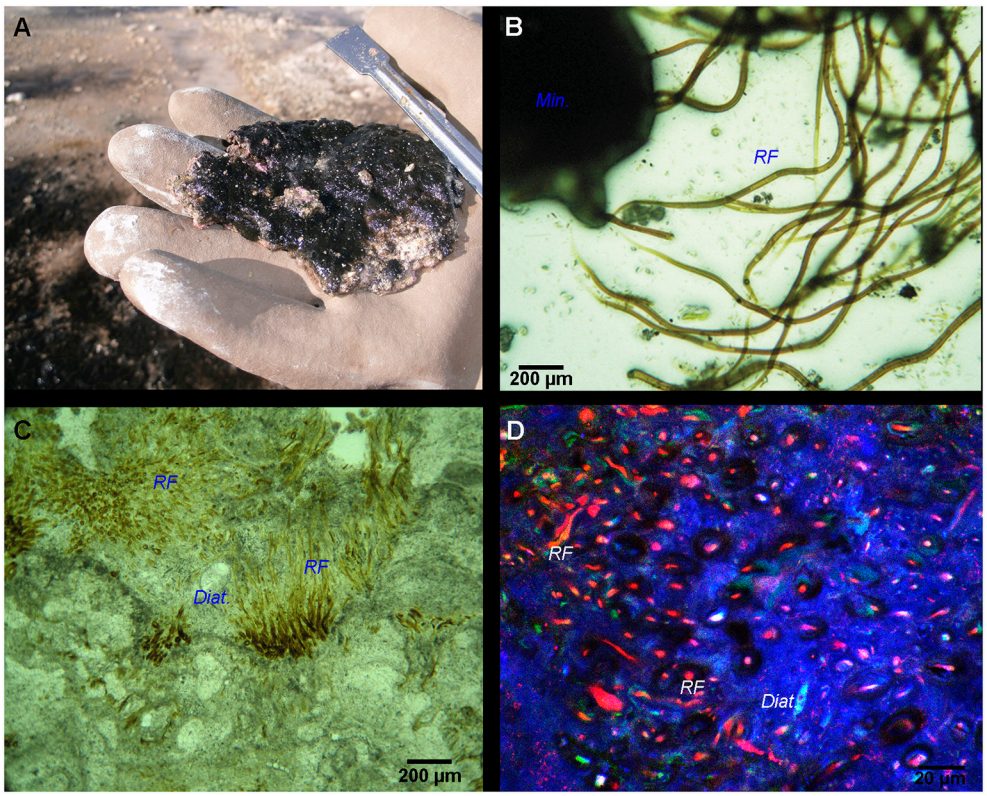

FIGURE 2 | (A) Black pustular mat with visible white-colored carbonate precipitates. **(B)** Optical microscopy image of the BP mat highlighting *Rivularia* filaments (*RF*) associated with minerals (*Min.*). **(C)** Paintbrush-like palisade fabric of *Rivularia*-like filaments encrusted by carbonates and preserved inside an oncoid lamination alternating with other lamination types (like sparry, botryoidal and micritic). Encrusted diatoms (*Diat.*) can also be found. **(D)** CLSM image of the same lamination enclosing *Rivularia*-like filaments whose remaining pigments show red fluorescence. The mineralized portion of the oncoid appears in blue due to laser reflection on solid carbonates.

A description of the main bacterial sequences detected in 2013 and 2015 using general bacterial primers is given in **Table 2**. Bacteroidetes, Proteobacteria and Verrucomicrobia were the most abundantly detected phyla. Only one sequence of cyanobacteria was detected. Among the bacterial phyla, Bacteroidetes belonging to the *Lewinella* genus were identified. Their cultivable representatives (*Lewinella cohaerens*, *Lewinella persica*) correspond to orange to black chemoorganotrophic bacteria (Khan et al., 2007). Interestingly, members of the Gammaproteobacteria found in both 2013 and 2015, samples have closest uncultivated bacteria (98% identities) that were only detected in the Altiplano at Salar de Ascotan in Chile (EF632661). Bacteria belonging to the Myxococcales order were also observed in both samples. They were affiliated to bacteria from the semiarid "Tablas de Dainiel National Park" wetland (Central Spain, FJ516764).

The other detected bacterial species were specific to the BP mats collected in 2013 or 2015. In the BP mat collected in 2013, numerous bacteria affiliated to marine species were identified. Bacteroidetes closely related to *Winogradskyella echinorum* (JQ661183, 97% identity; Nedashkovskaya et al., 2009) were detected. Most of the observed Alphaproteobacteria clones belonged to the Rhodobacteraceae family. One OTU was closely related to the *Tropicibacter* genus (97% identity; Lucena et al., 2013) and another one to *Sulfitobacter noctilucicola* (NR_134206, 99% identity; Kwak et al., 2014). An additional member of Alphaproteobacteria was closely related (98% identity) to the aerobic phototrophic marine bacteria *Marivita cryptomonadis* (NR_044514). Finally, Verrucomicrobia members affiliated to the *Haloferula* genus were distinguished. They were close to *Haloferula chungangensis* (NR_109435), a heterotrophic ureolytic bacterium from marine sediments (Kang et al., 2014). Conversely, the sulfur-bearing filamentous cells observed using CLSM and SEM in association with *Rivularia* (**Figures 3A,D,E**) were not clearly identified in our 16S rRNA gene sequences retrieved by bulk DNA extraction. Although the unidentified sulfur-bearing filament bacteria were morphologically similar to *Thiotrix* species (Howarth et al., 1999), further efforts will be required to identify them by testing new protocol of DNA extraction retrieving additional 16S rRNA encoding gene sequences and performing laser microdissection.

In the BP mat collected in 2015, several detected bacteria were closely related to uncultivated bacteria from the Guerrero Negro hypersaline microbial mats belonging to Bacteroidetes (JN453999), Alphaproteobacteria (JN530502, JN436614) and Verrucomicrobia (JN480742). Other identified Bacteroidetes

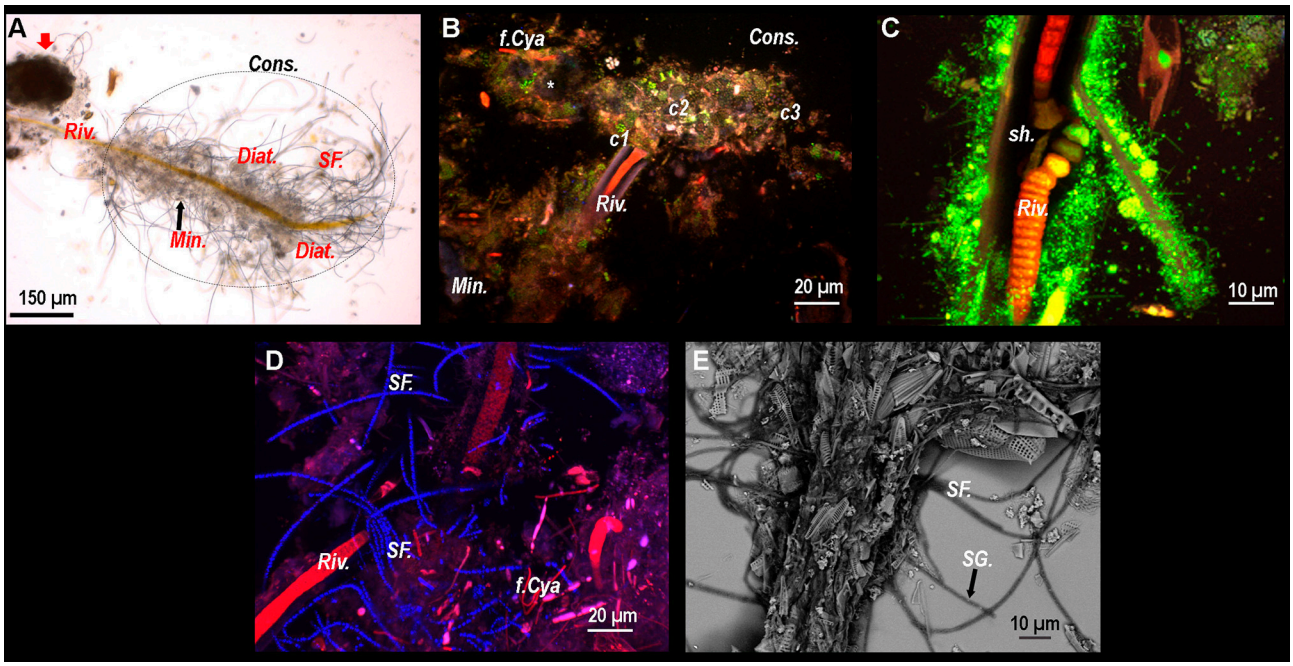

FIGURE 3 | (A) Optical microscopy image of a *Rivularia* filament (*Riv.*) with which numerous microorganisms are associated, hence suggesting the presence of a consortium (*Cons.*) (dotted circle). A large mineral aggregate is also visible near the filament (red arrow). Sulfur filaments (*SF.*), diatoms (*Diat.*) and mineral grains (*Min.*) can also be observed around the filament. From **(B–D)**: Composite CSLM images obtained over an integrated depth of 50 µm by concomitant excitations at 405, 488, and 543 nm and collection between 425 and 475 nm, 500 and 530 nm, and 560 and 660 nm, respectively. **(B)** Composite CLSM image of a consortium surrounding a *Rivularia* filament distinguished in red due to its photosynthetic pigments. Inside the consortium, abundant cocci-shaped cells are observed thanks to Syto®9 staining (green) (*c1*, *c2,* and *c3*). Minerals appear in light blue due to laser reflection (white asterisk). Other filamentous cyanobacteria (*f.Cya*) are observed. **(C)** High magnification composite CLSM image of a *Rivularia* filament where cells are visible (in red) inside the sheath (*sh.*), which is covered by a myriad of Syto®9-stained cells. **(D)** Detail of a *Rivularia* filament associated with sulfur-bearing bacterial filaments (bright blue dots due to laser reflection). **(E)** Magnified SEM image in backscattered electron mode showing a *Rivularia* filament and the associated sulfur-bearing filaments (black arrow) with sulfur grains (*SG.*) appearing as bright dots. **(A,B,D,E)** were obtained on BP13 mat samples, while **(C)** was observed on BP15 mat sample after laser microdissection.

were close to bacteria from El Tatio hot springs (GU437622), a high altitude (4400 meters above sea level) geothermal site with low sulfide and high arsenic concentrations in Chile (Engel et al., 2013). These Bacteroidetes were also related to *Psychroflexus salinarum* (NR108235; 96% identity), which correspond to dark orange bacteria isolated from marine solar saltern (Yoon et al., 2008). Moreover, three bacterial sequences affiliated to Bacteroidetes already found associated with diatom detritus were also observed in this sample (AY298788; 98% identity). Similarly to the results obtained for the 2013 BP mat, several sequences affiliated to the *Roseobacter* clade were detected and belonged to the *Oceanicola* genus (98% identities, KY770546), the *Octadecabacter* genus (98% identity with KX073749) and the *Roseinatronobacter* genus (97% identities with KJ486297), all these bacteria being aerobic phototrophic bacteria.

As observed for Bacteria, the Archaea communities were clearly different in BP mats collected in 2013 and in 2015 (**Table 3**). In 2013 BP samples, we detected only methanogenic archaea. Sequences affiliated to the obligate acetoclastic methanogenic *Methanosaeta harundinacea* (Ma et al., 2006) (CP003117, 99% identity). In addition, some sequences were related to *Methanolinea tarda* (NR_028163, 97% identity), a strain using H_2 and formate for growth and methane production (Imachi et al., 2008). Diverse other methanogenic archaea were detected, notably some closely affiliated to *Methanogenium cariaci* (99% identities) a marine methanogenic archaea (N_104730, 99% identities), which uses hydrogen and carbon dioxide as substrates for growth (Romesser et al., 1979). In 2015 BP, the archaea detected were affiliated to the Thermoplasmatales order. The sequences were related to 16S rRNA gene sequences of uncultivated archaea retrieved in hypersaline mats (EU585947, EU585956, HM480251).

pufLM Genes Cluster Detection

The phylogenetic analysis of the *puflM* genes cluster detected in 2013 (BP13) showed that at least 18 different sequences of aerobic anoxygenic phototrophic bacteria (AAnPB) were present in the analyzed BP mat. As also noticed for the 16S rRNA encoding genes, two groups of AAnPB seemed to be endemic of high altitude Andean lakes as the partial *pufLM* sequences were close to sequences detected in a high altitude salt lake in Chile (FN813741 and FN813748) (**Figure 5**).

Associated Carbonate Minerals in BP Mats

Most of the *Rivularia* filaments were observed in the superficial pustular zone of the BP mats. They showed a tangled

TABLE 1 | Taxonomic affiliations of the bacterial 16S rRNA gene sequences retrieved using general bacterial primers after laser microdissection from the BP consortia collected in 2015.

	Taxonomy	Nb	Closest environmental bacteria	Closest cultivated bacteria
4c-1	Bacteroidetes; Flammeovirgaceae; *Marivirga*	4		KT324862 100%, *Marivirga* sp. CR-23
4c-14	Bacteroidetes; Flammeovirgaceae; *Marivirga*	5	AF170787 98%, Antarctic quartz stone sublithic communities	NR112183 98%, *Marivirga sericea* strain IFO 15983
3c-4	Bacteroidetes; Flavobacteriaceae	3	AF170787 96%, phycosphere of *Enteromorpha prolifera*	JQ069961 96% *Maribacter* sp. BSw21901
3c-13	Bacteroidetes; Flavobacteriaceae; *Maribacter*	3		JQ988061 99%, *Maribacter* sp. T28
3c-34	Bacteroidetes; Flavobacteriaceae	2		NR_043453 99%, *Psychroserpens mesophilus*
3s-2	Bacteroidetes; Flavobacteriaceae	8		JQ 687107 99%, *Winogradskyella* sp. KYW 630
3s-13	Bacteroidetes; Flavobacteriaceae; *Winogradskyella*	4		NR_137338 95%, *Winogradskyella litoriviva*
3c-11	Bacteroidetes; Flavobacteriaceae; *Winogradskyella*	1	KY190901 95%, marine sediment, Antartica	AY771731 95%, *Winogradskyella thalassocola*
3c-25	Cyanobacteria; SubsectionIV; FamilyII; *Rivularia*	14	JN825310 99%, microbialites from Alchichica alkaline lake	AM230675 99%, *Rivularia atra* BIR MGR1
3c-38	Cyanobacteria; SubsectionIV; FamilyII; *Rivularia*	14		KY296608 100%, *Rivularia* sp. PUNA_NP3_PCI185B
3c-57	Cyanobacteria; SubsectionIV; FamilyII; *Rivularia*	2	JN825310 99%, microbialites from Alchichica alkaline Lake	AM230670 99%, *Calothrix* sp. XP9A
3c-51	Cyanobacteria; SubsectionI; FamilyI; *Gloeocapsa*	3	GQ340127 98%, water column Marathonas Reservoir	GQ375048 98%, *Limnococcus limneticus*
3c-43	Proteobacteria; Gammaproteobacteria; HTA4	2	JQ586297 98%, arctic marine sediment	EF492067 97%, Candidatus *Berkiella cookevillensis*
3s-16	Proteobacteria; Gammaproteobacteria; Legionellaceae; *Legionella*	2		LT906452 96%, *Legionella pneumophila*
4c-9	Unclassified	6	AB630669 96%, aquatic moss pillars	
3c-15	Unclassified	3	KJ998102 97%, Guerrero Negro intertidal mat	
3c-45	Unclassified	1	KJ998102 95%, Guerrero Negro intertidal mat	

Nb stands for number of clones.

arrangement with variable amounts of EPS-associated mineral aggregates and diatoms located between the cyanobacterial filaments (**Figure 6A**). The lower (i.e., inner) part of the BP mats showed *Rivularia* filaments together with calcium carbonate precipitates within an EPS matrix and diatoms (**Figure 6B**). Locally and within the carbonates, some tubular hollow structures were observed (**Figure 6B**). They probably corresponded to entombed microbial filaments. The diameter of these hollow structures was variable, being similar or lower than that of fresh *Rivularia* filaments (**Figure 6B**).

XRD analyses of bulk samples of the BP mats showed that they were mainly composed of Mg-calcite, with a lower amount of aragonite (Supplementary Figure S1). At the microscale, as observed using SEM, different types of carbonate particles were identified, with the predominance of sub-spherical to subhedral carbonate particles with diameters varying from 80 to 700 nm (**Figure 6C**) along with almost perfect tiny carbonate spheres (**Figure 6E**). Occasionally more irregular anhedral carbonate particles of similar size were also observed (**Figure 6D**). Sub-spherical to subhedral particles were typically associated with EPS and sometimes clustered into irregularly shaped aggregates of various sizes (usually up to ∼200 μm in diameter). These aggregates were closely associated to the EPS matrix where abundant diatoms and other microorganisms were also present (**Figures 6C–F**). They occasionally clumped together and form wavy to irregularly shaped horizontal lamina.

Another distinct group of calcium carbonate particles was represented by irregular bunches of elongated, needle- and spindle-like particles (**Figure 6F**). The individual needle-shaped particles could be up to 2 μm long and formed irregularly distributed clusters or patches that were not typically associated with the EPS matrix. As suggested by XRD data and given the acicular shape these particles, these needles could be aragonite. While the precipitation of the nanometer-sized sub-spherical to spherical calcium carbonate grains appeared to be limited to the EPS matrix of the top-most layers of the mat, the larger subhedral and euhedral grains were mostly present in the inner parts of the mat, where degraded diatoms and cyanobacterial sheaths were present.

Calcein Staining of Resin-Embedded BP Mat: Calcium Localization

In order to study the micro-scale relationships between microorganisms and carbonate precipitates within the consortium, resin-embedded microbial mat fragments stained with calcein were analyzed by CLSM. Calcein stained the

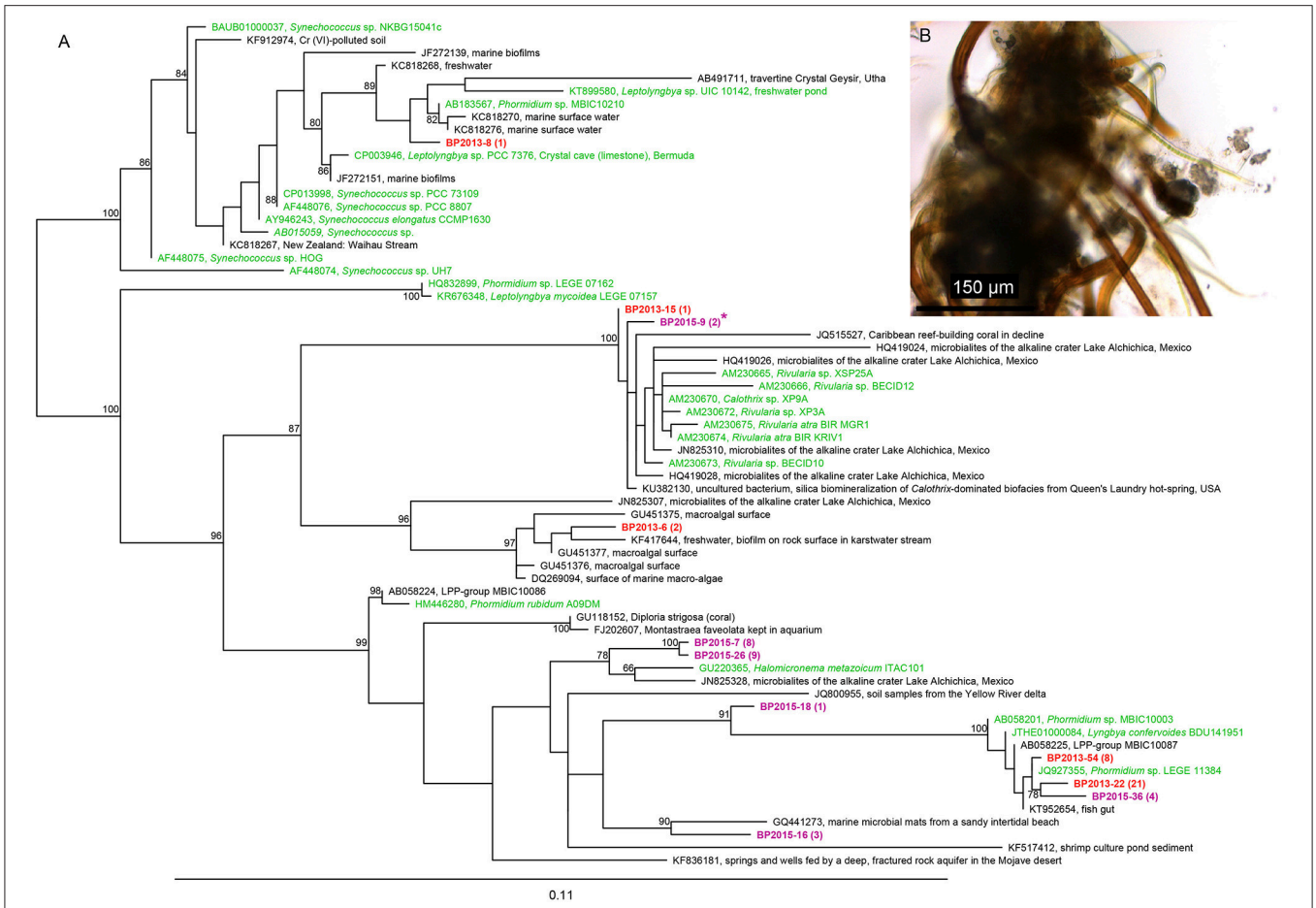

FIGURE 4 | (A) Phylogenic tree of the 16S rRNA encoding gene sequences of cyanobacteria retrieved using the cyanobacterial specific primers in the black pustular mats in 2013 (red) or 2015 (purple). Numbers in parentheses represent the number of clones obtained for each operational taxonomic unit (OTU) defined at a sequence similarity ≥97%. The cyanobacteria sequence identified in the consortium isolated by laser microdissection corresponds to BP2015-9*. The tree was constructed with the ARB software (Ludwig et al., 2004) by Maximum Likelihood analysis using 1,097 positions, by including the closest possible uncultivated (black) and cultivated (green) relatives as well as more distant representatives of cultivated species. Bootstrap values for nodes (>70% support) based on 1,000 replicates are displayed as percentages. **(B)** Optical microscopy image of one of the consortia isolated by laser microdissection and showing *Rivularia* filaments.

active parts of mats displaying free divalent cations close to the minerals and the subspherical aggregates located in between the *Rivularia* filaments (**Figures 7A,B**). Besides, the cocci cells (*c1*) already observed in **Figure 3**, were also visible with abundant calcein staining around the colonies (**Figure 7B**), all in close spatial relationship with the *Rivularia* sheaths (**Figure 7D**). Interestingly, calcein accumulated in between the *Rivularia* sheaths and cells (**Figures 7A–D**). Some bright spots were also detected at this level (**Figures 7B–D**), suggesting a possible mechanism of calcium accumulation or trafficking. As only Ca^{2+} was detectable using SEM-EDXS around the cells stained with calcein (Supplementary Figure S2), this calcein coloration should mainly reveal Ca^{2+} accumulation rather than Mg^{2+} accumulation.

Transmission Electron Microscopy Observations of a Cyanobacterial Filament

In order to explore the possibility of calcium accumulation inside the filaments, as suggested by the bright spots observed in **Figures 7B–D**, FIB ultrathin sections were milled from resin-embedded BP mat samples showing calcein-stained *Rivularia* filaments. This procedure allowed exploring the free Ca and Mg content of cyanobacterial sheaths without any interference coming from the surrounding minerals.

A longitudinal *Rivularia* filament stained with calcein was selected with others for FIB milling after CLSM observation (Supplementary Figure S3 and **Figure 8A**) and transversally milled (**Figure 8B**). HAADF-STEM observation of the FIB section with associated STEM-EDXS mapping of calcium (Ca, yellow) and carbon (C, red), is shown in **Figures 8C,D**. These two elements exhibited opposite distributions. Calcium-rich areas (white and black dotted lines) corresponded to low-carbon areas. Localized calcium globules were also detected (black and white arrows in **Figures 8C,D**, respectively). No clear or very low Mg signal was detected in the analyzed samples, supporting the idea of Ca accumulation within the filaments. These observations were consistent with CLSM observations showing high calcein fluorescence between the *Rivularia* sheaths

TABLE 2 | Taxonomic affiliations of the bacterial 16S rRNA gene sequences using general bacterial primers retrieved from the BP mats collected in 2013 (gray) and 2015 (white).

	Taxonomic affiliation	Nb	Closest uncultured bacterium	Closest cultivated bacterium
BPb2015-4	Bacteroidetes; Cryomorphaceae;	1	JQ197952 98%, sea water	CP003156 89%, *Owenweeksia hongkongensis*
BPb2015-3	Bacteroidetes; Flavoceae; *Psychroflexus*	3	AY298788 98%, diatom detritus Southern Ocean sea water	EU000243 97%, *Donghaeana dokdonensis*
BPb2015-15	Bacteroidetes; Flavoceae; *Psychroflexus*	1	GU437550 94%, sediment El Tatio Geyser Field, Chile	
BPb2015-2	Bacteroidetes; Flavoceae; *Psychroflexus*	1	JN453999 95%, Guerrero Negro hypersaline microbial mat	
BPb2015-27	Bacteroidetes; Flavoceae; *Psychroflexus*	1	GU437622 97%, sediment El Tatio Geyser Field, Chile	NR_108235 96%, *Psychroflexus salinarum*
BPb2015-30	Bacteroidetes; Flavoceae; *Psychroflexus*	1	EF190068 94%, Qinghai oilfield	
BPb2013-6	Bacteroidetes; Flavoceae; *Winogradskyella*	2		JQ661183 97%, *Winogradskyella echinorum*
BPb2013-36	Bacteroidetes; Flavoceae; *Winogradskyella*	3		JQ661183 97%, *Winogradskyella echinorum*
BPb2013-13	Bacteroidetes; Flavobacteraceae	1		KJ475165 94%, *Psychroserpens damuponensis*
BPb2013-19	Bacteroidetes; Flavobacteraceae	1	AY298788 98%, diatom detritus	CP025116 96%, *Nonlabens* sp. MB-3u-79
BPb2013-2	Bacteroidetes; Saprospiraceae; *Lewinella*	1		EU371935 95%, *Lewinella persicus*
BPb2013-32	Bacteroidetes; Saprospiraceae; *Lewinella*	1		JQ661170 95%, *Lewinella agarilytica*
BPb2015-12	Bacteroidetes; Saprospiraceae; *Lewinella*	1	JQ753202 96%, Antarctic sea ice	NR_112672 94%, *Lewinella cohaerens*
BPb2015-21	Bacteroidetes; Saprospiraceae; *Lewinella*	4		KY009734 96%, *Lewinella* sp. SD302
BPb2015-33	Bacteroidetes;	1	FJ213812 94%, Altiplano, Salar de Ascotan, Chile	
BPb2015-14	Cyanobacteria; SubsectionIII; Phormidium	1		JQ927355 98%, *Phormidium* sp. LEGE 11384
BPb2015-26	Proteobacteria	1	LC213232 96%	
BPb2015-17	Proteobacteria; Alphaproteobacteria; Hyphomonadaceae	1	JN530502 96%, Guerrero Negro hypersaline microbial mat	NR_148267 94%, *Hyphomonas beringensis*
BPb2015-1	Proteobacteria; Alphaproteobacteria; Hyphomonadaceae	1	JN436614 99%, Guerrero Negro hypersaline microbial mat	CP017718 98%, *Hyphomonas* sp. Mor2
BPb2015-22	Proteobacteria;Alphaproteobacteria; Parvularculaceae	2	GU326496 97%, desalinisation plant	
BPb2013-3	Proteobacteria; Alphaproteobacteria; Rhodobacteraceae	1	AM990873 97%, Mediterranean Sea	HE962517 95%, *Tropicibacter mediterraneus*
BPb2013-30	Proteobacteria; Alphaproteobacteria; Rhodobacteraceae	1	GQ441231 96%, marine microbial mats sandy beach	KJ486297 93%, *Roseinatronobacter* sp. MOL1.10
BPb2013-5	Proteobacteria; Alphaproteobacteria; Rhodobacteraceae	1	GU083689 96%, Inner Mongolia, Xiarinur soda lake	NR_044285 96%, *Rhodobaca barguzinensis*
BPb2013-8	Proteobacteria; Alphaproteobacteria; Rhodobacteraceae	1	KJ475514 97%, Oil-derived marine aggregates	JX861563 97%, *Tropicibacter* sp. MCCC1A07686l
BPb2015-18	Proteobacteria; Alphaproteobacteria; Rhodobacteraceae	1		KY770546 98%, *Oceanicola* sp. strain 7002-119
BPb2015-9	Proteobacteria; Alphaproteobacteria; Rhodobacteraceae	1		KJ486297 97%, *Roseinatronobacter* sp. MOL1.10
BPb2013-16	Proteobacteria; Alphaproteobacteria; Rhodobacteraceae; *Marivita*	1	KY770575 98%, phycosphere	NR_044514 98%, *Marivita cryptomonadis*
BPb2015-11	Proteobacteria; Alphaproteobacteria; Rhodobacteraceae; *Octadecabacter*	1		KX073749 98%, *Octadecabacter* sp. HDSW-34
BPb2013-7	Proteobacteria; Alphaproteobacteria; Rhodobacteraceae; *Sulfitobacter*	1		NR_134206 99%, *Sulfitobacter noctilucicola* costal
BPb2015-24	Proteobacteria; Alphaproteobacteria; Rhodobacteraceae	1		KF418804 94%, *Sulfitobacter* sp. S19SW

(Continued)

TABLE 2 | Continued

	Taxonomic affiliation	Nb	Closest uncultured bacterium	Closest cultivated bacterium
BPb2015-6	Proteobacteria; Gammaproteobacteria; Alteromonadaceae*; Marinobacter*	1		NR_145917 93%, *Marinobacter confluentis*
BPb2013-11	**Proteobacteria; Gammaproteobacteria;**	**1**	**EF632661 98%, Chile: Altiplano, Salar de Ascotan**	
BPb2015-34	**Proteobacteria; Gammaproteobacteria;**	**1**	**EF632661 98%, Chile: Altiplano, Salar de Ascotan**	
BPb2015-28		1		
BPb2015-23	Proteobacteria; Gammaproteobacteria; Oceanospirillaceae*;Nitrincola*	1		FJ764761 96%, *Nitrincola* sp. E-044
BPb2015-5	Proteobacteria; Gammaproteobacteria; OM182 clade	1	HM127577 98%, Qinghai Lake	NR_112620 91%, *Thioprofundum hispidum*
BPb2013-28	Proteobacteria; Gammaproteobacteria	1	EF632659 99%, aquatic environment Altiplano Chile	MG264256 98%, *Wenzhouxiangella marina*
BPb2015-55-CYA	**Proteobacteria; Deltaproteobacteria; Myxococcales**	**7***	**FJ516764 97%, wetland (Central Spain)**	
BPb2013-14-CYA	**Proteobacteria; Deltaproteobacteria; Myxococcales**	**6***	**FJ516764 99%, wetland (Central Spain)**	
BPb2013-10	Verrucomicrobia; Verrucomicrobiaceae; *Haloferula*	3	KY190897 95%, marine sediment from Potter Cove	NR_109435 95%, *Haloferula chungangensis*
BPb2015-7	Verrucomicrobia	2	JN480742 96%, Guerrero Negro hypersaline microbial mat	

Two non-cyanobacterial sequences were retrieved with the specific cyanobacterial primers (*). For the sequences retrieved using the cyanobacterial specific primers, please refer to ***Figure 4****. Strictly identical sequences retrieved in BP2013 and BP2015 are indicated in bold. Nb stands for number of clones.*

and the cells. Nevertheless, in this case no crystalline phase was detected inside the *Rivularia* sheaths or cells.

Characterization of the Structure and Mineralogy of *Rivularia*-Rich Laminations in Oncoids Associated With the BP Mats

SEM and CLSM observations indicated that, in the mat, carbonate precipitation seemed to occur within the EPS excreted by the microbial consortium found associated with the *Rivularia* filaments, which dominate the black pustular mat. The corresponding laminations within the associated oncoids should then be considered as biologically-induced and may have then registered direct or indirect traces of biological activity. We then investigated these laminations in oncoids in order to characterize potential biomarkers to be searched for in fossil stromatolites. Synchrotron-based deep UV fluorescence imaging was first carried out on a cross-section from an oncoid associated with the BP mats collected in 2013 (**Figure 9**). Optical microscopy observations of this cross section highlighted the presence of different laminations presenting variable colors (**Figure 9A**). Among them, brown-beige laminations were clearly distinguishable from other ones and were marked by the presence of numerous encrusted *Rivularia*-like filaments (**Figure 9A**). Full-field fluorescence images were collected on a transect crossing *Rivularia*-rich laminations (**Figure 9B**) after excitation at 275 nm. Similar imaging was performed on other *Rivularia*-rich laminations (**Figure 9C**) for consistency. Reconstructed RGB images indicated that the fluorescence signal was different in these laminations compared to the bulk carbonated matrix of the oncoid (in white in **Figure 9A**). These laminations (**Figure 9B** images 2 and 4, and **Figure 9C**) display fluorescence emission in the range 327–357 nm (detected with the Blue filter) while white laminations were dominated by a mix of fluorescence emission signals collected with the green and red filters (leading to a yellow color; **Figures 9B,C**). These observations were consistent for the whole sample and indicated that *Rivularia*-rich laminations presented a different structure or composition compared to the other laminations. In order to decipher the origin of this specific signal, hyperspectral fluorescence images were acquired on the same sample. An example of the collected fluorescence emission signal is given **Figure 9C**. Spectra were characterized by two bands at 316 and 341 nm and a large massif above 400 nm. The latter one could not be properly deconvoluted due to optical artifacts occurring above 400 nm. The two other bands at 316 and 341 nm were likely emerging from organic compounds related to cell remnants (main fluorescence emission at 312, 340, and 410 nm; Jamme et al., 2013) trapped in the mineralized matrix. The difference in fluorescence emission signals observed between *Rivularia*-rich laminations and other laminations could then correspond to a different content in organic compounds. However, carbonate minerals are known to fluoresce when excited in the UV range. The variable fluorescence patterns from one lamination to another one might then also be induced by differences in the lamination mineralogy.

The mineralogy of *Rivularia*-rich laminations was then investigated. Bulk XRD analyses were first performed on powdered oncoid associated with BP mat (**Figure 10A**) and indicated the predominance of Mg-rich calcite (90%) associated with minor aragonite (10%). Microscale ATR-FTIR analyses were then performed on the cross-section analyzed by S-DUV

TABLE 3 | Taxonomic affiliations of the archaeal 16S rRNA gene sequences using general archaeal primers retrieved from the BP mats collected in 2013 (gray) and 2015 (white). Nb stands for number of clones.

	Taxonomic affiliation	Nb	Closest uncultured archaeon	Closest cultivated archaeon
2015BPar-1	unclassified	1	EU585947 95%, hypersaline microbial mat	
2015BPar-21	Euryarchaeota; Thermoplasmatales; Marine Benthic Group D and DHVEG-1	2	EU585947 99%, hypersaline microbial mat	
2015BPar-30	Euryarchaeota; Thermoplasmatales; Marine Benthic Group D and DHVEG-1	2	EU585956 98%, hypersaline microbial mat	
2015BPar-19	Euryarchaeota; Thermoplasmatales; Marine Benthic Group D and DHVEG-1	1	EU585961 96%, hypersaline microbial mat	
2015BPar-16	Euryarchaeota; Thermoplasmatales; Marine Benthic Group D and DHVEG-1	1	EU585964 97%, hypersaline microbial mat	
2015BPar-13	Euryarchaeota; Thermoplasmatales; Marine Benthic Group D and DHVEG-1	1	HM480251 99%, hypersaline microbial mat	
2015BPar-9	Euryarchaeota; Thermoplasmatales; Marine Benthic Group D and DHVEG-1	1	EU585964 98%, hypersaline microbial mat	
2013BPar-30	Euryarchaeota; Methanosarcinales; Methanosaetaceae; Methanosaeta	1	HG001405 99%, salt marsh sediment	CP003117 98%, *Methanosaeta harundinacea*
2013BPar-26	Euryarchaeota; Methanosarcinales; Methanosaetaceae; Methanosaeta	6	KX581173 99%, marine sediment	CP003117 99%, *Methanosaeta harundinacea*
2013BPar-3	Euryarchaeota; Methanosarcinales; Methanosarcinaceae;	2	KP987245 99%, subsurface sediments	KF952458 95%, *Methanosalsum zhilinae*
2013BPar-24	Euryarchaeota; Methanosarcinales; Methanosarcinaceae;	3	KP987245 99%, subsurface sediments	NR_102894 97%, *Methanosalsum zhilinae*
2013BPar-2	Euryarchaeota; Methanomicrobiales; Methanoregulaceae; Methanolinea	2	MG062727 99%, anaerobic granules	NR_112799 96%, *Methanolinea mesophila*
2013BPar-9	Euryarchaeota; Methanomicrobiales; Methanoregulaceae; Methanolinea;	6	AB236052 98%, marine sediment	NR_028163 97%, *Methanolinea tarda*
2013BPar-11	Euryarchaeota; Methanomicrobiales; Methanomicrobiaceae; Methanogenium	2		NR_104730 99%, *Methanogenium cariaci*

fluorescence imaging, specifically in the areas presenting a "blue" fluorescence pattern (**Figure 9B** images 2 and 4, and **Figure 9C**). Most of the acquired ATR-FTIR spectra ($n \approx 66$) presented a similar pattern and are summarized in **Figure 10B**. The position of main CO_3^{2-} vibrational bands (ν_2 asymmetric bending at 870 cm^{-1}; ν_3 asymmetric stretching at 1,400 cm^{-1}; $\nu_1 + \nu_4$ at 1,800 cm^{-1}) were compared to carbonate standards and mainly corresponded to calcite (e.g., spectra a and b in **Figure 10B**). Some spectra presented patterns that might indicate a mixed composition between calcite and other carbonates depending on the position in the lamination. The low spatial resolution of the ATR tip ($20 \times 20\,\mu m$) precluded the identification of individualized pure components at the microscale. However, some spectra acquired very close to *Rivularia*-like cell remnants presented shifts from the typical calcite ν_2 asymmetric bending band at 1,789 cm^{-1} (vs. 1,796 cm^{-1} for calcite), along with a marked shoulder in the ν_3 asymmetric stretching band (black arrow in spectrum c displayed in **Figure 10B**). It should correspond to a mix between calcite and aragonite. Similarly, analyses in a white lamination, far from the assumed influence of *Rivularia*-rich lamination, presented a shift of the ν_2 asymmetric bending toward 1,803 cm^{-1}. It may highlight a mixed composition between calcite and dolomite (spectrum d in **Figure 10B**) and should be indicative of the presence of Mg-bearing carbonate, consistently with bulk XRD analyses. These combined analyses seem to confirm that the *Rivularia*-rich laminations should be distinguishable from the other ones from a spectroscopic point of view. Even if we cannot non-ambiguously conclude, they may present a higher organic content than other laminations (without *Rivularia* filaments) and/or a different mineralogy.

DISCUSSION

The different microscopic observations and microbial diversity analyses carried out in this study highlight the likely influence of the microbial consortium observed around *Rivularia* filaments in the carbonate precipitation process. Thus, the role of *Rivularia* and of the related consortium in the mineralization processes is discussed. In parallel, the composition of the corresponding laminations in oncoids, comparatively to other laminations, is discussed in order to characterize potential biosignatures to be searched for in fossil stromatolites.

The most abundantly detected cyanobacterial 16S rRNA gene sequences using the cyanobacterial specific primer were affiliated to the *Phormidium* and *Rivularia* genus. The large filamentous cyanobacteria of around 15 μm in diameter, observed by optical microscopy and CLSM, were identified as *Rivularia* using laser microdissection (**Table 1**, **Figure 4**). A striking observation is that

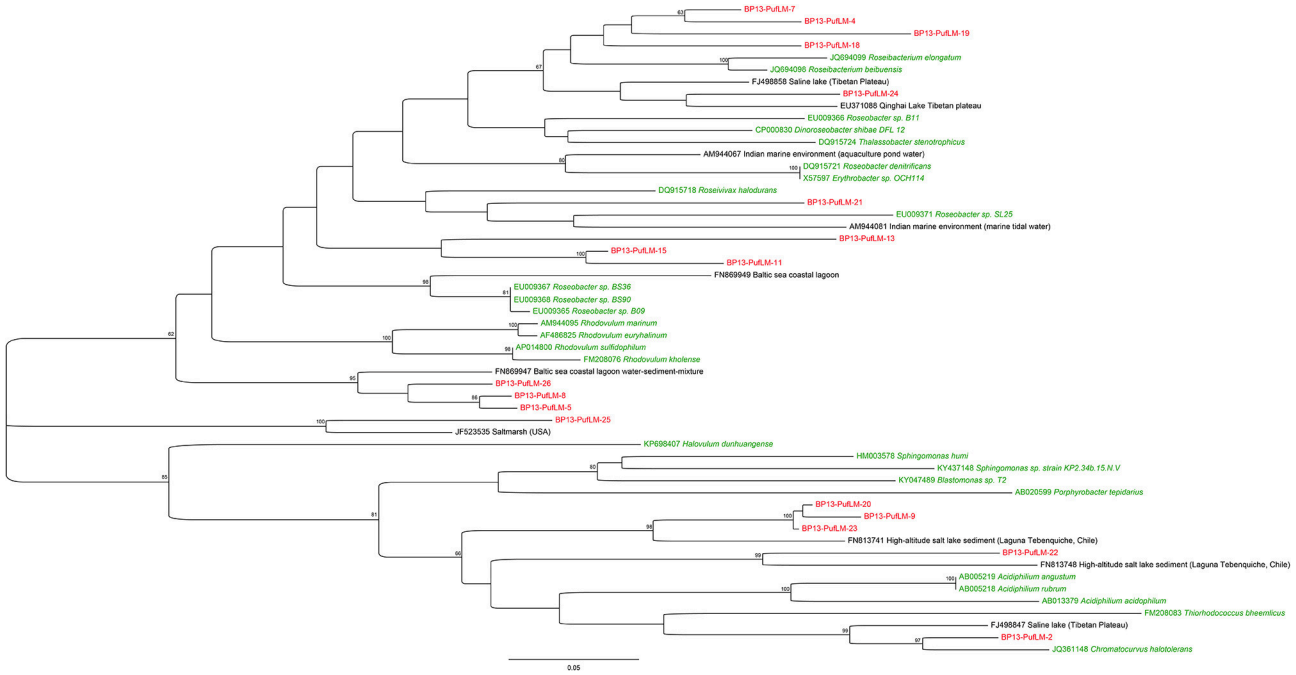

FIGURE 5 | Maximum Likelihood phylogenetic analysis of partial *pufLM* operons detected in the black pustular mat collected in 2013. The evolutionary history of the retrieved partial *pufLM* operons and of the partial *pufLM* operons of the closest uncultivated (black) and cultivated (green) relatives was inferred by using the Jukes-Cantor model (Jukes and Cantor, 1969). The tree with the highest log likelihood (−6611.4021) is shown. The percentage of trees in which the associated taxa clustered together is shown next to the branches. The tree is drawn to scale, with branch lengths measured in the number of substitutions per site. Evolutionary analyses were conducted using MEGA7 (Tamura et al., 2013).

calcein stained the space between the cells and the sheath of the *Rivularia* filaments (**Figure 7**). It suggests a possible mechanism of Ca^{2+} concentration and may have implications for carbonate precipitation. This could be due to the difference between the cell wall and the sheath surface that was observed for *Calothrix* sp. (strain KC97; Phoenix et al., 2002), a cyanobacteria presenting a morphology similar to the one of the *Rivularia* sp. *Calothrix* sp. has a spatially dual-layer system composed of a reactive cell wall, and a poorly-reactive sheath. The sheath may then inhibit detrimental biomineralization or HCO_3^- diffusion. On the contrary, the cell wall, which contains a high density of electronegative sites, may trap cations (Phoenix et al., 2000, 2002). A similar process should be proposed for the *Rivularia* of Laguna Negra. It would explain the specific accumulation of Ca^{2+} observed close to the cell wall surface rather than on the external sheath itself. Conversely, it has been shown that living cyanobacterial cells are capable of self-protection against solid carbonate incrustation through shedding of mineralized S-layer (Thompson et al., 1997; Douglas and Beveridge, 1998) and/or by metabolically maintaining positive surface potential to avoid Ca^{2+} adsorption and subsequent entombment within solid carbonates (Martinez et al., 2008, 2010). On the other hand, in cyanobacteria, as for all organisms, intracellular calcium is strongly regulated by independent processes of Ca^{2+} uptake and active efflux (Smith and Wilkins, 1988). The normal levels of Ca^{2+} are maintained very low in order to prevent toxicity. If external Ca^{2+} concentrations are higher, as it is typically the case in hypersaline lakes, calcium uptake may involve low passive permeability of Ca^{2+} sensitive trans-membrane channels (Singh and Mishra, 2014). In the case of the Andean *Rivularia* sp. identified in this study, further efforts should be devoted to understand why *Rivularia* filaments are capable to keep free Ca^{2+} ions between the cells and the sheaths without inducing carbonate precipitation, and if this calcium could bind to the S-layer domains (e.g., glutamate and aspartate residues) or to the cell wall domains to control the flux of calcium in and out of cells.

Despite the alkalinizing activity of *Rivularia* cyanobacteria and contrary to what was described for freshwater *Rivularia* (Pentecost and Ulrich, 2010), a remarkable observation of the present study is that the *Rivularia* filaments did not present any carbonate precipitation close to their sheath (**Figures 3**, **6**, **7**). Calcification in cyanobacteria depends on local environmental conditions (Arp et al., 2001; Riding, 2006) and only occurs in waters supersaturated with respect to calcium carbonates. However, only certain genera calcify and none of them are obligate calcifiers (Merz, 1992). The microorganisms located on the cyanobacterial sheath may metabolically modify the local physico-chemical conditions and induce or preclude carbonate precipitation. We assessed the influence of the activity of epiphytic bacteria on carbonation, based on the results obtained by 16S rRNA encoding genes sequencing following laser microdissection and whole genome amplification. Most of the bacteria associated with the *Rivularia* sheaths were affiliated to known epiphytic members of the Bacteroidetes phylum. Some identified species were affiliated to the *Maribacter* genus that

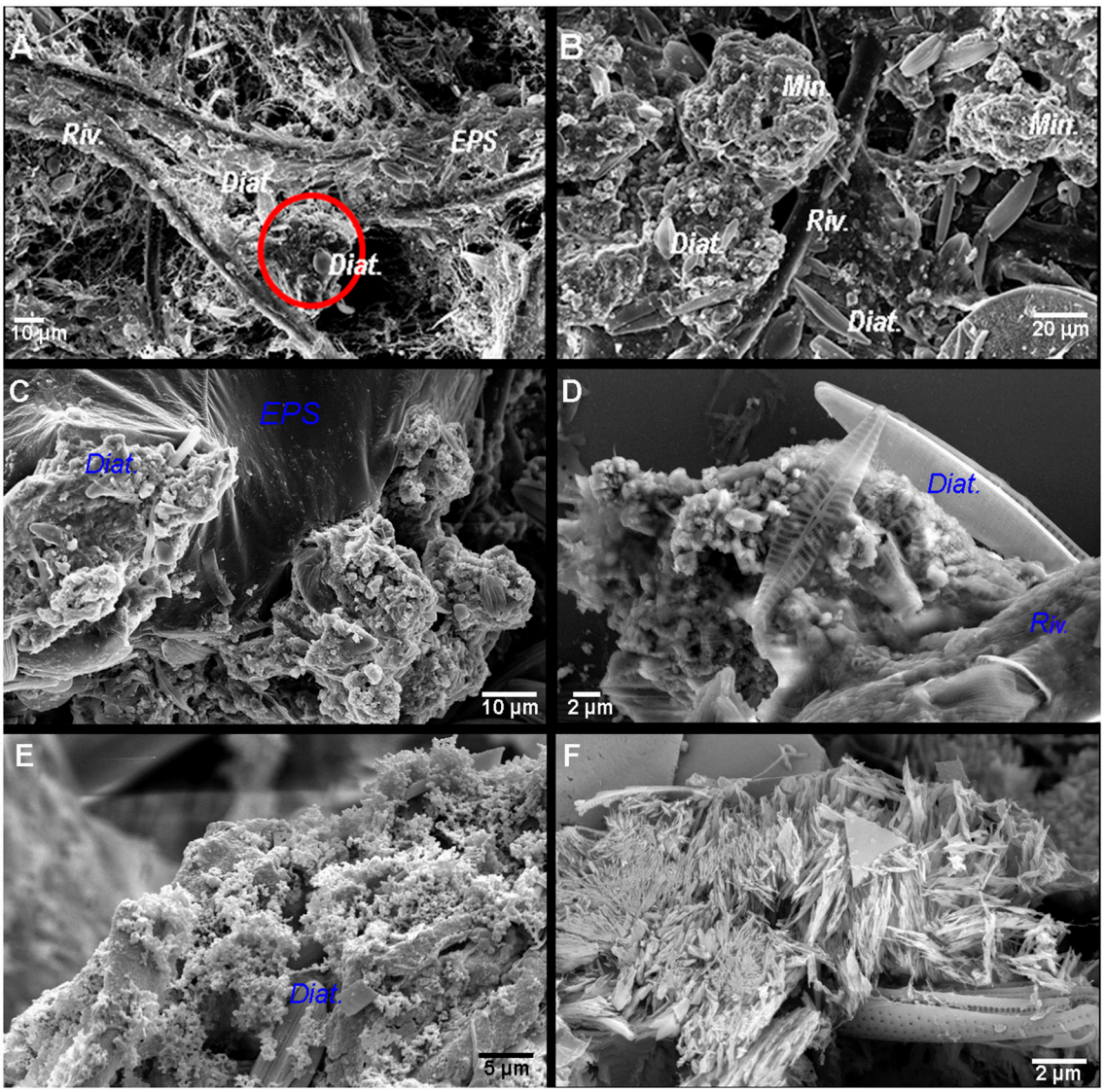

FIGURE 6 | (A) SEM images of the surface of the black pustular mat where *Rivularia* filaments (*Riv.*) and exopolymeric substances (*EPS*) are observed. The red circle highlights a mineral aggregate with diatoms (*Diat.*). **(B)** Below the black pustular surface, mineral aggregates (*Min.*) with diatoms are abundant; some *Rivularia* filaments can also be observed. From **(C–D)**, SEM images in backscattered electron mode of the carbonate minerals associated with the *Rivularia* filaments in BP mats. **(C)** Aggregates formed by sub-spherical to subhedral carbonate particles associated with the EPS matrix where diatoms frustules are also observed. **(D)** Magnified view of a mineral aggregate with subspherical carbonate grains and associated diatoms. **(E)** Aggregate composed of submicrometric carbonate spherules entombing abundant diatoms frustules. **(F)** Elongated needle-like carbonates.

encompasses heterotrophic bacteria associated with brown algae (Nedashkovskaya et al., 2004). Their activity may accordingly induce acidic conditions by producing CO_2 around *Rivularia* sheaths, hence precluding carbonate precipitation (Dupraz and Visscher, 2005; Dupraz et al., 2009) and explaining the absence of carbonation on *Rivularia* sheaths in Laguna Negra.

On the contrary, the results obtained in this study indicated that carbonate precipitation occurred within the EPS matrix excreted by the diverse bacterial consortium associated with *Rivularia*. To identify potential calcifiers in the BP mats, the influence of the whole microbial community retrieved by bulk phylogenetic analyses was then assessed in light of microscopic observations. SEM and CLSM observations indicated that calcification might start with the precipitation of small isolated granules of calcium carbonates dispersed throughout the EPS matrix surrounding diatoms and coccoid pigmented cells (*c1*) (**Figures 3**, **7**) but not in direct contact with the *Rivularia* sheath. Diatoms and other microorganisms such as Myxococcales and methanogenic archaea are known to produce large amounts of EPS (Bapteste et al., 2005; Scholten et al., 2005). These EPS should serve as nucleation sites for carbonate precipitation following organo-mineralization

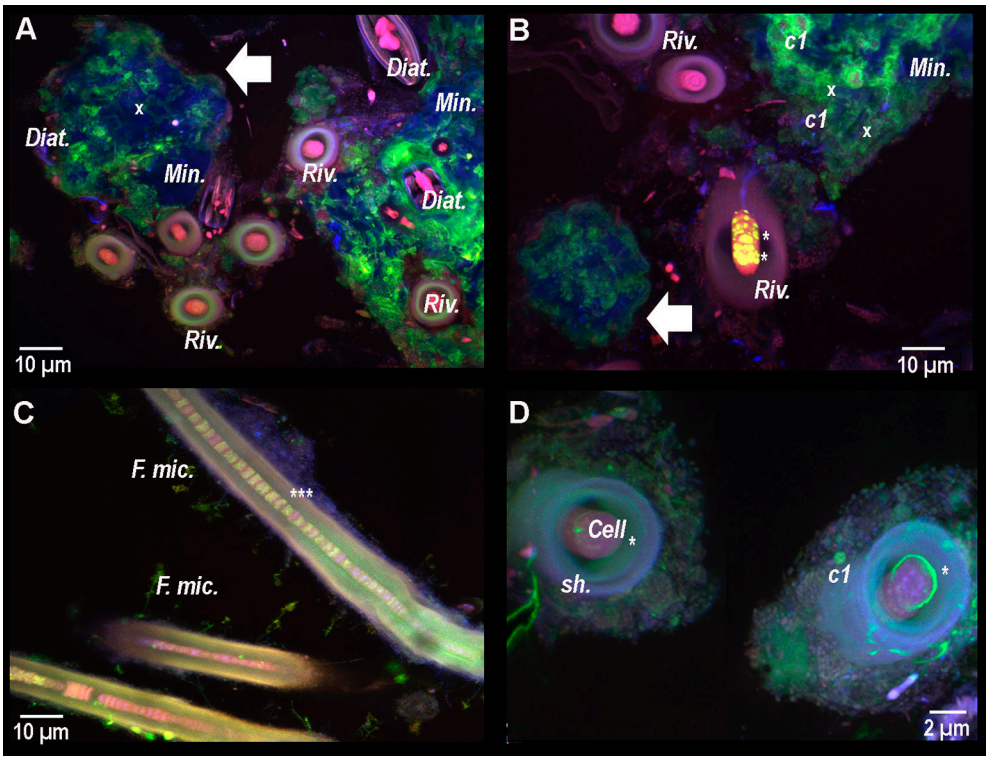

FIGURE 7 | Composite CLSM images of a resin-embedded black pustular microbialite, stained with calcein. Images were obtained with concomitant excitations at 405, 488, and 543 nm and collection between 425 and 475 nm, 500 and 530 nm, and 560 and 660 nm, respectively. Fluorescence emission between 500 and 530 nm emerges specifically from calcein (in green). **(A)** Mineral aggregates (*Min.* and white arrow) are observed in blue. Their surfaces are partially stained with calcein, hence indicating the presence of free Ca^{2+} ion. Inside and surrounding the mineral aggregate, diatom frustules (x) and living diatoms (*Diat.*) are visible thanks to their photosynthetic pigments. Some *Rivularia* filaments (*Riv.*) seem to be separated from the mineralized aggregates, while other filaments are close but not entombed in the aggregate and occur with diatoms. Calcein stained the space inside the filaments, i.e., between the sheath and the cells. In **(B)** yellow/light green dots are observed in one of the *Rivularia* filament (*). Calcein also strongly stained the contours of the pigmented *c1* cocci-shaped cell colonies that were found closely associated with the mineral aggregates (white arrow). **(C)** Close up view of calcein-stained *Rivularia* filaments. The dye also stained some other filamentous microorganisms associated with the *Rivularia* sheath (*F. mic.*). Inside the *Rivularia* filament, some green dots are distinguishable (***). **(D)** Image of two transversally-cut *Rivularia* filaments, where calcein fluorescence (*) was also found between the cells and the sheath (*sh.*); as in **(C)**, calcein also stained the *c1* colonies.

processes (Perry et al., 2007; Defarge et al., 2009). This is consistent with the micritic anhedral globular textures observed by SEM, characteristic of carbonate precipitation occuring in an organic matrix (Dupraz et al., 2009). The primary amorphous grains would be bound to EPS surface charges and would then grow into larger subhedral to euhedral carbonate grains. The precipitation of these carbonates would be favored by the supersaturation of the waters relatively to calcite (Gomez et al., 2014) and by some local alkalinization induced by microbial activity. Notably, in addition to the photosynthetic activity of *Rivularia*, diatoms may also have promoted local alkalinization. Furthermore, some of the bacteria identified in the whole microbial community may present potential alkalinizing metabolisms favoring carbonate precipitation. Among them are the Myxococcales identified in the BP mats of Laguna Negra. Some bacteria belonging to this order are known to favor mineral precipitation (Jimenez-López et al., 2007), such as *Myxococcus xanthus*, which induces carbonate precipitation by ammonification, resulting in an increase of the alkalinity in the culture medium (González-Muñoz et al., 2010). Of likely greater interest, the pigmented coccoid bacteria (*c1*, **Figure 3**) may correspond to some of the aerobic anoxygenic phototrophic bacteria (AAnPB) affiliated to the marine *Roseobacter* clade (**Figure 5** and **Table 2**). Abundant and diverse AAnPB were detected in the BP mats (**Table 2**). The phylogenetic analysis of the 16S rRNA and *pufLM* encoding genes showed that specific AAnPB develop in hypersaline high altitude Andean lakes. Members of the *Roseobacter* clade are known to interact with marine phytoplankton, including diatoms, also abundant in Andean lakes (Maidana and Seeligmann, 2006; Farías et al., 2013, 2014; Barbieri et al., 2014). This association may allow microbes to use metabolic niches that would be inaccessible otherwise (Overmann and van Gemerden, 2000; Schink, 2002; Orphan et al., 2008). For example, *Roseobacter*-related species are able to use glycolate excreted by eukaryotic phytoplankton during autotrophic photorespiration (Fogg, 1983; Grossart et al., 2005). Members of the *Roseobacter* clade are phototrophic bacteria but lack genes for inorganic carbon fixation (Lenk et al., 2012; Luo and Moran, 2014; Zhang et al., 2016). Consequently, these bacteria cannot favor carbonate precipitation *via* alkalinization

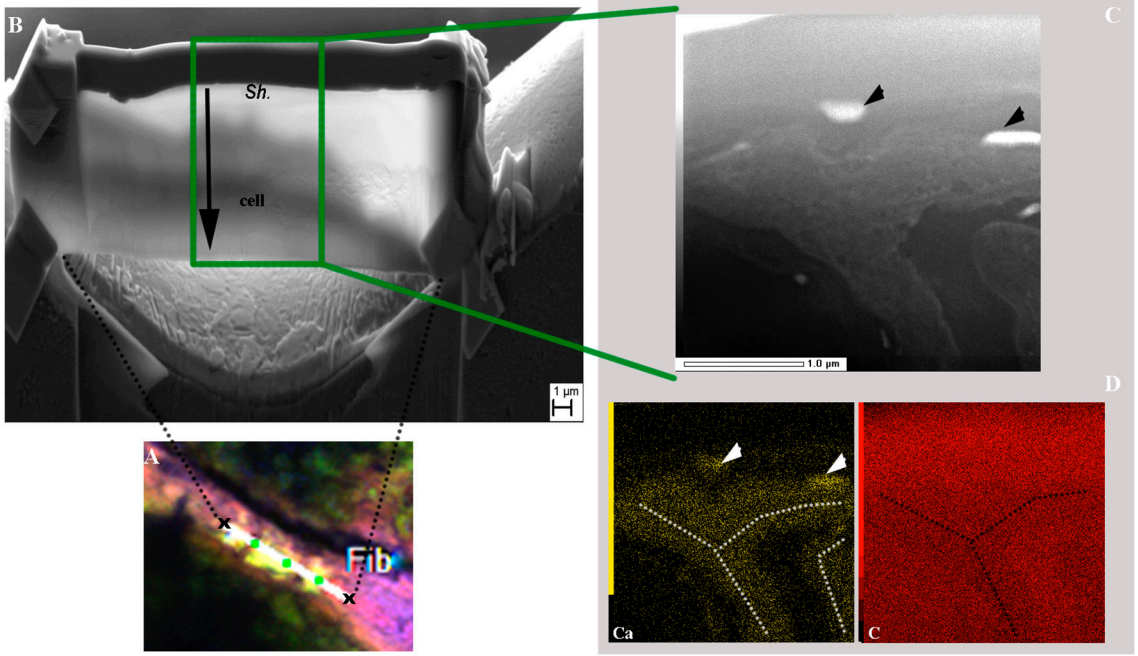

FIGURE 8 | SEM and TEM observations of a FIB section longitudinally milled on a cyanobacteria filament stained with calcein as shown in the CLSM image displayed in **(A)** (see Supplementary Figure S3 for location of the selected area and associated scale). **(B)** SEM image of the ultrathin section after milling. The upper part of the section corresponds to the filament sheath (*Sh.*) and the lower part (end of black arrow) to the cyanobacteria cell. **(C)** HAADF-STEM image of the FIB section showing the filament along its longer axis and the different phases within the filament. The black arrowheads indicate regions with strong electron absorption. **(D)** Associated STEM-EDXS elemental maps for calcium (Ca; in yellow) and carbon (**C**; in red) displaying opposite distributions. Ca-rich areas are highlighted by white arrowheads and white dotted lines.

linked to photoautotrophy (Dupraz and Visscher, 2005). On the contrary, most of the members of the *Roseobacter* clade are ureolysers and some are denitrifyers (Luo and Moran, 2014). Both ureolysis (Zhu and Dittrich, 2016) and denitrification (Erşan et al., 2015) increase pH in the surrounding medium and favor carbonate precipitation. Furthermore, it has been shown that denitrification activity of the *Roseobacter denitrificans* strain was increased by light stimulus (Doi and Shioi, 1991). Even if we cannot preclude the influence on carbonate formation of other microbial strains, such as methanogenic archaea (Michaelis et al., 2002; Roberts et al., 2004; Scholten et al., 2005; Kenward et al., 2009), we suggest that phototrophy, ureolysis and denitrification associated with the activity of AAnPB may be important drivers of alkalinization and carbonate precipitation in the BP mats of Laguna Negra.

Overall, *Rivularia* cyanobacteria favored the development of a large microbial consortium that indirectly promoted carbonate precipitation via organo-mineralization processes, and hence participated to the formation of stromatolites. The corresponding laminations in oncoids should then be considered as biologically-induced. They may present some direct or indirect markers of biological activity or cell remnants that may furnish biosignatures that could be searched for in the geological record. We then investigated stromatolites associated to the black pustular mat at Laguna Negra. We focused on laminations that presented *Rivularia*-like encrusted cells and we compared them to micritic and botryoidal laminations of the stromatolites, which may have a purely chemical origin. The laminations of interest presented well-preserved filaments that may have been encrusted *in vivo* or rapidly after death while preserving the original sheath morphology and sizes (Riding, 1977; Merz-Prei and Riding, 1999; Couradeau et al., 2014). The morphology of the mat could indeed be preserved if the carbonate formation process is fast enough to cover the EPS (Kazmierczak et al., 2015), hence creating mineral coatings on cells or groups of cells. Besides, these encrusted filaments presented a strong fluorescence signal after CLSM that could be attributed to cell photosynthetic pigments (**Figure 2D**). Pigments are recalcitrant molecules that can be preserved in sediments (Leavitt et al., 1997). They could be used as molecular fossils of photosynthetic organisms (Brocks and Pearson, 2005). The analysis of the *Rivularia*-rich laminations of oncoids associated with BP mats using S-DUV also clearly highlighted a different fluorescence signal compared to other laminations after excitation in the deep UV range (**Figure 9**). The origin of the fluorescence pattern could not be fully elucidated but could be attributed either to (i) a different mineralogy or (ii) a higher content in organic compounds trapped in the mineral matrix relatively to other laminations. Punctual FTIR analyses of the *Rivularia*-like laminations seemed to indicate a possible higher proportion of aragonite relatively to calcite or Mg-calcite

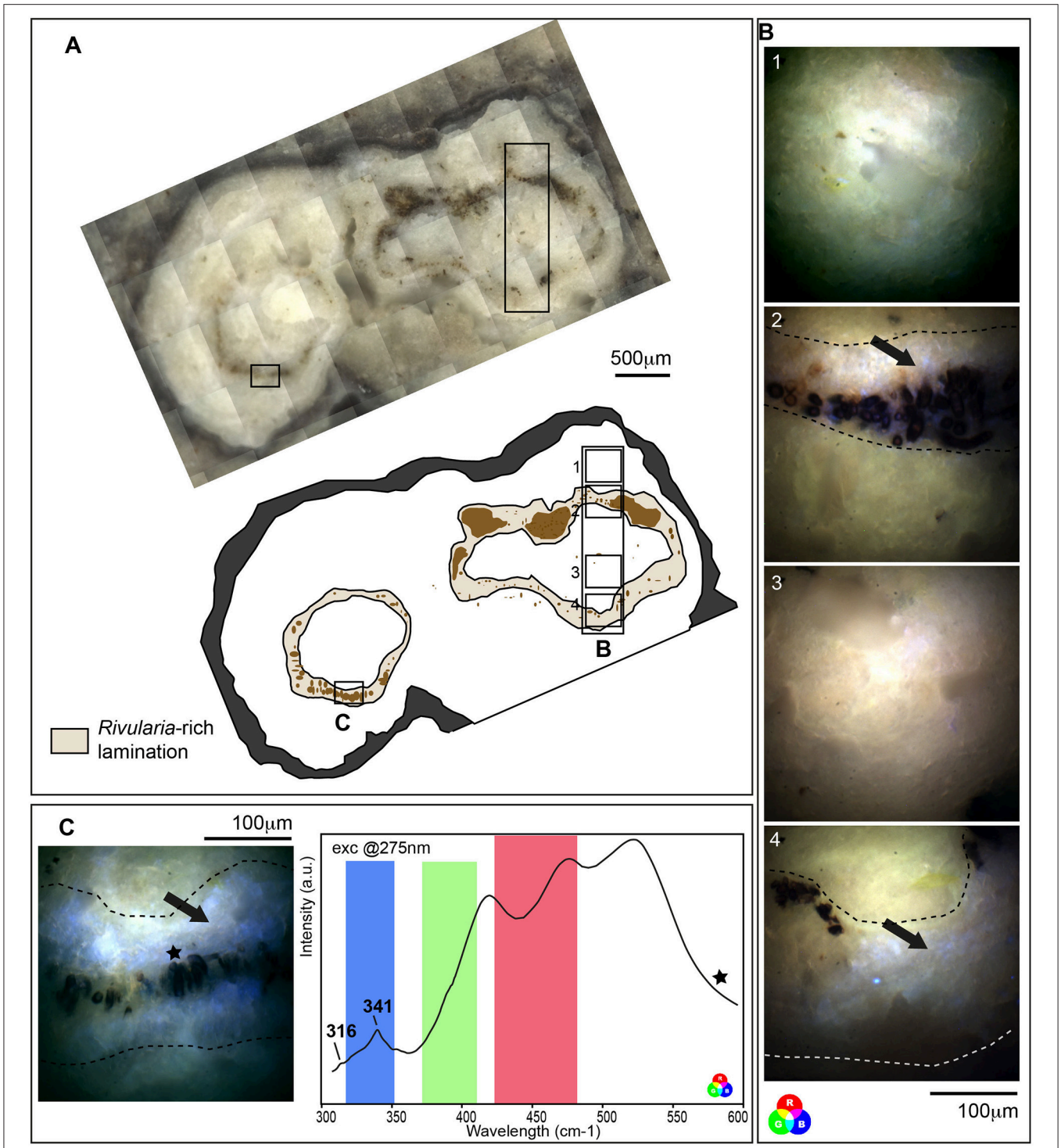

FIGURE 9 | Fluorescence emission signal after synchrotron-based deep UV excitation at 275 nm of a cross section of an oncoid associated with a black pustular mat. **(A)** Optical microscopy observation and schematic representation of the cross section highlighting *Rivularia*-rich laminations with encrusted *Rivularia*-like cells. The localization of areas of interest analyzed by S-DUV fluorescence imaging is given. **(B)** Composite RGB images of 4 areas of interest were reconstructed using the fluorescence signal collected with filters between 327 and 353 nm (Blue), 370 and 410 nm (Green) and 420 and 480 nm (Red). They were surimposed on the optical image. An intense fluorescence signal was observed using the blue filter between 327 and 353 nm (black arrows) in *Rivularia*-rich laminations (underlined by dot lines in **B,C**) while the rest of the matrix is marked by a mixed fluorescence collected using the green and red filters. **(C)** The fluorescence emission signal associated with *Rivularia*-rich laminations was recorded and showed two bands at 316 and 341 cm^{-1}. The fluorescence ranges covered by the three filters are indicated with respective colors and the precise localization where the spectrum was collected is given by a black star on the associated full-field RGB fluorescence image.

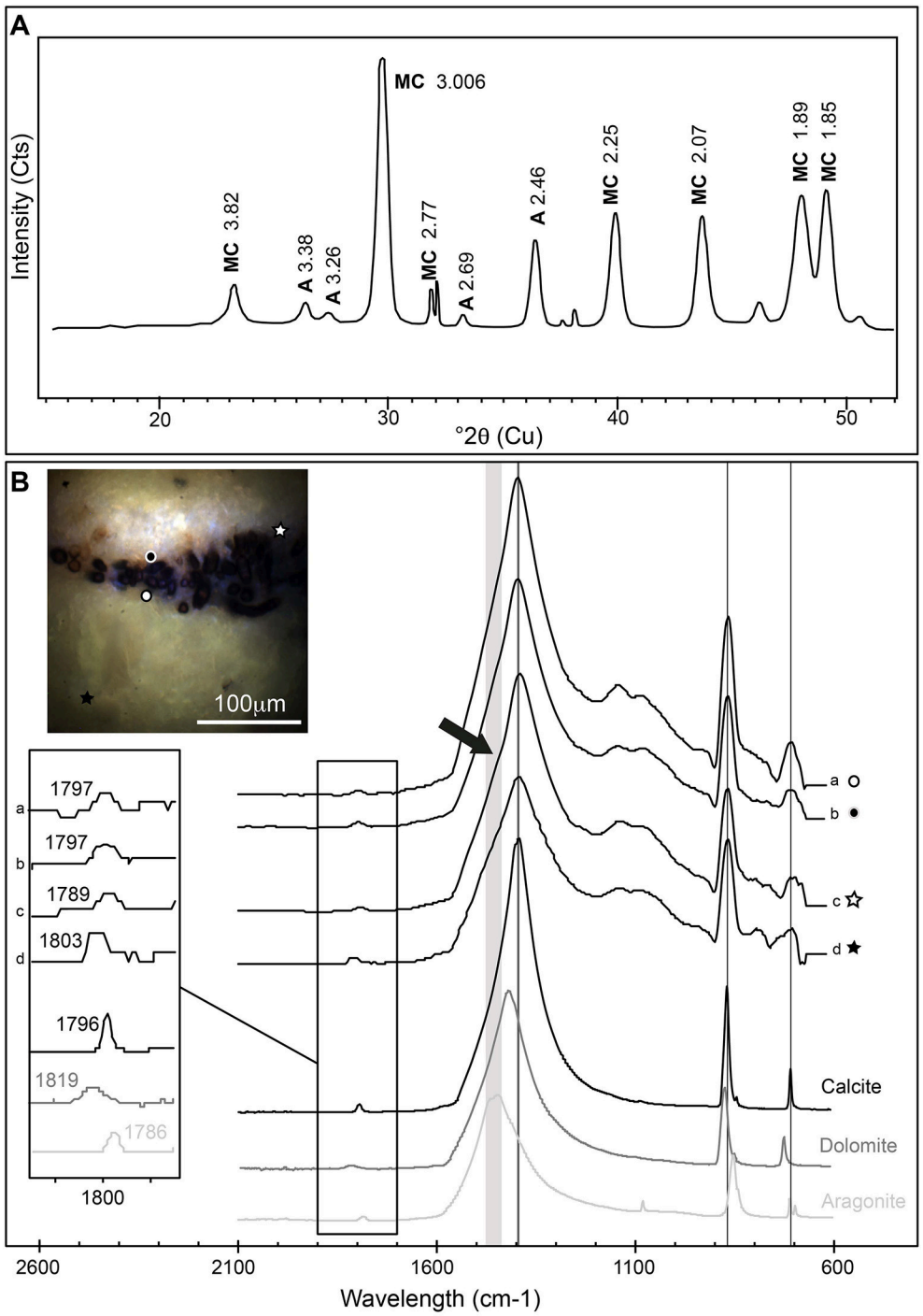

FIGURE 10 | (A) X-ray powder diffractogram obtained on a *Rivularia*-rich lamination. It shows Mg-rich calcite (MC) and aragonite **(A)** (Cts stands for counts). **(B)** ATR-FTIR spectra obtained on a *Rivularia*-rich lamination from a cross section of an oncoid associated with a black pustular mat also analyzed by S-DUV (**Figure 9B**). The precise localization of the spectra is given in the associated full-field RGB fluorescence emission image (white and black circles and stars). ATR-FTIR spectra were compared to standard spectra of calcite, aragonite and dolomite (Rruff database; http://rruff.info/) and showed the predominance of calcite mixed with either a Mg-carbonate or aragonite, detected by the shift of the CO_3^{2-} vibration bands at 1,796 cm^{-1} and a shoulder on the CO_3^{2-} asymmetric stretching band around 1,400 cm^{-1} (black arrow).

in these areas compared to other laminations. This could partly explain the different fluorescence pattern of this lamination. In that case, the presence of aragonite-rich laminations relatively to calcite-rich laminations may be a clue of biological activity (Lepot et al., 2008). Besides, the presence in the deep UV fluorescence emission spectrum extracted from this lamination (**Figure 9C**) of typical peaks associated with biological organic remnants at 316 and 341 cm^{-1} (Jamme et al., 2013) seemed to confirm the biological influence on these laminations. On the contrary, the absence of these signals in the other laminations may indicate that micritic and botryoidal laminations were either of pure chemical origin or did not preserve biological organic remnants if they were initially present. In the latter case, we may postulate that the presence of *Rivularia* sheaths, which favor the development of a large microbial consortium and are quite resistant to degradation, may have induced the preservation of a larger amount of biological organic remnants during mineralization comparatively to other laminations. It has important consequences for the search for biological traces in the fossil record. Indeed, these results are consistent with Lepot et al. (2008) who assumed a biological origin for stromatolites from the 2,724-Myr-old Tumbiana formation (Australia) based on the association of aragonite nanocrystals with organic globules in these formations. Specific laminations such as the ones rich in *Rivularia*-like structures presenting both higher aragonite together with a high organic content should then be tracked in order to decipher the biological origin of some laminations in fossil stromatolites.

CONCLUSION

By combining microscopic observations jointly with phylogenetic analyses, this study provides potential pathways for carbonate precipitation in the black pustular mat at Laguna Negra. Mineralization does not initiate directly on the *Rivularia* sheath or in the *Rivularia* sheath-cell interspace. This could be respectively related to the activity of epiphytic bacteria and to the capacity of *Rivularia* to locally change calcium concentrations by shedding a possible mineralized S-layer or by maintaining a positive surface potential to avoid Ca^{2+} adsorption. However, *Rivularia* play a critical role in favoring and structuring the development of a large microbial consortium excreting a well-developed EPS matrix. Carbonate precipitation then occurred *via* organo-mineralization processes, the EPS matrix serving as a template for mineral nucleation. In addition to the alkalinizing activity of *Rivularia* and diatoms, the presence of putative AAnPB of the *Roseobacter* clade suggests that ureolysis and denitrification can be important metabolisms triggering carbonate precipitation by favoring local alkalinization. With progressive precipitation, *Rivularia* get entombed with intact sheath and photosynthetic pigments. The microspectroscopic analyses of the corresponding laminations rich in *Rivularia*-sheaths structures in stromatolites indicate that a close combination of aragonite and a high organic content should then be considered as potential evidence of microbially-mediated processes of formation of stromatolites, providing biosignatures to be searched for in the fossil record.

AUTHOR CONTRIBUTIONS

EG, EM, and CP were responsible for the design of the study. EG, EM, CP, BM, LL, and FG performed experimental procedures and collected data. EG, KB, FG, and EM conducted FIB section, SEM and TEM. EG, EM, and LL performed DNA extraction and PCR. CP and EG performed FTIR analyses; CP, EG, BM, EM, FJ, and MR performed synchrotron-based Deep UV imaging experiment. ES performed XRD analyses. EM, CP, and EG interpreted the findings and drafted the manuscript. All authors critically reviewed content and approved the final version for publication.

FUNDING

This work was supported by grants from SECYT-UNC 2014-2016 project, International cooperation program CONICET-CNRS Coopinter n°252891 RD2910 (2014-2016), Programme de coopération CONICET/Université Paris Diderot (2013-2014), CNRS/CONICET Bernardo Houssay Fellow (2016), EMBO short-term fellow (number 6682), and the French INSU 2015-INTERRVIE program (PI: EG).

ACKNOWLEDGMENTS

The authors would like to thank M. Bisbal, P. Gil, G. Fernandez, and G. Paglini for their help with laboratory facilities in Argentina (IMMF-CONICET, INVIV-UNC). We also thank C. Mas for helping with confocal microscopy in Cordoba (CIQUIBIC-UNC), A. Mors for his help during field trips. We also thank O. Boudouma for assistance during SEM experiments at the Service Commun de Microscopie Electronique à Balayage (UPMC, Paris, France) and J. Cohen for laser microdissection experiments. Permission for sample collection was granted by the Ministerio de Ambiente y Desarrollo Sustentable, Catamarca, Argentina (number 18-10-2013, DPGA161 and 26-02-2015, DPGA:011 respectively). Part of this work was supported by the IPGP multidisciplinary program PARI and by Région Ile-de-France SESAME Grant No. 12015908. We acknowledge SOLEIL for provision of synchrotron beamtime (proposal n°20150267). This is IPGP contribution n°3940.

SUPPLEMENTARY MATERIAL

The Supplementary Material for this article can be found online at: https://www.frontiersin.org/articles/10.3389/fmicb.2018.00996/full#supplementary-material

REFERENCES

Allwood, A. C., Walter, M. R., Kamber, B. S., Marshall, C. P., and Burch, I. W. (2006). Stromatolite reef from the early Archaean era of Australia. *Nature* 441, 714–718. doi: 10.1038/nature04764

Aloisi, G., Gloter, A., Kruger, M., Wallmann, K., Guyot, F., and Zuddas, P. (2006). Nucleation of calcium carbonate on bacterial nanoglobules. *Geology* 34, 1017–1020. doi: 10.1130/G22986A.1

Altermann, W., Kazmierczak, J., Oren, A., and Wright, T. (2006). Cyanobacterial calcification and its rock-building potential during 3.5 billion years of Earth history. *Geobiology* 4, 147–166. doi: 10.1111/j.1472-4669.2006.00076.x

Altschul, S. F., Madden, T. L., Schäffer, A. A., Zhang, J., Zhang, Z., Miller, W., et al. (1997). Gapped BLAST and PSI-BLAST: a new generation of protein database search programs. *Nucleic Acids Res.* 25, 3389–3402. doi: 10.1093/nar/25.17.3389

Arp, G., Reimer, A., and Reitner, J. (2001). Photosynthesis-induced biofilm calcification and calcium concentrations in Phanerozoic oceans. *Science* 292, 1701–1704. doi: 10.1126/science.1057204

Awramik, S. M., and Sprinkle, J. (1999). Proterozoic stromatolites: the first marine evolutionary biota. *Hist. Biol.* 13, 241–253. doi: 10.1080/08912969909386584

Bapteste, E., Brochier, C., and Boucher, Y. (2005). Higher-level classification of the Archaea: evolution of methanogenesis and methanogens. *Archaea* 1, 353–363. doi: 10.1155/2005/859728

Barbieri, R., Cavalazzi, B., Stivaletta, N., and López-García, P. (2014). Silicified biota in high-altitude, geothermally influenced ignimbrites at El Tatio geyser field, Andean Cordillera (Chile). *Geomicrobiology J.* 31, 493–508. doi: 10.1080/01490451.2013.836691

Benzerara, K., Menguy, N., López-Garcia, P., Yoon, T.-H., Kazmierczak, J., Tyliszczak, T., et al. (2006). Nanoscale detection of organic signatures in carbonate microbialites. *Proc. Natl. Acad. Sci. U.S.A.* 103, 9440–9445. doi: 10.1073/pnas.0603255103

Berelson, W. M., Corsetti, F. A., Pepe-Ranney, C., Hammond, D. E., Beaumont, W., and Spear, J. R. (2011). Hot spring siliceous stromatolites from Yellowstone National Park: assessing growth rate and laminae formation. *Geobiology* 9, 411–424. doi: 10.1111/j.1472-4669.2011.00288.x

Bosak, T., Greene, S., and Newman, D. K. (2007). A likely role for anoxygenic photosynthetic microbes in the formation of ancient stromatolites. *Geobiology* 5, 119–126. doi: 10.1111/j.1472-4669.2007.00104.x

Bosence, D., Gibbons, K., Le Heron, D. P., Morgan, W. A., Pritchard, T., and Vining, B. A. (2015). "Microbial carbonates in space and time: introduction" in *Microbial Carbonates in Space and Time: Implications for Global Exploration and Production*, *Vol.* 418, eds D. W. J. Bosence, K. Gibbons, D. P. Le Heron, T. Pritchard and B. A. Vining (London: Geological Society, Special Publications), 1–15.

Braissant, O., Cailleau, G., Dupraz, C., and Verrecchia, A. P. (2003). Bacterially induced mineralization of calcium carbonate in terrestrial environments: the role of exopolysaccharides and amino acids. *J. Sediment. Res.* 73, 485–490. doi: 10.1306/111302730485

Braissant, O., Decho, A., Dupraz, C., Glunk, C., Przekop, K., and Visscher, P. (2007). Exopolymeric substances of sulfate-reducing bacteria: interactions with calcium at alkaline pH and implication for formation of carbonate minerals. *Geobiology* 5, 401–411. doi: 10.1111/j.1472-4669.2007.00117.x

Brocks, J. J., and Pearson, A. (2005). Building the tree of life. *Rev. Mineral. Geochem.* 59, 233–258. doi: 10.2138/rmg.2005.59.10

Buick, R., Dunlop, J. S. R., and Groves, D. I. (1981). Stromatolite recognition in ancient rocks: an appraisal of irregularly laminated structures in an Early Archaean chert-barite unit from North Pole, Western Australia. *Alcheringa* 5, 161–181. doi: 10.1080/03115518108566999

Burne, R., and Moore, L. (1987). Microbialites: organosedimentary deposits of benthic microbial communities. *Palaios* 2, 241–254. doi: 10.2307/3514674

Chagas, A. A. P., Webb, G. E., Burne, R. V., and Southam, G. (2016). Modern lacustrine microbialites: towards a synthesis of aqueous and carbonate geochemistry and mineralogy. *Earth Sci. Rev.* 162, 338–363. doi: 10.1016/J.EARSCIREV.2016.09.012

Couradeau, E., Benzerara, K., Gérard, E., Moreira, D., Tavera, R., and Lopez Garcia, P. (2014). *In situ* microscale cyanobacterial calcification in modern microbialites. *Biogeosciences* 10, 5255–5266. doi: 10.5194/bg-10-5255-2013

Defarge, C., Gautret, P., Reitner, J., and Trichet, J. (2009). Defining organominerals: comment on 'defining biominerals and organominerals: direct and indirect indicators of life'. *Sediment. Geol.* 213, 152-155. doi: 10.1016/j.sedgeo.2008.04.002

Diehl, H., and Ellingboe, J. L. (1956). Indicator for titration of calcium in presence of magnesium using disodium dihydrogen ethylenediamine tetraacetate. *Anal. Chem.* 28, 882–884. doi: 10.1021/ac60113a030

Doi, M., and Shioi, Y. (1991). Enhancement of denitrifying activity in cells of *Roseobacter denitrificans* grown aerobically in the light. *Plant Cell Physiol.* 32, 365-370. doi: 10.1093/oxfordjournals.pcp.a078089

Douglas, S., and Beveridge, T. J. (1998). Mineral formation by bacteria in natural microbial communities. *FEMS Microbiol. Ecol.* 26, 79–88. doi: 10.1111/j.1574-6941.1998.tb00494.x

Dupraz, C., Reid, R. P., Braissant, O., Decho, A. W., Norman, R. S., and Visscher, P. T. (2009). Processes of carbonate precipitation in modern microbial mats. *Earth Sci. Rev.* 96, 141–152. doi: 10.1016/j.earscirev.2008.10.005

Dupraz, C., and Visscher, P. T. (2005). Microbial lithification in marine stromatolites and hypersaline mats. *Trends Microbiol.* 13, 429–438. doi: 10.1016/j.tim.2005.07.008

Engel, A. S., Johnson, L. R., and Porter, M. L. (2013). Arsenite oxidase gene diversity among *Chloroflexi* and *Proteobacteria* from El Tatio geyser Field, Chile. *FEMS Microbiol. Ecol.* 83, 745–756. doi: 10.1111/1574-6941.12030

Erşan, Y. C., de Belie, N., and Boon, N. (2015). Microbially induced $CaCO_3$ precipitation through denitrification: an optimization study in minimal nutrient environment. *Biochem. Engineer. J.* 101, 108–118. doi: 10.1016/j.bej.2015.05.006

Farías, M. E., Contreras, M., Rasuk, M. C., Kurth, D., Flores, M. R., Poire, D. G., et al. (2014). Characterization of bacterial diversity associated with microbial mats, gypsum evaporites and carbonate microbialites in thalassic wetlands: Tebenquiche and La Brava, Salar de Atacama, Chile. *Extremophiles* 18, 311–329. doi: 10.1007/s00792-013-0617-6

Farías, M. E., Rascovan, N., and Toneatti, D. M. (2013). The discovery of stromatolites developing at 3570 m above sea level in a high-altitude volcanic lake Socompa, Argentinean Andes. *PLoS ONE* 8:e53497. doi: 10.1371/journal.pone.0053497

Fernandez, A., Rasuk, M. C., Visscher, P., Contreras, M., Novoa, F., Poire, D., et al. (2015). Microbial diversity in sediment ecosystems (evaporites domes, microbial mats and crusts) of hypersaline Laguna Tebenquiche, Salar de Atacama, Chile. *Front. Microbiol.* 7:1284. doi: 10.3389/fmicb.2016.01284

Fogg, G. (1983). The ecological significance of extracellular products of phytoplankton photosynthesis. *Bot. Mar.* 26, 3–14. doi: 10.1515/botm.1983.26.1.3

Foster, J. S., Green, S. J., Ahrendt, S. R., Golubic, S., Reid, P. R., Hetherington, K. L., et al. (2009). Molecular and morphological characterization of cyanobacterial diversity in the stromatolites of Highborne Cay, Bahamas. *ISME J.* 3, 573–587. doi: 10.1038/ismej.2008.129

Garcial-Pichel, F., and Castenholz, W. (1991). Characterization and biological implications of sytonemin a cyanobacterial sheath pigment. *J. Phycol.* 27, 395–409. doi: 10.1111/j.0022-3646.1991.00395.x

Gérard, E., Ménez, B., Couradeau, E., Moreira, D., Benzerara, K., Tavera, R., et al. (2013). Specific carbonate-microbe interactions in the modern microbialites of Lake Alchichica (Mexico). *ISME J.* 7, 1997–2009. doi: 10.1038/ismej.2013.81

Giuliani, A., Jamme, F., Rouam, V., Wien, F., Giorgetta, J. L., Lagarde, B., et al. (2009). DISCO: a low-energy multipurpose beamline at synchrotron SOLEIL. *J. Synchrotron Radiat.* 16, 835–841. doi: 10.1107/S0909049509034049

Glunk, C., Dupraz, C., Braissant, O., Gallagher, K. L., Verrecchia, E. P., and Visscher, P. T. (2011). Microbially-mediated carbonate precipitation in a hypersaline lake, Big Pond (Eleuthera, Bahamas). *Sedimentology* 58, 720–736. doi: 10.1111/j.1365-3091.2010.01180.x

Gomez, F., Kah, L., Bartley, K., and Astini, R. (2014). Microbialites in a high-altitude Andean lake: multiple controls on carbonate precipitation and lamina accretion. *Palaios* 29, 233–249. doi: 10.2110/palo.2013.049

Gomez, F. J., Llewski, C., Boidi, F. J., Farias, M. E., and Gérard, E. (2018). Calcium carbonate precipitation in diatom-rich microbial mats: the Laguna Negra hypersaline lake, Catamarca, Argentina. *J. Sediment. Res.* 88.

González-Muñoz, M. T., Rodriguez-Navarro, C., Martínez-Ruiz, F., Arias, J. M., Merroun, M. L., and Rodriguez-Gallego, M. (2010). "Bacterial biomineralization: new insights from *Myxococcus*-induced mineral precipitation," in *Tufas and Speleothems: Unravelling the Microbial and*

Physical Controls, *Vol. 336*, eds H. M. Pedley and M. Rogerson (London: Geological Society; Special Publications), 31–50.

Grossart, H.-P., Levold, F., Allgaier, M., Simon, M., and Brinkhoff, T. (2005). Marine diatom species harbour distinct bacterial communities. *Environ. Microbiol.* 7, 860–873. doi: 10.1111/j.1462-2920.2005.00759.x

Grotzinger, J. P., and Knoll, A. H. (1999). Stromatolites in Precambrian carbonates: evolutionary mileposts or environmental dipsticks? *Annu. Rev. Earth Planet. Sci.* 27, 313–358. doi: 10.1146/annurev.earth.27.1.313

Guiry, M. D., and Morrison, L. (2015). "Internet information resources for marine algae," in *Marine Algae Biodiversity, Taxonomy, Environmental Assessment, and Biotechnology*, eds L. Pereira and J. L Neto (Boca Raton, FL: CRC Press, Taylor & Francis), 357–376.

Heaney, P., Vicenzi, E., Giannuzzi, L., and Livi, K. (2001). Focused ion beam milling: a method of site-specific sample extraction for microanalysis of Earth and planetary materials. *Am. Mineral.* 86, 1094–1099. doi: 10.2138/am-2001-8-917

Hirose, S., Nagashima, K. V. P., Matsuura, K., and Haruta, S. (2012). Diversity of purple phototrophic bacteria, inferred from *pufM* gene, within epilithic biofilm in Tama River, Japan. *Microbes Environ.* 27, 327–329. doi: 10.1264/jsme2.ME11306

Howarth, R., Richard, F., Seviur, E., Seviou, R., Blackall, L., Pickup, R., et al. (1999). Phylogenetic relationships of filamentous sulfur bacteria (*Thiothrix* spp. and Eikelboom type 021 N bacteria) isolated from waste water treatment plants and description of *Thiothrix eikelboomii* sp. nov., *Thiothrix unzii* sp. nov., *Thiothrix fructosivorans* sp. nov. and *Thiothrix defluvii* sp. nov. *Int. J. Syst. Evol. Microbiol.* 49, 1817–1827. doi: 10.1099/00207713-49-4-1817

Imachi, H., Sakai, S., Sekiguchi, Y., Hanada, S., Kamagata, Y., Ohashi, A., et al. (2008). *Methanolinea tarda* gen. nov., sp. nov., a methane-producing archaeon isolated from a methanogenic digester sludge. *Int. J. Syst. Evol. Microbiol.* 58, 294–301. doi: 10.1099/ijs.0.65394-0

Jamme, F., Kascakova, S., Villette, S., Allouche, F., Pallu, S., Rouam, V., et al. (2013). Deep UV autofluorescence microscopy for cell biology and tissue histology. *Biol. Cell.* 105, 277–288. doi: 10.1111/boc.201200075

Jamme, F., Villette, S., Giuliani, A., Rouam, V., Wien, F., Lagarde, B., et al. (2010). Synchrotron UV fluorescence microscopy uncovers new probes in cells and tissues. *Microsc. Microanal.* 16, 507–514. doi: 10.1017/S1431927610093852

Jimenez-López, C., Jroundi, F., Rodriguez-Gallego, M., Arias, J. M., and González-Muñoz, M. T. (2007). "Biomineralization induced by *Myxobacteria*" in *Communicating Current Research and Educational Topics and Trends in Applied Microbiology*, Vol. 1, ed A. Méndez-Vilas (Badajoz: Formatex), 143–154.

Jukes, T. H., and Cantor, C. R. (1969). "Evolution of protein molecules," in *Mammalian Protein Metabolism III*, ed H. N. Munro (New York, NY: Academic Press), 21–132.

Kang, C.-H., Han, S.-H., Shin, Y., Oh, S. J., and So, J.-S. (2014). Bioremediation of Cd by microbially induced calcite precipitation. *Appl. Biochem. Biotechnol.* 172, 2907–2915. doi: 10.1007/s12010-014-0737-1

Kazmierczak, J., Fenchel, T., Kühl, M., Kempe, S., Kremer, B., Łacka, B., et al. (2015). $CaCO_3$ precipitation in multilayered cyanobacterial mats: clues to explain the alternation of micrite and sparite layers in calcareous stromatolites. *Life* 5, 744–769. doi: 10.3390/life5010744

Kempe, S., Kazmierczak, J., Landmann, G., Konuk, T., Reimer, A., and Lipp, A. (1991). Largest known microbialites discovered in Lake Van, Turkey. *Nature* 349, 605–608. doi: 10.1038/349605a0

Kenward, P. A., Goldstein, R. H., Gonzalez, L. A., and Roberts, J. A. (2009). Precipitation of low-temperature dolomite from an anaerobic microbial consortium: the role of methanogenic Archaea. *Geobiology* 7 , 556-565. doi: 10.1111/j.1472-4669.2009.00210.x

Khan, S. T., Nakagawa, Y., and Harayama, S. (2007). *Sediminibacter furfurosus* gen. nov., sp. nov. and *Gilvibacter sediminis* gen. nov., sp. nov., novel members of the family *Flavobacteriaceae. Int. J. Syst. Evol. Microbiol.* 57, 265–269. doi: 10.1099/ijs.0.64628-0

Knoll, A. H. (2003). Biomineralization and evolutionary history. *Rev. Mineral. Geochem.* 54, 329–356. doi: 10.2113/0540329

Koblizek, M. (2015). Ecology of aerobic anoxygenic phototrophs in aquatic environments. *FEMS Microbiol. Rev.* 39, 854–870. doi: 10.1093/femsre/fuv032

Kwak, M. J., Lee, J. S., Lee, K. C., Kim, K. K., Eom, M. K., Kim, B. K., et al. (2014). *Sulfitobacter geojensis* sp. nov., *Sulfitobacter noctilucae sp.* nov., and *Sulfitobacter noctilucicola sp. nov.,* isolated from coastal seawater. *Int. J. Syst. Evol. Microbiol.* 64, 3760–3767. doi: 10.1099/ijs.0.065961-0

Leavitt, P. R., Vinebrooke, R. D., Donald, D. B., Smol, J. P., and Schindler, D. W. (1997). Past ultraviolet radiation environments in lakes derived from fossil pigments. *Nature* 388, 457–459. doi: 10.1038/41296

Lenk, S., Moraru, C., Hahnke, S., Arnds, J., Richter, M., Kube, M., et al. (2012). *Roseobacter* clade bacteria are abundant in coastal sediments and encode a novel combination of sulfur oxidation genes. *ISME J.* 6, 2178–2187. doi: 10.1038/ismej.2012.66

Lepot, K., Benzerara, K., Brown, G. E. Jr., and Philippot, P. (2008). Microbially influenced formation of 2,724-million-year-old stromatolites. *Nat. Geosci.* 1, 118–121. doi: 10.1038/ngeo107

Logan, B. W. (1961). Cryptozoon and associated stromatolites from the recent, Shark Bay, Western Australia. *J. Geol.* 69, 517–533.

Lucena, T., Ruvira, M. A., Macián, M. C., Pujalte, M. J., and Arahal, D. R. (2013). Description of *Tropicibacter mediterraneus* sp. nov. and *Tropicibacter litoreus* sp. nov. *Syst. Appl. Microbiol.* 36, 325–329. doi: 10.1016/j.syapm.2013.04.001

Ludwig, W., Strunk, O., Westram, R., Richter, L., Meier, H., Yadhukumar, Buchner, A., et al. (2004). ARB: a software environment for sequence data. *Nucleic Acids Res.* 32, 1363–1371. doi: 10.1093/nar/gkh293

Luo, H., and Moran, M. A. (2014). Evolutionary ecology of the marine *Roseobacter* clade. *Microbiol. Mol. Biol. Rev.* 78 , 573-587. doi: 10.1128/MMBR.00020-14.

Ma, K., Liu, X., and Dong, X. (2006). *Methanosaeta harundinacea* sp. nov., a novel acetate-scavenging methanogen isolated from a UASB reactor. *Int. J. Syst. Evol. Micr.* 56, 127–131. doi: 10.1099/ijs.0.63887-0

Maidana, N. I., and Seeligmann, C. (2006). Diatomeas (*Bacillariophyceae*) de ambientes acuáticos de altura de la Provincia de Catamarca, Argentina II. *Bol. Soc. Argent. Bot.* 41, 1–13.

Martinez, R. E., Gardés, E., Pokrovsky, O. S., Schott, J., and Oelkers, E. H. (2010). Do photosynthetic bacteria have a protective mechanism against carbonate precipitation at their surfaces? *Geochim. Cosmochim. Acta* 74, 1329–1337. doi: 10.1016/j.gca.2009.11.025

Martinez, R. E., Pokrovsky, O. S., Schott, J., and Oelkers, E. H. (2008). Surface charge and zeta potential of metabolically active and dead cyanobacteria. *J. Colloid Interface Sci.* 323, 317–325. doi: 10.1016/j.jcis.2008.04.041

Meister, P. (2013). Two opposing effects of sulfate reduction on calcite and dolomite precipitation in marine, hypersaline and alkaline environments. *Geology* 41, 499–502. doi: 10.1130/G34185.1

Merz, M. U. E. (1992). The biology of carbonate precipitation by cyanobacteria. *Facies* 26, 81–102. doi: 10.1007/BF02536920

Merz-Prei, M., and Riding, R. (1999). Cyanobacterial tufa calcification in two freshwater streams: Ambient environment, chemical thresholds and biological processes. *Sediment. Geol.* 126, 103–124. doi: 10.1007/BF02539795

Michaelis, W., Seifert, R., Nauhaus, K., Treude, T., Thiel, V., Blumenberg, M., et al. (2002). Microbial reefs in the Black sea fueled by anaerobic oxidation of methane. *Science* 297, 1014–1015. doi: 10.1126/science.1072502

Nedashkovskaya, O., Kim, S., Kyun Han, S., Lysenko, A. M., Rohde, M., Rhee, M. S., et al. (2004). *Maribacter* gen. nov., a new member of the family *Flavobacteriaceae,* isolated from marine habitats, containing the species *Maribacter sedimenticola* sp. nov., *Maribacter aquivivus* sp. nov., *Maribacter orientalis* sp. nov. and *Maribacter ulvicola* sp. nov. *Int. J. Syst. Evol. Microbiol.* 54, 1017–1023. doi: 10.1099/ijs.0.02849-0

Nedashkovskaya, O., Vancanney, T., Seung, B., and Zhukova, N. (2009). *Winogradskyella echinorum* sp. nov., a marine bacterium of the family *Flavobacteriaceae* isolated from the sea urchin *Strongylocentrotus intermedius. Int. J. Syst. Evol. Microbiol.* 59, 1465–1468. doi: 10.1099/ijs.0.005421-0

Nutman, A. P., Bennett, V. C., Friend, C. R. L., Van Kranendonk, M. J., and Chivas, A. R. (2016). Rapid emergence of life shown by discovery of 3,700-million-year-old microbial structures. *Nature* 537, 535–538. doi: 10.1038/nature19355

Orphan, V. J., Jahnke, L. L., Embaye, T., Turk, K. A., Pernthaler, A., Summons, R. E., et al. (2008). Characterization and spatial distribution of methanogens and methanogenic biosignatures in hypersaline microbial mats of Baja California. *Geobiology* 6, 376–393. doi: 10.1111/j.1472-4669.2008.00166.x

Overmann, J., and van Gemerden, H. (2000). Microbial interactions involving sulfur bacteria: implications for the ecology and evolution

of bacterial communities. *FEMS Microbiol. Rev.* 24, 591–599. doi: 10.1111/j.1574-6976.2000.tb00560.x

Oz, A., Sabehi, G., Koblízek, M., Massana, R., and Béjà, O. (2005). *Roseobacter*-like bacteria in Red and Mediterranean Sea aerobic anoxygenic photosynthetic populations. *Appl. Environ. Microbiol.* 71 , 344–353. doi: 10.1128/AEM.71.1.344

Pagani, I., Chertkov, O., Lapidus, A., Lucas, S., Del Rio, T. G., Tice, H., et al. (2011). Complete genome sequence of *Marivirga tractuosa* type strain (H-43). *Stand. Genomic Sci.* 4, 154–162. doi: 10.4056/sigs.1623941

Pentecost, A., and Ulrich, F. (2010). Photosynthesis and calcification of the stromatolitic freshwater cyanobacterium *Rivularia*. *Eur. J. Phycol.* 45, 345–353. doi: 10.1080/09670262.2010.492914

Perry, R. S., McLoughlin, N., Lynne, B. Y., Sephton, M. A., Oliver, J. D., Perry, C. C., et al. (2007). Defining biominerals and organominerals: direct and indirect indicators of life. *Sed. Geol.* 201, 157–179. doi: 10.1016/j.sedgeo.2007.05.014

Phoenix, V., Martinez, R., Konhauser, K., and Ferris, F. (2002). Characterization and implications of the cell surface reactivity of *Calothrix* sp. strain KC97. *Appl. Environ. Microbiol.* 68, 4827–4834. doi: 10.1128/AEM.68.10.4827–4834.2002

Phoenix, V. R., Adams, D. G., and Konhauser, K. O. (2000). Cyanobacterial viability during hydrothermal biomineralisation. *Chem. Geol.* 169, 329-338. doi: 10.1016/S0009-2541(00)00212-6

Pruesse, E., Peplies, J., and Glöckner, F. O. (2012). SINA: accurate high-throughput multiple sequence alignment of ribosomal RNA genes. *Bioinformatics* 28, 1823–1829. doi: 10.1093/bioinformatics/bts252.

Quast, C., Pruesse, E., Yilmaz, P., Gerken, J., Schweer, T., Yarza, P., et al. (2013). The SILVA ribosomal RNA gene database project: improved data processing and web-based tools. *Nucleic Acids Res.* 41, D590–D596. doi: 10.1093/nar/gks1219

Reitner, J., Paul, J., Arp, G., and Hause-Reitner, D. (1996). "Lake Thetis domal microbialites. A complex framework of calcified biofilms and organomicrites (Cervantes, Western Australia)," in *Global and Regional Controls on Biogenic Sedimentation. I. Reef Evolution Research Reports*, Vol. SB2, eds J. Reitner, F. Neuweiler, and F. Gunkel (Göttingen: Göttinger Arb. Geol. Paläont, Sonderband), 85–89.

Riding, R. (1977). "Skeletal stromatolites" in *Fossil Algae-Recent Results and Developments*, ed E. Flügel (Berlin; Germany: Springer), 57–60.

Riding, R. (2006). Cyanobacterial calcification, carbon dioxide concentrating mechanisms, and Proterozoic–Cambrian changes in atmospheric composition. *Geobiology* 4, 299–316. doi: 10.1111/j.1472-4669.2006.00087.x

Roberts, J. A., Bennet, P. C., Gonzalez, L. A., Macpherson, G. L., , and Milliken, K. L. (2004). Microbial precipitation of dolomite in methanogenic groundwater. *Geology* 32, 277–280, doi: 10.1130/G20246.1.

Romesser, J. A., Wolfe, R. S., Mayer, F., Spiess, E., and Walther-Mauruschat, A. (1979). *Methanogenium*, a new genus of marine methanogenic bacteria, and characterization of *Methanogenium cariaci* sp. nov. and *Methanogenium marisnigri* sp. nov. *Arch. Microbiol.* 121, 147-153. doi: 10.1007/BF00689979

Saghaï, A., Zivanovic, Y., Zeyen, N., Moreira, D., Benzerara, K., Deschamps, P., et al. (2015). Metagenome-based diversity analyses suggest a significant contribution of non-cyanobacterial lineages to carbonate precipitation in modern microbialites. *Front. Microbiol.* 6:797. doi: 10.3389/fmicb.2015.00797

Schink, B. (2002). Synergistic interactions in the microbial world. *Antonie Van Leeuwenhoek* 81, 257–261. doi: 10.1023/A:1020579004534

Schneider, C. S., Rasband, W. S., and Eliceiri, W. (2012). NIH Image to ImageJ: 25 years of image analysis. *Nat. Methods* 9, 671–675. doi: 10.1038/nmeth.2089

Scholten, J. C. M., Joye, S. B., Hollibaugh, J. T., and Murrell, J. C. (2005). Molecular analysis of the sulfate reducing and archaeal community in a meromictic soda lake (Mono Lake, California) by targeting 16S rRNA, *mcrA*, *apsA*, and *dsrAB* genes. *Microbial. Ecol.* 50, 29–39. doi: 10.1007/s00248-004-0085-8

Singh, S., and Mishra, A. (2014). Regulation of calcium ion and its effect on growth and developmental behavior in wild type and *ntcA* mutant of *Anabaena* sp. PCC 7120 under varied levels of $CaCl_2$. *Microbiology* 83, 235–246. doi: 10.1134/S002626171403014X

Smith, R. J., and Wilkins, A. (1988). A correlation between intracellular calcium and incident irradiance in *Nostoc* 6720. *New Phytol.* 109, 157–161. doi: 10.1111/j.1469-8137.1988.tb03703.x

Stamatakis, A., Hoover, P., and Rougemont, J. (2008). A rapid bootstrap algorithm for the raxml web servers. *Syst. Biol.* 57, 758–771. doi: 10.1080/10635150802429642

Tamura, K., Stecher, G., Peterson, D., Filipski, A., and Kumar, S. (2013). MEGA6: Molecular Evolutionary Genetics Analysis Version 6.0. *Mol. Biol. Evol.* 30, 2725–2729. doi: 10.1093/molbev/mst197

Thompson, J. B., Schultz-Lam, S., Beveridge, T. J., and Des Marais, D. J. (1997). Whiting events: biogenic origin due to the photosynthetic activity of cyanobacterial picoplankton. *Limnol. Oceanogr.* 42, 133–141. doi: 10.4319/lo.1997.42.1.0133

Thoury, M., Echard, J.-P., Réfrégiers, M., Berrie, B., Nevin, A., Jamme, F., et al. (2011). Synchrotron UV-visible multispectral luminescence micro imaging of historical samples. *Anal. Chem.* 83, 1737-1745. doi: 10.1021/ac102986h

Walter, M. R., Bauld, J., and Brock, T. D. (1972). Siliceous algal and bacterial stromatolites in hot spring and geyser effluents of Yellowstone national park. *Science* 178, 402–405. doi: 10.1126/science.178.4059.402

Yilmaz, P., Parfray, L. W., Yarza, P., Gerken, J., Pruesse, E., Quast, C., et al. (2014). The SILVA and "All-species Living Tree Project (LTP)" taxonomic frameworks. *Nucleic Acids Res.* 42, D643–D648. doi: 10.1093/nar/gkt1209.

Yoon, J., Matsuo, Y., Katsuta, A., Jang, J. H., Matsuda, S., Adachi, K., et al. (2008). Haloferula rosea gen. nov., sp. nov., *Haloferula harenae* sp. nov., *Haloferula phyci* sp. nov., *Haloferula helveola* sp. nov. and *Haloferula sargassicola* sp. nov., five marine representatives of the family *Verrucomicrobiaceae* within the phylum '*Verrucomicrobia*'. *Int. J. Syst. Evol. Microbiol.* 58, 2491–2500. doi: 10.1099/ijs.0.2008/000711-0

Zhang, Y., Sun, Y., Jiao, N., Stepanauskas, R., and Luo, H. (2016). Ecological genomics of the uncultivated marine *Roseobacter* lineage CHAB-I-5. *Appl. Environ. Microbiol.* 82, 2100–2111. doi: 10.1128/AEM.03678-15

Zhu, T., and Dittrich, M. (2016). Carbonate precipitation through microbial activities in natural environment, and their potential in biotechnology: a review. *Front. Bioeng. Biotechnol.* 4:4. doi: 10.3389/fbioe.2016.00004

Zippel, B., and Neu, T. R. (2011). Characterization of glycoconjugates of extracellular polymeric substances in tufa-associated biofilms by using fluorescence lectin-binding analysis. *Appl. Environ. Microbiol.* 77, 505–516. doi: 10.1128/AEM.01660-10

Conflict of Interest Statement: The authors declare that the research was conducted in the absence of any commercial or financial relationships that could be construed as a potential conflict of interest.

frontiers in Microbiology

ORIGINAL RESEARCH
published: 25 May 2018
doi: 10.3389/fmicb.2018.00997

Microscale Biosignatures and Abiotic Mineral Authigenesis in Little Hot Creek, California

*Emily A. Kraus[1], Scott R. Beeler[2], R. Agustin Mors[3], James G. Floyd[4], GeoBiology 2016[5], Blake W. Stamps[1], Heather S. Nunn[4], Bradley S. Stevenson[4], Hope A. Johnson[6], Russell S. Shapiro[7], Sean J. Loyd[8], John R. Spear[1] and Frank A. Corsetti[5]**

[1] Geo- Environmental- Microbiology Laboratory, Department of Civil and Environmental Engineering, Colorado School of Mines, Golden, CO, United States, [2] Department of Earth and Planetary Sciences, Washington University in St. Louis, St. Louis, MO, United States, [3] Laboratorio de Paleobiología y Geomicrobiología Experimental, Centro de Investigaciones en Ciencias de la Tierra (CONICET-UNC), Córdoba, Argentina, [4] Department of Microbiology and Plant Biology, The University of Oklahoma, Norman, OK, United States, [5] Department of Earth Sciences, University of Southern California, Los Angeles, CA, United States, [6] Department of Biological Sciences, California State University, Fullerton, Fullerton, CA, United States, [7] Geological and Environmental Sciences, California State University, Chico, Chico, CA, United States, [8] Department of Geological Sciences, California State University, Fullerton, Fullerton, CA, United States

OPEN ACCESS

Edited by:
Christophe Dupraz, Stockholm University, Sweden

Reviewed by:
Trinity L. Hamilton, University of Minnesota Twin Cities, United States
Dirk De Beer, Max-Planck-Gesellschaft (MPG), Germany

***Correspondence:**
Frank A. Corsetti
fcorsett@usc.edu

Specialty section:
This article was submitted to Aquatic Microbiology, a section of the journal Frontiers in Microbiology

Received: *01 December 2017*
Accepted: *27 April 2018*
Published: *25 May 2018*

Citation:
Kraus EA, Beeler SR, Mors RA, Floyd JG, GeoBiology 2016, Stamps BW, Nunn HS, Stevenson BS, Johnson HA, Shapiro RS, Loyd SJ, Spear JR and Corsetti FA (2018) Microscale Biosignatures and Abiotic Mineral Authigenesis in Little Hot Creek, California. Front. Microbiol. 9:997. doi: 10.3389/fmicb.2018.00997

Hot spring environments can create physical and chemical gradients favorable for unique microbial life. They can also include authigenic mineral precipitates that may preserve signs of biological activity on Earth and possibly other planets. The abiogenic or biogenic origins of such precipitates can be difficult to discern, therefore a better understanding of mineral formation processes is critical for the accurate interpretation of biosignatures from hot springs. Little Hot Creek (LHC) is a hot spring complex located in the Long Valley Caldera, California, that contains mineral precipitates composed of a carbonate base (largely submerged) topped by amorphous silica (largely emergent). The precipitates occur in close association with microbial mats and biofilms. Geological, geochemical, and microbiological data are consistent with mineral formation via degassing and evaporation rather than direct microbial involvement. However, the microfabric of the silica portion is stromatolitic in nature (i.e., wavy and finely laminated), suggesting that abiogenic mineralization has the potential to preserve textural biosignatures. Although geochemical and petrographic evidence suggests the calcite base was precipitated via abiogenic processes, endolithic microbial communities modified the structure of the calcite crystals, producing a textural biosignature. Our results reveal that even when mineral precipitation is largely abiogenic, the potential to preserve biosignatures in hot spring settings is high. The features found in the LHC structures may provide insight into the biogenicity of ancient Earth and extraterrestrial rocks.

Keywords: carbonate–silicate microbialite, hot spring biofilm, biosignature, stromatolite, microbial mat

INTRODUCTION

Differentiating morphological biosignatures from abiogenic mineral assemblages remains a problem in the interpretation of the evolution of life in the geologic rock record and for the search for life on other planets. The environments of early Earth and Mars are thought to have been similar, containing aqueous geothermal activity, which could provide the potential to preserve traces of life (McKay and Stoker, 1989; Walter and Des Marais, 1993; Preston et al., 2008; Wordsworth, 2016). Detection of surface silica deposits associated with hydrothermal features on Mars (Squyres et al., 2008) and their resemblance to biotically-influenced silica structures on Earth (Ruff and Farmer, 2016) highlights the need for further study of active modern hot springs with silica precipitation. The discovery of hot-spring-associated biosignatures on Mars has been a goal of astrobiological research for decades, largely guided by insight gained from Earth analog systems (NASA, 1995; Cady et al., 2003).

Earth's modern hot springs exhibit strong thermal and chemical gradients that generate energetically favorable redox conditions for microbial life (Meyer-Dombard et al., 2005, 2011; Spear et al., 2005; Inskeep et al., 2010). Rapid mineral precipitation tends to occur in these systems as inorganic carbon- and silica-containing waters reach the surface and interact with the atmosphere. When these waters reach the surface, rapid physico-chemical changes occur due to degassing, cooling, evaporation, and water mixing, which can drive carbonate and silica precipitation abiotically (Fouke et al., 2000; Konhauser et al., 2004; Pentecost, 2005; Fouke, 2011). Due to rapid mineralization, microorganisms and/or traces of their activity can be preserved in the rock record (e.g., Cady and Farmer, 1996). Recent findings have demonstrated the ability of similar silica-rich deposits to preserve some of the earliest signs of life on Earth (Djokic et al., 2017), but abiotically-synthesized microstructures resembling biological morphologies have been shown to self-assemble in an experimental setting, casting doubt on solely using morphological features as biogenic indicators (García-Ruiz et al., 2003).

Microorganisms can induce mineral precipitation by changing local chemical microenvironments on micrometer scales through metabolic activity. For example, metabolic reactions such as photosynthesis, sulfate reduction, and denitrification have been shown to drive carbonate mineral precipitation by increasing relative alkalinity, thus increasing the saturation state of calcite (Dupraz and Visscher, 2005; Visscher and Stolz, 2005; Baumgartner et al., 2006; Chrachri et al., 2018). In addition, microbes can control mineral nucleation by the production of negatively charged surfaces, like exopolymeric substances (EPS), providing a surface for mineral nucleation, which has been observed in silica precipitation in hot springs (Konhauser and Ferris, 1996; Farmer and Des Marais, 1999; Phoenix et al., 2000; Benning et al., 2004). Thus, several processes can influence carbonate precipitation and silicification in different ways. Microbial control can be direct, as in carbonates (Dupraz and Visscher, 2005), or marginal to absent, as in silicification, by imparting an influence on the resulting mineral textures (Konhauser et al., 2004).

Disentangling the main physio-chemical and microbiological controls in mineral precipitation is necessary to better understand biosignature preservation in the sedimentary record; thus, the study of modern active hot spring systems yields valuable insight into Earth's history and beyond. Little Hot Creek (LHC) is a hot spring system in the Long Valley Caldera of California, containing mineral precipitates with a carbonate base and an amorphous silica/carbonate top. The precipitates occur in close association with microbial mats and biofilms in the spring. The phage community structure, geochemistry, isotopic characteristics, mineralogy, microbial community of LHC sediments, and microbial mat structures have been described in some detail previously (Breitbart et al., 2004; Vick et al., 2010; Bradley et al., 2017; Wilmeth et al., in review). The mineral precipitate microbial communities, physical structure, and mineralogy have not been characterized, affording an opportunity to investigate the generation of silica- and carbonate-based biosignatures. Here, we investigate the biogenicity of LHC precipitates using geochemical modeling, petrography, microscopy, high-throughput DNA sequencing, and isotopic data to better inform how the structures formed.

MATERIALS AND METHODS

Site Description and Aqueous Geochemistry

Little Hot Creek 1 (LHC) (Vick et al., 2010) is a 28-m-long channelized hot spring in the hydrothermally-active Long Valley Caldera of California at 37°41′26.1′′N 118°50′39.9′′W. Samples for water geochemistry and four mineralized structures within the hot spring were collected for biological, isotopic, and petrographic sampling under a United States Forest Service Research Permit (#MLD15053) (**Figure 1**). All structures were rooted in the spring bottom or side and ranged in size, with the largest structure approximately 15 cm long, 10 cm wide, and 9 cm thick. The above-water mineral surfaces were covered in biofilms of varying colors and/or white grainy material. Spring water was collected several centimeters directly upstream of the chosen mineralized structures via syringe and passed through a 0.45 μm filter to fill 15 ml Falcon® tubes with no headspace for triplicate measurements of anions and cations. Samples for cation analysis were acidified with drops of nitric acid and triplicate samples of four milliliters of 0.45 μm filtered water was injected into pre-evacuated Exetainer® vials (Labco Limited, Lampeter, Wales, United Kingdom) for dissolved inorganic carbon (DIC) measurements. Temperature and pH were measured at the point of water collection with a Mettler Toledo SevenGo Duo™ pH meter (Mettler Toledo, Columbus, OH, United States) at each site.

To empirically assess the isotopic evolution of dissolved inorganic carbon downstream at LHC, one source fluid degassing experiment was performed on-site contemporaneously with sample collection. This experiment was conducted on spring source waters to remove potential impacts from spring channel biology and mineral precipitates. One and a half liters of water was collected from the source of LHC in an open container

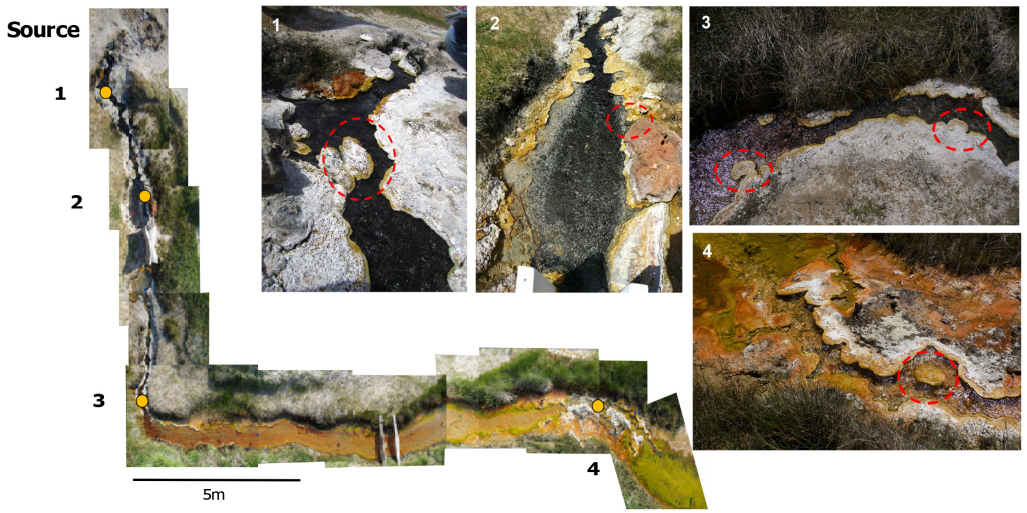

FIGURE 1 | A photomosaic of Little Hot Creek 1. Sampling sites are indicated by yellow dots. Dashed red circles show the precipitate structures that were removed from LHC for sampling.

and placed on a stir plate to mimic fluid turbulence exhibited along the flow path (the complexity of LHC outflow morphology produces local variability in turbulence; stirring was meant to mimic but not perfectly reconstruct turbulence). At 30-s intervals 4 ml of water was removed, passed through a sterile 0.45 μm filter, and injected into an evacuated Exetainer® vial to analyze for DIC concentration and isotopic composition. Temperature and pH were recorded concurrently at each sampling time point. The entire duration of the source fluid experiment lasted 15 min.

Cation and anion concentrations were analyzed using inductively coupled plasma atomic emission spectroscopy (ICP-AES; Optima 5300, PerkinElmer, Fremont, CA, United States) and ion chromatography (IC; ICS-90, Dionex, Sunnyvale, CA, United States), respectively. The maximum allowable sodium concentration in the ICP-AES instrument is 500 mg/L and the maximum allowable chloride concentration in the IC instrument is 300 mg/L; therefore, samples were diluted accordingly using ultrapure water and then acidified to a pH of less than 2 using nitric acid for ICP only. Dissolved inorganic carbon (DIC) concentrations and $\delta^{13}C$ values were determined on waters from LHC and the degassing experiment using a cavity ringdown spectrometer [(CRDS), 2121-i, Picarro, Santa Clara, CA, United States]. Samples were acidified using an AutoMate carbonate preparation device (AutoMate FX, Inc., Bushnell, FL, United States) to quantitatively convert DIC to CO_2(g). CO_2(g) is passed via ultra-high purity N_2 carrier gas to the CRDS. The CRDS provides simultaneous DIC concentration and $\delta^{13}C$ data. DIC concentration and $\delta^{13}C$ replicates are generally better than ±0.3 mM and 0.5‰, respectively.

Calculation of saturation indices and geochemical modeling were performed with PHREEQC-I version 3.3.7 (Parkhurst and Appelo, 2013). PHREEQC-I enables modeling of saturation state with respect to temperature and elemental activities. This allows for the ability to assess changes in saturation state as these parameters change during physico-chemical processes such as evaporation, cooling, and degassing. Measured source water values were used as the initial parameters for all geochemical modeling performed.

Solid Carbonate Stable Isotope Analysis

Solid samples were powdered using either a rotary tool (Dremel Co., Racine, WI, United States) fitted with a 1.5 mm carbide drill bit or mortar and pestle. Powdered samples (5–7 mg) were placed into evacuated Exetainer® vials in triplicate. Carbonate powders were then dissolved in 3 ml of 10% phosphoric acid overnight. Acid-produced CO_2(g) was passed via ultra-high purity N_2 carrier gas to the CRDS. The CRDS provides simultaneous total inorganic carbon (TIC) content and $\delta^{13}C$ data. TIC concentration and $\delta^{13}C$ replicates are generally better than ±0.2 wt% and 0.1‰, respectively.

Petrography and Microscopy of LHC Precipitates

Large (51 mm × 75 mm) and small (27 mm × 46 mm) format thin sections were made from several of the samples. Photomosaics of select thin sections were produced on a Zeiss Axioscope petrographic microscope (Carl Zeiss Microscopy, LLC, Thornwood, NY, United States) in the petrography lab at the University of Southern California. Samples of LHC mineral precipitates and associated biofilms were processed for biologic microscopy. Partially lithified precipitate material was homogenized by finely grinding approximately 1 g of material with a mortar and pestle with sterile phosphate buffered saline. The homogenized material was placed onto glass slides and imaged on an Olympus BX41 (Olympus Corporation, Shinjuku, Tokyo, Japan). Images were collected under 400× using brightfield, fluorescent green light (540 – 560 nm) to detect the presence of photosynthetic organisms, and DAPI (4′6′-diamidino-2-phenylindole) stain under UV light to

highlight DNA in organisms associated with mineral precipitates. Environmental scanning electron microscopy (ESEM) was done on mineral precipitates from Sites 3 and 4 (**Figure 1**). Small sections from the top mineral precipitate (approximately 3 mm × 3 mm × 3 mm) were prepared without chemical fixation, sputter coating, or dehydration steps. ESEM was performed on a Hitachi TM-1000 Tabletop SEM (Hitachi Global, Tokyo, Japan) equipped with a back-scatter electron (BSE) detector, an accelerating voltage of 15 kV, and a working distance of 8.4 – 8.7 mm.

DNA Extraction and Sequencing From LHC Precipitates

Sterile spatulas were used to scrape partially lithified, carbonaceous material and overlying green/brown biofilm from the upstream, submerged edge of each of the four mineralized structures. Three technical replicates were collected from each. Three technical replicate samples were also taken from the above-water, precipitate-top portions of the structures at Sites 1, 2, and 4 (**Figure 1**). Three samples for metagenomic sequencing were collected from the leading, submerged edge of the mineral structure at Site 4. Samples were immediately suspended in 750 μL Xpedition™ Lysis/Stabilization Solution (Zymo Research Co., Irvine, CA, United States), and homogenized for 1 min on-site using a custom designed lysis head attached to a reciprocating saw. Samples in the field were then maintained at room temperature (∼25°) stably in the Lysis/Stabilization Solution for several hours and stored at −20°C in the laboratory until completion of nucleic acid extraction. Within 2–3 days, DNA was extracted from these preserved samples using the Zymo Research Xpedition Soil/Fecal DNA MiniPrep Extraction kit (Zymo Research Co.) following manufacturer's instructions.

Libraries of partial bacterial, archaeal, and eukaryotic small subunit (SSU) rRNA genes were amplified from each DNA extraction using PCR with primers that spanned the V4 and V5 hypervariable regions of the 16S ribosomal RNA gene (16S rRNA gene) between position 515 and 926 (*Escherichia coli* numbering), producing a ∼400 bp fragment for Bacteria and Archaea, and a 600 bp fragment for the Eukarya 18S rRNA gene. These primers evenly amplify a broad distribution of SSU rRNA genes from all three domains of life (Parada et al., 2015). The forward primer 515F-Y (**GTA AAA CGA CGG CCA G** CCG TGY CAG CMG CCG CGG TAA-3′) contains the M13 forward primer (in bold) fused to the gene-specific forward primer (underlined), while the reverse primer 926R (5′-CCG YCA ATT YMT TTR AGT TT-3′′) was unmodified from Parada et al. (2015). 5 PRIME HotMasterMix (Quanta Biosciences, Beverly, MA, United States) was used for all reactions at a final reaction volume of 50 μL. Reactions were purified using Agencourt® Ampure® XP paramagnetic beads (Beckman Coulter Inc., Indianapolis, IN, United States) at an 0.8x final concentration. After purification, 4 μL of PCR product was used in a barcoding reaction to attach a unique 12 bp barcode to each library in duplicate 50 μL reactions. Duplicate reactions were pooled, purified using AmpureXP beads to a final volume of 40 μL, quantified using the Qubit™ dsDNA HS assay kit (Thermo Fisher Scientific Inc., Waltham, MA, United States), and pooled in equimolar amounts before concentration using an Amicon® Ultra 0.5 ml centrifugal filter unit with Ultracel-30K membrane (Millipore Sigma, Billerica, MA, United States) to a final volume of 80 μL. To mitigate the effects of reagent contamination (Salter et al., 2014), triplicate extraction blanks (DNA extraction with no sample addition) and negative PCR controls (PCR with no template DNA added) were sequenced. The pooled, prepared library was then submitted for sequencing on the Illumina MiSeq (Illumina Inc., San Diego, CA, United States) using V2 PE250 chemistry at the Oklahoma Medical Research Foundation (OMRF) Clinical Genomics Center[1].

Small sub-unit (SSU) rRNA gene analyses were carried out within QIIME version 1.9.1 (Caporaso et al., 2010b). Briefly, paired-end reads were joined using PEAR (Zhang et al., 2014), barcodes were extracted, and de-multiplexed prior to operational taxonomic unit (OTU) clustering. Chimeras were filtered prior to clustering using usearch61 (Edgar, 2010) and representative sequences for each OTU were assigned a taxonomic identity by mothur (Schloss et al., 2009) against the SILVA r128 database (Yilmaz et al., 2013) clustered to a 97% similarity. Finally, sequences were aligned with PyNAST (Wang et al., 2007; Caporaso et al., 2010a) against the SILVA r128 database and FastTree (Price et al., 2010) was used to produce a phylogenetic tree to generate a weighted UniFrac distance matrix (Lozupone and Knight, 2005). A BIOM file (McDonald et al., 2012) was generated and used to generate bar charts of the relative abundances of OTUs in each sample. A phylogenetic tree of OTUs belonging to the Cyanobacteria phylum with greater than 100 sequence counts (40 OTUs total) was constructed. Evolutionary history was inferred by using the Maximum Likelihood method based on the Tamura-Nei model (Tamura and Nei, 1993). Initial tree(s) for the heuristic search were obtained automatically by applying Neighbor-Join and BioNJ algorithms to a matrix of pairwise distances estimated using the Maximum Composite Likelihood (MCL) approach, and then selecting the topology with superior log likelihood value. A total of a thousand trees were produced to generate bootstrap values. All positions containing gaps and missing data were eliminated. A total of 417 positions were in the final dataset. Evolutionary analyses were conducted in MEGA7 (Kumar et al., 2016).

The metagenomic libraries were prepared from three samples of precipitate material collected from the upstream edge of the Site 4 mineral structure using the Nextera XT library preparation kit (Illumina Inc., San Diego CA, United States) following manufacturer's instructions. Briefly, DNA from each sample was normalized to a total amount of 1 ng as input into the tagmentation reaction. After limited-cycle amplification, samples were cleaned, normalized using a bead-based method (Illumina Inc.), pooled at an equimolar ratio, and sequenced on the Illumina NextSeq 500 using high output PE150 chemistry at the OMRF Clinical Genomics Center. Metagenomic sequencing

[1]https://omrf.org/

TABLE 1 | Water chemistry values along the flow path of Little Hot Creek.

Site	pH	T (°C)	$\Omega_{Calcite}$	DIC (mM)	Na^+ (mM)	K^+ (mM)	Ca^{2+} (mM)	F^-(mM)	Cl^-(mM)	SO_4^{2-} (mM)
1	6.70	81.2	2.1	15.7	16.8	0.7	1.3	0.5	5.0	1.1
2	6.80	79.6	1.5	14.9	17.5	0.7	0.7	0.5	5.3	1.2
3	7.07	76.7	2.1	13.7	17.5	0.7	0.7	0.5	4.9	1.1
4	7.45	70.7	7.2	12.8	17.3	0.8	1.0	0.5	5.1	1.1

Site 1 is closest to the hot spring source and Site 4 is closest to the output.

reads were demultiplexed and had barcodes removed prior to being uploaded to MG-RAST (Meyer et al., 2008; Wilke et al., 2015). The MG-RAST pipeline removed adapters and completed a quality control step before analysis and annotated using the KEGG Orthology database (Kanehisa, 2002) for functionality and against the RefSeq database (Pruitt et al., 2007) for taxonomic assignments.

RESULTS

Little Hot Creek Water Geochemistry

The water chemistry of Little Hot Creek exhibits substantial variability from source to outflow (**Table 1**). Waters near the hot spring source are hot and mildly acidic (81.2°C, and pH = 6.7 at the sampling location closest to source). Waters become cooler and more alkaline as they move downstream over a 28 m transect (70.7°C, and pH = 7.45 at the final sampling location). The concentration of DIC decreases from 15.7 mM closest to the source to 12.8 mM at the output. All other measured geochemical parameters display little variability along the flow path (**Table 1**). Data collected in 2015 from LHC show a decrease in the dissolved silica concentration from 1.49 mM near the source to 1.36 mM at the output (2015 Agouron International Geobiology Course, unpublished data). LHC waters are undersaturated with respect to amorphous silica at all sampling locations.

The stable carbon isotopic composition of the carbonate portion of the precipitates ($\delta^{13}C_{CARB}$), the measured DIC isotopic values from LHC water ($\delta^{13}C_{DIC}$), and the expected isotopic values for DIC of water from which a precipitate formed ($\delta^{13}C_{EXP}$), given equilibrium fractionation and a calcite-bicarbonate enrichment factor of 1.0‰ (Romanek et al., 1992), are shown in **Figure 2**. $\delta^{13}C_{CARB}$ varies between −2.2 and −0.2‰ with a mean value of −1.2‰. No clear pattern is observed in $\delta^{13}C_{CARB}$ from top to bottom within individual precipitates or between precipitates along the flow path. $\delta^{13}C_{EXP}$ varies between −3.2‰ and −1.2‰ with a mean value of −2.2‰. $\delta^{13}C_{DIC}$ is depleted relative to $\delta^{13}C_{EXP}$ with values ranging from −4.8‰ and −3.1‰ and a mean value of −3.9‰. However, $\delta^{13}C_{DIC}$ increases toward the average $\delta^{13}C_{EXP}$ moving downstream and is comparable to the most depleted $\delta^{13}C_{EXP}$ value at the final sampling location. The degassing experiment fluids exhibited a progressive decrease in DIC in association with ^{13}C enrichment. The fluid DIC contents decreased from 14.7 to 13.5 mM and $\delta^{13}C$ values increased from −5.2 to −3.3‰. Carbon contents and isotope composition were strongly correlated aside from the first six samples.

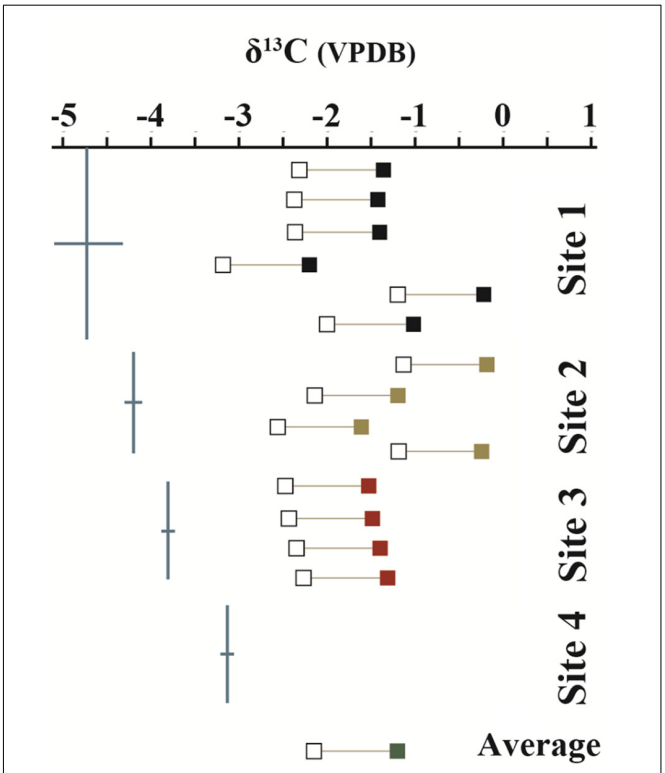

FIGURE 2 | Measured $\delta^{13}C$ values of mineral precipitates (closed boxes) and DIC from hot spring waters (blue lines). Open boxes show the expected isotopic values of the water from which a mineral structure precipitated under equilibrium conditions. Mineral precipitate values are plotted in order from top to bottom of sampled structure. No data was collected from the mineral precipitate of Site 4 due to the loss of the sample during transport. $\delta^{13}C$ values are referenced to the Vienna PeeDee Belemnite (VPDB) standard.

Petrography

The precipitate sample from Site 1 near the hot spring source was used for petrographic analysis (**Figure 3A**). The precipitate was 19.5 cm long by 9 cm wide, protruded ∼2–3 cm above water surface, and extended ∼4–5 cm below the water surface. The precipitate consists of an upper, subaerially exposed, partially lithified portion and a lower, subaqueous highly lithified portion (**Figure 3B**). The top portion has a white crenulated fabric with a light-pink tinge in the center. Beneath the white domal crenulations, dark green mats were encapsulated. Along the upstream margin, the edges of the upper layer are smooth and light yellow to red in color. The lower subaqueous portion is very well lithified and black in color with a rough surface.

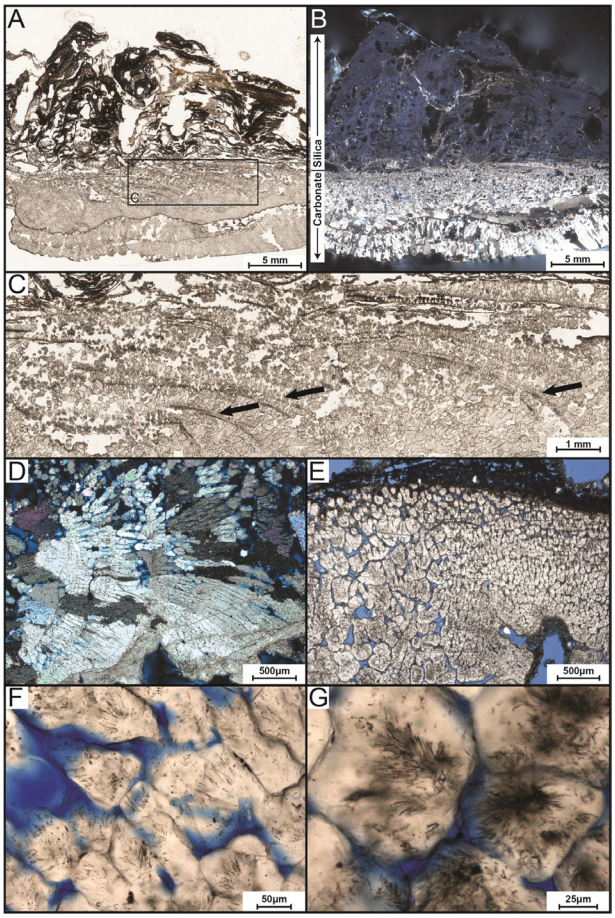

FIGURE 3 | Transmitted-light petrographic photomicrographs of LHC precipitates in thin section. **(A)** Plane-polarized transmitted light photomosaic of LHC precipitate (inset box enlarged in **C**). Light-colored area toward the bottom of the image is calcite and wavy-laminated, darker area toward the top is amorphous silica. **(B)** Cross-polarized transmitted light photomosaic revealing bladed calcite crystals in lower portion and amorphous silica in the upper portion (same field of view as **A**). Amorphous silica is opaque under cross-polarized light, so a minor amount of reflected light was cast across the thin section to enhance the visibility of the upper silica portion. **(C)** Inset image from **(A)**. Arrows point to several curved, downward dipping surfaces that indicate progressive growth of the bladed calcite from left to right. **(D)** Crossed-polarized photomicrograph of bladed calcite from the lower portion of the precipitate indicating growth from left to right. **(E)** Plane-polarized transmitted light image of bladed calcite crystals with cloudy appearance caused by pervasive endolithic activity (blue areas represent pore space). **(F,G)** Plane-polarized transmitted light photomicrographs of endoliths within calcite crystals.

In thin section, two different zones were recognized, aligning with those observed in the hand sample (**Figures 3A,B**). The upper zone is laminated and consists of mixed amorphous silica and micritic calcite. The laminae are domal, wavy, and characterized by a low degree of inheritance [i.e., stromatolitic in appearance (Walter, 1976)]. The lower zone consists of bladed calcite crystal fans that grew perpendicular to or slightly downward from the surface (**Figures 3C,D**). Curved, downward dipping surfaces spaced approximately 100 µm apart are visible within the lower carbonate portion (**Figure 3C**). Within this zone, the bladed calcite crystals appear cloudy under lower magnification (**Figures 3D,E**). Higher magnification (400×) reveals a network of tubular structures (up to 2 µm in diameter and 20 µm in length) that extend into the calcite (**Figures 3F,G**).

Microbial Communities of LHC Precipitates

Biofilm and lithified material were collected from leading edges and silica/calcite tops from four precipitates at four locations in LHC. SSU rRNA gene libraries were sequenced to identify microorganisms present on precipitate leading edges, tops, and interior (Accession SRX3004381). The relative abundances of bacterial and archaeal OTUs are shown at the phylum level in **Figure 4**. Eukarya were found to constitute a low percentage (0–0.7%) of the microbial community in both SSU rRNA and metagenomic data and were not investigated further for this study (Supplementary Table S1). The precipitate top communities (sampled at Sites 1 and 2) contained higher relative abundances of Cyanobacteria than the adjacent leading edges. And while no precipitate tops were sampled at Site 3 or 4, Cyanobacteria relative abundance increased at leading edges. Of the Cyanobacteria at Site 4, the metagenomic data identified the orders Chroococcales (average of 85.4% of sequences), Nostocales (6.8%), Oscillatoriales (4.6%), Prochlorales (0.8%), Gloeobacterales (1.8%), and unclassified reads (0.6%) (Supplementary Table S1). The genus *Synechococcus* comprised 90.2% of the reads attributed to Chroococcales. A maximum likelihood tree of Cyanobacteria OTUs (with greater than 100 sequences in the dataset) showed most OTUs to be most closely related to *Synechococcus* sp. JA-3-3Ab(CP000239) (Supplementary Figure S2), a photosynthetic cyanobacterium previously isolated from microbial mats in Yellowstone National Park's Octopus Spring (Allewalt et al., 2006; Steunou et al., 2006).

Microscopy of precipitate tops indicated the presence of photosynthetic cyanobacteria populations (Supplementary Figure S1). Fluorescence microscopy revealed the most abundant cellular morphology to be rod-shaped and approximately 3 µm in length. A lesser number of coccoidal organisms was noted as well, which is the one known morphology of *Synechococcus,* the most abundant Cyanobacteria identified in sequence data. It was difficult to detect organisms entrained within the mineral grains, but when grains were examined under green light (550 nm), organisms capable of photosynthesis became more evident as they fluoresced red. Samples were stained with DAPI (4′6′-diamidino-2-phenylindole) and exposed to ultraviolet light to fluoresce DNA allowing for easier imaging of organisms associated with mineral grains. Images of mineral precipitates were taken at low magnification (200×) on an ESEM that showed filamentous organisms, potentially cyanobacteria, in close association with mineral grains on LHC precipitate tops (Supplementary Figure S1E). Under higher magnification (1200×) an amorphous matrix, potentially exopolymeric substance (EPS), appeared to be in

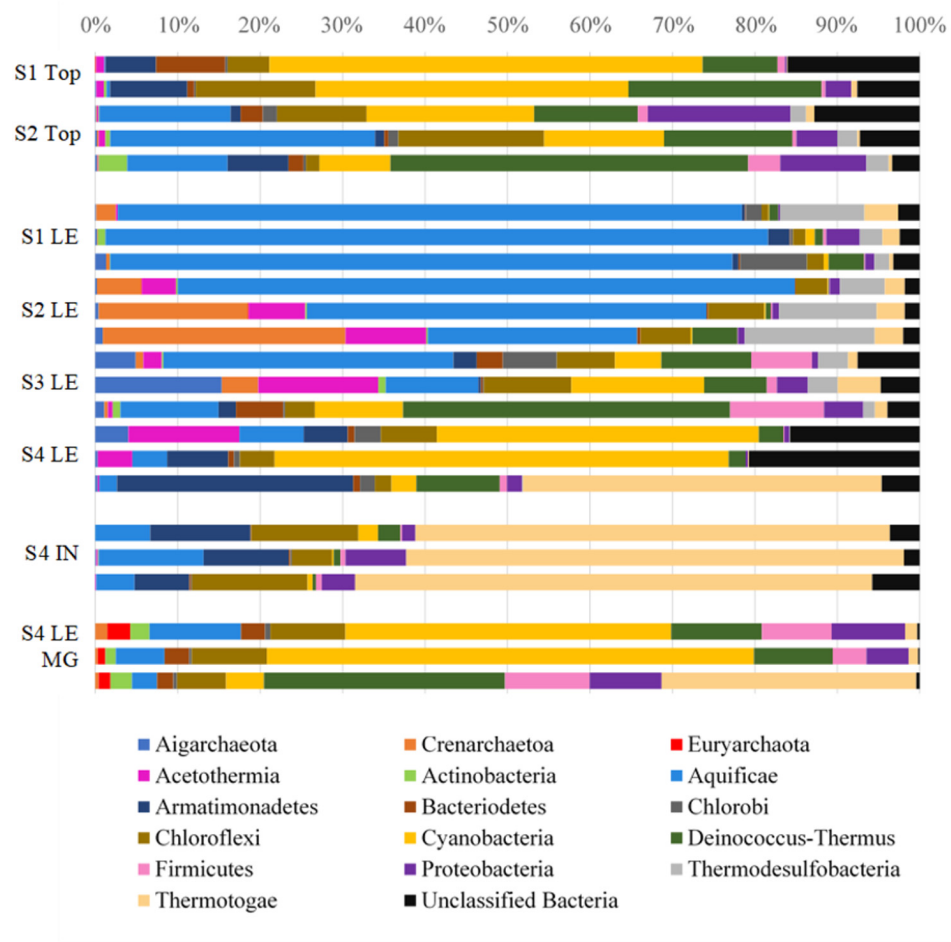

FIGURE 4 | Relative abundances of bacterial and archaeal phyla in LHC precipitates. S1, S2, S3, S4 indicates Site number where a sample was taken, followed by the type of sample taken: top, leading edge (LE), precipitate interior (IN), and leading-edge metagenome (LE MG). Each bar represents the microbial community of a biological replicate. Cyanobacteria are most abundant in the precipitate top portions and at the leading edge of the Site 4 precipitate. Aquificae is heavily represented in the warmest parts of the hot spring closer to the source and Thermotogae dominates the interior mineral material.

close association with the mineral grains as well (Supplementary Figure S1F).

In addition to SSU rRNA sequencing, metagenomic libraries were generated from the leading edge of the Site 4 precipitate (Accessions mgm4709842.3, mgm4709411.3, mgm4709423.3). A total of 4,868,811 sequences were produced from 788,297,300 base pairs (Supplementary Table S2). The relative abundances of metagenomic 16S rRNA sequences associated with taxa were in general agreement with the SSU rRNA sequencing results for the sampling site (**Figure 4** and Supplementary Table S1). The metagenomic reads were run against the KEGG Orthologs database within MG-RAST to identify genes associated with photosynthesis, which could affect carbonate precipitation through the biological consumption of CO_2 (Zhu and Dittrich, 2016). Photosynthesis and phycobilisome-associated genes were a major constituent of the metabolic makeup at Site 4, accounting for 21.6, 33.2, and 2.7% of all energy metabolism-associated sequences in samples (**Table 2**).

DISCUSSION

A Geochemical Model for Precipitate Formation

Metabolic reactions carried out by microorganisms have been shown to impact aqueous geochemistry and drive mineral precipitation in a number of environments (Dupraz and Visscher, 2005; Visscher and Stolz, 2005; Baumgartner et al., 2006). Thus, the intimate association of microorganisms with the studied mineral precipitates at Little Hot Creek suggests the possibility of a biological role in their formation. Indeed, photosynthesis can increase the saturation state of calcite, and genes associated with this metabolism were observed in metagenomic libraries from the Site 4 precipitate. However, the rapid physico-chemical changes that occur when the geothermal waters emerge at the surface and equilibrate with the atmosphere could also drive mineral formation. Geochemical modeling was performed to assess the effects of physico-chemical processes on the saturation states of calcite and amorphous silica, which were identified as the primary

TABLE 2 | Metabolic gene annotations from the KEGG Orthology database and MG-RAST.

	Percentage of annotated genes		
Energy metabolism	**MG 4A**	**MG 4B**	**MG 4C**
Oxidative phosphorylation	54.6	50.5	78.6
Photosynthesis	13.5	20.9	1.6
Photosynthesis antenna proteins	7.1	10.5	0.7
C fixation in photosynthetic organisms	1.0	1.7	0.4
C fixation in prokaryotes	5.2	3.3	8.8
Methane metabolism	10.9	6.3	6.1
Nitrogen metabolism	2.3	1.6	2.1
Sulfur metabolism	5.4	5.1	1.7

Genes associated with photosynthetic metabolism (photosynthesis, photosynthesis antenna proteins, and carbon fixation in photosynthetic organisms) constitute 21.6, 33.2, and 2.7% of the metabolic annotations in the three samples from Site 4.

mineral phases within the precipitates at LHC from petrographic analysis. Measured geochemical values from sampling Site 1 were used as the starting parameters for all models.

Figure 5 demonstrates the progressive DIC loss and ^{13}C-enrichment of LHC and source fluid experiment waters follow a Rayleigh-type evolutionary trend as has been observed in other hot springs (Usdowski et al., 1979; Michaelis et al., 1985; Fouke et al., 2000). Similar systems produce a predictable relationship between the isotope composition of the residual DIC and the fraction of DIC remaining (f). Linear regression of $\delta^{13}C_{DIC}$ versus ln(f) yields a slope that is approximately equal to the fractionation (in ‰) between the lost product and reactant DIC (ε_{P-DIC}). The fractionation associated with LHC DIC evolution ($\varepsilon \approx -7.80$) is similar to that measured in the degassing experiment ($\varepsilon_{CO2-DIC} \approx -8.67$). Both fractionations conform to CO_2 degassing, a common phenomenon impacting hot springs

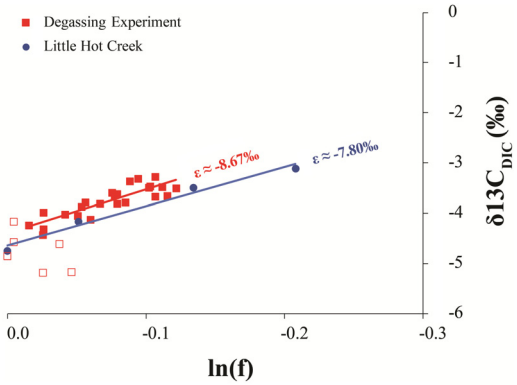

FIGURE 5 | Comparison of the Rayleigh fractionation from the degassing experiment and measured values from LHC1. The slope of a regression line of the natural log of the fraction of DIC remaining in the system (lnf) and its isotopic composition ($\delta^{13}C_{DIC}$) is approximately equal to the fractionation factor of the process. Open squares are the first six sampling points of the degassing experiment when mixing was likely incomplete, thus this data was not included in the regression analysis.

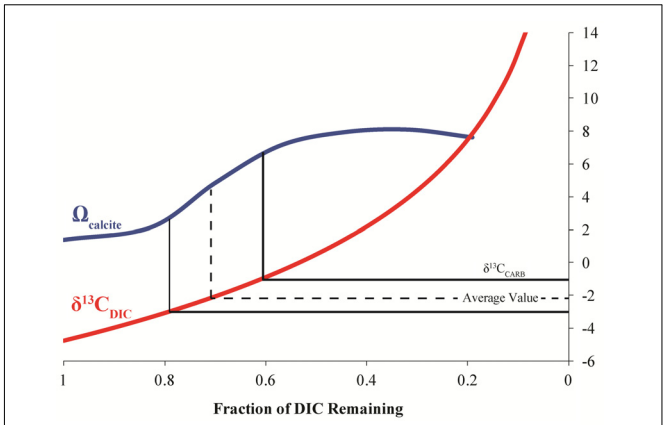

FIGURE 6 | Model results for the evolution of calcite saturation state (Ω) and $\delta^{13}C_{DIC}$ for degassing of LHC waters. The measured isotopic values from the precipitates ($\delta^{13}C_{CARB}$) occur at the greatest slope in the modeled increase of calcite saturation state.

(Renaut and Jones, 2000). This suggests that other factors impacting LHC (biological and mineral precipitation related) do not yield significant isotope fractionation of spring DIC (recall that the fluid experiment was conducted outside of the spring, in the absence of spring biota and mineral precipitates). However, CO_2 degassing can promote mineral formation by increasing pH and thus the saturation state of carbonate minerals as discussed below.

Because of the similarity between experimentally determined isotopic fractionations, the effect of degassing on calcite formation at LHC was modeled. Degassing was modeled by decreasing the concentration of DIC while allowing pH to vary to keep alkalinity constant as degassing removes DIC without affecting alkalinity. Model results indicate that degassing can drive an increase in the saturation state (Ω) of calcite, indicating that calcite precipitation becomes more thermodynamically favorable as CO_2 is degassed (**Figure 6**). A Rayleigh fractionation model for carbon isotopic fractionation during degassing predicts a concurrent isotopic enrichment in carbon during the modeled rise in saturation state (Usdowski et al., 1979; Michaelis et al., 1985; Fouke et al., 2000). Intriguingly, the modeled isotopic values during the greatest increase in saturation state match those expected for waters in equilibrium with calcite measured from the precipitates ($\delta^{13}C_{EXP}$). Further, the modeled saturation values are comparable to those measured at the final sampling location of LHC. The agreement between isotope compositions predicted from the model and measured values indicate that degassing alone can drive mineral formation and generate the $\delta^{13}C$ values of the LHC precipitates.

While degassing can explain the precipitation of calcite, it has less of an effect on the saturation state of amorphous silica. Primarily, silica saturation is controlled by the concentration of dissolved silica and temperature; therefore evaporation and/or cooling of waters could potentially increase silica saturation at LHC (Berelson et al., 2011). Modeling was performed to assess the effects of these processes on silica saturation at LHC (**Figure 7**).

Reducing temperature from the source temperature of 81.2–25°C alone is incapable of increasing the saturation state of silica to values where precipitation is thermodynamically favorable. Evaporation alone can drive silica to supersaturation when around 70% of water has been evaporated. However, evaporation also drives an increase of calcite saturation to values much higher than that of silica implying that calcite precipitation would be more quantitatively important in this scenario. In contrast, the combined effects of cooling and evaporation increase the saturation state of both mineral phases nearly equally, indicating that formation of each mineral would be equally favorable. This result is consistent with mixed calcite and silica layers observed petrographically and suggests that evaporation and cooling may be responsible for the precipitation of silica at LHC. Additionally, this result explains silica precipitation abiotically without any influence from microorganisms.

Based on the results of geochemical modeling, a multi-step growth model was developed describing mineral precipitate formation at LHC through physico-chemical processes alone (**Figure 8**). In this model, degassing increases the saturation state of calcite moving along the flow path promoting carbonate precipitation by nucleating at a point along the edge of the stream. Sequential precipitation leads to continued calcite formation and growth of the precipitate extending into the stream, as indicated by the curved, down-dipping growth lines observed in thin section (**Figure 3C**). As the precipitate grows and extends further into the stream, it forms a platform at the air water interface where water begins to splash onto its surface, which cools and evaporates leading to the precipitation of the upper layer of amorphous silica. Water splashing onto surfaces near hot spring environments leading to silica precipitation has been observed in other hot springs (Cady and Farmer, 1996; Mountain et al., 2003). This model indicates carbonate and silica precipitation can be fully explained through degassing and evaporation alone and is consistent with the results of geochemical modeling as well as field measurements and observations. Thus, from a thermodynamic standpoint, mineral precipitate formation at LHC can be explained through wholly abiotic processes, and microbial metabolic processes are not needed to generate substantial mineral deposition in LHC although they cannot be ruled out as an additional contributor.

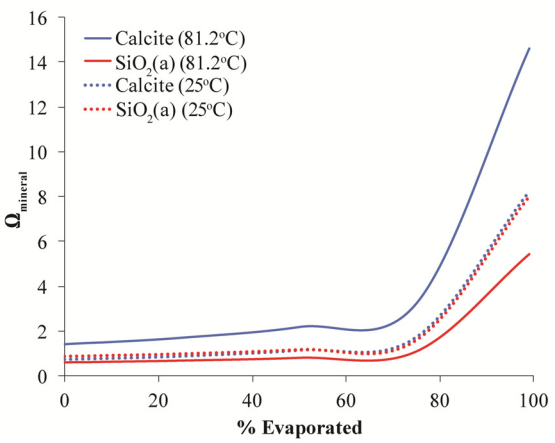

FIGURE 7 | Model results for evolution of the saturation state of calcite (blue lines) and amorphous silica (red lines) during evaporation at 81.2°C and (solid lines) and 25°C (dashed lines). The saturation state of both minerals begins to increase when ~70% of water has been evaporated. At high temperature calcite precipitation is more thermodynamically favorable than silica precipitation. However, at cooler temperatures both minerals are equally favorable.

Biological Controls on Precipitate Morphogenesis

The removal of CO_2 through physio-chemical or biological processes can shift carbonate equilibrium to favor the precipitation of $CaCO_3$ (e.g., Dupraz et al., 2009). Photosynthesis may drive carbonate precipitation through the biological removal of aqueous CO_2 and the concomitant increase in alkalinity. This removal and subsequent carbon fixation process can be represented by the simplified equation: $106\ CO_2 + 16\ NO_3^- + HPO_4^{2-} + 122\ H_2O + 18H^+ \rightarrow C_{106}N_{16}H_{263}O_{110}P + 138\ O_2$ (Bradley et al., 2017). Metagenomic functional annotations demonstrated photosynthetic genes present in the three sampled depths at Site 4 and SSU rRNA data shows Cyanobacteria are found on precipitate tops and leading edges. Active cyanobacteria populations in LHC may be altering geochemical gradients on micrometer scales to promote localized precipitation via photosynthesis. However, LHC fluids degas CO_2 readily as they reach the surface and equilibrate with the atmosphere along the stream's length. Modeling results indicate carbonate and silica precipitation can be fully explained through degassing and evaporation alone, and metabolic processes are not needed to generate substantial mineral deposition. The bladed morphology of the calcite crystals is also suggestive of abiogenic precipitation (e.g., Grotzinger and Knoll, 1999; Riding, 2008), consistent with the geochemical results.

Microscale biogenic morphological features such as altered mineral structure, low inheritance between mineral layers, asymmetric laminae couples, micritization, and the inclusion of benthic microfossils can be collectively diagnostic of biotic influence (Walter and Des Marais, 1993). Inheritance and micritization are two features that can be utilized in determining biogenicity of a deposit. Inheritance describes the relationship between laminations. High inheritance, where the overlying lamination mimics the underlying lamination, indicates predominantly abiogenic precipitation. Low inheritance, where the overlying lamination differs from the underlying lamination, is typically a property of microbial mats (e.g., Grotzinger and Rothman, 1996; Grotzinger and Knoll, 1999; Frantz et al., 2014; Petryshyn et al., 2016). Micritization is the formation of micrite brought on by the alteration of minerals by endolithic microorganisms via boring and is observable as darkened granular material in petrographic thin section (Bathurst, 1966). Additionally, other trace fossils and mineral alterations can be utilized to this end, and morphological evidence of biological involvement can be highly variable across different geochemical environments. Thus, microorganisms can not only influence the

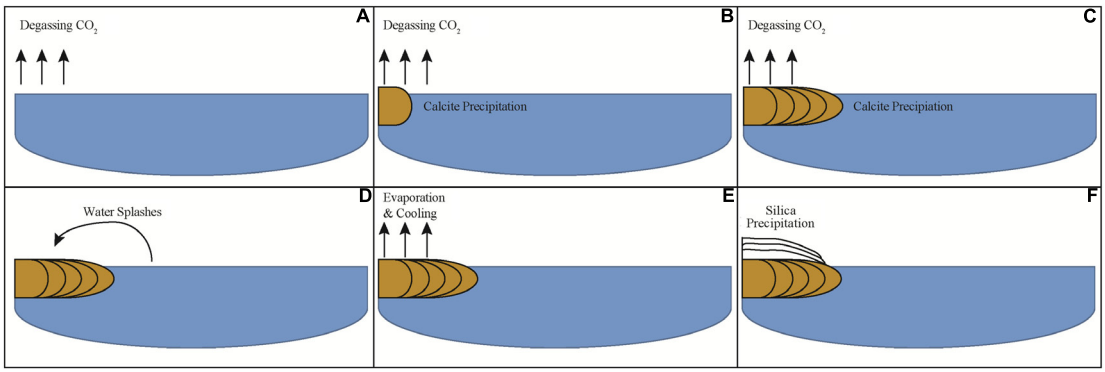

FIGURE 8 | Schematic model of mineral precipitate formation at a cross-section of Little Hot Creek. **(A)** CO_2 degasses from water increasing the saturation state for calcite. **(B)** When sufficient CO_2 has degassed calcite begins to precipitate. **(C)** As degassing continues calcite continues to precipitate leading the mineral structure to extend perpendicularly into the stream. **(D)** When the structure extends far enough out into the stream water begins to splash onto its surface. **(E)** Water that has splashed onto the precipitate evaporates and cools. **(F)** Silica precipitates once the water cools and evaporates sufficiently.

precipitate morphological features during mineral formation, but also after deposition.

Petrographic and microscopic analyses suggest a microbial role in shaping the emergent silica/calcite layer of the LHC precipitates. The LHC silica/calcite layer contained domed and wavy fabrics with micritization and a low degree of inheritance that is most parsimoniously explained as the result of precipitation occurring on an irregular surface formed by a microbial mat on the precipitates. As evaporation and decreasing temperature drive precipitation of dissolved silica, it will adsorb and precipitate onto cells of microbial biofilms regardless of microbial activities (Konhauser et al., 2004; Orange et al., 2013; Spear and Corsetti, 2013). Additionally, ESEM images from this layer show microbial filaments intimately associated with minerals implying they impart some impact on mineral formation.

The presence of filamentous cells, the genomic identification of photosynthesis and Cyanobacteria on the precipitate tops and leading edges, and previous studies of hot spring microbialites indicates Cyanobacteria likely play a role in shaping the emergent precipitate, even if they did not actively play a role in mineral precipitation via metabolism or cell wall/sheath interaction. Previous studies have noted this phyla in mats on the surface of microbialites and several mm into the surface, likely due to the above layer providing protection from predation and UV light filtration through mineral grains (Walker et al., 2005). Cyanobacteria have been implicated as 'builders' of stromatolitic microfabrics in microbialites recovered from Obsidian Pool Prime in Yellowstone National Park, producing very finely-laminated structures with high inheritance between layers (Berelson et al., 2011; Mata et al., 2012; Pepe-Ranney et al., 2012; Spear and Corsetti, 2013), and genesis of similar microfabrics in hot spring environments due to cyanobacterial colonization have been seen elsewhere (e.g., Konhauser et al., 2001). Many of the most abundant Cyanobacteria OTUs identified in LHC are most closely related to a *Synechococcus* from Octopus Spring, another alkaline siliceous hydrothermal spring. Though environmental conditions of mineral formation between LHC and these other hot springs differ, preventing direct comparison, but instead provide insight into the variance of biogenic textures that can be produced with differing geochemistry. We postulate that cyanobacteria are involved in producing the mineral textures seen in LHC but cannot determine the mechanisms of formation. The differentiation and variability in textural clues of biogenicity highlights the need for geochemical context and environmental parameters in biosignature identification.

Endolithic Microborings in the Abiogenic Calcite Base

In contrast to the mineral texture of the silica/calcite layer, the lower calcite layer is comprised of crystal fans that are typically interpreted as abiotic fabrics (Riding, 2008). However, the tubular dark structures observed in this abiogenic calcite layer (**Figures 3F,G**) resemble microborings made by euendoliths. Euendoliths are a type of endolithic organisms that actively bore into rock, leaving tube cavities (Golubic et al., 1981). Textural clues such as microboring distribution, size, directionality, and relation to external surfaces and fluid paths are key to determine the biogenicity of these structures (McLoughlin et al., 2007). Besides endolithic organisms, other explanations have been put forth for tunneling features in carbonates such as organic matter within rocks acting as a dissolution agent or high fluid pressures pushing harder mineral grains through a mineral precipitate (producing ambient inclusion trails) (McLoughlin et al., 2007). However, abiotic mineral dissolution at heterogeneities and ambient inclusion trails would not leave borings of the morphology we see in precipitates from LHC (see McLoughlin et al., 2010 for a review). The tube structures appear to have well-defined, circular cross-sections with similar diameters and varied lengths up to 20 μm, and the tubes propagate into the calcite from external surfaces of the crystals as if a microbe were tunneling inward.

Euendolithic cyanobacteria are commonly found in microbialites and other carbonate surfaces. It's been suggested that these phototrophic endoliths actively transport Ca^{2+} away

from the microboring front to lower the saturation state of $CaCO_3$ and utilize the mineral as a carbon source in times of aqueous DIC limitation (Garcia-Pichel et al., 2010; Ramírez-Reinat and Garcia-Pichel, 2012). This mechanism allows carbonate dissolution to occur despite photosynthetic activity acting to promote carbonate precipitation and provides an explanation of the behavior as evolutionarily adaptive (Garcia-Pichel, 2006). Additionally, some lineages of Cyanobacteria (including the genus Synechococcus) are capable of generating intracellular carbonate inclusions, and this ability is not rare (Benzerara et al., 2014). Internal carbonate biomineralization could lower the alkalinity generated during photosynthesis, thereby decreasing $CaCO_3$ saturation on the microscale (Benzerara et al., 2014). These metabolic interactions highlight the complexities and feedbacks in mineral-microbe relationships and how difficult it can be to tease apart such reactions.

We cannot directly demonstrate that Cyanobacteria are the euendolithic microorganisms responsible for the borings in LHC, but believe the microboring structures preserved in the calcite can act as a trace fossil of microbial activity. These endolithic signatures do not require rapid mineralization for preservation like the silica/calcite morphological biosignatures. These observations suggest that even in the absence of a direct influence of microbial activity on mineral formation, microorganisms may secondarily alter microfabrics and create biosignatures under similar environmental conditions.

CONCLUSION

Examination of the biogenicity of mineral precipitates from Little Hot Creek revealed that, while abiotic processes can explain their formation thermodynamically, their morphogenesis suggests a microbial contribution, highlighting the need for interdisciplinary approaches (e.g., geochemistry, modeling, and petrography) when investigating the role of life in the formation of mineralized structures. Genomic and microscopic evidence of the microbial communities associated with the mineral precipitates indicated that Cyanobacteria were likely involved in the generation of stromatolitic microfabrics on LHC precipitate tops, while thermophiles, typical of other hot springs, reside within precipitate interiors and leading edges. This study underscores the necessity of utilizing multiple analytical tools and fields of expertise to understand the formation of geologically and astrobiologically important structures in the field of geobiology. At Little Hot Creek, geochemical investigation alone would not indicate life was involved with the formation of the precipitates. However, the addition of the microscopic textural investigation reveals a biological role in the formation and modification of the precipitates. Interpretation of potentially microbially influenced minerals from the geologic record or other planets requires a broad suite of techniques to avoid misinterpretation of the biogenicity of the structures.

AUTHOR CONTRIBUTIONS

JS, FC, HJ, SL, BWS, HN, and BSS led the design of the study. Fieldwork and laboratory analyses were conducted by all authors. All authors interpreted results. EK wrote the manuscript with contributions from all other authors. SB wrote the geochemical results and discussion.

FUNDING

This research was funded by the Agouron Institute, the Center for Dark Energy Biosphere Investigations (C-DEBI) at the University of Southern California (USC), and the USC Wrigley Institute. JS was supported by the Zink Sunnyside Family Fund. EK was supported by the NASA Astrobiology Institute Rock-Powered Life grant.

ACKNOWLEDGMENTS

We would like to thank student participants and instructors from the 2016 International Geobiology Course, who assisted with sample collection and laboratory analyses, and insightful discussion of the results. We would also like to thank the students of the 2014 and 2015 International Geobiology Courses who helped lay the groundwork for this study. A permit was granted to JS from the United States Forest Service (Permit #MLD15053) to conduct fieldwork and sample the LHC system.

SUPPLEMENTARY MATERIAL

The Supplementary Material for this article can be found online at: https://www.frontiersin.org/articles/10.3389/fmicb.2018.00997/full#supplementary-material

REFERENCES

Allewalt, J. P., Bateson, M. M., Revsbech, N. P., Slack, K., and Ward, D. M. (2006). Effect of temperature and light on growth of and photosynthesis by *Synechococcus* isolates typical of those predominating in the octopus spring microbial mat community of Yellowstone National Park. *Appl. Environ. Microbiol.* 72, 544–550. doi: 10.1128/AEM.72.1.544-550.2006

Bathurst, R. (1966). Boring algae, micrite envelopes and lithification of molluscan biosparites. *Geol. J.* 5, 15–32. doi: 10.1002/gj.3350050104

Baumgartner, L. K., Reid, R. P., Dupraz, C., Decho, A. W., Buckley, D. H., Spear, J. R., et al. (2006). Sulfate reducing bacteria in microbial mats: changing paradigms, new discoveries. *Sediment. Geol.* 185, 131–145. doi: 10.1016/j.sedgeo.2005.12.008

Benning, L. G., Phoenix, V. R., Yee, N., and Konhauser, K. O. (2004). The dynamics of cyanobacterial silicification: an infrared micro-spectroscopic investigation. *Geochem. Cosmochim. Acta* 68, 743–757. doi: 10.1016/S0016-7037(03)00488-5

Benzerara, K., Skouri-Panet, F., Li, J., Ferard, C., Gugger, M., Laurent, T., et al. (2014). Intracellular Ca-carbonate biomineralization is widespread in cyanobacteria. *Proc. Natl. Acad. Sci. U.S.A.* 111, 10933–10938. doi: 10.1073/pnas.1403510111

Berelson, W. M., Corsetti, F. A., Pepe-Ranney, C., Hammond, D. E., Beaumont, W., and Spear, J. R. (2011). Hot spring siliceous stromatolites from Yellowstone

National Park: assessing growth rate and laminae formation. *Geobiology* 9, 411–424. doi: 10.1111/j.1472-4669.2011.00288.x

Bradley, J. A., Daille, L. K., Trivedi, C. B., Bojanowski, C. L., Stamps, B. W., Stevenson, B. S., et al. (2017). Carbonate-rich dendrolitic cones: insights into a modern analog for incipient microbialite formation, Little Hot Creek, Long Valley Caldera, California. *NPJ Biofilms Microbiomes* 3:32. doi: 10.1038/s41522-017-0041-2

Breitbart, M., Wegley, L., Leeds, S., Schoenfeld, T., and Rohwer, F. (2004). Phage community dynamics in hot springs. *Appl. Environ. Microbiol.* 70, 1633–1640. doi: 10.1128/AEM.70.3.1633-1640.2004

Cady, S. L., and Farmer, J. D. (1996). Fossilization processes in siliceous thermal springs: trends in preservation along thermal gradients. *Ciba Found. Symp.* 202, 150–173. Available at: http://www.ncbi.nlm.nih.gov/pubmed/9243015 doi: 10.1002/9780470514986

Cady, S. L., Farmer, J. D., Grotzinger, J. P., Schopf, J. W., and Steele, A. (2003). Morphological biosignatures and the search for life on Mars. *Astrobiology* 3, 351–368. doi: 10.1089/153110703769016442

Caporaso, J. G., Bittinger, K., Bushman, F. D., DeSantis, T. Z., Andersen, G. L., and Knight, R. (2010a). PyNAST: a flexible tool for aligning sequences to a template alignment. *Bioinformatics* 26, 266–267. doi: 10.1093/bioinformatics/btp636

Caporaso, J. G., Kuczynski, J., Stombaugh, J., Bittinger, K., Bushman, F. D., Costello, E. K., et al. (2010b). QIIME allows analysis of high-throughput community sequencing data. *Nat. Methods* 7, 335–336. doi: 10.1038/nmeth.f.303

Chrachri, A., Hopkinson, B. M., Flynn, K., Brownlee, C., and Wheeler, G. L. (2018). Dynamic changes in carbonate chemistry in the microenvironment around single marine phytoplankton cells. *Nat. Commun.* 9:74. doi: 10.1038/s41467-017-02426-y

Djokic, T., Van Kranendonk, M. J., Campbell, K. A., Walter, M. R., and Ward, C. R. (2017). Earliest signs of life on land preserved in ca. 3.5 Ga hot spring deposits. *Nat. Commun.* 8:15263. doi: 10.1038/ncomms15263

Dupraz, C., Reid, R. P., Braissant, O., Decho, A. W., Norman, R. S., and Visscher, P. T. (2009). Processes of carbonate precipitation in modern microbial mats. *Earth Sci. Rev.* 96, 141–162. doi: 10.1016/j.earscirev.2008.10.005

Dupraz, C., and Visscher, P. T. (2005). Microbial lithification in marine stromatolites and hypersaline mats. *Trends Microbiol.* 13, 429–438. doi: 10.1016/j.tim.2005.07.008

Edgar, R. C. (2010). Search and clustering orders of magnitude faster than BLAST. *Bioinformatics* 26, 2460–2461. doi: 10.1093/bioinformatics/btq461

Farmer, J. D., and Des Marais, D. J. (1999). Exploring for a record of ancient Martian life. *J. Geophys. Res.* 104, 26977–26995. doi: 10.1029/1998JE000540

Fouke, B. W. (2011). Hot-spring systems geobiology: abiotic and biotic influences on travertine formation at Mammoth Hot Springs, Yellowstone National Park, USA. *Sedimentology* 58, 170–219. doi: 10.1111/j.1365-3091.2010.01209.x

Fouke, B. W., Farmer, J. D., Des Marais, D. J., Pratt, L., Sturchio, N. C., Burns, P. C., et al. (2000). Depositional facies and aqueous-solid geochemistry of travertine-depositing hot springs (Angel Terrace, Mammoth Hot Springs, Yellowstone National Park, USA). *J. Sediment. Res.* 70, 565–585. doi: 10.1306/2DC40929-0E47-11D7-8643000102C1865D

Frantz, C., Petryshyn, V., Marenco, P., Berelson, W., Tripati, A., and Corsetti, F. (2014). Dramatic local environmental change during the Early Eocene Climatic Optimum detected using chemical analyses of a Green River Formation stromatolite. *Palaeogeogr. Palaeoclimatol. Palaeoecol.* 105, 1–15. doi: 10.1016/j.palaeo.2014.04.001

Garcia-Pichel, F. (2006). Plausible mechanisms for the boring on carbonates by microbial phototrophs. *Sediment. Geol.* 185, 205–213. doi: 10.1016/j.sedgeo.2005.12.013

Garcia-Pichel, F., Ramirez-Reinat, E., and Gao, Q. (2010). Microbial excavation of solid carbonates powered by P-type ATPase-mediated transcellular Ca^{2+} transport. *Proc. Natl. Acad. Sci. U.S.A.* 107, 21749–21754. doi: 10.1073/pnas.1011884108

García-Ruiz, J. M., Hyde, S. T., Carnerup, A. M., Christy, A. G., Van Kranendonk, M. J., and Welham, N. J. (2003). Self-assembled silica-carbonate structures and detection of ancient microfossils. *Science* 302, 1194–1197. doi: 10.1126/science.1090163

Golubic, S., Friedmann, I., and Schneider, J. (1981). The lithobiontic ecological niche, with special reference to microorganisms. *J. Sediment. Res.* 51, 475–478. doi: 10.1306/212F7CB6-2B24-11D7-8648000102C1865D

Grotzinger, J. P., and Knoll, A. H. (1999). Stromatolites in Precambrian carbonates; evolutionary mileposts or environmental dipsticks? *Annu. Rev. Earth Planet. Sci.* 27, 313–358. doi: 10.1146/annurev.earth.27.1.313

Grotzinger, J. P., and Rothman, D. H. (1996). An abiotic model for stromatolite morphogenesis. *Nature* 383, 423–425. doi: 10.1038/383423a0

Inskeep, W. P., Rusch, D. B., Jay, Z. J., Herrgard, M. J., Kozubal, M. A., Richardson, T. H., et al. (2010). Metagenomes from high-temperature chemotrophic systems reveal geochemical controls on microbial community structure and function. *PLoS One* 5:e9773. doi: 10.1371/journal.pone.0009773

Kanehisa, M. (2002). The KEGG database. *Novartis Found. Symp.* 247, 91–101; discussion 101–103, 119–128, 244–252. doi: 10.1002/0470857897.ch8

Konhauser, K. O., and Ferris, F. G. (1996). Diversity of iron and silica precipitation by microbial mats in hydrothermal waters, Iceland: implications for Precambrian iron formations. *Geology* 24, 323–326. doi: 10.1130/0091-7613(1996)024<0323:DOIASP>2.3.CO;2

Konhauser, K. O., Jones, B., Phoenix, V. R., Ferris, G., and Renaut, R. W. (2004). The microbial role in hot spring silicification. *Ambio* 33, 552–558. doi: 10.1579/0044-7447-33.8.552

Konhauser, K. O., Phoenix, V. R., Bottrell, S. H., Adams, D. G., and Head, I. M. (2001). Microbial-silica interactions in Icelandic hot spring sinter: possible analogues for some Precambrian siliceous stromatolites. *Sedimentology* 48, 415–433. doi: 10.1046/j.1365-3091.2001.00372.x

Kumar, S., Stecher, G., and Tamura, K. (2016). MEGA7: molecular evolutionary genetics analysis version 7.0 for bigger datasets. *Mol. Biol. Evol.* 33, 1870–1874. doi: 10.1093/molbev/msw054

Lozupone, C., and Knight, R. (2005). UniFrac: a new phylogenetic method for comparing microbial communities. *Appl. Environ. Microbiol.* 71, 8228–8235. doi: 10.1128/AEM.71.12.8228-8235.2005

Mata, S. A., Harwood, C. L., Corsetti, F. A., Stork, N. J., Eilers, K., Berelson, W. M., et al. (2012). Influence of gas production and filament orientation on stromatolite microfabric. *Palaios* 27, 206–219. doi: 10.2110/palo.2011.p11-088r

McDonald, D., Clemente, J. C., Kuczynski, J., Rideout, J. R., Stombaugh, J., Wendel, D., et al. (2012). The biological observation matrix (BIOM) format or: how I learned to stop worrying and love the ome-ome. *Gigascience* 1:7. doi: 10.1186/2047-217X-1-7

McKay, C. P., and Stoker, C. R. (1989). The early environment and its evolution on Mars: implication for life. *Rev. Geophys.* 27:189. doi: 10.1029/RG027i002p00189

McLoughlin, N., Brasier, M. D., Wacey, D., Green, O. R., and Perry, R. S. (2007). On biogenicity criteria for endolithic microborings on early earth and beyond. *Astrobiology* 7, 10–26. doi: 10.1089/ast.2006.0122

McLoughlin, N., Staudigel, H., Furnes, H., Eickmann, B., and Ivarsson, M. (2010). Mechanisms of microtunneling in rock substrates: distinguishing endolithic biosignatures from abiotic microtunnels. *Geobiology* 8, 245–255. doi: 10.1111/j.1472-4669.2010.00243.x

Meyer, F., Paarmann, D., D'Souza, M., Olson, R., Glass, E. M., Kubal, M., et al. (2008). The metagenomics RAST server - a public resource for the automatic phylogenetic and functional analysis of metagenomes. *BMC Bioinformatics* 9:386. doi: 10.1186/1471-2105-9-386

Meyer-Dombard, D. R., Shock, E. L., and Amend, J. P. (2005). Archaeal and bacterial communities in geochemically diverse hot springs of Yellowstone National Park, USA. *Geobiology* 3, 211–227. doi: 10.1111/j.1472-4669.2005.00052.x

Meyer-Dombard, D. R., Swingley, W., Raymond, J., Havig, J., Shock, E. L., and Summons, R. E. (2011). Hydrothermal ecotones and streamer biofilm communities in the Lower Geyser Basin, Yellowstone National Park. *Environ. Microbiol.* 13, 2216–2231. doi: 10.1111/j.1462-2920.2011.02476.x

Michaelis, J., Usdowski, E., and Menschel, G. (1985). Partitioning of 13C and 12C on the degassing of CO_2 and the precipitation of calcite-Rayleigh-type fractionation and a kinetic model. *Am. J. Sci.* 285, 318–327. doi: 10.2475/ajs.285.4.318

Mountain, B. W., Benning, L. G., and Boerema, J. A. (2003). Experimental studies on New Zealand hot spring sinters: rates of growth and textural development. *Can. J. Earth Sci.* 40, 1643–1667. doi: 10.1139/e03-068

NASA (1995). *An Exobiological Strategy for Mars Exploration, SP-530*. Washington, DC: National Aeronautics and Space Administration.

Orange, F., Lalonde, S. V., and Konhauser, K. O. (2013). Experimental simulation of evaporation-driven silica sinter formation and microbial silicification in hot spring systems. *Astrobiology* 13, 163–176. doi: 10.1089/ast.2012.0887

Parada, A., Needham, D. M., and Fuhrman, J. A. (2015). Every base matters: assessing small subunit rRNA primers for marine microbiomes with mock communities, time-series and global field samples. *Environ. Microbiol.* 18, 1403–1414. doi: 10.1111/1462-2920.13023

Parkhurst, D. L., and Appelo, C. A. J. (2013). *Description of Input and Examples for PHREEQC Version 3–A Computer Program for Speciation, Batch-Reaction, One-Dimensional Transport, and Inverse Geochemical Calculations: U.S. Geological Survey Techniques and Methods*. Available at: http://pubs.usgs.gov/tm/06/a43

Pentecost, A. (2005). *Travertine*. Netherlands: Springer.

Pepe-Ranney, C., Berelson, W. M., Corsetti, F. A., Treants, M., and Spear, J. R. (2012). Cyanobacterial construction of hot spring siliceous stromatolites in Yellowstone National Park. *Environ. Microbiol.* 14, 1182–1197. doi: 10.1111/j.1462-2920.2012.02698.x

Petryshyn, V. A., Corsetti, F. A., Frantz, C. M., Lund, S. P., and Berelson, W. M. (2016). Magnetic susceptibility as a biosignature in stromatolites. *Earth Planet. Sci. Lett.* 437, 66–75. doi: 10.1016/J.EPSL.2015.12.016

Phoenix, V. R., Adams, D. G., and Konhauser, K. O. (2000). Cyanobacterial viability during hydrothermal biomineralisation. *Chem. Geol.* 169, 329–338. doi: 10.1016/S0009-2541(00)00212-6

Preston, L. J., Benedix, G. K., Genge, M. J., and Sephton, M. A. (2008). A multidisciplinary study of silica sinter deposits with applications to silica identification and detection of fossil life on Mars. *Icarus* 198, 331–350. doi: 10.1016/j.icarus.2008.08.006

Price, M. N., Dehal, P. S., and Arkin, A. P. (2010). FastTree 2 – approximately maximum-likelihood trees for large alignments. *PLoS One* 5:e9490. doi: 10.1371/journal.pone.0009490

Pruitt, K. D., Tatusova, T., and Maglott, D. R. (2007). NCBI reference sequences (RefSeq): a curated non-redundant sequence database of genomes, transcripts and proteins. *Nucleic Acids Res.* 35, D61–D65. doi: 10.1093/nar/gkl842

Ramírez-Reinat, E. L., and Garcia-Pichel, F. (2012). Prevalence of Ca^{2+}-ATPase-mediated carbonate dissolution among cyanobacterial euendoliths. *Appl. Environ. Microbiol.* 78, 7–13. doi: 10.1128/AEM.06633-11

Renaut, R. W., and Jones, B. (2000). "Microbial precipitates around continental hot springs and geysers," in *Microbial Sediments*, eds R. E. Riding and S. M. Awramik (Berlin: Springer), 187–195. doi: 10.1007/978-3-662-04036-2_21

Riding, R. (2008). Abiogenic, microbial and hybrid authigenic carbonate crusts: components of Precambrian stromatolites. *Geol. Croat.* 61, 73–103.

Romanek, C. S., Grossman, E. L., and Morse, J. W. (1992). Carbon isotopic fractionation in synthetic aragonite and calcite: effects of temperature and precipitation rate. *Geochim. Cosmochim. Acta* 56, 419–430. doi: 10.1016/0016-7037(92)90142-6

Ruff, S. W., and Farmer, J. D. (2016). Silica deposits on Mars with features resembling hot spring biosignatures at El Tatio in Chile. *Nat. Commun.* 7:13554. doi: 10.1038/ncomms13554

Salter, S. J., Cox, M. J., Turek, E. M., Calus, S. T., Cookson, W. O., Moffatt, M. F., et al. (2014). Reagent and laboratory contamination can critically impact sequence-based microbiome analyses. *BMC Biol.* 12:87. doi: 10.1186/s12915-014-0087-z

Schloss, P. D., Westcott, S. L., Ryabin, T., Hall, J. R., Hartmann, M., Hollister, E. B., et al. (2009). Introducing mothur: open-source, platform-independent, community-supported software for describing and comparing microbial communities. *Appl. Environ. Microbiol.* 75, 7537–7541. doi: 10.1128/AEM.01541-09

Spear, J. R., and Corsetti, F. A. (2013). "The evolution of geobiology in the context of living stromatolites," in *The Web of Geological Sciences: Advances, Impacts and Interactions*, ed. M. E. Bickford (Boulder, CO: Geological Society of America).

Spear, J. R., Walker, J. J., McCollom, T. M., and Pace, N. R. (2005). Hydrogen and bioenergetics in the Yellowstone geothermal ecosystem. *Proc. Natl. Acad. Sci. U.S.A.* 102, 2555–2560. doi: 10.1073/pnas.0409574102

Squyres, S. W., Arvidson, R. E., Ruff, S., Gellert, R., Morris, R. V., Ming, D. W., et al. (2008). Detection of silica-rich deposits on Mars. *Science* 320, 1063–1067. doi: 10.1126/science.1155429

Steunou, A.-S., Bhaya, D., Bateson, M. M., Melendrez, M. C., Ward, D. M., Brecht, E., et al. (2006). In situ analysis of nitrogen fixation and metabolic switching in unicellular thermophilic cyanobacteria inhabiting hot spring microbial mats. *Proc. Natl. Acad. Sci. U.S.A.* 103, 2398–2403. doi: 10.1073/pnas.0507513103

Tamura, K., and Nei, M. (1993). Estimation of the number of nucleotide substitutions in the control region of mitochondrial DNA in humans and chimpanzees. *Mol. Biol. Evol.* 10, 512–526.

Usdowski, E., Hoefs, J., and Menschel, G. (1979). Relationship between 13C and 18O fractionation and changes in major element composition in a recent calcite-depositing spring—A model of chemical variations with inorganic $CaCO_3$ precipitation. *Earth Planet. Sci. Lett.* 42, 267–276. doi: 10.1016/0012-821X(79)90034-7

Vick, T. J., Dodsworth, J. A., Costa, K. C., Shock, E. L., and Hedlund, B. P. (2010). Microbiology and geochemistry of Little Hot Creek, a hot spring environment in the Long Valley Caldera. *Geobiology* 8, 140–154. doi: 10.1111/j.1472-4669.2009.00228.x

Visscher, P. T., and Stolz, J. F. (2005). Microbial mats as bioreactors: populations, processes, and products. *Palaeogeogr. Palaeoclimatol. Palaeoecol.* 219, 87–100. doi: 10.1016/j.palaeo.2004.10.016

Walker, J. J., Spear, J. R., and Pace, N. R. (2005). Geobiology of a microbial endolithic community in the Yellowstone geothermal environment. *Nature* 434, 1011–1014. doi: 10.1038/nature03447

Walter, M. E. (1976). *Stromatolites. Developments in Sedimentology 20*. Amsterdam: Elsevier, 790.

Walter, M. R., and Des Marais, D. J. (1993). Preservation of biological information in thermal spring deposits: developing a strategy for the search for fossil life on Mars. *Icarus* 101, 129–143. doi: 10.1006/icar.1993.1011

Wang, Q., Garrity, G. M., Tiedje, J. M., and Cole, J. R. (2007). Naive Bayesian classifier for rapid assignment of rRNA sequences into the new bacterial taxonomy. *Appl. Environ. Microbiol.* 73, 5261–5267. doi: 10.1128/AEM.00062-07

Wilke, A., Bischof, J., Harrison, T., Brettin, T., D'Souza, M., Gerlach, W., et al. (2015). A RESTful API for accessing microbial community data for MG-RAST. *PLoS Comput. Biol.* 11:e1004008. doi: 10.1371/journal.pcbi.1004008

Wordsworth, R. (2016). The climate of early Mars. *Annu. Rev. Earth Planet. Sci.* 41, 381–408. doi: 10.1146/annurev-earth-060115-012355

Yilmaz, P., Parfrey, L. W., Yarza, P., Gerken, J., Pruesse, E., Quast, C., et al. (2013). The SILVA and "all-species living tree project (LTP)" taxonomic frameworks. *Nucleic Acids Res.* 42, D643–D648. doi: 10.1093/nar/gkt1209

Zhang, J., Kobert, K., Flouri, T., and Stamatakis, A. (2014). PEAR: a fast and accurate Illumina Paired-End reAd mergeR. *Bioinformatics* 30, 614–620. doi: 10.1093/bioinformatics/btt593

Zhu, T., and Dittrich, M. (2016). Carbonate precipitation through microbial activities in natural environment, and their potential in biotechnology: a review. *Front. Bioeng. Biotechnol.* 4:4. doi: 10.3389/fbioe.2016.00004

Conflict of Interest Statement: The authors declare that the research was conducted in the absence of any commercial or financial relationships that could be construed as a potential conflict of interest.

frontiers in Microbiology

ORIGINAL RESEARCH
published: 13 June 2018
doi: 10.3389/fmicb.2018.01223

Viral Communities of Shark Bay Modern Stromatolites

Richard Allen White III[1,2,3,4,5], *Hon L. Wong*[4,6], *Rendy Ruvindy*[4,6], *Brett A. Neilan*[4,6] and *Brendan P. Burns*[4,6]*

[1] Institute of Biological Chemistry, Washington State University, Pullman, WA, United States, [2] Crop and Soil Sciences, Washington State University, Pullman, WA, United States, [3] Plant Pathology, Washington State University, Pullman, WA, United States, [4] Australian Centre for Astrobiology, University of New South Wales, Sydney, NSW, Australia, [5] RAW Molecular Systems (RMS) LLC, Spokane, WA, United States, [6] School of Biotechnology and Biomolecular Science, University of New South Wales, Sydney, NSW, Australia

Single stranded DNA viruses have been previously shown to populate the oceans on a global scale, and are endemic in microbialites of both marine and freshwater systems. We undertook for the first time direct viral metagenomic shotgun sequencing to explore the diversity of viruses in the modern stromatolites of Shark Bay Australia. The data indicate that Shark Bay marine stromatolites have similar diversity of ssDNA viruses to that of Highbourne Cay, Bahamas. ssDNA viruses in cluster uniquely in Shark Bay and Highbourne Cay, potentially due to enrichment by phi29-mediated amplification bias. Further, pyrosequencing data was assembled from the Shark Bay systems into two putative viral genomes that are related to *Genomoviridae* family of ssDNA viruses. In addition, the cellular fraction was shown to be enriched for antiviral defense genes including CRISPR-Cas, BREX (bacteriophage exclusion), and DISARM (defense island system associated with restriction-modification), a potentially novel finding for these systems. This is the first evidence for viruses in the Shark Bay stromatolites, and these viruses may play key roles in modulating microbial diversity as well as potentially impacting ecosystem function through infection and the recycling of key nutrients.

Keywords: ssDNA viruses, viral defense, CRISPR-Cas, BREX, Shark Bay, stromatolites, viral metagenomics

OPEN ACCESS

Edited by:
Jamie S. Foster,
University of Florida, United States

Reviewed by:
Kenneth Stedman,
Portland State University,
United States
Maureen Coleman,
The University of Chicago,
United States

***Correspondence:**
Brendan P. Burns
Brendan.burns@unsw.edu.au

Specialty section:
This article was submitted to Aquatic Microbiology, a section of the journal Frontiers in Microbiology

Received: *30 November 2017*
Accepted: *22 May 2018*
Published: *13 June 2018*

Citation:
White RA III, Wong HL, Ruvindy R, Neilan BA and Burns BP (2018) Viral Communities of Shark Bay Modern Stromatolites. Front. Microbiol. 9:1223. doi: 10.3389/fmicb.2018.01223

INTRODUCTION

Viruses represent the largest genetic repository and most abundant host-associated replicating entities on the planet (Breitbart and Rohwer, 2005; Suttle, 2005, 2007). Viruses infect all living organisms and viruses have been proposed to influence critical biochemical processes, such as photosynthesis and carbon fixation (Suttle, 2005, 2007; Thompson et al., 2011). Environmental viral metagenomics (i.e., viromics) has revealed that >90% of genes are hypothetical or uncharacterized (Angly et al., 2006), and thus it is likely that new genes will be found amongst viruses. A recent metagenomic study that exhaustively analyzed 3,042 geographically diverse samples revealed extensive global viral diversity, including recovering ∼125,000 partial DNA viral genomes, and yet more than 75% of the viral genes were hypothetical or uncharacterized (Paez-Espino et al., 2016). This indicated that more than two-thirds of all viral protein coding genes have currently no known function. The field of viromics currently has many tools for obtaining genomes and benchmarking (Roux et al., 2017), quantification of dsDNA and ssDNA viruses (Roux et al., 2016), and is truly coming of age (Sullivan et al., 2017). Viruses play a key role in carbon cycling representing >20% of all microbial biomass lysed daily in marine ecosystems

(Suttle, 2007). This massive genetic repository of billions of uncharacterized and hypothetical genes is formidable, however, linking viruses to ecosystems could provide greater understanding of the role of viruses in global processes.

Previous viral metagenomic studies have suggested that linking various viral genotypes to certain environments to establish viral biogeography is challenging. Often the same viral genotype is found in a variety of ecosystems suggesting that viruses have a cosmopolitan distribution (Breitbart and Rohwer, 2005). A viral metagenomic study that contrasted this concept of cosmopolitan viral biogeography suggested that viral ecotypes do exist in nature (Desnues et al., 2008). It was found that single-stranded DNA microphages from Highbourne Cay stromatolites were endemic and these specific viruses were not found among any other cross-examined ecosystem, including marine, freshwater, terrestrial or metazoan-associated systems. However, this is the only study to date that exists for viral communities among modern microbialites (Desnues et al., 2008).

However, the use of multiple-displacement amplification (MDA) using phi29 polymerase has been well documented to bias amplification toward ssDNA viruses over dsDNA viruses (Kim and Bae, 2011). This can make viral biogeography analyses challenging as absolute quantification of viral ecotypes can be difficult due to this amplification bias, however, general diversity is still maintained (Kim and Bae, 2011). Due to strand displacement events, the phi29 polymerase appears to amplify circular DNA more efficiently than linear DNA in diverse nucleic acid pools found in viromes in environmental ecosystems (Kim and Bae, 2011). A recent study found on average that phi29 polymerase amplification bias toward ssDNA viruses was systematically over-represented >10-fold, and that this method on average captured 2–15 times more ssDNA viral genomes (Roux et al., 2016). However, many studies have used this method (phi29 mediated amplification) to selectively enrich and amplify ssDNA viruses and measure diversity in ocean water (Rosario et al., 2009a), reclaimed water (Rosario et al., 2009b), human feces (Reyes et al., 2010), and modern microbialites (Desnues et al., 2008).

Modern stromatolites are analogs to early microbial ecosystems, some dating back 3.5 billion years (Gya) (Dupraz and Visscher, 2005; Van Kranendonk et al., 2008; Dupraz et al., 2009). However, modern marine stromatolites are less extensively distributed compared to the early Earth (Van Kranendonk et al., 2008), with Shark Bay and Highbourne Cay harboring some of the most well-studied examples. Several studies have characterized the extensive microbial diversity in the Shark Bay ecosystem, including novel bacterial, archaeal, and eukaryotic groups (Burns et al., 2004; Goh et al., 2009; Edgecomb et al., 2014; Wong et al., 2015, 2017; Ruvindy et al., 2016; Suosaari et al., 2016). To date no study has delineated the viral contribution to overall biological diversity of the modern stromatolites of Shark Bay, and the aim here was thus to describe the diversity of viruses in Shark Bay stromatolites for the first time. This was achieved by analyzing the purified viral fraction (e.g., free viral particles) and cellular fraction (i.e., lysogenic/prophage or viruses in active infection amongst the cellular fraction) via filtration then direct shotgun sequencing and comparing to similar microbialite viromes prepared in the same manner (e.g., Highbourne Cay, Pozas Azules II and Rios Mesquites).

MATERIALS AND METHODS

Sampling, Viral Metagenomic Library Construction, and Sequencing

Columnar stromatolites were collected and sampled in 2009 from the south-eastern shore of Hamelin Pool, Shark Bay, Western Australia (26°25 S, 114°130 E) as described previously (Burns et al., 2004; Ruvindy et al., 2016). Samples were collected at low tide using a sterile spatula. At the time of sampling, the temperature was recorded as 27.4°C, salinity 68 (Practical Salinity Unit; PSU) and pH 7.9. Samples were placed in sterile specimen containers and stored at 4°C during transportation for ∼30 min. DNA was extracted immediately upon sample return. Viral and cellular fraction metagenomes were purified, amplified with MDA via phi29 polymerase, and sequenced as described (Desnues et al., 2008). Briefly, ∼5 g of Shark Bay stromatolite material was shaken in 30 ml of SM buffer (0.1 M NaCl, 1 mM $MgSO_4$, 0.2 M Tris pH 7.5, 0.01% gelatin within 0.02 μm filtered seawater for 1 h (Desnues et al., 2008). Filtration was used to separate the microbial fraction from the viral fraction using 0.22 μm filters. The Shark Bay cellular fraction (i.e., microbial cellular fraction) was the stromatolite and cellular material collected on the 0.22 μm filter, and the flow through was considered the viral particle fraction. The viral particle fraction was then further purified using cesium chloride density gradient centrifugation (Thurber et al., 2009), and checked for bacterial and eukaryotic cells using SYBR straining and epifluorescence microscopy (Thurber et al., 2009). Both the viral and microbial fraction DNA were isolated using formamide/CTAB extraction (Sambrook et al., 1989), then amplified with phi29-based MDA via GenomiPhi (GE Healthcare) following the manufacturer's recommendations. Subsequently, ∼10 μg DNA was sequenced using 454 pyrosequencing (Margulies et al., 2005).

Quality Control of Sequencing Data and Assembly

The 454-pyrosequencing data (raw SFF files) were converted to FASTQ format and binned by molecular barcode (multiplex identifier). Data were examined for quality using FastQC[1]. Shark Bay metagenome barcodes were removed by Tagcleaner (Schmieder et al., 2010), sequences were trimmed for low quality (>Q_{25}), poly-A/T/N tails, de-duplicated (100% extract match), and ambiguous bases/sequences (>100 bp) and sequences with complexity (>70) on entropy scales removed by PRINSEQ (Schmieder and Edwards, 2011). High quality reads for the Shark Bay Virome (not cellular fraction) were assembled in order to find putative viral genomes and increase contig size using Ray DeNovo Assembler using (Kmer size = 31) (Boisvert et al., 2010, 2012, **Table 1**).

[1]www.bioinformatics.babraham.ac.uk/projects/fastqc/

Annotation and Analysis

High quality reads and viral-assembled contigs were loaded onto MetaVir[2] and updated using MetaVir2 to analyze the Shark Bay Virome and Shark Bay Cellular fraction (Roux et al., 2011, 2014). Basic local alignment search tool (BLAST) based comparison in MetaVir was implemented (*e*-value $\leq 10^{-3}$, 10^{-5}, 10^{-7}) against the NCBI refseq database (updated refseq 2017-01-11), and normalized to genome length using the built-in Genome-relative Abundance and Average Size (GAAS) normalization tool (Angly et al., 2006; Roux et al., 2011). KO EC numbers (directly KEGG mapped), refseq and SEED subsystem annotations, were analyzed by MG-RAST. MG-RAST was used for the main taxonomic and functional annotation (Meyer et al., 2008) of both microbial and viral fractions, and MetaVir2 employed for virome analysis. To search for antiviral gene homologs amongst the viral and cellular fraction, high quality reads were translated to predicted proteins using prodigal (Hyatt et al., 2010), and were annotated against the PFAM/TIGRFAM and KEGG using BLAST, InterProScan 5, and GhostKoala (Jones et al., 2014; Kanehisa et al., 2016).

Principal coordinate analyse (PCA) analysis was undertaken using GAAS outputs from MetaVir2 and R libraries Ecodist (dissimilarity-based functions for ecological analysis), pvclust (hierarchical clustering with *P*-values via Multiscale Bootstrap Resampling), ward clustering, and Bray–Curtis distance metrics at a 1000 replicates against the viromes and microbial fractions for Highboune Cay, Pozas Azules II, Ríos Mesquites microbialites (Desnues et al., 2008).

Phylogenetic Analysis

Marker gene identification was completed using reference trees provided by MetaVir2 for major capsid protein for *Microviridae* (VP1), auxiliary metabolic gene (AMG) phoH which is widespread in phage genomes but whose function remains unknown (Goldsmith et al., 2011), and replication-associated protein (Rep) found in ssDNA viruses.

Of the VP1 contigs, those with sequence length lower than 160 were deleted. Reference viral replication proteins

[2]http://metavir-meb.univ-bpclermont.fr/

TABLE 1 | Metagenomic statistics including read analysis, assembly stats, and annotations for MetaVir2 and MG-RAST.

Reads	Viral fraction	Cellular fraction	Assembly	Viral fraction
Raw data			**Contigs >100 bp**	
Number	92298	73371	Number	504
Total length (bp)	39623558	31023655	Total length (bp)	149063
Average (bp)	429	423	Average (bp)	295
GC%	48%	44%	N50 (bp)	353
			Median (bp)	172
After QC data			Largest (bp)	4099
Number	62294	59805	**Contigs >500 bp**	
Artificial duplicate reads	23699	8842	Number	49
Total length (bp)	28413896	26636206	Total length (bp)	57537
Average (bp)	456	445	Average (bp)	1174
GC%	47%	44%	N50 (bp)	1473
			Median (bp)	924
MG-RAST predictions			Largest (bp)	4099
Predicted protein features	39127	50281		
Predicted rRNA features	3321	3746		**Cellular fraction**
Identified protein features	2452	23704	**Contigs >100 bp**	
Identified rRNA features	0	64	Number	N/A
Identified functional categories	2033	21025	Total length (bp)	N/A
Failed QC (duplicates/length)	30,004 (32.51%)	13,566 (18.49%)	Average (bp)	N/A
Unknown	1,000 (1.08%)	197 (0.27%)	N50 (bp)	N/A
Predicted feature	61,294 (66.41%)	59,608 (81.24%)	Median (bp)	N/A
Unknown protein	30,514 (49.78%)	20,191 (33.87%)	Largest (bp)	N/A
Annotated protein	30,780 (50.22%)	38,473 (64.54%)	**Contigs >500 bp**	
Ribosomal RNA	0 (0.00%)	944 (1.58%)	Number	N/A
			Total length (bp)	N/A
MetaVir2 predictions*			Average (bp)	N/A
50 on score	6.55%	10.62%	N50 (bp)	N/A
E-value (10^{-3}) + GAAS	9.04%	15.50%	Median (bp)	N/A
E-value (10^{-5}) + GAAS	7.42%	12.57%	Largest (bp)	N/A
E-value (10^{-7}) + GAAS	6.53%	10.54%		

**Represents a significant viral hit. GAAS is genome length normalization.*

(phoH, VP1, Rep) and proteins obtained from the Shark Bay virome (viral fraction) were aligned using MUSCLE (Edgar, 2004), and alignment gaps were removed with UGENE[3] (Okonechnikov et al., 2012). Maximum likelihood phylogenetic trees were constructed using IQ-TREE v. 1.6.1 with a total of 1000 bootstrap replicates, and visualized with iTOL (Letunic and Bork, 2016; Hoang et al., 2017).

[3]http://ugene.net/

Data Availability

The assembled data Shark Bay virome and microbial fraction have been deposited in MetaVir and are available under project names "Shark Bay Virome" and "Shark Bay Microbes," and additionally in MG-RAST as "Shark Bay Virome," and "Shark Bay Microbes." All codes and scripts can be found on github.com/raw937. Both pre-assembled and assembled reads have been deposited in the Sequence Read Archive (SRA) under accession numbers SRR7160500 and SRZ187061, and BioProject

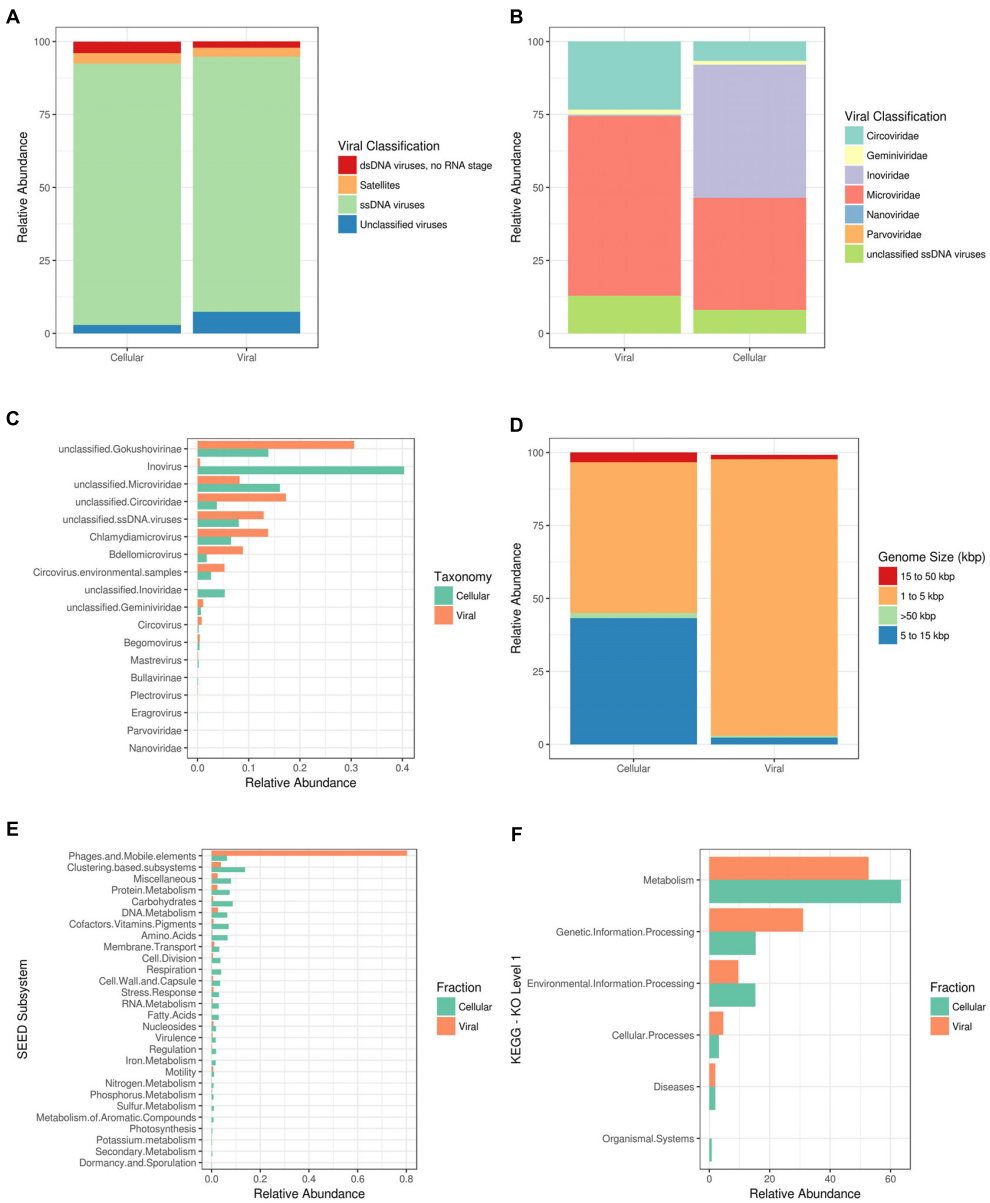

FIGURE 1 | Shark Bay viral and cellular fraction comparison. MG-RAST Functional annotations using KEGG (KO) and SEED where based on BLAT based comparison (*e*-value $\leq 10^{-5}$) against respective database. **(A)** Viral taxonomic classification characterization by nucleic acid state in MetaVir2. **(B)** Viral taxonomic classification characterization by viral family in MetaVir2. **(C)** Viral taxonomic classification characterization by viral genus in MetaVir2 by cellular or viral fraction metagenome. **(D)** GAAS predictive viral genome size estimations in MetaVir2. **(E)** SEED subsystem functional annotations in MG-RAST. **(F)** KEGG (KO) level 1 functional annotations in MG-RAST. MetaVir2 viral (BLAST) based comparison (*e*-value $\leq 10^{-5}$) against NCBI viral refseq database and normalized to genome length using the built-in Genome-relative Abundance and Average Size (GAAS) normalization tool (Angly et al., 2006).

identifier "Viral communities of Shark Bay modern stromatolites" (PRJNA471212).

RESULTS AND DISCUSSION

General Properties of the Shark Bay Stromatolite Cellular and Viral Fraction Metagenomes

DNA sequences for viral and cellular fractions from Shark Bay stromatolites were determined for viral homology and taxonomy using MetaVir2, and MG-RAST for functional annotation. Both the cellular and viral fraction have >50,000 sequences of ∼400 bp, with between 26 and 28 Mbp total sequence length (**Table 1**). The viral fraction contained 50% annotated proteins with another 50% unknown proteins with no rRNA sequences, whereas the microbial fraction contained 64% annotated proteins with 33% unknown and 1.5% rRNAs based on MG-RAST (**Table 1**). The lack of rRNA in the viral fraction, negative PCR results for bacterial 16S rDNA, and epifluorescence microscopy indicating no cells after filtration and CsCl gradient, suggests a relatively pure viral fraction. MetaVir2 predicted viral sequences based on BLAST to refseq (2017-01-11) found that regardless of the *e*-value (10^{-3}, 10^{-5}, 10^{-7} with GAAS normalization) that >5% have a significant viral hit to known viruses within the database, whereas the cellular fraction had >10% for significant viral hits (**Table 1**). An *e*-value of 10^{-5} with GAAS normalization was chosen for all further taxonomic and viral genome size estimation using MetaVir2, and an *e*-value of 10^{-5} for MG-RAST functional annotation for its conservative value while providing the most significant hits to known databases. Assembly was completed on the viral fraction only in an attempt to find circular ssDNA putative genomes and longer contigs (**Table 1**). Ray assembly of the Shark Bay viral fraction yielded few contigs (49 at >500 bp, 500 at >100 bp) suggesting sparse sampling of the available ssDNA viruses found at Shark Bay (**Table 1**).

Shark Bay Stromatolite Virome and ssDNA Virus Diversity

ssDNA viruses were the most abundant amongst the viral sequences due to the enrichment of phi29-based MDA of the Shark Bay stromatolite viral fraction (i.e., free viral particles). It is important to note that few sequences within the Shark Bay virome had representative annotated hits to known viral genomes, and downstream analyses described are based on known annotated viral genomes present within MetaVir2. More than 85% of reads relating to viruses in the viral and cellular fraction from Shark Bay were ssDNA viruses (*e*-value $\leq 10^{-5}$ with GAAS normalization) (**Figure 1A**). *Microviridae* represented >50% of annotated ssDNA virus sequences within the viral fraction and >30% in the cellular fraction (**Figure 1B**). The cellular fraction had ∼40% *Inoviridae* sequences whereas the viral fraction had <1% (**Figure 1B**). The *Inoviridae* sequences were ∼35% inovirus in the cellular fraction with some unclassified members (**Figure 1C**). *Microviridae* in Shark Bay are likely directly infecting hosts, as *Microviridae* are rarely lysogenic with the exception of the proviruses that infect *Bacteroidetes* (Krupovic and Forterre, 2011). *Microviridae* as a group are more often found to be lytic than lysogenic, and thus the higher presence of *Microviridae* annotated sequences in the cellular fraction in the present study could potentially be active infection (Szekely and Breitbart, 2016). Chlamydiamicroviruses composed 12% of the *Microviridae* sequences amongst the Shark Bay virome (**Figure 1C**), and these were dominated by subfamily Gokushovirinae at 27% (**Figure 1C**). The gokushoviruses have been shown to be widespread in many marine ecosystems (Hopkins et al., 2014). Amongst the Chlamydiamicroviruses sequences within the

TABLE 2 | KEGG ontology (KO) EC numbers for the Shark Bay virome annotations reads.

EC description	EC number	Abundance
DNA (cytosine-5-)-methyltransferase	2.1.1.37	36
Ribonucleoside-diphosphate reductase	1.17.4.1	11
DNA helicase	3.6.4.12	8
GDP-mannose 4,6-dehydratase	4.2.1.47	5
Riboflavin kinase	2.7.1.26 2.7.7.2	5
Methyltransferases	2.1.1.-	4
Carbon-oxygen lyases/Hydro-lyases	4.2.1.-	3
Spermidine dehydrogenase	1.5.99.6	3
DNA-directed DNA polymerase	2.7.7.7	2
Nicotinamidase	3.5.1.19 3.5.1.-	2
Ribonucleoside-triphosphate reductase	1.17.4.2	2
Nucleotidyltransferases	2.7.7.-	2
Thymidylate synthase	2.1.1.148	2
Sarcosine oxidase	1.5.3.1	2
Leucyl aminopeptidase	3.4.11.1	2
Xanthine dehydrogenase	1.17.1.4	1
Aspartate carbamoyltransferase	2.1.3.2	1
Deoxyuridine-triphosphatase	3.6.1.23	1
Histidine permease	3.6.3.21	1
Amidophosphoribosyltransferase	2.4.2.14	1
Indolepyruvate decarboxylase	4.1.1.74	1
NAD+ synthase (glutamine-hydrolysing)	6.3.5.1	1
Allantoicase	3.5.3.4	1
Peptidyl-dipeptidase A	3.4.15.1	1
Dihydrofolate reductase	1.5.1.3 2.1.1.45	1
GDP-L-fucose synthase	1.1.1.271	1
DNA-directed RNA polymerase	2.7.7.6	1
UDP-*N*-acetylglucosamine-1-carboxyvinyltransferase	2.5.1.7	1
Tryptophan synthase	4.2.1.20	1
3-oxoacyl-[acyl-carrier-protein] reductase	1.1.1.100	1
Oxidoreductases with NAD+ or NADP+ as acceptors	1.1.1.-	1
Protoporphyrinogen oxidase	1.3.3.4	1

MG-RAST cut-offs were at 1e-5 e-value, min% identity of 60%, and minimum alignment length of 50 bp.

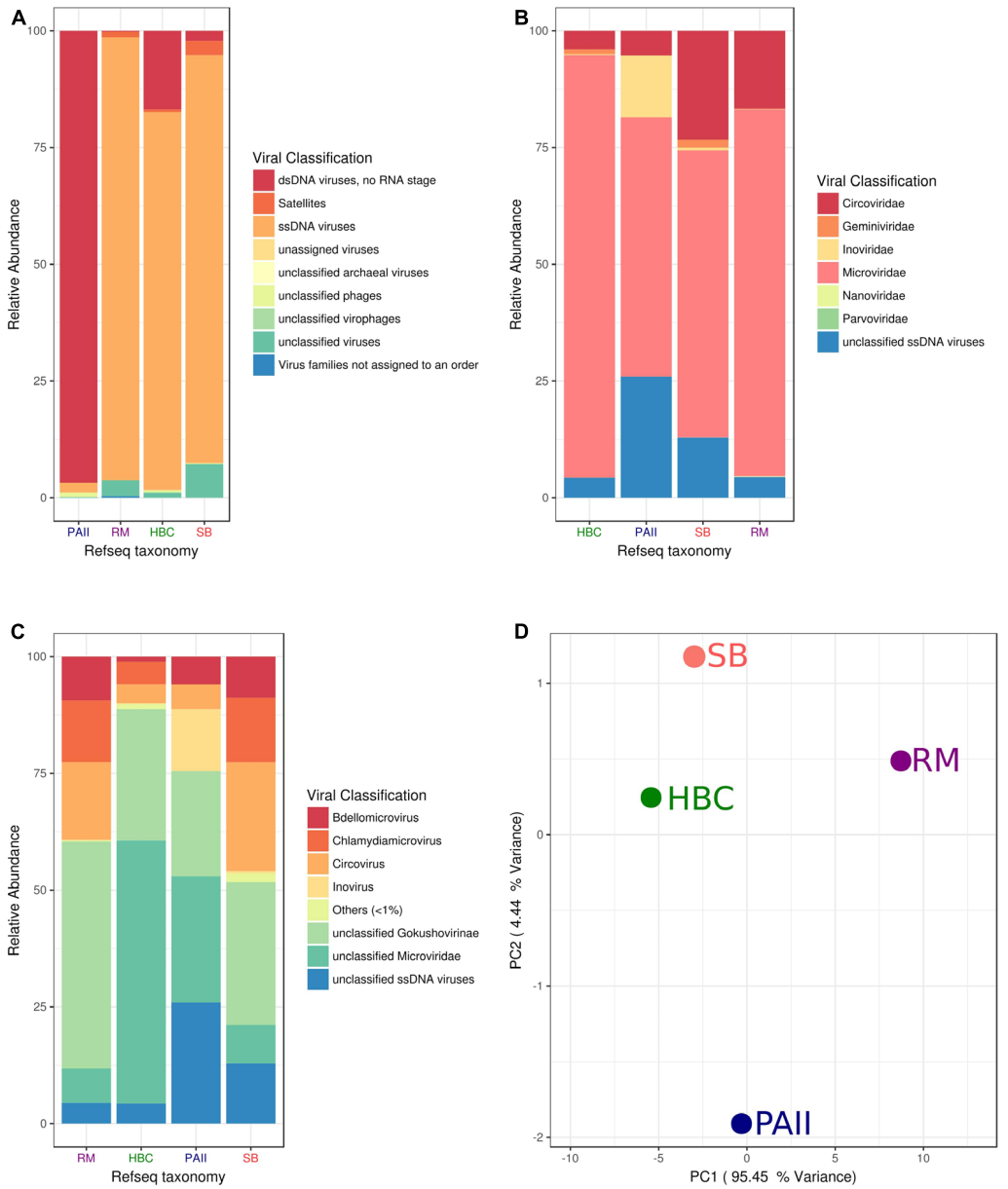

FIGURE 2 | Viral fraction comparison Shark Bay against Highbourne Cay, Rios Mesquites and Pozas Azules II microbialite sites. **(A)** Viral taxonomic classification characterization by nucleic acid state in MetaVir2. **(B)** Viral taxonomic classification characterization by viral family in MetaVir2. **(C)** Viral taxonomic classification characterization by viral genus in MetaVir2. **(D)** Principal coordinate analyses (PCA) comparing the viral diversity in disparate stromatolite locations. PCA were constructed from similarity matrices utilizing protein coding sequence recruitment using NCBI viral refseq database (refseq update 2017-1-11) and normalized to genome length using the built-in GAAS. Proportion variance (PC) was explained by each component printed next to the PC1/PC2 axes labels. MetaVir2 viral (BLAST) based comparison (*e*-value $\leq 10^{-5}$) against NCBI viral refseq database and normalized to genome length using the built-in Genome-relative Abundance and Average Size (GAAS) normalization tool (Angly et al., 2006). MG-RAST Functional annotations using KEGG (KO) and SEED where based on BLAT based comparison (*e*-value $\leq 10^{-5}$) against respective database. SB, Shark Bay; HBC, Highbourne Cay; PAII, Pozas Azule II; RM, Rio Mesquites.

Shark Bay virome, some sequences were most similar to chlamydia phage 3 and 4-like sequences (Supplementary Table 1). Bdellomicrovirus sequences also comprised ∼8% of the Shark Bay *Microviridae* sequences, and this virus is known to infect the bacterium *Bdellovibrio*.

Genome-relative abundance and average size normalization allowed for general prediction of the relative viral genome size for both cellular and viral fraction using MetaVir2 with large differences between the two fractions. Greater than 90% of the predicted genome sizes within the viral fraction were 1–5 kbp (**Figure 1D**). In contrast ∼50% was represented in the predictive genome size of 1–5 kbp (**Figure 1D**) in the cellular fraction. The other ∼40% were predicted to be viral genomes of 5–15 kbp (**Figure 1D**). The likely reason for this selectively lower viral

TABLE 3 | BLAST results against NCBI against long contigs and putative viral genomes in the Shark Bay viral fraction.

	Gene	Max score	Total score	Query cover %	*E*-value	Ident %	Accession
contig-7000012_1784							
Uncultured virus	Viral replication-associated protein (Rep)	172	172	56.00	1.00E-44	34.00	AUM61732.1
Uncultured virus	Viral replication-associated protein (Rep)	171	171	57.00	4.00E-43	33.00	AUM62051.1
Sewage-associated circular DNA virus-30	Viral replication-associated protein (Rep)	166	166	52.00	2.00E-41	32.00	YP_009117070.1
contig-1000003_2028							
Sewage-associated circular DNA virus-18	Viral replication-associated protein (Rep)	170	170	50.00	2.00E-43	31.00	YP_009116898.1
Uncultured virus	Viral replication-associated protein (Rep)	169	169	47.00	1.00E-42	33.00	AUM61781.1
Uncultured virus	Viral replication-associated protein (Rep)	164	164	49.00	2.00E-41	34.00	AUM61982.1
Contig-1000009_1678							
Ralstonia picketti	Hypothetical protein	636	636	55.00	0	99.00	WP_024972784.1
Cellulophaga phage phi47:1	Hypothetical protein CDPG_00080	629	629	54.00	0	99.00	AGF91683.1
Cellulophaga phage phi47:1	Hypothetical protein CDPG_00081	276	276	27.00	3.00E-87	100.00	AGF91684.1
contig-1000007_1202							
Pseudanabaena sp. 'Roaring Creek	Hypothetical protein	45.8	45.8	13.00	0.019	45.00	WP_055077263.1
Synechococcus sp. PCC 7502	Hypothetical protein	42	42	11.00	0.093	50.00	WP_015169903.1
Oscillatoriales cyanobacterium USR001	Hypothetical protein BCD67_24715	39.3	39.3	15.00	2.1	31.00	OCQ97517.1
Nocardia transvalensis	Patatin	41.2	41.2	22.00	3.7	34.00	WP_040746262.1
contig-4_4099							
Uncultured prokaryote	Hypothetical protein	48.1	48.1	11.00	0.037	27.00	CRY97485.1
Uncultured prokaryote	Hypothetical protein	41.6	41.6	3.00	5.3	46.00	CRY96835.1
Actinoplanes subtropicus	Recombinase family protein	42.7	42.7	4.00	6.7	39.00	WP_084599775.1
contig-2000010_3827							
Uncultured prokaryote	Hypothetical protein	75.9	75.9	11.00	6.00E-11	34.00	CRY96346.1
Azospirillum sp. 51_20	Hypothetical protein	72.4	72.4	4.00	2.00E-09	57.00	OLA80278.1
Sphingopyxis terrae	Hypothetical protein	69.7	69.7	4.00	7.00E-09	52.00	WP_082813420.1
contig-1000002_2208							
Tateyamaria omphalii	DNA ligase-associated DEXH box helicase	42.4	42.4	18.00	4.5	29.00	WP_076628122.1
Streptomyces	MULTISPECIES: serine/threonine protein kinase	42	42	19.00	7.1	28.00	WP_103536509.1
Contig-9_1603							
No hits							
Contig-8_1554							
No hits							
Contig-7_1473							
No hits							

genome is due to the phi29-mediated amplification, and future work is needed to amplify the majority of viral nucleic acids without dsDNA or ssDNA biases.

The top functional genes present and SEED subsystems for Shark Bay viral fraction included >80% in related to phages, prophages, transposable elements, and/or plasmids (**Figure 1E**). KEGG KO level 1 annotation for both viral and cellular fraction suggested metabolism >40% represented most functional calls by KEGG (**Figure 1F**). KEGG EC included phage viral structural genes (e.g., capsids, tails, **Table 2**) and DNA metabolism related genes (e.g., DNA 5-cytosine methylase, ribonucleoside-diphosphate reductase, and DNA helicase, **Table 2**). These functional genes potentially facilitate key processes in the Shark Bay stromatolite host communities, including viral attachment, protection of viral genetic material, and viral replication (Hofer, 2016).

Surprisingly, no haloarchaeal viruses were identified here, although haloarchaea are prominent in the Shark Bay microbialite systems (Burns et al., 2004; Allen et al., 2009; Wong et al., 2017), and have been hypothesized to 'fill the niche' as potentially major players in nutrient cycles. Despite the lack of haloarchaeal viruses/phage amongst our data, there were unclassified sequences from assembled contigs ∼25% or ∼1.08% unassembled reads (**Table 1**) with no hits to public databases, and haloarchaeal viral genes could putatively be amongst these. In addition, two of the putative viral contigs which contain only replication protein genes could be associated with haloarchaea.

Comparison Between Shark Bay Virome and Microbial Fraction With Other Microbialite Ecosystems

Shark Bay viral and cellular fraction metagenomes were compared to previously reported microbialite ecosystems (Highbourne Cay, Pozas Azules II, and Rios Mesquites). *Microviridae* sequence dominance within the Highbourne Cay viromes has been previously noted (Desnues et al., 2008), and the Shark Bay viromes were very similar in viral taxonomic composition (**Figure 2A**). Highbourne Cay, Rios Mesquites and Shark Bay viromes had >80% of sequences as ssDNA viruses

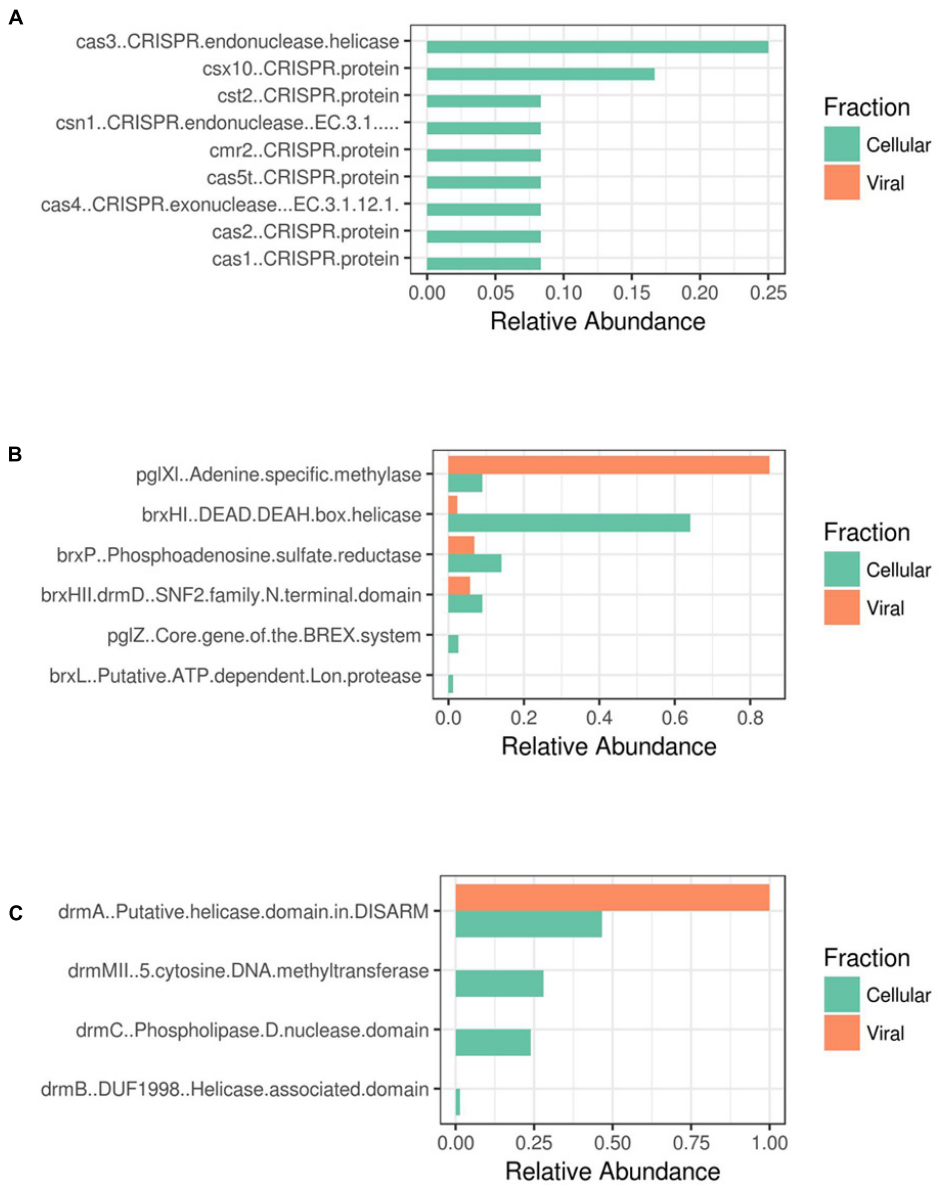

FIGURE 3 | Antiviral resistance genes amongst Shark Bay viral and cellular fraction. **(A)** CRISPR-Cas associated genes **(B)** BREX associated genes **(C)** DISARM associated genes. The relative abundance is the number of hits from GhostKoala and the Pfam database using InterProScan 5.

(**Figure 2A**), which may be attributed to phi29-mediated bias. Of those ssDNA sequences, Highbourne Cay, Rios Mesquites and Shark Bay >50% were of *Microviridae*-like sequences, with Shark Bay virome having >20% of circoviridae origin (**Figure 2B**). Pozas Azules II had >90% as dsDNA virus sequences (Desnues et al., 2008). Data here was normalized to 100% for ssDNA virus sequences for Pozas Azules II to compare ssDNA viruses across all four sites, with Pozas Azules II possessing >50% *Microviridae*-like sequences after normalization comprising the bulk of the ssDNA sequences in that ecosystem. There were some compositional differences between Shark Bay and Highbourne Cay viromes, as Shark Bay had >25% of the sequences with similarity to *Chlamydia* phage 3 and 4 (represented as Chlamydiamicrovirus), whereas Highbourne Cay had >20% of the sequences with similarity to unclassified *Microviridae* (**Figure 2C**). Shark Bay ssDNA virus sequences were highly similar and clustered with Highbourne Cay viromes (**Figure 2D**). The presence of the high levels of ssDNA sequences explained the majority of principal coordinate clustering observed (**Figure 2D**).

Long Viral Contigs and Putative Viral Genomes in Shark Bay Stromatolites

Two of the contigs obtained from the Shark Bay viral fraction (the largest contigs) have no BLAST hits to any reference sequence in NCBI databases. SB contig-2000010_3827 (3827 bp) and contig-4_4099 (4099 bp) have low *E*-values ($\sim 1 \times 10^3$) to hypothetical proteins or recombinases (**Table 3**). Two of the contigs (7000012_1784 and 1000003_2028) are putative viral genomes as they are circular and have homologs to replication protein (e.g., *Rep*), and related to Sewage-associated circular DNA virus-30 and Sewage-associated circular DNA virus-18 respectively (**Table 3**). Both of these viruses, Sewage-associated circular DNA virus-30 and Sewage-associated circular DNA virus-18,

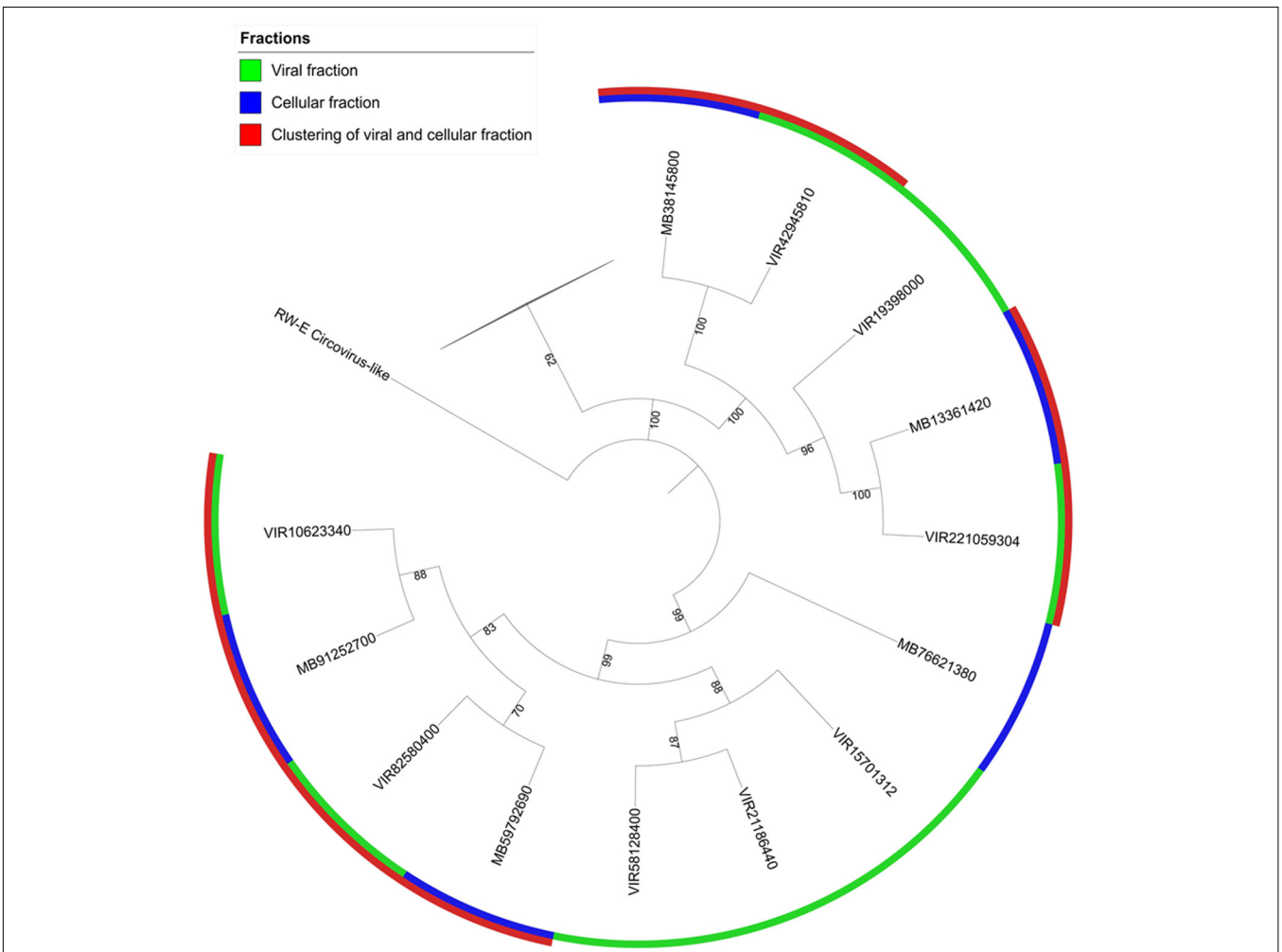

FIGURE 4 | Phylogenetic analysis of microbial and viral fractions from Shark Bay stromatolites for the Replication-associated protein (Rep) in CRESS viruses. Maximum likelihood phylogenetic tree of *Rep* protein sequences found in CRESS viruses in Shark Bay stromatolites. Protein sequence alignments were performed using MUSCLE and gaps in alignment were removed with UGENE. The tree was constructed with IQ-TREE v. 1.6.1 with 1000 bootstrap replicates and was visualized with iTOL. Number indicates bootstrap values, nodes with bootstrap values lower than 70 were not shown and represented by the collapsed branch. The collapsed branches in this figure represent reference sequences from Rosario et al. (2009a) for the replication (rep) protein that have lower than 70 bootstrap values.

are novel circular replication-associated protein encoding single-stranded (CRESS) DNA viral genomes (Kraberger et al., 2015). These viruses are classified now as novel *Genomoviridae* within CRESS family (Krupovic et al., 2016), whereas the hosts of these viruses are unknown most members infect eukaryotes associated with infecting plants and animals not bacteria. These viruses could be introduced to microbialite systems by seabirds endemic to an area (Desnues et al., 2008), a scenario that could also potentially be occurring in Shark Bay.

Environmental Relevance of ssDNA Viruses in Shark Bay

Eukaryotic grazers represent a potential destabilizing factor by grazing nutrient rich stromatolites, including Shark Bay

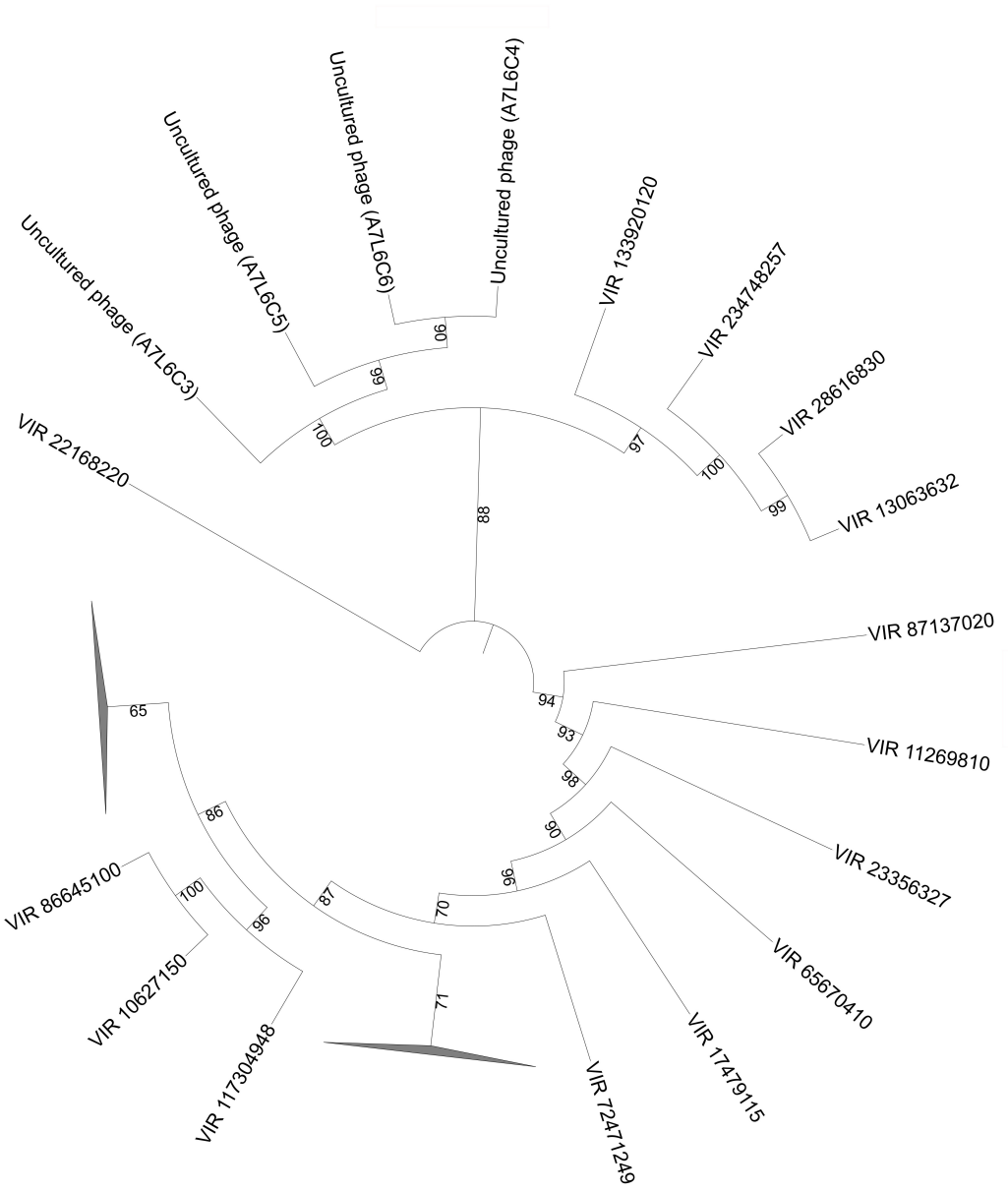

FIGURE 5 | Phylogenetic analysis of viral fractions from Shark Bay stromatolites for the major capsid protein (VP1) in *Microviridae* viruses. Maximum likelihood phylogenetic tree of VP1 protein sequences obtained from *Microviridae* viruses in Shark Bay stromatolites. Reference sequences were retrieved from the Uniprot database. Short sequences (<160 amino acid) were removed prior to alignment. Alignments were performed using MUSCLE and gaps in alignment were removed with UGENE. The tree was constructed with IQ-TREE v. 1.6.1 with 1000 bootstrap replicates and was visualized with iTOL. Number indicates bootstrap values, nodes with bootstrap values lower than 70 were not shown and represented by the collapsed branch. The collapsed branches in this figure represent reference sequences from Desnues et al. (2008) for major capsid protein (VP1) that have lower than 70 bootstrap values.

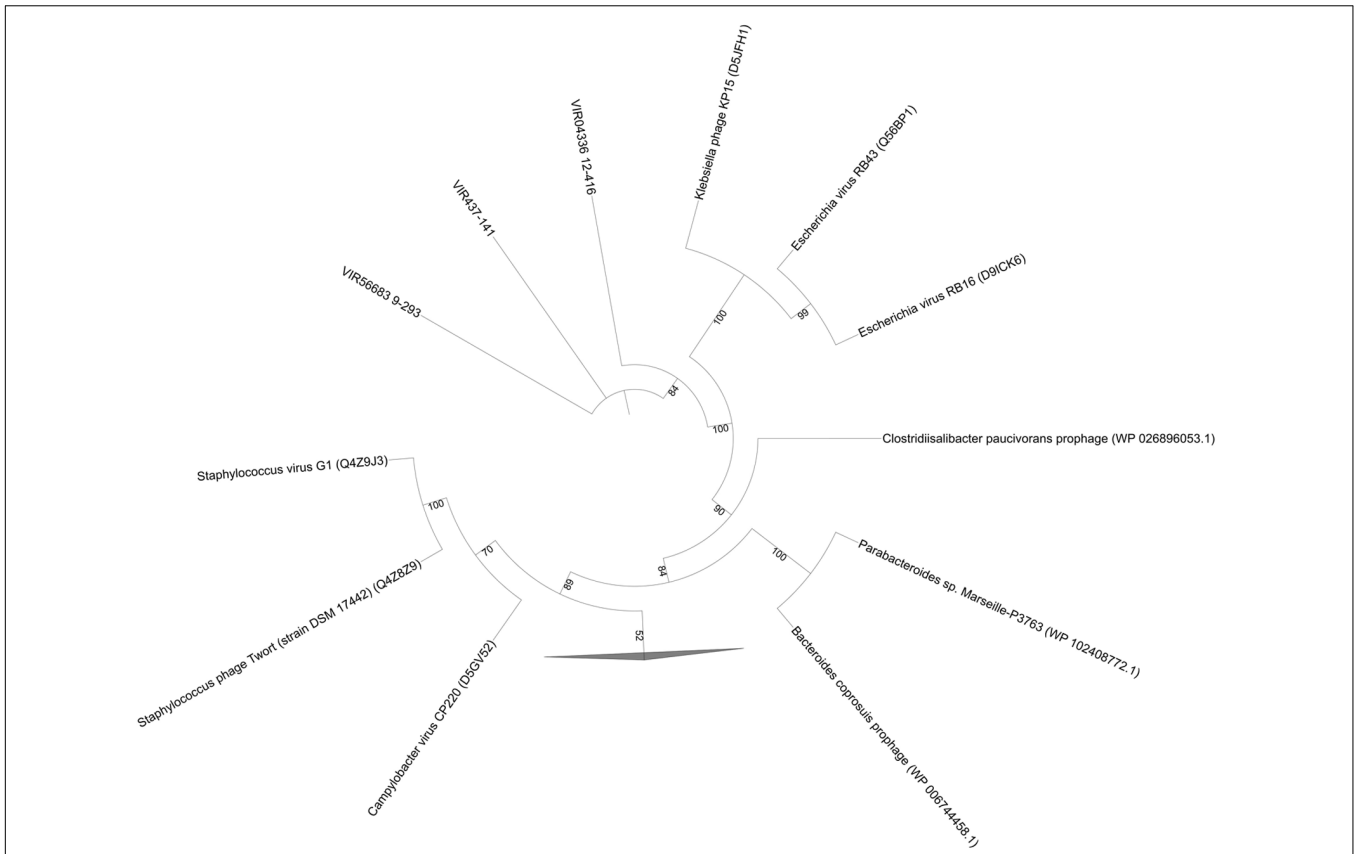

FIGURE 6 | Phylogenetic analysis of viral fractions from Shark Bay stromatolites for phoH (of the pho regulon) in dsDNA viruses. Maximum-likelihood tree of phoH protein sequences obtained from dsDNA viruses. Reference sequences were retrieved from Uniprot database. Alignments were performed using MUSCLE and gaps in alignment were removed with UGENE. The tree was constructed with IQ-TREE v. 1.6.1 with 1000 bootstrap replicates and was visualized with iTOL. Number indicates bootstrap values, nodes with bootstrap values lower than 70 were not shown and represented by the collapsed branch. The collapsed branches in this figure represent reference sequences from Goldsmith et al. (2011) for the phosphate starvation inducible protein (phoH) that have lower than 70 bootstrap values.

TABLE 4 | BLAST results against NCBI for phoH sequences in the Shark Bay viral fraction.

phoH sequences	Gene name	Species	Max score	Total score	Query cover %	*E*-value	Ident %	Accession
Sequence VIR56683 9-293	PhoH family protein	*Parabacteroides* sp. Marseille-P3763	110	110	96.00	1.00E-26	56.00	WP_102408772.1
	PhoH family protein	*Bacteroides coprosuis*	110	110	96.00	2.00E-26	58.00	WP_006744458.1
	PhoH family protein	*Defluviitoga tunisiensis*	110	110	97.00	2.00E-26	50.00	WP_045087935.1
Sequence VIR437-141	hypothetical protein D478_16524	*Brevibacillus agri* BAB-2500	112	112	98.00	3.00E-30	56.00	ELK40902.1
	PhoH family protein	*Clostridiisalibacter paucivorans*	119	119	98.00	1.00E-29	60.00	WP_026896053.1
	ATPase	*Bacillus boroniphilus* JCM 21738	107	107	98.00	3.00E-28	54.00	GAE45877.1
Sequence VIR04336 12-416	PhoH family protein	*Moorella thermoacetica*	148	148	98.00	3.00E-40	52.00	WP_075517747.1
	PhoH family protein	*Clostridiisalibacter paucivorans*	147	147	100.00	1.00E-39	52.00	WP_026896053.1
	PhoH family protein	*Alteribacillus iranensis*	145	145	99.00	3.00E-39	50.00	WP_091657652.1

stromatolites (Farmer, 1992; Edgecomb et al., 2014). Marine geminiviruses and circoviruses infect a wide range of eukaryotic organisms, including protists, marine arthropods, and other grazers (Rosario et al., 2009a; Saccardo et al., 2011). We hypothesize that the marine viruses identified in the present study may infect eukaryotic grazers, with the viruses acting act

as a top–down control. Viral mediated lysis of eukaryotic grazers may help stabilize the stromatolite ecosystems in Shark Bay, that could otherwise be disrupted by excessive grazing. While the aforementioned viruses are obligate eukaryotic-associated, the Shark Bay virome contains viruses similar to those also capable of infecting bacteria, such as the *Bdellomicroviruses* (**Figure 2**). Future studies are needed in eukaryotic circular Rep-encoding ssDNA (CRESS) viruses within Shark Bay stromatolites and other environments, to measure the rates of viral mediated lysis of eukaryotes amongst phytoplankton and zooplankton, as such top–down control could have global impacts of nutrient cycling in the ocean. Single cell techniques may elucidate such viral-host (e.g., protist-viral) interactions (Gavelis et al., 2015). Recent studies employing iTag deep amplicon sequencing of bacterial communities in Shark Bay microbialites indeed identified *Bdellovibrio* as one of the prominent community members (Wong et al., 2015). Thus, the potential for infection by this group of viruses with known microbialite hosts in Shark Bay is present, and future work will help clarify the extent of this process in these ecosystems.

Microbial Viral Defense Mechanisms in Shark Bay Stromatolites

Furthermore, metagenomic analysis of Shark Bay stromatolites has revealed putative viral defense mechanisms present. Evidence of CRISPR-Cas, BREX (bacteriophage exclusion), and DISARM (defense island system associated with restriction-modification) (Goldfarb et al., 2015; Ofir et al., 2018) in both the viral and cellular fraction metagenomes from Shark Bay were found in the present study (**Figure 3**). The genetic basis of one such mechanism, CRISPR (clustered, regularly interspaced, short palindromic repeat systems), was also identified in the Shark Bay microbial metagenomes (Ruvindy et al., 2016). When compared to the viral fraction, an enrichment of CRISPR-Cas genes was observed in the cellular fraction with none in the viral fraction (**Figure 3A**). BREX genes are also more abundant in the cellular fraction than the viral fraction (**Figure 3B**), with the viral fraction having an abundance of Adenine-specific methylase that may putatively be used against host methylation of viral DNA (**Figure 3B**). DISARM genes were also enriched in the cellular vs. viral fraction (**Figure 3C**), including the primary helicases. This is the first evidence of DISARM and BREX in metagenomes enriched in cellular fractions associated with stromatolites. CRISPR systems have been identified as an adaptive microbial immune system that provides acquired immunity against viruses (Horvath and Barrangou, 2010), and thus there may be an interplay between the viral populations identified in the present study and the defense mechanisms characterized in host Shark Bay populations.

A recent study of freshwater microbialites in Pavilion Lake, BC suggested that T4-like phage (e.g., *Myoviridae*) and large algal viruses (e.g., Phycodnaviridae) dominated the viral sequences in the water compared to microbialites, whereas the microbialites possessed genes related to viral defense (e.g., CRISPR, phage shock and phage excision) (White et al., 2016a). Future metagenomic sequencing efforts in Shark Bay should target in detail the two novel viral defense systems of BREX and DISARM, to help complete our understanding of the viral load in the modern microbialites of Shark Bay.

Phylogenetics of Shark Bay Stromatolite Viral Fraction

Circovirus-like viruses were also detected in Shark Bay viromes (**Figure 2C**), which are thought to associate with and potentially infect eukaryotic grazers, such as insects, snails, and other marine arthropods (Rosario et al., 2009a). Closely related Rep-encoding sequences were found in both the cell and viral fractions, indicative of the potential active infection amongst bacterial cells (**Figure 4**). Phylogenetic tree constructed indicates there are four pairs of contigs from microbial fraction and viral fraction that clustered together (**Figure 4**). These viruses in the viral fraction were found amongst the microbialite itself suggesting potential active infection by ssDNA could be occurring in Shark Bay stromatolites. Eukaryotic grazers can feed on cyanobacterial mats that are the basal unit of stromatolite formation, stability and construction, and thus the presence of viruses that infect and inhibit these grazers could be a top–down control and maintenance of the stromatolite ecosystem in Shark Bay.

Viral capsid protein gene (VP1) for microphages (i.e., *Microviridae*) was first described in stromatolites from Highbourne Cay, Rios Mesquites, and Pozas Azules II (Desnues et al., 2008). In the present study, the VP1 sequences obtained in the Shark Bay viral fraction have expanded the quantity of known VP1 sequences (**Figure 5**), and BLAST results also indicate that the branches are derived from uncultured phages. The potential hosts for these VP1-like sequences are likely bacterial hosts over eukaryotes due to their homology to uncultured phages.

As mentioned above, PhoH is a viral AMG with unknown function. Phosphorus limitation has been reported in previous studies in Shark Bay (Smith and Atkinson, 1984; Atkinson, 1987; Wong et al., 2015), as well as in freshwater microbialites (White et al., 2015, 2016a,b). The pho regulon as well as a high abundance of alkaline phosphatases were found amongst the columnar stromatolite (microbial fraction) analyzed here (**Figure 6**), as well as in a previous study (Ruvindy et al., 2016). This regulon has also been identified in soda lake microbialites of Mexico (Valdespino-Castillo et al., 2014). After further BLAST analysis of the phoH sequences in the present study, it was confirmed by manual examination of the reference genomes that they are viral phoH sequences from prophage in these bacterial genomes (**Table 4** and **Figure 6**). Inducible prophages are often found in marine systems that infect large groups of bacteria including marine aerobic anoxygenic phototrophic bacteria (AAPB) (Zheng et al., 2014). These prophage appeared to be integrated into the genomes of *Clostridiisalibacter paucivorans* and *Bacteroides coprosuis* DSM18011 (**Table 4** and **Figure 6**). Other reference genomes in public databases are in draft form and annotations were unclear and unreliable, as the phoH accessions resided in regions of unknown or hypothetical proteins. While phoH has been found to be a core gene in T4-like phages, its function within ecosystems remains to be elucidated (Roux et al., 2015). However, we acknowledge that

further investigation is warranted, and a more complete virome is needed for Shark Bay microbialites in order to ascertain whether phoH genes and complete pho regulons regulate phosphate uptake under low-phosphate conditions within Shark Bay.

Potential Role of Viruses in Shark Bay

Viruses are also well known as major players in marine nutrient cycling (Suttle, 2007), and they may also play such a role in Shark Bay systems. All viruses including ssDNA, dsDNA, and RNA viruses, are agents of cellular lysis due to infection and death. We hypothesize that the ssDNA viruses found in Shark Bay may be putative drivers of nutrient cycling mediated through eukaryotic and bacterial cell lysis, which releases dissolved nutrients (e.g., C, P, N, S) to be utilized by other microbial community members as has been shown elsewhere (Bratbak et al., 1992; Gobler et al., 1997; Scanlan and Wilson, 1999; Jover et al., 2014). Viruses in Shark Bay are also likely to replenish dissolved organic carbon (DOC) upon cell lysis, thus also playing a role in the carbon cycle (Bratbak et al., 1992). However, further work is needed to delineate the exact role of viruses in biogeochemical cycling in these communities.

CONCLUSION

Data from the present study document for the first-time viral diversity amongst Shark Bay stromatolites. Although complete viral diversity remains to be captured due to potential phi29 polymerase MDA bias toward ssDNA viruses, the virome (i.e., viral fraction) revealed significant ssDNA viral diversity. Future work is needed on the viruses in microbialites and stromatolites of Shark Bay, potentially employing a long-read technology such as PacBio, Oxford Nanopore or Illumina Moleculo (White et al., 2016a), which could result in longer contigs, improved assemblies, and novel viral genomes. Microbialites and stromatolites provide modern models to ancient early complex ecosystems, and the data presented here is of significant value to our understanding of some of the first complex microbial ecosystems on Early Earth. Future work employing deeper sequencing and targeting other viruses will help further our understanding of viral diversity in these ecosystems in addition to the ssDNA viruses described here, and determine their exact contribution to functional complexity in Shark Bay.

AUTHOR CONTRIBUTIONS

RAW conducted the data analysis, assemblies, and wrote the manuscript sections. HW and RR conducted the data analysis, phylogenetic analysis, and contributed to manuscript sections. BN and BB coordinated and designed the research, and wrote manuscript sections. All the authors read and approved the manuscript.

FUNDING

This work was funded by the Australian Research Council.

ACKNOWLEDGMENTS

The authors would like to acknowledge the support of Forest Rohwer and Mya Breitbart in helping establish this project and facilitating sequencing.

SUPPLEMENTARY MATERIAL

The Supplementary Material for this article can be found online at: https://www.frontiersin.org/articles/10.3389/fmicb.2018.01223/full#supplementary-material

REFERENCES

Allen, M. A., Goh, F., Burns, B. P., and Neilan, B. A. (2009). Bacterial, archaeal and eukaryotic diversity of smooth and pustular microbial mat communities in the hypersaline lagoon of Shark Bay. *Geobiology* 7, 82–96. doi: 10.1111/j.1472-4669.2008.00187.x

Angly, F. E., Felts, B., Breitbart, M., Salamon, P., Edwards, R. A., Carlson, C., et al. (2006). The marine viromes of four oceanic regions. *PLoS Biol.* 4:e368. doi: 10.1371/journal.pbio.0040368

Atkinson, M. (1987). Low phosphorus sediments in a hypersaline marine bay. *Estuar. Coast. Shelf Sci.* 24, 335–347. doi: 10.1016/0272-7714(87)90054-0

Boisvert, S., Laviolette, F., and Corbeil, J. (2010). Ray: simultaneous assembly of reads from a mix of high-throughput sequencing technologies. *J. Comput. Biol.* 17, 1519–1533. doi: 10.1089/cmb.2009.0238

Boisvert, S., Raymond, F., Godzaridis, E., Laviolette, F., and Corbeil, J. (2012). Ray Meta: scalable de novo metagenome assembly and profiling. *Genome. Biol.* 13:R122. doi: 10.1186/gb-2012-13-12-r122

Bratbak, G., Heldal, M., Thingstad, T. F., Riemann, B., and Haslund, O. H. (1992). Incorporation of viruses into the budget of microbial C-transfer: a first approach. *Mar. Ecol. Prog. Ser.* 83, 273–280. doi: 10.3354/meps083273

Breitbart, M., and Rohwer, F. (2005). Here a virus, there a virus, everywhere the same virus? *Trends. Microbiol.* 6, 278–284. doi: 10.1016/j.tim.2005.04.003

Burns, B. P., Goh, F., Allen, M., and Neilan, B. A. (2004). Microbial diversity of extant stromatolites in the hypersaline marine environment of Shark Bay, Australia. *Environ. Microbiol.* 6, 1096–1101. doi: 10.1111/j.1462-2920.2004.00651.x

Desnues, C., Rodriguez-Brito, B., Rayhawk, S., Kelley, S., Tran, T., Haynes, M., et al. (2008). Biodiversity and biogeography of phages in modern stromatolites and thrombolites. *Nature* 452, 340–343. doi: 10.1038/nature06735

Dupraz, C., Reid, R. P., Braissant, O., Decho, A. W., Norman, R. S., and Visscher, P. T. (2009). Processes of carbonate precipitation in modern microbial mats. *Earth Sci. Rev.* 96, 141–162. doi: 10.1016/j.earscirev.2008.10.005

Dupraz, C., and Visscher, P. T. (2005). Microbial lithification in marine stromatolites and hypersaline mats. *Trends Microbiol.* 13, 429–438. doi: 10.1016/j.tim.2005.07.008

Edgar, R. C. (2004). MUSCLE: multiple sequence alignment with high accuracy and high throughput. *Nucleic Acids Res.* 32, 1792–1797. doi: 10.1093/nar/gkh340

Edgecomb, V. P., Bernhard, J. M., Summons, R. E., Orsi, W., Beaudoin, D., and Visscher, P. T. (2014). Active eukaryotes in microbialites from Highbourne Cay, Bahamas, and Hamelin Pool (Shark Bay), Australia. *ISME J.* 8, 418–429. doi: 10.1038/ismej.2013.130

Farmer, J. D. (1992). "Grazing and bioturbation in modern microbial mats," in *The Proterozoic Biosphere – A multidisciplinary Study*, eds J. W. Schopf and C. Klein, (New York, NY: Cambridge University Press), 295–297.

Gavelis, G. S., White, R. A. III, Suttle, C. A., Keeling, P. J., and Leander, B. S. (2015). Single-cell transcriptomics using spliced leader PCR: evidence for multiple losses of photosynthesis in polykrikoid dinoflagellates. *BMC Genomics* 16:528. doi: 10.1186/s12864-015-1636-8

Gobler, C. J., Hutchins, D. A., Fisher, N. S., Cosper, E. M., and Saňudo-Wilhelmy, S. (1997). Release and bioavailability of C, N, P, Se, and Fe following viral lysis of a marine Chrysophyte. *Limnol. Oceanogr.* 42, 1492–1504. doi: 10.4319/lo.1997.42.7.1492

Goh, F., Allen, M. A., Leuko, S., Kawaguchi, T., Decho, A. W., Burns, B. P. et al. (2009). Determining the specific microbial populations and their spatial distribution within the stromatolite ecosystem of Shark Bay. *ISME J.* 4, 383–396. doi: 10.1038/ismej.2008.114

Goldfarb, T., Sberro, H., Weinstock, E., Cohen, O., Doron, S., Charpak-Amikam, Y., et al. (2015). BREX is a novel phage resistance system widespread in microbial genomes. *EMBO J.* 34, 169–183. doi: 10.15252/embj.201489455

Goldsmith, D. B., Crosti, G., Dwivedi, B., McDaniel, L. D., Varsani, A., Suttle, C. A., et al. (2011). Development of *phoH* as a novel signature gene for assessing marine phage diversity. *Appl. Environ. Microbiol.* 77, 7730–7739. doi: 10.1128/AEM.05531-11

Hoang, D. T., Chernomor, O., von Haeseler, A., Minh, B. Q., and Vinh L. S. (2017). UFBoot2: improving the ultrafast bootstrap approximation. *Mol. Biol. Evol.* 35, 518–522. doi: 10.1093/molbev/msx281

Hofer, U. (2016). Viral Pathogenesis: Tracing the steps of Zika virus. *Nat. Rev. Microbiol.* 14:401. doi: 10.1038/nrmicro.2016.80

Hopkins, M., Kailasan, S., Cohen, A., Roux, S., Tucker, K. P., Shevenell, A., et al. (2014). Diversity of environmental single-stranded DNA phages revealed by PCR amplification of the partial major capsid protein. *ISME J.* 8, 2093–2103. doi: 10.1038/ismej.2014.43

Horvath, P., and Barrangou, R. (2010). CRISPR/Cas, the immune system of bacteria and archaea. *Science* 327, 167–170. doi: 10.1126/science.1179555

Hyatt, D., Chen, G. L., Locascio, P. F., Land, M. L., Larimer, F. W., and Hauser, L. J. (2010). Prodigal: prokaryotic gene recognition and translation initiation site identification. *BMC Bioinformatics* 11:119. doi: 10.1186/1471-2105-11-119

Jones, P., Binns, D., Chang, H. Y., Fraser, M., Li, W., McAnulla, C., et al. (2014). InterProScan 5: genome-scale protein function classification. *Bioinformatics* 30, 1236–1240. doi: 10.1093/bioinformatics/btu031

Jover, L. F., Effler, T. C., Buchan, A., Wilhelm, S. W., and Weitz, J. S. (2014). The elemental composition of virus particles: implications for marine biogeochemical cycles. *Nat. Rev. Microbiol.* 12, 519–528. doi: 10.1038/nrmicro3289

Kanehisa, M., Sato, Y., and Morishima, K. (2016). BlastKOALA and GhostKOALA: KEGG tools for functional characterization of genome and metagenome sequences. *J. Mol. Biol.* 428, 726–731. doi: 10.1016/j.jmb.2015.11.006

Kim, K. H., and Bae, J. W. (2011). Amplification methods bias metagenomic libraries of uncultured single-stranded and double-stranded DNA viruses. *Appl. Environ. Microbiol.* 77, 7663–7668. doi: 10.1128/AEM.00289-11

Kraberger, S., Argüello-Astorga, G. R., Greenfield, L. G., Galilee, C., Law, D., Martin, D. P., et al. (2015). Characterisation of a diverse range of circular replication-associated protein encoding DNA viruses recovered from a sewage treatment oxidation pond. *Infect. Genet. Evol.* 31, 73–86. doi: 10.1016/j.meegid.2015.01.001

Krupovic, M., and Forterre, P. (2011). *Microviridae* goes temperate: microvirus-related proviruses reside in the genomes of *Bacteroidetes*. *PLoS One* 6:e19893. doi: 10.1371/journal.pone.0019893

Krupovic, M., Ghabrial, S. A., Jiang, D., and Varsani, A. (2016). Genomoviridae: a new family of widespread single-stranded DNA viruses. *Arch. Virol.* 161, 2633–2643. doi: 10.1007/s00705-016-2943-3

Letunic, I., and Bork, P. (2016). Interactive tree of life (iTOL) V3: an online tool for the display and annotation of phylogenetic and other trees. *Nucleic Acids Res.* 44, W242–W245. doi: 10.1093/nar/gkw290

Margulies, M., Egholm, M., Altman, W. E., Attiya, S., Bader, J., BembeN, L. A., et al. (2005). Genome sequencing in microfabricated high-density picolitre reactors. *Nature* 437, 376–380. doi: 10.1038/nature03959

Meyer, F. D., Paarmann, M., D'Souza, R., Olson, E. M., Glass, M., Kubal, T., et al. (2008). The metagenomics RAST server - A public resource for the automatic phylogenetic and functional analysis of metagenomes. *BMC Bioinform.* 9:386. doi: 10.1186/1471-2105-9-386

Ofir, G., Melamed, S., Sberro, H., Mukamel, Z., Silverman, S., Yaakov, G., et al. (2018). DISARM is a widespread bacterial defence system with broad anti-phage activities. *Nat. Microbiol.* 3, 90–98. doi: 10.1038/s41564-017-0051-0

Okonechnikov, K., Golosova, O., Fursov, M., and Ugene team (2012). Unipro UGENE: a unified bioinformatics toolkit. *Bioinformatics* 28, 1166–1167. doi: 10.1093/bioinformatics/bts091

Paez-Espino, D., Eloe-Fadrosh, E. A., Pavlopoulos, G. A., Thomas, A. D., Huntermann, M., Mikhailova, N., et al. (2016). Uncovering Earth's virome. *Nature* 536, 425–430. doi: 10.1038/nature19094

Reyes, A., Haynes, M., Hanson, N., Angly, F. E., Heath, A. C., Rohwer, F., et al. (2010). Viruses in the faecal microbiota of monozygotic twins and their mothers. *Nature* 466, 334–338. doi: 10.1038/nature09199

Rosario, K., Duffy, S., and Breitbart, M. (2009a). Diverse circovirus-like genome architectures revealed by environmental metagenomics. *J. Gen. Virol.* 90, 2418–2424. doi: 10.1099/vir.0.012955-0

Rosario, K., Nilsson, C., Lim, Y. W., Ruan, Y., and Breibart, M. (2009b). Metagenomic analysis of viruses in reclaimed water. *Environ. Microbiol.* 11, 2806–2820. doi: 10.1111/j.1462-2920.2009.01964.x

Roux, S., Emerson, J. B., Eloe-Fadrosh, E. A., and Sullivan, M. B. (2017). Benchmarking viromics: an *in silico* evaluation of metagenome-enabled estimates of viral community composition and diversity. *Peer J.* 5:e3817. doi: 10.7717/peerj.3817

Roux, S., Enault, F., Ravet, V., Pereira, O., and Sullivan, M. B. (2015). Genomic characteristics and environmental distributions of the uncultivated Far-T4 phages. *Front. Microbiol.* 6:199. doi: 10.3389/fmicb.2015.00199

Roux, S., Faubladier, M., Mahul, A., Paulhe, N., Bernard, A., Debroas, D., et al. (2011). Metavir: a web server dedicated to virome analysis. *Bioinformatics* 27, 3074–3075. doi: 10.1093/bioinformatics/btr519

Roux, S., Solonenko, N. E., Dang, V. T., Poulos, B. T., Schwenck, S. M., Goldsmith, D. B., et al. (2016). Towards quantitative viromics for both double-stranded and single-stranded DNA viruses. *Peer J.* 4:e2777. doi: 10.7717/peerj.2777

Roux, S., Tournayre, J., Mahul, A., Debroas, D., and Enault, F. (2014). Metavir 2: new tools for viral metagenome comparison and assembled virome analysis. *BMC Bioinform.* 15:76. doi: 10.1186/1471-2105-15-76

Ruvindy, R., White, R. A. III, Neilan, B. A., and Burns, B. P. (2016). Unravelling core microbial metabolisms in the hypersaline microbialites of Shark Bay using high-throughput metagenomics. *ISME. J.* 10, 183–196. doi: 10.1038/ismej.2015.87

Saccardo, F., Cettul, E., Palmano, S., Noris, E., and Firrao, G. (2011). On the alleged origin of geminiviruses from extrachromosomal DNAs of phytoplasmas. *BMC Evol. Biol.* 11:185. doi: 10.1186/1471-2148-11-185

Sambrook, J., Fritsch, E. F., and Maniatis, T. (1989). *Molecular Cloning*, 2nd Edn, Vol. 1. Cold Spring Harbor, NY: Cold Spring Harbor Laboratory Press.

Scanlan, D. J., and Wilson, W. H. (1999). Application of molecular techniques to addressing the role of P as a key effector in marine ecosystems. *Hydrobiologia* 401, 149–175. doi: 10.1007/978-94-011-4201-4_12

Schmieder, R., and Edwards, R. (2011). Quality control and preprocessing of metagenomic datasets. *Bioinformatics* 27, 863–864. doi: 10.1093/bioinformatics/btr026

Schmieder, R., Lim, W. Y., Rohwer, R., and Edwards, R. (2010). TagCleaner: identification and removal of tag sequences from genomic and metagenomic datasets. *BMC Bioinformat.* 11:341. doi: 10.1186/1471-2105-11-341

Smith, S. V., and Atkinson, M. J. (1984). Phosphorus limitation of net production in a confined aquatic ecosystem. *Nature* 307, 626–627. doi: 10.1038/307626a0

Sullivan, M. B., Weitz, J. S., and Wilhelm, S. (2017). Viral ecology comes of age. *Environ. Microbiol. Rep.* 9, 33–35. doi: 10.1111/1758-2229.12504

Suosaari, E. P., Reid, R. P., Playford, P., Foster, J. S., Stolz, J. F., Casaburi, G., et al. (2016). New multi-scale perspectives on the stromatolites of Shark Bay. Western Australia. *Sci. Rep.* 6:20557. doi: 10.1038/srep20557

Suttle, C. A. (2005). Viruses in the sea. *Nature* 437, 356–361. doi: 10.1038/nature04160

Suttle, C. A. (2007). Marine viruses - major players in the global ecosystem. *Nat. Rev. Microbiol.* 5, 801–812. doi: 10.1038/nrmicro1750

Szekely, A. J., and Breitbart, M. (2016). Single-stranded DNA phages: from early molecular biology tools to recent revolutions in environmental microbiology. *FEMS Microbiol. Lett.* 363:fnw027. doi: 10.1093/femsle/fnw027

Thompson, L. R., Zeng, Q., Kelly, L., Huang, K. H., Singer, A. U., Stubbe, J., et al. (2011). Phage auxiliary metabolic genes and the redirection of cyanobacterial host carbon metabolism. *Proc. Natl. Acad. Sci. U.S.A.* 108, E757–E764. doi: 10.1073/pnas.1102164108

Thurber, R. V., Haynes, M., Breitbart, M., Wegley, L., and Rohwer, F. (2009). Laboratory procedures to generate viral metagenomes. *Nat. Protoc.* 4, 470–483. doi: 10.1038/nprot.2009.10

Valdespino-Castillo, P. M., Alcántara-Hernández, R. J., Alcocer, J., Merino-Ibarra, M., Macek, M., and Falcón, L. I. (2014). Alkaline phosphatases in microbialites and bacterioplankton from Alchichica soda lake, Mexico. *FEMS Microbiol. Ecol.* 90, 504–519. doi: 10.1111/1574-6941.12411

Van Kranendonk, M. J., Philippot, P., Lepot, K., Bodrokos, S., and Piranjno, F. (2008). Geological setting of Earth's oldest fossils in the ca. 3.5 GA Dresser formation, Pilbara Craton, Western Australia. *Precambrian Res.* 167, 93–124. doi: 10.1016/j.precamres.2008.07.003

White, R. A. III, Bottos, E. M., Roy-Chowdhury, T., Zucker, J. D., Brislawn, C. J., Nicora, C. D., et al. (2016a). Moleculo long-read sequencing facilitates assembly and genomic binning from complex soil metagenomes. *mSystems* 1, e00045-16. doi: 10.1128/mSystems.00045-16

White, R. A. III, Chan, A. M., Gavelis, G. S., Leander, B. S., Brady, A. L., Slater, G. F., et al. (2016b). Metagenomic analysis suggests modern freshwater microbialites harbour a distinct core microbial community. *Front. Microbiol.* 6:1531. doi: 10.3389/fmicb.2015.01531

White, R. A. III, Power, I. M., Dipple, G. M., Southam, G., and Suttle, C. A. (2015). Metagenomic analysis reveals that modern microbialites and polar microbial mats have similar taxonomic and functional potential. *Front. Microbiol.* 6:966. doi: 10.3389/fmicb.2015.00966

Wong, H. L., Smith, D. L., Visscher, P. T., and Burns, B. P. (2015). Niche differentiation of bacterial communities at a millimeter scale in Shark Bay microbial mats. *Sci. Rep.* 5:15607. doi: 10.1038/srep15607

Wong, H. L., Visscher, P. T., White, R. A. III, Smith, D.-L., Patterson, M., and Burns, B. P. (2017). Dynamics of archaea at fine spatial scales in Shark Bay mat microbiomes. *Sci. Rep.* 7:46160. doi: 10.1038/srep46160

Zheng, Q., Zhang, R., Xu, Y., White, R. A. III., Wang, Y., Luo, T., et al. (2014). A marine inducible prophage vB_CibM-P1 isolated from the aerobic anoxygenic phototrophic bacterium citromicrobium bathyomarinum JL354. *Sci. Rep.* 4:7118. doi: 10.1038/srep07118

Conflict of Interest Statement: The authors declare that the research was conducted in the absence of any commercial or financial relationships that could be construed as a potential conflict of interest.

frontiers in Microbiology

ORIGINAL RESEARCH
published: 25 June 2018
doi: 10.3389/fmicb.2018.01359

Comparative Metagenomics Provides Insight Into the Ecosystem Functioning of the Shark Bay Stromatolites, Western Australia

*Joany Babilonia[1], Ana Conesa[2,3], Giorgio Casaburi[1], Cecile Pereira[2,4], Artemis S. Louyakis[1], R. Pamela Reid[5] and Jamie S. Foster[1]**

[1] Space Life Science Lab, Department of Microbiology and Cell Science, University of Florida, Gainesville, FL, United States, [2] Department of Microbiology and Cell Science, Genetics Institute, Institute for Food and Agricultural Sciences, University of Florida, Gainesville, FL, United States, [3] Genomics of Gene Expression Laboratory, Prince Felipe Research Center, Valencia, Spain, [4] EURA NOVA, Marseille, France, [5] Rosenstiel School of Marine and Atmospheric Science, University of Miami, Miami, FL, United States

OPEN ACCESS

Edited by:
Dennis A. Bazylinski, University of Nevada, Las Vegas, United States

Reviewed by:
Virginia Helena Albarracín, Center for Electron Microscopy (CIME), Argentina
Brendan Paul Burns, University of New South Wales, Australia

***Correspondence:**
Jamie S. Foster
jfoster@ufl.edu

Specialty section:
This article was submitted to Aquatic Microbiology, a section of the journal Frontiers in Microbiology

Received: *07 January 2018*
Accepted: *05 June 2018*
Published: *25 June 2018*

Citation:
Babilonia J, Conesa A, Casaburi G, Pereira C, Louyakis AS, Reid RP and Foster JS (2018) Comparative Metagenomics Provides Insight Into the Ecosystem Functioning of the Shark Bay Stromatolites, Western Australia. Front. Microbiol. 9:1359. doi: 10.3389/fmicb.2018.01359

Stromatolites are organosedimentary build-ups that have formed as a result of the sediment trapping, binding and precipitating activities of microbes. Today, extant systems provide an ideal platform for understanding the structure, composition, and interactions between stromatolite-forming microbial communities and their respective environments. In this study, we compared the metagenomes of three prevalent stromatolite-forming microbial mat types in the Spaven Province of Hamelin Pool, Shark Bay located in Western Australia. These stromatolite-forming mat types included an intertidal pustular mat as well as a smooth and colloform mat types located in the subtidal zone. Additionally, the metagenomes of an adjacent, non-lithifying mat located in the upper intertidal zone were also sequenced for comparative purposes. Taxonomic and functional gene analyses revealed distinctive differences between the lithifying and non-lithifying mat types, which strongly correlated with water depth. Three distinct populations emerged including the upper intertidal non-lithifying mats, the intertidal pustular mats associated with unlaminated carbonate build-ups, and the subtidal colloform and smooth mat types associated with laminated structures. Functional analysis of metagenomes revealed that amongst stromatolite-forming mats there was an enrichment of photosynthesis pathways in the pustular stromatolite-forming mats. In the colloform and smooth stromatolite-forming mats, however, there was an increase in the abundance of genes associated with those heterotrophic metabolisms typically associated with carbonate mineralization, such as sulfate reduction. The comparative metagenomic analyses suggest that stromatolites of Hamelin Pool may form by two distinctive processes that are highly dependent on water depth. These results provide key insight into the potential adaptive strategies and synergistic interactions between microbes and their environments that may lead to stromatolite formation and accretion.

Keywords: stromatolite, microbial mat, comparative metagenomics, Hamelin Pool, Shark Bay

INTRODUCTION

Stromatolites are one of the most prevalent and recognizable components of the fossil record, dating back more than 3.7 Ga years (Grotzinger and Knoll, 1999; Nutman et al., 2016). These lithified, organosedimentary structures are a type of microbialite, formed by the sediment trapping, binding and/or carbonate precipitating activities of microorganisms in response to their local environment (Awramik et al., 1976; Burne and Moore, 1987). Stromatolites are distinguished from other microbialites by the presence of laminated microstructures, which are formed through iterative successions of sedimentation, microbial mat growth, and lithification (Reid et al., 2000; Dupraz and Visscher, 2005; Pace et al., 2018). These long-lived microbialite ecosystems have had a profound impact on the habitability of the planet, as they are attributed to changing the global redox conditions via oxygenic photosynthesis (Des Marais, 1991; Lyons et al., 2014). These properties make contemporary microbialites ideal model systems for investigating carbon cycling and the underlying processes associated with the precipitation and dissolution of calcium carbonate (Riding, 2000; Dupraz and Visscher, 2005; Dupraz et al., 2009).

Modern microbialite ecosystems are widespread and are found in a diverse range of environments including, but not limited to, lacustrine ecosystems (e.g., Cuatro Ciénegas, Mexico; Lake Alchichica, Mexico; Pavilion and Kelly Lake, British Columbia) (Osborne et al., 1982; Ferris et al., 1997; Laval et al., 2000; Souza et al., 2006; Couradeau et al., 2011; Theisen et al., 2015; Chagas et al., 2016; White et al., 2016), freshwater systems (e.g., Deer Cave and Giblin River; Lundberg and McFarlane, 2011; Proemse et al., 2017); geothermal springs (e.g., Yellowstone National Park, WY, United States) (Inskeep et al., 2004; Pepe-Ranney et al., 2012), open marine environments (e.g., Exuma Sound, The Bahamas) (Dravis, 1983; Dill et al., 1986; Reid et al., 2000; Khodadad and Foster, 2012), and hypersaline waters (e.g., Kiritimati Atoll, Great Salt Lake) (Burns et al., 2004; Schneider et al., 2013; Ruvindy et al., 2016; Suosaari et al., 2016a; Lindsay et al., 2017).

Of the many extant examples of living, accreting microbialites, the largest, most extensive marine stromatolite-forming ecosystem is within the hypersaline embayment of Hamelin Pool, Shark Bay, Western Australia, a UNESCO world heritage site (**Figure 1A**; Playford, 1990; Reid et al., 2003; Suosaari et al., 2016a,b). Since their discovery in the 1950's, the stromatolites of Hamelin Pool have served as important models to understand the formation of both modern and ancient stromatolite systems (Logan et al., 1974; Playford and Cockbain, 1976; Walter, 1976; Reid et al., 2003). Based on these pioneering studies, the stromatolite-forming microbial mats of Hamelin Pool are morphologically characterized into three canonical types: (1) 'colloform' mats, which form structures with moderately laminated carbonate fabrics; (2) 'smooth' mats, which are associated with highly laminated structures; and (3) 'pustular' stromatolite-forming mats, which exhibit no internal lamination (Logan et al., 1974; Playford and Cockbain, 1976). Historically, all carbonate build-ups within Hamelin pool have been referred to as 'stromatolites' regardless of the degree of lamination (Logan et al., 1974; Awramik et al., 1976; Playford, 1990; Jahnert and Collins, 2012; Suosaari et al., 2016a).

Each of these distinctive stromatolite-forming mat types is found in different tidal zones within the pool (Playford and Cockbain, 1976; Jahnert and Collins, 2011; Suosaari et al., 2016b). The colloform stromatolite mats are the most seaward, located in the subtidal zone and can be found in depths up to four meters, whereas the pustular stromatolite-forming mats are the most shoreward in the intertidal zone (**Figure 1B**). In addition to these three prevalent stromatolite-forming mat communities, there are non-lithifying microbial mats in the upper intertidal zone including a smooth mat type and a pustular mat type (Wong et al., 2015; Suosaari et al., 2016b). These non-lithifying mats do not develop carbonate build-ups, but rather form extensive sheets, or fields of mats, along the coastline (Suosaari et al., 2016a).

The locations of the dominant stromatolite-forming mat types and morphological variations of stromatolites within Hamelin Pool have been extensively surveyed (Jahnert and Collins, 2013; Suosaari et al., 2016a,b). A recent mapping effort revealed eight geographical zones, or "Provinces," each with distinctive and differentiated stromatolite macrostructures (**Figure 1A**; Suosaari et al., 2016a,b). One of the largest zones is Spaven Province, located along the western edge of the pool, spanning more than 20 km. The Spaven Province is distinguished by elongated and nested stromatolites, with the direction of the elongation being perpendicular from the shore (Suosaari et al., 2016b). All three of the canonical stromatolite-forming mat types, as well as the non-lithifying mats, are present within the Spaven Province; however, no in-depth metagenomic analyses have been completed for stromatolite-forming mats in this portion of Hamelin Pool.

Over the past decade, several studies have begun to characterize the microbial diversity associated with the stromatolite-forming and non-lithifying mats within the southern region of Hamelin Pool by targeting the SSU rRNA gene (Burns et al., 2004; Papineau et al., 2005; Goh et al., 2009; Wong et al., 2015, 2017; Suosaari et al., 2016a). These studies indicate that microbial populations within the different mat types are distinctive, with minimal heterogeneity (Wong et al., 2015; Suosaari et al., 2016a). More recently, metagenomic sequencing was used to compare the non-stromatolite forming smooth and pustular mats, with an intertidal, columnar stromatolite build-up from the Nilemah province (Ruvindy et al., 2016). These results indicated that the stromatolite-forming communities exhibit a metabolic potential that is distinct from that of non-lithifying smooth and pustular mats.

In this study, we build on this previous work by comparing the metagenomes of the three main lithifying stromatolite-forming mats (i.e., colloform, smooth, and pustular) to assess whether there are distinctive metagenomic signatures for each type. We also examine the non-lithifying pustular sheet-forming mat in the upper intertidal zone, as a control, to ascertain whether there are significant differences between the lithifying and non-lithifying mats within the Spaven Province. By employing a comparative metagenomic approach, the metabolic potential for each of the dominant mat types can be identified,

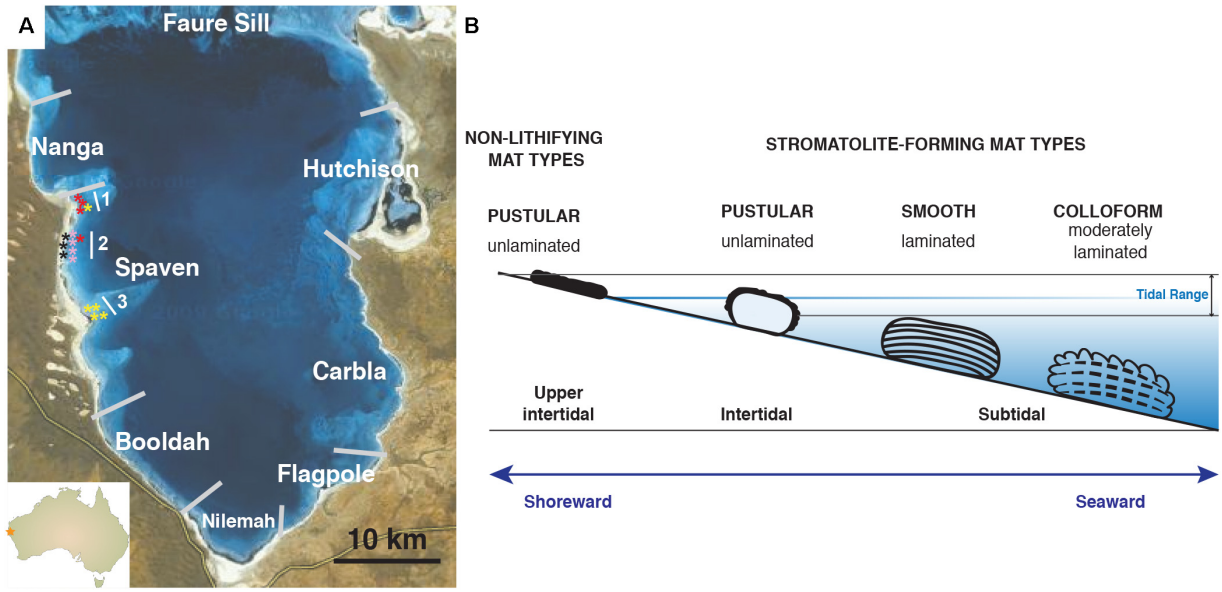

FIGURE 1 | Overview of Hamelin Pool collection site and locations of stromatolite-forming and non-lithifying mat types within the pool. **(A)** Map of Provinces located within Hamelin Pool, Shark Bay. The stars reflect the collection sites of the colloform (yellow), smooth (red), pustular (pink), and non-lithifying mats (black) within the Spaven Province. The numbers 1, 2, 3 reflect transects associated with the collection of the mat types. **(B)** Cartoon depicting the position within the pool of the distinct microbial structures targeted in this study. Bar = 10 km.

thereby advancing our understanding of microbes and processes associated with stromatolite formation and accretion within Hamelin Pool.

MATERIALS AND METHODS

Sample Collection

Stromatolite-forming and non-lithifying mats were collected from the Spaven Province of Hamelin Pool, Shark Bay, Western Australia in April 2014. Although the various mat types are found throughout Hamelin Pool, relative abundance at specific locations is variable. Replicate stromatolite heads collected for this study spanned approximately 10 km within the Spaven Province (**Table 1** and **Figure 1A**). Samples from each replicate head and non-lithifying sheet mats were collected using a sterile Harris 8.0 mm Uni-Core sampler (Ted Pella, Inc., Redding, CA, United States), immediately placed in RNAlater (Life Technologies, Inc., Grand Island, NY, United States), and stored at −20°C. Upon returning to the Space Life Science Lab, cores were stored at −20°C until DNA extraction.

DNA Extraction and Sequencing

Total genomic DNA was isolated (n = 8–10 extractions) from each replicate mat type samples using a xanthogenate bead beating method as previously described (Foster et al., 2009; Khodadad and Foster, 2012). Several modifications were made due to the high exopolysaccharide content of the mats. Each extraction replicate (60 mg) underwent three freeze-thaw cycles in liquid nitrogen, followed by immediate vortexing at max speed for 5 min with zirconia beads (Biospec Products, 2.0, 0.7, 0.1 mm diameter). All samples were visually inspected after the freeze-thaw incubations to ensure sufficient cell lysis. For those samples that did not exhibit full cell lysis due to extensive carbonate precipitate within the stromatolite-forming mat, samples were ground in liquid nitrogen prior to DNA extraction. Following extraction, DNA precipitation was conducted with 100% cold ethanol at −80°C, centrifuged, re-suspended in 70% cold ethanol, centrifuged and air dried for 2–5 min. DNA recovery was achieved with the DNeasy PowerSoil Kit (Qiagen, Germantown, MD, United States). Lastly, a second round of DNA precipitation was conducted with a final 0.3 M sodium acetate solution with cold 100% ethanol at −80°C to ensure removal of exopolysaccharides. DNA concentration was measured with Qubit® 2.0 fluorometer (Thermo Fisher Scientific, Waltham, MA, United States), normalized, and replicate extractions (n = 8 – 10) were pooled. DNA was sequenced at the University of Florida's Interdisciplinary Center for Biotechnology Research using the NextSeq 500/550 High Output v2 Kit (paired-end, 150 cycles) on a NextSeq 500 sequencing system (Illumina, San Diego, CA, United States). All raw reads have been deposited in the NCBI Sequence Read Archive under BioProject number PRJNA429237.

Taxonomic Classification and Functional Annotation of Metagenomes

Raw sequences were quality filtered using sickle v1.33 with default parameters (e.g., minimum values of 20 bp length and Phred score of >20) for paired-end reads (Joshi and Fass, 2011). The range of alignment lengths for all 16 metagenomes

ranged from 9 to 106 bp with a median of 48 bp. Additionally, the bit scores ranged from 20 to 125 with a median of 58 for all 16 metagenomes. For taxonomic classification, SSU rRNA sequences were recovered with SortMeRNA v2.1 using default parameters (Kopylova et al., 2012) against the SILVA_128 SSU Ref NR99 (Quast et al., 2013) database. Next, the SSU rRNA sequences were analyzed with QIIME version 1.9.1 (Caporaso et al., 2010) using the UCLUST method [open-reference operational taxonomic unit (OTU) picking] against the Silva[1] and Greengenes v13.8 (DeSantis et al., 2006) databases. For further taxonomic analysis, the subsequent OTU table was inputted into MEGAN version 6.7.15, using the lowest common ancestor method with default parameters (Huson et al., 2016).

Quality controlled reads were annotated using BLASTx v2.2.26+ directly on the unassembled reads (Altschul et al., 1990) against the 2016 non-redundant UniProtKB/Swiss-Prot database (The UniProt Consortium, 2017) and filtered with an *E*-value cut-off of 10^{-3}. An assembly free approach was used due to the variable taxonomic abundances within the stromatolite-forming mats, which has been shown to increase chimera formation frequency (Howe and Chain, 2015; Ghurye et al., 2016). Filtered BLAStx hits were programmatically linked to KEGG Orthology (KO) (Kanehisa et al., 2004) identifiers using the UniProt Retrieve/ID mapping tool. Unique KOs with their respective counts were then inputted into MEGAN to facilitate annotation of KEGG pathways (Huson et al., 2016). Pathway information for KOs not included in the MEGAN database, which was 62.3%, were identified via manual lookup on the KEGG website[2].

[1]http://www.arb-silva.de/

[2]http://www.genome.jp/kegg/kegg2.html

Visualization and Statistical Analysis

To preserve the biological variability and variances within the metagenomic library sizes, the raw OTU table (absolute count) was normalized using the DESeq2 normalization technique (Love et al., 2014) with QIIME. Taxonomic diversity analysis was performed on each of the samples from the normalized OTU counts. For alpha diversity metrics, Shannon–Weaver (Shannon and Weaver, 1949) and Faith's Phylogenetic Diversity (Faith, 1992) were used and significance of the diversity indices was performed with an adonis test (i.e., an analog of the nonparametric permutational manova) using 999 permutations. Beta-diversity metrics were generated from the unweighted UniFrac distance matrix and significance was determined using an adonis test. Phyla abundances were compared between any two mat types using a Wilcoxon test and statistical significance was et at p-value < 0.05 and visualized using the R package MetacodeR (Foster et al., 2017). Differential abundance analysis of the KEGG orthologs was conducted using the DESeq2 v1.16.1 statistical package in R (Love et al., 2014), which has been shown to be highly effective in comparing metagenomic data (McMurdie and Holmes, 2014; Rodriguez-R et al., 2015; Warden et al., 2016). As input, DESeq2 requires un-normalized count data for the statistical model to hold as it is designed to account for library size differences internally. Statistically significant differences between pairs of mat types were identified using a negative binomial Wald test; raw p-values were corrected for using the Benjamin–Hochberg adjustment and all adjusted p-values < 0.05 were considered to indicate differentially abundant KEGG orthologs between the mat types. Orthologs (i.e., KEGG level 4) were then mapped to their respective pathways (i.e., KEGG level 3) and results of the differential analysis were visualized with ggplot2 (Wickham, 2009). PCoA of the DESeq2 normalized gene counts was conducted using vegan

TABLE 1 | Sample collection metadata.

Mat Type Sample[a]	Quality trimmed[b]	Annotated[c]	Filtered[d]	KEGG Annotated[e]	SSU rRNA[f]
Colloform 1	25,640,027	24,440,441	5,783,177	4,278,942	83,075
Colloform 2	25,853,795	24,806,582	6,337,080	4,783,657	76,945
Colloform 3	32,157,886	30,577,393	7,762,622	5,850,001	73,383
Colloform 4	13,882,116	13,000,926	2,837,561	2,093,877	60,831
Colloform 5	16,491,656	15,816,629	3,894,429	2,911,914	51,761
Smooth 1	12,067,338	11,623,865	2,828,663	2,122,546	45,709
Smooth 2	15,005,964	14,327,705	3,867,244	2,977,815	29,858
Smooth 3	24,026,888	22,637,278	5,074,119	3,768,477	81,085
Smooth 4	37,762,998	35,922,198	8,845,909	6,690,571	104,499
Pustular 1	43,977,296	41,753,668	10,976,883	8,126,808	114,975
Pustular 2	6,650,194	6,369,761	1,503,861	1,077,965	30,704
Pustular 3	14,791,472	14,113,834	3,943,770	2,988,764	42,968
Pustular 4	26,210,855	24,847,807	7,149,138	5,279,132	66,797
Non-lithifying 1	25,326,367	23,995,391	6,602,867	4,956,857	68,162
Non-lithifying 2	25,929,115	24,674,737	6,720,601	5,008,672	76,140
Non-lithifying 3	25,964,103	24,811,097	6,584,807	4,893,546	90,516

[a]Each mat type sample represents a different sampled head. [b]Reads were trimmed with sickle and quality trimmed sequences retained a Phred score > 20. [c]Quality sequences were annotated with BLASTx against the Uniprot Swiss-prot database. [d]Sequences were filtered with a BLASTx e-value cutoff of <0.001. [e]Number of filtered sequences with an annotation to a KEGG Orthology (KO) level 4 gene. [f]SSU rRNA sequences were mined with SortMeRNA against the SILVA database.

v2.4-4 (Oksanen, 2017) with Bray–Curtis distances as input and visualized with ggplot2.

RESULTS

Site Description of Stromatolite-Forming Mats in Spaven Province

Within the Spaven Province, the three canonical, stromatolite-forming mat types were abundant; however, only the colloform and smooth mat types were associated with the elongated, nested stromatolite morphology characteristic of the Province (**Figures 2A,B**). Both the colloform and smooth stromatolites ranged from between 50 and 75 cm high and several meters in length. The pustular stromatolite-forming mats were associated with rounded, discrete heads that ranged from 30 to 50 cm in height and up to 1 m in width (**Figure 2C**). The non-lithifying mats formed sheets that extended for 100s of meters in the intertidal to supratidal zones (**Figure 2D**). The surfaces of each mat type showed distinctive features. The colloform stromatolites (**Figure 2E**) exhibited convoluted surfaces, whereas the smooth stromatolite-forming mats typically had flat, relatively unbroken surfaces (**Figure 2F**). Both the stromatolite-forming and non-lithifying pustular mats exhibited nodular surfaces, although the surface community on the stromatolite-forming pustular mats was darkly pigmented and often crusty compared to the non-lithifying mats (**Figures 2G,H**). In cross-section, all three of the stromatolite-forming mats exhibited extensive precipitation with a pronounced layer of cyanobacteria a few mm beneath the surface (**Figures 2I–K**), whereas the non-lithifying mat did not exhibit any lithification and often crumbled upon examination (**Figure 2L**).

Environmental data collected at the time of sampling as part of an independent study (Suosaari et al., 2016a,b) showed no significant temperature or tidal differences throughout the 20 km area of Spaven Province. The annual mean pH of the Spaven Province is 8.1 (Oehlert and Suosaari, personal communication) and the April water temperatures in Spaven Province at the collection sites ranged from 25.2 to 26°C at noon (the time of collection); salinity varied from 54.5 to 56 ppt.

Overview of Metagenomic Sequencing of Spaven Stromatolite-Forming Mats

Replicate metagenomic libraries were generated for each of the colloform, smooth, and pustular stromatolite-forming mats (**Table 1**). Additionally, libraries were also created for non-lithifying pustular mats to enable a direct comparison with the stromatolite-forming mats. The high-throughput sequencing effort produced a total of 16 metagenomes that contained 380,819,456 raw reads with an average of 23,801,216 per sample. For downstream analysis, an average of 2.4% of the sequences were removed to produce high-quality libraries (Phred quality score > 20; **Table 1**).

For taxonomic classification, initial assessment of the data revealed that the stromatolite-forming mat communities were more than 99% bacterial with archaea and eukaryotes comprising less than 1% of the total recovered reads. Few viral sequences were recovered and viruses were likely missed due to the DNA extraction and library preparation approaches used in this study. Bioinformatic mining of the SSU rRNA sequences from the metagenomes was conducted, producing an average of 65,588 SSU rRNA sequences per sample (**Table 1**). For functional annotation, all sequences were blasted against the UniProtKB/Swiss-Prot database, rendering the deduction of functionality from manually curated protein products and filtered with an *e*-value < 0.001, generating an average of 4,238,097 reads/sample (**Table 1**) that contained a KEGG Orthology (KO) identifier.

Comparison of Overall Microbial Diversity by Mat Type and Location

The taxa of the replicate metagenomes were compared using a principal coordinates analysis (PCoA) computed from the unweighted UniFrac distances between samples (**Figure 3**). When all OTUs (i.e., bacteria, archaea, eukaryotes) associated with the metagenomes were analyzed, three groupings were discernable (**Figure 3A**; adonis, $p = 0.001$; $R^2 = 0.27$). First, the non-lithifying mats formed a cluster that was distinctive from the three stromatolite-forming mats. Second, the pustular stromatolite-forming mats formed a separate, although less cohesive, grouping, suggesting there is a higher level of heterogeneity within that mat type. Lastly, the colloform and smooth stromatolite-forming mats formed a single grouping, indicating a high degree of similarity between these two mat types. As sample collection spanned several km, the taxa of the metagenomes were also compared based on location within Spaven Province; **Figure 3B**). The taxonomic differences between the mat types was weakly linked to the collection area (adonis, $p = 0.01$; $R^2 = 0.16$) and clustered primarily based on mat type.

Taxonomic Assessment of the Spaven Stromatolite-Forming Mats

Analysis of the 16 metagenomes revealed 33 bacterial, 3 archaeal and 3 eukaryotic phyla or superphyla. The overall alpha diversity within the different mat types was examined using both Shannon-Wiener Diversity and Faith's Phylogenetic Diversity metrics (Supplementary Figures S1A,B). No statistical differences for either metric were observed ($p > 0.05$), indicating that the overall level of microbial diversity between the different mat types was comparable. The indices values were, however, much higher than previous reports (Allen et al., 2009; Goh et al., 2009; Garby et al., 2013; Wong et al., 2015; Suosaari et al., 2016b) likely reflecting the use of newer sequencing platforms (e.g., Illumina) that lead to an increase in the overall microbial diversity detected within all mat types compared to previous technologies.

In all the different mat types, the dominant bacterial phyla included the Proteobacteria (55–69%) and Cyanobacteria (15–29%), with the Planctomycetes (5–7%), Bacteroidetes (3–7%), Verrucomicrobia (2–3%), Chloroflexi (2–5%), and Actinobacteria (0.25–2%) phyla present in all of the mat types (**Figure 4A** and Supplementary Figure S1C). At much lower abundances (relative abundance < 1% across all replicates),

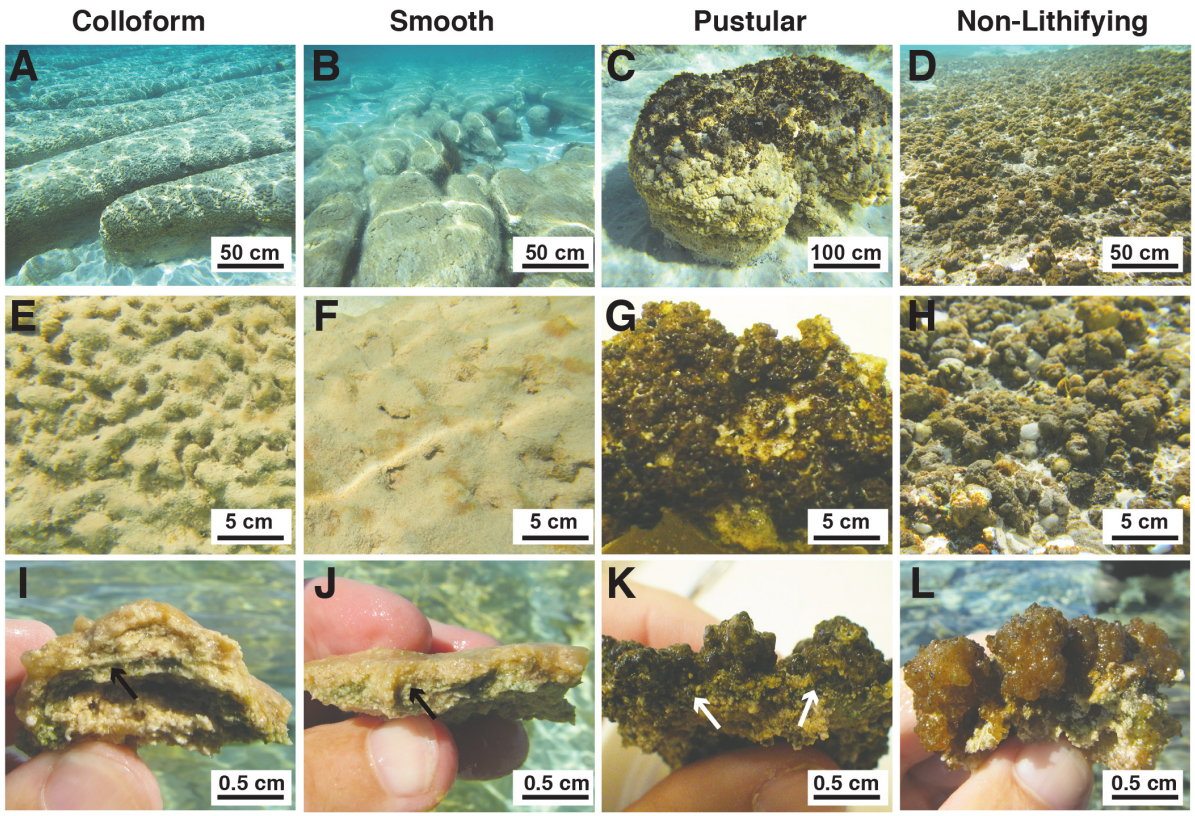

FIGURE 2 | Morphological features of mat types targeted in this study. **(A–D)** Underwater images depicting the macroscopic morphologies of the elongated nested build-ups associated with the colloform **(A)** and smooth **(B)** mat types, as well as the circular carbonate build-ups associated with the pustular **(C)** stromatolite-forming mats. The non-lithifying pustular mats form extensive sheets within the upper intertidal zone. **(A,B)** Bar = 50 cm; **(C,D)** Bar = 100 cm. **(E–H)** Surface images of the mat types showing the convoluted colloform **(E)**, flat smooth **(F)**, and nodular surfaces of the lithifying **(G)** and non-lithifying **(H)** pustular mats. Bar = 5 cm. **(I–L)** Cross-section of the mat surfaces depicting the domal structure of the colloform mat **(I)**, flat surfaces of the smooth mats **(J)**, heavily pigmented nodular structure of the lithifying pustular mat **(K),** and lighter pigmentation in the non-lithifying pustular mats **(L)**. Bar = 0.5 cm. Arrows indicate cyanobacterial layer within the stromatolite forming mats.

a total of 26 additional bacterial phyla were observed (Supplementary Figure S1D). Although bacteria dominated all mat types, the recovered archaea were predominantly Thaumarchaeota (Supplementary Figure S1E) whereas the eukaryotic taxa were primarily associated with the Opisthokonta and the SAR supergroup, which includes the stramenopiles, alveolates and Rhizarias (Supplementary Figure S1F). These results are consistent with previously documented taxa within the southern region of Hamelin Pool (Burns et al., 2004; Goh et al., 2009; Edgcomb et al., 2014; Wong et al., 2015; Ruvindy et al., 2016; Suosaari et al., 2016a).

Although few differences were observed between mat types at the phylum-level, in-depth pairwise comparisons of the bacteria revealed significant differences at lower taxonomic levels (Wilcoxon test, $p < 0.05$) and are visualized as differential abundance heat trees in **Figure 4B**. The most pronounced differences occurred between the stromatolite-forming mat types and the non-lithifying mats. There was a pronounced overall enrichment of Proteobacteria, in particular, Alpha-, Delta- and Gammaproteobacteria taxa in the non-lithifying mats compared to the stromatolite-forming mat types (**Figure 4B** and Supplementary Figure S2); however, some individual proteobacterial taxa were enriched in the stromatolite-forming mats. For example, in the smooth mats, there was a statistically significant enrichment of Desulfovibrionales compared to the non-lithifying mats, whereas in the colloform mats increases in several Rhodobacterales taxa were observed. In the colloform and smooth stromatolite-forming mats, there was also an enrichment of Bacteroidetes, specifically in the Flavobacteriales. The colloform mats also were enriched in Saprospirales and Cytophagales compared to the non-lithifying mats.

Differences were also observed between the three dominant stromatolite-forming mat types. The most pronounced difference was an enrichment of the coccoid cyanobacteria Synechococcales within the pustular mats compared to the colloform and smooth mat types (**Figure 4B** and Supplementary Figure S3; Wilcoxon test, $p < 0.05$). There was also a differential abundance of two different Chroococcales lineages. The colloform and smooth mats were enriched in the genus *Chroococcus,* whereas the pustular mats were enriched in the Gomphosphaeriaceae family. Both the smooth and colloform mats showed an enrichment of Verrucomicrobia and Bacteroidetes compared to the pustular

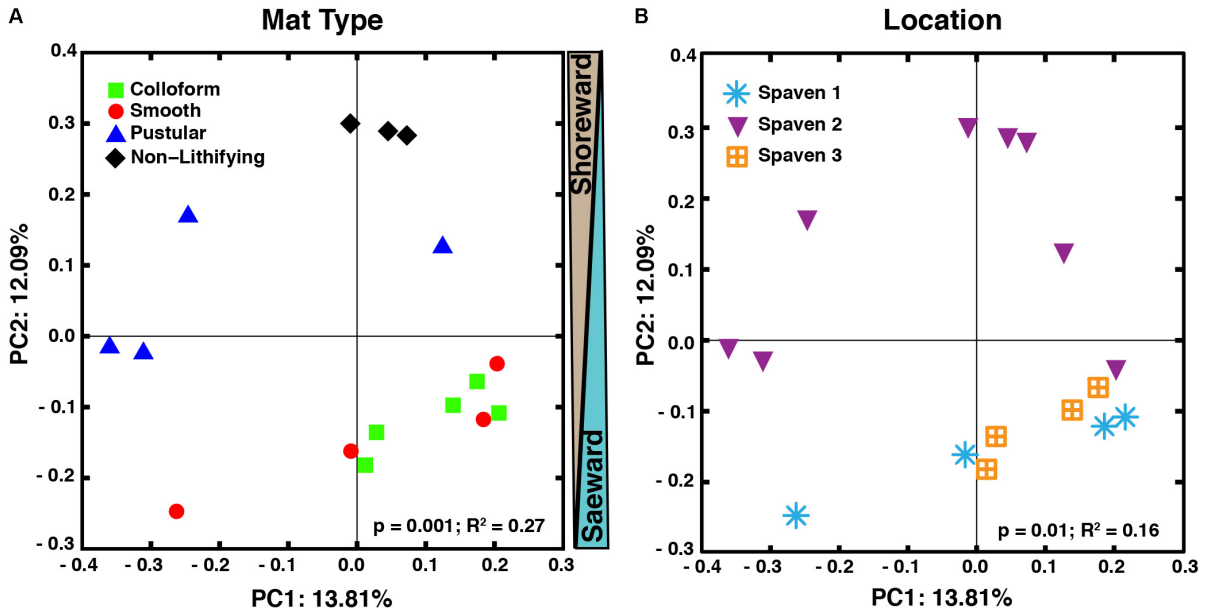

FIGURE 3 | Comparison of microbial diversity between lithifying stromatolite-forming mats and non-lithifying microbial mats in Spaven Province. Principal coordinates analysis plotting the unweighted Unifrac distances between samples according to mat type **(A)** and the three collection transects (Spaven 1, 2, 3) within Spaven Province **(B)**.

stromatolite-forming mats. There were very few differences observed between the colloform and smooth stromatolite-forming mats with an increased abundance of the Cytophagales in the colloform mats and a few enriched Alphaproteobacteria (Rhodobacterales and Rhizobiales) in the smooth stromatolite-forming mats (**Figure 4B**).

Comparison of the Functional Genes Within the Stromatolite-Forming Mats

To complement the taxonomic comparison, an ortholog-based comparison between the different mat types was performed using PCoA analysis of KEGG orthologies (**Figure 5**). When all annotated genes were considered, there were primarily two distinct clusters, one that included the colloform and smooth stromatolite-forming mats and a second that contained the pustular stromatolite-forming mats and non-lithifying mats (**Figure 5A**; adonis, $p = 0.001$; $R^2 = 0.40$).

In an effort to further characterize the metabolic differences between the mat types, pairwise comparisons of the differentially abundant genes were conducted with DESeq2 (**Table 2**; Love et al., 2014). There were 1232 differentially abundant genes ($p < 0.05$) between the non-lithifying mats and the colloform stromatolite-forming mats and 1033 between the non-lithifying mats and smooth stromatolite-forming mats, respectively (**Table 2**). A PCoA visualization was performed with statistically significant genes ($p < 0.001$), as was determined by differential abundance analysis with DESeq2 (**Figure 5B**). This approach more clearly revealed differences between the non-lithifying and pustular mat types, however, the colloform and smooth mats were still tightly clustered.

Interestingly, there were only four significant differentially abundant genes ($p < 0.05$) between the colloform and the smooth stromatolite-forming mat types, suggesting the genetic profiles of the microbes in these communities are highly similar. For those pairwise comparisons that had >1000 differentially abundant genes, filtering criteria were employed to identify those genes with a p-value < 0.001 and an absolute log2-fold change > 1 (**Table 2** and Supplementary Table S1).

In pairwise comparisons between the shoreward, non-lithifying mats and the stromatolite-forming mats, there were enrichments in numerous glycan and polysaccharide biosynthesis and degradation genes in the colloform and smooth stromatolite-forming mats, such as beta-porphyranases, fuctosidases, fructosideases, and rhamnotransferases (Supplementary Figures S4–S7). These genes were associated with a wide distribution of taxa including Chroococcales, Planctomycetales, several orders of Bacteroidetes, Firmicutes, and Proteobacteria (Supplementary Figures S8–S12). There was also a prevalence of genes associated with dissimilatory sulfur metabolism in the colloform and smooth stromatolite-forming mats compared to the non-lithifying mats, such as genes encoding thiosulfate reductases, dimethyl sulfoxide reductases (Supplementary Figures S4–S7 and Supplementary Table S1). There were fewer significant differences between the non-lithifying and pustular stromatolite-forming mats with the highest differentially abundant gene with regard to fold change associated with pigment transport in the pustular stromatolite and several uncharacterized proteins (Supplementary Figures S4–S7 and Supplementary Table S1).

In the upper intertidal, non-lithifying mats there was a higher representation of genes associated with oxidative and osmotic stress responses, including nitric oxide reductases,

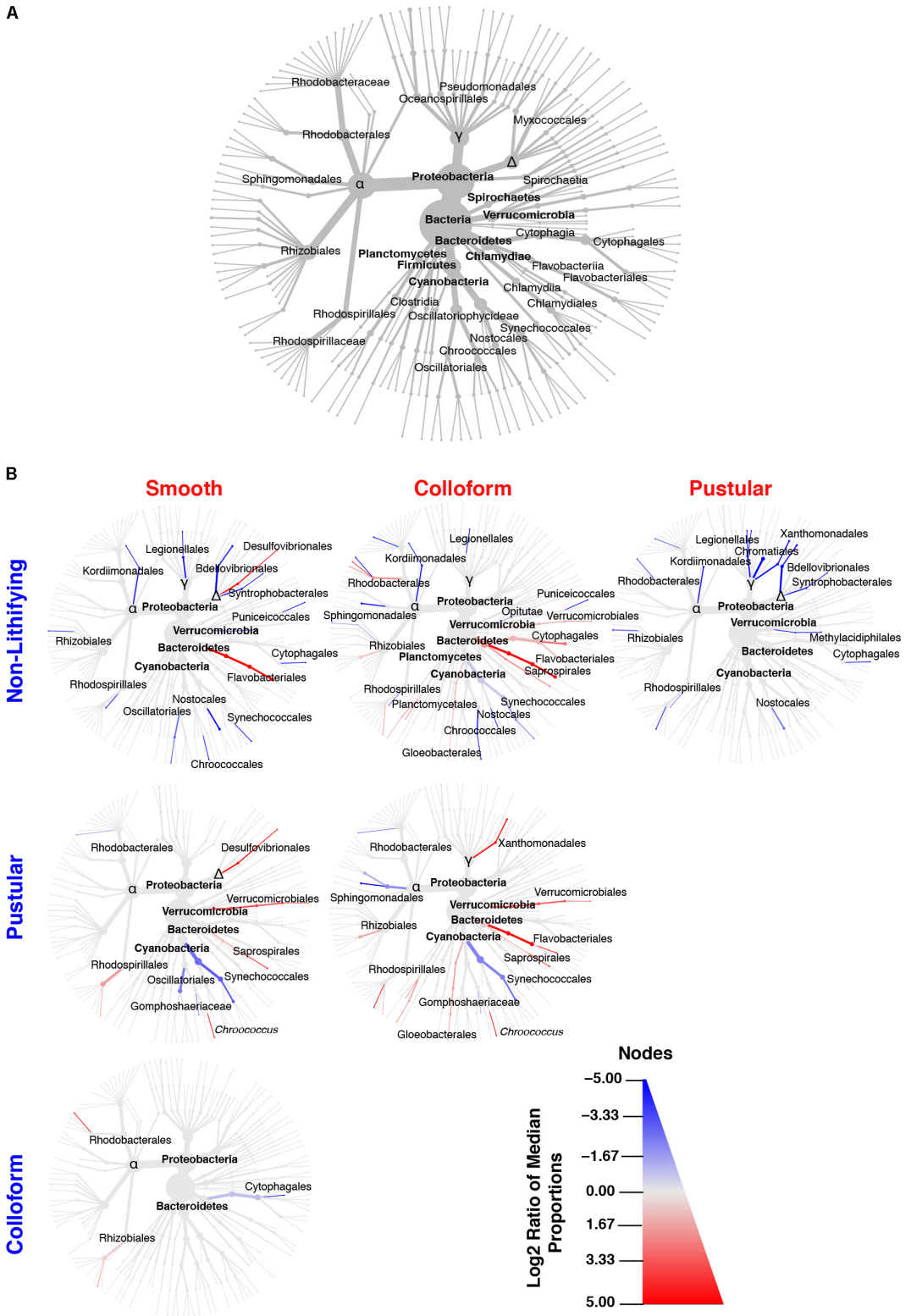

FIGURE 4 | Taxonomic distribution of bacteria within the targeted mat types. **(A)** Overview of the top 35 bacterial taxa recovered from the 16 metagenomic libraries generated in this study and serves as orientation for **(B)**. **(B)** Differential heat trees of pairwise comparisons between different mat types highlighting significant taxonomic enrichments (Wilcoxon test, $p < 0.05$). The color of each taxon represents the log-2 ratio of the median of the proportions observed with each mat type and corresponds to the different pairwise comparisons listed along the columns or rows. Node/edge color and size display the relative proportion for each taxon with lines in red reflecting those taxa enriched in mats along the *x*-axis and lines in blue enriched along the *y*-axis.

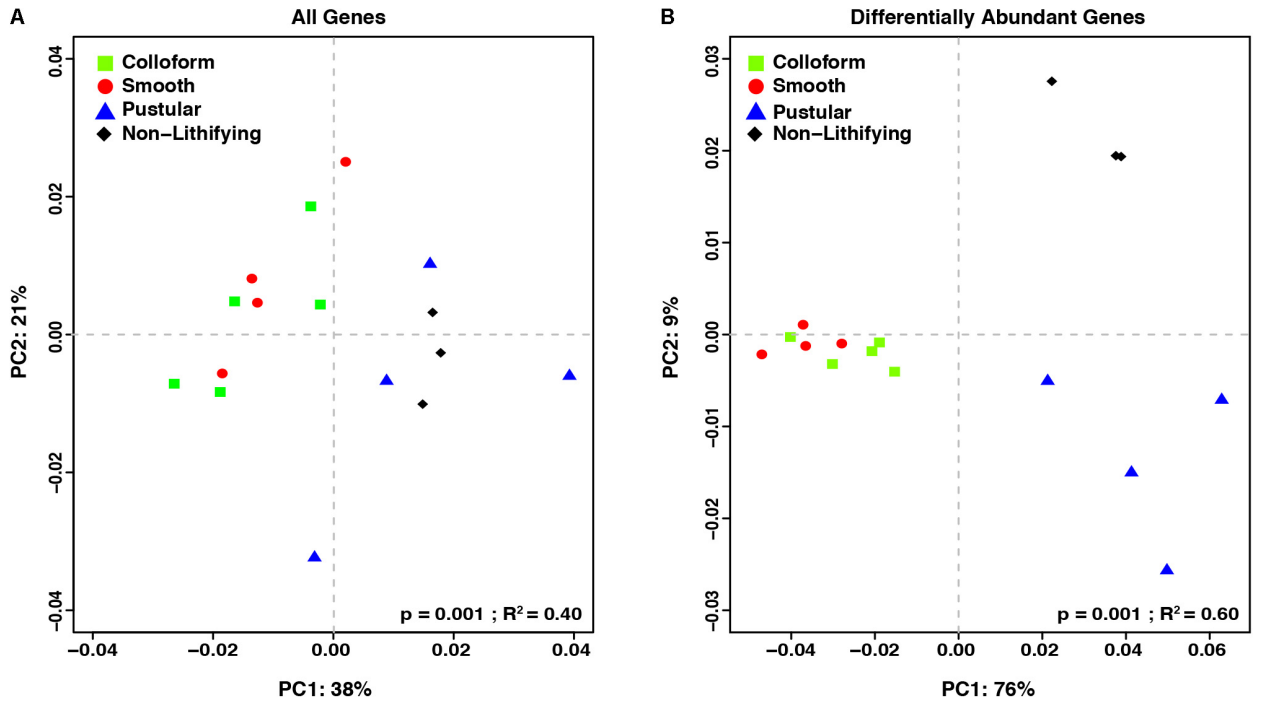

FIGURE 5 | Comparison of the functional gene profiles between the stromatolite-forming and non-lithifying mat types. Principal coordinate analysis (PCoA) of all DESeq2 normalized KEGG level 4 gene counts of **(A)** all recovered genes and **(B)** differentially abundant genes (p-value < 0.001) from the different mat types.

peroxidases, glucosylglycerol-phosphate synthase (GgpP), and glycine betaine/proline transporters (Supplementary Figures S4–S7). These genes were associated with a wide range of Proteobacteria, including several methylotrophic bacteria and purple-sulfur bacteria (Supplementary Figures S8–S12). There was also a significant enrichment of genes associated with metalloid and heavy metal cycling in the non-lithifying mats, such as arsenite transporters (e.g., *arsAB*), arsenite-mycothiol transferase (arsC) for removal, arsenic resistance genes (e.g., *arsH*), and arsenite oxidases (e.g., *aoxAB*) as well as genes that are part of the cobalt-zinc-cadmium efflux system (Supplementary Figures S4–S7). Genes associated with arsenate reductase were recovered from the non-lithifying mats, but they were not differentially abundant compared to the stromatolite-forming mat types. The genes associated with arsenic metabolism were widespread in the Actinobacteria, Cyanobacteria, and Firmicutes phyla, whereas the genes associated with the cobalt-zinc-cadmium system were found only in the Firmicutes and cyanobacterial Synechococcales (Supplementary Figures S8–S12).

In pairwise comparisons between the different stromatolite-forming mats, the most significant differentially abundant genes were observed in the pustular stromatolite-forming mats (**Figure 6** and Supplementary Figures S4–S7). There was an increase in the abundance of genes associated with carbon-concentrating mechanisms and photosynthesis compared to the colloform and smooth stromatolite-forming mats (p < 0.001; **Figure 6** and Supplementary Figures S4–S7). These differentially abundant photosynthesis genes were associated with both photosystem I and II pathways, as well as numerous antenna proteins that included phycocyanins and the blue phycocyanobilin (Supplementary Table S1). The differentially abundant photosynthesis genes were widely distributed in the coccoid Chroococcales and Synechococcales orders as well as the filamentous Nostocales cyanobacteria (**Figure 7** and Supplementary Figures S8–S12). As with the non-lithifying mats, the colloform and smooth stromatolite-forming mats were enriched in genes associated with heterotrophic metabolisms, such as methane and sulfur reduction metabolisms. Differentially abundant genes associated with these pathways included co-methyltransferase, heterodisulfide reductase, thioredoxin reductase, adenylylsulfate (APS) reductases

TABLE 2 | Differential gene abundance comparison between lithifying and non-lithifying mat types abundance mat types.

Pairwise Comparison	Genes[a] p < 0.05	Genes p < 0.001	Unique[b] pathways (p < 0.001)
Colloform vs. Smooth	4	–	–
Pustular vs. Smooth	1,070	394	108
Pustular vs. Colloform	1,248	318	98
Non-Lithifying vs. Colloform	1,232	261	105
Non-Lithifying vs. Smooth	1,033	231	92
Non-Lithifying vs. Pustular	210	36	28

[a]*KEGG Level 4 genes.* [b]*Unique KEGG Level 3 pathways.*

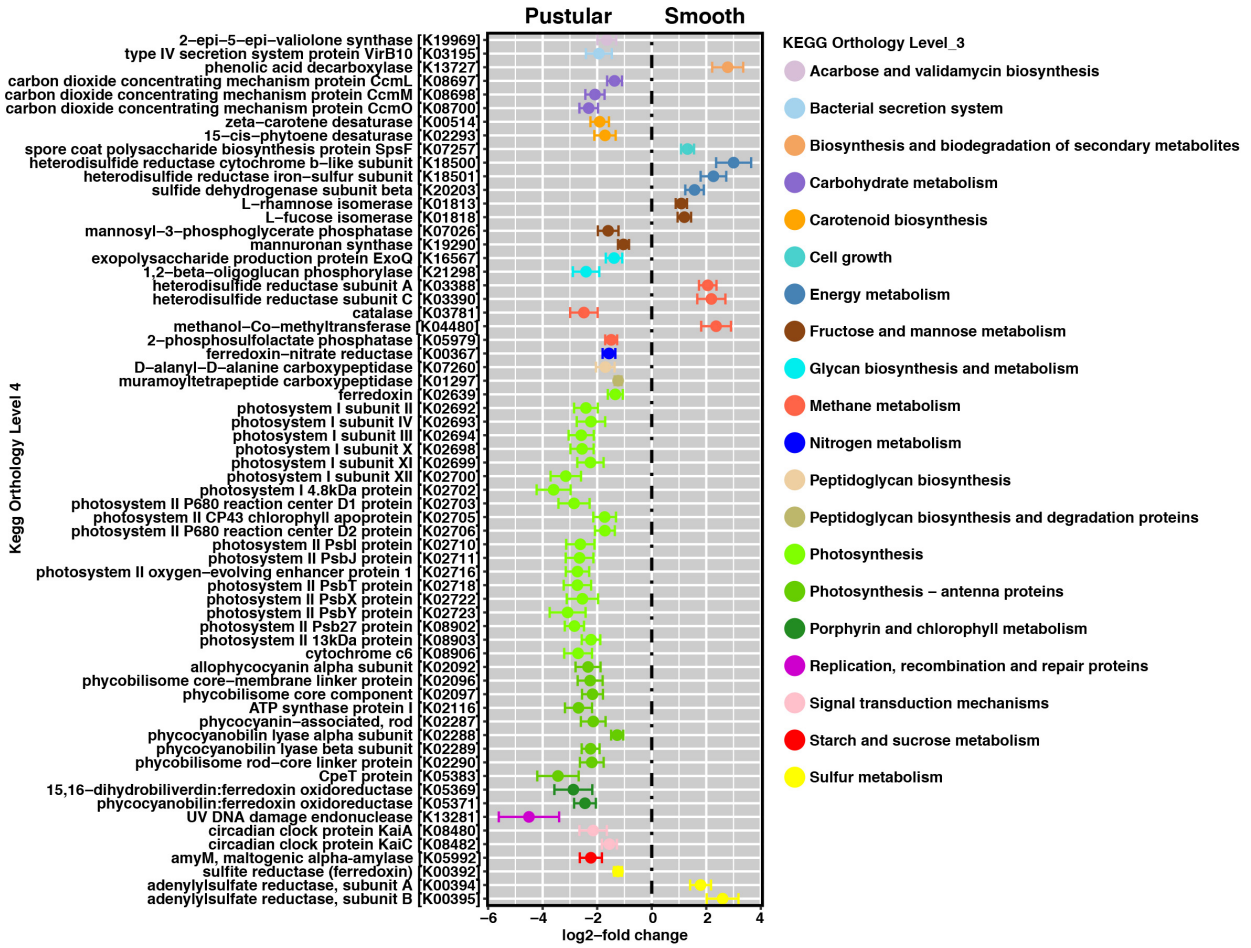

FIGURE 6 | Pairwise comparison of differentially abundant genes between pustular and smooth stromatolite-forming mats. Representative differentially abundant genes ($p < 0.001$) colored by their respective pathways. A positive log2-fold change designates differential abundance in the smooth mat type and a negative log2-fold change designates differential abundance within the pustular mats. Lines indicate the standard error of the mean.

and sulfide dehydrogenases (Supplementary Table S1). The methanogenesis genes were associated with Euryarchaeota (e.g., Methanobacteriales, Methanococcales, Methanopyrales, and Methanosarcinales), whereas the dissimilatory sulfur reduction genes were derived from the Desulfovibrionales (Supplementary Figures S8–S12).

DISCUSSION

Hamelin Pool represents the largest known marine habitat for actively accreting stromatolites; however, little is known about the molecular pathways underlying the different stromatolite-forming mat types in this ecosystem. In this study, the metagenomes of the three canonical microbial mat types associated with carbonate build-ups were compared to each other and to an adjacent sheet-forming mat to assess differences in the metabolic signatures of lithifying and non-lithifying microbial mats. The results of this study provide evidence that: (1) the stromatolite-forming mats types have distinct taxonomic and functional gene profiles compared to non-lithifying mats; (2) colloform and smooth stromatolite-forming mats exhibit distinctive surface morphologies, yet show few taxonomic and functional gene differences; and (3) intertidal pustular stromatolite-forming mats are enriched in photosynthetic genes compared to the colloform and smooth stromatolite-forming mats, suggesting two distinctive metabolic processes driving stromatolite formation within Hamelin Pool.

The metagenomic comparisons in this study provided an important, in-depth analysis of those differentially abundant metabolic pathways between lithifying and non-lithifying mat communities. Our current study expands upon previous metagenomic analyses (Ruvindy et al., 2016) to examine all three of the prevalent lithifying mat types. Our results revealed that one of the pronounced differences within the non-lithifying mats compared to the subtidal stromatolite-forming mat types was the enrichment of genes associated with metalloid cycling ($p < 0.001$), in particular, genes associated with arsenic metabolism. The presence of arsenic metabolism has been

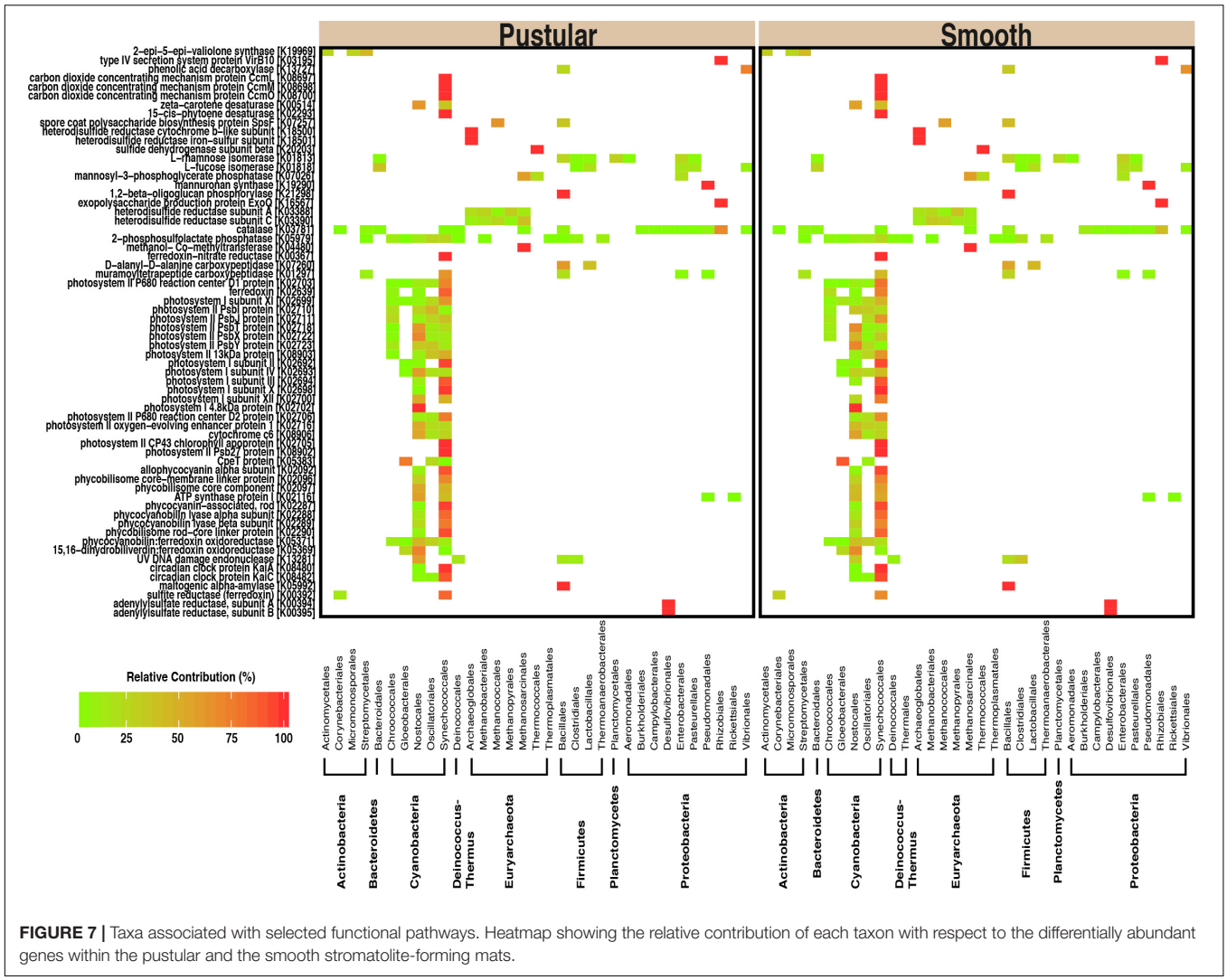

FIGURE 7 | Taxa associated with selected functional pathways. Heatmap showing the relative contribution of each taxon with respect to the differentially abundant genes within the pustular and the smooth stromatolite-forming mats.

previously reported in the non-lithifying mats of the southern Nilemah Province within Hamelin Pool (Ruvindy et al., 2016), hypersaline hot spring biofilms from Mono Lake (Kulp et al., 2008), as well as within the high altitude stromatolites of Socompa Lake, Argentina (Kurth et al., 2017). The increase in abundance of these genes associated with metal cycling within the mats of the upper zone may reflect the hypersaline nature of these habitats (Hamelin Pool. 66 – 88 ppt; Mono Lake 84 ppt; Socampa Lake ∼90 ppt; Farías et al., 2013). For example, evaporation can increase the abundance and availability of metalloids, such as arsenic and boron, within microbial communities (Kulp et al., 2007). Additionally, under extreme saline conditions some metabolisms, such as sulfate reduction and methanogenesis, are diminished (Oren, 1999; Kulp et al., 2007; Wong et al., 2017) and reliance on arsenic cycling, particularly under anoxic conditions, may reflect an important metabolic strategy for these mat communities exposed to the energetically taxing high salt and desiccation conditions of the upper, intertidal zone.

Another pronounced difference within the non-lithifying mats compared to the stromatolite-forming mat types in Spaven Province was the enrichment of oxidative (e.g., nitric oxide reductases, peroxidases) and osmotic stress (e.g., glycine betaine/proline synthesis and transport) genes in the upper tidal non-lithifying mats, whereas genes typically associated with UV stress were found to be evenly represented in all of the different mat types examined. The enriched oxidative and osmotic stress genes in the non-lithifying mats corresponded to several of observed osmoadaptive genes and pathways recovered from hypersaline mat environments, including Hamelin Pool (Goh et al., 2010; Goh et al., 2011; Gudhka et al., 2015; Gunde-Cimerman et al., 2018). As there is a pronounced desiccation gradient within the pool (Burne and Johnson, 2012; Suosaari et al., 2016b), the enrichment of genes associated with the production of osmoregulation and oxidative stress responses in the non-lithifying mats likely reflects the dynamic tidal extremes within the pool. Additionally, several taxonomic analyses of the non-lithifying mats in the Nilemah Province of Hamelin Pool have shown distinctive gradations of key functional groups of microbes, such as sulfate-reducing bacteria and methanogens, at different tidal regimes further suggesting that water levels

are influencing the mat communities (Wong et al., 2017). The enriched genes associated with pigment transport were associated with cyanobacteria and may reflect the higher light and salt selection pressures on the cyanobacteria within this mat type, as several cyanobacteria have shown differential pigment production and transport responses to light and salt stress (Riethman et al., 1988; Sudhir and Murthy, 2004). Several comparative genomic studies of marine cyanobacteria have revealed genome expansion as the result of nutrient or light stresses (Swingley et al., 2008) and light pressures can be a major driver of genome differences in pigments and the photosynthesis apparatus between closely related cyanobacterial ecotypes (Rocap et al., 2003).

Over the course of a year, the water levels within the pool can vary by as much as two meters and are highly dependent on seasonal, meteorological and astronomical effects (Burne and Johnson, 2012; Playford et al., 2013; Suosaari et al., 2016b). Although water levels are typically higher during the austral summer and fall, which coincided with the April collection of the samples used in this study, the location of Spaven Province on the eastern margin of the pool experiences the largest meteorological effect of tidal variation throughout the year, spanning 1.67 m (Suosaari et al., 2016a), indicating the non-lithifying mats would experience frequent exposure and desiccation throughout the diel cycle. Temperatures within the pool can also fluctuate between 11 and 33°C through the year (Suosaari et al., 2016a); however, due to the shallowness of the pool, there is no vertical temperature stratification within the water column (Burling et al., 2003). Therefore, it is more likely that water depth, has a stronger influence than temperature on driving the differences in the metagenomes between the mat types.

The concept that water depth influences the morphology and community composition of the stromatolite-forming mats has long been suggested (e.g., Logan, 1961; Logan et al., 1974; Golubic and Hofmann, 1976; Playford, 1990; Jahnert and Collins, 2011, 2012; Playford et al., 2013; Suosaari et al., 2016a; Wong et al., 2017). More recent studies suggest that water level and the underlying shelf physiography may be two of the most important drivers of microbial mat zonation within Hamelin Pool (Suosaari et al., 2016b). The PCoA comparisons of both the taxonomic and functional gene diversity (**Figures 3**, **5**) of the different mat types provide support for these concepts, as the stromatolite-forming mats formed three distinct clusters that corresponded with the upper tidal, intertidal and subtidal zones.

Interestingly, within the subtidal zone, the colloform and the smooth stromatolite-forming mats showed few taxonomic and functional gene differences. In fact, only four of the 15,378 recovered genes were significantly different between colloform and smooth stromatolites (**Table 2** and Supplementary Figure S5) indicating that these two subtidal mat types share almost identical metabolic potential. Despite the similar metabolic profiles between the two subtidal stromatolite-forming mat types, each of the associated carbonate build-ups exhibited different surface morphologies, with the colloform mats exhibiting a convoluted surface and the smooth mats having a flat, even surface. These differences could reflect differential gene expression between the two mats, as other metatranscriptomic analyses of Bahamian thrombolites have shown that the metatranscriptome can vary significantly throughout diel and seasonal cycles and does not fully reflect the metagenome (Mobberley et al., 2015; Louyakis et al., 2018).

Alternatively, the differences in morphology may reflect environmental factors impacting the mat surfaces, specifically, the shear forces of winds and currents. Although water circulation within Hamelin Pool is restricted due to the presence of the Faure Sill in the northern part of the pool, it is primarily driven by the wind resulting in Langmuir circulation, which are shallow, counter-rotating gyres that align with the winds (Playford et al., 2013; Suosaari et al., 2016b). In the Spaven Province, current velocities range from as low as 0.001 m/s to a maximum of 0.54 m/s with a mean of 0.125 m/s (Suosaari et al., 2016b). Waves driven by the wind could be differentially impacting the colloform and smooth stromatolite-forming mat communities in the Spaven Province resulting in the disparate morphologies. Additional analyses, such as metatranscriptomics and proteomics, will be required to ascertain whether the colloform and smooth microbial communities exhibit differential microbial activities that account for the differences in morphology or whether these differences are the product of extrinsic factors.

One key difference amongst the stromatolite-forming mat communities was the enrichment of genes associated with photosynthesis in the pustular mats, including genes associated with photosystems I/II, as well as a range of pigments and antennae proteins. These differentially abundant genes were widely distributed within the cyanobacteria and were associated with the coccoid Chroococcales and Synechococcales, as well as the filamentous Nostocales orders. Due to the paucity of sequenced genomes for cyanobacteria, many of the genes were unable to be identified beyond the order level. However, over the past few decades, microscopic analyses of the pustular mats have shown that *Entophysalis* spp., which belongs to the order Chroococcales as well as the filamentous Nostocales *Scytonema* spp. and *Dichothrix* spp., dominate the pustular mat types (Logan et al., 1974; Golubic and Hofmann, 1976; Collins and Jahnert, 2014; Suosaari et al., 2016a). These taxa have long been thought to play a key role in the formation of stromatolites, both in living and in ancient systems (Golubic and Hofmann, 1976; Golubic and Campbell, 1981). Additionally, recent metagenomic and metatranscriptomic examination of the unlaminated thrombolites of Highborne Cay, The Bahamas have shown that the filamentous *Dichothrix* spp. and its associated coccoid cyanobacteria are the most transcriptionally active taxa within the thrombolite communities, with most transcripts associated with photosynthesis (Mobberley et al., 2015; Louyakis et al., 2017, 2018). These results coupled with stable isotope analyses of the calcium carbonate have revealed that the primary metabolism driving precipitation in the intertidal Bahamian thrombolites is photosynthesis (Louyakis et al., 2017).

The enrichment of photosynthetic genes in the pustular stromatolite-forming mats of Hamelin Pool suggests that, like the Bahamian thrombolites, photosynthesis may be the

primary metabolism driving precipitation in this mat type. Additionally, as the carbonate build-ups associated within the pustular mats are typically unlaminated, and have been called stromatolites rather than thrombolites for historical reasons (Logan, 1961; Logan et al., 1974; Golubic and Hofmann, 1976; Playford, 1990; Jahnert and Collins, 2012, 2013; Playford et al., 2013), the processes associated with pustular carbonate build-ups may be distinct from the other lithifying mat structures and may be more thrombolite-like. Additional research into the biogeochemical and transcriptional activities of the filamentous *Dichothrix* spp. and coccoid *Entophysalis* spp. is needed to fully elucidate the role of these abundant taxa in the formation of the pustular-associated carbonate structures.

Whereas the pustular stromatolite-forming mats harbored an increase in photosynthesis genes, the colloform and smooth stromatolite-forming mats exhibited a differential abundance of genes associated with certain heterotrophic pathways known to promote carbonate precipitation. For example, there was a differential abundance of genes associated with dissimilatory sulfate reduction and methanogenesis in the colloform and smooth mats. Previous research on the stromatolites of Highborne Cay, The Bahamas has shown a strong correlation between sulfate-reducing activity and lithified micritic lamination (Visscher et al., 1998, 2000). Bicarbonate is a product of sulfate reduction, which can alter the local pH within the mat microenvironment, thereby promoting carbonate precipitation (Dupraz and Visscher, 2005; Visscher and Stolz, 2005; Dupraz et al., 2009). Methanogenesis can also increase the local pH subsequently facilitating conditions for carbonate precipitation (Visscher and Stolz, 2005) and several genes associated with that pathway were enriched in the lithifying colloform and smooth mats compared to the pustular stromatolite-forming mats.

In addition to creating localized geochemical environments that favor carbonate precipitation (Dupraz et al., 2009), nucleation sites must also be available. The primary nucleation sites of the lithifying mats are within the exopolymeric substances (EPS) secreted outside the cells forming a matrix (Braissant et al., 2007; Dupraz et al., 2009). The EPS matrix provides a multi-faceted role for the mat community, not only acting as nucleation sites for carbonate precipitation but also serves as a protective barrier against environmental stressors and enhances community stability in high-energy environments (Decho et al., 2005; Decho and Gutierrez, 2017). Within the EPS, negatively charged acidic groups can bind Ca^{2+}, thereby sequestering it within the matrix (Kawaguchi and Decho, 2002) and through modification to the EPS, either by environmental or metabolic degradation, the ions can be released, thus increasing local calcium concentration available for mineralization (Visscher et al., 2000; Dupraz and Visscher, 2005; Dupraz et al., 2009).

In the colloform and smooth stromatolite-forming mats, there was an increase in the abundance of genes associated with formation and degradation of EPS. Specifically, there was an increase in the abundance of metabolic enzymes associated with modification of dicarboxylic acids (e.g., maleic acid) and deoxyhexoses (e.g., fucose and rhamnose) from a wide range of taxa including Bacteroidetes, Firmicutes, Planctomycetes, and Proteobacteria compared to the pustular stromatolite-forming mats. This enrichment suggests that the EPS material of the colloform and smooth stromatolite-forming mats is highly labile and may fuel heterotrophic activity within the mats. The processing and restructuring of the EPS by heterotrophic activity may change the physiochemical properties of the EPS matrix, thereby influencing the morphology and mineralogy of the precipitates within colloform and smooth stromatolites. Together, these results suggest the processes facilitating carbonate precipitation in the laminated colloform and smooth stromatolite-forming mats may rely more on heterotrophic processes than in the unlaminated pustular stromatolite-forming mat type.

In summary, our results provide the first metagenomic comparison of the three dominant stromatolite-forming mat types within Hamelin Pool. Our results reveal key metabolic differences amongst the different stromatolite-forming mat communities, in particular between the intertidal and subtidal zones. The results suggest that carbonate precipitation in the unlaminated, pustular mat build-ups may be primarily photosynthesis driven, whereas, in the laminated colloform and smooth stromatolite structures, carbonate precipitation may be the product of a synergism between autotrophic and heterotrophic processes in the associated mats. More in-depth analysis of the microbial activities within each of these lithifying mat types will be required to more fully understand the metabolic drivers of carbonate precipitation within Hamelin Pool. Taken together, this comparative metagenomic analysis has provided confirmation of many of the prior geological and morphological-based studies in Hamelin Pool, thereby providing important insight into the feedbacks between microbial mat communities and their environments, which together drive stromatolite formation.

AUTHOR CONTRIBUTIONS

JF and PR conducted all the fieldwork. JB conducted the experiments, sequencing analysis, and wrote the first draft of the manuscript. AC, GC, CP, AL, and JF assisted in developing the bioinformatic pipeline and analysis of the data. All authors assisted in the writing and editing of the manuscript.

FUNDING

This work was funded by a NASA Exobiology and Evolutionary Biology program (NNX14AK14G) awarded to JF and PR. JB was supported by the NSF Graduate Research Fellowship Program and a NASA Earth and Space Science Fellowship.

ACKNOWLEDGMENTS

The authors would also like to thank the late Dr. Phillip Playford for discussions regarding this project as well as his discovery

and pioneering work on the stromatolite systems of Shark Bay. We thank Erica Suosaari for her geological expertise and for help in navigating through Hamelin Pool. We thank Amanda Oehlert, Jessica Babilonia, Lexi Duscher, and Michael Morrison for their technical assistance. We also thank Bush Heritage Australia for logistical assistance and to the Western Australia Department of Parks and Wildlife (formerly Department of Environment and Conservation) and the federal Department of Sustainability, Environment, Population, and Communities for sampling permits. This manuscript is Hamelin Stromatolite Contribution Series #5.

SUPPLEMENTARY MATERIAL

The Supplementary Material for this article can be found online at: https://www.frontiersin.org/articles/10.3389/fmicb.2018.01359/full#supplementary-material

REFERENCES

Allen, M. A., Goh, F., Burns, B. P., and Neilan, B. A. (2009). Bacterial, archaeal and eukaryotic diversity of smooth and pustular microbial mat communities in the hypersaline lagoon of Shark Bay. *Geobiology* 7, 82–96. doi: 10.1111/j.1472-4669.2008.00187.x

Altschul, S. F., Gish, W., Miller, W., Myers, E. W., and Lipman, D. J. (1990). Basic local alignment search tool. *J. Mol. Biol.* 215, 403–410. doi: 10.1016/S0022-2836(05)80360-2

Awramik, S. M., Margulis, L., and Barghoorn, E. S. (1976). "Evoulutionary processes in the formation of stromatolites," in *Stromatolites*, ed. M. R. Walter (Amsterdam: Elsevier), 149–162.

Braissant, O., Decho, A. W., Dupraz, C., Glunk, C., Przekop, K. M., and Visscher, P. T. (2007). Exopolymeric substances of sulfate-reducing bacteria: interactions with calcium at alkaline pH and implication for formation of carbonate minerals. *Geobiology* 5, 401–411. doi: 10.1111/j.1472-4669.2007.00117.x

Burling, M. C., Pattiaratchi, C. B., and Ivey, G. N. (2003). The tidal regime of Shark Bay, Western Australia. *Estuar. Coast. Shelf Sci.* 57, 725–735. doi: 10.1016/s0272-7714(02)00343-8

Burne, R. V., and Johnson, K. (2012). Sea level variation and the zonation of microbialites in Hamelin Pool, Shark Bay, Western Australia. *Mar. Freshw. Res.* 63, 994–1004. doi: 10.1071/MF12184

Burne, R. V., and Moore, L. S. (1987). Microbialites: organosedimentary deposits of benthic microbial communities. *PALAIOS* 2, 241–254. doi: 10.2307/3514674

Burns, B. P., Goh, F., Allen, M., and Neilan, B. A. (2004). Microbial diversity of extant stromatolites in the hypersaline marine environment of Shark Bay, Australia. *Environ. Microbiol.* 6, 1096–1101. doi: 10.1111/j.1462-2920.2004.00651.x

Caporaso, J. G., Kuczynski, J., Stombaugh, J., Bittinger, K., Bushman, F. D., Costello, E. K., et al. (2010). QIIME allows analysis of high-throughput community sequencing data. *Nat. Methods* 7, 335–336. doi: 10.1038/nmeth.f.303

Chagas, A. A. P., Webb, G. E., Burne, R. A., and Southam, G. (2016). Modern lacustrine microbialites; towards a synthesis of aqueous and carbonate geochemistry and mineralogy. *Earth Sci. Rev.* 162, 338–363. doi: 10.1016/j.earscirev.2016.09.012

Collins, L. B., and Jahnert, R. J. (2014). Stromatolite research in the Shark Bay world heritage area. *J. R. Soc. West. Aust.* 97, 189–219.

Couradeau, E., Benzerara, K., Moreira, D., Gerard, E., Kazmierczak, J., Tavera, R., et al. (2011). Prokaryotic and eukaryotic community structure in field and cultured microbialites from the alkaline Lake Alchichica (Mexico). *PLoS One* 6:e28767. doi: 10.1371/journal.pone.0028767

Decho, A. W., and Gutierrez, T. (2017). Microbial extracellular polymeric substances (EPSs) in ocean systems. *Front. Microbiol.* 8:922. doi: 10.3389/fmicb.2017.00922

Decho, A. W., Visscher, P. T., and Reid, R. P. (2005). Production and cycling of natural microbial exopolymers (EPS) within a marine stromatolites. *Palaeogeogr. Palaeoclimatol. Palaeoecol.* 219, 71–86. doi: 10.1016/j.palaeo.2004.10.015

Des Marais, D. J. (1991). Microbial mats, stromatolites and the rise of oxygen in the Precambrian atmosphere. *Palaeogeogr. Palaeoclimatol. Palaeoecol.* 97, 93–96. doi: 10.1016/0031-0182(91)90185-T

DeSantis, T. Z., Hugenholtz, P., Larsen, N., Rojas, M., Brodie, E. L., Keller, K., et al. (2006). Greengenes, a chimera-checked 16S rRNA gene database and workbench compatible with ARB. *Appl. Environ. Microbiol.* 72, 5069–5072. doi: 10.1128/AEM.03006-05

Dill, R. F., Shinn, E. A., Jones, A. T., Kelly, K., and Steinen, R. P. (1986). Giant subtidal stromatolites forming in normal salinity water. *Nature* 324, 55–58. doi: 10.1038/324055a0

Dravis, J. J. (1983). Hardened subtidal stromatolites. *Bahamas. Science* 219, 385–386. doi: 10.1126/science.219.4583.385

Dupraz, C., Reid, R. P., Braissant, O., Decho, A. W., Norman, R. S., and Visscher, P. T. (2009). Processes of carbonate precipitation in modern microbial mats. *Earth Sci. Rev.* 96, 141–162. doi: 10.1016/j.earscirev.2008.10.005

Dupraz, C., and Visscher, P. T. (2005). Microbial lithification in marine stromatolites and hypersaline mats. *Trends Microbiol.* 13, 429–438. doi: 10.1016/j.tim.2005.07.008

Edgcomb, V. P., Bernhard, J. M., Summons, R. E., Orsi, W., Beaudoin, D., and Visscher, P. T. (2014). Active eukaryotes in microbialites from Highborne Cay, Bahamas, and Hamelin Pool (Shark Bay), Australia. *ISME J.* 8, 418–429. doi: 10.1038/ismej.2013.130

Faith, D. P. (1992). Conservation evaluation and phylogenetic diversity. *Biol. Conserv.* 61, 1–10. doi: 10.1016/0006-3207(92)91201-3

Farías, M. E., Rascovan, N., Toneatti, D. M., Albarracin, V. H., Flores, M. R., Poire, D. G., et al. (2013). The discovery of stromatolites developing at 3570 m above sea level in a high-altitude volcanic lake Socompa, Argentinean Andes. *PLoS One* 8:e53497. doi: 10.1371/journal.pone.0053497

Ferris, F. G., Thompson, J. B., and Beveridge, T. J. (1997). Modern freshwater microbialites from Kelly Lake, British Columbia, Canada. *PALAIOS* 12, 213–219. doi: 10.2307/3515423

Foster, J. S., Green, S. J., Ahrendt, S. R., Hetherington, K. L., Golubic, S., Reid, R. P., et al. (2009). Molecular and morphological characterization of cyanobacterial diversity in the marine stromatolites of Highborne Cay, Bahamas. *ISME J.* 3, 573–587. doi: 10.1038/ismej.2008.129

Foster, Z. S., Sharpton, T. J., and Grunwald, N. J. (2017). Metacoder: an R package for visualization and manipulation of community taxonomic diversity data. *PLoS Comput. Biol.* 13:e1005404. doi: 10.1371/journal.pcbi.1005404

Garby, T. J., Walter, M. R., Larkum, A. W., and Neilan, B. A. (2013). Diversity of cyanobacterial biomarker genes from the stromatolites of Shark Bay, Western Australia. *Environ. Microbiol.* 15, 1464–1475. doi: 10.1111/j.1462-2920.2012.02809.x

Ghurye, J. S., Cepeda-Espinoza, V., and Pop, M. (2016). Metagenomic assembly: overview, challenges and applications. *Yale J. Biol. Med.* 89, 353–362.

Goh, F., Allen, M. A., Leuko, S., Kawaguchi, T., Decho, A. W., Burns, B. P., et al. (2009). Determining the specific microbial populations and their spatial distribution within the stromatolite ecosystem of Shark Bay. *ISME J.* 3, 383–396. doi: 10.1038/ismej.2008.114

Goh, F., Barrow, K. D., Burns, B. P., and Neilan, B. A. (2010). Identification and regulation of novel compatible solutes from hypersaline stromatolite-associated cyanobacteria. *Arch. Microbiol.* 192, 1031–1038. doi: 10.1007/s00203-010-0634-0

Goh, F., Jeon, Y. J., Barrow, K., Neilan, B. A., and Burns, B. P. (2011). Osmoadaptive strategies of the archaeon *Halococcus hamelinensis* isolated from a hypersaline stromatolite environment. *Astrobiology* 11, 529–536. doi: 10.1089/ast.2010.0591

Golubic, S., and Campbell, S. E. (1981). "Biogenically formed aragonite concretions in marine Ribularia," in *Phanerozoic Stromatolites,* ed. C. Monty (Berlin: Springer).

Golubic, S., and Hofmann, J. J. (1976). Comparison of Holocene and mid-Precambrian Entophysalidaceae (Cyanophyta) in stromatolitic alga mats: cell division and degradation. *J. Paleontol.* 50, 1074–1082.

Grotzinger, J. P., and Knoll, A. H. (1999). Stromatolites in Precambrian carbonates: evolutionary mileposts or environmental dipsticks? *Annu. Rev. Earth Planet. Sci.* 27, 313–358. doi: 10.1146/annurev.earth.27.1.313

Gudhka, R. K., Neilan, B. A., and Burns, B. P. (2015). Adaptation, ecology, and evolution of the halophilic stromatolite archaeon *Halococcus hamelinensis* inferred through genome analyses. *Archaea* 2015:241608. doi: 10.1155/2015/241608

Gunde-Cimerman, N., Plemenitas, A., and Oren, A. (2018). Strategies of adaptation of microorganisms of the three domains of life to high salt concentrations. *FEMS Microbiol. Rev.* 42, 353–375. doi: 10.1093/femsre/fuy009

Howe, A., and Chain, P. S. (2015). Challenges and opportunities in understanding microbial communities with metagenome assembly (accompanied by IPython Notebook tutorial). *Front. Microbiol.* 6:678. doi: 10.3389/fmicb.2015.00678

Huson, D. H., Beier, S., Flade, I., Gorska, A., El-Hadidi, M., Mitra, S., et al. (2016). MEGAN community edition - interactive exploration and analysis of large-scale microbiome sequencing data. *PLoS Comput. Biol.* 12:e1004957. doi: 10.1371/journal.pcbi.1004957

Inskeep, W. P., Macur, R. E., Harrison, G., Bostick, B. C., and Fendorf, S. (2004). Biomineralization of As(V)-hydrous ferric oxyhydroxide in microbial mats of an acid-sulfate-chloride geothermal spring, Yellowstone National Park. *Geochim. Cosmochim. Acta* 68, 3141–3155. doi: 10.1016/j.gca.2003.09.020

Jahnert, R. J., and Collins, J. B. (2012). Characteristics distribution and morphogenesis of subtidal microbial systems in Shark Bay, Australia. *Mar. Geol.* 30, 115–136. doi: 10.1016/j.margeo.2012.02.009

Jahnert, R. J., and Collins, L. B. (2011). Significance of subtidal microbial deposits in Shark Bay, Australia. *Mar. Geol.* 286, 106–111. doi: 10.1016/j.margeo.2011.05.006

Jahnert, R. J., and Collins, L. B. (2013). Controls on microbial activity and tidal flat evolution in Shark Bay, Western Australia. *Sedimentology* 60, 1071–1099. doi: 10.1111/sed.12023

Joshi, N., and Fass, J. (2011). *Sickle: A Sliding-Window, Adaptive, Quality-Based Trimming Tool for FastQ Files (Version 1.33)*. Available at: https://github.com/najoshi/sickle

Kanehisa, M., Goto, S., Kawashima, S., Okuno, Y., and Hattori, M. (2004). The KEGG resource for deciphering the genome. *Nucleic Acids Res.* 32, D277–D280. doi: 10.1093/nar/gkh063

Kawaguchi, T., and Decho, A. W. (2002). Isolation and biochemical characterization of extracellular polymeric secretions (EPS) from modern soft marine stromatolites (Bahamas) and its inhibitory effect on $CaCO_3$ precipitation. *Prep. Biochem. Biotechnol.* 32, 51–63. doi: 10.1081/PB-120013161

Khodadad, C. L., and Foster, J. S. (2012). Metagenomic and metabolic profiling of nonlithifying and lithifying stromatolitic mats of Highborne Cay, The Bahamas. *PLoS One* 7:e38229. doi: 10.1371/journal.pone.0038229

Kopylova, E., Noe, L., and Touzet, H. (2012). SortMeRNA: fast and accurate filtering of ribosomal RNAs in metatranscriptomic data. *Bioinformatics* 28, 3211–3217. doi: 10.1093/bioinformatics/bts611

Kulp, T. R., Han, S., Saltikov, C. W., Lanoil, B. D., Zargar, K., and Oremland, R. S. (2007). Effects of imposed salinity gradients on dissimilatory arsenate reduction, sulfate reduction, and other microbial processes in sediments from two California soda lakes. *Appl. Environ. Microbiol.* 73, 5130–5137. doi: 10.1128/AEM.00771-07

Kulp, T. R., Hoeft, S. E., Asao, M., Madigan, M. T., Hollibaugh, J. T., Fisher, J. C., et al. (2008). Arsenic(III) fuels anoxygenic photosynthesis in hot spring biofilms from Mono Lake, California. *Science* 321, 967–970. doi: 10.1126/science.1160799

Kurth, D., Amadio, A., Ordonez, O. F., Albarracin, V. H., Gartner, W., and Farias, M. E. (2017). Arsenic metabolism in high altitude modern stromatolites revealed by metagenomic analysis. *Sci. Rep.* 7:1024. doi: 10.1038/s41598-017-00896-0

Laval, B., Cady, S. L., Pollack, J. C., McKay, C. P., Bird, J. S., Grotzinger, J. P., et al. (2000). Modern freshwater microbialite analogues for ancient dendritic reef structures. *Nature* 407, 626–629. doi: 10.1038/35036579

Lindsay, M. R., Anderson, C., Fox, N., Scofield, G., Allen, J., Anderson, E., et al. (2017). Microbialite response to an anthropogenic salinity gradient in Great Salt Lake, Utah. *Geobiology* 15, 131–145. doi: 10.1111/gbi.12201

Logan, B. W. (1961). Cryptozoon and associated stromatolites from the recent, Shark Bay, Western Australia. *J. Geol.* 69, 517–533. doi: 10.1086/626769

Logan, B. W., Hoffman, P., and Gebelein, C. D. (1974). "Alga mats, cryptalgal fabrics and structures, Hamelin Pool, Western Australia," in *Evolution and diagenesis of quaternary carbonate sequences, Shark Bay, Western Australia*, ed. B. W. Logan (Tulsa, OK: American Association of Petrology), 140–194.

Louyakis, A. S., Gourle, H., Casaburi, G., Bonjawo, R. M. E., Duscher, A. A., and Foster, J. S. (2018). A year in the life of a thrombolite: comparative metatranscriptomics reveals dynamic metabolic changes over diel and seasonal cycles. *Environ. Microbiol.* 20, 842–861. doi: 10.1111/1462-2920.14029

Louyakis, A. S., Mobberley, J. M., Vitek, B. E., Visscher, P. T., Hagan, P. D., Reid, R. P., et al. (2017). A study of the microbial spatial heterogeneity of Bahamian thrombolites using molecular, biochemical, and stable isotope analyses. *Astrobiology* 17, 413–430. doi: 10.1089/ast.2016.1563

Love, M. I., Huber, W., and Anders, S. (2014). Moderated estimation of fold change and dispersion for RNA-seq data with DESeq2. *Genome Biol.* 15:550. doi: 10.1186/s13059-014-0550-8

Lundberg, J., and McFarlane, D. A. (2011). Subaerial freshwater phosphatic stromatolites in Deer Cave, Sarawak—A unique geobiological cave formation. *Geomorphology* 128, 57–72. doi: 10.1016/j.geomorph.2010.12.022

Lyons, T. W., Reinhard, C. T., and Planavsky, N. J. (2014). The rise of oxygen in Earth's early ocean and atmosphere. *Nature* 506, 307–315. doi: 10.1038/nature13068

McMurdie, P. J., and Holmes, S. (2014). Waste not, want not: why rarefying microbiome data is inadmissible. *PLoS Comput. Biol.* 10:e1003531. doi: 10.1371/journal.pcbi.1003531

Mobberley, J. M., Khodadad, C. L., Visscher, P. T., Reid, R. P., Hagan, P., and Foster, J. S. (2015). Inner workings of thrombolites: spatial gradients of metabolic activity as revealed by metatranscriptome profiling. *Sci. Rep.* 5:12601. doi: 10.1038/srep12601

Nutman, A. P., Bennett, V. C., Friend, C. R., Van Kranendonk, M. J., and Chivas, A. R. (2016). Rapid emergence of life shown by discovery of 3,700-million-year-old microbial structures. *Nature* 537, 535–538. doi: 10.1038/nature19355

Oksanen, J. (2017). *Vegan: An Introduction to Ordination. R Package Version*. Available at: https://cran.r-project.org/web/packages/vegan/vignettes/intro-vegan.pdf

Oren, A. (1999). Bioenergetic aspects of halophilism. *Microbiol. Mol. Biol. Rev.* 63, 334–348.

Osborne, R. H., Licari, G. R., and Link, M. H. (1982). Modern lacustrine stromatolites, Walker Lake, Nevada. *Sediment. Geol.* 32, 39–61. doi: 10.1016/0037-0738(82)90013-6

Pace, A., Bourillot, R., Bouton, A., Vennin, E., Braissant, O., Dupraz, C., et al. (2018). Formation of stromatolite lamina at the interface of oxygenic-anoxygenic photosynthesis. *Geobiology* 16, 378–398. doi: 10.1111/gbi.12281

Papineau, D., Walker, J. J., Mojzsis, S. J., and Pace, N. R. (2005). Composition and structure of microbial communities from stromatolites of Hamelin Pool in Shark Bay, Western Australia. *Appl. Environ. Microbiol.* 71, 4822–4832. doi: 10.1128/AEM.71.8.4822-4832.2005

Pepe-Ranney, C., Berelson, W. M., Corsetti, F. A., Treants, M., and Spear, J. R. (2012). Cyanobacterial construction of hot spring siliceous stromatolites in Yellowstone National Park. *Environ. Microbiol.* 14, 1182–1197. doi: 10.1111/j.1462-2920.2012.02698.x

Playford, P. E. (1990). "Geology of the Shark Bay area, Western Australia," in *Research in Shark Bay*, eds P. F. Berry, S. D. Bradshaw, and B. R. Wilson (Perth: Western Australia Museum), 13–31.

Playford, P. E., and Cockbain, A. E. (1976). "Modern algal stromatolites at Hamelin Pool, a hypersaline barred basin in Shark Bay, Western Australia," in *Stromatolites - Developments in Sedimentology*, ed. M. R. Walter (Amsterdam: Elsevier), 389–411.

Playford, P. E., Cockbain, A. E., Berry, P. F., Roberts, A. P., Haines, P. W., and Brooke, B. P. (2013). *The Geology of Shark Bay*. Berlin: Geological Survey of Western Australia, 299.

Proemse, B. C., Eberhard, R. S., Sharples, C., Bowman, J. P., Richards, K., Comfort, M., et al. (2017). Stromatolites on the rise in peat-bound karstic wetlands. *Sci. Rep.* 7:15384. doi: 10.1038/s41598-017-15507-1

Quast, C., Pruesse, E., Yilmaz, P., Gerken, J., Schweer, T., Yarza, P., et al. (2013). The SILVA ribosomal RNA gene database project: improved data processing and web-based tools. *Nucleic Acids Res.* 41, D590–D596. doi: 10.1093/nar/gks1219

Reid, R. P., James, N. P., Macintyre, I. G., and Dupraz, C. P. (2003). Shark Bay stromatolites: microfabrics and reinterpretation of origins. *FACIES* 49, 299–324.

Reid, R. P., Visscher, P. T., Decho, A. W., Stolz, J. F., Bebout, B. M., Dupraz, C., et al. (2000). The role of microbes in accretion, lamination and early lithification of modern marine stromatolites. *Nature* 406, 989–992. doi: 10.1038/35023158

Riding, R. (2000). Microbial carbonates: the geological record of calcified bacterial-algal mats and biofilms. *Sedimentology* 47, 179–214. doi: 10.1046/j.1365-3091.2000.00003.x

Riethman, H., Bullerjahn, G. S., Reddy, K. J., and Sherman, L. A. (1988). "Regulation of cyanobacterial pigment-protein composition and organization by environmental factors," in *Molecular Biology of Photosynthesis*, ed. Govinedjee (Dordrecht: Springer), 229–257.

Rocap, G., Larimer, F. W., Lamerdin, J., Malfatti, S., Chain, P., Ahlgren, N. A., et al. (2003). Genome divergence in two Prochlorococcus ecotypes reflects oceanic niche differentiation. *Nature* 424, 1042–1047. doi: 10.1038/nature01947

Rodriguez-R, L. M., Overholt, W. A., Hagan, C., Huettel, M., Kostka, J. E., et al. (2015). Microbial community successional patterns in beach sands impacted by the Deepwater Horizon oil spill. *ISME J.* 9, 1928–1940. doi: 10.1038/ismej.2015.5

Ruvindy, R., White, R. A. III, Neilan, B. A., and Burns, B. P. (2016). Unravelling core microbial metabolisms in the hypersaline microbial mats of Shark Bay using high-throughput metagenomics. *ISME J.* 10, 183–196. doi: 10.1038/ismej.2015.87

Schneider, D., Arp, G., Reimer, A., Reitner, J., and Daniel, R. (2013). Phylogenetic analysis of a microbialite-forming microbial mat from a hypersaline lake of the Kiritimati atoll, Central Pacific. *PLoS One* 8:e66662. doi: 10.1371/journal.pone.0066662

Shannon, C. E., and Weaver, W. (1949). *The Mathematical Theory of Communication.* Urbana, IL: University of Illinois Press.

Souza, V., Espinosa-Asuar, L., Escalante, A. E., Eguiarte, L. E., Farmer, J., Forney, L., et al. (2006). An endangered oasis of aquatic microbial biodiversity in the Chihuahuan desert. *Proc. Natl. Acad. Sci. U.S.A.* 103, 6565–6570. doi: 10.1073/pnas.0601434103

Sudhir, P., and Murthy, S. D. S. (2004). Effects of salt stress on basic processes of photosynthesis. *Photosynthetica* 42, 481–486. doi: 10.1007/S11099-005-0001-6

Suosaari, E. P., Reid, R. P., Abreau, T. A., Playford, P. E., Holley, D. K., McNamara, K. J., et al. (2016a). Environmental pressures influencing living stromatolites in Hamelin Pool, Shark Bay, Western Australia. *PALAIOS* 31, 483–496. doi: 10.2110/palo.2016.023

Suosaari, E. P., Reid, R. P., Playford, P. E., Foster, J. S., Stolz, J. F., Casaburi, G., et al. (2016b). New multi-scale perspectives on the stromatolites of Shark Bay, Western Australia. *Sci. Rep.* 6:20557. doi: 10.1038/srep20557

Swingley, W. D., Chen, M., Cheung, P. C., Conrad, A. L., Dejesa, L. C., Hao, J., et al. (2008). Niche adaptation and genome expansion in the chlorophyll d-producing cyanobacterium *Acaryochloris marina*. *Proc. Natl. Acad. Sci. U.S.A.* 105, 2005–2010. doi: 10.1073/pnas.0709772105

The UniProt Consortium (2017). UniProt: the universal protein knowledgebase. *Nucleic Acids Res.* 45, D158–D169. doi: 10.1093/nar/gkw1099

Theisen, C. H., Sumner, D. Y., Mackey, T. J., Lim, D. S., Brady, A. L., and Slater, G. F. (2015). Carbonate fabrics in the modern microbialites of Pavilion Lake: two suites of microfabrics that reflect variation in microbial community morphology, growth habit, and lithification. *Geobiology* 13, 357–372. doi: 10.1111/gbi.12134

Visscher, P. T., Reid, R. P., and Bebout, B. M. (2000). Microscale observations of sulfate reduction: correlation of microbial activity with lithified micritic laminae in modern marine stromatolites. *Geology* 28, 919–922. doi: 10.1130/0091-7613(2000)28<919:MOOSRC>2.0.CO;2

Visscher, P. T., Reid, R. P., Bebout, B. M., Hoeft, S. E., Macintyre, I. G., and Thompson, J. A. (1998). Formation of lithified micritic laminae in modern marine stromatolites (Bahamas): the role of sulfur cycling. *Am. Mineral.* 83, 1482–1493. doi: 10.2138/am-1998-11-1236

Visscher, P. T., and Stolz, J. F. (2005). Microbial mats as bioreactors: populations, processes and products. *Palaeogeogr. Palaeoclimatol. Palaeoecol.* 219, 87–100. doi: 10.1016/j.palaeo.2004.10.016

Walter, M. R. (1976). *Developments in Sedimentology: Stromatolites*. Amsterdam: Elsevier.

Warden, J. G., Casaburi, G., Omelon, C. R., Bennett, P. C., Breecker, D. O., and Foster, J. S. (2016). Characterization of microbial mat microbiomes in the modern thrombolite ecosystem of Lake Clifton, Western Australia using shotgun metagenomics. *Front. Microbiol.* 7:1064. doi: 10.3389/fmicb.2016.01064

White, R. A., Chan, A. M., Gavelis, G. S., Leander, B. S., Brady, A. L., Slater, G. F., et al. (2016). Metagenomic analysis suggests modern freshwater microbialites harbor a distinct core microbial community. *Front. Microbiol.* 6:1531. doi: 10.3389/fmicb.2015.01531

Wickham, H. (2009). *ggplot2: Elegant Graphics for Data Analysis*. Berlin: Springer Science & Business Media. doi: 10.1007/978-0-387-98141-3

Wong, H. L., Smith, D. L., Visscher, P. T., and Burns, B. P. (2015). Niche differentiation of bacterial communities at a millimeter scale in Shark Bay microbial mats. *Sci. Rep.* 5:15607. doi: 10.1038/srep15607

Wong, H. L., Visscher, P. T., White Iii, R. A., Smith, D. L., Patterson, M. M., and Burns, B. P. (2017). Dynamics of archaea at fine spatial scales in Shark Bay mat microbiomes. *Sci. Rep.* 7:46160. doi: 10.1038/srep46160

Conflict of Interest Statement: The authors declare that the research was conducted in the absence of any commercial or financial relationships that could be construed as a potential conflict of interest.

frontiers in Microbiology

ORIGINAL RESEARCH
published: 13 July 2018
doi: 10.3389/fmicb.2018.01464

Environmental and Biological Influences on Carbonate Precipitation Within Hot Spring Microbial Mats in Little Hot Creek, CA

Dylan T. Wilmeth[1], Hope A. Johnson[2], Blake W. Stamps[3], William M. Berelson[1], Bradley S. Stevenson[4], Heather S. Nunn[4], Sharon L. Grim[5], Megan L. Dillon[6], Olivia Paradis[1], Frank A. Corsetti[1] and John R. Spear[3]**

[1] Department of Earth Sciences, University of Southern California, Los Angeles, CA, United States, [2] Department of Biological Science, California State University, Fullerton, Fullerton, CA, United States, [3] Geo- Environmental- Microbiology Laboratory, Department of Civil and Environmental Engineering, Colorado School of Mines, Golden, CO, United States, [4] Department of Microbiology and Plant Biology, University of Oklahoma, Norman, OK, United States, [5] Geomicrobiology Laboratory, Department of Earth and Environmental Sciences, University of Michigan, Ann Arbor, MI, United States, [6] Department of Earth and Planetary Sciences, University of California, Davis, Davis, CA, United States

OPEN ACCESS

Edited by:
Christophe Dupraz,
Stockholm University, Sweden

Reviewed by:
David Moreira,
Centre National de la Recherche Scientifique (CNRS), France
Karim Benzerara,
Centre National de la Recherche Scientifique (CNRS), France

***Correspondence:**
Dylan T. Wilmeth
dylan.wilmeth@gmail.com
John R. Spear
jspear@mines.edu

Specialty section:
This article was submitted to Aquatic Microbiology, a section of the journal Frontiers in Microbiology

Received: 01 December 2017
Accepted: 12 June 2018
Published: 13 July 2018

Citation:
Wilmeth DT, Johnson HA, Stamps BW, Berelson WM, Stevenson BS, Nunn HS, Grim SL, Dillon ML, Paradis O, Corsetti FA and Spear JR (2018) Environmental and Biological Influences on Carbonate Precipitation Within Hot Spring Microbial Mats in Little Hot Creek, CA. Front. Microbiol. 9:1464. doi: 10.3389/fmicb.2018.01464

Microbial mats are found in a variety of modern environments, with evidence for their presence as old as the Archean. There is much debate about the rates and conditions of processes that eventually lithify and preserve mats as microbialites. Here, we apply novel tracer experiments to quantify both mat biomass addition and the formation of $CaCO_3$. Microbial mats from Little Hot Creek (LHC), California, contain calcium carbonate that formed within multiple mat layers, and thus constitute a good test case to investigate the relationship between the rate of microbial mat growth and carbonate precipitation. The laminated LHC mats were divided into four layers via color and fabric, and waters within and above the mat were collected to determine their carbonate saturation states. Samples of the microbial mat were also collected for 16S rRNA analysis of microbial communities in each layer. Rates of carbonate precipitation and carbon fixation were measured in the laboratory by incubating homogenized samples from each mat layer with $\delta^{13}C$-labeled HCO_3^- for 24 h. Comparing these rates with those from experimental controls, poisoned with NaN_3 and $HgCl_2$, allowed for differences in biogenic and abiogenic precipitation to be determined. Carbon fixation rates were highest in the top layer of the mat (0.17% new organic carbon/day), which also contained the most phototrophs. Isotope-labeled carbonate was precipitated in all four layers of living and poisoned mat samples. In the top layer, the precipitation rate in living mat samples was negligible although abiotic precipitation occurred. In contrast, the bottom three layers exhibited biologically enhanced carbonate precipitation. The lack of correlation between rates of carbon fixation and biogenic carbonate precipitation suggests that processes other than autotrophy may play more significant roles in the preservation of mats as microbialites.

Keywords: microbial mat, carbonate precipitation, biomineralization, carbon fixation, hot spring

INTRODUCTION

Microbial mats have been preserved within the rock record over 3.5 billion years (Walter et al., 1980; Noffke et al., 2006; Schopf, 2006; Bosak et al., 2009). Structures attributed to microbial precipitation of carbonate minerals, commonly termed microbialites, are particularly common in the geologic past (Awramik and Sprinkle, 1999; Grotzinger and Knoll, 1999; Riding, 2000; Bosak et al., 2013). Despite the ubiquity of microbial mats in a variety of modern aqueous environments, few appear to be mineralized in a way that would lead to the preservation of a microbialite. When identified, modern microbial mats that precipitate minerals provide potential analogs for the formation of ancient microbialites (Reid et al., 2000; Visscher et al., 2000; Dupraz et al., 2004, 2009; Dupraz and Visscher, 2005; Vasconcelos et al., 2006; Mata et al., 2012).

The metabolic activity within microbial mats and the physicochemical changes in the surrounding environment can influence mineral saturation states and induce mineral precipitation (Grotzinger and Knoll, 1999). This study defines mineralization that occurs when the activities of living microbes act to enhance precipitation as *biogenic precipitation* (see also "organomineralization *sensu stricto*" in Trichet and Defarge, 1995, "microbially induced precipitation" in Dupraz et al., 2009). Mineralization within mats that is independent of living microbial activity is defined as *abiogenic precipitation* (see also "biologically influenced precipitation" in Frankel and Bazylinski, 2003; Dupraz et al., 2009). Three factors can influence the precipitation of calcium carbonate within microbial mats, whether biogenic or abiogenic in nature: the concentrations of CO_3^{2-} ions, Ca^{2+} ions, and surface chemistry or nucleation centers (Dupraz et al., 2009). The first two factors relate to the saturation state of calcium carbonate, defined as omega (Ω), the product of calcium and carbonate ion concentrations divided by the solubility constant K_{sp}' for the appropriate mineral (where the symbol ' accounts for the activities of Ca^{2+} and CO_3^{2-}). When calcium carbonate is at equilibrium in solution, $\Omega = 1$, with under- and over-saturated solutions bearing lower and higher values, respectively. The third factor relates to the potential for locations within microbial mats to serve as nuclei for carbonate minerals to form (Arp et al., 1999a; Dupraz et al., 2009).

Certain metabolisms have been studied as candidates for inducing biogenic carbonate precipitation, including oxygenic photosynthesis (Pentecost and Riding, 1986; Merz-Preiß and Riding, 1999; Riding, 2000), anoxygenic photosynthesis (Bundeleva et al., 2012), sulfate reduction (Visscher et al., 2000; Dupraz et al., 2004; Baumgartner et al., 2006; Gallagher et al., 2012), and anaerobic oxidation of methane (Michaelis et al., 2002). For example, cyanobacteria increase saturation through carbon fixation by raising pH and removing CO_2. Cyanobacteria can also produce abundant exopolymeric substances which can serve as nucleation centers for carbonate precipitation (De Philippis et al., 1998; Obst et al., 2009). However, precipitation induced via cyanobacterial photosynthesis occurs primarily in freshwater environments with low dissolved inorganic carbon and high calcium concentrations, and is not correlated with areas of increased carbon fixation (Arp et al., 1999a,b, 2001; Merz-Preiß and Riding, 1999). In lakes with high dissolved inorganic carbon, aragonite precipitation is only associated with cyanobacteria which contain an external fibrous layer on cell walls (Couradeau et al., 2013; Gérard et al., 2013). Finally, internal accumulation of calcium has been observed in multiple cyanobacterial lineages from lacustrine environments and hot springs (Ragon et al., 2014; Cam et al., 2018). Therefore, external environmental factors, cellular morphologies, and intracellular chemistry can affect precipitation in microbial mats even when metabolisms that increase carbonate saturation are abundant.

One method used to examine biologically induced precipitation is the comparison of metabolic rates with patterns of carbonate mineralization within microbial mats. However, studies directly comparing rates of precipitation and metabolic activity remain limited. Within modern Bahamian stromatolites, laminae with high sulfate reduction rates coincide with zones of carbonate precipitation (Visscher et al., 2000; Dupraz et al., 2004). Rates of sulfate reduction were measured using incubations with ^{35}S-labeled SO_4^{2-}, while carbonate precipitation was assessed through petrographic analysis (Visscher et al., 2000). In contrast, numerical models of metabolic impact on carbonate saturation hypothesize that sulfate reduction coupled with H_2S oxidation decreases Ω (Aloisi, 2008). Bundeleva et al. (2012) found a correlation between carbonate precipitation and biomass production through anoxygenic photoheterotrophic growth with pure cultures of the proteobacterium *Rhodovulum* in supersaturated solutions ($\Omega = 10$–120).

Measuring carbonate precipitation rates within microbial mats complements constraints on microbialite growth rates determined in studies of stromatolite accretion. Previous hypotheses have suggested that stromatolite laminae form daily via the diurnal activity of cyanobacteria (Doemel and Brock, 1974; Golubic and Focke, 1978; Pepe-Ranney et al., 2012). In contrast, studies of Holocene stromatolites using ^{14}C dating suggest seasonal or even multiyear lamination rates (Chivas et al., 1990; Berelson et al., 2011; Petryshyn et al., 2012). The variability in stromatolite accretion rates is likely due to the variety of biogenic and abiogenic precipitation mechanisms within microbial mats. Comparing precipitation rates in relation to specific metabolisms or physicochemical processes in turn provides constraints for modern and ancient microbialite growth.

This study examines the effects of microbial metabolism and environmental factors on nascent carbonate precipitation within microbial mats from Little Hot Creek (LHC), California by focusing on the rate of carbon fixation into biomass and concomitant carbonate precipitation. Isotope labeling experiments were used to compare rates of carbonate precipitation and autotrophic production of organic carbon during incubations with ^{13}C enriched bicarbonate. Rates of precipitation were compared between active and poisoned microbial mats to discern biogenic from abiogenic carbonate production.

SITE DESCRIPTION AND PREVIOUS WORK

Little Hot Creek is a stream sourced from hydrothermal springs within the Long Valley Caldera of eastern California (**Figures 1A,B**). The source of LHC is on the eastern flank of a resurgent dome formed by a rising magma chamber beneath the caldera (Sorey et al., 2003). Thermal waters emerge at ∼80°C from several vents (Vick et al., 2010). The vents discharge into LHC, where the waters cool to ∼50°C over the course of approximately 30 m. Several recent studies have characterized the microbiology and geochemistry of parts of the site. Vick et al. (2010) examined the microbial complement of the LHC source vents, and determined that groups related to the *Aquificae* and *Thermodesulfobacteria*, among others, were present in the hottest portions of the system, where the thermal waters discharge onto the surface. Source vent environments had circumneutral pH (6.75) and calcium concentrations ∼0.55 mM (Vick et al., 2010). Breitbart et al. (2004) examined phage–microbial interactions in LHC streams from several vent sources. While specific taxa were not described, the microbial communities at one location several meters downstream (74°C, pH 7.7) had a turnover rate of under one day based on labeled thymidine incubations (Breitbart et al., 2004). Dendrolitic cone structures in microbial mats from a cooler, adjacent pool (45°C) have also been studied as a potential analog for ancient microbialites (Bradley et al., 2017; Kraus et al., 2018).

Extensive microbial mats occur 25 m downstream from source waters, where flow velocity decreases as the creek bed widens from <1 to 8 m across (**Figure 1C**). Textures and mat thickness differ between wholly subaqueous mats and those at the creek surface. Subaqueous mats occur toward the center of the creek and are predominantly green with small orange patches (**Figure 1C**). Portions of the subaqueous mats several centimeters wide are partially detached from the creek bed, forming "rollover structures" (Hagadorn and Mcdowell, 2012) and exposing patches of underlying sediment. The resulting voids indicate a maximum mat thickness of 1–2 cm. In contrast, surficial mats are orange to tan, and usually extend from creek margins up to 1 m into LHC (**Figures 1C,D**), with smaller patches in the middle of the stream. Surficial mats rise up to 10 cm above the LHC creek bed, often reaching the creek's surface. Surficial mat textures are clotted, and do not exhibit rollover features seen in subaqueous mats.

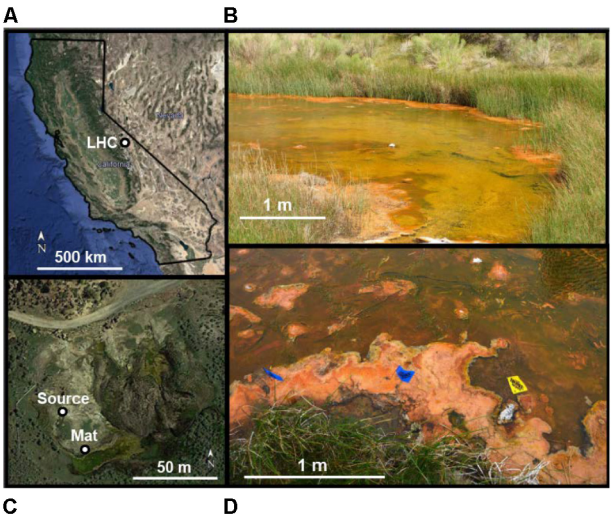

FIGURE 1 | Location of Little Hot Creek (LHC) microbial mats. **(A)** Map of California. **(B)** View of mat location area looking east (downstream). Mat sampling and field geochemistry was performed on left-hand creek margin. Green areas toward the center of creek flow represent subaqueous mats, orange areas on creek margins represent mats at creek surfaces. **(C)** Aerial overview of LHC source and mat location. **(D)** Location of mat sampling and field geochemistry. Creek flow is from right to left. The yellow flag represents the Upstream location for field geochemistry, while the left blue flag represents the Downstream location (see **Table 1**). The orange surficial mat was sampled between the middle blue flag and the yellow flag (see **Figure 2A**).

METHODS

Field Geochemical Analysis

Microbial mats and creek waters were sampled ∼30 m downstream from LHC headwaters (**Figure 1B**). Temperature, pH, calcium concentrations, TCO_2 ($H_2CO_3 + HCO_3^- + CO_3^{2-}$), and $\delta^{13}C$ of the TCO_2 were measured in pore waters 1 and 5 cm deep within the sampled mat. Measurements were also made in stream waters 20 cm upstream, and 80 cm downstream from the mat. All field geochemical measurements were performed at the same time (June 2015), except for pH values within mat pore water, which were measured in August 2015. Temperature, TCO_2, $\delta^{13}C$, calcium concentrations, and stream water pH values were virtually identical in June and August, increasing the confidence in using August pore water pH values to calculate saturation states. Saturation states of calcium carbonate within and around the LHC mat were calculated in CO2SYS (Pierrot et al., 2006) using pH data from a SevenGo Duo pH meter (Mettler Toledo) and TCO_2 data obtained using a cavity ring-down spectrometer (CRDS; Picarro). Samples for calcium analysis were collected from the stream using a clean 20 mL syringe, filtered onsite with a 0.45 micron filter, and preserved with two drops of HCl. Calcium concentration was measured on the acidified sample using a microwave induced plasma-optical emission spectrometer (Agilent).

Mat Extraction and Description

A piece of surficial microbial mat was selected for removal from LHC (**Figure 2A**). After extraction, the sampled mat was placed in a container lined with sterile aluminum foil, along with LHC water from around the mat to prevent desiccation, and was stored and transported on ice before laboratory analyses. The sampled LHC mat was divided into four layers based on texture and color (**Figure 2B**). Minerals from all layers were examined

using an environmental scanning electron microscope (SEM). No preparation of sample was required for SEM examination.

Incubation Experiments

The rates of biogenic carbonate precipitation and autotrophic production of organic carbon in each layer were determined using incubation experiments with ^{13}C-labeled HCO_3^-. Prior to incubation, each layer was homogenized and separated into two sample groups – one for organic $\delta^{13}C$ analysis and the other for inorganic $\delta^{13}C$ analysis. In both groups, three sets of triplicate samples ∼2–3 mg each, (9 total) were prepared from each layer: (i) "Negative Control": $\delta^{13}C$ values of mat carbonates and organic carbon were obtained without incubation or addition of $\delta^{13}C$ label; (ii) "Poisoned Control": Mat samples were placed into 2 mL glass vials containing 10 μL of 300 mM NaN_3 and saturated $HgCl_2$ solution to poison the mat, filled and capped without headspace with LHC water amended with 5 mM HCO_3^- and a $\delta^{13}C$ label of +2000 ‰; (iii) "Living": Mat samples were placed into 2 mL vials and filled and capped without headspace with LHC water amended with 5 mM HCO_3^-, and a $\delta^{13}C$ label of +2000 ‰. **Table 1** gives the initial carbonate parameters for the stream and microbial mat pore water.

For both carbonate precipitation and organic carbon production experiments, Poisoned Controls and Living samples were incubated for 24 h at 40°C. To account for changing metabolism over a diel cycle, the incubator was set on a 12-h light/dark cycle. After incubation, samples for organic $\delta^{13}C$ analyses were treated with 1M HCl until effervescence ceased. All incubations were washed with phosphate-buffered saline (PBS) three times by centrifugation, decanting of the supernatant, and suspension of the pellet, in order to remove labeled HCO_3^- that was not incorporated into carbonates or organic material. After HCl treatment and the PBS wash, all samples were oven-dried at 60°C.

Dried samples were ground, weighed (1–3 mg) and measured for % C and $\delta^{13}C$ on a Picarro CRDS (Santa Clara, CA, United States) (Supplementary Tables S1 and S2). Samples analyzed for carbonates were acidified with phosphoric acid in a closed vessel, with evolved CO_2 passing into the Picarro CRDS. Organic carbon was analyzed on de-carbonated samples by oxidizing dried material at 1000°C in a Costech Elemental Analyzer and passing CO_2 into the Picarro. The averages of triplicate $\delta^{13}C$ measurements for Living and Poisoned Control incubations were compared with averages of Negative Control samples from respective layers. Heavier $\delta^{13}C$ values in Living and Poisoned Control incubated samples compared to Negative Control samples indicated incorporation of labeled HCO_3^- by carbonate precipitation (in the case of carbonate analysis) or production of autotrophic organic carbon (in samples combusted via EA).

An analysis of the significance of different isotope values for different treatments was determined by comparing $\delta^{13}C$ triplicate averages (Δ_{avg}) with distributions of potential Δ_{avg} values using bootstrap analyses (Efron, 1979; Efron and Tibshirani, 1986). After calculating the experimental Δ_{avg} between two triplicate averages (Δ_{avg}^{exp}), $\delta^{13}C$ values from all six samples were resampled at random to create two novel triplicate sets. The difference in these two resampled triplicate sets produced a new Δ_{avg} value (Δ_{avg}^{res}). $\delta^{13}C$ values were resampled with replacement, which indicates that a single $\delta^{13}C$ value can be selected multiple times. For example, resampling with replacement can produce two triplicates where all six $\delta^{13}C$ values are the same, producing a Δ_{avg}^{res} of 0. Repeating the resampling process 1000 times produced distributions of Δ_{avg}^{res} values which were then compared with the measured Δ_{avg}^{exp}. Values of Δ_{avg}^{exp} greater than 95% of Δ_{avg}^{res} distributions (p = 0.05) were evaluated as non-random representations of $\delta^{13}C$ that increased during incubation experiments, supporting the hypothesis that carbonate precipitation or carbon fixation occurred. Values of Δ_{avg}^{exp} were also compared with the Δ_{avg} that could be produced by machine variability alone on two identical triplicates (Δ_{avg}^{mac}). The standard deviation (σ) for multiple CRDS $\delta^{13}C$ measurements is conservatively ±0.1 ‰ (Subhas et al., 2015) σ for a triplicate average is 0.058 ‰ ($0.1 \times 3^{-0.5}$), and σ for Δ_{avg} is 0.082 ‰ [$(0.058^2 + 0.058^2)^{0.5}$]. The Δ_{avg}^{exp} values which were larger than

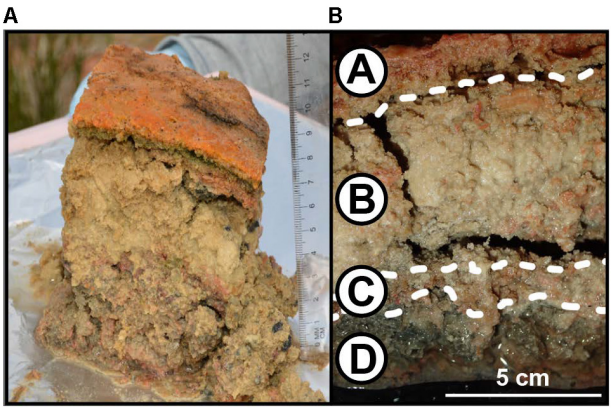

FIGURE 2 | Structure of LHC microbial mats. **(A)** Microbial mat sample immediately after extraction. Note the distinct textural difference between the mat surface (Layer A) and the layers below (Layers B, C, and D). Scale bar is in cm. **(B)** Microbial mat after transport from field to laboratory. Layer A represents the mat surface, Layer D represents the mat bottom.

TABLE 1 | Field measurements of stream water and pore water at LHC taken in June 2015.

Location	Upstream 20 cm	Downstream 80 cm	Mat porewater: 1 cm (A/B boundary)	Mat porewater: 5 cm (Layer B)
T (°C)	52.4	38.1	38.8	48.4
TCO_2 (mM)	11.91	11.88	11.52	11.59
$\delta^{13}C$ (‰)	−2.58	−2.49	−2.06	−2.23
pH	8.34	8.29	8.10*	8.30*
Ω	4.62	3.50	3.23	4.27

**Indicates measurements taken in August 2015. Upstream and Downstream locations are relative to the sampled mat.*

2σ (0.164 ‰) have less than 5% probability of machine variability as an origin, while Δ_{avg}^{exp} values less than σ have a 14% or higher probability.

The amount of new inorganic or organic carbon produced during incubations was calculated using an isotope mass balance approach. Our primary assumption was that new carbonate or autotrophic organic carbon would incorporate the heavier $\delta^{13}C$ value of the HCO_3^- label with no significant fractionation. In making our isotope mass balance, we use the fractional abundance of $^{13}C/(^{12}C + {}^{13}C)$] in Living and Poisoned Control samples with the bicarbonate label before and after incubation as per Hayes (1983).

$$\text{Percent new growth} = (1 - (F_{\text{Living}} - F_{HCO_3^-})/ (F_{\text{Poisoned control}} - F_{HCO_3^-})) \times 100 \quad (1)$$

F represents the $^{13}C/^{12}C$ ratio in each component measured, and HCO_3^- denotes the bicarbonate spike value. Abiogenic carbonate production rates were calculated by replacing the fractional abundances for Living and Poisoned Control with Poisoned Control and Negative Control, respectively. The solution to Eq. 1 was turned into a rate by dividing percent new carbon production by the incubation time (24 h), and were expressed as % new carbon/day.

DNA and Community Composition Analysis

The bacterial and archaeal composition of LHC mats was determined by sequencing amplified libraries of small subunit ribosomal RNA (16S rRNA) genes. Field samples of all layers were amplified and sequenced in triplicate, with subsequent single analyses of mat samples taken from each layer immediately before and after incubation.

Extraction of DNA from each sample was performed using the *Xpedition* Soil/Fecal DNA MiniPrep kit according to manufacturer's instructions (Zymo Research Corp., Irvine, CA, United States). Extracted DNA was amplified using primers that spanned the V4 region of the 16S rRNA gene between positions 519 and 802 (*Escherichia coli* numbering), producing a product of approximately 266 bp. The primer pair amplified a broad distribution of both the Bacteria and Archaea (Klindworth et al., 2013). The forward primer (M13L-519F: 5′-**GTA AAA CGA CGG CCA GCA** CMG CCG CGG TAA-3′) contained the M13 forward primer (in bold), followed by the 16S rRNA gene-specific sequence (underlined) to allow for barcoding of each sample in a separate reaction (Stamps et al., 2016). The reverse primer (785R: 5′-TAC NVG GGT ATC TAA TCC-3′) was taken directly from the "S-D-Bact07850b-A-18" reverse primer in Klindworth et al. (2013).

Each 50 μL PCR reaction consisted of: 1× 5 PRIME HOT master mix (5 PRIME Inc., Gaithersburg, MD, United States), 0.2 μM of each primer, molecular grade water, and 4 μL of extracted template DNA. The thermal cycling used for PCR was the same as described in Stamps et al. (2016). Positive (*E. coli*) and negative (no template) controls were also amplified along with sample template reactions. The amplified DNA molecules were then purified using AMPure XP paramagnetic beads (Beckman Coulter Inc., Indianapolis, IN, United States) at a final concentration of 0.8× v/v. A second, six cycle PCR was used to add a unique 12 bp barcode to each previously amplified sample using a forward primer containing the unique barcode + M13 forward sequence (5′-3′) and the original 785R primer (A mapping file is available at 10.5281/zenodo.1067761). The final barcoded PCR products were again cleaned and concentrated using AMPure XP paramagnetic beads at a final concentration of 0.8× (v/v), quantified using the QuBit dsDNA HS assay (Life Technologies, Carlsbad, CA, United States), pooled in equimolar amounts, and concentrated to a final volume of 80 μL using two Amicon Ultra-0.5 mL 30K Centrifugal Filters (EMD Millipore, Billerica, MA, United States).

The final pooled library was sequenced using the Illumina MiSeq platform (Illumina, San Diego, CA, United States) and the PE250 V2 chemistry. After sequencing, reads were merged and de-multiplexed using QIIME (Caporaso et al., 2010), filtered at a minimum quality score of 20 before being clustered into sub-operational taxonomic units (sOTUs) using Deblur (Amir et al., 2017). Raw reads were deposited into the NCBI sequencing read archive (SRA) under the accession number SRX2830741. An R markdown notebook and all required data to recreate the 16S rRNA gene analyses presented here are available at 10.5281/zenodo.1067761. Taxonomy was assigned using mothur (Schloss et al., 2009) against the SILVA database (Release 128) (Pruesse et al., 2007).

RESULTS

Environmental Characterization

The LHC mat sampled for biomass and precipitation experiments was a surficial mat ∼30 m from source waters, extending 50 cm from the shoreline into creek flow (**Figure 1D**). The total mat thickness was 10 cm with a gradational contact between the deepest layer (D) and the underlying sediment. Unconsolidated mineral crystals were noted within the mat as granulated textures during extraction, but no lithified structures such as carbonate crusts or continuous nodules or layers were observed. Temperature, pH, TCO_2, and $\delta^{13}C$ data from upstream, downstream, and pore waters within the mat collected prior to extraction are shown in **Table 1**. The temperature of surface waters decreased from 52.4°C upstream to 38.1°C downstream of the sampled mat. The temperature at the mat surface was 34.1°C, increasing to 48.4°C at 3 cm mat depth. The pH of stream waters above the mat in June 2015 decreased from 8.34 upstream to 8.29 downstream. The pH within mats in August 2015 increased from 8.10 to 8.30 with depth. TCO_2 of creek waters decreased downstream, while $\delta^{13}C$ values of TCO_2 became slightly heavier. With increasing mat depth, TCO_2 increased and $\delta^{13}C$ values of TCO_2 decreased (see **Table 1**). Mat pore waters were supersaturated with respect to calcium carbonate, with Ω increasing from 3.23 at 0.5 cm depth to 4.27 at 10 cm.

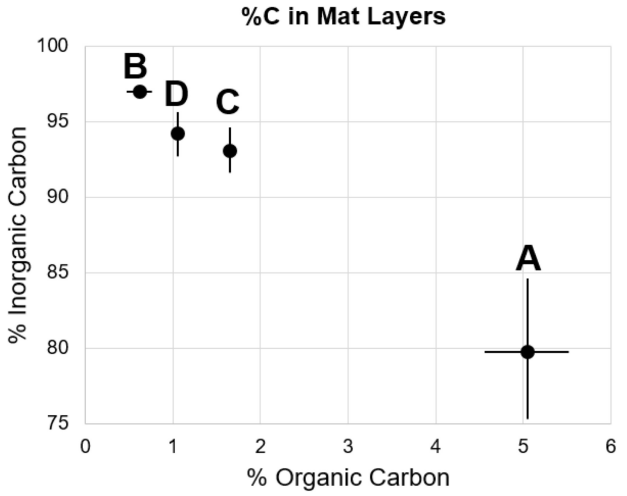

FIGURE 3 | Percent organic and inorganic carbon of mat layers. Points represent triplicate averages, error bars represent one standard deviation.

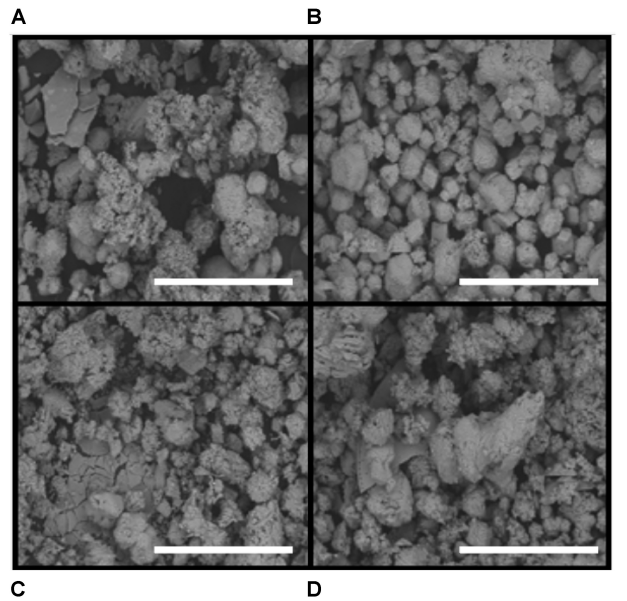

FIGURE 4 | Scanning electron microscope (SEM) images of carbonate precipitates. Scale bar is 500 μm. **(A)** Layer A. **(B)** Layer B. **(C)** Layer C. **(D)** Layer D. Note the presence of euhedral crystals, particularly in Layer B, an indication of precipitation within mat layers as opposed to trapping and binding of detrital carbonates.

A Layered Mat With Extensive Carbonate Precipitation

The microbial mat contained four layers that were visually defined, labeled A through D from top to bottom (**Figure 2B**). Layer A was 1 cm thick and graded from bright orange at the mat–water interface to olive green at the boundary with Layer B. Layer A was extremely cohesive, with isolated pieces retaining shape when separated from the mat. Layer B was 3 cm thick, tan, and lacked the cohesiveness of Layer A. Layer C was 1 cm thick, light pink, and was more cohesive than Layers B or D, but less than Layer A. Layer D was 5 cm thick and gray, with similar consistency to Layer B. Weight percentages of organic and inorganic carbon were inversely correlated within these mat layers (**Figure 3** and Supplementary Table S2). Layer A had the highest amount of organic carbon (5.1 wt%) and the lowest amount of carbonate (79.7 wt%), while Layers B, C, and D varied between 0.6–1.7 wt% organic carbon and 93.1–96.9 wt% carbonate. Despite the high weight percentage carbonate, the mat was not lithified and was easily disarticulated with a spatula.

Upon removal of the organic matter, carbonate crystals were visible in all layers via SEM (**Figure 4**). Many carbonates formed individual rhombs up to 200 μm in diameter, with an average width of 50 μm. Carbonate crystals within LHC mats are euhedral and lack evidence for erosion such as rounding. Euhedral crystal morphologies indicate *in situ* precipitation, as opposed to trapping and binding of detrital carbonates. Crystal abundance broadly corresponded with measured carbonate weight percentage, with Layer A exhibiting less carbonate than Layers B through D (**Figure 3**). While the weight percentage of carbonate was high in all layers, the carbonate crystals were not interlinked and did not form a solid framework.

Production Rates of Organic and Inorganic Carbon

Carbon fixation will produce more enriched $\delta^{13}C_{org}$ values in mat samples incubated with labeled bicarbonate than un-incubated samples. In all layers, $\delta^{13}C_{org}$ values were not heavier ($p > 0.05$, see Supplementary Table S3 and **Figure 5**) in poisoned than un-incubated samples, indicating little to no microbial activity in the poisoned incubations after addition of NaN_3 and $HgCl_2$ and also indicating that the addition of bicarbonate spike did not reside on the sample surface. In contrast, organic $\delta^{13}C$ values were heavier in living than poisoned samples in each layer, implying uptake of labeled bicarbonate through autotrophic production of organic carbon (**Figure 5**). Layers A and B exhibited the highest rates of autotrophic carbon production (both 0.17% new organic carbon/day, $P = 0.01$, 0.003, respectively), followed by Layer D (0.07% new organic carbon/day, $P = 0.01$, see **Figure 6**). Production rates in Layer C were an order of magnitude lower than the other three layers (0.011% new organic carbon/day, $P = 0.036$).

Analogous to the carbon fixation experiment, carbonate precipitation will also produce heavier $\delta^{13}C_{inorg}$ values in mat samples incubated with labeled bicarbonate than in un-incubated samples. In Layers A, C, and D, $\delta^{13}C_{inorg}$ values were higher in poisoned than un-incubated samples ($P = 0.021$, 0.010, and 0.013, respectively, see **Figure 7** and Supplementary Table S3). The incorporation of labeled ^{13}C into carbonates in poisoned samples provides evidence for abiogenic precipitation in the absence of active metabolisms. Poisoned samples from Layer B did not have heavier $\delta^{13}C_{inorg}$ values than un-incubated samples

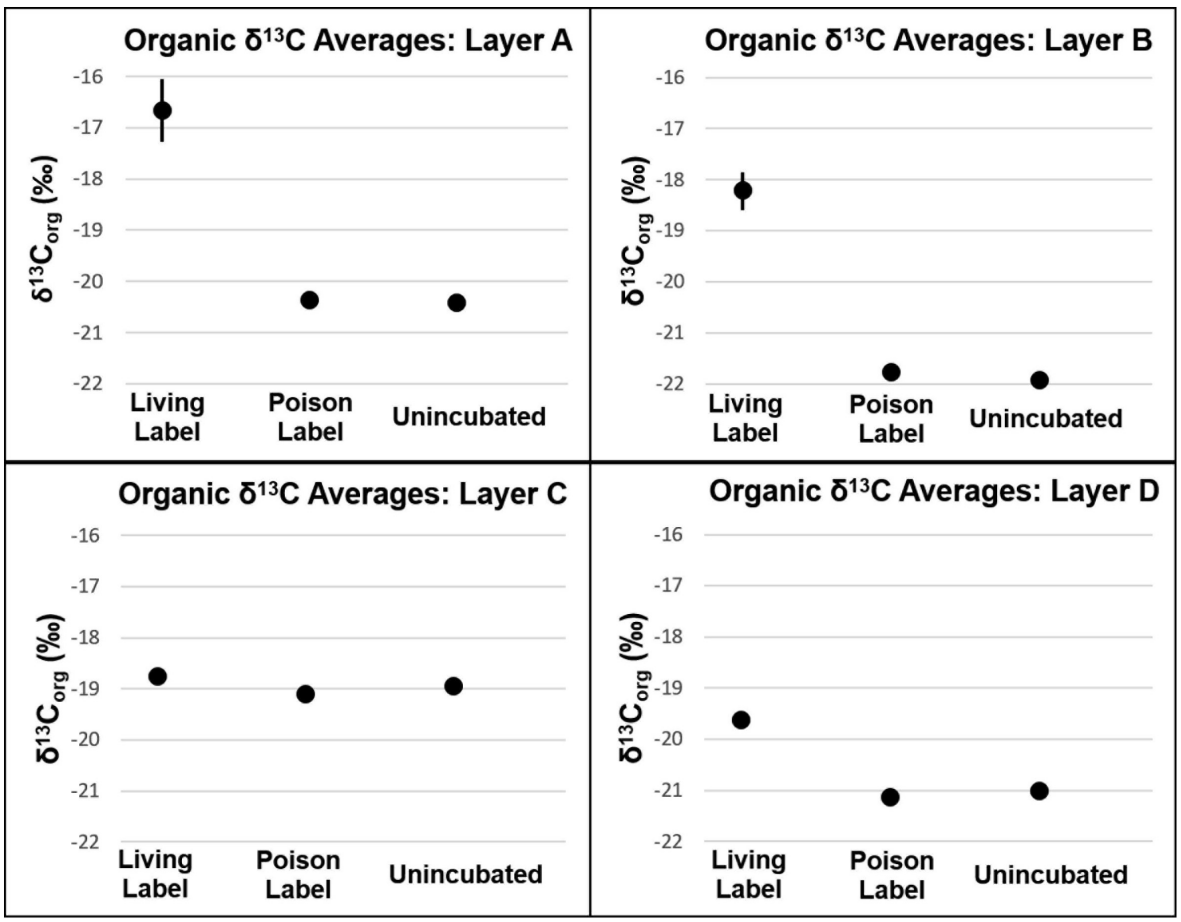

FIGURE 5 | $\delta^{13}C$ of organic carbon of mat layers after incubation experiments. Points represent triplicate averages, error bars represent one standard deviation.

(**Figure 6**, $P = 0.071$). This result shows that the incorporation of spike into carbonate is not an artifact of experiment design, but that abiotic precipitation did not occur in Layer B.

The lack of a difference between living and poisoned carbonate production in Layer A (**Figure 7**, $P = 0.38$) indicates that microbial activity/presence did not foster additional carbonate production at the mat's surface. While the Δ^{exp}_{avg} measured in Layer B was slightly lower than the 95% confidence interval in bootstrap analysis ($P = 0.058$), a comparison with Δ^{mac}_{avg} shows only a 12% probability of machine variability explaining the observed data, similar to the probability of machine variability in Layer C (10%), which has Δ^{exp}_{avg} higher than the 95% confidence interval ($P = 0.034$). The similarity in machine error probability between Layer C, which passes the bootstrap confidence interval test for precipitation, and Layer B, which falls just short of the confidence interval, increases confidence that some biogenic carbonate precipitation occurred in Layer B. Inorganic $\delta^{13}C$ values in Layer D were heavier in living than in poisoned samples ($P = 0.038$). The incorporation of additional labeled ^{13}C into carbonates in living relative to poisoned samples from Layers B, C, and D is evidence that microbial activity plays a role in increasing the carbonate content of these layers.

Mat Communities With Depth

Cyanobacteria and Bacteroidetes were the most abundant phyla in the surface Layer A (see **Figure 8**). Members of the phylum Cyanobacteria composed ∼37–40% of the community, including the genera *Calothrix, Leptolyngbya, Synechococcus*, and *Phormidium*. The phylum Bacteroidetes (∼18–23%) held the most abundant taxa in Layer A, an uncultured member of the Saprospiraceae (17–22%). The rest of the community was predominantly composed of members of the phyla Chloroflexi (∼6–23%), Acidobacteria (∼5–9%), Verrucomicrobia (3–9%), and Planctomycetes (∼3–6%). Compared to samples preserved immediately in the field, the Chloroflexi from Layer A seemed to respond favorably during the 24 h experimental incubation, more than doubling in relative abundance (from ∼9 to 18%). The microbial community in Layer B may have contained abundant novel taxa, as no taxonomic classification was given to 10–12% of these sequences, and while of quality sequence, they remain unclassified. Ignavibacteria responded favorably during transportation prior to incubation, more than doubling from ∼7 to 16%. Additionally, Aminicenantes (Candidate Phylum OP8) increased from 5.9 to 15.1% during incubations. The other most abundant classified taxa in Layer B were members of the

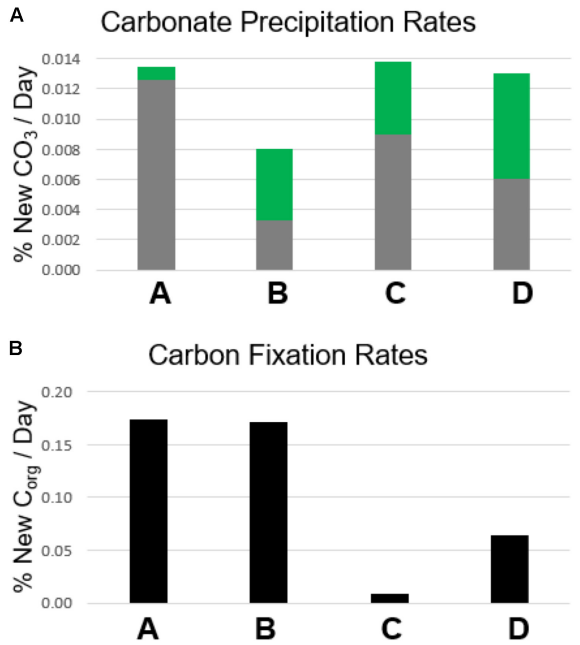

FIGURE 6 | Rates of calcium carbonate precipitation and autotrophic organic carbon production. **(A)** Carbonate precipitation rates. Gray bars represent the amount of new carbonate precipitated in poisoned incubation samples as a percentage of the carbonate present prior to incubation. Green bars represent the additional amount of new carbonate precipitated in living incubation samples compared with poisoned incubation samples. **(B)** Carbon fixation rates. Bars represent the amount of organic carbon produced through carbon fixation in living incubation samples as a percentage of the organic carbon present prior to incubation.

phyla Proteobacteria (3–9%), Chlorobi (4–7%), Planctomycetes (3–12%), and Chloroflexi (1–4%).

Layers C and D had very similar communities based on 16S rRNA gene analysis. Aminicenantes was the most abundant phylum in Layers C and D, at 15–73% and 46–67%, respectively. The phylum did not respond favorably during transportation in Layer C, decreasing from ∼70% from samples taken immediately in the field to 14.9 and 30.1% immediately prior to and after laboratory incubation, respectively. Unclassified taxa also formed a major fraction of the community (∼10–13% in C and ∼8–25% in D). Although the Ignavibacteriae were a relatively minor fraction of the microbial community in samples from Layer C preserved in the field (∼2%), they increased in relative abundance over fivefold during incubations (5.5–27%). The rest of the sequences in Layers C and D were members of the phyla Chloroflexi, Nitrospirae, Planctomycetes, and Bathyarchaeota, present as 2–5% of the community.

DISCUSSION

Correlating Carbon Fixation With Carbonate Precipitation Within Mat Layers

Autotrophic production of organic carbon occurred in all layers of non-poisoned mats during the incubation experiments (**Figure 6**). The rate of this carbon fixation in Layers A and B at the top of the mat (0.17% new organic carbon/day) was more than twice as fast as that within Layer D (0.07% new organic carbon/day), and more than an order of magnitude greater than within Layer C (0.01% new organic carbon/day). Rates of carbon fixation in Layers A and B are nearly identical to rates measured by Bradley et al. (2017) from *in situ* incubations of surficial cones from LHC mats (0.15–0.17% new organic carbon/day), suggesting that meaningful rates can be determined using homogenized samples for the upper layers of the mat. Future comparisons between mats with preserved structure and homogenized mats have the potential to determine the effects of laboratory manipulations on rates in lower, light-limited and potentially anaerobic layers.

Autotrophic microbial communities have different abundances in each LHC mat layer. Previous incubations of hot spring microbial mats provide evidence for autotrophy by members of the phyla Cyanobacteria and Chloroflexi (van der Meer et al., 2005). Within LHC, members of the phylum Cyanobacteria were far more abundant in Layer A (35–39%) than in Layer B (0.5–1.5%) (**Figure 8**). Members of the phylum Chloroflexi were less abundant than Cyanobacteria in Layer A (8–24%), but relatively more abundant in Layer B (3–8%) (**Figure 8**). Despite differing abundances of Cyanobacteria and Chloroflexi, carbon fixation rates were nearly equal in Layers A and B (0.17% new organic carbon/day). Conversely, while Layers A and B had similar rates of carbon fixation with different microbial communities, Layers C and D had similar communities but Layer D had higher rates of carbon fixation (**Figure 6**). Chloroflexi are relatively common in both layers, but decreased from 14.2 to 2.3% during incubation in Layer C, potentially decreasing net carbon fixation. Finally, it is possible that future examination and identification of the ∼14–26% of unclassified taxa in Layers B, C, and D will yield further information on carbon-fixing organisms within the LHC mats.

Biogenic carbonate precipitation within the LHC mat occurred during incubation of Layers B, C, and D (**Figure 7** and Supplementary Table S3). In contrast, the highest rates of carbon fixation were in Layers A and B, with rates similar to *in situ* incubations of LHC cones (Bradley et al., 2017). Yet, the different carbonate precipitation rates in Layers A and B (**Figure 7** and Supplementary Table S3) did not support a positive correlation between carbon fixation and biogenic carbonate precipitation rates. While *in situ* rates within the lower LHC mat layers are not available for comparison, biogenic carbonate precipitation and carbon fixation did occur in these layers, and there was also no apparent correlation between the two processes. There also appears to be no correlation between biogenic and abiogenic carbonate precipitation in LHC mats. Both styles produce carbonate in Layers C and D, while only biogenic precipitation is prevalent in Layer B. Layer A had the highest rate of abiogenic precipitation with no major biogenic influence. Finally, abiogenic carbonate precipitation has no clear correlation with carbonate saturation states within LHC mats. Calcium carbonate was supersaturated at all points above and within mats, with Ω increasing with depth, from 3.23 at 0.5 cm (Layer A) to 4.27 at 10 cm (Layer D). However, abiogenic

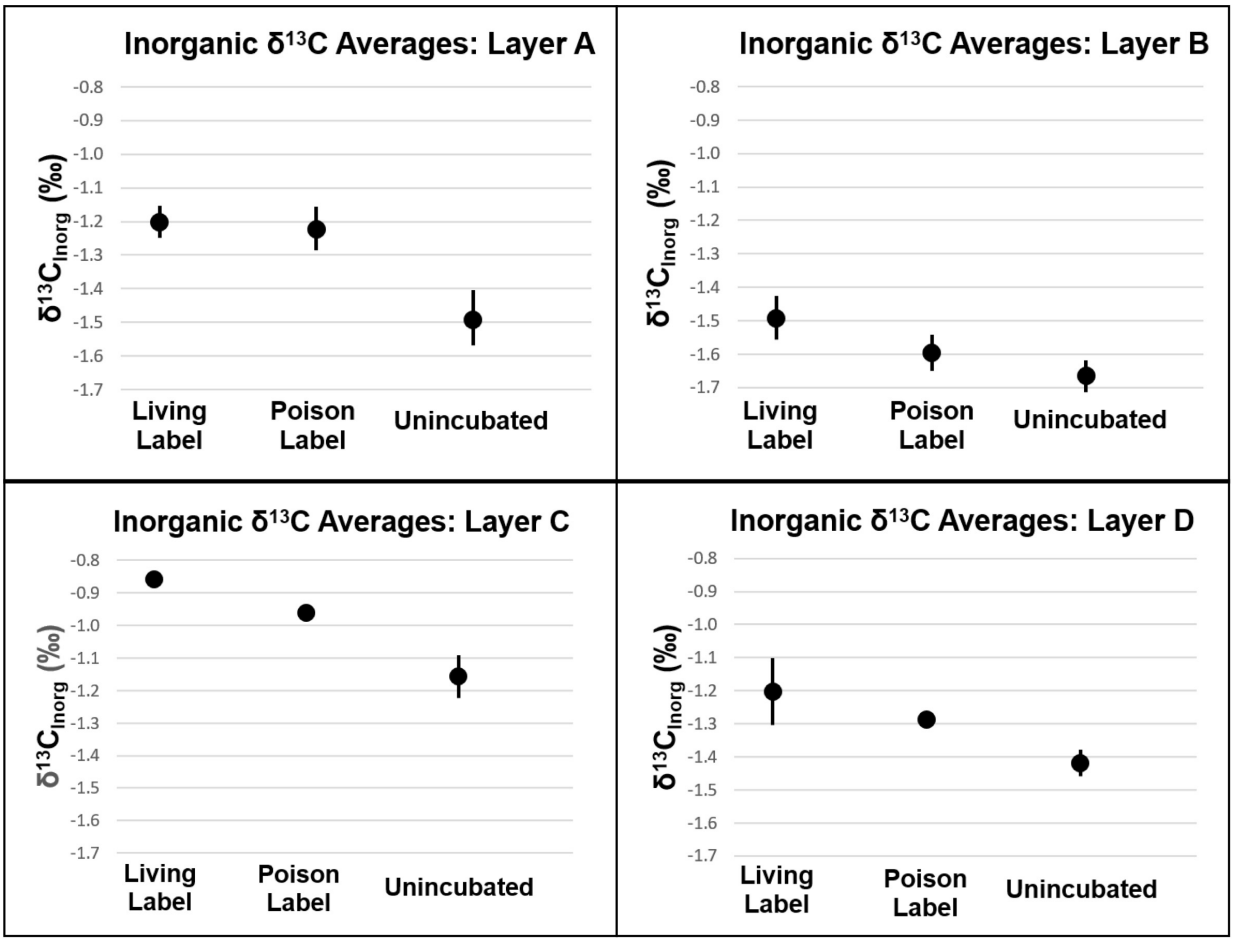

FIGURE 7 | $\delta^{13}C$ of inorganic carbon of mat layers after incubation experiments. Points represent triplicate averages (except for Layer B Living Label, which is the average of two samples), error bars represent one standard deviation.

precipitation rates were highest in Layer A at the top of the mat, and were marginal within Layer B immediately below, with intermediate values in Layers C and D. This is in contrast with previous experiments in abiotic systems, which observe a positive correlation between precipitation rate and saturation (Shiraki and Brantley, 1995).

Layer B had the highest weight percentage of carbonate (96.9%, **Figure 3** and Supplementary Table S2), but only biogenic precipitation occurred during incubation. Conversely, Layer A has the highest abiogenic precipitation rates, and total precipitation rates (biogenic + abiogenic) equivalent to those of Layers C and D, but the lowest carbonate percentage (79.7%). One explanation for this discrepancy is spatial differentiation of communities as LHC mats grow over time. Taxa with higher motility have the potential to move to more habitable environments when conditions become less habitable (Stal, 1995; Nadeau et al., 1999). Cyanobacteria have been shown to exhibit motile behavior in reaction to light availability, ultraviolet radiation, and chemical gradients within mats (Richardson and Castenholz, 1987; Bebout and Garcia-Pichel, 1995; Ramsing et al., 1997). Carbonate precipitation has the potential to limit light availability in LHC mats, forcing motile photoautotrophs to move upward, differentiating a thin, relatively organic-rich and carbonate-poor layer (Layer A) on top of carbonate-rich, organic-poor layers below (Layers B, C, and D).

Precipitation Rates Compared With Microbialite Formation

Precipitation rates from LHC mats not only provide valuable information about the dynamics of modern mat growth, but can also help constrain conditions for microbialite formation and preservation in deep time. Averaging all four layers, LHC mats are 91 wt% carbonate, with a precipitation rate of 0.012% new carbonate per day. The average dry sample mass is 0.002 mg. Therefore, a typical incubation sample had 0.0018 g of carbonate (0.002 grams total × 0.91 grams carbonate/grams total), and 2.2 E-7 grams of carbonate are precipitated every day (0.0018 grams carbonate × 0.00012 grams new carbonate/grams carbonate). At measured rates, a lithified microbialite with 100 wt% carbonate would take two more years to produce. This

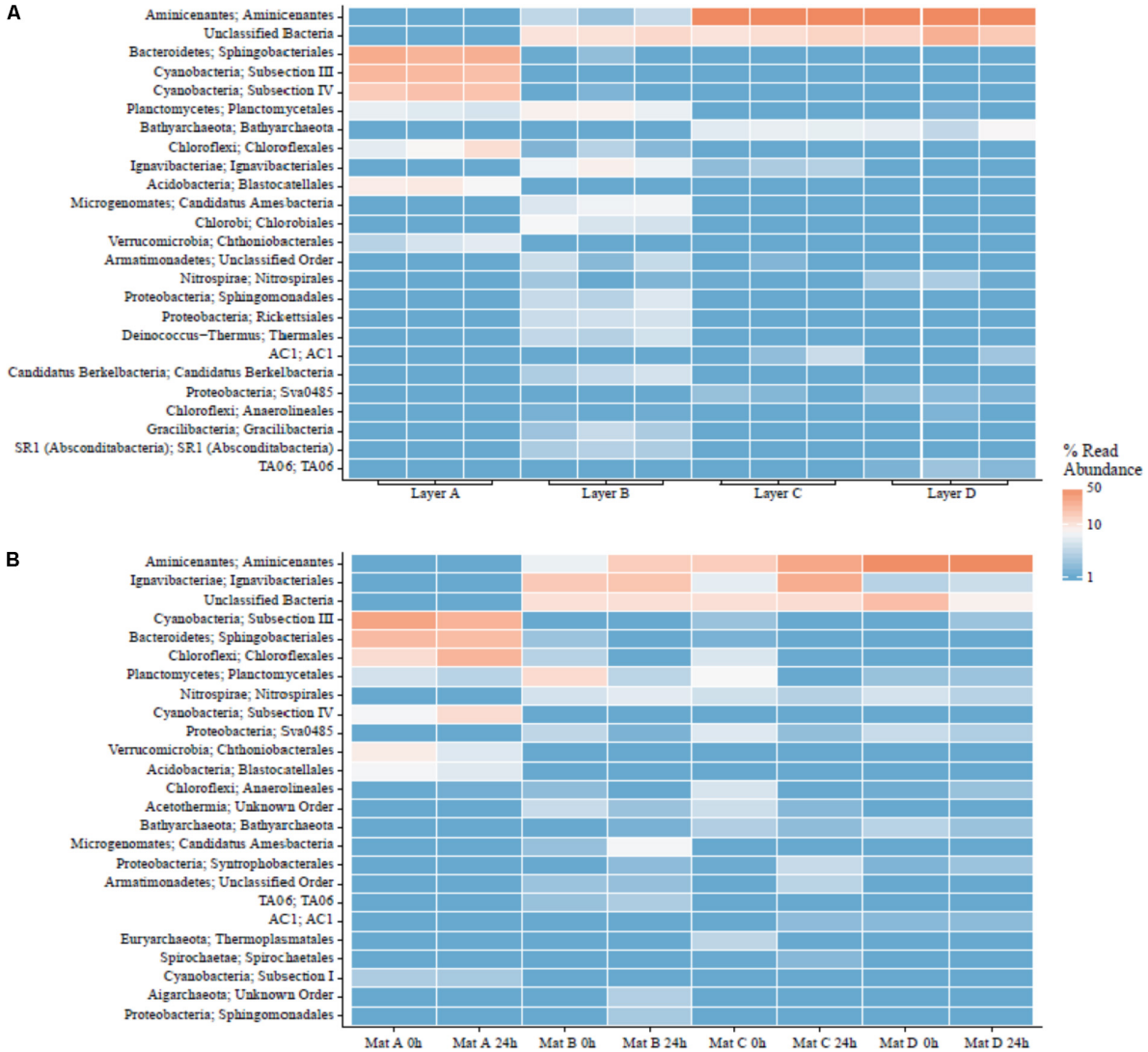

FIGURE 8 | Major orders in LHC mat layers. **(A)** Field triplicates. **(B)** Laboratory samples prior to and after incubation experiments.

hypothesis will be easily testable with future observations of LHC mats.

There are three potential solutions to the discrepancy between the rates of precipitation observed within LHC mats and the lack of lithified microbialites in the same location. (i) The incubation experiments represent a "snapshot" of microbial mat processes instead of long-term, steady state conditions. While the short-term nature of the experiments explains the differences between laboratory and field observations, the explanation does not include, perhaps, a specific process that inhibits microbialite formation at LHC. While a few clades changed in abundance during transportation or incubation, the majority remained relatively stable, indicating that major changes in mat community composition during experiments are unlikely to explain the discrepancy. (ii) Metabolisms within LHC mats in the field inhibit precipitation or promote dissolution which may not have been recognized in the lab experiments. Although the communities of each layer during incubations are relatively representative of field abundances, we introduced more light and aerobic conditions to lower layers such as C and D. Such changes could promote metabolisms that are not normally active in field communities, either processes that promote carbonate precipitation, or inhibit carbonate dissolution. (iii) Organic carbon production dilutes carbonate mineralization. In this scenario, carbonate precipitation in LHC mats could be equal or potentially higher than observed in the incubation experiments. However, if production rates of organic carbon are consistently higher than carbonate precipitation rates, then the microbial mat will never completely lithify into a microbialite (see Supplementary Materials). While all three explanations merit further investigation on mats from LHC and other environments, dilution of carbonate mineralization through organic carbon production provides the best explanation with the current set of observations.

Hypotheses for ancient microbial growth rates vary between short-term diurnal cycles based on modern cyanobacterial motility (Doemel and Brock, 1974; Golubic and Focke, 1978), and slower growth over many months or years (Chivas et al., 1990; Petryshyn et al., 2012; Frantz et al., 2014). Evidence from LHC suggests that elements of both ideas are at work in modern mats. Patterns of LHC mat communities and carbonate growth suggest that cyanobacterial motility does separate modern mats into upper organic-rich and lower carbonate-rich zones, but on slower timescales than thought by previous hypotheses. At observed precipitation rates, a minimum of 23 years is required for a hypothetical LHC mat starting with no carbonate present to fully lithify, all things being equal. However, if production rates of organic carbon consistently outpace carbonate precipitation rates in this mat, it is possible that the mats may never become fully lithified. It is possible to speculate that the paucity of microbialites versus the ubiquity of microbial mats in modern environments may reside in the balance between rates of organic carbon production versus carbonate precipitation, where times of abundant microbialite formation in the past may represent conditions where carbonate precipitation rates were equal to or greater than microbial growth rates.

Our study of 1-day growth rate experiments shows (i) Rates of autotrophic carbon fixation are not correlated with rates of biogenic carbonate precipitation within certain microbial mats. The results corroborate previous work demonstrating that carbon fixation only precipitates calcium carbonate in specific chemical environments (Merz-Preiß and Riding, 1999; Arp et al., 2001). The uppermost layers of LHC mats have the highest carbon fixation rates as well as abundant autotrophic communities, but biogenic precipitation only occurred in Layers B, C, and D. (ii) Mats with consistently higher rates of organic carbon production than carbonate precipitation are unlikely to produce lithified microbialites. This hypothesis is supported by recent research indicating higher rates of primary productivity in unlithified microbial mats than within recently formed stromatolites (Schuler et al., 2017). (iii) Individual microbial mat layers can host both biogenic and abiogenic carbonate precipitation. Abiogenic precipitation occurred in the uppermost LHC layer, and in concert with biogenic precipitation in the lower two layers. (iv) Layers with the highest carbonate production rates do not always correspond with areas of high carbonate percentage. The uppermost LHC layer had the lowest percentage of carbonate (79.7%), but the highest rate of abiogenic carbonate precipitation, while the immediately adjacent layer was 96.9% carbonate, but had the lowest rates of total carbonate precipitation during incubations. Comparing differences in carbonate percentage and production rate can potentially provide growth histories of microbial mats.

AUTHOR CONTRIBUTIONS

DW assisted with mat collection, field geochemistry, laboratory experiments, data analysis and interpretation, and wrote the initial manuscript draft. SG and MD assisted with mat collection, field geochemistry, laboratory experiments, data analysis and interpretation. HJ and WB designed and ran laboratory analyses, and assisted with geochemical interpretation. BSS, BWS, and HN performed 16S rRNA analyses, and assisted with biological interpretation. OP assisted with field geochemical sampling and saturation state calculation. FC co-directed and secured funding for the 2015 International Geobiology Course, and assisted with interpreting significance to modern and ancient lithified microbialites. JS co-directed and secured funding for the 2015 International Geobiology Course. All authors contributed in the writing and editing of the manuscript.

FUNDING

This work was supported in part through funding for the 2015 International Geobiology Course from the Agouron Institute.

ACKNOWLEDGMENTS

A permit was granted to JS from the U.S. Forest Service (Permit #MLD15053) to conduct fieldwork and sample LHC. We acknowledge all members of the 2015 International Geobiology Course in their assistance, including Caitlin Bojanowski, James Bradley, Joy Buongiorno, Luoth Chou, Leslie Daille, Gabriela Libanori, Katie Rempfert, Danielle Santiago, Chris Trivedi, Lennart van Maldegem, Feifei Zhang, Laura Zinke, Emma Bertran, Jonah Duckles, Sean Loyd, Victoria Petryshyn, and Russell Shapiro. We thank Nick Rollins for analyzing and reducing data, and Julien Emile-Geay and Jeffrey Thompson for their assistance on statistical analyses.

SUPPLEMENTARY MATERIAL

The Supplementary Material for this article can be found online at: https://www.frontiersin.org/articles/10.3389/fmicb.2018.01464/full#supplementary-material

REFERENCES

Aloisi, G. (2008). The calcium carbonate saturation state in cyanobacterial mats throughout Earth's history. *Geochim. Cosmochim. Acta* 72, 6037–6060. doi: 10.1016/j.gca.2008.10.007

Amir, A., McDonald, D., Navas-Molina, J. A., Kopylova, E., Morton, J. T., Zech, et al. (2017). Deblur rapidly resolves single-nucleotide community sequence patterns. *mSystems* 2:e00191-16. doi: 10.1128/mSystems.00191-16

Arp, G., Reimer, A., and Reitner, J. (1999a). Calcification in cyanobacterial biofilms of alkaline salt lakes. *Eur. J. Phycol.* 34, 393–403. doi: 10.1080/09670269910001736452

Arp, G., Reimer, A., and Reitner, J. (2001). Photosynthesis-induced biofilm calcification and calcium concentrations in phanerozoic oceans. *Science* 292, 1701–1704. doi: 10.1126/science.1057204

Arp, G., Thiel, V., Reimer, A., Michaelis, W., and Reitner, J. (1999b). Biofilm exopolymers control microbialite formation at thermal springs discharging

into the alkaline Pyramid Lake, Nevada, USA. *Sediment. Geol.* 126, 159–176. doi: 10.1016/S0037-0738(99)00038-X

Awramik, S. M., and Sprinkle, J. (1999). Proterozoic stromatolites: the first marine evolutionary biota. *Hist. Biol.* 13, 241–253. doi: 10.1080/08912969909386584

Baumgartner, L. K., Reid, R. P., Dupraz, C., Decho, A. W., Buckley, D. H., Spear, J. R., et al. (2006). Sulfate reducing bacteria in microbial mats: Changing paradigms, new discoveries. *Sediment. Geol.* 185, 131–145. doi: 10.1016/j.sedgeo.2005.12.008

Bebout, B. M., and Garcia-Pichel, F. (1995). UV B-induced vertical migrations of cyanobacteria in a microbial mat. *Appl. Environ. Microbiol.* 61, 4215–4222.

Berelson, W. M., Corsetti, F. A., Pepe-Ranney, C., Hammond, D. E., Beaumont, W., and Spear, J. R. (2011). Hot spring siliceous stromatolites from Yellowstone National Park: assessing growth rate and laminae formation. *Geobiology* 9, 411–424. doi: 10.1111/j.1472-4669.2011.00288.x

Bosak, T., Knoll, A. H., and Petroff, A. P. (2013). The Meaning of Stromatolites. *Annu. Rev. Earth Planet. Sci.* 41, 21–44. doi: 10.1146/annurev-earth-042711-105327

Bosak, T., Liang, B., Sim, M. S., and Petroff, A. P. (2009). Morphological record of oxygenic photosynthesis in conical stromatolites. *Proc. Natl. Acad. Sci. U.S.A.* 106, 10939–10943. doi: 10.1073/pnas.0900885106

Bradley, J. A., Daille, L. K., Trivedi, C. B., Bojanowski, C. L., Stamps, B. W., Stevenson, B. S., et al. (2017). Carbonate-rich dendrolitic cones: insights into a modern analogue for incipient microbialite formation, Little Hot Creek, Long Valley Caldera, California. *NPJ Biofilms Microbiomes* 3:32. doi: 10.1038/s41522-017-0041-2

Breitbart, M., Wegley, L., Leeds, S., Schoenfeld, T., and Rohwer, F. (2004). Phage community dynamics in hot springs. *Appl. Environ. Microbiol.* 70, 1633–1640. doi: 10.1128/AEM.70.3.1633-1640.2004

Bundeleva, I. A., Shirokova, L. S., Bénézeth, P., Pokrovsky, O. S., Kompantseva, E. I., and Balor, S. (2012). Calcium carbonate precipitation by anoxygenic phototrophic bacteria. *Chem. Geol.* 291, 116–131. doi: 10.1016/j.chemgeo.2011.10.003

Cam, N., Benzerara, K., Georgelin, T., Jaber, M., Lambert, J. F., Poinsot, M., et al. (2018). Cyanobacterial formation of intracellular Ca-carbonates in undersaturated solutions. *Geobiology* 16, 49–61. doi: 10.1111/gbi.12261

Caporaso, J. G., Kuczynski, J., Stombaugh, J., Bittinger, K., Bushman, F. D., Costello, E. K., et al. (2010). QIIME allows analysis of high-throughput community sequencing data. *Nat. Methods* 7, 335–336. doi: 10.1038/nmeth.f.303

Chivas, A. R., Torgersen, T., and Polach, H. A. (1990). Growth rates and Holocene development of stromatolites from Shark Bay, Western Australia. *Aust. J. Earth Sci.* 37, 113–121. doi: 10.1080/08120099008727913

Couradeau, E., Benzerara, K., Gérard, E., Estève, I., Moreira, D., Tavera, R., et al. (2013). Cyanobacterial calcification in modern microbialites at the submicrometer scale. *Biogeosciences* 10, 5255–5266. doi: 10.5194/bg-10-5255-2013

De Philippis, R., Margheri, M. C., Materassi, R., and Vincenzini, M. (1998). Potential of unicellular cyanobacteria from saline environments as exopolysaccharide producers. *Appl. Environ. Microbiol.* 64, 1130–1132.

Doemel, W. N., and Brock, T. D. (1974). Bacterial stromatolites: origin of laminations. *Science* 184, 1083–1085. doi: 10.1126/science.184.4141.1083

Dupraz, C., Reid, R. P., Braissant, O., Decho, A. W., Norman, R. S., and Visscher, P. T. (2009). Processes of carbonate precipitation in modern microbial mats. *Earth Sci. Rev.* 96, 141–162. doi: 10.1016/j.earscirev.2008.10.005

Dupraz, C., and Visscher, P. T. (2005). Microbial lithification in marine stromatolites and hypersaline mats. *Trends Microbiol.* 13, 429–438. doi: 10.1016/j.tim.2005.07.008

Dupraz, C., Visscher, P. T., Baumgartner, L. K., and Reid, R. P. (2004). Microbe-mineral interactions: early carbonate precipitation in a hypersaline lake (Eleuthera Island, Bahamas). *Sedimentology* 51, 745–765. doi: 10.1111/j.1365-3091.2004.00649.x

Efron, B. (1979). Bootstrap methods: another look at the jackknife. *Ann. Stat.* 7, 1–26. doi: 10.1214/aos/1176344552

Efron, B., and Tibshirani, R. (1986). Bootstrap methods for standard errors. *Stat. Sci.* 1, 54–75. doi: 10.1214/ss/1177013815

Frankel, R. B., and Bazylinski, D. A. (2003). Biologically induced mineralization by bacteria. *Rev. Mineral. Geochem.* 54, 95–114. doi: 10.2113/0540095

Frantz, C. M., Petryshyn, V. A., Marenco, P. J., Tripati, A., Berelson, W. M., and Corsetti, F. A. (2014). Dramatic local environmental change during the early Eocene climatic optimum detected using high resolution chemical analyses of green river formation stromatolites. *Palaeogeogr. Palaeoclimatol. Palaeoecol.* 405, 1–15. doi: 10.1016/j.palaeo.2014.04.001

Gallagher, K. L., Kading, T. J., Braissant, O., Dupraz, C., and Visscher, P. T. (2012). Inside the alkalinity engine: the role of electron donors in the organomineralization potential of sulfate-reducing bacteria. *Geobiology* 10, 518–530. doi: 10.1111/j.1472-4669.2012.00342.x

Gérard, E., Ménez, B., Couradeau, E., Moreira, D., Benzerara, K., Tavera, R., et al. (2013). Specific carbonate–microbe interactions in the modern microbialites of Lake Alchichica (Mexico). *ISME J.* 7, 1997–2009. doi: 10.1038/ismej.2013.81

Golubic, S., and Focke, J. W. (1978). Phormidium hendersonii howe: identity and significance of a modern stromatolite building microorganism. *J. Sediment. Res.* 48, 751–764. doi: 10.1306/212F7559-2B24-11D7-8648000102C1865D

Grotzinger, J. P., and Knoll, A. H. (1999). Stromatolites in Precambrian carbonates: evolutionary mileposts or environmental dipsticks? *Annu. Rev. Earth Planet. Sci.* 27, 313–358. doi: 10.1146/annurev.earth.27.1.313

Hagadorn, J. W., and Mcdowell, C. (2012). Microbial influence on erosion, grain transport and bedform genesis in sandy substrates under unidirectional flow. *Sedimentology* 59, 795–808. doi: 10.1111/j.1365-3091.2011.01278.x

Hayes, J. M. (1983). "Practice and principles of isotopic measurements in organic geochemistry," in *Organic Geochemistry of Contemporaneous and Ancient Sediments*, eds W. G. Meinschein (Bloomington, Ind: SEPM).

Klindworth, A., Pruesse, E., Schweer, T., Peplies, J., Quast, C., Horn, M., et al. (2013). Evaluation of general 16S ribosomal RNA gene PCR primers for classical and next-generation sequencing-based diversity studies. *Nucleic Acids Res.* 41:e1. doi: 10.1093/nar/gks808

Kraus, E. A., Beeler, S. R., Mors, R. A., Floyd, J. G., Stamps, B. W., Nunn, H. S., et al. (2018). Microscale biosignatures and abiotic mineral authigenesis in Little Hot Creek, California. *Front. Microbiol.* 9:997. doi: 10.3389/fmicb.2018.00997

Mata, S. A., Harwood, C. L., Corsetti, F. A., Stork, N. J., Eilers, K., Berelson, W. M., et al. (2012). Influence of gas production and filament orientation on stromatolite microfabric. *Palaios* 27, 206–219. doi: 10.2110/palo.2011.p11-088r

Merz-Preiß, M., and Riding, R. (1999). Cyanobacterial tufa calcification in two freshwater streams: ambient environment, chemical thresholds and biological processes. *Sediment. Geol.* 126, 103–124. doi: 10.1016/S0037-0738(99)00035-4

Michaelis, W., Seifert, R., Nauhaus, K., Treude, T., Thiel, V., and Blumenberg, M. (2002). Microbial reefs in the black sea fueled by anaerobic oxidation of methane. *Science* 297, 1013–1015. doi: 10.1126/science.1072502

Nadeau, T.-L., Howard-Williams, C., and Castenholz, R. W. (1999). Effects of solar UV and visible irradiance on photosynthesis and vertical migration of *Oscillatoria* sp.(Cyanobacteria) in an Antarctic microbial mat. *Aquat. Microb. Ecol.* 20, 231–243. doi: 10.3354/ame020231

Noffke, N., Eriksson, K. A., Hazen, R. M., and Simpson, E. L. (2006). A new window into Early Archean life: Microbial mats in Earth's oldest siliciclastic tidal deposits (3.2 Ga Moodies Group, South Africa). *Geology* 34, 253–256. doi: 10.1130/G22246.1

Obst, M., Dynes, J. J., Lawrence, J. R., Swerhone, G. D. W., Benzerara, K., Karunakaran, C., et al. (2009). Precipitation of amorphous $CaCO_3$ (aragonite-like) by cyanobacteria: A STXM study of the influence of EPS on the nucleation process. *Geochim. Cosmochim. Acta* 73, 4180–4198. doi: 10.1016/j.gca.2009.04.013

Pentecost, A., and Riding, R. (1986). "Calcification in cyanobacteria," in *Biomineralization in Lower Plants and Animals*, eds B. S. C. Leadbeater and R. Riding (Oxford: Clarendon Press), 73–90.

Pepe-Ranney, C., Berelson, W. M., Corsetti, F. A., Treants, M., and Spear, J. R. (2012). Cyanobacterial construction of hot spring siliceous stromatolites in Yellowstone National Park. *Environ. Microbiol.* 14, 1182–1197. doi: 10.1111/j.1462-2920.2012.02698.x

Petryshyn, V. A., Corsetti, F. A., Berelson, W. M., Beaumont, W., and Lund, S. P. (2012). Stromatolite lamination frequency, Walker Lake, Nevada: implications for stromatolites as biosignatures. *Geology* 40, 499–502. doi: 10.1130/G32675.1

Pierrot, D., Lewis, E., and Wallace, D. W. R. (2006). *MS Excel Program Developed for CO_2 System Calculations. ORNL/CDIAC-105a*. Oak Ridge, TN: Carbon Dioxide Information Analysis Center.

Pruesse, E., Quast, C., Knittel, K., Fuchs, B. M., Ludwig, W., Peplies, J., et al. (2007). SILVA: a comprehensive online resource for quality checked and aligned

ribosomal RNA sequence data compatible with ARB. *Nucleic Acids Res.* 35, 7188–7196. doi: 10.1093/nar/gkm864

Ragon, M., Benzerara, K., Moreira, D., Tavera, R., and Lopez-Garcia, P. (2014). 16S rDNA-based analysis reveals cosmopolitan occurrence but limited diversity of two cyanobacterial lineages with contrasted patterns of intracellular carbonate mineralization. *Front. Microbiol.* 5:331. doi: 10.3389/fmicb.2014.00331

Ramsing, N. B., Ferris, M. J., and Ward, D. M. (1997). Light-induced motility of thermophilic Synechococcus isolates from Octopus Spring, Yellowstone National Park. *Appl. Environ. Microbiol.* 63, 2347–2354.

Reid, R. P., Visscher, P. T., Decho, A. W., Stolz, J. F., Bebout, B. M., Dupraz, C., et al. (2000). The role of microbes in accretion, lamination and early lithification of modern marine stromatolites. *Nature* 406, 989–992. doi: 10.1038/35023158

Richardson, L. L., and Castenholz, R. W. (1987). Diel vertical movements of the cyanobacterium *Oscillatoria terebriformis* in a sulfide-rich hot spring microbial mat. *Appl. Environ. Microbiol.* 53, 2142–2150.

Riding, R. (2000). Microbial carbonates: the geological record of calcified bacterial-algal mats and biofilms. *Sedimentology* 47, 179–214. doi: 10.1046/j.1365-3091.2000.00003.x

Schloss, P. D., Westcott, S. L., Ryabin, T., Hall, J. R., Hartmann, M., Hollister, E. B., et al. (2009). Introducing mothur: open-source, platform-independent, community-supported software for describing and comparing microbial communities. *Appl. Environ. Microbiol.* 75, 7537–7541. doi: 10.1128/AEM.01541-09

Schopf, J. W. (2006). Fossil evidence of Archaean life. *Philos. Trans. R. Soc. B Biol. Sci.* 361, 869–885. doi: 10.1098/rstb.2006.1834

Schuler, C. G., Havig, J. R., and Hamilton, T. L. (2017). Hot spring microbial community composition, morphology, and carbon fixation: implications for interpreting the ancient rock record. *Front. Earth Sci.* 5:97. doi: 10.3389/feart.2017.00097

Shiraki, R., and Brantley, S. L. (1995). Kinetics of near-equilibrium calcite precipitation at 100°C: an evaluation of elementary reaction-based and affinity-based rate laws. *Geochim. Cosmochim. Acta* 59, 1457–1471. doi: 10.1016/0016-7037(95)00055-5

Sorey, M. L., McConnell, V. S., and Roeloffs, E. (2003). Summary of recent research in Long Valley Caldera, California. *J. Volcanol. Geotherm. Res.* 127, 165–173. doi: 10.1016/S0377-0273(03)00168-9

Stal, L. J. (1995). Physiological ecology of cyanobacteria in microbial mats and other communities. *New Phytol.* 131, 1–32. doi: 10.1111/j.1469-8137.1995.tb03051.x

Stamps, B. W., Lyles, C. N., Suflita, J. M., Masoner, J. R., Cozzarelli, I. M., Kolpin, D. W., et al. (2016). Municipal solid waste landfills harbor distinct microbiomes. *Front. Microbiol.* 7:534. doi: 10.3389/fmicb.2016.00534

Subhas, A. V., Rollins, N. E., Berelson, W. M., Dong, S., Erez, J., and Adkins, J. F. (2015). A novel determination of calcite dissolution kinetics in seawater. *Geochim. Cosmochim. Acta* 170, 51–68. doi: 10.1016/j.gca.2015.08.011

Trichet, J., and Defarge, C. (1995). Non-biologically supported organomineralization. *Bull. Inst. Oceanogr.* 14, 203–236.

van der Meer, M. T. J., Schouten, S., Bateson, M. M., Nübel, U., Wieland, A., Kühl, M., et al. (2005). Diel variations in carbon metabolism by green nonsulfur-like bacteria in alkaline siliceous hot spring microbial mats from placePlaceNameYellowstone PlaceTypeNational Park. *Appl. Environ. Microbiol.* 71, 3978–3986. doi: 10.1128/AEM.71.7.3978-3986.2005

Vasconcelos, C., Warthmann, R., McKenzie, J. A., Visscher, P. T., Bittermann, A. G., and van Lith, Y. (2006). Lithifying microbial mats in Lagoa Vermelha, Brazil: Modern Precambrian relics? *Sediment. Geol.* 185, 175–183. doi: 10.1016/j.sedgeo.2005.12.022

Vick, T. J., Dodsworth, J. A., Costa, K. C., Shock, E. L., and Hedlund, B. P. (2010). Microbiology and geochemistry of Little Hot Creek, a hot spring environment in the Long Valley Caldera. *Geobiology* 8, 140–154. doi: 10.1111/j.1472-4669.2009.00228.x

Visscher, P. T., Reid, P. R., and Bebout, B. M. (2000). Microscale observations of sulfate reduction: correlation of microbial activity with lithified micritic laminae in modern marine stromatolites. *Geology* 28, 919–922. doi: 10.1130/0091-7613(2000)28<919:MOOSRC>2.0.CO;2

Walter, M. R., Buick, R., and Dunlop, J. S. R. (1980). Stromatolites 3,400-3,500 Myr old from the North Pole area, Western Australia. *Nature* 284, 443–445. doi: 10.1038/284443a0

Conflict of Interest Statement: The authors declare that the research was conducted in the absence of any commercial or financial relationships that could be construed as a potential conflict of interest.

frontiers in Microbiology

ORIGINAL RESEARCH
published: 15 October 2018
doi: 10.3389/fmicb.2018.02180

The Complete Genome and Physiological Analysis of the Microbialite-Dwelling *Agrococcus pavilionensis* sp. nov; Reveals Genetic Promiscuity and Predicted Adaptations to Environmental Stress

Richard Allen White III[1], Greg Gavelis[2], Sarah A. Soles[3], Emma Gosselin[4], Greg F. Slater[3], Darlene S. S. Lim[5,6], Brian Leander[5] and Curtis A. Suttle[1,2,4,7]*

[1] Department of Microbiology and Immunology, University of British Columbia, Vancouver, BC, Canada, [2] Department of Zoology, University of British Columbia, Vancouver, BC, Canada, [3] School of Geography and Earth Sciences, McMaster University, Hamilton, ON, Canada, [4] Department of Earth, Ocean and Atmospheric Sciences, The University of British Columbia, Vancouver, BC, Canada, [5] Bay Area Environmental Research Institute, Petaluma, CA, United States, [6] NASA Ames Research Center, Moffett Field, CA, United States, [7] Canadian Institute for Advanced Research, Toronto, ON, Canada

OPEN ACCESS

Edited by:
Pieter T. Visscher, University of Connecticut, United States

Reviewed by:
Haley M. Sapers, California Institute of Technology, United States
Jamie S. Foster, University of Florida, United States
Artemis S. Louyakis, University of Connecticut, United States

***Correspondence:**
Richard Allen White III
raw937@gmail.com

Specialty section:
This article was submitted to Aquatic Microbiology, a section of the journal Frontiers in Microbiology

Received: *05 January 2018*
Accepted: *24 August 2018*
Published: *15 October 2018*

Citation:
White RA III, Gavelis G, Soles SA, Gosselin E, Slater GF, Lim DSS, Leander B and Suttle CA (2018) The Complete Genome and Physiological Analysis of the Microbialite-Dwelling Agrococcus pavilionensis sp. nov; Reveals Genetic Promiscuity and Predicted Adaptations to Environmental Stress. Front. Microbiol. 9:2180. doi: 10.3389/fmicb.2018.02180

Members of the bacterial genus *Agrococcus* are globally distributed and found across environments so highly diverse that they include forests, deserts, and coal mines, as well as in potatoes and cheese. Despite how widely *Agrococcus* occurs, the extent of its physiology, genomes, and potential roles in the environment are poorly understood. Here we use whole-genome analysis, chemotaxonomic markers, morphology, and 16S rRNA gene phylogeny to describe a new isolate of the genus *Agrococcus* from freshwater microbialites in Pavilion Lake, British Columbia, Canada. We characterize this isolate as a new species *Agrococcus pavilionensis* strain RW1 and provide the first complete genome from a member of the genus *Agrococcus.* The *A. pavilionensis* genome consists of one chromosome (2,627,177 bp) as well as two plasmids (HC-CG1 1,427 bp, and LC-RRW783 31,795 bp). The genome reveals considerable genetic promiscuity via mobile elements, including a prophage and plasmids involved in integration, transposition, and heavy-metal stress. *A. pavilionensis* strain RW1 differs from other members of the *Agrococcus* genus by having a novel phospholipid fatty acid iso-C15:1Δ^4, β-galactosidase activity and amygdalin utilization. Carotenoid biosynthesis is predicted by genomic metabolic reconstruction, which explains the characteristic yellow pigmentation of *A. pavilionensis*. Metabolic reconstructions of strain RW1 genome predicts a pathway for releasing ammonia via ammonification amino acids, which could increase the saturation index leading to carbonate precipitation. Our genomic analyses suggest signatures of environmental adaption to the relatively cold

and oligotrophic conditions of Pavilion Lake microbialites. *A. pavilionensis* strain RW1 in modern microbialites has an ecological significance in Pavilion Lake microbialites, which include potential roles in heavy-metal cycling and carbonate precipitation (e.g., ammonification of amino acids and filamentation which many trap carbonate minerals).

Keywords: actinobacteria, microbialite, cosmopolitan, oligotrophic, metabolic potential

INTRODUCTION

Microbialites represent the oldest evidence of life on the planet with fossils dating back to around 3.7 billion years ago (Nutman et al., 2016). These structures consist of a specialized microbial mat that lithifies carbonates into two main structural types, (1) thrombolites composed of non-laminated clots, or (2) stromatolites defined by laminated layers (Burne and Moore, 1987; Perry et al., 2007). Microbialites are still present today and represent natural laboratories of early microbial ecosystems, which allow for testing hypotheses around the basic principles of microbial ecology including questions regarding community composition (Wong et al., 2015, 2017), community assembly (Havemann and Foster, 2008), functional traits, and diversity (Breitbart et al., 2009; Saghaï et al., 2015; White et al., 2015, 2016b; Ruvindy et al., 2016; Louyakis et al., 2018) and the discovery of novel taxa (Burns et al., 2012).

While heterotrophs and photoautotrophs—mainly cyanobacteria—have been described and isolated from a range of microbial mats, including microbialites, little work has been done on pigmented heterotrophic bacteria within microbialites. It has been suggested that a variety of pigments could come from non-phototrophic bacteria (Nübel et al., 1999; Lionard et al., 2012). Actinobacteria have also been identified in the pigmented layers in microbial mats (Bottos et al., 2008; Lionard et al., 2012), and it is thought that carotenoids are responsible for their characteristic coloration (Nübel et al., 1999; Mueller et al., 2005; Klassen, 2010). Given that these groups seemingly lack metabolism for oxygenic or anoxygenic photosynthesis, fundamental questions include (1) what is the function of pigmentation in these heterotrophic bacteria? And (2) what are the potential roles of heterotrophic bacteria in cold microbialites or microbial mats? We enriched and isolated >100 pigmented bacteria from microbialites in Pavilion Lake, in southeastern British Columbia, Canada (50.8°N, 121.7°W). Based on their growth in the dark, they were either mixotrophs or heterotrophs. Among our enrichments the one isolate described here; which belongs to the *Agrococcus* genus and is a Gram-positive member of the phylum *Actinobacteria*.

Pavilion Lake is a cold, oligotrophic ecosystem (mean total phosphorus, 3.3 $\mu g\ L^{-1}$), with dimictic, circumneutral waters (median pH 8.3; mean calcium carbonate, 182 $mg\ L^{-1}$) (White et al., 2016b). Characterization of the limnology of Pavilion Lake is described in detail Lim et al. (2009). Pavilion Lake microbialites are calcium carbonate-based thrombolites with thin (∼5 mm) microbial mats dominated by cyanobacteria that change morphology as a function of lake depth (White et al., 2016b). Characterization of the limnology of Pavilion Lake is described in detail Lim et al. (2009). Our *Agrococcus* strain was isolated and enriched from a Pavilion microbialite (i.e., a thrombolite) at 20 m depth, where the water temperature remains around 4 to 10°C throughout the year (Lim et al., 2009). Bacteria at this depth should be adapted to cold temperature, low phosphorus, and alkaline conditions.

The genus *Agrococcus* was described based on two strains of *Agrococcus jenensis* isolated from soil and the surface of sandstone (Groth et al., 1996). The genus *Agrococcus* is classified within the family *Microbacteriaceae*, within the phylum *Actinobacteria.* All *Agrococcus* members have diaminobutyric acid within their cell walls (Groth et al., 1996). Diaminobutyric acid may impart the distinctive lemon-yellow color, although its role in pigmentation is unknown (Groth et al., 1996). *Agrococcus* spp. have been isolated from a wide range of environments, including air (Zlamala et al., 2002), a coal mine (Dhanjal et al., 2011), cheese (Bora et al., 2007), cold-desert soil (Mayilraj et al., 2006), forest soil (Zhang et al., 2010), a medieval wall painting (Wieser et al., 1999), dried seaweed (Lee, 2008), and the phyllosphere of potato plants (Behrendt et al., 2008). There are eight described species of *Agrococcus,* yet little is known about the genome, metabolism, evolution, or physiology of this genus.

To explore the potential role of this genus in microbialite communities, we herein characterize the new species *Agrococcus pavilionensis* strain RW1, using both classical bacteriological examination (e.g., chemotaxonomic investigation of its metabolism) along with modern genome-centric approaches. We provide the first complete reference genome (i.e., closed gapless chromosome with two plasmids) from the *Agrococcus* genus. Our genomic analyses suggest signatures of environmental adaption to the relatively cold and oligotrophic conditions of Pavilion Lake microbialites. Promiscuous mobile elements were found in two plasmids involved in heavy-metal resistance and DNA transposition. The genomes of *A. pavilionensis* RW1 and *A. lahaulensis* K22-21 both encode a carotenogenic gene cluster that could be responsible for producing the characteristic lemon-yellow pigmentation found in isolates of *Agrococcus spp.* We also discuss further the potential roles of *A. pavilionensis* RW1 in microbialite formation.

MATERIALS AND METHODS

Isolation, Growth Conditions, Microscopy, Phage Induction, Biochemical and Antibiotic Susceptibility Tests

Agrococcus pavilionensis strain RW1 was isolated by plating 0.5 g of a thrombolytic microbialite collected from a depth of 20 m in

Pavilion Lake, British Columbia (50.86677 °N, 121.74191 °W). Plating occurred in lysogeny broth (LB) [1% (w/v) tryptone, 0.5% (w/v) yeast extract, 1% (w/v) NaCl, pH 7], and incubated at 10°C for 1 week as an enrichment culture (**Figure 1**). The enrichment culture was selected for pigmented single colonies then were streaked for isolation on LB agar plates [solidified with 1.5% (w/v) agar] at 30°C for 3 days. Solidified LB agar was also used for assessing growth at various temperatures (4, 11, 16, 20, 25, 30, 35, 42, and 50°C), at pH 7 and 1% (w/v) NaCl. To assess the effect of pH (5, 6, 6.5, 7, 7.5, 8, 8.5, 9, 10, 10.5, and 11) on growth, standard solidified LB was used at 30°C and at a concentration of 1% (w/v) NaCl. To test the effect of salinity on growth, different amounts of NaCl were added to achieve final salinities of 0–6, 9, 12, 13, and 16% on solidified LB (pH 7). The cultures were grown at 30°C and maintained in LB medium or on agar at 1% NaCl, pH 7 and at 30°C. M-agar medium [0.5% (w/v) tryptone, 0.25% (w/v) yeast extract, 1% (w/v) NaCl, 1.5% (w/v) agar, pH 7]. A diluted version of LB agar medium, was used to determine filamentous growth under carbon-limitation. Strain characteristics, including colony morphology and cell morphologies, were determined by standard methods (Murry et al., 1994). Oxidase tests, biochemical enzyme assays, and carbohydrate utilization tests were completed using API20E (BioMérieux) test strips on cultures re-suspended in sterile water. Antibiotic susceptibility of strain RW1 was determined by the Kirby-Bauer method using antibiotic disks on solidified LB (Collee et al., 1996).

Prophage induction assays were done either by adding 0.2 μg ml^{-1} of mitomycin C or by heating cultures to 45°C for 5 min, incubating at 30°C for 3–10 h, and monitoring changes in turbidity until a decrease of OD_{600} to 0.1 or less (starting OD_{600} = 0.6). At several time points (3, 5, and 10 h), cells were pelleted at 3,250 × g and the supernatant filter-sterilized twice through a 0.22 μm pore-size Millex Durapore PVDF membrane (Millipore) filters before plating using a double agar overlay plaque assay (Kropinski et al., 2009).

Light and scanning electron microscopy (SEM) was completed on exponentially growing cells in LB medium. Cells were harvested after 48 h and viewed under oil immersion at 1,500 times magnification for light microscopy. For SEM, cultures in liquid LB were filtered at 72 h onto a 0.2 μm pore-size Supor polycarbonate membrane (Pall, Port Washington, NY, United States). Cells were fixed in 2.5% glutaraldehyde in phosphate-buffered saline (PBS) [137 mM NaCl, 2.7 mM KCL, 10 mM $Na_2HPO_4 2H_2O$, 2 mM KH_2PO_4, pH 7.4] for 30 min on ice. Cells were washed with PBS and post-fixed in 1% OsO_4 for 1 h. Stained cells were passed through a graded ethanol series (25, 50, 70, 95, and 100%) at 10-min intervals, and critical-point dried in 100% EtOH. A sputter coater applied 5 nm of gold/palladium alloy onto the cells before imaging by SEM using a Hitachi S4700 microscope.

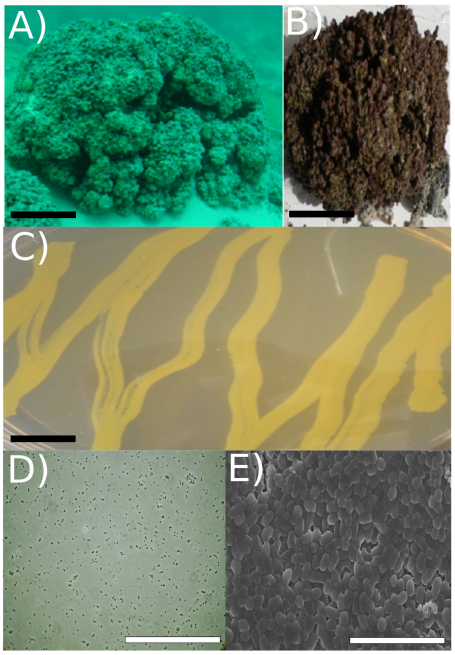

FIGURE 1 | Strain RW1 isolation environment, culture plate illustration, and microscopy. **(A)** Picture of Pavilion Lake microbialite (i.e., thrombolite) taken underwater (20 m depth sample, scale bar: ∼1 m). **(B)** Pavilion Lake microbialite (i.e., thrombolite) taken at sample station (20 m depth sample, scale bar: ∼15 cm). **(C)** Culture plate (∼24 h growth, the black scale bar ∼10 mm). **(D)** Light microscopy (∼72 h growth, scale bar: ∼80 μm); **(E)** SEM (∼72 h growth, scale bar: ∼5 μm). All microscopy (i.e., SEM/light) and culture plate photo (C-E) were completed at strain RW1 standard growth parameters on solidified LB-agar at 30°C, pH 7 and concentration 1% (w/v) NaCl.

Chemotaxonomic Analysis of Phospholipids

Phospholipid fatty acids (PLFAs) were extracted from cultures grown in 25 ml LB medium for 4 days at 22°C using triplicate biological replicates. Cultures were transferred into pre-combusted vials for an overnight solvent extraction in a 1:2:0.8 ratio of dichloromethane (DMC): methanol (MeOH): PBS [137 mM NaCl, 2.7 mM KCL, 10 mM Na_2HPO_4 $2H_2O$, 2 mM KH_2PO_4, pH 7.4] solution (Bligh and Dyer, 1959). The extract was filtered through a separatory funnel where DCM and water were added to achieve a mixture of MeOH-:DCM:water of 1:1:0.9 (Bligh and Dyer, 1959). The lower organic phase was removed and purified into polar, neutral, and non-polar fractions using liquid chromatography through silica gel. Phospholipids present in the polar fraction were subjected to mild alkaline methanolysis to produce fatty acid methyl esters (FAMEs) (Guckert et al., 1985). FAMEs were separated, identified, and quantified using gas chromatography mass spectrometry (GC/MS) (Agilent Technologies Inc., Santa Clara, CA, United States) with a DB-5MS capillary column (30 m × 0.32 mm I.D. ×0.25 μm film thickness) at a temperature regime of 50°C (1 min), 20°C min^{-1} to 130°C, 4°C min^{-1} to 160°C, and 8°C min^{-1} to 300°C (5 min). PLFAs were identified by retention time and mass spectra relative to those of reference standards (Bacterial Acid Methyl Ester Mix, Matreya Inc., Pleasant Gap, PA, United States; and Supelco 37 Component FAME Mix, Sigma-Aldrich Co., Bellefonte, PA, United States). A modified picolinyl ester derivatization was used to determine the branching point in unknown compounds (Dowd, 1998; Destaillats and Angers, 2002). Dimethyl disulfide

adduct derivatives were prepared to determine the double-bond position in unsaturated fatty acids (Nichols et al., 1986).

DNA Extraction, PCR, and Illumina Library Construction

DNA was extracted from early log-phase colonies of *Agrococcus pavilionensis* strain RW1 grown on LB agar plates using a QIAamp DNA Mini Kit, followed by MinElute PCR purification cleanup columns (Qiagen Germantown, MD, United States). We amplified 16S rRNA by using the universal primers 27f and 1492r (Lane, 1991), and a second PCR using primers 341f and 907r to obtain sequence overlap between the 27f and 1492r to complete the full-length 16S rRNA gene (Muyzer et al., 1993; Muyzer and Smalla, 1998). PCR products were sequenced using standard Sanger method on an ABI3730 (Applied Biosystems, Foster City, CA, United States). The Illumina MiSeq library was constructed using the NxSeq Library Prep Kit (Lucigen, Middleton, WI, United States) without the final 14-cycle PCR enrichment to avoid PCR bias. Quality control of the resulting library was completed using Agilent high-sensitivity DNA chips and digital droplet PCR (Hindson et al., 2011; White and Suttle, 2013; White et al., 2013a,b).

Phylogenetic Analysis

Sanger sequences obtained from the 27f-1492r and 341f-907r PCR products were merged into a full-length 16S rRNA gene sequence using Consed (Gordon et al., 1998) with manual editing. BLAST analysis of both the full-length PCR product and the whole-genome assembled 16S rRNA gene suggested that our culture was a member of the *Agrococcus* genus. The phylogenetic position of *A. pavilionensis* strain RW1 was assessed using the error-corrected whole-genome assembled 16S rRNA gene (∼99% similar to PCR amplified) rather than the PCR amplified sequence.

Multiple locus sequencing typing (MLST) marker analysis was completed by extracting protein sequences from rpoB (β subunit of bacterial RNA polymerase, ∼1156 amino acids), RecA (recombination protein A, ∼352 amino acids), gyrB (DNA gyrase subunit B, ∼679 amino acids), and ppK (Polyphosphate kinase, ∼752 amino acids, from both draft and completed genomes by BLASTP analysis or from prior MLST analysis (*A. jenensis* strain DSM9580 only, Stackebrandt et al., 2007) then concatenated into a ∼2939 amino acid sequence. All phylogenetic analyses were aligned using muscle-default parameters (−400 gap open with zero gaps extended) then clustered using UPGMB. Trees were then constructed using maximum likelihood with bootstrapping (1000 replicates) and the Jukes-Cantor substitution model for 16S rRNA gene full-length sequences (as default parameters), and Jones-Taylor-Thronton model (as default parameters) for ∼2939 amino acid MLST concatenated sequences in MEGA (Edgar, 2004; version 5.10, Tamura et al., 2011).

Whole-Genome Assembly and Genome Finishing

Read-error correction and Celera assembly (including plasmid pHC-CG425) and read partitioning were done as described (White et al., 2013b). Ray assembly of the bacterial genome using the error-corrected reads and phiX removal were done as described (White et al., 2013b,c).

A method to align two or more genomes, progressiveMauve, was used to find the best representative assembly and contig order, and to complete the genome (Darling et al., 2010). Contigs from Celera and Ray assemblies were pooled, then the remaining gaps were closed by recursive alignments in Mauve. The draft *A. lahaulensis* genome from NCBI (version ASM42510v1) was used for genome ordering. The ordered and aligned overlapping contigs were merged using the EMBOSS union script, yielding three circular contigs (Rice et al., 2000).

To confirm the three circular contigs as separate circular genomes, read-mapping was used. Error-corrected, phiX-removed reads were mapped back to the genome and plasmids using Bowtie2 (version 2.3.4) with the very sensitive local option (Langmead and Salzberg, 2012). The Bowtie2 read-mapping output file (Sam file) was visually inspected by the Tablet program (Milne et al., 2013).

Annotation was completed on RAST using SEED (Aziz et al., 2008); RAST server parameters used SEED subsystems with FIGfam under the Glimmer 3 option (Meyer et al., 2009). In addition to RAST, metabolic pathways were predicted using MetaPathways, a modular pipeline for gene prediction and annotation that uses pathway tools and the MetaCyc database to construct environmental pathway/genome databases (ePGBDs) (Paley and Karp, 2006; Konwar et al., 2013; Caspi et al., 2014).

Annotations were further analyzed for comparison to the *A. lahaulensis* strain K22-21 and analyzed for genome synteny, average amino acid identity, and phage lifestyle prediction. The genome circular plot was constructed using CGViewer (Grant and Stothard, 2008). *Agrococcus lahaulensis* strain K22-21, Celera (k0-k1250), and Ray (k0-k1250v2) assemblies were mapped to the completed genome of the *A. pavilionensis* strain RW1 using tBLASTx at an Expect (E) value of $1e^{-3}$ with 50% identity and 25 bp overlap. Synteny plots were completed in the RAST server module using a BLAST-based dot plot format (Aziz et al., 2008). Average amino acid identity (AAIr) analysis and functional gene similarities were calculated on the RAST server module, then parsed by a web-based tool (Aziz et al., 2008; Krebs et al., 2013). RAST-server annotation predicted a prophage element in the genome, which was analyzed for lifestyle preference (lytic or lysogenic) using the phage classification toolset (PHACTS) (McNair et al., 2012).

FR-hit program was used for metagenomic recruitment for the *Agrococcus* genomes using default parameters with a minimum identity >70% and an Expect (E) value $>1e^{-5}$ (Niu et al., 2011). The recruitments were then visualized with the R library ggplot2 (Wickham, 2009).

Data Availability

Agrococcus pavilionensis strain RW1 is listed at NCBI under BioProject accession PRJNA201450. The Celera assembly (k0-k1250) of *Agrococcus pavilionensis* RW1 is under RefSeq

NZ_ASHR00000000.1 and assembly GCF_000400485.1 at NCBI. The *Agrococcus lahaulensis* strain K22-21 is listed at NCBI under BioProject accession PRJNA188801.

RESULTS AND DISCUSSION

Morphology and Growth Characteristics

The cells were coccoid during log phase (∼48 h) and were irregular rod-like or coccoid in stationary phase (∼72 h) (**Figure 1**). The cell size of *A. pavilionensis* strain RW1 was 0.5 to 0.7 μm in diameter, which is similar to other described members of the genus (Zhang et al., 2010; **Table 1**). On solidified LB, colonies were bright yellow, smooth and circular, and were typically 0.5 to 2 mm in diameter after ∼72 h of growth at 30°C.

The morphology of *A. pavilionensis* strain RW1 shared features with other members of the genus but had a novel phenotype of filament-like growth. This growth form emerged in low-carbon conditions (i.e., diluted LB or M-agar), and had pale-yellow to white colonies with irregularly branching filaments. These could potentially act as nucleation points for carbonate precipitation within the Pavilion Lake microbialite mat. However, further study of carbonate precipitation and nucleation on *Agrococcus pavilionensis* strain RW1 is ongoing. While filamentous growth morphology is common among actinobacteria (e.g., isolates of *Streptomyces* spp.), this phenotype has not been reported for other members of the *Microbacteriaceae* (Doroghazi and Metcalf, 2013). Further experimentation is needed to confirm whether this is a unique adaptation of *A. pavilionensis* strain RW1 to microbialites or whether this phenotype is more widely spread across the genus of *Agrococcus* under low-carbon conditions.

Agrococcus pavilionensis strain RW1 grows on under many conditions. Growth occurred from pH 6 to 10, at 0 to 6% added NaCl, and over a temperature range of 11 to 42°C on LB agar (**Table 1**). A close relative, *A. lahaulensis* strain K22-21, has a narrower temperature range of growth (between 30 and 37°C) but can grow at salt concentrations as high as 7% (Mayilraj et al., 2006; **Table 1**). Contrary to expectations for a cold-water isolate, *Agrococcus pavilionensis* strain RW1 had the highest reported growth temperature for the genus (Zhang et al., 2010), at 42°C, and had no observed growth at or below 4°C (**Table 1**), while it exhibited slow growth at 10°C. This suggests that growth of *A. pavilionensis* RW1 within microbialites may be seasonal. Water temperatures in Pavilion Lake at 20 m range from 4 to 10°C throughout the year (Lim et al., 2009).

PLFA Characterization and Comparative Analysis

Phospholipid fatty acid is commonly used to distinguish bacterial isolates in classical bacterial strain naming. The PLFA composition of *A. pavilionensis* RW1 was distinct from other strains of *Agrococcus* spp., including its close relative *A. lahaulensis*. *Agrococcus pavilionensis* RW1 had half the amount of iC16:0 but three times as much C16:0 compared to *A. lahaulensis* (Mayilraj et al., 2006; **Table 2**). The branched unsaturated PLFA iC15:1Δ^4 was 3.5% of the total PLFAs found in *A. pavilionensis* RW1. It was only found in trace amounts (<1%) in *A. versicolor* strain K 114/01^T (Behrendt et al., 2008; **Table 2**). Branched monoenoic PLFAs such as iC15:1Δ^4 are typically used as biomarkers for anaerobic sulfate-reducing bacteria. Yet *A. pavilionensis* RW1 grows aerobically and does not reduce sulfate (Kohring et al., 1994). Branched PLFAs found in *A. pavilionensis* RW1 are known biomarkers for Gram-positive bacteria (Kaur et al., 2005). Although the PLFA profiles between *A. pavilionensis* RW1 and *A. lahaulensis* K22-21 are quite similar, the differences support the phylogenetic inference that the two isolates are from different taxonomic groups.

Unsaturated branched PLFAs found in *A. pavilionensis* RW1 may be a survival adaptation to cold temperatures present in Pavilion Lake since unsaturated fatty acids are used to compensate for a decrease in membrane fluidity found at cold temperatures (Los and Murata, 2004). *A. lahaulensis* was isolated from cold soil in Lahaul-Spiti Valley in the Indian Himalayas, which also contains unsaturated, branched PLFAs (Mayilraj et al., 2006). These features of unsaturated, branched PLFAs may therefore facilitate the adaption to colder temperatures of both *A. pavilionensis* and *A. lahaulensis*.

Evolutionary Placement of *Agrococcus pavilionensis* Strain RW1

Phylogenetic analysis of the 16S rRNA gene indicates that *A. pavilionensis* RW1 was most closely related to a clade containing *A. lahaulensis* K22-21, and an isolate from human-skin (**Figure 2**). However, a full-length 16S rRNA sequence alone was unable to resolve whether *A. pavilionensis* RW1 and *A. lahaulensis* are different species. MLST analysis suggests that *A. pavilionensis* strain RW1 and *A. lahaulensis* are in the same clade, but was unable to resolve whether they are separate species (**Figure 3**). MLST needs a minimum of seven loci to assign a species-level classification of closely related bacterial species. Only four loci are available for the genus *Agrococcus* (Maiden et al., 2013), so speciation could not be assigned by MLST alone.

Fortunately, a draft genome is available for *A. lahaulensis,* making it possible to infer their relationship based on an analysis of synteny between the two genomes. We mapped the assemblies of *A. lahaulensis* K22-21 and *A. pavilionensis* RW1 (both Ray and Celera) against the final circular chromosome of *A. pavilionensis* RW1 using tBLASTx. Only the *A. lahaulensis* assembly showed gaps (**Figure 4** and **Supplementary Table S1**). Synteny plots revealed 12 large gaps between the genomes of *A. pavilionensis* RW1 and *A. lahaulensis,* K22-21, along with 1752 non-conserved intergenic regions in *A. lahaulensis* (**Figure 5**). A comparison of functional gene annotations for *A. pavilionensis* RW1 and *A. lahaulensis* K22-21, using both SEED (RAST-based) and MetaCyc (MetaPathways-based), revealed >200 conserved genes, demonstrating that only a small core genome is conserved between the isolates (**Figure 5**). Thus, while they are closely related, it seems

TABLE 1 | Comparison of physiological properties of selected strains of *Agrococcus* spp. – No growth (–), Growth (+), Data not available (NA), Temperature (temp).

	Strain RW1	***A. lahaulensis*: *K22-21***	***A. baldri-V-108***	***A. citreus*[1] *D-I/Ia***	***A. jenensis*[1] *2002-39/1***	***A. terreus*[1] *DNG5***
Habitat	Microbialite	Desert soil	Air	Painting	Sandstone	Forest soil
Cell size (μm)						
Length	0.5–0.7	1.0–1.5	1.1–1.7	1.1–1.7	0.7–1.7	0.8–1.0
Width	0.3–0.5	0.6–1.0	0.7–1.0	0.7–1.0	0.7–1.0	0.4–0.5
Growth range(°C)						
11	+	NA	NA	NA	NA	NA
30	+	+	+	+	+	+
37	+	+	W	+	V	+
42	+	–	–	NA	–	NA
pH growth						
6	+	+	NA	NA	NA	+
7	+	+	+	+	+	+
10	+	+	NA	NA	NA	–
NaCl tolerance						
0%	+	NA	NA	NA	NA	+
6%	+	+	+	+	NA	–
7%	–	+	NA	+	NA	–

All growth measurements for A. pavilionensis strain RW1 were taken after 3 days. [1]Groth et al. (1996); Wieser et al. (1999); Zlamala et al. (2002); Zhang et al. (2010). Strain RW1 was measured directly on LB agar plates if colonies were present >100 growth (+) was used and if no colonies were present (–) was used. Weak growth (W) and variable growth (V) were described for two observations in the various references strains in there various manuscripts but were listed as no growth (–) in our table.

TABLE 2 | Selected cellular phospholipid fatty acids of selected strains of *Agrococcus* spp.

	Strain RW1	***A. lahaulensis*[1] *K22-21***	***A. baldri*[1] *V-108***	***A. citreus*[1] *D-1/1a***	***A. jenensis*[1] *2002-39/1***
C14:0	ND	ND	ND	tr	tr
iC14:0	ND	ND	ND	tr	tr
C15:0	ND	ND	ND	tr	ND
iC15:Δ4	3.5 ± 0.1	ND	ND	ND	ND
iC15:I	ND	ND	ND	ND	1.9
aiC15:I	ND	tr	ND	ND	0
iC15:0	8.8 ± 0.2	9.9	5.7	10	12.2
aiC15:0	46.6 ± 2.4	48.4	44.9	53.1	57.8
C16:0	5.5 ± 0.7	1.8	3	1.7	2
iC16:0	2.8 ± 0.6	5.8	7.5	12	12.6
iC17:0	3.1 ± 0.5	4.8	1.5	1.7	1.9
aiC17:0	29.7 ± 1.0	27.6	24.3	13.2	9.3
aiC17:I	ND	ND	ND	ND	ND
C18:0	ND	ND	ND	tr	tr

Values are percentages of total phospholipid fatty acids. Not detected (ND), Trace (<1%, tr). Strain RW1: A. pavilionensis [1]Mayilraj et al. (2006).

that their subclade within the genus shows high genomic plasticity.

Average amino acid identity between the two genomes supports classifying *A. pavilionensis* RW1 and *A. lahaulensis* K22-21 as different species. This is a robust measure for bacterial species classification based on whole-genome sequences and comparable to DNA-DNA hybridization (Konstantinidis and Tiedje, 2005). The standard cutoff to distinguish isolates as different bacterial species is <70% similarity by DNA-DNA hybridization. This corresponds to <95% average amino acid identity (Konstantinidis and Tiedje, 2005). The average amino acid identity for *A. pavilionensis* RW1 and *A. lahaulensis* K22-21 was only 86.2%, based on bidirectional whole-genome best-hit protein analysis using RAST annotation. That supports the classification of the isolates as different species (Konstantinidis and Tiedje, 2005; Krebs et al., 2013; **Figure 5**).

Biochemical Properties and Antibiotic Susceptibility

Agrococcus pavilionensis RW1 shared many biochemical properties with other members of the genus. That included being Gram-positive, but negative for oxidase, arginine dihydrolase, lysine decarboxylase, ornithine decarboxylase, urease, use of citrate and inositol/myo-inositol, production of hydrogen sulfide, and indole and acetoin and positive for catalase (Behrendt et al.,

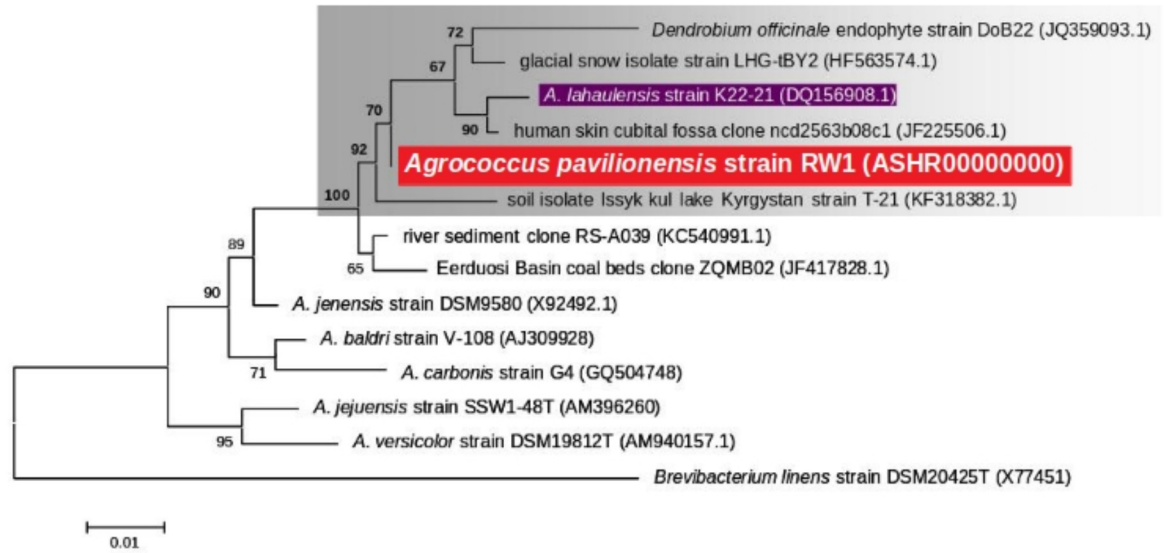

FIGURE 2 | Maximum likelihood tree based on 16S rRNA gene sequences (~1409 bp) showing the phylogenetic relationship among the different isolates of the genus *Agrococcus*. Bootstrap values greater than 50% are given at nodes. Bar represents a nucleotide substitution rate per 100 nucleotides.

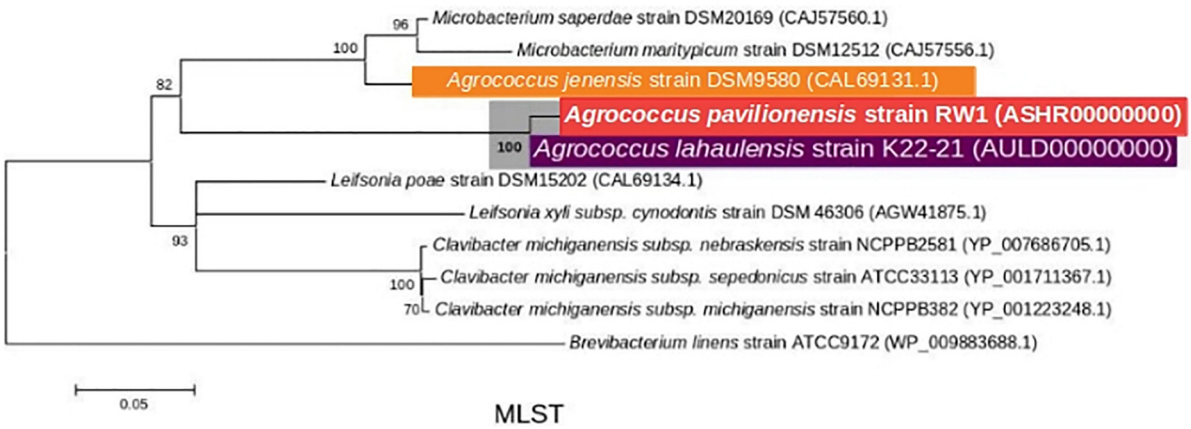

FIGURE 3 | Maximum-Likelihood tree based on MLST analysis (~2939 amino acid) showing the phylogenetic relationship among the different isolates of the genus *Agrococcus* and deeper relatives of the *Microbacteriaceae*. Bootstrap values greater than 50% are given at nodes. Bar represents a nucleotide substitution rate per 100 nucleotides.

2008). In contrast, *A. pavilionensis* RW1 was positive for β-galactosidase activity, whereas other isolates have only weak or no activity (Behrendt et al., 2008; **Table 3**), and *A. lahaulensis* has no predicted β-galactosidase activity or corresponding genes (Mayilraj et al., 2006; **Table 3**). Given the diversity of galactosidases in other microbial mat-dwelling heterotrophs, it is possible that β-galactosidase allows *A. pavilionensis* RW1 to digest exopolysaccharides or other carbohydrates within the mat, though this remains to be tested (Leyn et al., 2017).

Tests for antibiotic sensitivity in *A. pavilionensis* RW1 show a pattern that is similar to other isolates of *Agrococcus* spp., including being sensitive to penicillin, tetracycline, streptomycin, and rifampin (Wieser et al., 1999; **Table 4**). It is also sensitive to tobramycin, vancomycin, and clindamycin, but resistant to cefixime, sulfisoxazole, oxacillin, trimethoprim and a mixture of sulfamethoxazole/trimethoprim, antibiotics for which patterns of resistance in other strains are less clear, or for which comparable data are not available (**Table 4**). *Agrococcus citreus* and *A. jenensis* strain DSM9580^T and DSM9996 are sensitive to oxacillin at 5 μg and weakly sensitive to polymyxin (Wieser et al., 1999); whereas *A. pavilionensis* RW1 was resistant to oxacillin at 1 μg and sensitive to polymyxin (**Table 4**). The resistance of *A. pavilionensis* RW1 to 1 μg of oxacillin, while other *Agrococcus* spp. are sensitive to doses of 5 μg, suggests that *A. pavilionensis* RW1 could be sensitive to higher oxacillin concentrations (Wieser et al., 1999). β-lactamase is commonly involved in oxacillin resistance, but evidence for its occurrence was not found in the genomes of either *A. pavilionensis* RW1

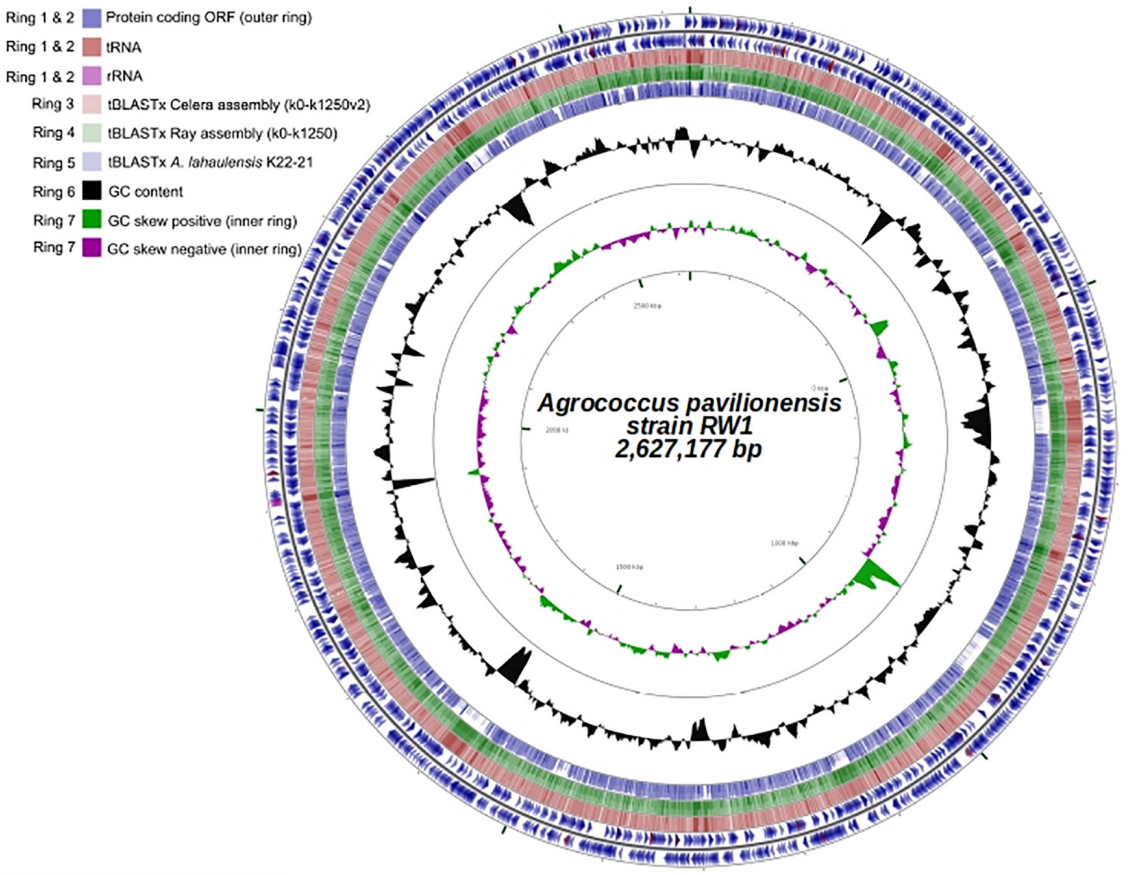

FIGURE 4 | Genome plot (~2.6 Mb) of *A. pavilionensis* strain RW1. Genome key (left corner): starts with the innermost ring, which is a genome ruler followed by GC skew (purple/green) and ends with two outer rings, which contain protein coding ORFs, tRNAs, and rRNAs.

or *A. lahaulensis* K22-21 (Hou et al., 2007). Although there were no putative antibiotic resistance genes predicted within the genome of *A. pavilionensis* RW1, pathways were predicted for aromatic compound degradation, including salicylate and gentisate catabolism, which may be involved in resistance. It is conceivable that this antibiotic resistance may be necessitated by exposure to toxic organic molecules produced by cyanobacterial mats, and that it may act as a survival mechanism (Neilan et al., 2013). To better understand antibiotic resistance in *Agrococcus* spp., more isolates should be tested in future studies.

Mobile DNA and Viral Elements

Mobile DNA elements, which are plasmid-encoded in *Agrococcus* sp. RW1, are predicted to function in integration, transposition, and heavy-metal resistance. Two plasmids (pHCCG425 and pLC-RRW783) discovered in *A. pavilionensis* RW1 are involved in integration, transposition, and heavy-metal resistance. The 1,427-bp plasmid pHC-CG425 has a GC content of 67.8% (4.7% less than the main chromosome) and two ORFs. One encodes a putative integrase, and the other encodes a hypothetical protein of unknown function. Meanwhile, pHC-CG425 plasmid shares strong similarities to gene clusters in other members of the phylum *Actinobacteria* including isolates of *Brevibacterium linens* and *Mycobacterium* spp. The second plasmid, pLC-RRW783, is 31,975 bp in length with a GC content of 70.6% (2% less than the main chromosome) and 36 ORFs (**Figure 6**), including putative coding sequences. Plasmid pLC-RRW783 contained ORFs annotated for mercuric reduction, arsenic resistance, various metal-dependent proteases, peptidases, ATPases, cadmium and unknown transporters, and an unclassified oxidoreductase. Seven ORFs in pLC-RRW783 have no predicted function and are annotated as hypothetical proteins.

Annotation of the genome of *A. pavilionensis* RW1 revealed a 34,174 bp prophage-like element that resembles *Siphoviridae* prophages found in actinobacteria. It has 43 predicted ORFs and a GC content of 70.1%, which is ~2% less than the GC content of the genome (**Supplementary Figure S1**). The addition of heat and mitomycin C did not result in induction, suggesting the prophage is incapable of entering the lytic cycle, or that the treatments were not suitable inducing agents (Zheng et al., 2014). By comparison, no prophage or phage-like genes are predicted in the genome of *A. lahaulensis* K22-21. The prophage in *A. pavilionensis* RW1 has a predicted coding sequence for a phage tail-length tape measure protein and a phage-protease

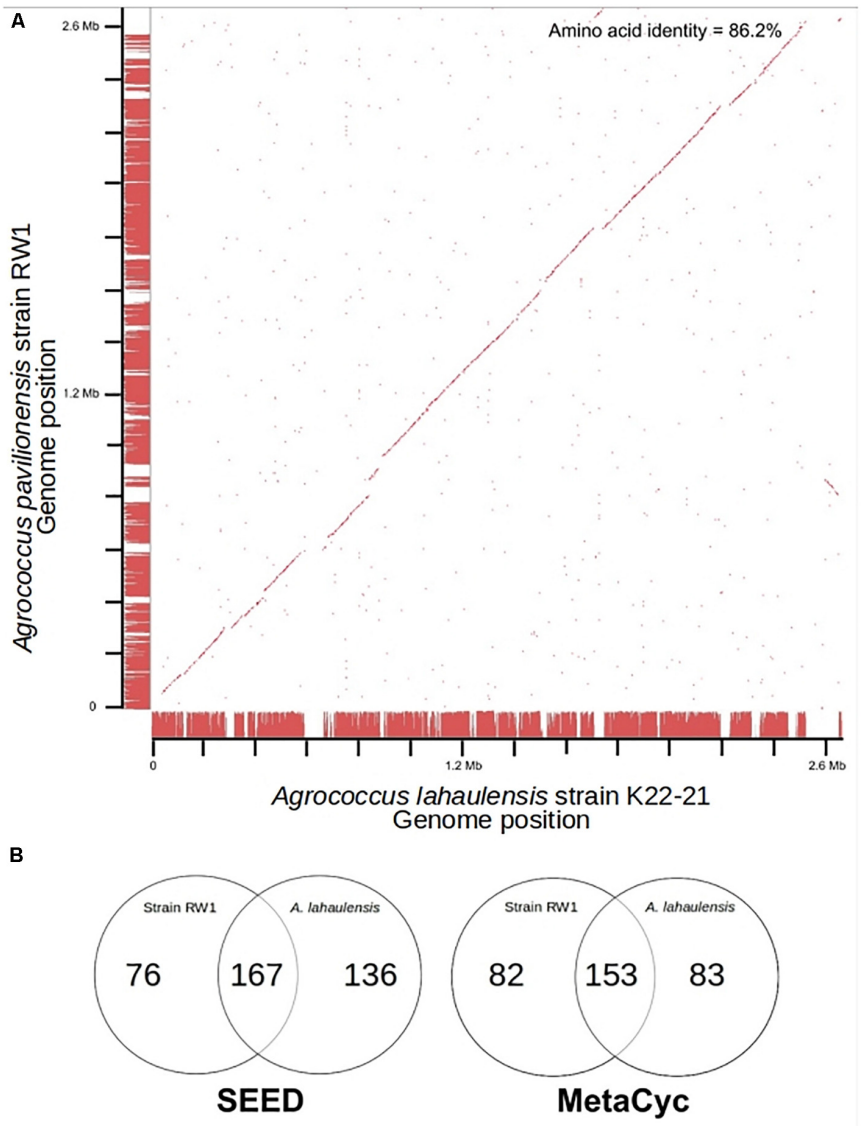

FIGURE 5 | Genome synteny and Venn diagrams of *A. pavilionensis* RW1 vs. *A. lahaulensis* K22-21. **(A)** RAST bidirectional BLAST genome synteny dot plot with Progressive Mauve alignments as axes. Red dots are positive BLAST hits based on the RAST genome comparison module. Red lines at the axes are regions of synteny based on Progressive Mauve. Amino acid identity was calculated by RAST functional module with a web-based tool (Krebs et al., 2013). **(B)** Venn Diagrams based on RAST SEED/FIGfams and Metapathways MetaCyc annotations.

gene that are related to sequences found in other phages of *Siphoviridae.* Those include VWB, phi-c31, and phi-BT1, as well as the *Mycobacterium* phage Brujita, which were found infecting *Streptomyces* spp. (Gregory et al., 2003; Van Dessel et al., 2005).

Nitrogen and Phosphorus Metabolism

Agrococcus pavilionensis RW1 encodes an incomplete ammonium utilization pathway that could also be involved in glutamine, glutamate, aspartate, and asparagine biosynthesis. It includes ORFs with similar coding sequences for glutamate-ammonia ligase adenyltransferase and for three NADPH glutamate synthase proteins. Glutamate-ammonia ligase adenyltransferase is conserved across related members in the phylum, including *Clavibacter michiganensis* and *Kocuria rhizophila.* It encodes about 1000 amino acids in length, whereas in *A. pavilionensis* RW1 it is truncated to 113 amino acids and is not predicted to be functional. The genomes of strain K22-21 and RW1 predicted ammonification of amino acids via aspartate, histidine, serine, glutamine, threonine ammonia lyases, and ammonium transporters. While both genomes encode a QacE-family quaternary ammonium compound efflux SMR transporter, strain RW1 encodes an extra copy. *Agrococcus pavilionensis* RW1 does release ammonium in late log phase or older cultures (via characteristic ammonium odor) Ammonium has been shown to increase carbonate biomineralization via ammonification through the deamination of amino acids

TABLE 3 | Biochemical properties of *Agrococcus* selected strains.

	Strain RW1	*A. lahaulensis*: K22-21	*A. baldri*: V-108	*A. citreus*[1] D-I/Ia	*A. jenensis*[1] 2002-39/1	*A. versicolor*[1] K114/01(T)
Hydrolysis of:						
Gelatinase	−	+	−	−	−	ND
Activity of:						
β-galactosidase	+	−	−	−	−	W
Assimilation of:						
D-glucose	+	−	+	−	+	+
D-mannitol	+	+	+	+	+	W
D-sorbitol	+	−	+	−	−	−
L-Rhamnose	+	+	−	−	−	−
D-sucrose	+	−	−	−	−	+
Amygdalin	+	−	−	−	−	−
L-arabinose	−	+	+	+	+	+

Not detected (ND), Weakly positive (W), Strain RW1: Agrococcus pavilionensis. [1]Behrendt et al., 2008.

TABLE 4 | Antibiotic susceptibility of selected strains of *Agrococcus* spp.

Antibiotic	Disk content	Strain RW1	*A. citreus*[1] DI/1aT	*A. jenensis*[1] DSM9580T
Sulfamethoxazole + Trimethoprim	23.75 + 1.25 μg	+	ND	ND
Penicillin	10 IU	−	−	−
Clindamycin	2 μg	−	ND	ND
Rifampin[μ]	5/30 μg	−	−	−
Polymyxin	300 IU	−	W	W
Cefixime	5 μg	+	ND	ND
Sulfisoxazole	300 μg	+	ND	ND
Oxacillin[μμ]	1/5 μg	+	−	−
Tetracycline	30 μg	−	−	−
Trimethoprim	5 μg	+	ND	ND
Tobramycin	10 μg	−	ND	ND
Vancomycin	30 μg	−	ND	ND
Streptomycin	10 μg	−	−	−

*Resistant (+), Sensitive (−), Weakly Sensitive (W), No Data (ND). *A. pavilionensis Strain RW1 was sensitive to 5 μg, whereas the other strains were sensitive at 30 μg. **A. pavilionensis Strain RW1 was resistant to 1 μg, whereas the other strains were sensitive at 5 μg. [1]Wieser et al. (1999).*

(Rodriguez-Navarro et al., 2003). Further experimental confirmation is needed to ascertain if *Agrococcus pavilionensis* RW1 ammonification leads to carbonate biomineralization.

Genes related to those encoding the phosphate (Pho) regulon for high-affinity uptake of phosphate. Included were the phosphate permease protein (PstA), phosphate regulon sensor protein (PhoR), and the phosphate-regulon transcriptional regulatory protein (PhoB). The phosphate-regulon proteins (PhoR/PhoB) and PstA were not predicted within the *A. lahaulensis* K22-21 genome. Exopolyphosphatase, a purine metabolism enzyme, is predicted in both *A. lahaulensis* K22-21 and *A. pavilionensis* RW1. Polyphosphate glucokinase is only predicted in the *A. lahaulensis* K22-21 genome. Pavilion Lake is oligotrophic, with low concentrations of total phosphorus (3.3 $\mu g\ L^{-1}$) (Lim et al., 2009). The phosphorus regulon (Pho) in the genome of *A. pavilionensis* RW1, which may be evidence of adaptation to low phosphate by encoding gene clusters linked to phosphorus regulation and acquisition. This machinery may represent an adaptation to the oligotrophic habitat where *A. pavilionensis* was found, since phosphate limitation has been found to actively induce the pho regulon in other bacteria (Suzuki et al., 2004). Indeed, genes associated with phosphorus adaptation and scavenging have also been found in metagenomic studies of other freshwater microbialites (Breitbart et al., 2009). Still, the response of the Pho regulon in *A. pavilionensis* RW1 under phosphorus limitation still has to be experimentally investigated.

Life in a Cold and Oligotrophic Microbialite Mat

Pavilion Lake microbialites exist in water that ranges in temperature from 4 to 10°C (Lim et al., 2009). This frigid environment is reflected in the genome of *A. pavilionensis* RW1, which has signatures of cold adaptation. These signatures include a single copy of *cspA* that encodes cold-shock protein A (CspA), a protein that is induced at cold temperatures (<10°C) and which is essential for growth at <10°C. It functions as a sort of molecular chaperone that binds mRNA, preventing

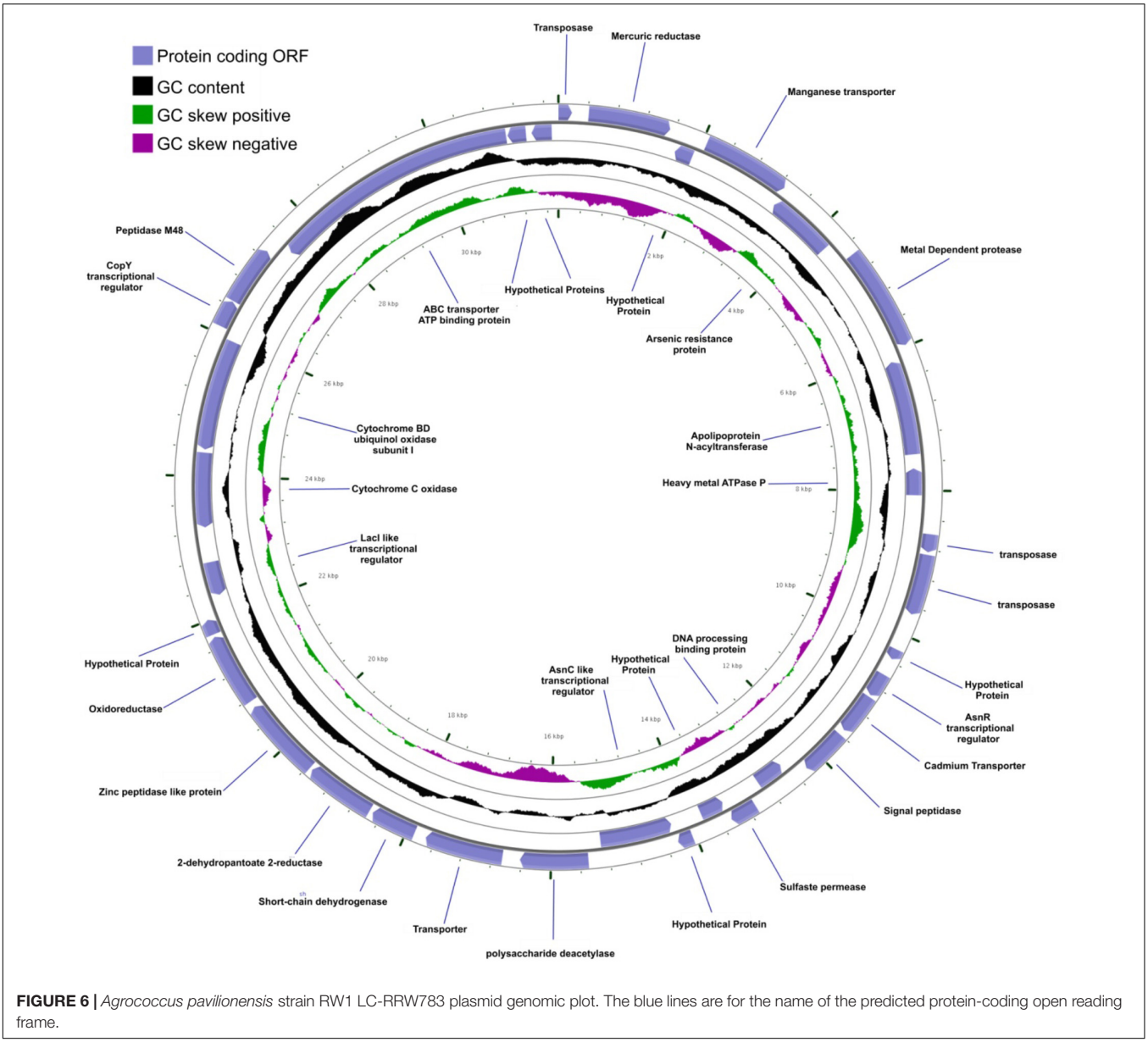

FIGURE 6 | *Agrococcus pavilionensis* strain RW1 LC-RRW783 plasmid genomic plot. The blue lines are for the name of the predicted protein-coding open reading frame.

secondary structure formation and ensuring translation at low temperatures (Yamanaka and Inouye, 1997). CspA is also expressed during sub-zero temperature growth in members of the genus *Exiguobacterium* (Rodrigues et al., 2008). *A. pavilionensis* RW1 also contains a rare branched unsaturated PLFA iC15:1Δ^4 and other branched unsaturated PLFAs, which could regulate membrane fluidity to combat the colder temperatures found in Pavilion Lake (Los and Murata, 2004).

Agrococcus pavilionensis RW1 was able to metabolize a wide range of carbon compounds. These include amygdalin (**Table 3**), which has not been reported for other *Agrococcus* spp., and is surprising because amygdalin-specific glycosylases were not predicted by the genome. Amygdalin utilization is known for its distant relative *Rhodococcus kunmingensis*, an actinobacteria isolated from soil (Wang et al., 2008). Analysis of the *A. pavilionensis* RW1 genome predicts carbohydrate utilization pathways for mannose, fructose, D-gluconate, trehalose, D-ribose, and glycogen, as well as for chitin, lactate, glycerate, deoxyribose, and deoxynucleoside catabolism. Carbohydrate utilization tests for D-glucose, D-mannitol, and D-sucrose validated the metabolic potential of the *A. pavilionensis* RW1 genome (**Table 3**). *Agrococcus pavilionensis* RW1 was able to grow on many more single-carbon sources compared to other members of the genus, possibly allowing access to carbon provided by cyanobacterial mats (Breitbart et al., 2009; **Table 3**).

Heavy Metal Metabolism and Detoxification

Agrococcus spp. appear to be a component of the Pavilion Lake microbialite community and potentially contribute to the detoxification of heavy metals. Such detoxification potential appears to be, an accessory feature of microbialite communities

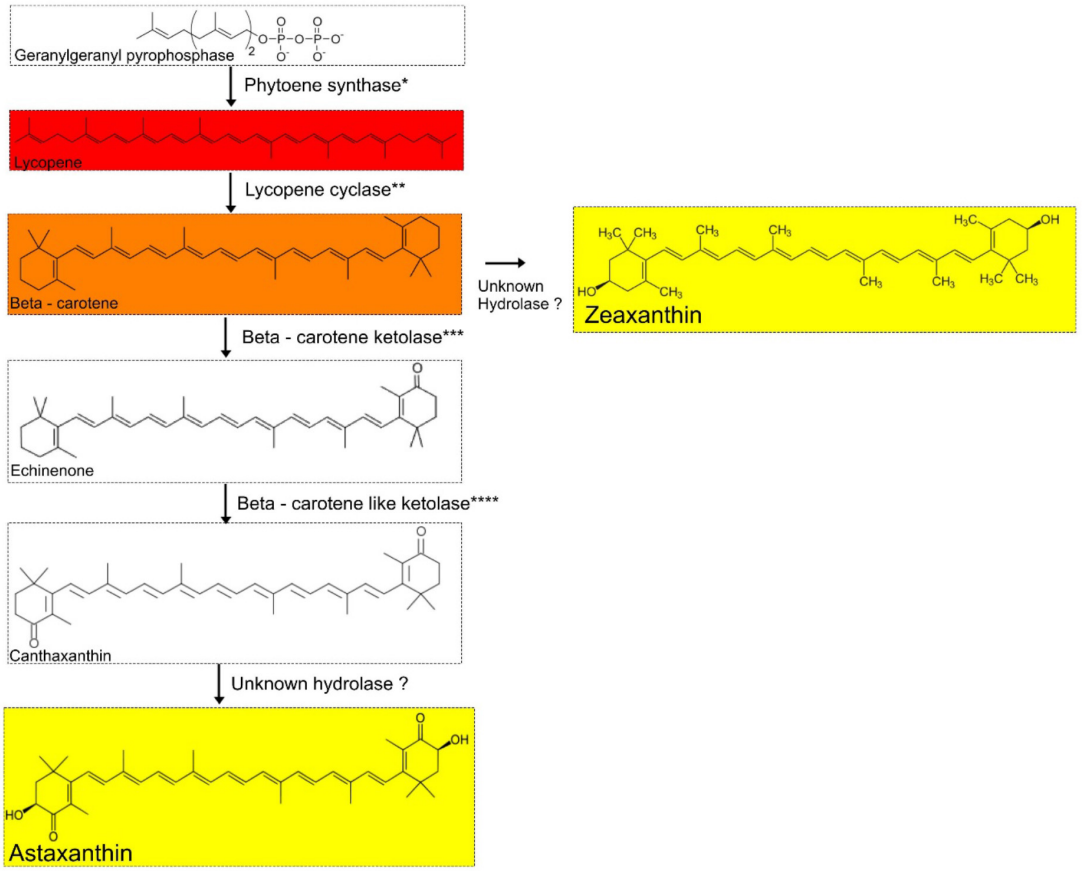

FIGURE 7 | Proposed carotenoid biosynthetic pathway for *Agrococcus* spp. Isolates of *Agrococcus* spp. have the genetic potential to accumulate C_{40} carotenoids (canthaxanthin and echinenone). Hydrolases are not predicted in the genomes of *A. pavilionensis* RW1 or *A. lahaulensis* K22-21. *Phytoene synthase, **Lycopene cyclase, ***Beta-carotene ketolase, ****Beta-carotene-like ketolase are predicted in the genomes of *A. pavilionensis* strain RW1 and *A. lahaulensis* strain K22-21.

(Ruvindy et al., 2016; White et al., 2016b; Kurth et al., 2017). Heavy-metal resistance genes, particularly those for arsenic resistance and metabolism, appear to be common in freshwater microbialites in Pavilion Lake (White et al., 2016b), as well as in microbialites from Socompa Lake in the Andes (Kurth et al., 2017) and in the marine stromatolites of Australia's Shark Bay (Ruvindy et al., 2016). We completed metagenomic-read recruitments from the 20 m Pavilion Lake microbialite metagenome (White et al., 2016b), comparing them to reads from our genome of *Agrococcus pavilionensis* strain RW1 (i.e., plasmids and chromosome). Using metagenomic-read recruitment, we confirm our *Agrococcus pavilionensis* strain RW1 is part of the Pavilion Lake microbial community (White et al., 2016b) We also obtained an assignment of previously unclassified actinobacterial sequences as 1% of metagenomic reads from the microbialite from which *A. pavilionensis* RW1 was isolated (**Supplementary Figure S2**). Metagenomic sequences recruited with the highest similarity (>95%) to the *A. pavilionensis* RW1 genome through tBLASTx ($1e^{-3}$) were predicted to be heavy-metal resistance genes. The metagenomic-read recruitment found hits to heavy-metal resistance genes contained on both the plasmid pLC-RRW783 and in the main chromosome of the *A. pavilionensis* RW1 genome. Sequences from the Pavilion Lake 20 m metagenome match the mercuric ion reductase and arsenic resistance genes (a*rsC* and a*rsR*) in the pLC-RRW783 plasmid. That means these heavy-metal resistance genes encoded in pLC-RRW783 plasmid could be mobile and potentially could be transferred to other bacteria. Together these data suggest that *A. pavilionensis* RW1 is a source of the heavy-metal resistance genes within the Pavilion Lake metagenome (White et al., 2016b). That adds new metabolic capabilities linking a cultured isolate directly to the Pavilion Lake microbialite community.

In other microbialite studies, these heavy-metal resistance genes are predominantly recruited to *Proteobacteria* and *Firmicute* phyla. However, some sequences were found relating to *Corynebacterium*, a distant relative of *Agrococcus* (Kurth et al., 2017). It is possible that members of distant phyla are transferring these heavy-metal resistance genes around by way of the horizontal gene transfer of plasmids (e.g., pLC-RRW783). Pavilion Lake water has undetectable levels of arsenic, cadmium, cobalt, copper, and chromium, along with very low levels of zinc (0.01 to 0.03 mg L^{-1}) (Lim et al., 2009). Thus, it is unclear why an organism from Pavilion Lake would carry gene clusters for heavy-metal resistance. Nevertheless, heavy metal resistance in

microbialite communities appears to be an accessory metabolism feature (Ruvindy et al., 2016; White et al., 2016b; Kurth et al., 2017). The pLC-RRW783 plasmid arsenic resistance genes (a*rsC* and a*rsR*) encoded in RW1 are glutathione-dependent, which appears to be common in low-arsenic environments (Escudero et al., 2013). Mercury was actively mined near Pavilion Lake in the 1940s (Stevenson, 1940), and could have been at a higher concentration at one time, suggesting these are vestiges from that era.

Generally, heavy metals including arsenic limit microbial growth which in turn would limit the growth of microbialites. However, we find two examples of thriving modern microbialite ecosystems in the presence of high arsenic, Laguna Brava (Sancho-Tomás et al., 2018) and Socompa Lake microbialites (Kurth et al., 2017). While the remnants of heavy-metal metabolism and detoxification are present in genomes of organisms currently in low heavy-metal environments Pavilion Lake (White et al., 2016b), and marine stromatolites of Shark Bay (Ruvindy et al., 2016).

The extracellular polymeric substances within cyanobacterial microbialite mats and biofilms bind heavy metals, then concentrate and remove them from the water column (Arp et al., 1999). Cyanobacteria are the primary producers in microbialites ecosystems (Dupraz et al., 2009), and are sensitive to heavy metals (Dudkowiak et al., 2011). Any heterotroph that removes and detoxifies heavy metals as a byproduct of their metabolism would be rewarded by substrates for growth (e.g., carbon, nitrogen, phosphorus, and metals) by healthy cyanobacterial mats. The removal and detoxification of these heavy metals would benefit the entire microbial communities within microbialites because high metal concentrations would lead to eventual collapse of microbial population levels. Initially, these genes may have conferred heavy-metal resistance, but now function under other stressors. Or they are still maintained to resist heavy metal, which would limit growth at the sub-micron level in cyanobacterial mats.

However, alternative hypotheses are possible, including that initially heavy-metal resistance genes are now serving alternative functions. Heavy-metal resistance genes can have secondary roles, as in *Rhodobacter sphaeroides*, where arsenic resistance genes have higher expression under high-salt stress (Tsuzuki et al., 2011). Metagenomic sequencing of Pavilion Lake microbialites revealed accessory metabolic genes related to heavy-metal and antibiotic resistance (White et al., 2016b). The heavy metal resistance genes in strain RW1 are retained in a low heavy-metal environment because they detoxify other substrates (e.g., antibiotics). Heavy metals drive co-selection of antibiotic resistance when aquatic systems are impacted by agriculture or other anthropogenic means (Seiler and Berendonk, 2012). Resistance in heavy metals has conferred resistance to antibiotics in a complex microbiome (e.g., chicken guts) (Nisanian et al., 2014). Further experimental evidence is needed to confirm whether these genes within strain RW1 confer heavy-metal resistance or other functions. In either case, strain RW1 carries these genes on plasmids and may be involved in transferring such accessory genes (e.g., heavy-metal resistance or antibiotic resistance) to the entire microbiome of Pavilion Lake.

Carotenoid Biosynthesis

The pathway responsible for the yellow pigmentation in the genus *Agrococcus* has not been described, although it has been suggested that diaminobutyric acid within the cell wall could impart the distinctive lemon-yellow colony color (Groth et al., 1996). However, other bacteria (e.g., *Cronobacter sakazakii*) have yellow colonies in the absence of diaminobutyric acid (Zhang et al., 2014). Actinobacterial isolates form yellow colonies and produce C_{40} carotenoids (e.g., canthaxanthin and echinenone) and C_{50} carotenoids (e.g., flavuxanthin) (Tao et al., 2007; Klassen, 2010). *Cronobacter sakazakii* strain BAA894 is a Gammaproteobacterium that produces yellow-pigmented colonies via a carotenoid biosynthetic pathway. When the *Cronobacter* carotenoid biosynthetic pathway was reconstructed and expressed in *E. coli,* the resulting colonies could produce lycopene, β-carotene, and cryptoxanthin, or zeaxanthin (Zhang et al., 2014). The production of zeaxanthin or zeaxanthin glycoside in *E. coli* changed the colony pigmentation from white to yellow (Zhang et al., 2014).

We screened *A. pavilionensis* RW1 and *A. lahaulensis* K22-21 for genes involved in carotenoid production; based on these results we propose a C_{40}/C_{50} carotenoid biosynthetic pathway (**Figure 7**). Both *A. pavilionensis* RW1 and *A. lahaulensis* K22-21 have the genetic potential to produce lycopene, β-carotene, canthaxanthin, echinenone, and zeaxanthin, or astaxanthin (**Figure 7**). The carotenoid biosynthetic pathways include predicted genes for phytoene synthase, phytoene dehydrogenase, beta-carotene ketolase, and the second beta carotene-like ketolase that probably converts echinenone to canthaxanthin, which t implies a C_{40}/C_{50} carotenoid pathway (Tao et al., 2007; **Figure 7**). Genes within the carotenogenic gene cluster of *A. pavilionensis* RW1 and *A. lahaulensis* K22-21 shared similarity to both *Brevibacterium linens*, a C_{50} carotenoid producer, and to *Cronobacter sakazakii* BAA894 (Krubasik and Sandmann, 2000).

The carotenoid biosynthetic pathway in *A. pavilionensis* RW1 and *A. lahaulensis* K22-21 is similar to that described for *Cronobacter sakazakii* BAA894 (Zhang et al., 2014). Zeaxanthin is the most likely pigment responsible for the yellow pigmentation in *Agrococcus* strains since its genome lacks the hydrolase gene necessary to convert zeaxanthin to other yellow pigments, such as astaxanthin, another yellow carotenoid that could be responsible (**Figure 7**). No hydrolase coding sequences were found in the genomes of *A. pavilionensis* RW1 or *A. lahaulensis* K22-21, which is the only type of enzyme known to convert β-carotene to zeaxanthin or canthaxanthin to astaxanthin (Klassen, 2010; Zhang et al., 2014).

The function of the yellow pigmentation in *A. pavilionensis* RW1 remains unclear, though we have excluded the possibility of phototrophy since bacteriorhodopsins and xanthorhodopsins were absent from its genome. A bacterial phytopathogen, *Pantoea stewartii*, has a phytoene synthase similar to strain RW1. It produces a yellow-pigmented carotenoid that has antioxidant properties (i.e., it is less sensitive to hydrogen peroxide stress), and it enables UV radiation protection (Mohammadi et al., 2012). The possibility that they function in photoprotection is a reasonable alternative, since the exceptionally clear waters of Pavilion Lake (due to low dissolved organic carbon) allow for

high penetration of solar UV radiation (Lim et al., 2009; Lionard et al., 2012). In this way, the yellow pigment in *Agrococcus pavilionensis* RW1 may act as a kind of protective sunscreen.

Carotenoids are known signal molecules beyond their role in pigmentation or photoprotection. Carotenoids can inhibit virulence factors in pathogens such as zeaxanthin, which inhibits *Pseudomonas aeruginosa* quorum-sensing systems and biofilm formation (Gökalsın et al., 2017). *Pantoea stewartii* yellow carotenoid, while providing both antioxidant properties and UV protection, also makes its carotenoids in a quorum-sensing dependent manner via the EsaI/EsaR system (Mohammadi et al., 2012). As with *Pseudomonas aeruginosa, Pantoea stewartii* losses virulence when its carotenoids production is limited (Mohammadi et al., 2012). In the non-pathogen *Rhodococcus* sp. SD-74, carotenoids are rapidly accumulated in biofilms (∼1 week). Bacterial cell aggregation or biofilm formation may trigger their synthesis (Zheng et al., 2013). We speculate that carotenoids in strain RW1 may help to trigger biofilm formation on carbonate minerals, initializing the steps in microbialite formation. Whether the function of carotenoids in strain RW1 is beyond the colony pigmentation presented here is unknown. Further investigations are needed to put strain RW1 into carotenoid roles in photoprotection, antioxidant properties, quorum-sensing, cell aggregation, and biofilm formation.

CONCLUSION

Our study provides a complete reference genome sequence for the first time from a member of the genus *Agrococcus*. Strain RW1 was isolated from a modern microbialite and possesses some features that distinguish it from previously characterized members of this genus. The presence of mobile elements, plasmids and a putative prophage in the genome implies much genetic promiscuity and could in part be responsible for high genomic plasticity as revealed by the low-gene similarities between *A. pavilionensis* RW1 and *A. lahaulensis* K22-21. The LC-RRW783 plasmid and the chromosome of *A. pavilionensis* encode genes related to heavy-metal resistance (and confer antibiotic resistance). Signatures of this encoding were also found in the metagenomic data from Pavilion Lake, confirming its presence and a potential role. In addition, the biochemical properties and physiological capabilities of *A. pavilionensis* RW1 were distinct from other members of the genus. *A. pavilionensis* RW1 possesses PLFA iC15:1Δ^4, has β-galactosidase activity, and uses amygdalin as a sole carbon source.

Phylogenetic analysis using either 16S rRNA gene or MLST could not resolve *A. pavilionensis* RW1 and *A. lahaulensis* K22-21 as different species and placed them consistently in the same clade. However, the whole-genome analysis did resolve that *A. pavilionensis* and *A. lahaulensis* are separate species based on relatively low functional gene conservation and less than 95% amino acid identity between the genomes. The presence of many non-conserved intergenic regions in *A. lahaulensis* also supports the classification of *A. pavilionensis* RW1 and *A. lahaulensis* K22-21 as separate species.

One of the most surprising aspects of *A. pavilionensis* was its high growth temperature, which may reflect its descent from a population of durable generalists, as seen in the diverse habitats where the genus can be found. However, the genome of *A. pavilionensis* also shows characteristics that may reflect adaptations to its present environment (or to conditions in the recent past, as in the case of heavy-metal resistance). These include a lipid profile ostensibly suited for cold climates, the possession of cold-shock proteins, and a low-phosphorous response regulon (Pho), all of which could be of use in a cold, oligotrophic environment. Other features may represent pre-adaptations; such as the carotenogenic gene cluster whose products could provide photoprotection in the clear water column of Pavilion Lake.

Strain RW1 was investigated for its potential role in Pavilion Lake microbialites, including candidate processes (e.g., ammonification and filament-like growth) by which actinobacteria may contribute to microbialite formation. These results provide a blueprint for future efforts to characterize stress response, pigment synthesis, and phage interactions in this widespread genus. Transcriptomics (including single cell) (Gavelis et al., 2015) and proteomics (White et al., 2016a; Callister et al., 2018) should be used in future experiments with strain RW1 to further elucidate functional profiles within the genome. *A. pavilionensis* strain RW1 represents a model system for further study of non-photosynthetic pigmented heterotrophic bacteria present within modern microbialites and microbial mats. Further exploration of microbialite-associated taxa is crucial to the understanding of these ecosystems and should include not only those driving the formation of the microbialite but also those contributing to the overall development and health of the community.

AUTHOR CONTRIBUTIONS

RW designed the study, collected and plated the isolate, performed growth studies, extracted DNA, prepared libraries, assembled and annotated the genome, and performed comparative genomic and phylogenetic analysis. SS performed PLFA, with financial support from GS. EG performed culturing experiments. RW preserved cells for scanning electron microscopy, which was imaged by GG. RW and GG wrote the manuscript. All authors participated in the manuscript drafting process.

FUNDING

Financial support for sample collection was provided by the MARSLIFE Project [9F052-10-0176] funded by the Canadian Space Agency. The laboratory work was supported by a Discovery Grant from the Natural Science and Engineering Council of Canada (CAS), and grants to CS from the Tula Foundation and the Canadian Institute for Advanced Research. Infrastructure support for laboratory work was provided to CS from the Canadian Foundation for Innovation and the British Columbia Knowledge Development Fund.

ACKNOWLEDGMENTS

Thanks to Donnie Reid and members of the dive team who recovered the microbialite from the lake, Amy M. Chan and Jan Finke who helped with sample collection and processing, and the other individuals associated with the PLRP team. We thank Sugandha Dandekar (Uma) and Hemani Wijesuriya at the UCLA Sequencing & Genotyping Core and the UBC NAPS facility for conducting the sequencing. We are grateful to the Ts'kw'aylaxw First Nation, Linda and Mickey Macri and the Pavilion Community, and British Columbia Parks for their continued support. We thank Dr. Julian Davies for antibiotic disks and Cedric Brimacombe for light microscopy. We thank Dr. Brendan P. Burns for his help editing the final manuscript.

SUPPLEMENTARY MATERIAL

The Supplementary Material for this article can be found online at: https://www.frontiersin.org/articles/10.3389/fmicb.2018.02180/full#supplementary-material

FIGURE S1 | Putative prophage genome from RAST annotation. The gray represents genes of hypothetical function. The red gene (label 1) is hypothetical phage gene homologous across strain RW1 and the representative phage/bacterial comparison genomes. The light blue (labeled 16) is phage terminase and tail proteins. The numbers represent genome locations.

FIGURE S2 | FR-Hit recruitment plot of Pavilion Lake 20 m microbialite reads (~7.5 Million) to *A. pavilionensis* strain RW1 isolated from 20 m microbialites and to *A. lahaulensis* strain K22-21.

TABLE S1 | Final assembly statistics. *Published in White and Suttle (2013).

REFERENCES

Arp, G., Reimer, A., and Reitner, J. (1999). Calcification in cyanobacterial biofilms of alkaline salt lakes. *Eur. J. Phycol.* 34, 393–403. doi: 10.1080/09670269910001736452

Aziz, R. K., Bartels, D., Best, A. A., DeJongh, M., Disz, T., Edwards, R. A., et al. (2008). The RAST server: rapid annotations using subsystems technology. *BMC Genomics* 9:75. doi: 10.1186/1471-2164-9-75

Behrendt, U., Schumann, P., and Ulrich, A. (2008). *Agrococcus versicolor* sp. nov., an actinobacterium associated with the phyllosphere of potato plants. *Int. J. Syst. Bacteriol.* 58, 2833–2838. doi: 10.1099/ijs.0.2008/001610-0

Bligh, E. G., and Dyer, W. J. (1959). A rapid method of total lipid extraction and purification. *Can. J. Biochem. Phys.* 37, 911–917. doi: 10.1139/y59-099

Bora, N., Vancanneyt, M., Gelsomino, R., Swings, J., Brennan, N., Cogan, T. M., et al. (2007). *Agrococcus casei* sp. nov., isolated from the surfaces of smear-ripened cheeses. *Int. J. Syst. Evol. Microbiol.* 57, 92–97. doi: 10.1099/ijs.0.64270-0

Bottos, E. M., Vincent, W. F., Greer, C. W., and Whyte, L. G. (2008). Prokaryotic diversity of arctic ice shelf microbial mats. *Environ. Microbiol.* 10, 950–966. doi: 10.1111/j.1462-2920.2007.01516.x

Breitbart, M., Hoare, A., Nitti, A., Siefert, J., Haynes, M., Dinsdale, E., et al. (2009). Metagenomic and stable isotopic analyses of modern freshwater microbialites in Cuatro Cienegas, Mexico. *Environ. Microbiol.* 11, 16–34. doi: 10.1111/j.1462-2920.2008.01725.x

Burne, R. V., and Moore, L. S. (1987). Microbialites: organosedimentary deposits of benthic microbial communities. *Palaios* 2, 241–254. doi: 10.2307/3514674

Burns, B. P., Gudhka, R. K., and Neilan, B. A. (2012). Genome sequence of the halophilic archaeon *Halococcus hamelinensis*. *J. Bacteriol.* 194, 2100–2101. doi: 10.1128/JB.06599-11

Callister, S. J., Fillmore, T. L., Nicora, C. D., Shaw, J. B., Purvine, S. O., Orton, D. J., et al. (2018). Addressing the challenge of soil metaproteome complexity by improving metaproteome depth of coverage through two-dimensional liquid chromatography. *Soil Biol. Biochem.* 125, 290–299. doi: 10.1016/j.soilbio.2018.07.018

Caspi, R., Altman, T., Billington, R., Dreher, K., Foerster, H., Fulcher, C. A., et al. (2014). The MetaCyc database of metabolic pathways and enzymes and the BioCyc collection of pathway/genome databases. *Nucleic Acids Res.* 42, D459–D471. doi: 10.1093/nar/gkt1103

Collee, J. G., Miles, R. S., and Watt, B. (1996). "Tests for the identification of bacteria," in *Mackie and McCartney Practical Medical Microbiology*, 14th Edn, eds J. G. Collee, A. G. Fraser, B. P. Marmion, and A. Simmons (London: Churchill Livingstone), 131–149.

Darling, A. E., Mau, B., and Perna, N. T. (2010). progressiveMauve: multiple genome alignment with gene gain, loss and rearrangement. *PLoS One* 5:e11147. doi: 10.1371/journal.pone.0011147

Destaillats, F., and Angers, P. (2002). One-step methodology for the synthesis of FA picolinyl esters from intact lipids. *JAOCS* 3, 253–256. doi: 10.1007/s11746-002-0469-7

Dhanjal, A., Kaur, I., Suresh, K., Schumann, P., Cameotra, S. S., Pukall, R., et al. (2011). *Agrococcus carbonis* sp. nov., isolated from soil of a coal mine. *Int. J. Syst. Bacteriol.* 61, 1253–1258. doi: 10.1099/ijs.0.024745-0

Doroghazi, J. R., and Metcalf, W. W. (2013). Comparative genomics of actinomycetes with a focus on natural product biosynthetic genes. *BMC Genomics* 14:611. doi: 10.1186/1471-2164-14-611

Dowd, M. (1998). Identification of the unsaturated heptadecyl fatty acids in the seed oils of *Thespesia populnea* and *Gossypium hirsutum*. *J. Am. Oil Chem. Soc.* 89, 1599–1609. doi: 10.1007/s11746-012-2071-5

Dudkowiak, A., Olejarz, B., Łukasiewicz, J., Banaszek, J., Sikora, J., and Wiktorowicz, K. (2011). Heavy metals effect on cyanobacteria *Synechocystis aquatilis* study using absorption, fluorescence, flow cytometry, and photothermal measurements. *Intern. J. Thermophys.* 32, 762–773. doi: 10.1007/s10765-010-0852-3

Dupraz, C., Reid, R. P., Braissant, O., Decho, A. W., Norman, R. S., and Visscher, P. T. (2009). Processes of carbonate precipitation in modern microbial mats. *Earth Sci. Rev.* 96, 141–162. doi: 10.1016/j.earscirev.2008.10.005

Edgar, R. C. (2004). MUSCLE: multiple sequence alignment with high accuracy and high throughput. *Nucleic Acids Res.* 32, 1792–1797. doi: 10.1093/nar/gkh340

Escudero, L. V., Casamayor, E. O., Chong, G., Pedrós-Alió, C., and Demergasso, C. (2013). Distribution of microbial arsenic reduction, oxidation and extrusion genes along a wide range of environmental arsenic concentrations. *PLoS One* 8:e78890. doi: 10.1371/journal.pone.0078890

Gavelis, S., White, R. A. III, Suttle, C. A., Keeling, P. J., and Leander, B. S. (2015). Single-cell transcriptomics using spliced leader PCR: evidence for multiple losses of photosynthesis in polykrikoid dinoflagellates. *BMC Genomics* 16:528. doi: 10.1186/s12864-015-1636-8

Gökalsın, B., Aksoydan, B., Erman, B., and Sesal, N. C. (2017). Reducing virulence and biofilm of *Pseudomonas aeruginosa* by potential quorum sensing inhibitor carotenoid: zeaxanthin. *Microb. Ecol.* 74, 466–473. doi: 10.1007/s00248-017-0949-943

Gordon, D. C., Abajian, C., and Green, P. (1998). Consed: a graphical tool for sequence finishing. *Genome Res.* 8, 195–202. doi: 10.1101/gr.8.3.195

Grant, J. R., and Stothard, P. (2008). The CGView server: a comparative genomics tool for circular genomes. *Nucleic Acids Res.* 36, 181–184. doi: 10.1093/nar/gkn179

Gregory, M. A., Till, R., and Smith, M. C. (2003). Integration site for *Streptomyces* phage phiBT1 and development of site-specific integrating vectors. *J. Bacteriol.* 185, 5320–5323. doi: 10.1128/JB.185.17.5320-5323.2003

Groth, I., Schumann, P., Weiss, N., Martin, K., and Rainey, F. A. (1996). *Agrococcus jenensis* gen. nov., sp. nov., a new genus of actinomycetes with diaminobutyric acid in the cell wall. *Int. J. Syst. Bacteriol.* 46, 234–239. doi: 10.1099/00207713-46-1-234

Guckert, J. B., Antworth, C. P., Nichols, P. D., and White, D. C. (1985). Phospholipid, ester-linked fatty acid profiles as reproducible assays for changes in prokaryotic community structure of estuarine sediments. *FEMS Microbiol. Ecol.* 31, 147–158. doi: 10.1111/j.1574-6968.1985.tb01143.x

Havemann, S. A., and Foster, J. S. (2008). A comparative characterization of the microbial diversity in an artificial microbialite model and a natural stromatolite. *Appl. Environ. Microbiol.* 74, 7410–7421. doi: 10.1128/AEM.01710-08

Hindson, B. J., Ness, K. D., Masquelier, D. A., Belgrader, P., Heredia, N. J., Makarewicz, A. J., et al. (2011). High-throughput droplet digital PCR system for absolute quantitation of DNA copy number. *Anal. Chem.* 83, 8604–8610. doi: 10.1021/ac202028g

Hou, Z., Meng, J. R., Zhao, J. R., Hu, B. Q., Liu, J., Yan, X. J., et al. (2007). Inhibition of beta-lactamase-mediated oxacillin resistance in Staphylococcus aureus by a deoxyribozyme. *Acta Pharmacol. Sin.* 28, 1775–1782. doi: 10.1111/j.1745-7254.2007.00646.x

Kaur, A., Chaudhary, A., Kaur, A., Choudhary, R., and Kaushik, R. (2005). Phospholipid fatty acid – a bioindicator of environment monitoring and assessment in soil ecosystem. *Curr. Sci.* 89, 1103–1112.

Klassen, J. L. (2010). Phylogenetic and evolutionary patterns in microbial carotenoid biosynthesis are revealed by comparative genomics. *PLoS One* 5:e11257. doi: 10.1371/journal.pone.0011257

Kohring, L. L., Ringelberg, D. B., Devereux, R., Stahl, D. A., Mittelman, M. W., and White, D. C. (1994). Comparison of phylogenetic relationships based on phospholipid fatty acid profiles and ribosomal RNA sequence similarities among dissimilatory sulfate–reducing bacteria. *FEMS Microbiol. Lett.* 119, 303–308. doi: 10.1111/j.1574-6968.1994.tb06905.x

Konstantinidis, K. T., and Tiedje, J. M. (2005). Genomic insights that advance the species definition for prokaryotes. *Proc. Natl. Acad. Sci. U.S.A.* 102, 2567–72. doi: 10.1073/pnas.0409727102

Konwar, K. M., Hanson, N. W., Pagé, A. P., and Hallam, S. J. (2013). MetaPathways: a modular pipeline for constructing pathway/genome databases from environmental sequence information. *BMC Bioinform.* 14:202. doi: 10.1186/1471-2105-14-202

Krebs, J. E., Gale, A. N., Sontag, T. C., Keyser, V. K., Peluso, E. M., and Newman, J. D. (2013). *A Web-Based Method to Calculate Average Amino Acid Identity (AAI) between Prokaryotic Genomes*. Available at: www.lycoming.edu/ newman/aai

Kurth, D., Amadio, A., Ordoñez, O. F., Albarracín, V. H., Gärtner, W., and Farías, M. E. (2017). Arsenic metabolism in high altitude modern stromatolites revealed by metagenomic analysis. *Sci. Rep.* 7:1024. doi: 10.1038/s41598-017-00896-0

Krubasik, P., and Sandmann, G. (2000). A carotenogenic gene cluster from *Brevibacterium linens* with novel lycopene cyclase genes involved in the synthesis of aromatic carotenoids. *Mol. Gen. Genet.* 263, 423–432. doi: 10.1007/s004380051186

Lane, D. J. (1991). "16S/23S rRNA sequencing," in *Nucleic Acid Techniques in Bacterial Systematics*, eds E. Stackebrandt and M. Goodfellow (New York, NY: John Wiley and Sons), 115–175.

Langmead, B., and Salzberg, S. (2012). Fast gapped-read alignment with Bowtie 2. *Nat. Methods* 9, 357–359. doi: 10.1038/nmeth.1923

Lee, S. D. (2008). Agrococcus jejuensis sp. nov., isolated from dried seaweed. *Int. J. Syst. Evol. Microbiol.* 58, 2297–2300. doi: 10.1099/ijs.0.65731-0

Leyn, S. A., Maezato, Y., Romine, M. F., and Rodionov, D. A. (2017). Genomic reconstruction of carbohydrate utilization capacities in microbial-mat derived consortia. *Front. Microbiol.* 8:1304. doi: 10.3389/fmicb.2017.01304

Lim, D. S. S., Laval, B. E., Slater, G., Antoniades, D., Forrest, A. L., Pike, W., et al. (2009). Limnology of Pavilion Lake B.C. - Characterization of a microbialite forming environment. *Fundam. Appl. Limnol.* 173, 329–351. doi: 10.1127/1863-9135/2009/0173-0329

Lionard, M., Péquin, B., Lovejoy, C., and Vincent, W. F. (2012). Benthic cyanobacterial mats in the high arctic: multi-layer structure and fluorescence responses to osmotic stress. *Front. Microbiol.* 3:140. doi: 10.3389/fmicb.2012.00140

Los, D. A., and Murata, N. (2004). Membrane fluidity and its roles in the perception of environmental signals. *Biochim. Biophys. Acta* 2, 142–157. doi: 10.1016/j.bbamem.2004.08.002

Louyakis, A. S., Gourlé, H., Casaburi, G., Bonjawo, R. M. E., Duscher, A. A., and Foster, J. S. (2018). A year in the life of a thrombolite: comparative metatranscriptomics reveals dynamic metabolic changes over diel and seasonal cycles. *Environ. Microbiol.* 20, 842–861. doi: 10.1111/1462-2920.14029

Maiden, M. C., van Rensburg, M. J., Bray, J. E., Earle, S. G., Ford, S. A., Jolley, K. A., et al. (2013). MLST revisited: the gene-by-gene approach to bacterial genomics. *Nat. Rev. Microbiol.* 11, 728–736. doi: 10.1038/nrmicro3093

Mayilraj, S., Suresh, K., Schumann, P., Kroppenstedt, R. M., and Saini, H. S. (2006). *Agrococcus lahaulensis* sp. nov., isolated from a cold desert of the Indian Himalayas. *Int. J. Syst. Evol. Microbiol.* 56, 1807–1810. doi: 10.1099/ijs.0.64247-0

McNair, K., Bailey, B. A., and Edwards, R. A. (2012). PHACTS, a computational approach to classifying the lifestyle of phages. *Bioinformatics* 28, 614–618. doi: 10.1093/bioinformatics/bts014

Meyer, F., Overbeek, R., and Rodriguez, A. (2009). FIGfams: yet another set of protein families. *Nucleic Acids Res.* 37, 6643–6654. doi: 10.1093/nar/gkp698

Milne, I., Stephen, G., Bayer, M., Cock, P. J. A., Pritchard, L., Cardle, L., et al. (2013). Using tablet for visual exploration of second-generation sequencing data. *Brief. Bioinform.* 14, 193–202. doi: 10.1093/bib/bbs012

Mohammadi, M., Burbank, L., and Roper, M. C. (2012). Biological role of pigment production for the bacterial phytopathogen *Pantoea stewartii* subsp. *stewartii*. *Appl. Environ. Microbiol.* 78, 6859–6865. doi: 10.1128/AEM.01574-1512

Mueller, D. R., Vincent, W. F., Bonilla, S., and Laurion, I. (2005). Extremotrophs, extremophiles and broadband pigmentation strategies in a high arctic shelf ecosystem. *FEMS Microbiol. Ecol.* 53, 73–87. doi: 10.1016/j.femsec.2004.11.001

Muyzer, G., De Waal, E. C., and Uitterlinden, A. G. (1993). Profiling of complex microbial populations by denaturing gradient gel electrophoresis analysis of polymerase chain reaction-amplified genes coding for 16S rRNA. *Appl. Environ. Microbiol.* 59, 695–700.

Muyzer, G., and Smalla, K. (1998). Application of denaturing gradient gel electrophoresis (DGGE) and temperature gradient gel electrophoresis (TGGE) in microbial ecology. *Antonie Van Leeuwenhoek* 73, 127–141. doi: 10.1023/A:1000669317571

Neilan, B. A., Pearson, L. A., Muenchhoff, J., Moffitt, M. C., and Dittmann, E. (2013). Environmental conditions that influence toxin biosynthesis in cyanobacteria. *Environ. Microbiol.* 5, 1239–1253. doi: 10.1111/j.1462-2920.2012.02729.x

Nichols, P. D., Gukert, J. B., and White, D. C. (1986). Determination of monounsaturated fatty acid double bond position and geometry for microbial monocultures and complex consortia by capillary GC-MS of their dimethyl disulfide adducts. *J. Microb. Methods* 5, 49–55. doi: 10.1016/0167-7012(86)90023-0

Nisanian, M., Holladay, S. D., Karpuzoglu, E., Kerr, R. P., Williams, S. M., Stabler, L., et al. (2014). Exposure of juvenile Leghorn chickens to lead acetate enhances antibiotic resistance in enteric bacterial flora. *Poult. Sci.* 93, 891–897. doi: 10.3382/ps.2013-03600

Niu, B., Zhu, Z., Fu, L., Wu, S., and Li, W. (2011). FR-HIT, a very fast program to recruit metagenomic reads to homologous reference genomes. *Bioinformatics* 27, 1704–1705. doi: 10.1093/bioinformatics/btr252

Nübel, U., Garcia-Pichel, F., Kühl, M., and Muyzer, G. (1999). Quantifying microbial diversity: morphotypes, 16S rRNA genes, and carotenoids of oxygenic phototrophs in microbial mats. *Appl. Environ. Microbiol.* 65, 422–430.

Nutman, A. P., Bennett, V. C., Friend, C. R. L., Van Kranendonk, M. J., and Chivas, A. R. (2016). Rapid emergence of life shown by discovery of 3,700-million-year-old microbial structures. *Nature* 537, 535–538. doi: 10.1038/nature19355

Paley, S. M., and Karp, P. D. (2006). The Pathway Tools cellular overview diagram and Omics Viewer. *Nucleic Acids Res.* 34, 3771–3778. doi: 10.1093/nar/gkl334

Perry, R. S., Mcloughlin, N., Lynne, B. Y., Sephton, M. A., Oliver, J. D., Perry, C. C., et al. (2007). Defining biominerals and organominerals: direct and indirect indicators of life. *Sed. Geol.* 201, 157–179. doi: 10.1016/j.sedgeo.2007.05.014

Rice, P., Longden, I., and Bleasby, A. (2000). EMBOSS: the european molecular biology open software suite. *Trends Genet.* 16, 276–277. doi: 10.1016/S0168-9525(00)02024-2

Rodrigues, D. F., Ivanova, N., He, Z., Huebner, M., Zhou, J., and Tiedje, J. M. (2008). Architecture of thermal adaptation in an *Exiguobacterium sibiricum* strain isolated from 3 million-year-old permafrost: a genome and transcriptome approach. *BMC Genomics* 9:547. doi: 10.1186/1471-2164-9-547

Rodriguez-Navarro, C., Rodriguez-Gallego, M., Ben Chekroun, K., and Gonzalez-Munoz, M. T. (2003). Conservation of ornamental stone by *Myxococcus xanthus*-induced carbonate biomineralization. *Appl. Environ. Microbiol.* 69, 2182–2193. doi: 10.1128/AEM.69.4.2182-2193

Ruvindy, R., White, R. A. III, Neilan, B. A., and Burns, B. P. (2016). Unraveling core microbial metabolisms in the hypersaline microbial mats of Shark Bay using high-throughput metagenomics. *ISME J.* 10, 183–196. doi: 10.1038/ismej.2015.87

Saghaï, A., Zivanovic, Y., Zeyen, N., Moreira, D., Benzerara, K., Deschamps, P., et al. (2015). Metagenome-based diversity analyses suggest a significant contribution of non-cyanobacterial lineages to carbonate precipitation in modern microbialites. *Front. Microbiol.* 6:797. doi: 10.3389/fmicb.2015.0079

Sancho-Tomás, M., Somogyi, A., Medjoubi, K., Bergamaschi, A., Visscher, P. T., Van Driesschee, E. S. A., et al. (2018). Distribution, redox state and (bio)geochemical implications of arsenic in present-day microbialites of Laguna Brava, Salar de Atacama. *Chem. Geol.* 490, 13–21. doi: 10.1016/j.chemgeo.2018.04.029

Seiler, C., and Berendonk, U. T. (2012). Heavy metal driven co-selection of antibiotic resistance in soil and water bodies impacted by agriculture and aquaculture. *Front. Microbiol.* 3:399. doi: 10.3389/fmicb.2012.00399

Stackebrandt, E., Brambilla, E., and Richert, K. (2007). Gene sequence phylogenies of the family Microbacteriaceae. *Curr. Microbiol.* 55, 42–46. doi: 10.1007/s00284-006-0569-5

Stevenson, J. S. (1940). *Mercury Deposits of British Columbia. Bulletin No.5*. Victoria, BC: British Columbia department of mines.

Suzuki, S., Ferjani, A., Suzuki, I., and Murata, N. (2004). The SphS-SphR two-component system is the exclusive sensor for the induction of gene expression in response to phosphate limitation in synechocystis. *J. Biol. Chem.* 279, 13234–13240. doi: 10.1074/jbc.M313358200

Tamura, K., Peterson, D., Peterson, N., Stecher, G., Nei, M., and Kumar, S. (2011). MEGA5: molecular evolutionary genetics analysis using maximum likelihood, evolutionary distance, and maximum parsimony methods. *Mol. Biol. Evol.* 28, 2731–2739. doi: 10.1093/molbev/msr121

Tao, L., Yao, H., and Cheng, Q. (2007). Genes from a *Dietzia* sp. for synthesis of C_{40} and C_{50} β-cyclic carotenoids. *Gene* 386, 90–97. doi: 10.1016/j.gene.2006.08.006

Tsuzuki, M., Moskvin, O. V., Kuribayashi, M., Sato, K., Retamal, S., Abo, M., et al. (2011). Salt stress-induced changes in the transcriptome, compatible solutes, and membrane lipids in the facultatively phototrophic bacterium *Rhodobacter sphaeroides*. *Appl. Environ. Microbiol.* 77, 7551–7559. doi: 10.1128/AEM.05463-11

Van Dessel, W., Van Mellaert, L., Liesegang, H., Raasch, C., De Keersmaeker, S., Geukens, N., et al. (2005). Complete genomic nucleotide sequence and analysis of the temperate bacteriophage VWB. *Virology* 331, 325–337. doi: 10.1016/j.virol.2004.10.028

Wang, Y. X., Wang, H. B., Zhang, Y. Q., Xu, L. H., Jiang, C. L., and Li, W. J. (2008). *Rhodococcus kunmingensis* sp. nov., an actinobacterium isolated from a rhizosphere soil. *Int. J. Syst. Evol. Microbiol.* 58, 1467–1471. doi: 10.1099/ijs.0.65673-65670

White, R. A. III, Callister, S. J., Moore, R. J., Baker, E. S., and Jansson, J. K. (2016a). The past, present, and future of microbiome analyses. *Nat. Protoc.* 11, 2049–2053. doi: 10.1038/nprot.2016.148

White, R. A. III, Chan, A. M., Gavelis, G. S., Leander, B. S., Brady, A. L., Slater, G. F., et al. (2016b). Metagenomic analysis suggests modern freshwater microbialites harbor a distinct core microbial community. *Front. Microbiol.* 6:1531. doi: 10.3389/fmicb.2015.01531

White, R. A. III, Grassa, C. J., and Suttle, C. A. (2013a). Draft genome sequence of Exiguobacterium pavilionensis strain RW-2, with wide thermal, salinity, and pH tolerance, isolated from modern freshwater microbialites. *Genome Announc.* 1:e597-13. doi: 10.1128/genomeA.00597-13

White, R. A., III Grassa, C. J., and Suttle, C. A. (2013b). First draft genome sequence from a member of the genus *Agrococcus*, isolated from modern microbialites. *Genome Announc.* 1:e391-13. doi: 10.1128/genomeA.00391-13

White, R. A., III Power, I. M., Dipple, G. M., Southam, G., and Suttle, C. A. (2015). Metagenomic analysis reveals that modern microbialites and polar microbial mats have similar taxonomic and functional potential. *Front. Microbiol.* 6:966. doi: 10.3389/fmicb.2015.00966

White, R. A., III and Suttle, C. A. (2013). The draft genome sequence of *Sphingomonas paucimobilis* strain HER1398 (*Proteobacteria*), host to the giant PAU phage, indicates that it is a member of the genus *Sphingobacterium* (*Bacteroidetes*). *Genome Announc.* 1:e598-13. doi: 10.1128/genomeA.00598-13

Wickham, H. (2009). *ggplot2: Elegant Graphics for Data Analysis*. New York, NY: Springer. doi: 10.1007/978-0-387-98141-3

Wieser, M., Schumann, P., Martin, K., Altenburger, P., Burghardt, J., Lubitz, W., et al. (1999). *Agrococcus citreus* sp. nov., isolated from a medieval wall painting of the chapel of Castle Herberstein (Austria). *Int. J. Syst. Bacteriol.* 49, 1165–1170. doi: 10.1099/00207713-49-3-1165

Wong, H. L., Smith, D. L., Visscher, P. T., and Burns, B. P. (2015). Niche differentiation of bacterial communities at a millimeter scale in Shark Bay microbial mats. *Sci. Rep.* 5:15607. doi: 10.1038/srep15607

Wong, H. L., Visscher, P. T., White, R. A. III, Smith, D. L., Patterson, M. M., and Burns, B. P. (2017). Dynamics of archaea at fine spatial scales in Shark Bay mat microbiomes. *Sci. Rep.* 7:46160. doi: 10.1038/srep46160

Yamanaka, K., and Inouye, M. (1997). Growth-phase-dependent expression of cspD, encoding a member of the CspA family in Escherichia coli. *J. Bacteriol.* 179, 5126–5130. doi: 10.1128/jb.179.16.5126-5130.1997

Zhang, J. Y., Liu, X. Y., and Liu, S. J. (2010). *Agrococcus terreus* sp. nov. and *Micrococcus terreus* sp. nov., isolated from forest soil. *Int. J. Syst. Evol. Microbiol.* 60, 1897–1903. doi: 10.1099/ijs.0.013235-0

Zhang, W., Hu, X., Wang, L., and Wang, X. (2014). Reconstruction of the carotenoid biosynthetic pathway of *Cronobacter sakazakii* BAA894 in *Escherichia coli*. *PLoS One* 9:e86739. doi: 10.1371/journal.pone.0086739

Zheng, Y. T., Toyofuku, M., Nomura, N., and Shigeto, S. (2013). Correlation of carotenoid accumulation with aggregation and biofilm development in *Rhodococcus* sp. SD-74. *Anal. Chem.* 85, 7295–7301. doi: 10.1021/ac401188f

Zheng, Q., Zhang, R., Xu, Y., White, III R. A., Wang, Y., Luo, T., et al. (2014). A marine inducible prophage vB_CibM-P1 isolated from the aerobic anoxygenic phototrophic bacterium *Citromicrobium bathyomarinum* JL354. *Sci. Rep.* 4:7118. doi: 10.1038/srep07118

Zlamala, C., Schumann, P., Kämpfer, P., Rosselló-Mora, R., Lubit, W., and Busse, H. J. (2002). *Agrococcus baldri* sp. nov., isolated from the air in the 'Virgilkapelle' in Vienna. *Int. J. Syst. Evol. Microbiol.* 52, 1211–1216.

Conflict of Interest Statement: The authors declare that the research was conducted in the absence of any commercial or financial relationships that could be construed as a potential conflict of interest.

The reviewer AL and handling Editor declared their shared affiliation at time of review.

frontiers in Microbiology

ORIGINAL RESEARCH
published: 28 November 2018
doi: 10.3389/fmicb.2018.02606

Understanding the Mechanisms Behind the Response to Environmental Perturbation in Microbial Mats: A Metagenomic-Network Based Approach

*Valerie De Anda[1], Icoquih Zapata-Peñasco[2], Jazmín Blaz[3], Augusto Cesar Poot-Hernández[4], Bruno Contreras-Moreira[5,6], Marcos González-Laffitte[7], Niza Gámez-Tamariz[1], Maribel Hernández-Rosales[7], Luis E. Eguiarte[1] and Valeria Souza[1]**

[1] Departamento de Ecología Evolutiva, Instituto de Ecología, Universidad Nacional Autónoma de México, Ciudad de México, Mexico, [2] Dirección de Investigación en Transformación de Hidrocarburos, Instituto Mexicano del Petróleo, Eje Central Lázaro Cárdenas, Ciudad de México, Mexico, [3] Laboratorio Nacional de Ciencias de la Sostenibilidad, Instituto de Ecología, Universidad Nacional Autónoma de México, Ciudad de México, Mexico, [4] Departamento de Ingeniería de Sistemas Computacionales y Automatización, Instituto de Investigaciones en Matemáticas Aplicadas y en Sistemas, UNAM, Ciudad Universitaria, Ciudad de México, Mexico, [5] Estación Experimental de Aula Dei, Consejo Superior de Investigaciones Científicas, Zaragoza, Spain, [6] Fundación ARAID, Zaragoza, Spain, [7] Instituto de Matemáticas, UNAM Juriquilla, Juriquilla, Mexico

To date, it remains unclear how anthropogenic perturbations influence the dynamics of microbial communities, what general patterns arise in response to disturbance, and whether it is possible to predict them. Here, we suggest the use of microbial mats as a model of study to reveal patterns that can illuminate the ecological processes underlying microbial dynamics in response to stress. We traced the responses to anthropogenic perturbation caused by water depletion in microbial mats from Cuatro Cienegas Basin (CCB), Mexico, by using a time-series spatially resolved analysis in a novel combination of three computational approaches. First, we implemented MEBS (Multi-genomic Entropy-Based Score) to evaluate the dynamics of major biogeochemical cycles across spatio-temporal scales with a single informative value. Second, we used robust Time Series-Ecological Networks (TS-ENs) to evaluate the total percentage of interactions at different taxonomic levels. Lastly, we utilized network motifs to characterize specific interaction patterns. Our results indicate that microbial mats from CCB contain an enormous taxonomic diversity with at least 100 phyla, mainly represented by members of the rare biosphere (RB). Statistical ecological analyses point out a clear involvement of anaerobic guilds related to sulfur and methane cycles during wet versus dry conditions, where we find an increase in fungi, photosynthetic, and halotolerant taxa. TS-ENs indicate that in wet conditions, there was an equilibrium between cooperation and competition (positive and negative relationships, respectively), while under dry conditions there is an over-representation of negative relationships. Furthermore, most of the

OPEN ACCESS

Edited by:
Jamie S. Foster, University of Florida, United States

Reviewed by:
Richard Allen White III, RAW Molecular Systems (RMS) LLC, United States
Stefan J. Green, University of Illinois at Chicago, United States

***Correspondence:**
Valeria Souza
souza@unam.mx

Specialty section:
This article was submitted to Aquatic Microbiology, a section of the journal Frontiers in Microbiology

Received: *29 March 2018*
Accepted: *11 October 2018*
Published: *28 November 2018*

Citation:
De Anda V, Zapata-Peñasco I, Blaz J, Poot-Hernández AC, Contreras-Moreira B, González-Laffitte M, Gámez-Tamariz N, Hernández-Rosales M, Eguiarte LE and Souza V (2018) Understanding the Mechanisms Behind the Response to Environmental Perturbation in Microbial Mats: A Metagenomic-Network Based Approach. Front. Microbiol. 9:2606. doi: 10.3389/fmicb.2018.02606

keystone taxa of the TS-ENs at family level are members of the RB and the microbial mat core highlighting their crucial role within the community. Our results indicate that microbial mats are more robust to perturbation due to redundant functions that are likely shared among community members in the highly connected TS-ENs with density values close to one (≈0.9). Finally, we provide evidence that suggests that a large taxonomic diversity where all community members interact with each other (low modularity), the presence of permanent of low-abundant taxa, and an increase in competition can be potential buffers against environmental disturbance in microbial mats.

Keywords: time series ecological networks, environmental perturbation, MEBS, microbial mats, rare biosphere, network motifs

INTRODUCTION

Understanding the responses and the mechanisms that constrain and promote microbial adaptation in face of environmental perturbation is crucial to evaluate the ecosystem impact at global scales. Microbial ecological studies have demonstrated that diverse microbial communities tend to be more stable over time by promoting functional redundancy, whereas after a disturbance the community richness and diversity tends to decline (Girvan et al., 2005; Gihring et al., 2011; Hunting et al., 2015). Recent studies suggest that the probability that the community will return to its previous state following a small perturbation (hereafter referred as microbial stability, see Allesina et al., 2015; Borrelli et al., 2015; Grilli et al., 2016) could be related to the great genetic reservoir of low abundant taxa, also known as the rare biosphere (RB), and the microbial interactions that could have a crucial role providing a buffer against environmental disturbances influencing both community assembly and stability (Hunt and Ward, 2015; Konopka et al., 2015; Lynch and Neufeld, 2015; Jousset et al., 2017; Karpinets et al., 2018; Rivett and Bell, 2018). Yet, to date it is unclear how microbial community dynamics (i.e., composition and relationships) are influenced by environmental constraints, which largely shape the degree of resistance, resilience, and functional redundancy of a microbial community (Allison and Martiny, 2008; Fuhrman, 2009; Newton et al., 2011; Bissett et al., 2013; Konopka et al., 2015).

Natural microbial communities are highly complex systems that are in constant flux through spatial and temporal scales, where even minor perturbation can significantly reorder the function of each community member and the interaction network (Konopka et al., 2015). In this study we focused on community level patterns in stable microbial communities during environmental perturbation and the possible mechanisms that facilitates or disrupts microbial community stability and their ability to adapt to change. Due to their capacity to perform most of the biogeochemical cycles in a physically and chemically reduced environment, microbial mats are excellent models of study. Microbial mats are successful ecological communities which have adapted continuously to environmental changes since the Archean Eon (van Gemerden, 1993; Guerrero et al., 2002; Bolhuis et al., 2014; Preisner et al., 2016). Here, we seek to identify the general patterns caused by environmental perturbation. If microbial mats are resilient and resistant over time, we expect that samples taken through time in fixed points in space would present similar community patterns regardless of the disturbance. In contrast, if these communities survived by a constant species turnover, we expect to see systematic differences reflected in the community composition, function, structure, and overall relationships.

Despite their importance, low abundance taxa have been routinely removed from microbial ecology studies (Jousset et al., 2017). Most existing studies using network inference focus on evaluating a small percentage of the strongest interaction pairs, or infer microbial relationships at one single taxonomic level or a few marker genes involved in several metabolic process ignoring if those genes are differentially abundant (Shaw et al., 2017).

In order to comprehensively evaluate complex microbial community dynamics under environmental disturbance, we suggest the implementation of three approaches to complement the standard taxonomic ecological analysis. (1) The analysis of robust time series ecological networks (TS-ENs) at different taxonomic level to access general patterns of microbial relationships. (2) The application of MEBS (Multigenomic Entropy Based Score) to capture the enrichment of biogeochemical cycles or other complex metabolic pathways (De Anda et al., 2017) to provide a quantifiable measure of community response to environmental perturbation. (3) The use of network motifs or building blocks of biological networks that have been applied to the study of development, regulatory, and neuronal networks (Shen-Orr et al., 2002; Prill et al., 2005; Tran et al., 2013), and in ecological food webs of plants and animals (Stouffer et al., 2007; Borrelli et al., 2015; Baiser et al., 2016). The latter is needed since network motifs studies offer the opportunity to bridge the gap between the dynamics of simple modules and the analysis of topological metrics describing the community as a whole (Delmas et al., 2018).

To examine the community response against anthropogenic perturbations caused by water depletion, we studied microbial mats at three sites in the Churince Lagoon in Cuatro Cienegas Basin (CCB) México during 2012–2014. CCB is an extremely oligotrophic oasis characterized by low P concentrations (PO_4^{3-} as low as 0.1 μM) but relatively high concentrations of inorganic N and thus high N: P ratios (>200:1 by atoms) (Lee et al., 2015, 2017). Paradoxically, despite this nutrient limitation, CCB is a World Wildlife Fund (WWF) hotspot

for biodiversity and a wetland of international importance under the RAMSAR convention and is a singularity biodiversity that persisted through time (Souza et al., 2018). However, despite the importance of this site, increasing demand for water by agricultural development (mainly for forage and feed for livestock) has generated critical conservation issues related to the drying of different aquatic systems in the basin. In particular, the desiccation process of the Churince Lagoon, a wetland with a rich input of deep water with magmatic influence (Wolaver et al., 2012) and a high, endemic biodiversity that now is in danger of disappearing (Souza et al., 2007, 2018; De Anda et al., 2018).

In order to focus on the dynamic response of these communities in the face of anthropogenic perturbation, we seek to address the following questions: How are the networks assembled from their basic building blocks? Can we detect the keystone taxa? Is it possible to discriminate between intrinsic community changes and those given by the environmental degradation? Finally, can we mechanistically predict the overall behavior in the community under environmental stress using network inference? To this end, we used high throughput Illumina sequencing to assess the community composition and function as well as the change in the structure and membership networks between sites during and after the anthropogenic perturbation. Our results indicate that even though microbial mats are resilient and resistant taxonomically and metabolically, their network of interactions change during the dry period. During this time, negative interactions predominate under stress while interactions are more balanced in wet conditions.

MATERIALS AND METHODS

Sample Collection and Processing

Microbial mats were sampled from a small (ca. 12 m × 4 m) pond named "Lagunita" that is part of the main Churince lake in CCB (26.84810° N, −102.14160° W). Under normal conditions Lagunita pond is shallow with variable water levels (<0.42 cm) (Lee et al., 2015, 2017; **Figure 1A**). However, during initial fieldwork, we found that long term water extraction for agriculture had finally overturned the water levels and Lagunita pond was almost dry, with a majority of its sediment exposed and in direct contact with the atmosphere, consequently desiccating and displaying green and yellow tonalities. With the exception of two wet patches, that were both covered with a thick white surface with a sulfide smell. We sampled microbial mats from one dry area (Site A: 26.848120°N, −102.141604°W) and two wet patches (Site B: 26.848093°N, −102.141608°W and C: 26.848084°N, −102.141577°W), all less than 3 meters from each other. We sampled seasonally (Autumn and Spring) from 2012 to 2014 (**Figure 1B**) resulting in a total of 12 samples (**Figure 1C**).

Triplicate samples of each mat were obtained for each time point (5 cm × 5 cm × 5 cm), using sterile Falcon tubes (50 mL) and then stored at 4°C and subsequently frozen in liquid nitrogen until processing in the lab. Physicochemical water parameters were registered at each sampling time using Hydrolab Mini Sonde 5 Multiprobe SE, with the exception of the initial (dry) sampling (as there was not water to measure). We took great care in preserving the mat structure and, even if we could not split the layers due to the mat consistency, we represented in our DNA isolation all the layers evenly, starting with the upper photic layer and ending with a similar sized black anoxic layer.

DNA Extractions

Approximately 0.5 g of microbial mats sample was extracted for each replicated sample according to Purdy (2005). Replicate samples for the same site and time point were pooled into a single sample, yielding a total of 12 DNA samples, each one with more than 5 μg of high molecular weight DNA.

Metagenomic Library Preparation, Sequencing and Quality Assessment

Metagenomic shotgun sequencing libraries were prepared and sequencing at CINVESTAV-LANGEBIO, Irapuato, Mexico. For each sample ∼5 μg of genomic DNA (DO 260/280 ≤1.8) was used with Illumina's TruSeq nano for library preparation, which supports shearing by Covaris ultrasonication. Fragments were selected according to agarose gel 0.7% at 70 mV in order to obtain an average insert size of 550 bp. Libraries were sequenced using the Illumina MiSeq Paired-End 2 × 300 bp technology with a run in a single plate generating 12Gb of sequence data for all 12 samples. Quality of raw reads was analyzed using FastQC v0.11 (Andrews, 2010). TruSeq Indexed Adapter and barcodes were removed using cutadapt v1.12 (Martin, 2011). Low quality sequences were discarded with Trimmomatic using a sliding window of 4 bp, an average quality per base of 20, and min read length of 36 bp (Bolger et al., 2014). The assembly of the trimmed reads was conducted with Megahit v1.1.1-2 using the option – presets meta-large (Li et al., 2014).

The coding regions were searched from the obtained contigs using Prodigal v2.6.3 (Hyatt et al., 2010) with the -a option, to obtain the translated amino acid sequences of the predicted coding regions and -p meta option. The peptide amino acid sequences were then scanned against Pfam-A v30 (Finn et al., 2015). The abundance profile of each Pfam domain in the metagenomic samples was obtained from a Perl script extract_pfam.pl which is part of the MEBS software suite (De Anda et al., 2017). The resulting FASTA files of sequence contigs have been deposited in the MG-RAST repository under project number mgp80319.

Taxonomy Assignment

We used the k-mer based taxonomic classification algorithm of One Codex (Minot et al., 2015) to assign microbial taxonomy of the Megahit derived contigs. Briefly, One Codex classifies unknown nucleotide sequences according to the set of signature sequences that are unique to a specific taxonomic group using oligonucleotides of 31 bp (k = 31). The taxonomic profiles obtained from the reference-based

FIGURE 1 | Sampling site and microbial mats samples description. **(A)** The Lagunita pond is located at Cuatro Cienegas Basin (CCB) in state of Coahuila, Mexico Map. Google Maps. Google, 15 Jun 2018. Web, 15 Jun 2018. Here is shown two contrasting conditions during the study period (dry and wet or "water" conditions). **(B)** Specific characteristics of the Lagunita pond are showed during the sampling period ranging from Autumn 2012 (time 1), to Spring 2014 (time 4). **(C)** Microbial mats were sampled seasonally from three geographically separated sites **(A–C)** during two-years resulting in a total of 12 samples (3 sites, 4 time points).

approach were used for downstream analyses described below.

Microbial Mats Diversity, Structure and Statistics

Several descriptors of alpha diversity were obtained from Phyloseq-estimate_richness function (McMurdie and Holmes, 2013) implemented in R (R Development Core Team, 2011). In order to estimate the sampling effort, rarefaction curves were obtained for each sampling site using the rarefaction function implemented in Vegan Library in R. Several statistical analyses were performed in order to test for differences between samples and estimate components of variation due to year, site, or water conditions. We first performed a permutational multivariate analysis of variance (PERMANOVA) using R-vegan function Adonis in order to establish the differences between sites and times. A pairwise comparison among samples for the same site

and water conditions was performed using the STAMP v2.1.3 program (Parks et al., 2014) in order to statistically identify the significant differences among genera within each sample by using Welch's *t*-test type two-sided, with the confidence interval (CI) method of Welch's inverted adjustment of 0.95. Then, we compared the taxonomic presence/absence profile from the microbial mats under dry condition versus those from the rest of the sampling, the particular and shared taxa across water conditions were plotted with Venn-Euler diagrams using a web-based tool[1]. Finally, we identified the core of microbial mats (those genera present across space and time in all microbial mat samples) using the *parse_pangenome_matrix.pl* script part of the software GET_HOMOLOGUES (Contreras-Moreira and Vinuesa, 2013).

Biogeochemical Cycling Dynamics

We used MEBS (De Anda et al., 2017) to evaluate the metabolic machinery of C, O, N, S, and Fe cycles in the microbial mats across time by using a single value measured in bits (informational units). Briefly, FASTA peptide sequences for each microbial mat, obtained with Prodigal, are taken as input of the main script *mebs.pl*. We used the -comp option to compute the metabolic completeness of sulfur and methane cycle (currently N and Fe cycles are also supported). Cycles enriched in a given sample are recognized by using the –fdr (False Discovery Rate). In this case we used a restrictive FDR of 0.0001. We performed ROC analysis described in De Anda et al. (2017) for each cycle, computing several cut-offs for fixed FDR rates. In this way, by using restrictive FDR we can control the rate of true positives and false positives obtained in each cycle. The exact values for each cycle are shown in the config file of MEBS github repository[2]. The details of those analyses will be published elsewhere, including the benchmark of each cycle across two-thousand non-redundant genomes.

To contrast the biogeochemical cycles across several environments, we used publicly available metagenomes from MG-RAST of stromatolites from Highborne Cay, Bahamas 4449591.3 4449590.3 (Khodadad and Foster, 2012), Polar Microbial mats 4445126.3 4445129.3 (Varin et al., 2012); freshwater microbial mats from CCB 4442467.3 4442466.3 4441363.3 4441347.3 (Bonilla-Rosso et al., 2012; Peimbert et al., 2012) and stromatolites from CCB, 4440060.4 4440067.3 (Desnues et al., 2008; Breitbart et al., 2009); microbial mats from Yellowstone 4443746.3 4443747.3 4443762.3 4443749.3 4443750.3 (Bhaya et al., 2007); purple sulfur bacteria biofilm (Wilbanks et al., 2014); hydrothermal vents 4487624.3 4487625.3 (Tang et al., 2013), 4449206.3 (Jiménez et al., 2012); microorganisms from the vent-associated polychaete worm *Alvinella pompejana* 4441102.3 (Grzymski et al., 2008); acid mine drainage 4441138.3 4441137.3 (AMD) (Jiao et al., 2011); polar cryoconite 4491734.3; freshwater microbialites from Pavilion Lake, Clinton Creek described in White et al. (2015, 2016); hypersaline microbial mats from marine environments described in Ruvindy et al. (2016) and Guerrero Negro (Kunin et al., 2008).

Network Inference

We used the time-series Lotka-Volterra-based network inference approach MetaMIS (Shaw et al., 2016) to infer the underlying interactions from microbial mats collected during and after the perturbation event. For each site, the non-normalized taxonomic classifications (ranging from Phylum to Family) were used to compute the consensus networks. Due to the large amount of network interactions generated at lower hierarchical levels and the limitation of computing power (Intel Core i7-4500U CPU @3.20 GHz processor and 16Gb RAM), we were not able to obtain the consensus networks at genera level. Considering that the three studied sites are very close together, we constructed a "high order-network" by concatenating the consensus networks of the three sites. We named it "global network" and it was constructed to find general patterns that could reflect the behavior of the mats within Lagunita pond.

The consensus networks inferred from MetaMIS can include several types of interaction patterns, yet we decided to further separate them into more simple networks displaying only either positive or negative relationships. For each site we obtained three different networks (consensus, positive and negative) resulting in a total of 36 Time-Series Ecological networks (TS-ENs). The global network was also separated by type of interaction at every taxonomic level, resulting in 12 global TS-ENs per sampling time. In total, we obtained 48 TS-ENs in our study.

Motif Discovery

Network motifs are defined as a set of recurring circuits on *n* nodes. Nodes can represent biological entities such as OTUs, species, genes or proteins. Network motifs are patterns of interactions from which the networks are built. These patterns occur in complex networks more often than expected in a random network (Milo, 2002; Alon, 2007; Baiser et al., 2016). In order to compare our data with those derived from the ecological theory developed in food webs and the tractable number of network motifs, we focused only on the 13 possible 3-node network motifs. For comparison, there are 199 and 9364 motifs for four and five node subgraphs, respectively, which require high computational performance (Stouffer et al., 2007). To calculate all significant network motifs of three nodes within the 48 TS-ENs, we used Mfinder v1.20 (Milo, 2002) with default options.

Network Statistics

To further evaluate the topological features of the 48 TS-ENs, we developed a software package called NetAn: Network Analyzer[3] that was built on broadly used python libraries that are freely available, such as Networkx (Hagberg et al., 2008). The main script *NetworkAnalysis.py* receives a list of interactions weighted or unweighted (-d and –u options, respectively) and computes several metrics. We focused on identifying key features that are showed to be significant in comparison with those in random networks. Therefore, we

[1]http://bioinformatics.psb.ugent.be/webtools/Venn/

[2]https://github.com/eead-csic-compbio/metagenome_Pfam_score/blob/master/config/config.txt

[3]https://github.com/valdeanda/NetAn

extracted properties of the directed networks such as density, hubs with maximum in-degree and out-degree and clustering coefficient, among others. Then we assumed the networks as non-directed and calculated further topological features such as modularity and communities using the Louvain method (Blondel et al., 2008).

Given that the real networks are very dense in terms of connections, we implemented a method to generate random networks that resemble the real ones using the option gnm_random_graph from Networkx python module. A hundred random networks were generated for each real one, with the same number of nodes and edges. Then, for each one same topological features were extracted and the average compared to those of real networks.

RESULTS

Study Field Site Overview

Lagunita pond shows a conductivity ranging from 6.47 to 11.59 mS cm^{-1}. At the end of the study, May 2014, salinity was almost double in concentration than in the year before, May 2013. Nevertheless, pH remained constant ≈8 for 2 years. Water physicochemical parameters during wet conditions are shown in **Supplementary Table 1**, and nutrients for Lagunita were extensively reported by Lee et al. (2015, 2017).

Metagenomic Analysis

The dataset comprising 12 libraries, consisting of more than 22 million read-pairs, of which ∼9.3% were discarded during quality control. The filtered reads were subsequently assembled, yielding 4,685,929 contigs (N50 ∼417 bp ± 34.36 std). Around 426,300 ± 116,000 std. proteins were detected with Prodigal (see details in **Supplementary Table 2**), which were then scanned against the Pfam-A v30 database for metabolic inference.

Microbial Mats Diversity and Community Structure

Despite the relatively low MiSeq coverage for the twelve metagenomes, we were able to identify 100 bacterial phyla, 168 classes, 302 orders, 539 families and 1431 genera. The number of phyla detected exceeds around three times the number of taxa observed in equivalent studies within mats from Lake Clifton, Australia (Warden et al., 2016), indicating highly diverse microbial mats occur in CCB. Within the total genera identified, 97.27% are found in low abundance ≤0.01 consistently across samples (**Figure 2A**), and the unclassified sequences are from the Bacteria domain, Rhodobacteraceae family, Proteobacteria phylum, Alphaproteobacteria, and Actinobacteria classes as well as Rhizobiales order, where the abundant taxa among samples with a relative abundance ≥0.01 (**Figure 2A1**). According to the rarefaction curves, the taxonomic assignment at genera level tends to reach an asymptotic behavior for almost all samples, with the exception of B1 since this sample had a lower number of raw reads (See **Supplementary Table 2**).

From the total genera identified, 373 were present across all samples, regardless of geographical distance and contrasting environmental conditions (**Supplementary Table 3**). This subset of taxa could be potentially associated with the microbial mat core. For visual comparisons, the overall abundance shift of the members of the microbial mat core across time are shown in **Figure 2B**. The vast majority of the core members (344 genera) belong to the RB indicating the presence of permanent rare taxa within microbial mats. Despite their lower abundance (<0.01), RB taxa show a constant presence across samples in all sites during the 2-year study period; hence they cannot be associated with sequencing errors or under-sampling. As expected from previous studies at CCB, a considerable proportion of the members of the microbial mat core, 30% (114 genera), belongs to unclassified sequences. It is worth mentioning that deeper sequencing could reveal a larger core than presented here, for example taxa at lower abundance in all samples.

Ecological Diversity Index

The alpha-diversity estimators across sites are shown in **Supplementary Figure 1**. In general, we observe that Site B is the less diverse, especially during dry conditions. Unexpectedly, microbial mats from site A are more diverse at the taxonomic level. The observed differences in richness and diversity between Chao and Shannon indexes may be due to the Shannon algorithm falling short when examining a large number of low abundant organisms (the RB), that in our case represent most of the taxa in the microbial mats. The trajectories of Shannon and Pielou indexes during the period of study indicate little variations of the three sites, pointing out a resilient microbial mat community (**Supplementary Figure 2**).

Due to the high percentage of low-abundance taxa, we used the genera presence/absence profile to highlight unique and shared taxa during contrasting water conditions (**Figure 3**).

During dry conditions we detected a diverse community of bacteria, but also Archaea, fungi, protists and lesser number of viruses. Furthermore, we observed the common presence of halophilic taxa, fungi, and protozoa during dry conditions in the three sampling sites (a detailed list is included in **Supplementary Table 4**). Interestingly, during dry conditions the shared taxa are mostly from the RB, with the exception of *Methanohalophilus* which was common between mats from sites A and C. These two sites in dry conditions also shared six taxa that were never detected during wet conditions. These taxa highlight the implication of a halotolerant and C-cycling community in these mats (i.e., *Gramella* and *Kordia* genus) (more details in **Supplementary Table 4**).

During wet conditions, representatives of fungi and protista were not found within wet patches, contrasting with site dry mat, where we observed a genus of the Leotiomyceta class (Ascomycota) (details in **Supplementary Table 5**). Interestingly, given the small spatial scale, many unique taxa exist in each separated community (especially in site B). In contrast to dry conditions, we found two taxa that are common in all the sites in the water conditions (*Ornatilinea* and Rikenellaceae) they belong to the RB (**Figure 4**).

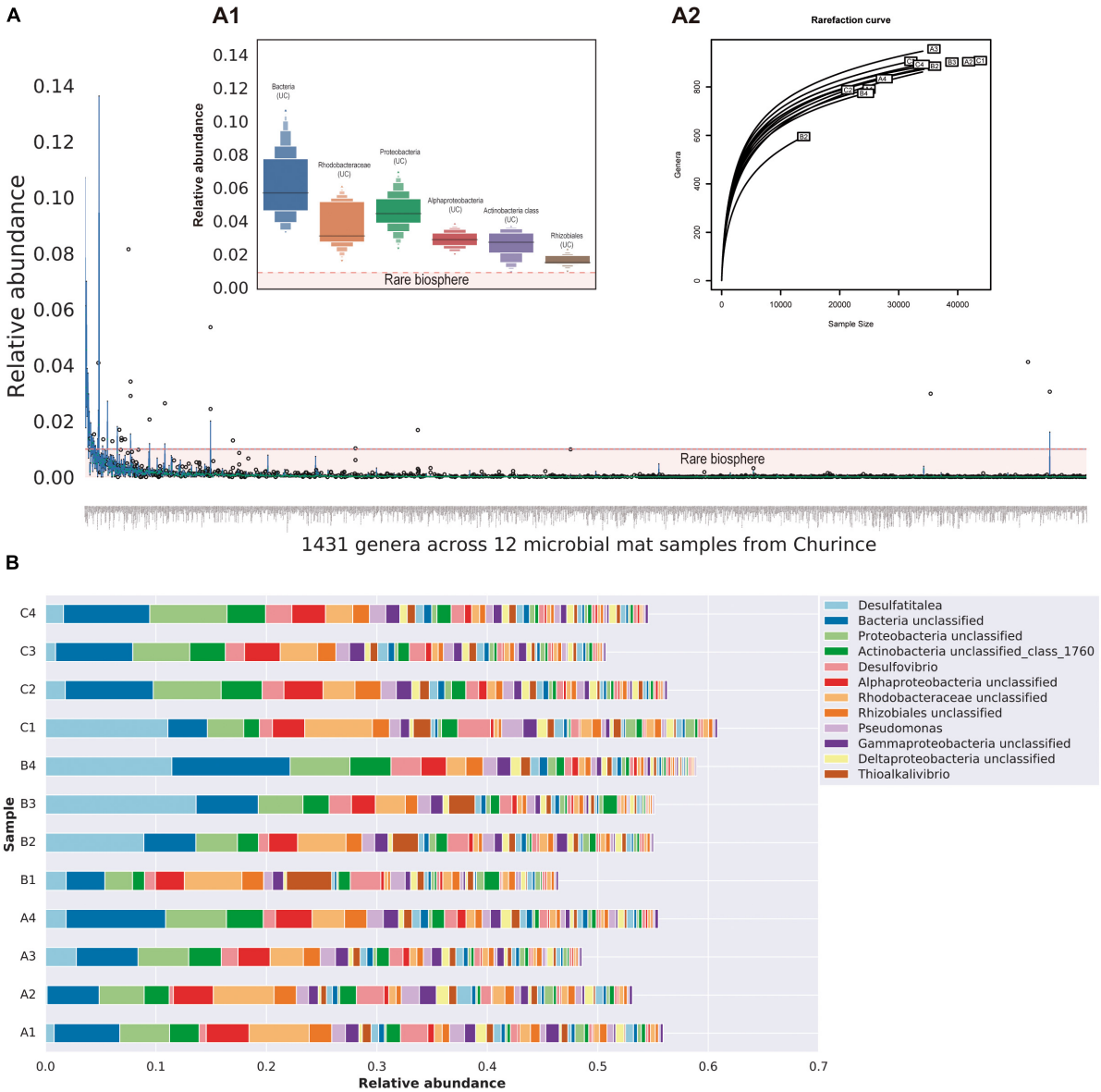

FIGURE 2 | Taxonomic diversity within microbial mats from Lagunita pond at genera level. **(A)** Boxplot distribution showing the relative abundance of the total genera found within microbial mats from Churince where each boxplot represents the distribution of each genera across 12 samples. The horizontal red line indicates the low abundant taxa or RB <0.01 of relative abundance. The inner figure **(A1)** indicates the distribution of the six most abundant genera (>0.01 relative abundance). The second inner figure **(A2)** shows the rarefaction curves of the 12 microbial mats at genera level. **(B)** Stacked bar plots of 58 members of the microbial mat core whose abundance is >0.001 for comparative purposes, this plot shows how the actual composition of each site **(A–C)** change over time (four time points).

Statistical Analysis

The analyses made to identify the proportion of sequences assigned to each genus that was enriched among dry and wet conditions (first versus other sampling points **Figure 4**) indicate that during dry conditions, unclassified sequences from Rhodobacteraceae, Alphaproteobacteria, Rhizobiales, *Paracoccus,* and *Thioalkalivibrio* were consistently over-represented in the three site points. However, when water conditions were restored unclassified sequences from Bacterial domain, Proteobacteria and Actinobacteria, as well as sulfate reducers (*Desulfovibrio* and *Desulfatitalea*), were enriched (**Figure 4A**).

To gain an insight into the low abundant taxa enriched during dry and wet conditions in **Figure 4B** we show the extender error bar in Welch's *t*-test to highlight the differentially abundant ($p < 0.005$ genera). In the case of dry conditions eight genera were observed: *Marinovum, Pannonibacter, Paracoccus*, unclassified Rhodobacteraceae, *Roseivivax, Oceanicola, Wenxinia, and Citreicella*. In contrast, we observed a total of 24 genera enriched during wet conditions, including the potential phosphorous

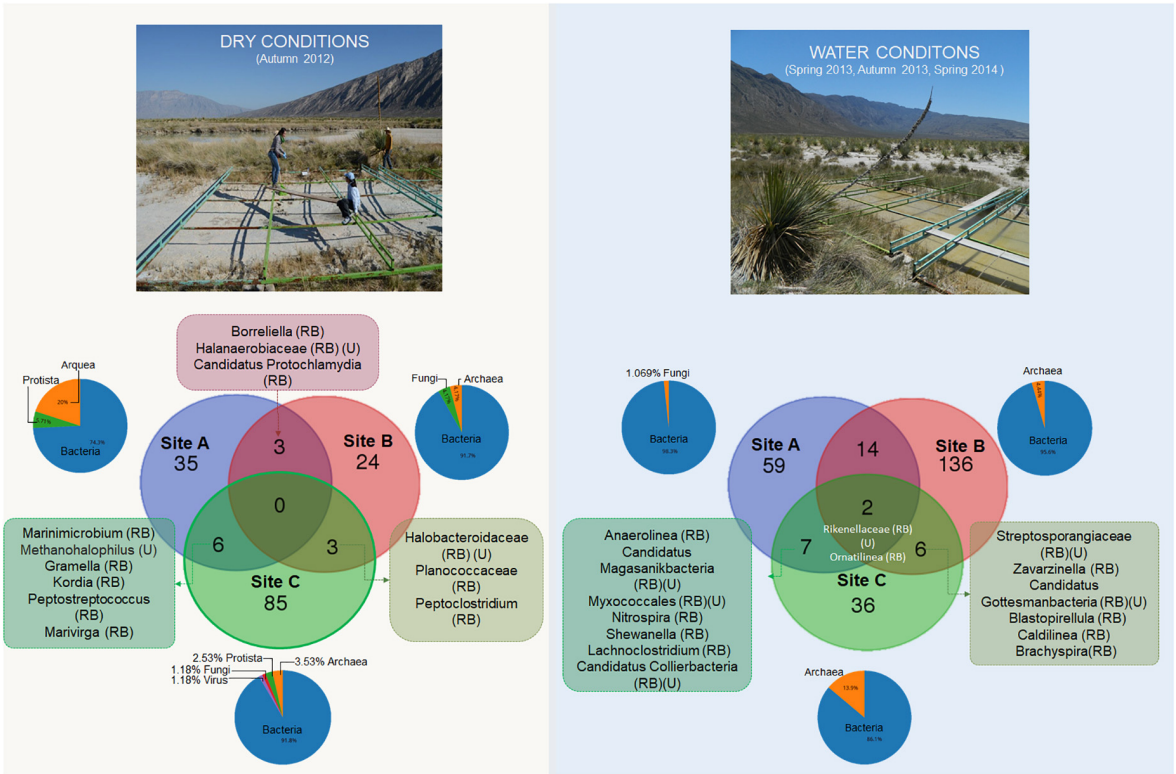

FIGURE 3 | Venn diagram analysis showing the shared and unique taxa at genus level during contrasting water conditions (RB) rare biosphere, (U) unclassified.

removal by Candidatus Accumulibacter, unclassified sequences from Nanoarchaeota, and *Ornatilinea*.

Specific statistical taxonomic differences across sites suggests a clear involvement of anaerobic taxa in mats from wet patches, whereas in the dry site we observed mostly photosynthetic and heterotrophic genera. Among the differentially abundant genera from microbial mats from site C compared with those from site A we found several representatives of sulfate reducing bacteria such as *Desulfococcus, Desulfosarcina, Desulfonatronospira, Desulfatibacillum, and Geoalkalibacter*. In contrast, site A was enriched with marine-related genera such as *Plesiocystis, Hyphomonas, Enhygromyxa, and Arenimonas* (**Supplementary Figure 3**). The same pattern was observed in mean proportions between mats from site A and B, being enriched with the genera *Spirochaeta,* unclassified candidatus *Daviesbacteria, Desulfonatrospira, Desulfobacterium* in site B, whereas unclassified cyanobacteria along with *Synechococcus, Nostococales*, and *Oscillatoriale*s are differentially abundant within site A (**Supplementary Figure 4**).

When comparing the differentially abundant genera from wet patches (site B and C), we observed a representation of an aerobic community enriched within site C (*Rhizobacter, Rhodospirillum, and Skermanella*) (**Supplementary Figure 5**). Despite the geographic closeness of the three sites, each one presents many elements unique from each community and a unique response of such taxa for perturbation being sulfate reducers common in wet patches.

PERMANOVA analysis indicates that the microbial mats have statistically different taxonomic composition ($p < 0.05$) depending on site and season, despite having several enriched taxa in common during contrasting water conditions. Moreover, when we compare samples metabolic composition, we found significant differences between sites ($p = 0.005$) but not across seasons ($p = 0.072$), indicating that in every site, the metabolic potential was maintained over time. This pattern can also be observed in detrending correspondence analysis (DCA) (**Figure 5**) where distribution of samples according to metabolic functions are clustered principally by site.

Dynamics of the Main Cycles Over Time

For comparative purposes, we used a restrictive FDR to avoid false positives and to detect the most enriched cycles within the microbial mats. By using this approach, we observed that methane and nitrogen cycles were over-represented in the microbial mats (with asterisks in **Supplementary Table 6** and bigger markers in **Figure 6**).

In the first case, the methane cycle, characterized by the usage of CH_4 compounds by methanotrophs, methanogens, and methylotroph, is always enriched within site B and becomes significant in all microbial mats after the aquifer recovery at the end of the period of study.

The dynamics of the nitrogen cycle, which includes pathways involved in the reduction and oxidation of both inorganic [nitrate

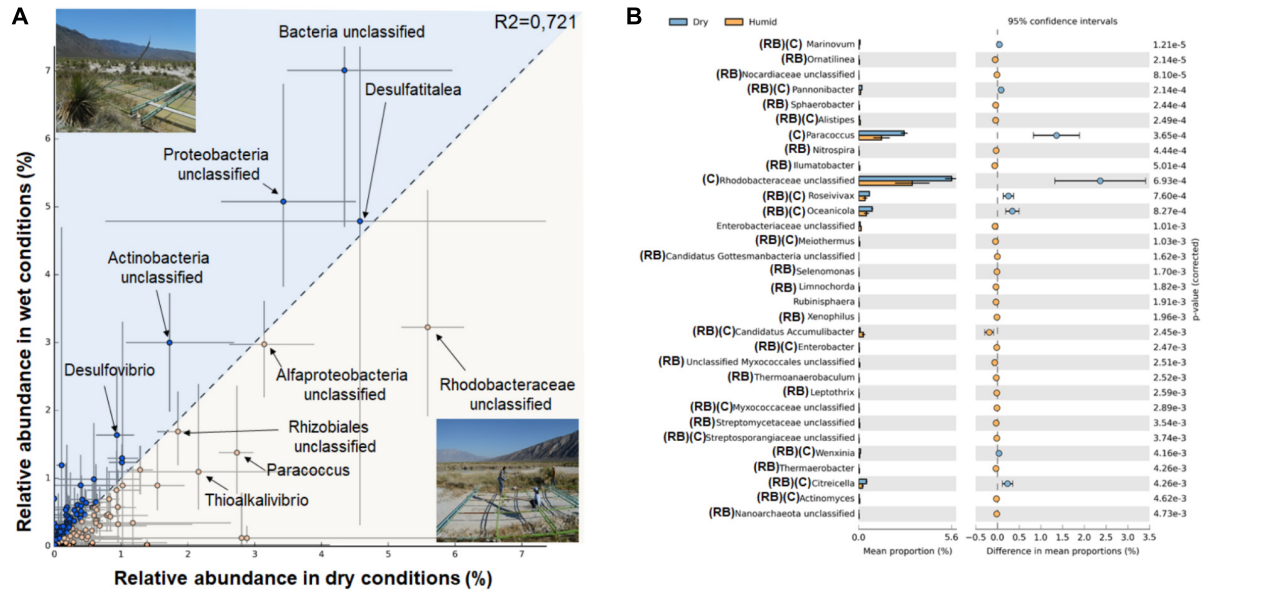

FIGURE 4 | Taxonomic statistical differences between dry and wet conditions. **(A)** Profile scatter plot of each site (A–C), x-axis (dry conditions) and y-axis (wet conditions) microbial mats with the difference in mean proportion among microbial mats within each site along with the associated confidence interval of this effect size (2th and 98th percentile). Points on each side of the gray dashed y = x line are enriched in one of the two samples, SD for proportion are shown as horizontal lines. A statistical hypothesis test is required to determine if the observed difference is large enough, to discount it being a sampling artifact safely, however, in dry conditions there is only one mat for each site therefore no *p*-values are indicated. **(B)** The error bar indicating all genera where Welch's *t*-test with confidence interval method DP Welch' inverted of 0.95 produces a *p*-value (<0.005). The difference in mean proportion between the microbial mats during dry and wet conditions are shown in blue and orange, respectively (RB, rare biosphere; C, microbial mat core).

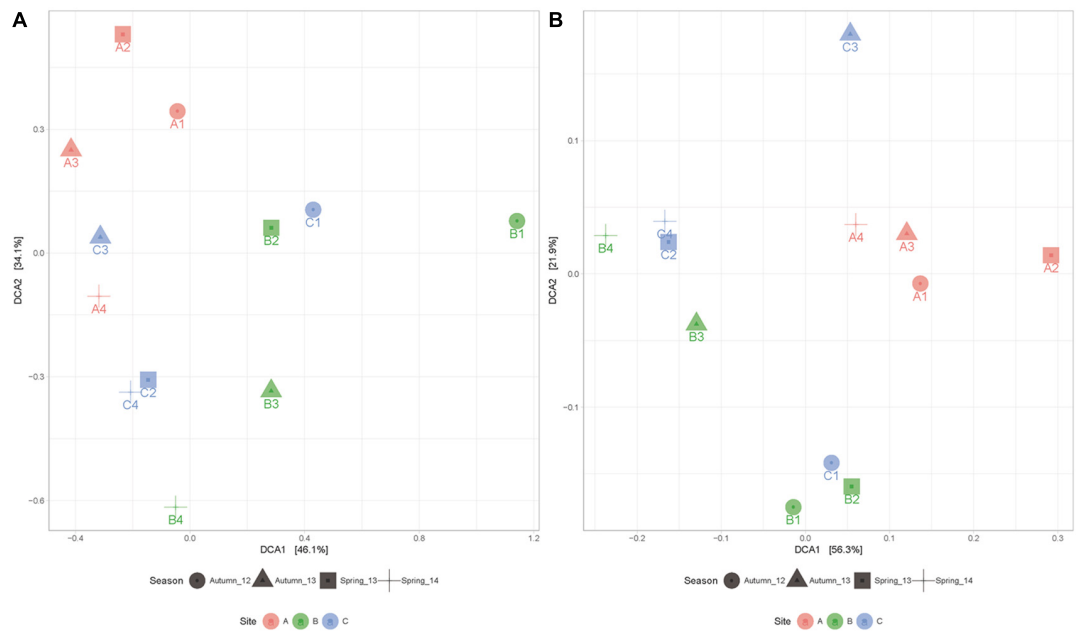

FIGURE 5 | Detrented correspondence analysis (DCA) according to taxonomic **(A)** and metabolic **(B)** composition of microbial mats explaining 80.2 and 78.2% of the variance among samples, respectively. These results are supported by PERMANOVA analysis.

(+5) to ammonia (−3)] and organic nitrogen compounds (i.e., taurine, urea, and choline degradation), follows an opposite behavior, since it is significant in all samples at the third sampling time in October 2013 (**Supplementary Table 6** and bigger markers in **Figure 6**). This is interesting since that sampling period corresponds to a moment of recovery of the aquifer after

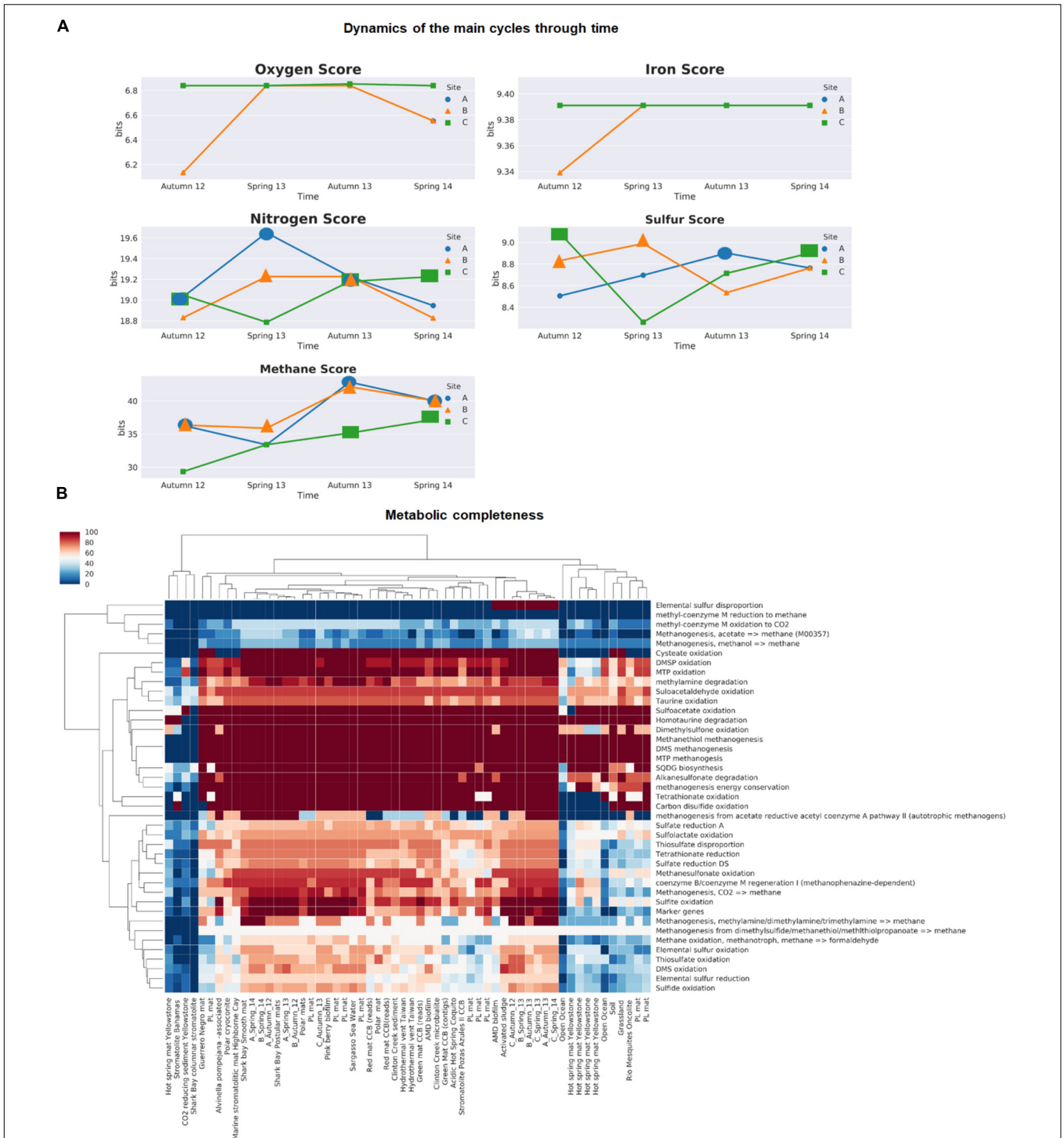

FIGURE 6 | Biogeochemical cycling within microbial mats across space and time using MEBS. **(A)** Dynamics of the main cycles within microbial mats samples during the two-year period of study by with a single value MEBS captured in bits. **(B)** Metabolic completeness in a color gradient, the more complete are red and the less shift to blue. Sulfur and methane cycle across 58 environments including those analyzed in this study and several environments such as hydrothermal vents, biofilms, microbial mats, stromatolites and soils. Samples from this study are named according to the site (A–C), and sampling season and year.

the closing of a canal that was draining the site. Furthermore, site C is the only one that becomes significant at the end of the period of study compared to the rest of the mats.

In our previous benchmark for the sulfur cycle (Figure 6 in De Anda et al., 2017), we observed that microbial mats from Churince CCB were among the most enriched in terms

of sulfur cycle compared with nearly 1000 metagenomes, with a sulfur score above the 95th distribution (>8.81 bits) are shown with bigger markers in **Figure 6A**. We observed a tendency that indicates that during dry conditions in site A, the overall machinery of the sulfur cycle was underrepresented compared to the wet patches sites B and C. These results agree with the anaerobic differentially abundant taxa within wet patches, suggesting that the water fluctuations largely determine the redox gradient within the mats affecting the anaerobic organisms.

In the case of the oxygen and iron cycle (**Figure 6A**), our results indicate that there is neither enrichment nor impoverishment of the above-mentioned cycles in the microbial mats from Lagunita pond. For example, in the case of photosynthesis (oxygen score), our results agree with the low proportion of cyanobacteria detected in the taxonomic profile, indicating an under representation of the oxygenic photosynthetic pathways in our community during the period of study. The iron cycle, represented by the reduction and oxidation of iron compounds including siderophores uptake, was under-represented during dry conditions within site B, but then become stable over time.

In general terms, the comparison of MEBS scores indicates that the sulfur, methane, and nitrogen cycles are over-represented in microbial mats from Lagunita, as well as in Pavillon Lake (White et al., 2016), both sites displaying similar patterns. Interestingly, Pavillon Lake is another analog of early Earth studied by NASA, in British Columbia and, as Lagunita, it is a non-extreme continental site with microbialites. However, the over-representation of the methane cycle is evident within microbial mats from our study, compared with the rest of environments including soil, microbialites, hydrothermal vents, biofilms, and open ocean samples (**Supplementary Table 6**).

For a closer look into the dynamics of sulfur and methane cycles, we employed the completeness module implemented in MEBS. As established previously, the metabolic completeness is defined as the full repertoire of protein domains involved in a given metabolic pathway such as sulfate reduction or methanogenesis (De Anda et al., 2017). As observed in **Figure 6B**, the complete repertoire of protein domains required to utilize the organic sulfur compounds such as sulfonates as Dimethylsulfoniopropionate (DMSP), [3-(methylsulfanyl) propanoate (MTP)] (Jonkers et al., 1998; Curson et al., 2008; Bullock et al., 2014), as well as the methanogenesis from organic sulfur compounds (methanethiol and DMS) were found in the majority of microbial mat samples with exception of hot-spring mats from Yellowstone and stromatolite from Bahamas. In addition, the dimethyl sulfide (DMS) oxidation pathway reported for aerobic microorganisms (such as *Thiobacillus*, *Hyphomicrobium*, methanogens and sulfate reducing bacteria) was also found to be 100% complete after the disturbance event in microbial mats from Lagunita and in site C during dry conditions.

The elemental sulfur disproportion represented by the sulfur oxygenase/reductase (SOR) protein isolated from the thermoacidophilic and chemolithoautotrophic crenarchaeote *Acidianus ambivalens* (Kletzin, 2008) was only found in microbial mats from Lagunita (after the desiccation event and in a wet patch from site C), and one biofilm from an Acid Drainage Mine (ADM), but was found to be absent in the rest of the metagenomes. The main pathways for oxidation and reduction of inorganic sulfur compounds (sulfate reduction, sulfide, and sulfite oxidation), are 80–100% present in all samples from microbial mats of Lagunita, but their completeness is not always observed in the rest of microbial mats (i.e., Yellowstone, or stromatolites from Bahamas) (**Figure 6B**).

Finally, we can argue that the fact that the methane cycle is over-represented in our samples, may be due to the majority of main pathways involved in the methanogenesis, as well as the oxidation of methane and methanesulfonate are almost complete in the Lagunita mats, contrary to their poor representation in the rest of the microbialites.

Network Inference Method Based on Time-Series Data

First, we evaluated whether the regenerated abundance profiles obtained from MetaMIS successfully reproduced the microbial abundance similar to the original by using the Bray Curtis Dissimilarity (BCD). As observed in **Supplementary Table 7**, a small BCD (mean 0.136 ± 0.021 std.) was obtained in the three sites at all taxonomic levels, suggesting that interactions revealed successfully the underlying interactive relations of the microbial mat communities. We also confirmed that the majority of taxa within microbial mats were found to be rare <0.1% (75% ± 3.06 std.).

From 1600 intermediate networks generated by MetaMIS, we obtained 48 TS-ENs that comprised the total number of interactions at every taxonomic level (**Supplementary Table 7** for details). We used NetAn to compute the several topological properties of real and random networks. Due to the high number of relationships (highly dense networks) and the method used to generate the random networks, it is not surprising that the structure of both real consensus and random networks are similar (**Table 1**). This data suggests that a large number of taxa (probably from the diverse RB) co-occur randomly, with exception of those that belong to the microbial mat core. This also suggests that this large RB co-occurs randomly, probably being part of the large and dynamic seed bank of the deep aquifer. Although several methods were tested to generate the random networks (data not shown), the values were similar to the real ones, indicating that small world properties (Zhou et al., 2010) do not characterize our TS-ENs.

Our results indicate that microbial mats are more robust to perturbation due to redundant functions that are likely shared among nodes or functional clades in the highly connected TS-ENs, with density values close to one (≈0.9) (Montoya et al., 2006; Steele et al., 2011; Faust and Raes, 2012a; Shaw et al., 2016). Consensus and negative networks displayed a higher clustering coefficient (∼0.9 and ∼0.7 respectively), while positive interaction networks showed much lower values (≈0.2–0.3). Networks with a high clustering coefficient are likely to contain more hubs or focal nodes than those with a lower coefficient (Proulx et al., 2005; Peura et al., 2015). Hence, the loss of these

TABLE 1 | Global network measures obtained from real (consensus) and random networks Std. of the values obtained across the span of taxonomic levels from Phylum to Family.

	Site A		Site B		Site C	
	Real	Random	Real	Random	Real	Random
Clustering Coefficient	0.9620 (±0.0247)	0.9268 (±0.0497)	0.9507 (±0.0034)	0.9106 (±0.0090)	0.9597 (±0.0069)	0.9288 (±0.0278)
Density	0.927 (±0.043)	0.9269 (±0.0498)	0.911 (±0.008)	0.9106 (±0.0090)	0.892 (±0.024)	0.8920 (±0.0278)
Diameter	2.000 (±0.707)	1.9625 (±0.0750)	2.000 (±0.000)	2.000 (±0.000)	2.500 (±0.500)	2.000 (±0.000)
Modularity	0.003 (±0.002)	0.0010 (±0.0014)	0.002 (±0.002)	0.0005 (±0.0008)	0.004 (±0.002)	0.0015 (±0.0014)
Radius	1.250 (±0.433)	1.1250 (±0.2500)	1.250 (±0.433)	1.0000 (±0.0000)	1.500 (±0.500)	1.0625 (±0.1250)
Mean degree	159.391 (±97.214)	159.3912 (±112.2527)	164.246 (±88.870)	164.2461 (±102.6182)	168.933 (±92.229)	168.9333 (±106.4964)
Communities	2.500 (±1.500)	1.7475 0.9531	2.250 (±1.090)	1.5600 (±0.5931)	3.000 (±1.581)	2.0850 (±0.8296)

hub nodes, which have been likened to 'keystone' species (Steele et al., 2011), reflects potential structural perturbations to the community and suggests some degree of community stress as bacterial associations have been fractured.

Our data indicates that negative relationships within mats may retain a greater number of hubs than positive interactions, suggesting an important role for competitive interactions in stressed conditions. As indicated by Grilli et al. (2016), positive modularity values indicate that interactions occur predominantly within groups, while negative values indicate that interactions are more frequent among groups. In our study, the consensus networks have associated positive values of modularity close to zero, indicating that taxa within microbial mats prefer those members from another network subsystem due to the highly densely connected network. However, when we separated the consensus networks by their type of interaction (+ or −), we found a subtle modularity increase to 0.2 in the negative networks, suggesting a preference for competitive interactions within the same subsystem (**Table 2**).

Our results indicate that modularity in our networks was very low compared to other reported biological networks (Baldassano and Bassett, 2016). The low modularity values indicate that our TS-ENs lack an evident modular architecture. Therefore, we can hypothesize that modularity values close to zero in the studied microbial mats point toward a community behavior as a complete module, where all the members are interacting with each other.

By comparing the properties of the TS-ENs by their type of interaction (positive and negative) against the random ones (**Table 2**), our data indicates that negative relationships may retain a greater number of hubs than positive interactions, highlighting again the important role of competitive interactions within the mats. We also found that modularity increased in the negative associations, suggesting large groups of mutually excluding taxa and a clear dominance of competitive interaction within the same subsystem, in agreement with the clustering coefficient mentioned for the consensus TS-ENs.

The consensus TS-ENs at family level are shown in **Figure 7**. To facilitate visual representation, we displayed only the 0.05% of the top relationships. The latter is done since the networks displaying the 100% of the total interactions are so densely connected that the network patterns and hubs cannot be appreciated clearly. At this level of low-resolution, we observed a crucial role of the family Rhodobacteraceae as a hub within the three sites, having more negative associations within site C. The

TABLE 2 | Global network measurements of random and real networks.

	Negative interactions			Positive interactions		
	A	B	C	A	B	C
Clustering coefficient	0.7334 (±0.020)	0.5838 (±0.025)	0.7139 (±0.026)	0.3270 (±0.038)	0.1953 (±0.020)	0.2580 (±0.022)
Random	0.5745 (±0.025)	0.5920 (±0.008)	0.4482 (±0.012)	0.3522 (±0.029)	0.3184 (±0.013)	0.4457 (±0.030)
Modularity*	0.09 (±0.02)	0.13 (±0.02)	0.24 (±0.01)	0.05 (±0.01)	0.06 (±0.02)	0.02 (±0.01)
Random	0.025 (±0.005)	0.023 (±0.005)	0.037 (±0.011)	0.052 (±0.013)	0.057 (±0.017)	0.037 (±0.007)
Diameter*	2.25 (±0.50)	2.50 (±0.58)	2.50 (±0.58)	2.25 (±0.50)	2.50 (±0.58)	2.50 (±0.58)
Random*	2 (±0.0)	2 (±0.0)	2 (±0.0)	2 (±0.0)	2 (±0.0)	2 (±0.0)
Number of hubs with max in degree	3.50 (±2.38)	2.25 (±0.96)	6.50 (±7.33)	1.50 (±1.00)	2.25 (±2.50)	1.25 (±0.50)
Random	1.32 (±0.13)	1.27 (±0.14)	1.29 (±0.13)	1.26 (±0.11)	1.26 (±0.04)	1.26 (±0.11)
Number of hubs with max out degree	1.00 (±0.00)	1.75 (±0.50)	1.00 (±0.00)	1.75 (±1.50)	1.50 (±1.00)	6.50 (±10.34)
Random	1.29 (±0.13)	1.22 (±0.06)	1.23 (±0.12)	1.20 (±0.07)	1.28 (±0.11)	1.21 (±0.09)

*Std (±) represent the values obtained across the span of taxonomic levels from Phylum to Family. Properties marked by * are calculated on the underlying non-directed network.*

TABLE 3 | Strongly interconnected taxa or hubs identify at family levels within TS-ENs of microbial mats.

Site	Type of interaction	Max in-degree (affected by *n* nodes)	*n*	Max out degree (affecting *n* nodes)	*n*
A	*Consensus*	1. Nannocystaceae (PG)(RB) 2. Desulfarculaceae (C) (PG) (RB): *Desulfarculus* 3. Bacteroidaceae (C)(RB): *Bacteroides* 4. Caulobacteraceae (C)(RB): *unclassified Caulobacteraceae* 5. Bradyrhizobiaceae (C): Bosea, unclassified Bradyrhizobiaceae, Bradyrhizobium 6. Unclassified Oscillatoriophycideae (UC)(PG)(RB) 7. Rhodobacterales (UC)(PG)(RB) 8. Actinobacteria phylum 201174 (UC)(PG)(RB)	337	1. Polyangiaceae (PG)(RB)	345
	Positives	1. Unclassified Chloroflexi (RB)	275	1. Unclassified Armatimonadetes (UC)(PG)(RB)	263
	Negatives	1. Unclassified Rhodobacterales (UC)(RB)	278	1. Pelobacteraceae (C)(RB)(PB): *Pelobacter*	275
B	*Consensus*	1. Unclassified Xanthomonadales (UC)(RB)(PG) 2. Beijerinckiaceae 3. Burkholderiaceae (C): *Burkholderia, unclassified Burkholderiaceae, Burkholderiales Genera incertae sedis unclassified, unclassified Burkholderiales* 4. Phyllobacteriaceae (C)(PG): *unclassified Phyllobacteriaceae* 5. Gemmantimonadaceae	318	1. Thermoactinomycetaceae (C)(RB)(PG): Thermoactinomyces 2. Actinomycetaceae (C)(RB)(PG): Actinomyces 3. Alcaligenaceae (C) (RB): *unclassified* Alcaligenaceae 4. Gemmantimonadaceae	325
	Positives	1. Staphylococcaceae (RB)	226	1. Fusobacteriaceae (RB)	246
	Negatives	1. Phyllobacteriaceae (C): *unclassified Phyllobacteriaceae*	298	1. Cystobacterineae (UC)(RB) 2. Cloacimonetes (UC)(RB)	289
C	*Consensus*	1. Unclassified Verrucomicrobia (UC)(RB) 2. Methylobacteriaceae (C) (PG):*(unclassified Methylobacteriaceae, Methylobacterium)*	335	1. Chromobacteriaceae (C)(RB)(PG): *unclassified Chromobacteriaceae* 2. Mycobacteriaceae (C)(RB):*Mycobacterium* 3. Symbiobacteriaceae (RB)	343
	Positives	1. Unclassified Archaea (RB)	252	1. Micrococcales (UC)(RB)(PG)	223
	Negatives	1. Rhizobiales (UC) 2. Alteromonadaceae 3. Methylococcaceae (C)(RB): *unclassified Methylococcaceae* 4. Bacillales (UC)(RB) 5. Corynebacteriales (UC)(RB) 6. Beijerinckiaceae (RB)	251	1. Bacteroidetes (UC)(RB)	222
Global (A+B+C)	*Consensus*	1. Desulfarculaceae (C) (RB): *Desulfarculus* 2. Pelobacteraceae (C)(RB): *Pelobacter* 3. Gemmatimonadaceae	391	1. Bacteroidales (UC)(RB) 2. Microgenomates group (UC) (RB) 3. Nocardiaceae (C) (RB): *Nocardia* 4. Nitrospiraceae (RB) 5. Prolixibacteraceae (RB)	393
	Positive	1. Moraxellaceae (RB)	349	1. Unclassified Eukaryota (UC)	352
	Negatives	1. Phyllobacteriaceae (C): unclassified Phyllobacteriaceae	367	1. Desulfobacteraceae (C): *Desulfatibacillum*, *Desulfatiglans*, *Desulfatirhabdium*, *Desulfatitalea, Desulfobacter*, unclassified Desulfobacteraceae, *unclassified* Desulfobacterales	362

C, core microbial mat (presence in all samples regardless of environmental conditions and abundances). UC, unclassified sequences belonging to the microbial mat core. PG, taxa with known members delivering public goods (i.e., metabolites, enzymes, and vitamins). RB, rare biosphere <1% (0.01) abundances.

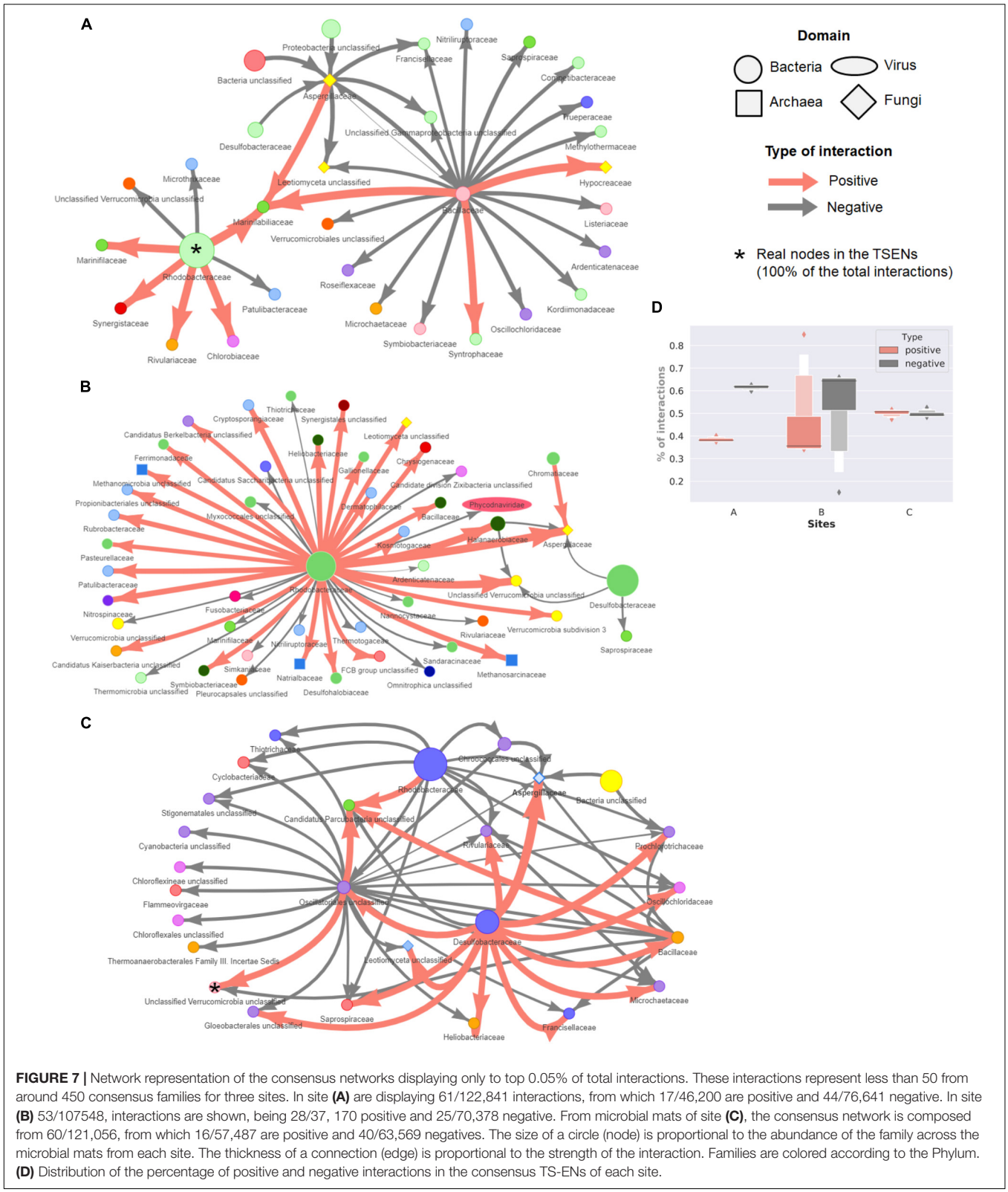

FIGURE 7 | Network representation of the consensus networks displaying only to top 0.05% of total interactions. These interactions represent less than 50 from around 450 consensus families for three sites. In site **(A)** are displaying 61/122,841 interactions, from which 17/46,200 are positive and 44/76,641 negative. In site **(B)** 53/107548, interactions are shown, being 28/37, 170 positive and 25/70,378 negative. From microbial mats of site **(C)**, the consensus network is composed from 60/121,056, from which 16/57,487 are positive and 40/63,569 negatives. The size of a circle (node) is proportional to the abundance of the family across the microbial mats from each site. The thickness of a connection (edge) is proportional to the strength of the interaction. Families are colored according to the Phylum. **(D)** Distribution of the percentage of positive and negative interactions in the consensus TS-ENs of each site.

family Desulfobacteraceae is also a key component within wet patches, having both negative and positive relations with fungi representatives (Aspergillaceae) in site B and C, respectively. However, these hubs came to light only when we focused on a small percentage of relationships. Therefore, in order to identify whether the hubs observed in this low level of resolution, we

identified the highly connected nodes either affecting (max out-degree) or being affected (max in-degree) by many links in the consensus, positive, negative, and global TS-ENs. Those hubs found in the consensus TS-ENs and in the low-resolution networks are highlighted with asterisks in **Figure 7**. In order to infer possible metabolic roles of the potential key stone taxa, we focused only on the nodes at family level, identifying those that were either part of the microbial mat core (C) rare biosphere (RB) or capable of delivering public goods (PG) to the system with prior reported evidence to perform such task (**Table 3**).

In the case of site A, we identified in the consensus TS-ENs eight hubs affected by 337 nodes, indicating a high interconnectivity within the overall system, and one hub affecting 345 nodes represented by the Polyangiaceae, a type of myxobacteria that is known for excreting hydrolytic enzymes and decomposing various and complex biopolymers (Brinkhoff et al., 2012). Interestingly, the number of hubs in the positive and negative networks decreases to some keystone taxa that belong to both the RB and the microbial mat core (see details in **Table 3**).

Our results indicate that the number of keystone taxa affected by, or affecting other members in the microbial mat community within site B is equivalent, being the majority members of both RB and microbial mat core. An interesting example within these hubs is the family Thermoactinomycetaceae, which is known for its protein degradative capacities, strong lipolytic activity, and alpha-amylase activity, as well as antimicrobial activity (Frikha Dammak et al., 2017).

By analyzing the consensus network from the microbial mats of site C, we found two hubs belonging to the microbial mat core; one is Verrucomicrobia, a lineage that is also part of the RB. Interestingly, this phylum is known to perform saccharolytic lifestyle commensal and mutualistic relationships with ciliates (Vannini et al., 2003).

Unexpectedly, within the positive networks, we observed a hub of unclassified sequences from the Eukarya domain whose presence could be potentially associated with an increase in the energy transfer, and therefore trophic complexity and potential resilience to environmental change (Duffy and Stachowicz, 2006).

For a visual comparison between low-level resolution networks and the consensus TS-ENs, we focused on the total amount of positive and negative interactions within sites. As observed in **Figure 7D**, site A displayed a larger percentage of negative interactions (0.616 mean $\pm$ 0.012 std.) compared with the positive ones (0.384 $\pm$ 0.011). In contrast, in the wet patches (especially in site C) approximately half of the interactions were found to be equally positive and negative (considering only average values).

Network Motifs

We focused on the representation of three-node motifs over 48 TS-ENs to observe whether these motifs could reflect the behavior of microbial mats from three sites during and after water depletion. In our study, we considered only those motifs whose probability of appearing is lower than a cutoff value (here $p = 0$ and $p \leq 0.05$) according to the distribution observed in randomized networks (Jin et al., 2007). As observed in **Figure 8**, these motifs appear numerous times on each particular network at every taxonomic level. For visual comparison, we normalized the abundance of each motif by the sum of the total across taxonomic levels. Therefore, an abundance of one indicates that a given motif is only found in that particular taxonomic level.

The occurrence of each motif can be observed consistently across the span of taxonomic levels when consensus networks are separated by type of interaction, either positive or negative. For example, motifs 6, 36, 78, 102, and 110 are under-represented in the negative TS-Ens, but are highly distributed across the positive interactions. This is particularly interesting since motif 6 (exploitative competition) occurs when some quantity of resources is consumed by an individual, thereby depriving other individuals of it. This type of competition has also been called consumptive competition (Kawata, 1997), and was never found among the negative TS-ENs within our microbial mats. The latter indicates that motif (6) can potentially have a different ecological connotation in microbial ecology, for example one bacteria delivering PG to the system. The same pattern is observed for the apparent competition motif (36) that occurs when two individuals that do not compete directly for resources affect each other indirectly as prey for the same predator (Lang and Benbow, 2013). However, in a microbial ecological context, the fact that this type of motif is mainly distributed across positive relationship could indicate beneficial relationships from two partners. For example, in the case of microbial mats from CCB, we suggest that this motif could correspond to a sulfate reducing bacteria using both organic compounds from a cyanobacteria and sulfate derived from purple bacteria to be used as the terminal electron acceptor in an energy-gaining respiratory process.

Furthermore, we found that motifs 12, 46, 108, and 238 are widely distributed across negative TS-ENs, but under-represented within the positive ones. These motifs seem to display more complex relationships, for example motif 238 represents the most mutually exclusive relationships in which all nodes exclude each other in a cycle form. Consistent with the ecological theory (Stouffer et al., 2007), the tri-trophic food chain motif (composed by prey, predator, and top-predator) was over-represented within negative networks compared to positive ones. However, since we also found the same motif in the positive interactions and in the consensus networks, it is possible that in our communities it represents both beneficial and negative interactions (Baiser et al., 2016).

The FeedForward-Loop (FFL) motif is one of the most significant motifs in *E. coli* and yeast, representing a structural stable motif with no feedback interaction and it has been found to be over-represented in transcriptional networks (Shen-Orr et al., 2002; Mangan and Alon, 2003). In ecological theory, the FFL involves omnivory, representing a predator consuming species from two lower trophic levels (Stouffer et al., 2007; Bascompte and Stouffer, 2009). In our TS-ENs, this motif must have at least one positive and one negative interaction since it is only found in the consensus TS-ENs. Another example is the Feedback-Loop (FBL), which has been recognized as an unstable network motif that is under-represented in gene regulatory neuronal

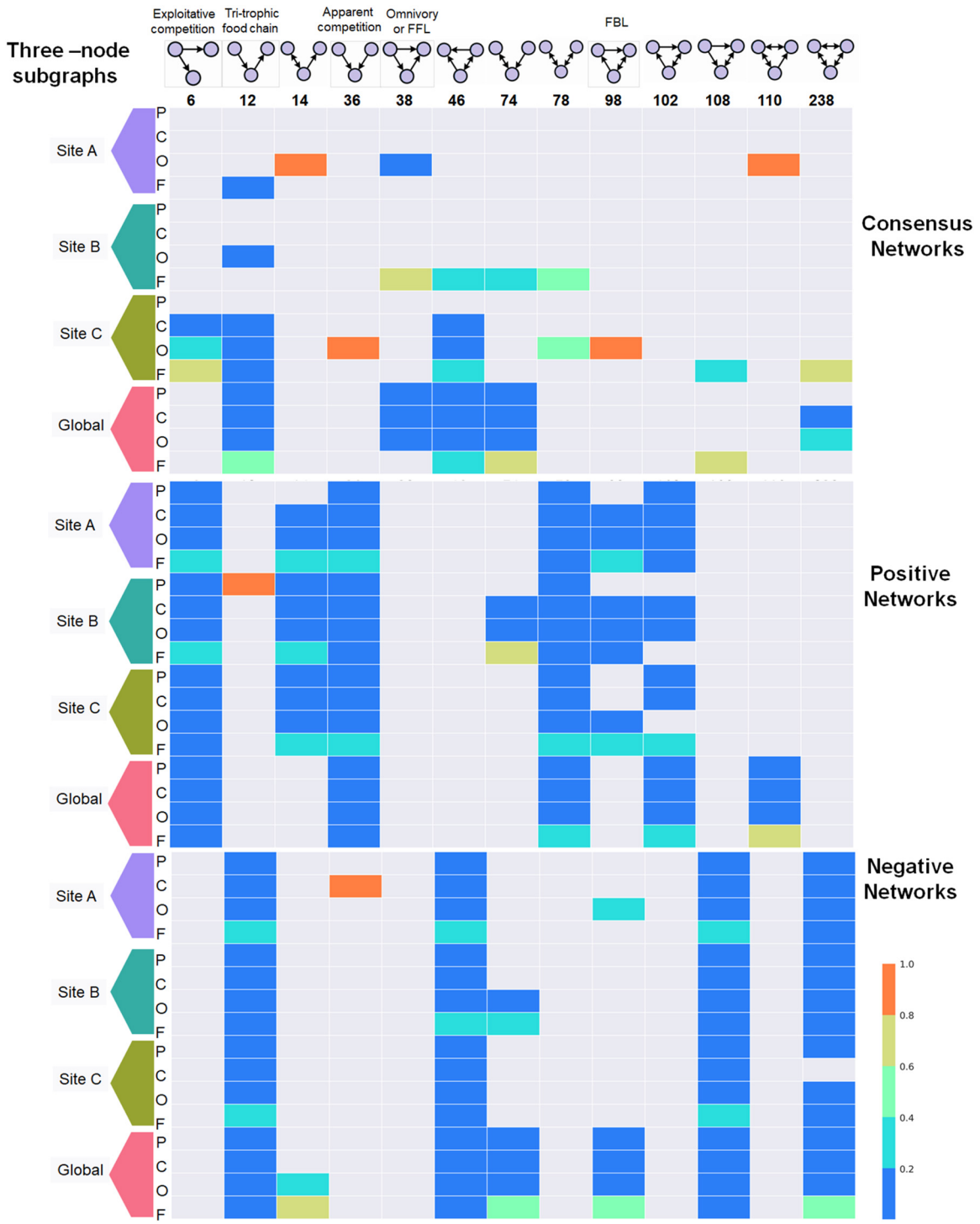

FIGURE 8 | Distribution of the 3-three-node subgraphs or network motifs across 48 microbial mat networks built across the taxonomic levels: Phylum (P), Class (C), Order (O), and Family (F). The top panel represents the motifs sorted by their ID identifier described in Mfinder. The motifs with specific ecological terminology are ID6, ID12, ID36, and ID38. The latter motif is also known as Feed Forward Loop (FFL) in regulatory networks. The ID98 represents Feedback Loop (FBL). To facilitate visual comparison, the abundance of each motif was normalized by its appearance across taxonomic levels. The relative abundance of each one indicates that a given motif is only found in that particular taxonomic lave (i.e., id 36 Site A in negative networks at class level). It is observed that particular motifs appear over-represented across the span of taxonomic levels when consensus networks are separated by type of interaction either positive or negative (i.e., Motif 108 in negative networks or motif 36 in positive ones). The color code in the bars indicate the scale from over representation (red) of a given motif in a given taxonomic level shifting to underrepresented (blue).

networks (de-Leon and Davidson, 2007). However, in our study, we observed an overrepresentation of this motif within the positive networks that could be an example of positive metabolic coupling occurring within microbial mats.

Finally, under the hypothesis that the environment can influence the strength and type of interactions between taxa, we expected to find similar interaction patterns in the microbial mats isolated from the wet patches. Interestingly, we only found that site B displayed a specific type of relationship, -the network motif ID74-. The latter indicates that specific local roles within site B that are not found within the microbial mats from the other sites, highlighting a very specific community dynamic and structure, even in the presence of the same environmental constraints.

DISCUSSION

The effects of wet versus dry conditions in Lagunita pond in Churince, CCB, on microbial communities were the main focus of our study. We observed that the lack of water in one site disrupted the fundamental characteristics of well-developed microbial mats, where the redox gradient includes a deep anaerobic environment that is fundamental for its function and stratification (Sorokin et al., 2006; Grimm et al., 2011; Higashioka et al., 2013; Eren et al., 2014). In contrast to normal wetland conditions, microbial mats from site A (the dry patch) were exposed to bright sunlight, in direct contact with the atmosphere losing their redox gradient and leading to a harsh photo-oxidative microenvironment at their surface. Given the remarkable physicochemical-zonation observed in microbial mats characterized by steep vertical gradients of oxygen, pH and sulfide (Chennu et al., 2015). Considering that metabolite exchanges in microbial communities give rise to ecological interactions that govern ecosystem diversity and stability (Zomorrodi and Segrè, 2017). It is expected that the lack of water has affected not only the community composition, structure and function, but also the community-level relationships.

Comparing our data with the analysis of microbialites from Pavilion lake (White et al., 2016), we found that they are supported by carbonate-rich structures associated with bacteria producing exo-polysaccharides (EPS). Here cyanobacteria are important in the organo-mineralization via dissimilatory sulfate reduction that precipitates compounds in carbonate stromatolites (White et al., 2016). Meanwhile, in our study system there is mostly gypsum and the mats at Lagunita are soft. Nevertheless, it is possible that a type of organo-mineralization occurs in wet conditions since we found cyanobacteria as well as unclassified sequences from Bacterial domain, Proteobacteria, Actinobacteria, and sulfate reducers such as *Desulfovibrio* and *Desulfatitalea* (also conforming the core and RB). This is interesting because in Pavilion Lake, the Deltaproteobacteria were assigned to the same genera of dissimilatory sulfate reducers that we observe in Lagunita (e.g., *Desulfobacterium* and *Desulfovibrio*). This suggests that even though the shape and consistency of the microbial communities are different, they are functionally similar to other marine and freshwater mats despite geographical and environmental differences.

Freshwaters Microbial Mats From Lagunita Are Highly Diverse

The large number of identified taxa (100 Phyla), mainly represented by low-abundant members within microbial mats indicate that this environment has a rich "seed pool" of genetic diversity. The latter suggests not only a large biological complexity at the micron scale (Minz et al., 1999a,b), but also a very dynamic structure with different ecotypes with apparently overlapping ecological features. As expected by the ecological theory on perturbations (Eng and Borenstein, 2018), the modifications of environmental conditions lead to changes in the proportion of species members in the community (measured at genera level).

When we explored the relationship between taxonomic and metabolic diversity estimated with ecological metrics (i.e., Shannon, Pielou, rarefaction curves) and the functional potential for several biogeochemical cycles by using MEBS algorithm, site A (dry in November 2012) was more diverse and resilient over time than expected, maybe because it was a fluctuating environment with wet winters until 2014. However, we believe that such resilience has been lost now that the lagoon has been permanently dry since 2016. Interestingly, even if wet patches do not display the same taxonomical dynamics as dry patches, they retained functional similarity. This functional core may be fulfilled by different key members of the RB. Another possible explanation for these results is the micro-dynamics of the deep aquifer. It is possible that site A was a little bit further from the micro-filtrations of deep water then the two neighboring sampling points (B and C), making it drier as the aquifer became depleted. Nevertheless, fluctuating environments have been shown to promote diversity in the different studied CCB environments (Bonilla-Rosso et al., 2012; Peimbert et al., 2012; Pajares et al., 2015).

Metabolic Dynamics in the Freshwaters Microbial Mats From Lagunita

By using MEBS, we were able to capture the fluctuation dynamics of the whole metabolic machinery involved in the main cycles, not only by focusing on a few marker genes, but rather by following the importance of the overall behavior over time. Our results indicate that the anaerobic cycles within microbial mats from the wet patches are maintained by the redox conditions probably related with the deep sulfur rich aquifer. This becomes more apparent when the aquifer recovered in 2013, due to the temporal closing of a canal 5 km away. When the water returned, the sulfur cycle became over-represented within the dry patch (site A, Autumn 2013). This is also evident in the potential methane cycling, where we observed microbial mats from the three sites were over-represented during the last two sampling periods (Autumn 2013 and Spring 2014) when water returned to the Lagoon.

Despite having no metagenomic samples before Autumn 2012, the Churince within CCB has been our focal study site for more than 15 years (Cerritos et al., 2011; Lee et al., 2015, 2017; Ponce-Soto et al., 2015). Long-term observations have seen the slow but dramatic decay of the ecosystem from a well-defined wetland to a nearly a dry desert with only a small spring and sections of the former river (Souza et al., 2007, 2018; De Anda et al., 2018). Sadly, this study was the last chance to understand the effect of perturbation and recovery on microbial mats from Churince, unless changes water usage policy start to allow the wetland to recover its deep aquifer.

Our results indicate that the sulfur cycle was only significantly overrepresented in microbial mats from site A after water recovery. We can suggest that perhaps site A could have had the potential for sulfur cycling under initial conditions, where low-abundant members of the microbial community were "waiting" the proper ecological conditions to develop particular metabolic features (i.e., elemental sulfur disproportionation in **Figure 6B**). Another hypothesis is that deep-water microbial migrants filled the empty ecological niche performing key metabolic processes within the mats. However, due to the large diversity of low-abundant members within the mats, we can argue that the "seed bank" hypothesis is more likely to occur, given the representation of the RB as key stone taxa in the TS-ENs.

There are other important keystone taxa that are dominant within mats, especially within dry conditions. For example, we can associate the abundance of the physiologically and metabolically versatile Rhodobacterales to their potential as primordial colonizers for the formation of biofilms in aquatic environments. This can explain their adaptation to dry environments by forming biofilms that are able to resist drying (Dang et al., 2008; Elifantz et al., 2013). Consistent with the visual structure of wet patches, the genera enriched among dry conditions were those implicated in the oxidation of inorganic reduced sulfur compounds (i.e., *Thioalkalivibrio*) which is a physiologically and metabolically taxon adapted to hyper-saline (up to saturation) and alkaline (pH up to 10.5) conditions (Foti et al., 2006; Sorokin et al., 2011). In contrast when the water levels were recovered, we detected an unknown diversity of unclassified Proteobacteria, along with the sulfate reducing bacteria *Desulfatitalea* [that is part of the microbial mat core and common in marine sediments (Higashioka et al., 2013)]. Our results confirm previous findings showing that sediments of the hypersaline lakes and lagoons may support a rich community of anaerobic halophilic bacteria, as the solubility of oxygen in hyper-saline brines is low and the amounts of organic matter available are often high (Oren, 1988, 2008).

Even if there are taxonomic shifts under environmental perturbation in the microbial mats of Lagunita, their resilience and resistance is evident when we compare their metabolic diversity, as the microbial mats originally sampled from wet-patches are metabolically similar. In addition, the anaerobic community that was shared -including purple sulfur bacteria and sulfur reducing bacteria- suggests the reestablishment of redox conditions and stability of the wet patches. This "elastic" property of the community is also supported by an overrepresentation of anaerobic cycles within these wet patches. Although there were shifts in the community composition, the retention of functionality indicates a shared function in response to water reestablishment toward a normal condition within the pond. More interesting is the finding that in Lagunita under stress or under recovery, there is a bacterial core that is constant, meaning a set of shared RB persist over time.

Although the three sites are very close in space, the fact that they have different dynamics and diversity along the time-series indicates site specific community dynamics. This is not surprising given the large microbial beta-diversity observed in CCB in general (Bonilla-Rosso et al., 2012; Espinosa-Asuar et al., 2015; Pajares et al., 2016) and in the studied Lagunita pond in particular (Lee et al., 2017). We believe that such community differentiation in the space could be due to historical factors –such as early colonizers establishing the ground rules of interactions-, but also by stochastic events such as virus predation of the dominant taxa following a "king of the hill" model (Taboada et al., 2018).

The changes in diversity and function of site A, in particular, confirm our hypothesis that water conditions in Lagunita and at the whole Churince Lagoon are important factors influencing metabolic function-composition within microbial mats. Even though the lack of water constitutes an obvious environmental filter for aquatic microbes (Pontarp et al., 2012; Monard et al., 2016), the fluctuation of such an important resource seems to be playing a critical role in the distribution and abundance of the taxa shaping microbial assemblies within the mats.

Microbial Mat Network Analysis

Modeling of interactions using networks is considered a powerful tool to understand the dynamics of succession within communities through time, as well as to analyze the stability within a system (Thébault and Fontaine, 2010; Coyte et al., 2015; Delmas et al., 2018). Unlike previous studies in which only the top 25% of interactions were used in the analysis (i.e., Weng et al., 2017), we used 100% of interactions, to gain information on the relationships among taxa given the importance of the RB in the diversity and function of the microbial mats of Lagunita.

In order to obtain the general patterns, we used the consensus network relationships and dissected them into positive and negative to find meaningful statistical properties. For instance, the network density or degree of network connectivity gives us an idea of how quickly perturbations may spread, by providing a measure of how dense the network is. A small diameter indicates presence of a densely connected nodes or hubs hence fast propagation among nodes, which may make the network more sensitive to perturbation (Delmas et al., 2018). The large network density obtained indicates that in Lagunita microbial mats, the networks of bacterial community are composed of highly connected groups. This was expected given the resilience of the system since a largely connected community is more robust to changes than low density networks (Sun et al., 2013).

It has been suggested that communities with modular organization of the type "small world" are more stable facing perturbations; modular arrangement allows different groups of nodes to perform different functions with some degree of independence (Newman, 2006). In practice, modularity values for biological networks typically fall in the range from about 0.3 to 0.7, and higher values are rare (Newman and Girvan, 2003). However, more recently, it has been suggested that it is not likely that the modularity maximum values (closer to one) always correspond to the best network for a stable community structure (Fortunato and Hric, 2016). Our study highlights the possibility that complex, densely connected networks can have modularity values that are lower than what it has been previously suggested (Newman and Girvan, 2003; Newman, 2006; Blondel et al., 2008; Poisot, 2013; Fortunato and Hric, 2016). In our study, the three microbial mat sampling sites are uniquely cohesive despite their large diversity. We consider that at CCB, the RB has been building complex bacterial communities that can survive under extremely unbalanced C: N: P conditions for a very long time (Souza et al., 2012) explaining the singularity of this site (Souza et al., 2018).

Building Blocks of Microbial Mats Networks

Although the networks described herein are highly dense and similar to those obtained from random networks, the appearance of each network motif do not occur randomly. Rather, their presence across the TS-ENs in all taxonomic levels increase the robustness of the analysis. Therefore, evaluating such motifs provides a link to understand the unique type of relationship dynamics in contrasting sampling points.

Recently these motifs have been used to define species trophic roles in the context of their community and therefore, the network's stability (Borrelli et al., 2015; Delmas et al., 2018). As far as we know, this is the first study to incorporate network motifs for the analysis of microbial mats under perturbation conditions. Further studies are needed to corroborate whether the overrepresentation of network motifs is specific to microbial mats or other environments, compared for example with neuronal, transcription and food webs (Tran et al., 2013; Borrelli et al., 2015).

Under the hypothesis than the environment can influence the strength and type of interactions among taxa, we expected to find similar interaction patterns among wet patches (sites B and C) while the dry patch at time 1 would be unique. Unexpectedly, site B was the only site that displayed a specific type of interaction, motif 74, a motif whose arrows suggest cross feeding among two members of the interaction, and a type of Black Queen dynamics toward the third member (Morris et al., 2012), suggesting a very unique mutualistic dynamic. In this site (B) we detected a wider range of interactions at the family level. Since all of these relationships are part of the microbial market and are context dependent (Mccully et al., 2017), we do not know what made site B unique. One possibility is that each site has a particular source of deep water by microfiltration. This idea may explain the specific RB dynamics within each site, since each one is "fed" from a slightly different seed bank.

To better understand why some motifs are found in high or low abundances within our microbial mats we need to explore not only the mathematical properties of such networks motif but also design experiments of direct interactions to understand the ecological meaning of generalists and specialists within each node.

Keystone Taxa Are Part of the Rare Biosphere and of the Microbial Mat Core

In general, we found that site B has a higher number of hubs in max out-degree (four in total); meanwhile site C has three and the site A has only one hub. This suggests that the dry patch is possibly more fragile because if a single hub is removed, more relationships may be lost compared to sites B and C (see **Table 3**). In addition, we observed that most hubs belonging either to the RB or microbial mat core seem to provide PG. This is particularly meaningful, given that in ecological studies there is no way to discriminate the role of particular taxa within natural systems by simply highlighting their low abundance. However, in our study we found a direct implication of the RB in microbial mats under environmental perturbation.

We also observed that some of the hubs, which were detected independently in the three sites, were also detected in the global network. Interestingly, unclassified members of Eukarya domain were identified as a hub with positive relationships. It has been observed that diverse communities of eukaryotes live in microbial mats including not only a broad range of taxa, but also a large functional diversity, including phototrophs from several algal phyla and a variety of heterotrophic organisms. In this context, microbial mats could provide different microhabitats under contrasting conditions, which gives protection against oxidative, osmotic, freeze-thaw, and dehydration stressors for all microorganisms embedded within the microbial mat matrix (Jungblut et al., 2012). A global positive interconnection among unknown eukaryotic taxa within the global network in microbial mats of Churince is important to highlight regarding the presence of saprophytic, phagotrophic, parasitic, and predatory eukaryotes that would increase the number of links within a mat for nutrient and energy transfer (Duffy and Stachowicz, 2006). It would be very interesting to test these ideas by experimentally removing certain taxa (using particular antibiotics, for instance) and observing if their disappearance affects the entire system.

Suggesting Possible Drivers of Microbial Mat's Stability

Our results are in agreement with other studies that have proposed negative interactions increase the resilience of microbial communities (Foster and Bell, 2012; Coyte et al., 2015; Zelezniak et al., 2015; Deng et al., 2016). In addition, it has been suggested that microbial cooperative networks (characterized by mutualism) are often unstable, while a higher proportion of competitive interaction pairs (-/-) help the host maintain a stable microbial community in the case of the human microbiome (Coyte et al., 2015). However, it is expected that when resources are limited (as is the case of our

extremely oligotrophic system), some species may outcompete others and stability is reached with one species per resource in the classic niche model (Borrelli et al., 2015). On the other hand, *in silico* studies suggested that modularity was able to have a positive effect on stability only when (a) the system is composed of two subsystems of about the same size and (b) the overall mean interaction strength is negative (Grilli et al., 2016). Here, consistent with the theory, we observed that in the stressed mat of site A the negative interactions are, on average, larger than the positive ones even though this site is the most resistant according to our ecological indexes.

However, under wet conditions there is an equilibrium between positive and negative interactions due to the metabolic interdependency based on cooperation or mutualistic relationships. This has been observed under nutrient-poor conditions where metabolic complementarity can provide group advantage (Morris et al., 2013). However, if this frail balance is tipped over by environmental disturbance, then the negative relationships exceed the positive ones. This type of behavior has been found in complex food webs due to low transformation of prey into predator (Allesina et al., 2015; Grilli et al., 2016). The latter do not apply for the CCB microbial mats since predators are virus and recycling of the nutrients are so efficient that we observe extremely low organic P (Lee et al., 2015). Furthermore, it has been suggested that large systems in which the positive interactions dominate, the negative ones are unstable and will likely lose stability through a "hop bifurcation" (conversion efficiency of resources of consumers) (Allesina et al., 2015). Hop bifurcation should be most common in the presence of an inverted biomass pyramid, typically occurring in planktonic or other aquatic systems (Allesina et al., 2015; Grilli et al., 2016). Moreover, it has been suggested that a strong network of interactions among organisms can provide a buffer against disturbance beyond the effect of functional redundancy, as alternative pathways (with different combinations of microbes) can be recruited to fulfill specific functions, thus increasing the negative interactions (Konopka et al., 2015). This is what we observed in our study: during wet conditions, the ratio of cooperation versus competition under equilibrium, however, negative interactions increase under dry conditions (see **Table 3**).

The hypothesis that closely coordinated metabolic associations promote homeostasis and become a buffer against stressful, resource-limited conditions has been previously described (Guerrero et al., 2002; Konopka et al., 2015; Wong et al., 2017). In general, is accepted that there is a metabolic and ecological congruence in a community as long as biogeochemical and environmental gradients allow individual niches to exist in close proximity. Thus, metabolically diverse microorganisms are oriented according to energetic, nutrient and ecological requirements and tolerances (Guerrero et al., 2002; Wong et al., 2017).

Metabolic dependencies based on the Black Queen hypothesis (Morris et al., 2012) are a starting point for the evolution of cooperative behavior, where the cross-feeding (bidirectional dependency) is obligated in communities were essential functions are costly for producers (Mas et al., 2016). To explore Black Queen ideas, we separated the effect of network complexity from specific traits of individual members in hubs. To find keystone candidate taxa important for the maintenance of structure and function of a community, we focused on microorganisms from the microbial mat core (present in all samples) and low abundant taxa (RB) to infer putative ecological niches and functional roles. We found that the majority of nodes are members of the RB and microbial mat core and despite their low abundance, their role in the community seems to be critical by establishing indirect, mutualistic relationships. An example of this is the case of a positive relationship between unclassified members of Oscillatoriales (cyanobacteria) and a sulfate reducing bacteria Desulfobacteraceae, along with a candidatus Parcubacteria and Rhodobacteraceae (heterotroph). In this example (see **Figure 7C**), the cyanobacteria release public goods in the form of carbon sources that are degraded by the candidatus Parcubacteria (Nelson and Stegen, 2015), making them available to Rhodobacteraceae. Therefore, by establishing mutualistic relationships, the RB is allowing co-occurrence of several small niches (Thébault and Fontaine, 2010; Zhou et al., 2010; Faust and Raes, 2012b; Mccully et al., 2017).

As aforementioned, in microbial mats the biogeochemical cycles through networks of metabolite exchange are structured along energetic gradients (Guerrero et al., 2002; Wong et al., 2017). As energy yields become limiting, these networks promote co-metabolic interactions to maximize energy disequilibrium (Wong et al., 2017). Thus, when there are more species than resources, some of them will invariably outcompete with others, in theory resulting in a final community with at most one species per resource, that should reach equilibrium and stability despite variable environmental parameter values (Borrelli et al., 2015).

CONCLUSION

Microbial mats from three close by sites within Lagunita in the Churince system of the CCB displayed a high microbial diversity. Most of this diversity is represented by members of the RB, but also included a particular core of microorganisms that were present in all samples across spatial-temporal scales. Our analysis shows that when the aquifer re-established its deep flow, the anaerobic-dependent functions within the sulfur and methane cycles also reestablish. This rebound was likely possible due to a large "seed bank" that makes the microbial mat redundant and diverse. In their interaction motifs, we detected a type of site-specific "fingerprint," even though they are few meters apart. The microbial mat under stressful conditions displayed more negative interactions than the wetter communities where mutualistic interaction balances with antagonism. This suggests an important role of the members of the RB in the permanence of these bacterial communities.

In conclusion, we suggest that the mechanisms behind microbial mats stability in Lagunita are related to an increase in

negative interaction during perturbation, low modularity, large taxonomic diversity (represented by a large number of rare taxa), and core microorganisms which can carry out essential functions in the community. We consider that at CCB, the RB has been building complex bacterial communities that can survive under extremely unbalanced C: N: P conditions for a very long time explaining the singularity and resilience of this site, and we hope that this biodiversity will allow this wetland to be reborn from its stored seed bank.

DATA AVAILABILITY STATEMENT

The data and scripts to reproduce all the figures for this study can be found in the following repository https://valdeanda.github.io/Time_series_mats/. The software developed for the network analysis is found at https://valdeanda.github.io/NetAn/.

AUTHOR CONTRIBUTIONS

VDA, IZ-P, LE, and VS conceived the project and worked on the manuscript. VDA and JB performed the fieldwork, sampling, sample processing, DNA extraction and ecological indexes analysis. VDA, AP-H, and BC-M conducted the bioinformatic metagenomic analysis. BC-M and MH-R provided computing resources and analysis interpretation. MG-L, MH-R, and VDA designed and implemented NetAn. IZ-P, MG-L, NG-T, MH-R, and VDA provided ecological interpretation of the network analysis. LE and VS contributed to sampling and fieldwork, provided expertise, logistics and resources to develop and supervised the project, as well as intellectual contributions to the work. All authors made contributions to the manuscript.

FUNDING

This work constitutes a partial fulfillment requirement for the Ph.D. degree of VDA at the graduate program Doctorado en Ciencias Biomédicas of the Universidad Nacional Autónoma de México who received fellowship 356832 of Consejo Nacional de Ciencia y Tecnología (CONACYT). The authors acknowledge the funding of WWF-Alianza Carlos Slim, and the support by the SEP Conacyt Project to VS and LE 1101OL34. The paper was written during VDA research stay in BC-M laboratory with the support of Beca Mixta Conacyt and during a sabbatical leave of LE and VS in the University of Minnesota in Peter Tiffin and Michael Travisano laboratories, with support of the program PASPA-DGAPA, UNAM.

ACKNOWLEDGMENTS

We would like to thank Manuel Rosas, Paola Vazquez, and Gabriel Yaxal Ponce for their valuable help during fieldwork and sampling collections. Emilio Morella and Silvia Barrientos for the technical support during DNA extractions. Laura Espinosa Asuar and Erika Aguirre Planter with technical logistics along all the study. Carlos Cantalapiedra, Ernesto Igartua Aguirre, Mirna Vazquez, Gabriel Yaxal Ponce, Paul O'Brien, and Maggie Langwing for their valuable comments and discussion. We also thank Craig Connolly and Kylie Holt who contributed to the editing processes greatly improving the manuscript. The first author acknowledges the laboratory of computational and structural biology and Aula Dei CSIC, for computing resources and support during the research stay. We also thank the LAVIS (Laboratorio Nacional de Visualización Científica Avanzada) from UNAM campus Juriquilla, Mexico for the provided computer infrastructure, as well as Alberto Luis Aguilar for the technical support during the development of the project.

SUPPLEMENTARY MATERIAL

The Supplementary Material for this article can be found online at: https://www.frontiersin.org/articles/10.3389/fmicb.2018.02606/full#supplementary-material

REFERENCES

Allesina, S., Grilli, J., Barabás, G., Tang, S., Aljadeff, J., and Maritan, A. (2015). Predicting the stability of large structured food webs. *Nat. Commun.* 6:7842. doi: 10.1038/ncomms8842

Allison, S. D., and Martiny, J. B. H. (2008). Resistance, resilience, and redundancy in microbial communities. *Proc. Natl. Acad. Sci. U.S.A.* 105, 11512–11519.

Alon, U. (2007). Network motifs: theory and experimental approaches. *Nat. Rev. Genet.* 8, 450–461. doi: 10.1038/nrg2102

Andrews, S. (2010). *FastQC: A Quality Control Tool for High Throughput Sequence Data*. Available at: http://www.bioinformatics.babraham.ac.uk/projects/fastqc

Baiser, B., Elhesha, R., and Kahveci, T. (2016). Motifs in the assembly of food web networks. *Oikos* 125, 480–491. doi: 10.1111/oik.02532

Baldassano, S. N., and Bassett, D. S. (2016). Topological distortion and reorganized modular structure of gut microbial co-occurrence networks in inflammatory bowel disease. *Sci. Rep.* 6:26087. doi: 10.1038/srep26087

Bascompte, J., and Stouffer, D. B. (2009). The assembly and disassembly of ecological networks. *Philos. Trans. R. Soc. B Biol. Sci.* 364, 1781–1787. doi: 10.1098/rstb.2008.0226

Bhaya, D., Grossman, A. R., Steunou, A.-S., Khuri, N., Cohan, F. M., Hamamura, N., et al. (2007). Population level functional diversity in a microbial community revealed by comparative genomic and metagenomic analyses. *ISME J.* 1, 703–713. doi: 10.1038/ismej.2007.46

Bissett, A., Brown, M. V., Siciliano, S. D., and Thrall, P. H. (2013). Microbial community responses to anthropogenically induced environmental change: towards a systems approach. *Ecol. Lett.* 16, 128–139. doi: 10.1111/ele.12109

Blondel, V. D., Guillaume, J.-L., Lambiotte, R., and Lefebvre, E. (2008). Fast unfolding of communities in large networks. *J. Stat. Mech. Theory Exp.* P10008, 1–12. doi: 10.1088/1742-5468/2008/10/P10008

Bolger, A. M., Lohse, M., and Usadel, B. (2014). Trimmomatic: a flexible trimmer for Illumina sequence data. *Bioinformatics* 30, 2114–2120. doi: 10.1093/bioinformatics/btu170

Bolhuis, H., Cretoiu, M. S., and Stal, L. J. (2014). Molecular ecology of microbial mats. *FEMS Microbiol. Ecol.* 90, 335–350. doi: 10.1111/1574-6941.12408

Bonilla-Rosso, G., Peimbert, M., Alcaraz, L. D., Hernández, I., Eguiarte, L. E., Olmedo-Alvarez, G., et al. (2012). Comparative metagenomics of two microbial mats at Cuatro Ciénegas Basin II: community structure and composition in

oligotrophic environments. *Astrobiology* 12, 659–673. doi: 10.1089/ast.2011.0724

Borrelli, J. J., Allesina, S., Amarasekare, P., Arditi, R., Chase, I., Damuth, J., et al. (2015). Selection on stability across ecological scales. *Trends Ecol. Evol.* 30, 417–425. doi: 10.1016/j.tree.2015.05.001

Breitbart, M., Hoare, A., Nitti, A., Siefert, J., Haynes, M., Dinsdale, E., et al. (2009). Metagenomic and stable isotopic analyses of modern freshwater microbialites in Cuatro Ciénegas, Mexico. *Environ. Microbiol.* 11, 16–34. doi: 10.1111/j.1462-2920.2008.01725.x

Brinkhoff, T., Fischer, D., Vollmers, J., Voget, S., Beardsley, C., Thole, S., et al. (2012). Biogeography and phylogenetic diversity of a cluster of exclusively marine myxobacteria. *ISME J.* 6, 1260–1272. doi: 10.1038/ismej.2011.190

Bullock, H. A., Reisch, C. R., Burns, A. S., Moran, M. A., and Whitman, W. B. (2014). Regulatory and functional diversity of methylmercaptopropionate coenzyme A ligases from the dimethylsulfoniopropionate demethylation pathway in Ruegeria pomeroyi DSS-3 and other proteobacteria. *J. Bacteriol.* 196, 1275–1285. doi: 10.1128/JB.00026-14

Cerritos, R., Eguiarte, L. E., Avitia, M., Siefert, J., Travisano, M., Rodríguez-Verdugo, A., et al. (2011). Diversity of culturable thermo-resistant aquatic bacteria along an environmental gradient in Cuatro Cienegas, Coahuila, México. *Antonie van Leeuwenhoek* 99, 303–318. doi: 10.1007/s10482-010-9490-9

Chennu, A., Grinham, A., Polerecky, L., de Beer, D., and Al-Najjar, M. A. A. (2015). Rapid reactivation of cyanobacterial photosynthesis and migration upon rehydration of desiccated marine microbial mats. *Front. Microbiol.* 6:1472. doi: 10.3389/fmicb.2015.01472

Contreras-Moreira, B., and Vinuesa, P. (2013). GET_HOMOLOGUES, a versatile software package for scalable and robust microbial pangenome analysis. *Appl. Environ. Microbiol.* 79, 7696–7701. doi: 10.1128/AEM.02411-13

Coyte, K. Z., Schluter, J., and Foster, K. R. (2015). The ecology of the microbiome: networks, competition, and stability. *Science* 350, 663–666. doi: 10.1126/science.aad2602

Curson, A. R. J., Rogers, R., Todd, J. D., Brearley, C. A., and Johnston, A. W. B. (2008). Molecular genetic analysis of a dimethylsulfoniopropionate lyase that liberates the climate-changing gas dimethylsulfide in several marine α-proteobacteria and *Rhodobacter sphaeroides*. *Environ. Microbiol.* 10, 757–767. doi: 10.1111/j.1462-2920.2007.01499.x

Dang, H., Li, T., Chen, M., and Huang, G. (2008). Cross-ocean distribution of rhodobacterales bacteria as primary surface colonizers in temperate coastal marine waters. *Appl. Environ. Microbiol.* 74, 52–60. doi: 10.1128/AEM.01400-07

De Anda, V., Zapata-Peñasco, I., Poot-Hernández, A. C., Eguiarte, L. E., Contreras-Moreira, B., and Souza, V. (2017). MEBS, a software platform to evaluate large (meta)genomic collections according to their metabolic machinery: unraveling the sulfur cycle. *Gigascience* 6, 1–17. doi: 10.1093/gigascience/gix096

De Anda, V., Zapata-Peñasco, I., and Souza, V. (2018). "Towards a comprehensive understanding of environmental perturbations in microbial mats from the Cuatro Ciénegas Basin by network inference," in *Ecosystem Ecology and Geochemistry of Cuatro Cienegas: How to Survive in an Extremely Oligotrophic Site*, eds S. V. Elser and J. F. García-Oliva (Berlin: Springer).

de-Leon, S. B.-T., and Davidson, E. H. (2007). Gene regulation: gene control network in development. *Annu. Rev. Biophys. Biomol. Struct.* 36, 191–212. doi: 10.1146/annurev.biophys.35.040405.102002

Delmas, E., Besson, M., Brice, M.-H., Burkle, L., Riva, G. V. D., Fortin, M.-J., et al. (2018). Analyzing ecological networks of species interactions. *bioRxiv* [Preprint]. doi: 10.1101/112540

Deng, Y., Zhang, P., Qin, Y., Tu, Q., Yang, Y., He, Z., et al. (2016). Network succession reveals the importance of competition in response to emulsified vegetable oil amendment for uranium bioremediation. *Environ. Microbiol.* 18, 205–218. doi: 10.1111/1462-2920.12981

Desnues, C., Rodriguez-Brito, B., Rayhawk, S., Kelley, S., Tran, T., Haynes, M., et al. (2008). Biodiversity and biogeography of phages in modern stromatolites and thrombolites. *Nature* 452, 340–343. doi: 10.1038/nature06735

Duffy, J. E., and Stachowicz, J. J. (2006). Why biodiversity is important to oceanography: potential roles of genetic, species, and trophic diversity in pelagic ecosystem processes. *Mar. Ecol. Prog. Ser.* 311, 179–189. doi: 10.3354/meps311179

Elifantz, H., Horn, G., Ayon, M., Cohen, Y., and Minz, D. (2013). Rhodobacteraceae are the key members of the microbial community of the initial biofilm formed in Eastern Mediterranean coastal seawater. *FEMS Microbiol. Ecol.* 85, 348–357. doi: 10.1111/1574-6941.12122

Eng, A., and Borenstein, E. (2018). Taxa-function robustness in microbial communities. *Microbiome* 6, 1–19. doi: 10.1186/s40168-018-0425-4

Eren, A. M., Morrison, H. G., Lescault, P. J., Reveillaud, J., Vineis, J. H., and Sogin, M. L. (2014). Minimum entropy decomposition?: unsupervised oligotyping for sensitive partitioning of high- throughput marker gene sequences. *ISME J.* 9, 968–979. doi: 10.1038/ismej.2014.195

Espinosa-Asuar, L., Escalante, A. E., Gasca-Pineda, J., Blaz, J., Peña, L., Eguiarte, L. E., et al. (2015). Aquatic bacterial assemblage structure in Pozas Azules, Cuatro Ciénegas Basin, Mexico: deterministic vs. stochastic processes. *Int. Microbiol.* 18, 105–115. doi: 10.2436/20.1501.01.240

Faust, K., and Raes, J. (2012a). Microbial interactions: from networks to models. *Nat. Rev. Microbiol.* 10, 538–550. doi: 10.1038/nrmicro2832

Faust, K., and Raes, J. (2012b). Microbial interactions: from networks to models. *Nat. Rev. Microbiol.* 10, 538–550. doi: 10.1038/nrmicro2832

Finn, R. D., Coggill, P., Eberhardt, R. Y., Eddy, S. R., Mistry, J., Mitchell, A. L., et al. (2015). The Pfam protein families database: towards a more sustainable future. *Nucleic Acids Res.* 44, D279–D285. doi: 10.1093/nar/gkv1344

Fortunato, S., and Hric, D. (2016). Community detection in networks: a user guide. *Phys. Rep.* 659, 1–44. doi: 10.1016/j.physrep.2016.09.002

Foster, K. R., and Bell, T. (2012). Competition, not cooperation, dominates interactions among culturable microbial species. *Curr. Biol.* 22, 1845–1850. doi: 10.1016/j.cub.2012.08.005

Foti, M., Ma, S., Sorokin, D. Y., Rademaker, J. L. W., Kuenen, J. G., and Muyzer, G. (2006). Genetic diversity and biogeography of haloalkaliphilic sulphur-oxidizing bacteria belonging to the genus *Thioalkalivibrio*. *FEMS Microbiol. Ecol.* 56, 95–101. doi: 10.1111/j.1574-6941.2006.00068.x

Frikha Dammak, D., Zarai, Z., Najah, S., Abdennabi, R., Belbahri, L., Rateb, M. E., et al. (2017). Antagonistic properties of some halophilic thermoactinomycetes isolated from superficial sediment of a solar saltern and production of cyclic antimicrobial peptides by the novel isolate *Paludifilum halophilum*. *Biomed. Res. Int.* 2017:1205258. doi: 10.1155/2017/1205258

Fuhrman, J. A. (2009). Microbial community structure and its functional implications. *Nature* 459, 193–199. doi: 10.1038/nature08058

Gihring, T. M., Zhang, G., Brandt, C. C., Brooks, S. C., Campbell, J. H., Carroll, S., et al. (2011). A limited microbial consortium is responsible for extended bioreduction of uranium in a contaminated aquifer. *Appl. Environ. Microbiol.* 77, 5955–5965. doi: 10.1128/AEM.00220-11

Girvan, M. S., Campbell, C. D., Killham, K., Prosser, J. I., and Glover, L. A. (2005). Bacterial diversity promotes community stability and functional resilience after perturbation. *Environ. Microbiol.* 7, 301–313. doi: 10.1111/j.1462-2920.2005.00695.x

Grilli, J., Rogers, T., and Allesina, S. (2016). Modularity and stability in ecological communities. *Nat. Commun.* 7:12031. doi: 10.1038/ncomms12031

Grimm, F., Franz, B., and Dahl, C. (2011). Regulation of dissimilatory sulfur oxidation in the purple sulfur bacterium allochromatium vinosum. *Front. Microbiol.* 2:51. doi: 10.3389/fmicb.2011.00051

Grzymski, J. J., Murray, A. E., Campbell, B. J., Kaplarevic, M., Gao, G. R., Lee, C., et al. (2008). Metagenome analysis of an extreme microbial symbiosis reveals eurythermal adaptation and metabolic flexibility. *Proc. Natl. Acad. Sci. U.S.A.* 105, 17516–17521. doi: 10.1073/pnas.0802782105

Guerrero, R., Piqueras, M., and Berlanga, M. (2002). Microbial mats and the search for minimal ecosystems. *Int. Microbiol.* 5, 177–188. doi: 10.1007/s10123-002-0094-8

Hagberg, A. A., Schult, D. A., and Swart, P. J. (2008). "Exploring network structure, dynamics, and function using NetworkX," in *Proceedings of the 7th Python Science Conference (SciPy 2008)*, Washington, DC, 11–15.

Higashioka, Y., Kojima, H., Watanabe, M., and Fukui, M. (2013). *Desulfatitalea tepidiphila* gen. nov., sp. nov., a sulfate-reducing bacterium isolated from tidal flat sediment. *Int. J. Syst. Evol. Microbiol.* 63, 761–765. doi: 10.1099/ijs.0.043356-0

Hunt, D. E., and Ward, C. S. (2015). A network-based approach to disturbance transmission through microbial interactions. *Front. Microbiol.* 6:1182. doi: 10.3389/fmicb.2015.01182

Hunting, E. R., Vijver, M. G., van der Geest, H. G., Mulder, C., Kraak, M. H. S., Breure, A. M., et al. (2015). Resource niche overlap promotes stability of bacterial community metabolism in experimental microcosms. *Front. Microbiol.* 6:105. doi: 10.3389/fmicb.2015.00105

Hyatt, D., Chen, G.-L., Locascio, P. F., Land, M. L., Larimer, F. W., and Hauser, L. J. (2010). Prodigal: prokaryotic gene recognition and translation initiation site identification. *BMC Bioinformatics* 11:119. doi: 10.1186/1471-2105-11-119

Jiao, Y., D'haeseleer, P., Dill, B. D., Shah, M., Verberkmoes, N. C., Hettich, R. L., et al. (2011). Identification of biofilm matrix-associated proteins from an acid mine drainage microbial community. *Appl. Environ. Microbiol.* 77, 5230–5237. doi: 10.1128/AEM.03005-10

Jiménez, D. J., Andreote, F. D., Chaves, D., Montaña, J. S., Osorio-Forero, C., Junca, H., et al. (2012). Structural and functional insights from the metagenome of an acidic hot spring microbial planktonic community in the Colombian Andes. *PLoS One* 7:e52069. doi: 10.1371/journal.pone.0052069

Jin, G., Zhang, S., Zhang, X. S., and Chen, L. (2007). Hubs with network motifs organize modularity dynamically in the protein-protein interaction network of yeast. *PLoS One* 2:1207. doi: 10.1371/journal.pone.0001207

Jonkers, H. M., Bruin, S., and Gemerden, H. (1998). Turnover of dimethylsulfoniopropionate (DMSP) by the purple sulfur bacterium *Thiocapsa roseopersicina* M11: ecological implications. *FEMS Microbiol. Ecol.* 27, 281–290. doi: 10.1111/j.1574-6941.1998.tb00544.x

Jousset, A., Bienhold, C., Chatzinotas, A., Gallien, L., Gobet, A., Kurm, V., et al. (2017). Where less may be more: how the rare biosphere pulls ecosystems strings. *ISME J.* 11, 853–862. doi: 10.1038/ismej.2016.174

Jungblut, A. D., Vincent, W. F., and Lovejoy, C. (2012). Eukaryotes in Arctic and Antarctic cyanobacterial mats. *FEMS Microbiol. Ecol.* 82, 416–428. doi: 10.1111/j.1574-6941.2012.01418.x

Karpinets, T. V., Gopalakrishnan, V., Wargo, J., Futreal, A. P., Schadt, C. W., and Zhang, J. (2018). Linking associations of rare low-abundance species to their environments by association networks. *Front. Microbiol.* 9:297. doi: 10.3389/fmicb.2018.00297

Kawata, M. (1997). Exploitative competition and ecological effective abundance. *Ecol. Model.* 94, 125–137. doi: 10.1016/S0304-3800(96)00008-7

Khodadad, C. L. M., and Foster, J. S. (2012). Metagenomic and metabolic profiling of nonlithifying and lithifying stromatolitic mats of Highborne Cay, The Bahamas. *PLoS One* 7:e38229. doi: 10.1371/journal.pone.0038229

Kletzin, A. (2008). "Oxidation of sulfur and inorganic sulfur compounds in acidianus ambivalens," in *Proceedings of the Microbial Sulfur Metabolism*, eds C. Dahl and C. G. Friedrich (Berlin: Springer). doi: 10.1007/978-3-540-72682-1_15

Konopka, A. E., Lindemann, S., and Fredrickson, J. K. (2015). Dynamics in microbial communities: unraveling mechanisms to identify principles. *ISME J.* 9, 1488–1495. doi: 10.1038/ismej.2014.251

Kunin, V., Raes, J., Harris, J. K., Spear, J. R., Walker, J. J., Ivanova, N., et al. (2008). Millimeter-scale genetic gradients and community-level molecular convergence in a hypersaline microbial mat. *Mol. Syst. Biol.* 4:198. doi: 10.1038/msb.2008.35

Lang, J. M., and Benbow, M. E. (2013). Species Interactions and Competition. *Nat. Educ. Knowledge* 4:8.

Lee, Z., Poret-Peterson, A. T., Siefert, J. L., Kaul, D., Moustafa, A., Allen, A. E., et al. (2017). Nutrient stoichiometry shapes microbial community structure in an Evaporitic Shallow Pond. *Front. Microbiol.* 8:949. doi: 10.3389/fmicb.2017.00949

Lee, Z. M., Steger, L., Corman, J. R., Neveu, M., Poret-Peterson, A. T., Souza, V., et al. (2015). Response of a stoichiometrically imbalanced ecosystem to manipulation of nutrient supplies and ratios. *PLoS One* 10:e0123949. doi: 10.1371/journal.pone.0123949

Li, D., Liu, C. M., Luo, R., Sadakane, K., and Lam, T. W. (2014). MEGAHIT: an ultra-fast single-node solution for large and complex metagenomics assembly via succinct de Bruijn graph. *Bioinformatics* 31, 1674–1676. doi: 10.1093/bioinformatics/btv033

Lynch, M. D. J., and Neufeld, J. D. (2015). Ecology and exploration of the rare biosphere. *Nat. Rev. Microbiol.* 13, 217–229. doi: 10.1038/nrmicro3400

Mangan, S., and Alon, U. (2003). Structure and function of the feed-forward loop network motif. *Proc. Natl. Acad. Sci. U.S.A.* 100, 11980–11985. doi: 10.1073/pnas.2133841100

Martin, H. (2011). Cutadapt removes adapter sequences from high-throughput sequencing reads. *EMBnet J.* 17, 10–12. doi: 10.14806/ej.17.1.200

Mas, A., Jamshidi, S., Lagadeuc, Y., Eveillard, D., and Vandenkoornhuyse, P. (2016). Beyond the black queen hypothesis. *ISME J.* 10, 2085–2091. doi: 10.1038/ismej.2016.22

Mccully, A. L., Lasarre, B., and Mckinlay, J. B. (2017). Recipient-biased competition for an intracellularly generated cross-fed nutrient is required for coexistence of microbial mutualists. *mBio* 8:e01620-17. doi: 10.1128/mBio.01620-17

McMurdie, P. J., and Holmes, S. (2013). Phyloseq: an r package for reproducible interactive analysis and graphics of microbiome census data. *PLoS One* 8:e61217. doi: 10.1371/journal.pone.0061217

Milo, R. (2002). Network motifs: simple building blocks of complex networks. *Science* 298, 824–827. doi: 10.1126/science.298.5594.824

Minot, S. S., Krumm, N., and Greenfield, N. B. (2015). One codex: a sensitive and accurate data platform for genomic microbial identification. *bioRxiv* [Preprint]. doi: 10.1101/027607

Minz, D., Fishbain, S., Green, S. J., Muyzer, G., Cohen, Y., Rittmann, B. E., et al. (1999a). Diversity of sulfate-reducing bacteria in oxic and anoxic regions of a microbial mat characterized by comparative analysis of dissimilatory sulfite reductase genes. *Appl. Environ. Microbiol.* 65, 4666–4671.

Minz, D., Fishbain, S., Green, S. J., Muyzer, G., Cohen, Y., Rittmann, B. E., et al. (1999b). Unexpected population distribution in a microbial mat community: sulfate-reducing bacteria localized to the highly oxic chemocline in contrast to a eukaryotic preference for anoxia. *Appl. Environ. Microbiol.* 65, 4659–4665.

Monard, C., Gantner, S., Bertilsson, S., Hallin, S., and Stenlid, J. (2016). Habitat generalists and specialists in microbial communities across a terrestrial-freshwater gradient. *Sci. Rep.* 6:37719. doi: 10.1038/srep37719

Montoya, J. M., Pimm, S. L., and Solé, R. V. (2006). Ecological networks and their fragility. *Nature* 442, 259–264. doi: 10.1038/nature04927

Morris, B. E. L., Henneberger, R., Huber, H., and Moissl-Eichinger, C. (2013). Microbial syntrophy: interaction for the common good. *FEMS Microbiol. Rev.* 37, 384–406. doi: 10.1111/1574-6976.12019

Morris, J. J., Lenski, R. E., and Zinser, E. R. (2012). The black queen hypothesis?: evolution of dependencies through adaptative gene loss. *mBio* 3:e0036-12. doi: 10.1128/mBio.00036-12.Copyright

Nelson, W. C., and Stegen, J. C. (2015). The reduced genomes of Parcubacteria (OD1) contain signatures of a symbiotic lifestyle. *Front. Microbiol.* 6:713. doi: 10.3389/fmicb.2015.00713

Newman, M. E. J. (2006). Modularity and community structure in networks. *Proc. Natl. Acad. Sci. U.S.A.* 103, 8577–8582. doi: 10.1073/pnas.0601602103

Newman, M. E. J., and Girvan, M. (2003). Finding and evaluating community structure in networks. *Phys. Rev. E Stat. Nonlin. Soft Matter Phys.* 69(2 Pt 2):026113. doi: 10.1103/physreve.69.026113

Newton, R. J., Jones, S. E., Eiler, A., McMahon, K. D., and Bertilsson, S. (2011). A guide to the natural history of freshwater lake bacteria. *Microbiol. Mol. Biol. Rev.* 75, 14–49. doi: 10.1128/MMBR.00028-10

Oren, A. (1988). Anaerobic degradation of organic compounds at high salt concentrations. *Antonie Van Leeuwenhoek* 54, 267–277. doi: 10.1007/BF00443585

Oren, A. (2008). Microbial life at high salt concentrations: phylogenetic and metabolic diversity. *Saline Syst.* 4, 1–13. doi: 10.1186/1746-1448-4-2

Pajares, S., Escalante, A. E., Noguez, A. M., García-Oliva, F., Martínez-Piedragil, C., Cram, S. S., et al. (2016). Spatial heterogeneity of physicochemical properties explains differences in microbial composition in arid soils from Cuatro Cienegas, Mexico. *PeerJ* 4:e2459. doi: 10.7717/peerj.2459

Pajares, S., Souza, V., and Eguiarte, L. E. (2015). Multivariate and phylogenetic analyses assessing the response of bacterial mat communities from an ancient oligotrophic aquatic ecosystem to different scenarios of long-term environmental disturbance. *PLoS One* 10:e0119741. doi: 10.1371/journal.pone.0119741

Parks, D. H., Tyson, G. W., Hugenholtz, P., and Beiko, R. G. (2014). STAMP: statistical analysis of taxonomic and functional profiles. *Bioinformatics* 30, 3123–3124. doi: 10.1093/bioinformatics/btu494

Peimbert, M., Alcaraz, L. D., Bonilla-Rosso, G., Olmedo-Alvarez, G., García-Oliva, F., Segovia, L., et al. (2012). Comparative metagenomics of two microbial mats at Cuatro Ciénegas Basin I: ancient lessons on how to cope with an environment under severe nutrient stress. *Astrobiology* 12, 648–658. doi: 10.1089/ast.2011.0694

Peura, S., Bertilsson, S., Jones, R. I., and Eiler, A. (2015). Resistant microbial cooccurrence patterns inferred by network topology. *Appl. Environ. Microbiol.* 81, 2090–2097. doi: 10.1128/AEM.03660-14

Poisot, T. (2013). An a posteriori measure of network modularity. *F1000Res.* 2:130. doi: 10.12688/f1000research.2-130.v1

Ponce-Soto, G. Y., Aguirre-von-Wobeser, E., Eguiarte, L. E., Elser, J. J., Lee, Z. M.-P., and Souza, V. (2015). Enrichment experiment changes microbial

interactions in an ultra-oligotrophic environment. *Front. Microbiol.* 6:246. doi: 10.3389/fmicb.2015.00246

Pontarp, M., Canbäck, B., Tunlid, A., and Lundberg, P. (2012). Phylogenetic analysis suggests that habitat filtering is structuring marine bacterial communities across the globe. *Microb. Ecol.* 64, 8–17. doi: 10.1007/s00248-011-0005-7

Preisner, E. C., Fichot, E. B., and Norman, R. S. (2016). Microbial mat compositional and functional sensitivity to environmental disturbance. *Front. Microbiol.* 7:1632. doi: 10.3389/fmicb.2016.01632

Prill, R. J., Iglesias, P. A., and Levchenko, A. (2005). Dynamic properties of network motifs contribute to biological network organization. *PLoS Biol.* 3:e030343. doi: 10.1371/journal.pbio.0030343

Proulx, S. R., Promislow, D. E. L., and Phillips, P. C. (2005). Network thinking in ecology and evolution. *Trends Ecol. Evol.* 20, 345–353. doi: 10.1016/j.tree.2005.04.004

Purdy, K. J. (2005). Nucleic acid recovery from complex environmental samples. *Methods Enzymol.* 397, 271–292. doi: 10.1016/S0076-6879(05)97016-X

R Development Core Team (2011). *A Language and Environment for Statistical Computing*. Vienna: R Development Core Team.

Rivett, D. W., and Bell, T. (2018). Abundance determines the functional role of bacterial phylotypes in complex communities. *Nat. Microbiol.* 3, 767–772. doi: 10.1038/s41564-018-0180-0

Ruvindy, R., White, R. A., Neilan, B. A., and Burns, B. P. (2016). Unravelling core microbial metabolisms in the hypersaline microbial mats of Shark Bay using high-throughput metagenomics. *ISME J.* 10, 183–196. doi: 10.1038/ismej.2015.87

Shaw, G. T.-W., Liu, A.-C., Weng, C.-Y., Chou, C.-Y., and Wang, D. (2017). Inferring microbial interactions in thermophilic and mesophilic anaerobic digestion of HOG waste. *PLoS One* 12:e0181395. doi: 10.1371/journal.pone.0181395

Shaw, G. T.-W., Pao, Y.-Y., and Wang, D. (2016). MetaMIS: a metagenomic microbial interaction simulator based on microbial community profiles. *BMC Bioinformatics* 17:488. doi: 10.1186/s12859-016-1359-0

Shen-Orr, S. S., Milo, R., Mangan, S., and Alon, U. (2002). Network motifs in the transcriptional regulation network of *Escherichia coli*. *Nat. Genet.* 31, 64–68. doi: 10.1038/ng881

Sorokin, D. Y., Kuenen, J. G., and Muyzer, G. (2011). The microbial sulfur cycle at extremely haloalkaline conditions of soda lakes. *Front. Microbiol.* 2:44. doi: 10.3389/fmicb.2011.00044

Sorokin, D. Y., Tourova, T. P., Lysenko, A. M., and Muyzer, G. (2006). Diversity of culturable halophilic sulfur-oxidizing bacteria in hypersaline habitats. *Microbiology* 152, 3013–3023. doi: 10.1099/mic.0.29106-0

Souza, V., Eguiarte, L. E., Travisano, M., Elser, J. J., Rooks, C., and Siefert, J. L. (2012). Travel, sex, and food: what's speciation got to do with it? *Astrobiology* 12, 634–640. doi: 10.1089/ast.2011.0768

Souza, V., Falcón, L. I., Elser, J. J., and Eguiarte, L. E. (2007). *Protecting a Window into the Ancient Earth: Towards a Precambrian Park at Cuatro Cienegas, Mexico*. Available at: http://www.evolutionary-ecology.com/citizen/citizen.html

Souza, V., Moreno-Letelier, A., Travisano, M., Alcaraz, L. D., Olmedo, G., and Eguiarte L. E. (2018). The lost world of Cuatro Cienegas Basin, a relictual bacterial niche in a desert oasis. *eLife* 7:e38278. doi: 10.7554/eLife.38278

Steele, J. A., Countway, P. D., Xia, L., Vigil, P. D., Beman, J. M., Kim, D. Y., et al. (2011). Marine bacterial, archaeal and protistan association networks reveal ecological linkages. *ISME J.* 5, 1414–1425. doi: 10.1038/ismej.2011.24

Stouffer, D. B., Camacho, J., Jiang, W., and Nunes Amaral, L. A. (2007). Evidence for the existence of a robust pattern of prey selection in food webs. *Proc. R. Soc. B Biol. Sci.* 274, 1931–1940. doi: 10.1098/rspb.2007.0571

Sun, M. Y., Dafforn, K. A., Johnston, E. L., and Brown, M. V. (2013). Core sediment bacteria drive community response to anthropogenic contamination over multiple environmental gradients. *Environ. Microbiol.* 15, 2517–2531. doi: 10.1111/1462-2920.12133

Taboada, B., Isa, P., Gutiérrez-Escolano, A. L., del Ángel, R. M., Ludert, J. E., Vázquez, N., et al. (2018). The geographic structure of viruses in the Cuatro Ciénegas Basin, a unique oasis in northern Mexico, reveals a highly diverse population on a small geographic scale. *Appl. Environ. Microbiol.* 84:e00465-18. doi: 10.1128/AEM.00465-18

Tang, K., Liu, K., Jiao, N., Zhang, Y., and Chen, C.-T. A. (2013). Functional metagenomic investigations of microbial communities in a shallow-sea hydrothermal system. *PLoS One* 8:e72958. doi: 10.1371/journal.pone.0072958

Thébault, E., and Fontaine, C. (2010). Stability of ecological communities and the architecture of mutualistic and trophic networks. *Science* 329, 853–856. doi: 10.1126/science.1188321

Tran, N. H., Choi, K. P., and Zhang, L. (2013). Counting motifs in the human interactome. *Nat. Commun.* 4:2241. doi: 10.1038/ncomms3241

van Gemerden, H. (1993). Microbial mats: a joint venture. *Mar. Geol.* 113, 3–25. doi: 10.1016/0025-3227(93)90146-M

Vannini, C., Petroni, G., Schena, A., Verni, F., and Rosati, G. (2003). Well-established mutualistic associations between ciliates and prokaryotes might be more widespread and diversified than so far supposed. *Eur. J. Protistol.* 39, 481–485. doi: 10.1078/0932-4739-00024

Varin, T., Lovejoy, C., Jungblut, A. D., Vincent, W. F., and Corbeil, J. (2012). Metagenomic analysis of stress genes in microbial mat communities from Antarctica and the High Arctic. *Appl. Environ. Microbiol.* 78, 549–559. doi: 10.1128/AEM.06354-11

Warden, J. G., Casaburi, G., Omelon, C. R., Bennett, P. C., Breecker, D. O., Foster, J. S., et al. (2016). Characterization of microbial mat microbiomes in the modern thrombolite ecosystem of lake clifton, western Australia using shotgun metagenomics. *Front. Microbiol.* 7:1064. doi: 10.3389/fmicb.2016.01064

Weng, F. C. H., Shaw, G. T. W., Weng, C. Y., Yang, Y. J., and Wang, D. (2017). Inferring microbial interactions in the gut of the Hong Kong whipping frog (*Polypedates megacephalus*) and a validation using probiotics. *Front. Microbiol.* 8:525. doi: 10.3389/fmicb.2017.00525

White, R. A., Chan, A. M., Gavelis, G. S., Leander, B. S., Brady, A. L., Slater, G. F., et al. (2016). Metagenomic analysis suggests modern freshwater microbialites harbor a distinct core microbial community. *Front. Microbiol.* 6:1531. doi: 10.3389/fmicb.2015.01531

White, R. A., Power, I. M., Dipple, G. M., Southam, G., and Suttle, C. A. (2015). Metagenomic analysis reveals that modern microbialites and polar microbial mats have similar taxonomic and functional potential. *Front. Microbiol.* 6:966. doi: 10.3389/fmicb.2015.00966

Wilbanks, E. G., Jaekel, U., Salman, V., Humphrey, P. T., Eisen, J. A., Facciotti, M. T., et al. (2014). Microscale sulfur cycling in the phototrophic pink berry consortia of the Sippewissett Salt Marsh. *Environ. Microbiol.* 16, 3398–3415. doi: 10.1111/1462-2920.12388

Wolaver, B. D., Crossey, L. J., Karlstrom, K. E., Banner, J. L., Cardenas, M. B., Ojeda, C. G., et al. (2012). Identifying origins of and pathways for spring waters in a semiarid basin using He, Sr, and C isotopes: Cuatro Cienegas Basin, Mexico. *Geosphere* 9, 113–125. doi: 10.1130/GES00849.1

Wong, H. L., Visscher, P. T., White, R. A., Smith, D. L., Patterson, M. M., and Burns, B. P. (2017). Dynamics of archaea at fine spatial scales in Shark Bay mat microbiomes. *Sci. Rep.* 7:46160. doi: 10.1038/srep46160

Zelezniak, A., Andrejev, S., Ponomarova, O., Mende, D. R., Bork, P., and Patil, K. R. (2015). Metabolic dependencies drive species co-occurrence in diverse microbial communities. *Proc. Natl. Acad. Sci. U.S.A* 112, 6449–6454. doi: 10.1073/pnas.1421834112

Zhou, J., Deng, Y., Luo, F., He, Z., Tu, Q., and Zhi, X. (2010). Functional molecular ecological networks. *mBio* 1:e00169-10. doi: 10.1128/mBio.00169-10

Zomorrodi, A. R., and Segrè, D. (2017). Genome-driven evolutionary game theory helps understand the rise of metabolic interdependencies in microbial communities. *Nat. Commun.* 8:1563. doi: 10.1038/s41467-017-01407-5

Conflict of Interest Statement: The authors declare that the research was conducted in the absence of any commercial or financial relationships that could be construed as a potential conflict of interest.

frontiers in Microbiology

ORIGINAL RESEARCH
published: 08 January 2019
doi: 10.3389/fmicb.2018.03189

The Complete Genome and Physiological Analysis of the Eurythermal Firmicute *Exiguobacterium chiriqhucha* Strain RW2 Isolated From a Freshwater Microbialite, Widely Adaptable to Broad Thermal, pH, and Salinity Ranges

Richard Allen White III[1†], Sarah A. Soles[2‡], Greg Gavelis[3‡], Emma Gosselin[4], Greg F. Slater[2], Darlene S. S. Lim[5,6], Brian Leander[3] and Curtis A. Suttle[1,4,7,8]*

[1] Department of Microbiology and Immunology, University of British Columbia, Vancouver, BC, Canada, [2] School of Geography and Earth Sciences, McMaster University, Hamilton, ON, Canada, [3] Department of Zoology, University of British Columbia, Vancouver, BC, Canada, [4] Department of Earth, Ocean and Atmospheric Sciences, University of British Columbia, Vancouver, BC, Canada, [5] Bay Area Environmental Institute, Petaluma, CA, United States, [6] NASA Ames Research Center, Moffett Field, CA, United States, [7] Department of Botany, University of British Columbia, Vancouver, BC, Canada, [8] Institute for the Oceans and Fisheries, University of British Columbia, Vancouver, BC, Canada

Members of the genus *Exiguobacterium* are found in diverse environments from marine, freshwaters, permafrost to hot springs. *Exiguobacterium* can grow in a wide range of temperature, pH, salinity, and heavy-metal concentrations. We characterized *Exiguobacterium chiriqhucha* strain RW2 isolated from a permanently cold freshwater microbialite in Pavilion Lake, British Columbia using metabolic assays, genomics, comparative genomics, phylogenetics, and fatty acid composition. Strain RW2 has the most extensive growth range for temperature (4–50°C) and pH (5–11) of known *Exiguobacterium* isolates. Strain RW2 genome predicts pathways for wide differential thermal, cold and osmotic stress using cold and heat shock cascades (e.g., *csp* and *dnaK*), choline and betaine uptake/biosynthesis (e.g., *opu* and *proU*), antiporters (e.g., *arcD* and *nhaC* Na^+/K^+), membrane fatty acid unsaturation and saturation. Here, we provide the first complete genome from *Exiguobacterium chiriqhucha* strain RW2, which was isolated from a freshwater microbialite. Its genome consists of a single 3,019,018 bp circular chromosome encoding over 3,000 predicted proteins, with a GC% content of 52.1%, and no plasmids. In addition to growing at a wide range of temperatures and salinities, our findings indicate that RW2 is resistant to sulfisoxazole and has the genomic potential for detoxification of heavy metals (via mercuric reductases, arsenic resistance pumps, chromate transporters, and cadmium-cobalt-zinc resistance genes), which may contribute to the metabolic potential of Pavilion Lake microbialites. Strain RW2 could also contribute to microbialite formation, as it is a robust biofilm former and encodes genes involved in the deamination of amino

OPEN ACCESS

Edited by:
Pieter T. Visscher, University of Connecticut, United States

Reviewed by:
Fabiano Thompson, Instituto Alberto Luiz Coimbra de Pós-Graduação e Pesquisa de Engenharia (COPPE), Brazil
Jennifer Mobberley, University of California, Santa Barbara, United States

***Correspondence:**
Richard Allen White III
raw937@gmail.com

†Present address:
Richard Allen White III, RAW Molecular Systems, Spokane, WA, United States; Crop and Soil Sciences, Washington State University, Pullman, WA, United States; Plant Pathology, Washington State University, Pullman, WA, United States; Australian Centre for Astrobiology, University of New South Wales, Sydney, NSW, Australia

‡*These authors have contributed equally to this work*

Specialty section:
This article was submitted to Aquatic Microbiology, a section of the journal Frontiers in Microbiology

Received: *08 January 2018*
Accepted: *10 December 2018*
Published: *08 January 2019*

Citation:
White RA III, Soles SA, Gavelis G, Gosselin E, Slater GF, Lim DSS, Leander B and Suttle CA (2019) The Complete Genome and Physiological Analysis of the Eurythermal Firmicute Exiguobacterium chiriqhucha Strain RW2 Isolated From a Freshwater Microbialite, Widely Adaptable to Broad Thermal, pH, and Salinity Ranges. Front. Microbiol. 9:3189. doi: 10.3389/fmicb.2018.03189

acids to ammonia (i.e., L-asparaginase/urease), which could potentially boost carbonate precipitation by lowering the local pH and increasing alkalinity. We also used comparative genomic analysis to predict the pathway for orange pigmentation that is conserved across the entire *Exiguobacterium* genus, specifically, a C_{30} carotenoid biosynthesis pathway is predicted to yield diaponeurosporene-4-oic acid as its final product. Carotenoids have been found to protect against ultraviolet radiation by quenching reactive oxygen, releasing excessive light energy, radical scavenging, and sunscreening. Together these results provide further insight into the potential of *Exiguobacterium* to exploit a wide range of environmental conditions, its potential roles in ecosystems (e.g., microbialites/microbial mats), and a blueprint model for diverse metabolic processes.

Keywords: exiguobacterium, microbialite, cosmopolitan, heavy metals, metabolic potential

INTRODUCTION

Microbialite fossils (i.e., the ancient stromatolites) represent the oldest evidence for life on the Earth (Nutman et al., 2016). Microbialites consist of a specialized microbial mat that lithifies carbonates into two main structural types, (1) thrombolites; composed of unlaminated clots, or (2) stromatolites; defined by laminated layers (Burne and Moore, 1987; Perry et al., 2007). Microbialites represent natural analogs for the early microbial ecosystems, which allow for testing hypotheses around the basic principles of microbial ecology including questions regarding community composition (Wong et al., 2015, 2017), community assembly (Havemann and Foster, 2008), functional traits and diversity (Breitbart et al., 2009; White et al., 2015, 2016; Ruvindy et al., 2016; Wong et al., 2018) and discovery of novel taxa (Burns et al., 2012; White et al., 2018b).

Our model microbialite ecosystem is Pavilion Lake a cold, oligotrophic ecosystem in southeastern British Columbia, Canada with dimictic circumneutral waters (median pH 8.3; mean calcium carbonate, 182 mg L^{-1}), (White et al., 2016). Characterization of the limnology of Pavilion Lake is described in detail Lim et al. (2009). Resident microbialites are calcium carbonate-based thrombolites whose morphological features vary with depth (White et al., 2016), though all have thin (∼5 mm) microbial mats dominated by cyanobacteria.

While both heterotrophs and photoautotrophs (i.e., cyanobacteria) have been described and isolated from a range of microbial mats including microbialites, little work has been done on pigmented heterotrophic bacteria within microbialites. *Firmicutes* have been identified in the pigmented layers in microbial mats (Bottos et al., 2008; Lionard et al., 2012), and it is thought that carotenoids are responsible for their characteristic coloration (Nübel et al., 1999; Mueller et al., 2005; Klassen, 2010; Fisher et al., 2019). Fundamental questions about heterotrophic non-phototrophic arise which include (1) what the function of pigments in these microbialite associated heterotrophic bacteria is? and (2) what is the role of pigmented heterotrophs in ecosystem functioning within microbialites? To address these questions, we enriched and isolated >100 pigmented bacteria from Pavilion Lake freshwater microbialites, and grew them in the dark to select for heterotrophic or mixotrophic strains.

Among these pigmented heterotrophic enrichments included *Exiguobacterium* "strain RW2," a Gram-positive member of the *Firmicutes*. Strain RW2 was isolated and enriched from a thrombolite at 20 m depth, where the water temperature remains around 4–10°C throughout the year (Lim et al., 2009) (**Figures 1A,B**). Bacteria at this depth should be adapted to cold temperature, low phosphorus, and alkaline conditions. Recently, we have described another heterotrophic pigmented isolate *Agrococcus pavilionensis* strain RW1 (White et al., 2013b, 2018a), that was co-isolated with strain RW2 from the same microbialite and enrichment.

Members of this genus have a cosmopolitan distribution due to their highly adaptable physiology. Isolates of *Exiguobacterium* represent two major clades, clade I, which is comprised of cold-adapted strains including *E. sibiricum* 255-15^T (Rodrigues et al., 2008), and clade II, whose members range from temperate (e.g., *E. aurantiacum* DSM6208^T) to hot environments (e.g., *E.* sp. AT1b) (Vishnivetskaya et al., 2009; Gutiérrez-Preciado et al., 2017), and include strain RW2. Due to the global distribution of *Exiguobacterium*, microbialites and/microbial mats appear to be another environment where they can adapt and colonize. Two *Exiguobacterium* strains have been directly isolated from microbialites: the present strain RW2 (formally *pavilionensis*) isolated from cold freshwater thrombolites (White et al., 2013a; Gutiérrez-Preciado et al., 2017), and strain S17, which was isolated from a warm (i.e., ∼20–24°C) freshwater stromatolite in Lake Socompa (Ordoñez et al., 2013, 2015). Based on average nucleotide identity (ANI), RW2 appears to be the same species as two other strains; strain N139 and GIC31 (formally *pavilionensis*, Gutiérrez-Preciado et al., 2017), and it represents the type strain. Strain N139 was isolated from the water column of Leguna Negra which contains microbialites/microbial mats with extreme temperature variation ranging from −5 to 42°C (Gomez-Javier et al., 2018; Mlewski et al., 2018). Remarkably, the third strain—GIC31 was isolated from glacial ice (Vishnivetskaya et al., 2009), potentially from a biofilm growing on top of the ice, but this is unknown. Another question arises (3) are strains RW2, N139, and GIC31 the same species? We use comparative genomics to determine the species placement of these three strains (i.e., RW2, N139, GIC31).

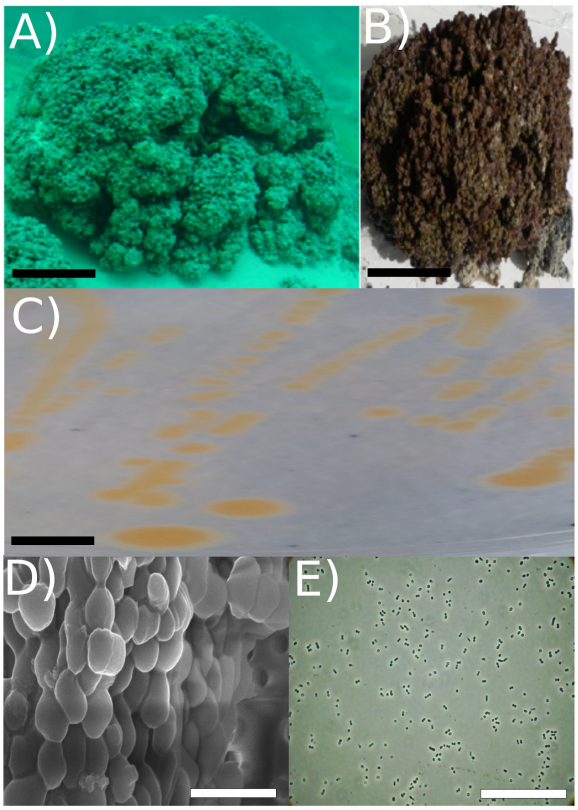

FIGURE 1 | Strain RW2 isolation environment, culture plate illustration, and microscopy. **(A)** Picture of Pavilion Lake microbialite (i.e., thrombolite) taken underwater (20 m depth sample, scale bar: ∼1 m). **(B)** Pavilion Lake microbialite (i.e., thrombolite) taken at sample station (20 m depth sample, scale bar: ∼15 cm). **(C)** Culture plate (∼24 h growth, the black scale bar ∼10 mm). **(D)** Light microscopy (∼24 h growth, scale bar: ∼80 μm); **(E)** SEM (∼72 h growth, scale bar: ∼5 μm). All microscopy (i.e., SEM/light) and culture plate photo **(C–E)** were completed at strain RW2 standard growth parameters on solidified M-agar at 30°C, pH 7 and concentration 1% (w/v) NaCl. Panels **(A,B)** adapted from White et al. (2018a).

At the time of this writing, the genus *Exiguobacterium* has sixteen named species (**Table 1**), which were isolated from diverse environments including permafrost (Rodrigues et al., 2006), deep-sea vents (Crapart et al., 2007) and hot springs (Vishnivetskaya et al., 2009, 2011). These widespread bacteria can tolerate of a wide range of pH (5–11), salinity (NaCl: 0–16%) and temperature (−12°C to 55°C) (White et al., 2013a) (**Table 1**). The first described member of the genus, *E. aurantiacum* DSM6208^T, was isolated from a potato processing plant (Collins et al., 1983). Consequently, isolates of *Exiguobacterium* spp. have been used as model organisms for understanding thermal adaptation to cold (i.e., −5°C) (Rodrigues et al., 2008; Vishnivetskaya et al., 2009), hot temperatures (i.e., 55°C) and heavy metal stress (Ordoñez et al., 2013, 2015). Currently, 60 genomes of *Exiguobacterium* are listed on NCBI, 17 of which are complete (**Supplementary Table S1**). However, no complete genomes are available from microbialites, from which only a draft-genome is available (White et al., 2013a).

Here, we present the first such complete genome of *Exiguobacterium* isolated from modern microbialites. We also characterize strain RW2 using standard bacteriological and physiological testing, comparative genomics, and phylogenetics (i.e., 16S rRNA gene phylogeny) to describe its placement in the genus, and its broad adaptation to ranges of salinity, pH, and temperature. Lastly, from a genomic standpoint, we assess the potential of strain RW2 to contribute important metabolic functions to the microbialite community in Pavilion Lake.

MATERIALS AND METHODS

Isolation, Growth Conditions, Biochemical and Antibiotic Susceptibility Tests

Strain RW2 was isolated by plating 0.5 g of homogenized thrombolytic microbialite, collected from 20 m depth in Pavilion Lake, British Columbia (50.86°N, 121.74°W), onto M-agar medium [0.5% (w/v) tryptone, 0.25% (w/v) yeast extract, 1% (w/v) NaCl, 1.5% (w/v) agar, pH 7], followed by incubation at 30°C for 3 days in the dark (White et al., 2013a) (**Figure 1C**). M-agar plates (1% NaCl, pH 7, 1.5% agar w/v) were also used for culture maintenance (at 30°C) and for assessing growth under the following conditions. Growth effects of temperature were measured at 4, 5, 11, 16, 18, 20, 25, 30, 37, 42, 45, and 50–55°C. At temperatures greater than 45°C, we used thicker M-agar plates at 4% (w/v) agar, to avoid dehydrating the plates. Growth effects of pH were measured at 4, 5, 6, 6.5, 7, 7.5, 8, 10, 10.5, 11, and 12 pH. Lastly, growth effects of salt were measured with 0, 1, 3, 6, 9, 12, 13, 16% added NaCl. Note that these percentages reflect that of added NaCl and not salinity, as tryptone and yeast extracts contain preexisting salts. Each condition was imposed for 72 h on triplicate plates. Standard colony forming unit (CFU) evaluation was used in that growth occurred only when >100 CFUs occurred on plates. All grow evaluations on plates were confirmed in liquid culture followed by optical density measurement.

We also assessed photoautotrophic and photoheterotrophic growth on MM9 minimal medium [20% glucose, 0.5% (w/v) tryptone, 0.25% (w/v) yeast extract], and on RCV medium (Beatty and Gest, 1981) in liquid medium and agar plates (1.5% agar w/v) grown both anaerobically, microaerophilically and aerobically with and without ambient sunlight on 8 h light and 16 dark cycle. No photoautotrophy or photoheterotrophy was observed.

Strain characteristics, including colony and cell morphologies, were determined by standard methods (Murray et al., 1994). Oxidase tests and biochemical enzyme assays and carbohydrate use were conducted in triplicate using API20E (BioMérieux) test strips following manufacturers instructions. Single isolated colonies from M-agar plates were washed via pelleting at 3,250 × *g* for 10 min three times in sterile distilled water then inoculated to API20E (BioMérieux) test strips, which includes a motility assay. Antibiotic susceptibility was determined by the Kirby-Bauer method using antibiotic disks on M-agar plates in triplicate (Collee et al., 1996).

TABLE 1 | Names and isolation location of *Exiguobacterium* species.

Species Name	Environment of Isolation	Reference	Isolation Notes
ICSP recognized species			
E. acetylicum	Creamery waste	Farrow et al., 1994	Levine and Soppeland, 1926 classified "*Flavobacterium acetylicum*" renamed "*Brevibacterium acetylicum*" then reclassified by Farrow et al. (1994)
E. antarcticum	Microbial mat/biofilm	Fruhling et al., 2002; Carneiro et al., 2012	Lake Fryxell mat in Antarctica
E. aestuarii	Marine tidal flat	Kim et al., 2005	Daepo beach in yellow sea near Mokpo City, Korea,
E. alkaliphilum	Wastewater drained sludge	Kulshreshtha et al., 2013	Beverage industry facility New Delhi, India
E. aquaticum	Freshwater lake	Raichand et al., 2012	Tikkar Tal Lake, Haryana, India
E. aurantiacum	Potato processing plant	Collins et al., 1983	**Type species for the genus**
E. himgiriensis	Soil	Singh et al., 2013	Lahaul-Spiti valley, Indian Himalayas
E. indicum	Glacial melt water	Chaturvedi and Shivaji, 2006	Hamta glacier (4270 m above sea level), Himalayans
E. martemiae	Brine shrimp cysts	Lopez-Cortes et al., 2006	*Artemia franciscana* cysts
E. mexicanum	Brine shrimp cysts	Lopez-Cortes et al., 2006	*Artemia franciscana* cysts
E. oxidotolerans	Fish processing plant	Yumoto et al., 2004	Hokkaido, Japan
E. profundum	Hydrothermal Vent	Crapart et al., 2007	Northeast Pacific rise at ∼2600 m
E. sibiricum	Permafrost	Rodrigues et al., 2006	Siberian permafrost (3 Mya old)
E. soli	Glacial moraine	Chaturvedi et al., 2008	McMurdo dry valleys, Antarctica
E. undae	Garden pond water	Fruhling et al., 2002	Wolfenbüttel, Lower Saxon Germany
Published strains discussed			
Strain RW2	Thrombolithic microbialite	White et al., 2013a	Pavilion lake 20 m microbialites
Strain S17	Stromatolithic microbialite	Ordoñez et al., 2013	Polyextremophile strain tolerate heavy metals (As)
Strain AT1b	Alkaline hot spring	Vishnivetskaya et al., 2011	Mammoth Terrace hot spring YNP, Wyoming, United States
Strain N139	Hypersaline lagoon	Gutiérrez-Preciado et al., 2017	Polyextremophile strain tolerate heavy metals (As)
Strain GIC31	Glacier ice	Vishnivetskaya et al., 2011, 2014	Greenland ice shelf

Official species names are recognized by the International Committee on Systematics of Prokaryotes (ICSP) and have been published in the International Journal of Systematic and Evolutionary Microbiology or another journal recognized by the ICSP. Isolates published in NCBI as genome announcements or other that are unnamed, not classically described, or not recognized by the ICSP are listed as Exiguobacterium sp.

Triplicate experiments in liquid culture were used to induce biofilm formation and measure timing (M-broth 30°C at pH 7 and 1% NaCl w/v) at low shaking (100 rpms) and without shaking. A positive biofilm in strain RW2 was a top film appeared over medium within the flask.

Phospholipid Fatty Acid Analysis (PLFA)

Phospholipid fatty acids (PLFAs) were extracted from cultures grown in triplicate M-agar plates for 72 h at multiple conditions for temperatures (4, 18, 30, 50°C at pH 7 and 1% NaCl, 1.5% agar w/v, 4% agar w/v at 50°C), pH (5, 7, 11 at 30°C at 1% NaCl w/v in 1.5% agar w/v) and added NaCl (5, 7, 11 at 30°C at 1% NaCl w/v in 1.5% agar w/v). All PLFA results were confirmed in liquid medium. Cultures were transferred into pre-combusted vials for an overnight solvent extraction in a 1:2:0.8 ratio of dichloromethane (DMC), methanol (MeOH) and phosphate-buffered saline (PBS) [137 mM NaCl, 2.7 mM KCL, 10 mM Na_2HPO_4 $2H_2O$, 2 mM KH_2PO_4, pH 7.4] (Bligh and Dyer, 1959). The extract was filtered through a separatory funnel where DMC and water were added to achieve a mixture of MeOH:DMC:water of 1:1:0.9 (Bligh and Dyer, 1959). The lower organic phase was removed and purified into polar, neutral, and non-polar fractions using liquid chromatography through silica gel. Phospholipids present in the polar fraction were subjected to mild alkaline methanolysis to produce fatty acid methyl esters (FAMEs) (Guckert et al., 1985). FAMEs were separated, identified, and quantified using gas chromatography-mass spectrometry (GC/MS) (Agilent Technologies Inc., Santa Clara, CA, United States) with a DB-5MS capillary column (30 m × 0.32 mm I.D. × 0.25 μm film thickness) under a temperature regime of 50°C (1 min), 20°C min^{-1} to 130°C, 4°C min^{-1} to 160°C, and 8°C min^{-1} to 300°C (5 min). PLFAs were identified by retention time and mass spectra relative to those of reference standards (Bacterial Acid Methyl Ester Mix, Matreya Inc., Pleasant Gap, PA, United States; and Supelco 37 Component FAME Mix, Sigma-Aldrich Co., Bellefonte, PA, United States). A modified picolinyl ester derivatization was used to determine the branching point in unknown compounds (Dowd, 1998; Destaillats and Angers, 2002). Dimethyl disulfide derivatives were prepared to determine the double bond position in unsaturated fatty acids (Nichols et al., 1986).

Light and Scanning Electron Microscopy (SEM)

Exponentially growing cells were harvested at 26 h after being transferred to liquid M-medium and were viewed by light microscopy under oil immersion at 100×. Flagella straining was completed as per Kodaka et al. (1982) then viewed by light microscopy after 26 h of growth. For SEM, a culture in stationary phase ∼72 h after being transferred to liquid M-medium was

pelleted at 3,250 × *g* for 10 min, then the M medium was exchanged and cells were fixed in 2.5% glutaraldehyde in PBS (137 mM NaCl, 2.7 mM KCL, 10 mM Na_2HPO_4 $2H_2O$, 2 mM KH_2PO_4, pH 7.4) solution for 30 min on ice. The fixed culture was filtered onto a 0.2 μm pore-size Supor polycarbonate membrane (Pall Port Washington, NY, United States). Cells on the filter were washed with PBS and post-fixed in 1% OsO_4 for 1 h. The cells and filter were passed through a graded ethanol series (25, 50, 70, 95, 100%) at 10 min intervals, and in 100% ethanol were critical-point dried with CO_2. A sputter coater applied 5 nm of gold/palladium alloy onto the cells before imaging by SEM using a Hitachi S4700 microscope.

Phylogenetic Analysis of 16S rRNA Gene Sequences

Thirty-two reference sequences were downloaded from NCBI representing all named typed (^{T}) strains of genus *Exiguobacterium*, with three typed strains of *Bacillus* spp. as outgroups. The whole-genome assembled 16S rRNA gene sequence was used for phylogenetic analysis. Alignments of 16S rRNA gene sequences were completed in MAFFT (v. 7.310) using the options (–localpair –maxinterate 1000) which is iterative refinement method incorporating local pairwise alignment information (L-INS-i) providing the most accurate alignment (Katoh et al., 2002). A maximum likelihood phylogenetic tree was constructed using IQ-TREE (v. 1.6.1) (Hoang et al., 2017) with a total of 1,000 bootstrap replicates using UFBoot2 (Trifinopoulos et al., 2016), and visualized with SeaView (v. 4) (Gouy et al., 2010). Strain RW2 16S rRNA gene sequence and alignments are available on github.com/strain_RW2.

Whole Genome Assembly and Annotation

DNA extraction, Illumina library preparation and sequencing, data cleaning, phiX spike-in removal, and draft genome assembly are described by White et al. (2013a). The genome was closed into a single circular contig (i.e., chromosome) without plasmids using comparative genome ordering, alignment, mapping, and manual editing. For comparison, scaffolding and contig ordering of the genome of strain AT1b was compared to strain RW2 which was downloaded from NCBI. Strain RW2 contigs were ordered and aligned in progressiveMauve to strain AT1b to visualize genome order (Darling et al., 2010; Vishnivetskaya et al., 2011). The remaining gaps between contigs were closed by recursive alignments using Mauve. The ordered contigs with overlaps were merged into a single circular contig using the EMBOSS union script (Rice et al., 2000). To estimate sequencing depth represented in the assembly for coverage estimation, reads used in the assembly were mapped back to the final circular genome using Bowtie2 with the very sensitive local option (Langmead and Salzberg, 2012). The Bowtie2 read mapping output file (Sam file) was visually inspected by the Tablet program (Milne et al., 2013). The contigs that were screened for overlaps and read mapping depth (>10×) were then merged manually, based on the reference genome of AT1b.

Annotation was conducted on the RAST annotation server using the Glimmer-3 option and standard RAST against the FIGfam database release-70 (Aziz et al., 2008). Metabolic pathways were predicted in strain RW2 using MetaPathways which uses pathway tools (Paley and Karp, 2006; Konwar et al., 2013; Caspi et al., 2014), against MetaCyc/BioCyc databases via a built-in LAST (Local Alignment Search Tool) (Kiełbasa et al., 2011) for homology matches of ≥180 bp ORFs (protein-coding open reading frames) and ≥50 alignment score. A metabolic model for strain RW2 was predicted using ModelSEED (Devoid et al., 2013). The Prokaryotic Genome Annotation Pipeline (PGAP) at NCBI was also used to compare to RAST annotation for strain RW2 (Tatusova et al., 2016). We manually curated the annotations produced by RAST and NCBI (PGAP)—retaining only annotations that were a consensus between both programs.

Comparative Genomic Analysis

All genomes available for *Exiguobacterium* were uploaded to RAST, for synteny, AAI via RAST annotations, and metabolic model comparisons in modelSEED. Metapathways was also used to predict pathways across the genomes using BioCyc/MetaCyc. To display genomic features a circular genome plot of strain RW2 was constructed using Cgviewer server[1] (Grant and Stothard, 2008, version V 1.0, date accessed Jan 1st, 2018). Genomes of strains RW2, S17, GIC31, and N139 were compared in CGViewer using tBLASTx (e-value of $1e^{-5}$, with 70% identity cutoff, and minimum 50 bp overlap) and then displayed in the CGviewer genome plot server (Grant and Stothard, 2008). Synteny plots were completed in the RAST server module using a BLAST-based dot plot format. Average amino-acid identity (AAI) and Reciprocal Orthology Score Average (ROSA) via functional gene similarities from RAST server annotations were calculated using with a web-based tool[2] (Krebs et al., 2013, date accessed January 1st, 2018).

For species classification, average nucleotide identity (ANI), AAI (non-RAST based), and digital DNA–DNA hybridization were used to compare strains (i.e., RW2, N139, and GIC31). ANI/AAI was completed using web server from Kostas lab[3] with default parameters based on the enveomics software package collections (Rodriguez-R and Konstantinidis, 2016, date accessed August 1st, 2018). Digital DNA–DNA hybridization for species determination was completed using GGDC (v. 2.1) web server (Meier-Kolthoff et al., 2013, 2014, date accessed August 1st, 2018).

Metagenomic Read Recruitment

The presence of strain RW2 within Pavilion Lake sediments, microbialites, and water column was previously described in a metagenomic study by White et al. (2016). We compared our genomic data to their published metagenomic data, by loading their predicted protein dataset onto MG-RAST (Meyer et al., 2008), and using RefSeq (protein level) annotations (using BLAT parameters, with matches of ≥60% similarity cutoff, ≥15 bp

[1]http://stothard.afns.ualberta.ca/cgview_server/

[2]http://lycofs01.lycoming.edu/~newman/AAI/html

[3]http://enve-omics.ce.gatech.edu/

overlap, and minimum E-value of 10^{-5}) to search for signatures of strain RW2 in their Pavilion Lake metagenomes. Reads assigned to *Exiguobacterium* from the metagenome were mapped to the strain RW2 using Bowtie2 with the very sensitive local option (Langmead and Salzberg, 2012). These results were subject to ANOVA statistical testing using the Statistical Analysis of Metagenomic Profiles package (STAMP) (Parks and Beiko, 2010). The program FR-hit was then used to assign metagenomic read recruitment of the 7.5 million Metagenomic sequences (250 bp paired-end MiSeq reads) to *Exiguobacterium* genomes from strain RW2, S17, and AT1b, using default parameters with a minimum identity > 70% and an E-value > $1e^{-5}$ (Niu et al., 2011). The recruitments were then visualized with the R library ggplot2 (Wickham, 2016).

Data Availability

Strain RW2 is listed at NCBI under bioproject accession PRJNA208114 and biosample accession SAMN02471612. The Ray assembly for the draft genome is listed under DDBJ/EMBL/GenBank under the accession number ATCL00000000, and RefSeq under NZ_ATCL00000000.1, as well as NCBI under GCA_000416965.1. Lastly, the complete genome, scripts, and supplementary data are posted on github.com/raw937/Strain_RW2/.

RESULTS

Classification of RW2 Related Strains Using Phylogenetics and Whole-Genome Analysis

Using 16S rRNA gene-based phylogeny, whole-genome ANI/AAI and digital DNA–DNA hybridization we will determine whether RW2, GIC31, and N139 are the same species. Currently, strains GIC31 and N139 are missing data required for classical bacteriological species determination via the IJSEM which include experimental fatty acid analysis, quinone characterization, peptidoglycan structure analysis, and DNA–DNA hybridization assays. However, a recent proposal from IJSEM suggests that genome-based ANI/AAI and 16S rRNA gene-based phylogeny can replace the experimental DNA–DNA hybridization and be used for naming/typing strains in the future (Chun et al., 2018).

We generated a maximum-likelihood phylogeny of 16S rRNA gene sequences from all fourteen typed strains of *Exiguobacterium* spp., fifteen sequences representing strains with complete genomes, and three typed strains of *Bacillus* spp. as outgroups. This positioned strain RW2 in clade II, along with *E.* sp. AT1b and *E. aurantiacum* DSM6208^T (**Figure 2**). *E. aurantiacum* DSM6208^T represents the first isolate of *Exiguobacterium,* from potato effluent (which contains soil) (Collins et al., 1983). Within clade II are two subclades; clade IIa and clade IIb, together containing isolates from a wide range of environments (**Figure 2**). Clade IIa stem from hot springs and both shallow and deep-sea marine ecosystems, whereas isolates of clade IIb stem terrestrial habitats including soil, microbialites (including strain RW2), and freshwater ecosystems (**Figure 2**). Clade IIb is well-supported, suggesting that it represents a true radiation into terrestrial habitats including lakes (i.e., strains N139, SH31, S17, RW2), glacial ice (i.e., strain GIC31), microbialites (i.e., strains S17, RW2), canals (i.e., strain HUD), and even the microbiomes of brine shrimp, which dwell in hypersaline vernal pools (i.e., strain DSM16483^T) and canals (i.e., strain HUD) (**Figure 2**). However, the subclade that contains strains RW2, N139, GIC31, and HUD is not well resolved (**Figure 2**). Strain HUD is currently classified by NCBI as a strain of *E. mexicanum*, but this is challenged by our 16S rRNA gene

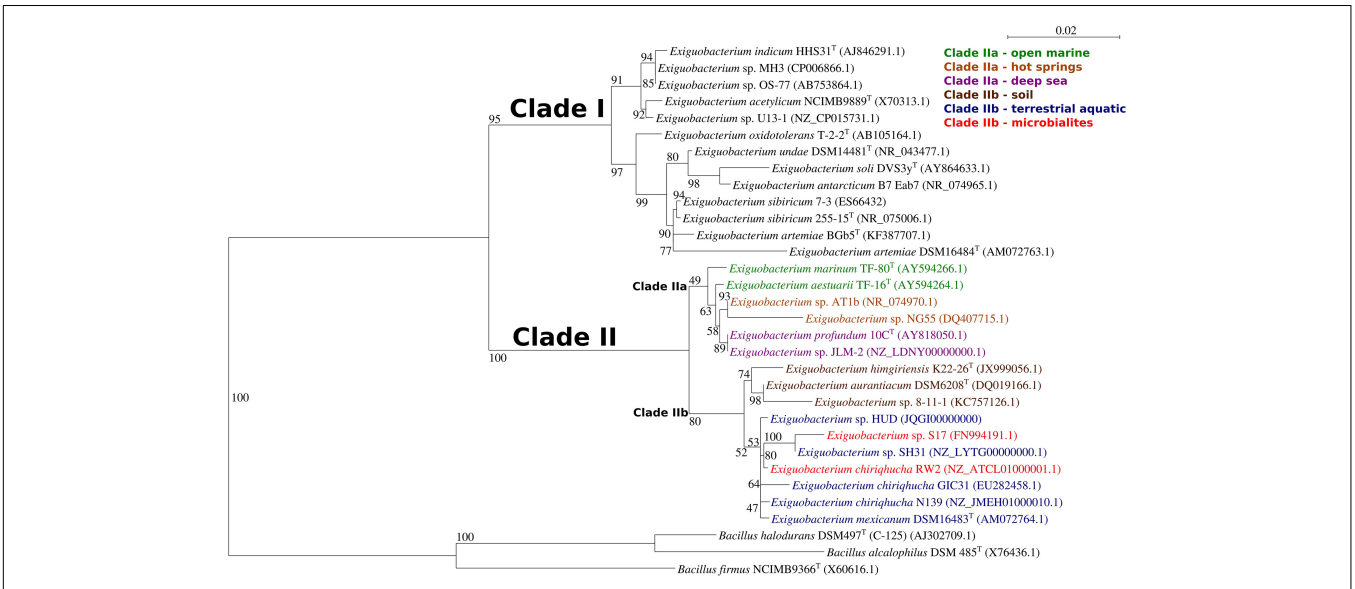

FIGURE 2 | Maximum-Likelihood tree based on 16S sequences showing the phylogenetic relationship among different isolates of the genus *Exiguobacterium.* Bootstrap values greater than 50% are given at nodes based on 1000 replications. Bar represents a nucleotide substitution rate per 1000 nucleotides. The named, typed strains are labeled (^{T}), other strains are published as in NCBI or as genome announcements.

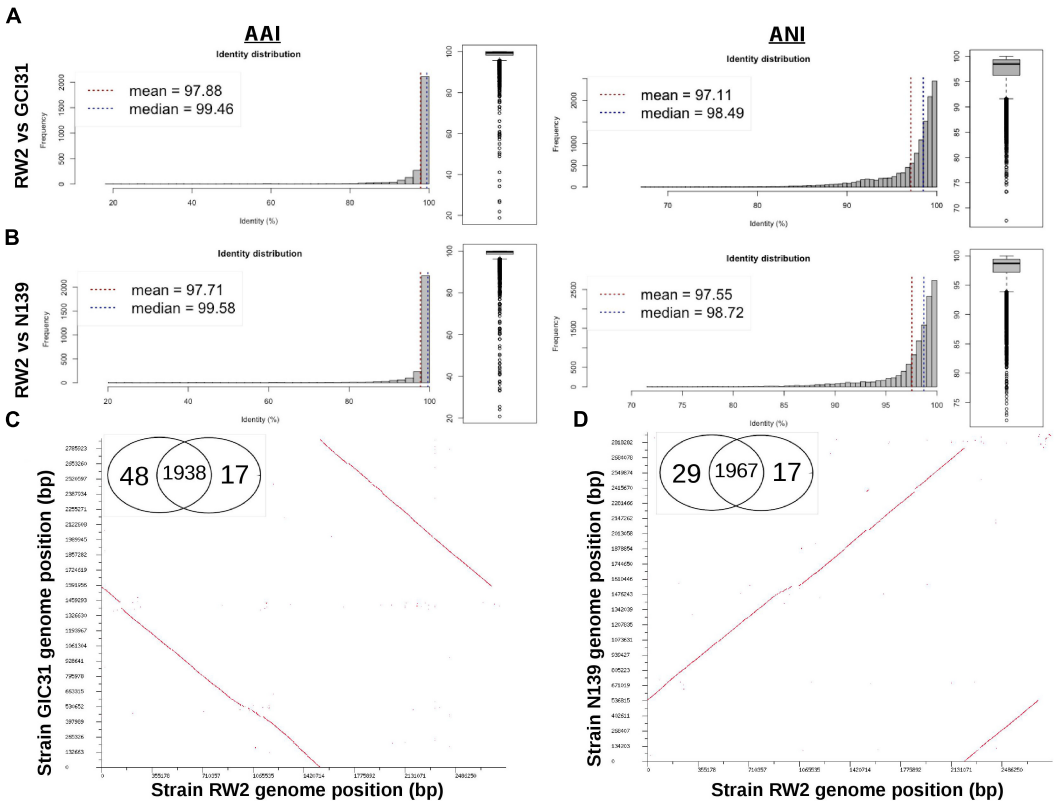

FIGURE 3 | Whole genome comparison of strain RW2, N139, and GIC31 for average amino acid identity (AAI), average nucleotide identity (ANI), genome synteny and Venn diagrams of RAST SEED functions. **(A)** Strain RW2 vs. GIC31 for AAI/ANI using enveomics. **(B)** Strain RW2 vs. N139 for AAI/ANI using enveomics. **(C)** Strain RW2 vs. GIC31 - BLAST dot-plots for genome synteny and Venn diagram. **(D)** Strain RW2 vs. N139 - BLAST dot-plots for genome synteny and Venn diagram. Genomes are listed in megabase pairs (Mb). Red dots are positive blast hits based on the RAST genome comparison module. Venn diagrams are listed by strain name based on RAST functional annotations (SEED/FigFams).

phylogeny, given that it does not branch with the type strain of *E. mexicanum* (strain DSM16483) (**Figure 2**). The genome of the type strain of *E. mexicanum* DSM16483^T is currently not available to compare to strain HUD or other strains related to strain RW2. There is high bootstrap support for a clade containing strain RW2 (as the basal member) along with strains SH31 and S17. By contrast, strains HUD, GIC31, and N139 branch earlier than this clade, where the tree topology is poorly resolved (i.e., the branches are polytomic) (**Figure 2**). The 16S rRNA gene of RW2 is 99% similar to GIC31 and N139 based on BLASTN, whereas N139 is 100% similar to GIC31. More representative 16S rRNA gene sequences are needed to resolve the polytomy within clade IIb (**Figure 2**).

Based on 16S rRNA gene sequence alone it is unclear whether strains RW2, GIC31, and N139 belong to the same species. Whole-genome analysis is needed to resolve this issue. Strain RW2, N139, and GIC31 have >97% similarity both on the nucleotide (ANI) and protein (AAI) level (**Figures 3A,B**). Based on standards established in *E. coli*, >95% similarity between the 16S rRNA gene sequence of two isolates is used as a cutoff for conspecificity (Rodriguez-R and Konstantinidis, 2016). Furthermore, our genomic analysis suggests that gene content and synteny are highly conserved across RW2, GIC31, and N139 (**Figures 3C,D**). Based on RAST functional assignment, all three strains have >1900 shared functions (97% shared) with <50 functions (3% distinct) that are unique to each strain (**Figures 3C,D**). Likewise inter-strain tBLASTx used in the CGViewer estimated >97% homology for GIC31 vs. RW2, >97% N139 vs. RW2 and 87% for S17 vs. RW2 (**Figure 4**). Lastly, Digital DNA–DNA hybridization (dDDH) estimated that RW2, GIC31, and N139 are the same species with >80% probability based on logistic regression, with >70% being the cut-off for species determination (**Table 2**). Both N139 and GIC31 contain plasmids, though we found no evidence of plasmids in strain RW2 (**Table 2**). The tBLASTx found (>97%) homology for GIC31 vs. RW2, N139 vs. RW2 and 87% for S17 vs. RW2 (**Figure 4**).

Morphology, Growth, and Characteristics of Strain RW2

Strain RW2 is a Gram-positive aerobe that is facultatively anaerobic. It subsists heterotrophically with no evidence of photoheterotrophy. After 48 h of growth at 30°C on M-agar, it forms bright orange, smooth, circular colonies that are typically 3 to 4 mm in diameter (**Figure 1C** and **Table 3**). In liquid M-medium at 30°C, the cells were coccoid after 24–48 h in

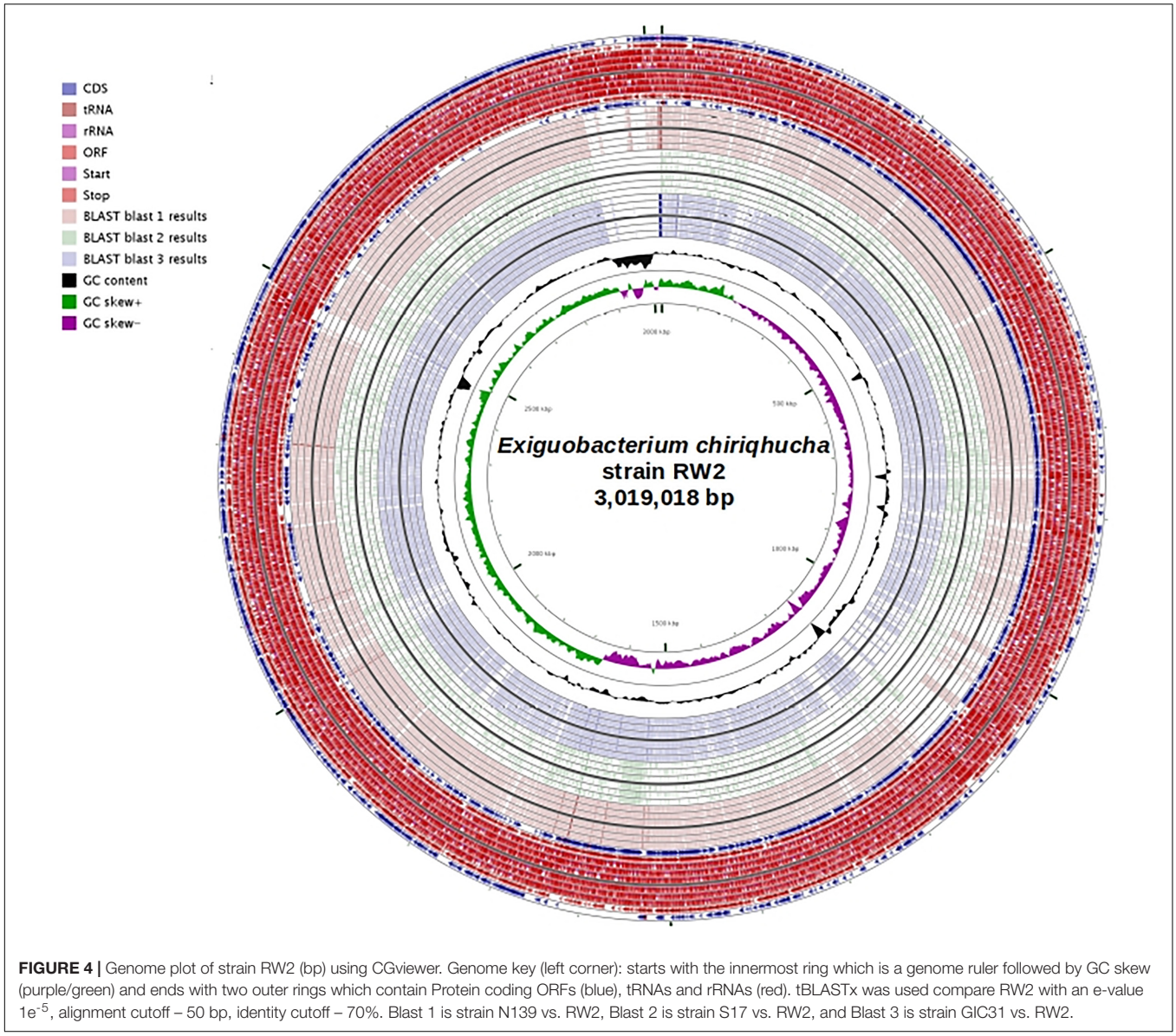

FIGURE 4 | Genome plot of strain RW2 (bp) using CGviewer. Genome key (left corner): starts with the innermost ring which is a genome ruler followed by GC skew (purple/green) and ends with two outer rings which contain Protein coding ORFs (blue), tRNAs and rRNAs (red). tBLASTx was used compare RW2 with an e-value $1e^{-5}$, alignment cutoff – 50 bp, identity cutoff – 70%. Blast 1 is strain N139 vs. RW2, Blast 2 is strain S17 vs. RW2, and Blast 3 is strain GIC31 vs. RW2.

logarithmic growth and irregularly shaped after 72 h in stationary phase, coincident with the beginning of biofilm formation under shaking (100 rpm) (**Figures 1D,E**). Biofilms first appeared within ∼72 h, and their growth culminated at 8 days for 30°C under shaking (100 rpm).

No flagella were observed in the electron microscopy (SEM) or under standard light microscopy (**Figures 1D,E**). Strain RW2 had a positive motility assay provided by API20E kit. The genome annotation of strain RW2 predicts a complete flagellum biosynthesis pathway (including the *fih, fli, fig* gene operons). Flagella staining and motility testing was positive, meaning that strain RW2 is motile with peritrichous flagella.

Strain RW2 grows at a wide range of temperatures, added salinity, and pHs. Ranging from 4 to 50°C, strain RW2 grows at the broadest range of temperatures currently reported for any isolate of *Exiguobacterium* genus) (**Table 3**) though we were not able to test its growth at subzero temperatures. Likewise, strain RW2 exhibits the broadest range of pH tolerance reported within the genus, from a pH of 5 to pH 11 (**Table 3**). We attempted to grow strain RW2 on minimal medium to test the absolute requirement of NaCl required for growth, but we were unsuccessful. We tested overall NaCl tolerance for growth by directly adding NaCl from 0 to 16% (w/vol) to M-agar/broth. Strain RW2 only grew at 0 and 7% (**Table 3**). Nevertheless, strain RW2 has a higher salt tolerance than other non-marine isolates, which do not grow above 7% added NaCl (**Table 3**). Interestingly, strain RW2 grows beyond the range of the temperature, pH, and salinity expected at 20 m depth in Pavilion Lake microbialites, where temperatures range from 4 to 10°C, and pH is very stable at 8.1–9.1 (Lim et al., 2009). This degree of abiotic tolerance makes RW2 unique among isolates of the genus.

TABLE 2 | Digital DNA–DNA hybridization (dDDH) using GGDC 2.1 for strain RW2, GIC31, N139.

	Value	Range	Notes
Strain RW2 vs. N139			
DDH (identities/HSP length – formula 2)			
Distance:	0.0256		
DDH estimate (GLM-based):	78.10%	75.2–80.8%	
Probability that DDH > 70% (i.e., same species):	89.02%		(via logistic regression)
Probability that DDH > 79% (i.e., same subspecies):	44.21%		(via logistic regression)
Strain RW2 vs. GIC31			
DDH (identities / HSP length – formula 2)			
Distance:	0.0302		
DDH estimate (GLM-based):	74.50%	71.4–77.3%	
Probability that DDH > 70% (i.e., same species):	85.09%		(via logistic regression)
Probability that DDH > 79% (i.e., same subspecies):	37.15%		(via logistic regression)

Cut-offs for same species with >80% probability based on logistic regression with >70% for species determination.

TABLE 3 | Morphology and growth properties under differential temperature, pH, and salinity.

	RW2	DVS3Y	DSM14480	DSM17290	DSM14481	DSM15368	JCM12280	DSM20416
Habitat of isolation	**Microbialite**	**Marine**	**Microbial mat**	**Permafrost**	**Garden Pond**	**Glacial Water**	**Fish processing**	**Creamery**
Colony size (mm)	2–4	2–3	2–3	2–3	2–4	2–4	1–5	2–5
Colony shape	Round	Round	Round	Round	Round	Round	Round	Irregular
Colony color	Orange	Orange	Orange	Orange	Orange	Yellow-orange	Orange	Yellow-orange
Growth temp (°C)								
−2.5	NA	+	+	+	+	w	w	−
4	+	+	+	+	+	+	+	−
37	+	+	+	+	+	−	+	w
40	+	−	+	+	+	−	+	−
45	+	−	−	−	−	−	−	−
50	+	−	−	−	−	−	−	−
Max pH for growth	50	30	41	40	41	30	40	37
4	−	−	−	−	−	−	−	−
5	+	−	−	−	−	−	−	−
11	+	−	−	−	−	−	−	−
Max NaCl (%) for growth								
5.80%	+	+	+	+	+	+	+	+
7.00%	+	−	−	−	−	−	−	−

All growth temperature measurements for strain RW2 were taken after 2 days, except at 4°C which took 10 days to grow. Non-strain RW2 data are from Chaturvedi et al. (2008). no growth (−), strong growth (+), weak growth (W), data not available (NA). DVS3Y – E. soli DVS3Y, DSM14480 – E. antarcticum DSM14480, DSM17290 – E. sibiricum DSM17290, DSM14481 – E. undae DSM14481, DSM15368 – E. indicum DSM15368, JCM12280 – E. oxidotolerans JCM12280, DSM20416 – E. acetylicum DSM20416. All isolates are further described in publications listed in ***Table 1****. DSM17290 – E. sibiricum DSM17290 also known as strain DSM 17290/JCM 13490/255-15 is described in* ***Table 1****.*

Genome Properties and Comparative Genome Analysis

The initial draft genome of strain RW2 was not complete and fragmented on 23 contigs (White et al., 2013a) (**Table 4**). With progressiveMauve, mapping, and manual finishing, we closed the strain RW2 genome into a single circular chromosome. This chromosome is 3,019,504 bp in length, with a GC content 52.05%, and no plasmids (**Table 4**). This is similar to the genome assembly of strain GIC31, which is likewise a single circular contig, with high coverage that suggests no evidence of plasmids (**Table 4**).

The draft and completed genomes of *Exiguobacterium* spp. were similar regarding genome size, GC content, and the number of protein-coding genes. Within the genus, genome sizes range from 2.82 to 3.16 Mb, with GC content ranging from 47.5 to 53%, containing from 2,941 to 3,323 genes that encode 2,772 to 3,332 predicted proteins (**Table 4**). Strain RW2 had lower numbers of rRNAs, tRNAs, and had 17 pseudogenes predicted (**Table 4**). Both S17 and 8-11-1 have lower synteny, possibly as a result of the fact that these are less complete genome assemblies (>25 contigs) (**Table 4** and **Supplementary Figure S1**). Among members of clade IIa, strain RW2 had the highest genome synteny to strain AT1b (**Supplementary Figure S1**). MetaCyc/BioCyc pathway predictions using Metapathways suggest that >90% of the pathways are shared even among genomes with <65% AAI (**Supplementary Figure S2**). Strain RW2 has the high AAI identity to strain S17 (87.76%, **Supplementary Figure S2**). It also

TABLE 4 | *Exiguobacterium* genome assembly and annotation statistics.

	***RW2**	**RW2**	**GIC31**	**N139**	**S17**	**OS-77**	**8-11-1**	**AT1b**	**MH3**	**B7**	**255-15**
Sequencing Method	Illumina MiSeq	Illumina MiSeq	PacBio	454 GS FLX	454 GS FLX	454 GS FLX	Illumina HiSeq	454Sanger	Illumina HiSeq	SOLiD	454Sanger
Assembler	–	Ray	HGAP	NewblerMIRA	Newbler	Newbler	Velvet	PhredPhrap	SOAPdenovo	VelvetEdena	PhredPhrap
Assembly Name	–	r23K55	–	ExiN39	ExiS17_1.0	ASM41419v1	V1	ASM2304v1	ASM49663v1	ASM29943v1	ASM1990v1
Genome coverage	–	300x	–	85x	63x	45x	300x	20x	140x	> 400x	–
No. Contigs	1	23	2	23	163	23	31	1	1	1	3
Scaffolds	–	–	2	23	–	5	–	–	–	–	–
Genome Size (bp)	3019504	3019504	2974642	2952486	3127363	3151479	2906962	2999895	3164195	2815863	3040786
N50	3019504	705844	2918587	1553709	34407	349882	340222	–	–	–	–
Largest Contig (bp)	3019504	947149	2918587	1553709	122784	929170	663994	–	–	–	–
G+C%	52.1	52.1	52.1		53.1	47.1	52.8	49	47.2	47.5	47.7
Annotation Method	NCBI	NCBI	NCBI	NCBI	NCBI	RAST	RAST	NCBI	NCBI	NCBI	NCBI
Gene No.	3148	3137	3072	3108	3268	–	–	3141	3332	2941	3155
Protein coding	3092	3079	2929	2965	3218	3265	2926	3020	3203	2772	3015
Pseudogenes	0	0	44	38	–	–	–	23	41	76	–
rRNAs	10	10	28	34	2	2	2	9	9	9	9
tRNAs	46	48	67	67	48	49	14	68	60	66	69
Plasmids	0	0	1	3	–	–	–	0	0	0	2

*–, not available; Members are listed by strain name: *Draft genome published White et al. (2013a); #complete genome presented here; RW2, GIC31, N139 – E. chiriqhucha strains; RW2, GIC31, N139 renamed in Gutiérrez-Preciado et al., 2017; S17 – E. sp strain S17 from Ordoñez et al. (2013); B7 – E. antarcticum strain B7 from Fruhling et al. (2002); OS-77 – E. sp strain OS-77 from Nonaka et al. (2014); 8-11-1 – E. sp strain 8-11-1 from Jiang et al. (2013); AT1b – E. sp strain AT1b from Vishnivetskaya et al. (2011); MH3 – E. sp strain MH3 from Tang et al. (2013); B7 – E. antarcticum strain B7 from Carneiro et al. (2012); 255-15 – E. sibiricum strain 255-15 from Rodrigues et al. (2008).*

shared over 50% of RAST functions with more distant relatives in the phylum *Firmicutes* (e.g., *Planococcus halocryophilus* and *Bacillus halodurans*, (**Supplementary Figure S1**). The rarity of unique genes in strain RW2 suggests that it has a restricted accessory genome (i.e., pan-genome) while a large core genome is highly conserved across strains of *Exiguobacterium.*

Potential Genomic Signatures of Physiological Adaptability

Strain RW2 has physiological adaptability to a range of thermal, salinity and pHs which we further inquired the genomic basis for such growth parameters. Cold shock proteins encoded by *cspA* to *cspI* are molecular chaperones that help to regulate protein-folding under cold conditions and prevent cryodamage (Kawahara, 2008). Interestingly, strain RW2 and the other clade II members seem to lack *cspA* and *cspB* genes, while members of clade I have multiple copies of *cspA* and *cspB* (e.g., *E. sibiricum* strain 255-15 and *E. antarcticum* B7). We compared the strain RW2 genome to a distantly related member of the firmicutes known as *Planococcus halocryophilus* which can grow at −15°C (Mykytczuk et al., 2013). *Planococcus halocryophilus* has only one copy of *cspA*, unlike *E. sibiricum* strain 255-15 and *E. antarcticum* B7 which have multiple copies of *cspA*. This suggests growth below −5°C mechanisms are required.

By contrast, strain RW2 is surprisingly thermotolerant and grows at >45°C (White et al., 2013a) (**Table 3**). Strain RW2 genome contains a complete heat shock gene cluster (*dnaJ, dnaK*, and *GrpE*), which encodes for chaperones that prevent denaturation and aggregation of proteins at high temperatures (Feder and Hofmann, 1999).

In regards to osmoregulation, choline and betaine uptake/biosynthesis pathways are effective systems for regulating osmolyte concentrations, including that of NaCl. Uptake pathways include the genes *bet*, *opu,* and *proU*, which encode ABC transport proteins (Sleator and Hill, 2002). We again compared the strain RW2 genome to *P. halocryophilus* as the latter can tolerate 18% added NaCl (Mykytczuk et al., 2013). Strain RW2 has no *bet* genes, one copy of *opuA* (type AA, AB, AC only), no *opuC*, two copies of *opuD,* and one copy of *proU* (*proX* only); whereas *P. halocryophilus* has one copy of *betT*, has two copies of *opuA* (type AA, AB, AC), one copy *opuC*, five copies of *opuD,* multiple copies of *proU* (two copies *proV/X*, and one *proW*) based on RAST annotations.

In regards to pH regulation, strain RW2 genomic evidence of regulation includes antiporters—including the arginine-ornithine antiporter (a*rcD*)—can facilitate survival under acidic conditions (Fulde et al., 2014). Strain RW2 has four copies of the *arcD* antiporter—the same number found in *E. marinum* DSM16307^{T} and *E. acetylicum* DSM20416^{T}, which dwell in saline marine environments. By contrast, close relatives of strain RW2, such as strain AT1b and S17 have only two copies of *arcD*; while *P. halocryophilus* has zero copies based on RAST annotation. Strains of the alkaliphilic *Bacillus* genus commonly regulate high pH with the *nhaC* Na^{+}/K^{+} antiporter (Ito et al., 1997). Strain RW2 has three copies of *nhaC* gene, which is the same in AT1b (clade II) and *P. halocryophilus*, whereas *E. sibiricum* 255-15 (clade I) which only has two copies based on NCBI annotation. The *mrp* and *tet(L)* gene cluster antiporters which also regulate high pH (Padan et al., 2005), were not found in strain RW2 or other members of the genus.

Fatty Acid Composition Under Differential Growth Conditions

Under all growth conditions, the PLFA profiles of strain RW2 were mainly comprised of saturated branched PLFAs, predominantly anteiso-C13:0, Iso-C13:0, Iso-C15:0, Iso-C17:0, and anteiso-C17:0 (**Table 5**). The percentages of iso-C17:0 and anteiso-C17:0 at 23.9% and 8.1%, respectively, are the highest reported for these PLFAs for any strain of *Exiguobacterium* spp. (**Table 5**). In strain RW2, the fourth most abundant phospholipid is Iso-C17:1Δ^{5}, at 5.5% (**Table 5**). This phospholipid is not found in other *Exiguobacterium* isolates (**Table 5**) and is consistent with strain RW2 being assigned as a new species. Iso-C17:1Δ^{5} varied by as much as 12% in response to altered growth conditions (**Table 6** and **Figure 5**).

The PLFA profiles of strain RW2 were found to undergo measurable changes over the experimental growth temperature range (4–50°C). Notably, large shifts were observed in the unique branched monoenoic PLFAs, including iso-C16:1Δ 5, iso-C17: 1Δ5, brC17:1Δ 5, iso-C18:1Δ5, and brC19:1 (**Table 6** and **Figure 5**). The mol % of each of these PLFAs decreased by >93% between 4 and 50°C, and iso-C16:1Δ5, iso-C18:1Δ5, and brC19:1—through present at 4°C, were not detected at all at 50°C (**Table 6** and **Figure 5**). Of all fatty acids, iso-C17:1Δ5 underwent the largest shift, decreasing from 17.0 ± 0.5 mol % at 4°C to 1.1 ± 0.3 mol % at 50°C (**Table 6** and **Figure 5**).

Phospholipid fatty acid profile shifted across added NaCl and pH growth conditions (**Table 6** and **Figure 5**). Similar to the temperature profiles, the notable differences were found in i-iso-C16:1Δ 5, iso-C17: 1Δ5, brC17:1Δ5, and iso-C18:1Δ5 (**Table 6** and **Figure 5**). Under the acidic pH 5, iso-C17:1Δ5 was found to comprise 7.0 ± 0.9 mol % of the total PLFAs; this value increased to 15.5 ± 1.6 mol % by pH 11 (**Table 6**). This shift was the major influence on the degree of unsaturation, which increased between pH 7 and pH 11 but displayed little change between pH 5 and pH 7 (**Table 6**). The monoenoic PLFAs were also found to increase between pH 7 and pH 11, while there were no differences observed in these PLFAs between pH 5 and pH 7 (**Table 6**).

Salinity (via added NaCl) had limited effects on the composition of the PLFA profile. The total mol % of branched monoenoic PLFAs displayed a minor decrease between 0 NaCl and 1% NaCl but remained constant after that. These values decreased to 0.12 and 2.1, respectively, at 1% NaCl and remained similar at 7% NaCl (**Table 6** and **Figure 5**). C14:0 and C17:0 were only detected at 7% NaCl (**Table 6**). On the contrary, the mol % of all branched PLFAs was the lowest at 7% NaCl. The average fatty acid chain length displayed no large changes with altered salinity (**Table 6** and **Figure 5**).

The strain RW2 genome predicts the synthesis of many fatty acids, lipids, and isoprenoids. Lipids synthesis predicted by the genome include diverse phospholipids (e.g., unsaturated/saturated) and branched phospholipids, fatty acids, cardiolipin, polyhydroxybutyrates, and isoprenoids. Lipid catabolism predicted in the strain

TABLE 5 | Selected phospholipid fatty acids from strains of *Exiguobacterium.*

	StrainRW2	DSM14481[a]	DSM6208[a]	7–3[a]	K22-24[b]	DSM16307[b]
$iC_{13:0}$	8.9 ± 1.4	12	18	9	12.2	1
$aC_{13:0}$	21.1 ± 2.9	11	12	11	16.4	16.8
$iC_{15:0}$	10.3 ± 0.2	11	4	13	14.2	14.1
$aC_{15:0}$	4.0 ± 0.9	2	ND	3	5.8	2.2
$C_{16:1\Delta\ 5}$	1.6 ± 0.1	18	10	8	2.4	3.6
$iC_{16:0}$	3.9 ± 0.2	ND	ND	2	3.8	6.9
$brC_{16:1}$	1.6 ± 0.1	ND	ND	ND	ND	ND
$C_{16:0}$	3.4 ± 0.4	13	27	17	2.8	4.7
$iC_{17:1\Delta\ 5}$	5.5 ± 0.3	ND	ND	ND	ND	ND
$iC_{17:0}$	23.9 ± 2.3	5	6	9	16.1	16.8
$C_{17:0}$	0	ND	ND	ND	tr	tr
$aC_{17:0}$	8.1 ± 1.0	ND	ND	3	4.8	3.6
$C_{18:1\Delta\ 5}$	0.2 ± 0.3	ND	ND	ND	ND	ND
$C_{18:0}$	0.2 ± 0.3	5	5	4	tr	tr
$iC_{18:0}$	0.2 ± 0.4	ND	ND	ND	1.6	tr

Values are % of total which are averaged from triplicate measurement with standard deviation included. Non-strain RW2 data are from [a]Rodrigues et al. (2006) and [b]Singh et al. (2013). No phospholipid detected or no data available (NA). Traces of phospholipid (<1%) detected (tr). This for standard growth conditions for strain RW2 [M-agar, 30°C, 1% NaCl (w/v) and pH 7, on 1.5% (w/v) agar]. DSM14481 – E. antarcticum DSM14481, DSM6208 – E. aurantiacum DSM6208 7-3 – E. sibiricum 7-3, K22-24 – E. himgiriensis K22-24b, DSM16307 – E. marinum DSM16307. All strains are further listed in ***Table 1****.*

TABLE 6 | Mole percentage distributions of PLFAs for strain RW2 grown under varying temperature, pH, and salinity conditions.

Fatty acid	4°C	18°C	30°C*	50°C	pH 5	pH 7*	pH 11	0% NaCl*	1% NaCl*	7% NaCl
$iC_{12:0}$	4.4 ± 0.2	3.9 ± 0.7	3.6 ± 0.8	3.4 ± 0.7	2.8 ± 0.5	3.6 ± 0.8	1.8 ± 0.6	3.1 ± 0.3	3.6 ± 0.8	2.9 ± 0.3
$iC_{13:0}$	11.8 ± 0.3	8.2 ± 2.0	8.9 ± 1.4	8.8 ± 0.5	8.0 ± 1.8	8.9 ± 1.4	8.2 ± 1.9	6.3 ± 0.6	8.9 ± 1.4	8.1 ± 0.1
$aC_{13:0}$	15.0 ± 0.5	15.2 ± 3.7	21.1 ± 2.9	20.1 ± 1.4	17.6 ± 4.0	21.1 ± 2.9	16.8 ± 3.7	15.8 ± 1.8	21.1 ± 2.9	19.5 ± 0.5
$iC_{14:0}$	2.4 ± 0.1	2.1 ± 0.1	0.4 ± 0.7	0.8 ± 0.7	1.1 ± 0.1	0.4 ± 0.7	0.7 ± 0.1	1.8 ± 0.4	0.4 ± 0.7	1.8 ± 0.2
$C_{14:0}$	0	0	0	0	0	0	0	0	0	1.6 ± 0.3
$iC_{15:0}$	4.9 ± 0.1	6.2 ± 0.3	10.3 ± 0.2	12.3 ± 0.2	10.2 ± 0.1	10.3 ± 0.2	15.9 ± 0.4	9.9 ± 0.7	10.3 ± 0.2	12.7 ± 0.4
$aC_{15:0}$	3.2 ± 0.1	3.6 ± 0.1	4.0 ± 0.9	3.6 ± 0.5	2.9 ± 0.2	4.0 ± 0.9	3.1 ± 0.2	3.9 ± 0.4	4.0 ± 0.9	3.6 ± 0.2
$iC_{16:1\Delta\ 5}$	1.8 ± 0.1	2.3 ± 0.1	1.6 ± 0.1	0	1.5 ± 0.2	1.6 ± 0.1	3.0 ± 0.2	2.1 ± 0.0	1.6 ± 0.1	1.7 ± 0.1
$iC_{16:0}$	1.8 ± 0.1	2.6 ± 0.1	3.9 ± 0.2	5.4 ± 0.2	4.3 ± 0.4	3.9 ± 0.2	2.8 ± 0.2	3.9 ± 0.3	3.9 ± 0.2	3.3 ± 0.1
$C_{16:1\Delta\ 5}$	2.3 ± 0.1	3.7 ± 0.4	2.3 ± 0.4	0	1.8 ± 0.2	2.3 ± 0.4	3.6 ± 0.5	2.8 ± 0.1	2.3 ± 0.4	2.7 ± 0.2
$C_{16:0}$	2.9 ± 0.1	3.3 ± 0.3	3.4 ± 0.4	8.7 ± 0.6	3.4 ± 0.3	3.4 ± 0.4	2.4 ± 0.3	3.5 ± 0.2	3.4 ± 0.4	5.8 ± 0.2
$iC_{17:1\Delta\ 5}$	17.0 ± 0.5	13.7 ± 1.8	5.5 ± 0.3	1.1 ± 0.3	7.0 ± 0.9	5.5 ± 0.3	15.5 ± 1.6	7.9 ± 0.7	5.5 ± 0.3	4.7 ± 0.5
$brC_{16:1}$	2.2 ± 0.1	3.6 ± 0.5	2.1 ± 0.5	0	1.9 ± 0.1	2.1 ± 0.5	3.4 ± 0.5	2.7 ± 0.2	2.1 ± 0.5	1.8 ± 0.2
$iC_{17:0}$	12.0 ± 0.6	16.5 ± 1.5	23.9 ± 2.3	24.1 ± 1.5	26.1 ± 3.8	23.9 ± 2.3	15.5 ± 1.5	24.4 ± 1.3	23.9 ± 2.3	17.1 ± 1.0
$aC_{17:0}$	3.5 ± 0.1	5.7 ± 0.6	8.1 ± 1.0	9.3 ± 0.3	8.0 ± 1.2	8.1 ± 1.0	6.3 ± 0.7	8.5 ± 0.4	8.1 ± 1.0	7.6 ± 0.2
$C_{17:0}$	1.1 ± 0.1	0	0	0	0	0	0	0	0	1.0 ± 0.2
$iC_{18:1\Delta\ 5}$	2.0 ± 0.1	1.5 ± 0.1	0.2 ± 0.3	0	0.2 ± 0.4	0.2 ± 0.3	0.5 ± 0.1	0	0.2 ± 0.3	0.9 ± 0.2
$iC_{18:0}$	1.8 ± 0.1	1.4 ± 0.2	0.2 ± 0.4	1.1 ± 0.3	0.9 ± 0.1	0.2 ± 0.4	0.3 ± 0.0	1.0 ± 0.2	0.2 ± 0.4	1.0 ± 0.2
$C_{18:1\Delta\ 5}$	2.9 ± 0.1	2.7 ± 0.6	0.2 ± 0.3	0	0.7 ± 0.1	0.2 ± 0.3	0.6 ± 0.1	1.0 ± 0.2	0.2 ± 0.3	1.0 ± 0.1
$C_{18:0}$	2.0 ± 0.1	1.7 ± 0.2	0.2 ± 0.3	1.4 ± 0.4	0.9 ± 0.1	0.2 ± 0.3	0.3 ± 0.1	1.0 ± 0.2	0.2 ± 0.3	1.1 ± 0.1
$brC_{19:1}$	2.4 ± 0.1	0	0	0	0	0	0	0	0	0
$iC_{19:0}$	1.5 ± 0.1	1.0 ± 0.1	0.1 ± 0.2	0	0.3 ± 0.3	0.1 ± 0.2	0	0.2 ± 0.3	0.1 ± 0.2	0
$aC_{19:0}$	1.3 ± 0.1	1.0 ± 0.1	0.1 ± 0.2	0	0.3 ± 0.3	0.1 ± 0.2	0	0.2 ± 0.3	0.1 ± 0.2	0
Degree of unsaturation	0.31	0.28	0.12	0.01	0.13	0.12	0.27	0.17	3.6 ± 0.8	0.13
Ratio i-PLFA/a-PLFAs	3.3	2.9	2.1	2.1	2.5	2.1	2.9	2.6	2.1	2.1
Average chain length*	15.6	15.6	15.2	15.2	15.5	15.2	15.5	15.5	15.2	15.2

**Average chain length = [(mol % i-12:0/100)*12] + [(mol % i-13:0/100)*13] +. . . [(mol % a-19:0/100)*19]*

**This for standard growth conditions for strain RW2 [M-agar, 30°C, 1% NaCl (w/v) and pH 7, on 1.5% (w/v) agar] all in triplicate. These values are % of total which are averaged from triplicate measurement with standard deviation included.*

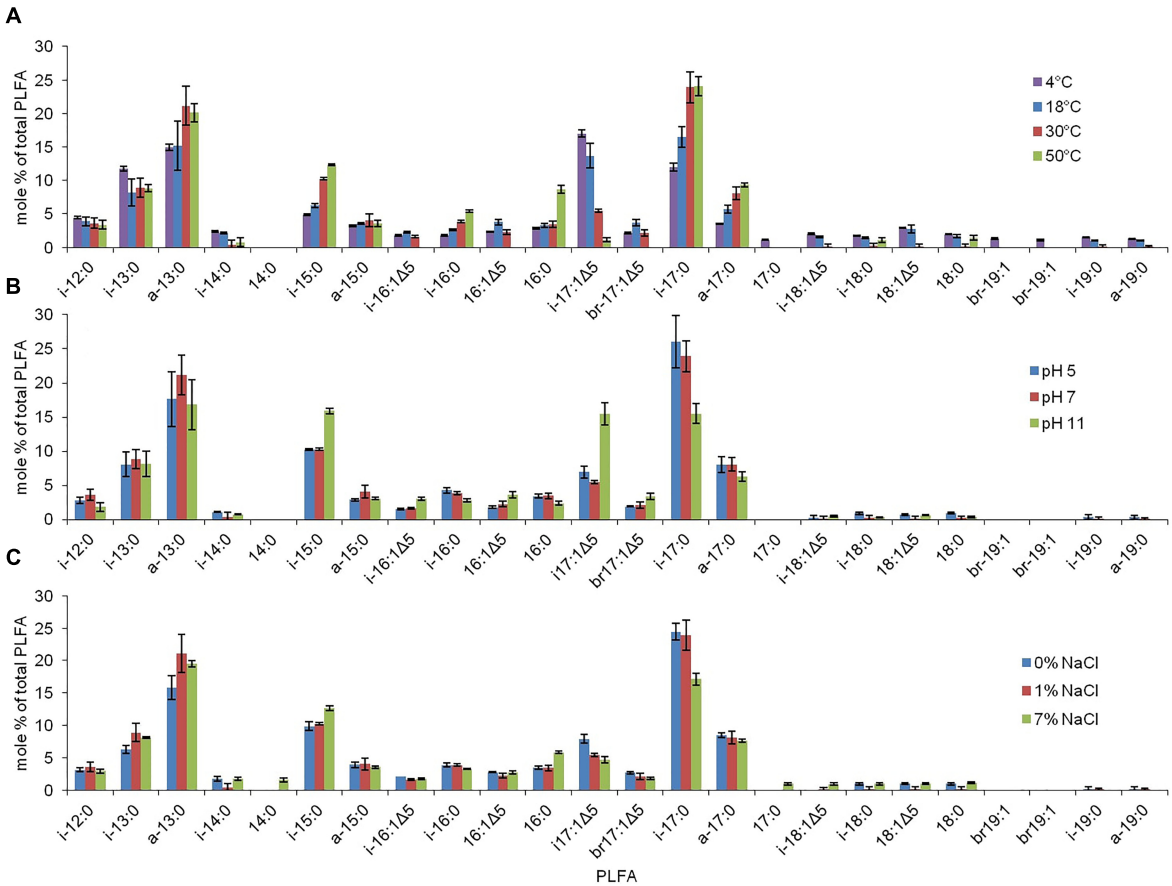

FIGURE 5 | The PLFA profiles associated with strain RW2 under varying growth conditions. **(A)** Temperature. **(B)** pH. **(C)** Salinity. Growth conditions for temperature were on M-agar plates, 1% NaCl, pH 7, 1.5% agar w/v (<45°C) and 4% agar w/v (>45°C). Growth conditions for pH were on M-agar plates, 1% NaCl, 30°C, 1.5% agar w/v. Growth conditions salinity (added NaCl w/v) were on M-agar plates, pH 7, 30°C, 1.5% agar w/v. These values are % of total which are averaged from triplicate measurement with standard deviation included.

RW2 include triacylglycerols, fatty-acids, isoprenoid, and polyhydroxybutyrate.

Resistance of Heavy Metals and Antibiotics Including Community Presence

After sequencing the metagenomes of Pavilion Lake (White et al., 2016), we questioned whether strain RW2 was part of the Pavilion Lake microbialite microbiome. With metagenomic recruitment analysis, we uncovered the presence of strain AT1b and unclassified *Exiguobacterium* spp., with the latter being significantly (p-value < 0.01) enriched within the microbialite, compared to the surrounding sediment and water column (**Supplementary Figure S3A**). We found no *Exiguobacterium* spp. reads present in the sediment metagenomes of Pavilion Lake (**Supplementary Figure S3A**).

This taxonomic resolution of MG-RAST was not sufficient to detect whether the hits were from strain RW2 or another *Exiguobacterium* spp. To calculate the presence and abundance of strain RW2, we recruited metagenomic reads (from the 20 m depth microbialite sample against genomic databases from strains RW2, AT1b, and S17. Strain RW2 recruited more reads (0.46% of reads) than S17 (0.33%) or AT1b (0.25%—with its genome achieving nearly complete coverage—as well as more reads with 100% identity hits (**Supplementary Figure S3B**). We further checked whether any of the 100–95% identity hits recruited from the metagenome were related to heavy metal resistance genes present in the genome of strain RW2, using tBLASTx ($1e^{-3}$). We found positive heavy metal gene recruitment to mercuric reductases, arsenic resistance pumps, multidrug and toxin efflux (MATE) resistance pumps, chromate transporters and cadmium-cobalt-zinc resistance genes.

By contrast, we could not determine which taxa were responsible for contributing antibiotic resistance genes to the Pavilion Lake microbialite metagenomes, other than *Proteobacteria* (White et al., 2016), which were affiliated with *gyrB* antibiotic resistance genes, known to encode multifunctional DNA repair proteins. Nevertheless, the assembled genome of strain RW2 encodes four copies of MATE resistant pumps, vancomycin B-type resistance proteins, tetracycline resistance MFS pumps, as well as four

antibiotic biosynthesis monooxygenases, which are involved in many diverse processes including the biosynthesis of antibiotics.

Little is known about antibiotic sensitivity and metabolism in *Exiguobacterium* spp. Other than *E. soli*, *E. indicum* and *E. acetylicum*, isolates of *Exiguobacterium* spp. are sensitive to clindamycin, as is strain RW2 (**Supplementary Table S2**). Additionally, strain RW2 was tested against eleven other antibiotics (**Supplementary Table S2**) and found only to possess resistance against sulfisoxazole (300 μg). The *sul* and *dhf* genes are found in organisms resistant to sulfisoxazole (Barman et al., 2010). This resistance may stem from the genomic presence of well-known sulfisoxazole resistance genes *sul* and *dhf* genes (encoding dihydropteroate synthase and dihydrofolate reductase), within the genomes of strain RW2, *E. indicum,* and *E. acetylicum*. While genes for vancomycin and tetracycline resistance were present in the genome of strain RW2, testing revealed the strain was sensitive to both antibiotics (**Supplementary Table S2**).

Carbohydrate, Amino Acid, and Nitrogen Metabolism

Biochemical tests indicated that strain RW2 uses a variety of monosaccharides, polysaccharides, and amino acids as carbon sources (**Table 7**). Pathways for lactose uptake were present, but only a *lacZ* (β-galactosidase) for lactose utilization appeared to be present (**Table 7**). Strain RW2 could not use D-mannitol, D-inositol, D-sorbitol, L-rhamnose, D-melibiose, and L-arabinose as sole carbon sources (**Table 7**). D-mannitol utilization was predicted by the genome, yet it was not assimilated as a sole carbon source, suggesting that only fermentation occurs (**Table 7**). Amygdalin was utilized by strain RW2 (**Table 7**), as is the case for several members of the genus. Although amygdalin metabolism was not specifically predicted in our RAST analysis of the genome, many general function beta-glucosidases were present in the genome, potentially lending this function. The genome of strain RW2 also appears to possess metabolic potential to perform various forms of fermentation including mixed acid, lactate, and acetyl-CoA fermentation to butyrate. Lastly, our analysis suggests diverse substrates including chitin, *N*-acetylglucosamine, maltose, maltodextrin, trehalose, glycerol, glycerol-3-phosphate, glycogen, fructose, gluconate, ribose, fructooligosaccharides (FOS), raffinose and deoxyribose can be used, although none were tested as growth substrates here.

Our genome analysis suggests that strain RW2—like other members of the genus—is auxotrophic for branched-chain amino acids, as biosynthetic pathways for isoleucine, leucine, and valine were predicted to be absent, while complete degradation pathways were present. Moreover, arginine dihydrolase was

TABLE 7 | Biochemical tests for selected strains of *Exiguobacterium*.

Activity for	RW2	DVS3Y	DSM14480	DSM17290	DSM14481	DSM15368	JCM12280	DSM20416
Catalase	+	+	+	+	+	+	+	+
Oxidase	−	+	+	+	+	+	+	+
β-Galactosidase	+	+	+	+	+	+	+	+
Arginine dihydrolase	+	+	+	+	+	+	+	+
Lysine decarboxylase	−	+	−	+	+	+	−	−
Ornithine decarboxylase	−	+	+	+	+	+	+	+
Urease	+	−	−	−	−	−	−	−
Tryptophan deaminase	−	−	+	+	−	−	+	+
Citrate utilization	+	−	−	+	−	+	+	+
Gelatinase	+	+	+	+	+	−	+	+
Production of:								
H_2S	−	−	−	−	−	−	−	−
Indole	−	−	−	−	−	−	−	−
Acetoin	−	+	+	+	+	+	+	+
Assimilation of:								
D-Mannitol	−	−	−	−	+	−	+	+
Inositol	−	+	−	−	−	+	−	−
D-Sorbitol	−	+	−	+	−	+	−	−
L-Rhamnose	−	+	−	−	−	+	−	−
D-Melibiose	−	−	−	+	−	−	−	−
Amygdalin	+	+	+	+	+	−	+	−
L-Arabinose	−	+	−	+	−	−	−	−
D-Glucose	+	+	+	+	+	+	+	+
D-Sucrose	+	+	+	+	+	+	+	+

All growth measurements for strain RW2 were taken after 24 h in triplicate. Non-strain RW2 data are from Chaturvedi et al. (2008). All are listed by strain name. All strain publications are further described in ***Table 1****.*

functional in strain RW2; whereas, tryptophan deaminase, lysine, and ornithine decarboxylases were not (**Table 7**). Further growth substrates should be tested to elucidate carbohydrate and amino acid utilization in strain RW2 further.

Strain RW2 genome is predicted to encode genes that generate ammonium from amino acids. An L-asparagine biosynthetic pathway is predicted to encode genes for aspartate aminotransferase, aspartate-ammonia ligase, and L-asparaginase. The enzyme L-asparaginase is known to hydrolyze L-asparagine to L-aspartate and ammonia, though we did not chemically validate its function in strain RW2. By contrast, urease—another enzyme capable of ammonification, via the catabolism of urea into ammonium and CO_2—was not found in the genome of strain RW2. Interestingly, cells of RW2 nonetheless measured as positive on a biochemical urease test, conducted in triplicate (**Table 7**). It is possible that a poorly annotated gene encodes this urease function; since there are five copies of unspecified aminohydrolases within the genome of strain RW2, and given that aminohydrolases represent the enzymatic superfamily to which urease belongs (EC 3.5.1.5).

Carotenoid Biosynthesis

The pathways responsible for the characteristic orange pigmentation of *Exiguobacterium* spp. are unknown, though the main candidate is that of carotenoid biosynthesis, as this pathway is commonly found in members of the *Firmicutes* (Klassen, 2010). Our comparative genomic analysis indicates that complete pathways for carotenoid C_{30} biosynthesis were present in all the published *Exiguobacterium* spp. genomes, including that of strain RW2 (**Figure 6**). Relevant enzymes include diapophytoene synthase (*crtM,* annotated as phytoene synthase), diapophytoene desaturase (*crtN,* annotated as phytoene desaturase), and diapophytoene desaturase (*crtNb,* annotated as the second copy of phytoene desaturase). Similar to the case in *Halobacillus halophilus* (Köcher et al., 2009) (**Figure 6**), all genes for the pathway are located on a single operon, specifically on a span of 5,673 bp, stretching from position 39,293 to 44,966 bp on the genome.

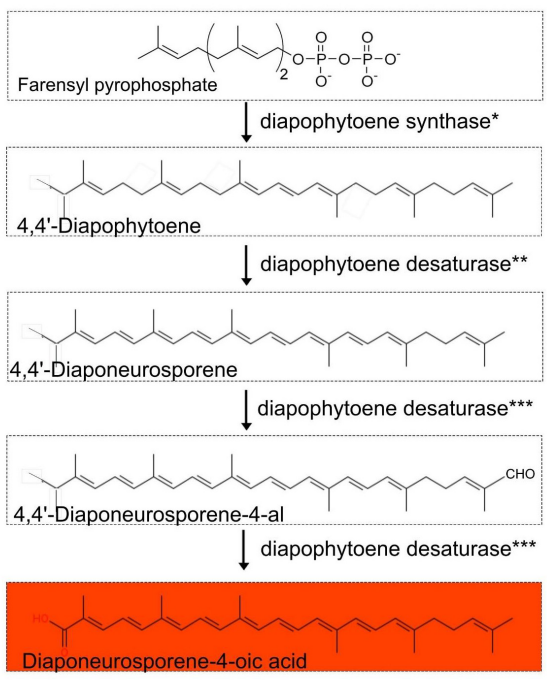

FIGURE 6 | Proposed carotenoid biosynthetic pathway (4-4′ diapocarotenoids C_{30} carotenoid-based) in the genus *Exiguobacterium*.*Diapophytoene synthase (*crtM*) annotated as phytoene synthase. **Diapophytoene desaturase (*crtN*) annotated as phytoene desaturase. ***Diapophytoene desaturase (*crtNb*) annotated as phytoene desaturase.

DISCUSSION

Exiguobacterium Coloration Is Based on C_{30} Carotenoids With Potential Functions

Based on our comparative genomic analysis of draft and completed genomes from NCBI, we predict that a 4-4' diapocarotenoids C_{30} carotenoid-based biosynthetic pathway is responsible for the orange pigmentation of *Exiguobacterium* colonies, with diaponeurosporene-4-oic as the final product. As reported in *Halobacillus halophilus*, genes encoding this pathway are arranged as an operon, and genetic ablation of the terminal gene (for diapophytoene desaturase) results in the accumulation of diaponeurosporene-4-oic acid and consequent orange pigmentation (Köcher et al., 2009).

To our knowledge, a hypothesis has not been advanced to explain the function of pigments in the genus *Exiguobacterium.* Low concentrations of dissolved organic carbon (DOC) in Pavilion Lake allow for high UV penetration, and carotenoids might provide a "sunscreen" function to cope with these conditions (Lim et al., 2009; Lionard et al., 2012). Three tested strains of *Exiguobacterium* are known to use photoenzymatic repair (PER) and nucleotide excision repair (NER) to recover from UV-B photodamage, but all had some form of UV-B resistance beyond PER and NER (Gutiérrez-Preciado et al., 2017). We hypothesize that 4-4' diapocarotenoids C_{30} carotenoids protect members of *Exiguobacterium* from UV-B damage, given the well-known role of carotenoids quenching and scavenging reactive oxygen species, releasing excessive light energy, and sunscreening (Wada et al., 2013). Further experimentation is needed to confirm if carotenoids indeed protect firmicutes against UV radiation.

Potential Contribution to Microbialite Formation and Maintenance

While strain RW2 has many of the physiological features of an environmental generalist, it was specifically enriched in the microbialite community at 20 m depth in Pavilion Lake. Specifically, its reads were absent in the sediment metagenome sampled nearby and are poorly represented in the metagenome

sampled from the water column overhead. Moreover, reads from strain RW2 comprised a higher proportion of total microbialite reads than those of strain S17 in Socompa Lake microbialites and strain AT1b in a hyperthermal microbial mat (Ordoñez et al., 2013, 2015). Together these data suggest that strain RW2 is a numerically significant component of the Pavilion Lake microbialites. Strain RW2 was found in lower amounts on the filters (i.e., water column metagenomes), and wasn't as prevalent as in the microbialite metagenomes. Filters can contain small amounts of microbialite microbial mat as they were sampled near the microbialites at depth; however, the water column metagenomes are distinctly different via PCA analysis from the microbialite metagenome (White et al., 2016).

Since we do not know how long strain RW2 has lived on freshwater microbialites, it is unclear how and to what extent it has co-evolved with this microbial community. Even in the absence of evolutionary specialization, there are several ways in which strain RW2 might contribute to microbialite formation and maintenance. For instance, biofilm formation has previously been nominated as a survival mechanism in nutrient-poor conditions (Shao et al., 2013), and this might apply to the cold, oligotrophic conditions from which strain RW2 was isolated (Lim et al., 2009). By adhering to sediment and precipitated carbonates, Firmicutes such as *Exiguobacterium* could, in turn, contribute to the coherence and spatial structure of microbialites like those found in Pavilion Lake and Laguna Negra (White et al., 2016; Gomez-Javier et al., 2018). But biofilm formation is not necessarily a consequence of co-evolution with microbialites since other strains form biofilms in the absence of microbialites, such as *Exiguobacterium* strain GIC31, which may grow directly on glacial ice. A few strains of *Exiguobacterium* isolates have been found to be endemic to Cuatro Ciénegas Basin which microbialites are found (Rebollar et al., 2012).

Several metabolic pathways predicted in strain RW2 might also contribute to microbialite formation by promoting inducing carbonate precipitation via urease or deamination of amino acids. For instance, the enzyme L-asparaginase generates ammonium as a by-product of the deamination of amino acids, thereby increasing alkalinity, which favors the precipitation of carbonate minerals (Castanier et al., 1999). Interestingly, our biochemical assay indicated that urease is also active in strain RW2; though we found no evidence of urease genes within its genome, nor that of any other *Exiguobacterium* strain. This suggests either (A) the presence of an uncharacterized "orphan enzyme" (perhaps any of the five amidohydrolases predicted in the genome of strain RW2), or (B) that a known enzyme is capable of an undescribed side reaction (Sorokina et al., 2014; Montgomery et al., 2015). Amidohydrolases belong to the same protein superfamily as urease; which is a future target for further characterization and investigation. In any case, urease—like asparaginase—can induce calcium carbonate precipitation, and it is found in carbonate precipitating members of *Bacillus* spp. (Hammes et al., 2003), though its actual involvement in biomineralization remains to be demonstrated.

More compelling is the possibility that strain RW2 contributes other metabolic functions—namely heavy-metal metabolism—since these *Exiguobacterium* genes are highly represented in the microbialite metagenome of Pavilion Lake. For reasons that are still unclear, heavy-metal metabolism appears to be an accessory feature of microbialite communities (Ruvindy et al., 2016; White et al., 2016; Kurth et al., 2017; Gomez-Javier et al., 2018). Generally, heavy metals (such as arsenic) limit microbial growth. However, we find three examples of thriving modern microbialite ecosystems in the presence of high arsenic; the microbialites of Laguna Brava (Sancho-Tomás et al., 2018), Socompa Lake (Kurth et al., 2017), and Laguna Negra (Gomez-Javier et al., 2018). The extracellular polymeric substances (EPS) within cyanobacterial microbialite mats and biofilms bind, concentrate, and remove heavy metals from the water column (Arp et al., 1999). Any heterotroph that eliminates and detoxifies heavy metals as a by-product of its metabolism would benefit the entire microbialite microbiome and would presumably be rewarded with more substrates for growth. Strangely, Pavilion Lake has low levels of zinc (0.01–0.03 mg L^{-1}) and undetectable levels of cobalt, copper, chromium, arsenic, and cadmium (Lim et al., 2009).

Genes predicted in the resistance of mercury, arsenic, chromate, cadmium, cobalt, zinc resistance were all found in Pavilion Lake microbialite microbiome based on recruitment of their metagenomic reads to the genome of strain RW2. While strain RW2 hasn't been tested for arsenic resistance; strain N139 can grow at 100 mM of arsenate (As [V]), and 2.5 mM of arsenite (As [III]) (Ordoñez et al., 2015). All three strains (RW2, GIC31, N139) have no *acr3* based on genome predictions; whereas S17 does and can grow at 10 mM As [II] (Ordoñez et al., 2015). We would predict that strain RW2 would have similar arsenic resistance as strain N139, high As [V] resistance but low As [III] due to the lack of the *acr3* gene.

Moreover, the genome of *Agrococcus pavilionensis* strain RW1—which was isolated from the same microbialite as strain RW2—also carried genes for heavy-metal resistance genes (White et al., 2013a). One possible explanation is that these genomic signatures are relicts from a time when Pavilion Lake had higher levels of dissolved heavy metals, as likely occurred in the early 20th century when mining operations were active in the region (Stevenson, 1940).

Another possibility is that metal resistance genes have other secondary alternative functions, as in *Rhodobacter sphaeroides* is known to have arsenic resistance genes expressed under high salt stress (Tsuzuki et al., 2011). For instance, the heavy metal resistance proteins genes in strain RW2 are retained in a low heavy metal environment because of the act as can also detoxification of other substrates (e.g., antibiotics). As such, heavy metal metabolism can drive co-selection of antibiotic resistance when aquatic systems that are impacted by agriculture or antibiotics introduced through wastewater and agricultural runoff anthropomorphic means (Seiler and Berendonk, 2012). Resistance in heavy metals has conferred resistance to antibiotics in a complex microbiome (e.g., chicken guts) (Nisanian et al., 2014). It is not clear whether this is the case for microbialites in Pavilion Lake, though strain RW2 also contributes antibiotic resistance genes to the metagenome of

these microbialites, including those for sulfisoxazole resistance (White et al., 2016).

Classification of the Strains as the Same Species

Using 16S rRNA gene sequence phylogeny, whole-genome ANI/AAI, and digital DNA–DNA hybridization; we confirmed that strain RW2, GIC31, and N139 belong to same bacterial species—the recently described *Exiguobacterium chiriqhucha* (Gutiérrez-Preciado et al., 2017). We also provide the first complete genomes for this species—represented by our assembly of strain RW2, as well as our the complete genome of strain GIC31. Each genome consists of a single circular chromosome, with strain GIC31 also possessing one plasmid.

Adaptation to a Wide Range of Abiotic Conditions

While strain RW2 has a modest tolerance for added salts, it exhibits both the highest thermal growth range (4–50°C) and broadest pH growth range (5–11 pH) ever reported for the genus *Exiguobacterium.* Strain RW2 genome encodes molecular chaperons (*csp* and *dnaK*), ABC transporters, antiporters, for thermal, freezing and osmotic stress adaptation. This is unusual, a few of these extremes would be expected in the permanently cold and alkaline habitat from which this isolate was obtained. Growth at such high temperatures and low salinities is not a requirement for life in Pavilion Lake. Though there are numerous hot springs in southwestern British Columbia (Lim et al., 2009), and geothermally heated microhabitats have been known to provide refugia for certain flora during glacial periods Alternately, if strain RW2 is a recent colonist of microbialite habitats, then these physiological tolerances might be holdovers from a more generalist lifestyle. But speculation aside, in the present environment of our isolate, cold and alkaline conditions are the most likely sources of abiotic stress.

Cold stress generally decreases membrane fluidity and causes ice crystal formation, leading to cryodamage of the cell (Ponder et al., 2005). At lower temperatures (4°C), strain RW2 synthesizes a higher proportion of branched, unsaturated fatty acids (i.e., iso-C16:1Δ5, iso-C18:1Δ5, and brC19:1), which likely help prevent membrane crystallization. This increase in unsaturated fatty acids is similar to that found in *P. halocryophilus* when grown at sub-zero temperatures (Mykytczuk et al., 2013).

Its thermotolerance is unique since, until now, *Exiguobacterium* spp., strains that grow at >45°C have only been isolated from such hyperthermal environments (Crapart et al., 2007). Conversely, the percentage of unsaturated fatty acids decreased at higher temperatures. Indeed, the largest change in the PLFA composition of strain RW2 was prompted by increasing the temperature to 50°C, as branched monoenoic (unsaturated) PLFAs decreased as much as 93% between 4 and 50°C. This changing membrane profile is a characteristic cellular response to heat stress, as high levels of saturated fats decrease membrane fluidity and thereby prevent phase transitions at high temperature (Hazel, 1995). As with its lipid profile, the genome of strain RW2 seems to reflect its broad thermal and pH tolerance. It possesses a full heat-shock protein cascade (i.e., *dnaJ, dnaK*, and *GrpE)*, as does its hot-spring dwelling relative, strain AT1b.

Strain RW2 considerable tolerance of acidity is surprising, as similar acidic pH tolerance has only been reported from marine isolates of *Exiguobacterium* (i.e., *E. profundum, E. aestuarii,* and *E. marinum*) which can grow at a pH of 5.5 (but not the upper limit of pH 11 as in strain RW2) (Kim et al., 2005; Crapart et al., 2007). Our genomic annotations indicate that strain RW2 possesses the antiporter encoded by *arcD* (Fulde et al., 2014), and a Na^+/K^+ antiporter encoded by *nhaC*, which—in other members of *Exiguobacterium*—are known to regulate responses to acidity and alkalinity, respectively (Ito et al., 1997). Under decreasing pH, PLFAs increased in saturation, presumably resulting in a more ordered and rigid membrane. Such increases in saturation are thought to help resist H^+ influxes under acidic conditions (Mykytczuk et al., 2013). Compared to its responses to pH and temperature, PLFA composition in strain RW2 was less affected by salinity, though the percent of saturated PLFAs increased slightly at low salinities as would be expected to increase membrane rigidity and reduce the risk of lysis (Ponder et al., 2005). It is also conceivable that strain RW2 could adapt to high pH via cardiolipin biosynthesis since alkaliphilic strains of *Bacillus* are known to upregulate this pathway under high pH (Clejan et al., 1986). Further experimental evidence is required to understand how strain RW2 regulates its responses to changes in pH.

Strain RW2 can grow from 0 to 7% added NaCl, and could potentially respond to regulate low salt stress higher osmotic stress by increasing intracellular NaCl concentration using via the choline and betaine uptake and biosynthesis pathways encoded in its genome. Halotolerance of strain RW2 is considerably lower than marine isolates found in the clade IIa, such as *Exiguobacterium aestuarii,* which can grow at 17% added NaCl (Kim et al., 2005). Genome prediction suggest strain RW2 potentially regulates NaCl stress via choline and betaine uptake and biosynthesis pathway. ABC transporter genes required for higher salinity growth were present in the genome of strain RW2 (i.e., *opuC, proW*). However, strain RW2 was missing the *bet* genes thought to be required for high salinity growth (>10%) (Mykytczuk et al., 2013). *P. halocryophilus* has *bet* genes required for high salinity growth and can grow in 18% added NaCl (Mykytczuk et al., 2013). The heat shock *dnaK* gene cluster also can also protect cells from hyperosmotic shock induced by salt (i.e., NaCl/KCl) and carbon substrates (e.g., sugars) (Bianchi and Baneyx, 1999). Overall, the temperature, pH, and salinity-based changes in its PLFA composition seem to reflect strain RW2 adaptability likely due to membrane restructuring.

CONCLUSION

Exiguobacterium chiriqhucha strain RW2 was isolated from microbialite cyanobacterial mat within a Pavilion Lake in

southeastern BC. Currently, strain RW2 has the widest pH and temperature growth range for any isolate of *Exiguobacterium*. We described the physiological, genomic, and fatty acid composition under different growth conditions for strain RW2 widely adaptability to various temperatures, pHs, and salinities. We revealed the putative pathway for the orange colony formation in *Exiguobacterium* as 4-4' diapocarotenoids C_{30} carotenoid-based biosynthetic pathway using comparative genomic analysis. We suggest the potential role of these carotenoid pigments as protective potentially against photodamage or act as quenchers for reactive oxygen.

Our results suggest that strain RW2 is present within microbialite microbiome of Pavilion Lake. Metagenomic recruitment suggest genes related to the detoxification of heavy metals and antibiotics are supplied by strain RW2 genome. Strain RW2 is a robust biofilm former, and putatively increases alkalinity leading to carbonate precipitation is deamination of amino acids to ammonia (i.e., L-asparaginase/urease).

The remarkable range of possible growth conditions and metabolic potential of strain RW2 may make this species relevant to industries that are exploring the use of *Exiguobacterium* spp. For example, its predicted heavy-metal tolerance makes it an excellent candidate for bioremediation applications (Park and Chon, 2016), and its ability to produce carotenoids may have applications in natural pigment biosynthesis. Strain RW2 is also highly amenable to cultivation because it can grow on a diverse set of nutrients. Lastly, the ability to catabolize urea despite the apparent lack of genes encoding urease may lead to the discovery of a hitherto unknown protein or enzymatic pathway that could function in the transformation of nitrogen.

AUTHOR CONTRIBUTIONS

RW designed the study, and collected and plated the isolate, performed growth studies, extracted DNA, prepared libraries, assembled and annotated the genome, performed comparative genomic and phylogenetic analysis. SS completed PLFA, with financial support from GS. EG performed culturing experiments. RW preserved cells for scanning electron microscopy, which were imaged by GG. RW and GG wrote the manuscript. All authors participated in the manuscript drafting process.

FUNDING

Financial support for sample collection was provided by the MARSLIFE Project (9F052-10-0176) funded by the Canadian Space Agency. The laboratory work was supported by a Discovery Grant from the Natural Science and Engineering Council of Canada (CAS), and grants to CS from the Tula Foundation and the Canadian Institute for Advanced Research. Infrastructure support for laboratory work was provided to CS from the Canadian Foundation for Innovation and the British Columbia Knowledge Development Fund.

ACKNOWLEDGMENTS

We are grateful to the entire Pavilion Lake Research Project (PLRP) research team, especially Donnie Reid for his exceptional leadership of field logistics and diving operations, as well as the PLRP science divers and the DeepWorker pilots for their help recovering samples from the lake. We also thank Danielle Winget, Kynan Suttle, Jan Finke, Marli Vlok, and Tyler Nelson for assistance with sample processing in the field. Microbialite morphology photographs in **Figure 1** are used with permission and copyrighted by Donnie Reid, Tyler Mackey, Amy M. Chan, Kynan Suttle, and RA. We thank the following individuals and their teams for providing the sequence data: Sugandha Dandekar (Uma) and Hemani Wijesuriya for the MiSeq data (UCLA Genotyping and Sequencing Core), Frederick Robidoux for the HiSeq data (McGill University and Genome Quebec Innovation Centre), and Sergio Pereira for the 454 FLX data (The Centre for Applied Genomics, SickKids Hospital, Toronto, ON, Canada). Special thanks to Niels W. Hanson and Kishori M. Konwar for R scripts for parsing metapathways data. Also, thank you, Brendan P. Burns, for your excellent comments on draft manuscripts. We are also grateful to Linda and Mickey Macri for hosting the PLRP and MARSLIFE projects and to the Ts'Kw'aylaxw First Nation and British Columbia Parks for their continued support of our research.

SUPPLEMENTARY MATERIAL

The Supplementary Material for this article can be found online at: https://www.frontiersin.org/articles/10.3389/fmicb.2018.03189/full#supplementary-material

FIGURE S1 | Genome synteny and functional Venn diagrams (SEED) with Amino acid identity score (AAIr) to strain RW2. Genomes are listed in megabase pairs (Mb). Red dots are positive blast hits based on the RAST genome comparison module. Amino acid identity (AAIr) was calculated using the RAST functional module with the web-based tool (Krebs et al., 2013). Venn diagrams are listed by strain name based on RAST functional annotations (SEED/FigFams).

FIGURE S2 | MetaCyc pathway annotations of genomes for isolates of *Exiguobacterium*. **(A)** Venn diagram high amino acid identity score (AAIr) to strain RW2 (>80% AAIr), within clade II. **(B)** Venn diagram low amino acid identity score (AAIr) to strain RW2 (<62% AAIr), within clade I. Labels on Venn diagrams, are listed by strain name with *Exiguobacterium* sp. for strains 8-11-1, AT1b, MH3, RW2, S17, followed *E. sibiricum* strain 255-15 and *E. antarcticum* strain B7.

FIGURE S3 | *Exiguobacterium* presence in Pavilion Lake microbialite metagenome. **(A)** *Exiguobacterium* STAMP post-havoc confidence interval plots (>95%) based on ANOVA parameters for novel metabolic potential differences for microbialites and surrounding environment (using multiple groups). **(B)** Metagenomic recruitment plot of Pavilion Lake 20 m microbialite reads (∼7.5 million) to three *Exiguobacterium* genetically related to strain RW2 isolated from 20 m microbialites (minimum identity > 70% and an E-value > $1e^{-5}$).

TABLE S1 | Complete genomes of *Exiguobacterium* published (as of July 2018).

TABLE S2 | Antibiotic susceptibility for selected strains *Exiguobacterium*. Resistant (+), sensitive (–), data not available (NA). Additional data are from [1]Chaturvedi et al. (2008). All growth measurements for strain RW2 were taken after 24 h. This for standard growth conditions for strain RW2 [M-agar, 30°C, 1% NaCl (w/v) and pH 7, on 1.5% (w/v) agar] all in triplicate.

REFERENCES

Arp, G., Reimer, A., and Reitner, J. (1999). Calcification in cyanobacterial biofilms of alkaline salt lakes. *Eur. J. Phycol.* 34, 393–403. doi: 10.1080/09670269910001736452

Aziz, R. K., Bartels, D., Best, A. A., DeJongh, M., Disz, T., Edwards, R. A., et al. (2008). The RAST server: rapid annotations using subsystems technology. *BMC Genomics* 9:75. doi: 10.1186/1471-2164-9-75

Barman, S., Chatterjee, S., and Koley, H. (2010). Plasmid-mediated streptomycin and sulfamethoxazole resistance in *Shigella flexneri* 3a. *Int. J. Antimicrob. Agents* 36, 348–351. doi: 10.1016/j.ijantimicag.2010.06.037

Beatty, J. T., and Gest, H. (1981). Biosynthetic and bioenergetic functions of citric acid cycle reactions in *Rhodopseudomonas capsulata*. *J. Bacteriol.* 148, 584–593.

Bianchi, A. A., and Baneyx, F. (1999). Hyperosmotic shock induces the σ32 and σE stress regulons of *Escherichia coli*. *Mol. Microbiol.* 34, 1029–1038. doi: 10.1046/j.1365-2958.1999.01664.x

Bligh, E. G., and Dyer, W. J. (1959). A rapid method of total lipid extraction and purification. *Can. J. Biochem. Phys.* 37, 911–917. doi: 10.1139/y59-099

Bottos, E. M., Vincent, W. F., Greer, C. W., and Whyte, L. G. (2008). Prokaryotic diversity of arctic ice shelf microbial mats. *Environ. Microbiol.* 10, 950–966. doi: 10.1111/j.1462-2920.2007.01516.x

Breitbart, M., Hoare, A., Nitti, A., Siefert, J., Haynes, M., Dinsdale, E., et al. (2009). Metagenomic and stable isotopic analyses of modern freshwater microbialites in Cuatro Cienegas, Mexico. *Environ. Microbiol.* 11, 16–34. doi: 10.1111/j.1462-2920.2008.01725.x

Burne, R. V., and Moore, L. S. (1987). Microbialites: organosedimentary deposits of benthic microbial communities. *Palaios* 2, 241–254. doi: 10.2307/3514674

Burns, B. P., Gudhka, R. K., and Neilan, B. A. (2012). Genome sequence of the halophilic archaeon *Halococcus hamelinensis*. *J. Bacteriol.* 194, 2100–2101. doi: 10.1128/JB.06599-11

Carneiro, A. R., Ramos, R. T., Dall'Agnol, H., Pinto, A. C., de Castro Soares, S., Santos, A. R., et al. (2012). Genome sequence of *Exiguobacterium antarcticum* B7, isolated from a biofilm in Ginger Lake, King George Island, Antarctica. *J. Bacteriol.* 194, 6689–6690. doi: 10.1128/JB.01791-12

Caspi, R., Altman, T., Billington, R., Dreher, K., Foerster, H., Fulcher, C. A., et al. (2014). The MetaCyc database of metabolic pathways and enzymes and the BioCyc collection of Pathway/Genome Databases. *Nucleic Acids Res.* 42, 459–471. doi: 10.1093/nar/gkt1103

Castanier, S., Le Metayer-Levrel, G., and Perthuisot, J. P. (1999). Ca-carbonates precipitation and limestone genesis the microbiogeologist point of view. *Sediment. Geol.* 126, 9–23. doi: 10.1016/S0037-0738(99)00028-7

Chaturvedi, P., Prabahar, V., Manorama, R., Pindi, P. K., Bhadra, B., Begum, Z., et al. (2008). *Exiguobacterium soli* sp. nov. A psychrophilic bacterium from the McMurdo dry valleys, Antarctica. *Int. J. Syst. Evol. Microbiol.* 58, 2447–2453. doi: 10.1099/ijs.0.2008/000067-0

Chaturvedi, P., and Shivaji, S. (2006). *Exiguobacterium indicum* sp. nov. A psychrophilic bacterium from the Hamta glacier of the Himalayan mountain ranges of India. *Int. J. Syst. Evol. Microbiol.* 56, 2765–2770. doi: 10.1099/ijs.0.64508-0

Chun, J., Oren, A., Ventosa, A., Christensen, H., Arahal, D. R., da Costa, M. S., et al. (2018). Proposed minimal standards for the use of genome data for the taxonomy of prokaryotes. *Int. J. Syst. Evol. Microbiol.* 68, 461–466. doi: 10.1099/ijsem.0.002516

Clejan, S., Krulwich, T. A., Mondrus, K. R., and Seto-Young, D. (1986). Membrane lipid composition of obligately and facultatively alkalophilic strains of *Bacillus* spp. *J. Bacteriol.* 168, 334–340. doi: 10.1128/jb.168.1.334-340.1986

Collee, J. G., Miles, R. S., and Watt, B. (1996). "Tests for the identification of bacteria," in *Mackie and McCartney Practical Medical Microbiology*, 14th Edn, eds J. G. Collee, A. G. Fraser, B. P. Marmion, and A. Simmons (London: Churchill Livingstone), 131–149.

Collins, M. D., Lund, B. M., Farrow, J. A. E., and Schleifer, K. H. (1983). Chemotaxonomic study of an alkaliphilic bacterium, *Exiguobacterium aurantiacum* gen nov., sp. nov. *J. Gen. Microbiol.* 129, 2037–2042.

Crapart, S., Fardeau, M. L., Cayol, J. L., Thomas, P., Sery, C., Ollivier, B., et al. (2007). *Exiguobacterium profundum* sp nov., a moderately thermophilic, lactic acid-producing bacterium isolated from a deep-sea hydrothermal vent. *Int. J. Syst. Bacteriol.* 57, 287–292. doi: 10.1099/ijs.0.64639-0

Darling, A. E., Mau, B., and Perna, N. T. (2010). progressiveMauve: multiple genome alignment with gene gain, loss, and rearrangement. *PLoS One* 5:e11147. doi: 10.1371/journal.pone.0011147

Destaillats, F., and Angers, P. (2002). One-step methodology for the synthesis of FA picolinyl esters from intact lipids. *JAOCS* 3, 253–256. doi: 10.1007/s11746-002-0469-7

Devoid, S., Overbeek, R., DeJongh, M., Vonstein, V., Best, A. A., and Henry, C. (2013). Automated genome annotation and metabolic model reconstruction in the SEED and Model SEED. *Methods Mol. Biol.* 985, 17–45. doi: 10.1007/978-1-62703-299-5_2

Dowd, M. (1998). Identification of the unsaturated heptadecyl fatty acids in the seed oils of *Thespesia populnea* and *Gossypium hirsutum*. *J. Am. Oil Chem. Soc.* 89, 1599–1609. doi: 10.1007/s11746-012-2071-5

Farrow, J. A. E., Wallbanks, S., and Collins, M. D. (1994). Phylogenetic interrelationships of round-spore-forming bacilli containing cell walls based on lysine and the non-spore-forming genera *Caryophanon*, *Exiguobacterium*, *Kurthia*, and *Planococcus*. *Int. J. Syst. Bacteriol.* 44, 74–82. doi: 10.1099/00207713-44-1-74

Feder, M. E., and Hofmann, G. E. (1999). Heat-shock proteins, molecular chaperones, and the stress response: evolutionary and ecological physiology. *Annu. Rev. Physiol.* 61, 243–282. doi: 10.1146/annurev.physiol.61.1.243

Fisher, A., Wangpraseurt, D., Larkum, A. W. D., Johnson, M., Kühl, M., Chen, M., et al. (2019). Correlation of bio-optical properties with photosynthetic pigment and microorganism distribution in microbial mats from Hamelin Pool, Australia. *FEMS Microbiol. Ecol.* 95:fiy219. doi: 10.1093/femsec/fiy219

Fruhling, A., Schumann, P., Hippe, H., Straubler, B., and Stackebrandt, E. (2002). *Exiguobacterium undae* sp nov. and *Exiguobacterium antarcticum* sp. nov. *Int. J. Syst. Evol. Microbiol.* 52, 1171–1176.

Fulde, M., Willenborg, J., Huber, C., Hitzmann, A., Willms, D., Seitz, M., et al. (2014). The arginine-ornithine antiporter *arcD* contributes to biological fitness of *Streptococcus suis*. *Front. Cell. Infect. Microbiol.* 4:107. doi: 10.3389/fcimb.2014.00107

Gomez-Javier, F., Mlewski, C., Jaquelina, F. B., Farías, M. E., and Gérard, E. (2018). Calcium carbonate precipitation in diatom-rich microbial mats: the Laguna Negra hypersaline lake, Catamarca, Argentina. *J. Sediment. Res.* 88, 727–742. doi: 10.2110/jsr.2018.37

Gouy, M., Guindon, S., and Gascuel, O. (2010). SeaView Version 4: a multiplatform graphical user interface for sequence alignment and phylogenetic tree building. *Mol. Biol. Evol.* 27, 221–224. doi: 10.1093/molbev/msp259

Grant, J. R., and Stothard, P. (2008). The CGView Server: a comparative genomics tool for circular genomes. *Nucleic Acids Res.* 36, W181–W184. doi: 10.1093/nar/gkn179

Guckert, J. B., Antworth, C. P., Nichols, P. D., and White, D. C. (1985). Phospholipid, ester-linked fatty acid profiles as reproducible assays for changes in prokaryotic community structure of estuarine sediments. *FEMS Microbiol. Ecol.* 31, 147–158. doi: 10.1111/j.1574-6968.1985.tb01143.x

Gutiérrez-Preciado, A., Vargas-Chávez, C., Reyes-Prieto, M., Ordoñez, O. F., Santos-García, D., Rosas-Pérez, T., et al. (2017). The genomic sequence of *Exiguobacterium chiriqhucha* str. N139 reveals a species that thrives in cold waters and extreme environmental conditions. *PeerJ.* 5:e3162. doi: 10.7717/peerj.3162

Hammes, F., Boon, N., de Villiers, J., Verstraete, W., and Siciliano, S. D. (2003). Strain-specific ureolytic microbial calcium carbonate precipitation. *Appl. Environ. Microbiol.* 69, 4901–4909. doi: 10.1128/AEM.69.8.4901-4909.2003

Havemann, S. A., and Foster, J. S. (2008). A comparative characterization of the microbial diversity in an artificial microbialite model and a natural stromatolite. *Appl. Environ. Microbiol.* 74, 7410–7421. doi: 10.1128/AEM.01710-08

Hazel, J. R. (1995). Thermal adaptation in biological-membranes - Is homeoviscous adaptation the explanation. *Annu. Rev. Physiol.* 57, 19–42. doi: 10.1146/annurev.ph.57.030195.000315

Hoang, D. T., Chernomor, O., von Haeseler, A., Minh, B. Q., and Vinh, L. S. (2017). UFBoot2: improving the ultrafast bootstrap approximation. *Mol. Biol. Evol.* 35, 518–522. doi: 10.1101/153916

Ito, M., Guffanti, A. A., Zemsky, J., Ivey, D. M., and Krulwich, T. A. (1997). Role of the nhaC-encoded Na^+/H^+ antiporter of alkaliphilic *Bacillus firmus* OF4. *J. Bacteriol.* 179, 3851–3857. doi: 10.1128/jb.179.12.3851-3857.1997

Jiang, X., Xue, Y., Wang, L., Yu, B., and Ma, Y. (2013). Genome sequence of a novel polymer-grade l-lactate-producing alkaliphile, *Exiguobacterium* sp. strain 8-11-1. *Genome Announc.* 1:e00616-13. doi: 10.1128/genomeA.00616-13

Katoh, K., Misawa, K., Kuma, K., and Miyata, T. (2002). MAFFT: a novel method for rapid multiple sequence alignment based on fast Fourier transform. *Nucleic Acids Res.* 30, 3059–3066. doi: 10.1093/nar/gkf436

Kawahara, H. (2008). *Psychrophiles: from Biodiversity to Biotechnology*. Heidelberg: Springer. 229–246. doi: 10.1007/978-3-540-74335-4_14

Kiełbasa, S. M., Wan, R., Sato, K., Horton, P., and Frith, M. C. (2011). Adaptive seeds tame genomic sequence comparison. *Genome Res.* 3, 487–493. doi: 10.1101/gr.113985.110

Kim, I. J., Lee, M. H., Jung, S. Y., Song, J. J., Oh, T. K., and Yoon, J. H. (2005). *Exiguobacterium aestuarii* sp. nov. and *E. marinum* sp. nov. isolated from tidal flat of the yellow sea in Korea. *Int. J. Syst. Evol. Microbiol.* 55, 885–889. doi: 10.1099/ijs.0.63308-0

Klassen, J. L. (2010). Phylogenetic and evolutionary patterns in microbial carotenoid biosynthesis are revealed by comparative genomics. *PLoS One* 5:e11257. doi: 10.1371/journal.pone.0011257

Köcher, S., Jurgen, B., Müller, V., and Sandmann, G. (2009). Structure, function, and biosynthesis of carotenoids in the moderately halophilic bacterium *Halobacillus halophilus*. *Arch. Microbiol.* 191, 95–104. doi: 10.1007/s00203-008-0431-1

Kodaka, H., Armfield, A. Y., Lombard, G. L., and Dowell, V. R. Jr. (1982). Practical procedure for demonstrating bacterial flagella. *J. Clin. Microbiol.* 16, 948–952.

Konwar, K. M., Hanson, N. W., Pagé, A. P., and Hallam, S. J. (2013). MetaPathways: a modular pipeline for constructing pathway/genome databases from environmental sequence information. *BMC Bioinformatics* 14:202. doi: 10.1186/1471-2105-14-202

Krebs, J. E., Gale, A. N., Sontag, T. C., Keyser, V. K., Peluso, E. M., and Newman, J. D. (2013). A web-based method to calculate average amino acid identity (AAI) between prokaryotic genomes. *BioTechniques*. Available at: http://lycofs01.lycoming.edu/∼newman/AAI/

Kulshreshtha, N. M., Kumar, R., Begum, Z., Shivaji, S., and Kumar, A. (2013). *Exiguobacterium alkaliphilum* sp. nov. isolated from alkaline wastewater drained sludge of a beverage factory. *Int. J. Syst. Evol. Microbiol.* 63(Pt 12), 4374–4379. doi: 10.1099/ijs.0.039123-0

Kurth, D., Amadio, A., Ordoñez, O. F., Albarracín, V. H., Gärtner, W., and Farías, M. E. (2017). Arsenic metabolism in high altitude modern stromatolites revealed by metagenomic analysis. *Sci. Rep.* 7:1024. doi: 10.1038/s41598-017-00896-0

Langmead, B., and Salzberg, S. (2012). Fast gapped-read alignment with Bowtie 2. *Nat. Methods* 9, 357–359. doi: 10.1038/nmeth.1923

Lim, D. S. S., Laval, B. E., Slater, G., Antoniades, D., Forrest, A. L., Pike, W., et al. (2009). Limnology of pavilion lake B.C. - characterization of a microbialite forming environment. *Fundam. Appl. Limnol.* 173, 329–351. doi: 10.1127/1863-9135/2009/0173-0329

Lionard, M., Péquin, B., Lovejoy, C., and Vincent, W. F. (2012). Benthic cyanobacterial mats in the high arctic: multi-layer structure and fluorescence responses to osmotic stress. *Front. Microbiol.* 3:140. doi: 10.3389/fmicb.2012.00140

Lopez-Cortes, A., Schumann, P., Pukall, R., and Stackebrandt, E. (2006). *Exiguobacterium mexicanum* sp nov. and *Exiguobacterium artemiae* sp. nov., isolated from the brine shrimp *Artemia franciscana*. *Syst. Appl. Microbiol.* 29, 183–190. doi: 10.1016/j.syapm.2005.09.007

Meier-Kolthoff, J. P., Auch, A. F., Klenk, H. P., and Göker, M. (2013). Genome sequence-based species delimitation with confidence intervals and improved distance functions. *BMC Bioinformatics* 14:60. doi: 10.1186/1471-2105-14-60

Meier-Kolthoff, J. P., Hahnke, R. L., Petersen, J., Scheuner, C., Michael, V., Fiebig, A., et al. (2014). Complete genome sequence of DSM30083T, the type strain (U5/41T) of *Escherichia coli*, and a proposal for delineating subspecies in microbial taxonomy. *Stand. Genomic Sci.* 9:2. doi: 10.1186/1944-3277-9-2

Meyer, F. D., Paarmann, M., D'Souza, R., Olson, E. M., Glass, M., Kubal, T., et al. (2008). The metagenomics RAST server – A public resource for the automatic phylogenetic and functional analysis of metagenomes. *BMC Bioinformatics* 9:386. doi: 10.1186/1471-2105-9-386

Milne, I., Stephen, G., Bayer, M., Cock, P. J. A., Pritchard, L., Cardle, L., et al. (2013). Using Tablet for visual exploration of second-generation sequencing data. *Brief. Bioinform.* 14, 193–202. doi: 10.1093/bib/bbs012

Mlewski, E. C., Pisapia, C., Gomez, F., Lecourt, L., Soto Rueda, E., Benzerara, K., et al. (2018). Characterization of pustular mats and related rivularia-rich laminations in oncoids from the Laguna Negra lake (Argentina). *Front. Microbiol.* 9:996. doi: 10.3389/fmicb.2018.00996

Montgomery, D. C., Sorum, A. W., and Meier, J. L. (2015). Defining the orphan functions of lysine acetyltransferases. *ACS Chem. Biol.* 10, 85–94. doi: 10.1021/cb500853p

Mueller, D. R., Vincent, W. F., Bonilla, S., and Laurion, I. (2005). Extremotrophs, extremophiles and broadband pigmentation strategies in a high arctic shelf ecosystem. *FEMS Microbiol. Ecol.* 53, 73–87. doi: 10.1016/j.femsec.2004.11.001

Murray, R. G. E., Doetsch, R. N., and Robinow, C. F. (1994). "Determination and cytological light microscopy," in *Methods for General and Molecular Bacteriology*, eds P. Gerhardt, R. G. E. Murray, W. A. Wood, and N. R. Krieg (Washington, DC: American Society for Microbiology), 21–41.

Mykytczuk, N. C., Foote, S. J., Omelon, C. R., Southam, G., Greer, C. W., and Whyte, L. G. (2013). Bacterial growth at −15 °C; molecular insights from the permafrost bacterium *Planococcus halocryophilus* Or1. *ISMEJ.* 7, 1211–1226. doi: 10.1038/ismej.2013.8

Nichols, P. D., Gukert, J. B., and White, D. C. (1986). Determination of monounsaturated fatty acid double bond position and geometry for microbial monocultures and complex consortia by capillary GC-MS of their dimethyl disulfide adducts. *J. Microbiol. Methods* 5, 49–55. doi: 10.1016/0167-7012(86)90023-0

Nisanian, M., Holladay, S. D., Karpuzoglu, E., Kerr, R. P., Williams, S. M., Stabler, L., et al. (2014). Exposure of juvenile Leghorn chickens to lead acetate enhances antibiotic resistance in enteric bacterial flora. *Poult. Sci.* 93, 891–897. doi: 10.3382/ps.2013-03600

Niu, B., Zhu, Z., Fu, L., Wu, S., and Li, W. (2011). FR-HIT, a very fast program to recruit metagenomic reads to homologous reference genomes. *Bioinformatics* 27, 1704–1705. doi: 10.1093/bioinformatics/btr252

Nonaka, K., Yoon, K.-S., and Ogo, S. (2014). Biochemical characterization of psychrophilic Mn-superoxide dismutase from newly isolated *Exiguobacterium* sp. OS-77. *Extremophiles* 18, 363–373. doi: 10.1007/s00792-013-0621-x

Nübel, U., Garcia-Pichel, F., Kühl, M., and Muyzer, G. (1999). Quantifying microbial diversity: morphotypes, 16S rRNA genes, and carotenoids of oxygenic phototrophs in microbial mats. *Appl. Environ. Microbiol.* 65, 422–430.

Nutman, A. P., Bennett, V. C., Friend, C. R., Van Kranendonk, M. J., and Chivas, A. R. (2016). Rapid emergence of life shown by discovery of 3,700-million-year-old microbial structures. *Nature* 537, 535–538. doi: 10.1038/nature19355

Ordoñez, O., Lanzarotti, E., Kurth, D., Cortez, N., Farias, M. E., and Turjanski, A. G. (2015). Genome comparison of two *Exiguobacterium* strains from high altitude andean lakes with different arsenic resistance: identification and 3D modeling of the Acr3 efflux pump. *Front. Environ. Sci.* 3:50. doi: 10.3389/fenvs.2015.00050

Ordoñez, O., Lanzarotti, E., Kurth, D., Gorriti, M., Revale, S., Cortez, N., et al. (2013). Draft genome sequence of the polyextremophilic *Exiguobacterium* sp. strain S17, isolated from hyperarsenic lakes in the Argentinian Puna. *Genome Announc.* 1:e00480-13. doi: 10.1128/genomeA.00480-13

Padan, E., Bibi, E., Ito, M., and Krulwich, T. A. (2005). Alkaline pH homeostasis in bacteria: new insights. *Biochim. Biophys. Acta* 1717, 67–88. doi: 10.1016/j.bbamem.2005.09.010

Paley, S. M., and Karp, P. D. (2006). The pathway tools cellular overview diagram and omics viewer. *Nucleic Acids Res.* 34, 3771–3778. doi: 10.1093/nar/gkl334

Parks, D. H., and Beiko, R. G. (2010). Identifying biologically relevant differences between metagenomic communities. *Bioinformatics* 26, 715–721. doi: 10.1093/bioinformatics/btq041

Park, J. H., and Chon, H. T. (2016). Characterization of cadmium biosorption by *Exiguobacterium* sp. isolated from farmland soil near Cu-Pb-Zn mine. *Environ. Sci. Pollut. Res. Int.* 23, 11814–11822. doi: 10.1007/s11356-016-6335-8

Perry, R. S., Mcloughlin, N., Lynne, B. Y., Sephton, M. A., Oliver, J. D., Perry, C. C., et al. (2007). Defining biominerals and organominerals: direct and indirect indicators of life. *Sediment. Geol.* 201, 157–179. doi: 10.1016/j.sedgeo.2007.05.014

Ponder, M. A., Gilmour, S. J., Bergholz, P. W., Mindock, C. A., Hollingsworth, R., Thomashow, M. F., et al. (2005). Characterization of potential stress responses in ancient Siberian permafrost psychroactive bacteria. *FEMS Microbiol. Ecol.* 53, 103–115. doi: 10.1016/j.femsec.2004.12.003

Raichand, R., Pareek, S., Singh, N. K., and Mayilraj, S. (2012). *Exiguobacterium aquaticum* sp. nov. a new member of the genus *Exiguobacterium*. *Int. J. Syst. Evol. Microbiol.* 62, 2150–2155. doi: 10.1099/ijs.0.035790-0

Rebollar, E. A., Avitia, M., Eguiarte, L. E., González-González, A., Mora, L., Bonilla-Rosso, G., et al. (2012). Water-sediment niche differentiation in ancient marine lineages of *Exiguobacterium* endemic to the Cuatro Cienegas Basin. *Environ. Microbiol.* 14, 2323–2333. doi: 10.1111/j.1462-2920.2012.02784.x

Rice, P., Longden, I., and Bleasby, A. (2000). EMBOSS: the european molecular biology open software suite. *Trends Genet.* 16, 276–277. doi: 10.1016/S0168-9525(00)02024-2

Rodrigues, D. F., Goris, J., Vishnivetskaya, T., Gilichinsky, D., Thomashow, M. F., and Tiedje, J. M. (2006). Characterization of *Exiguobacterium* isolates from the Siberian permafrost Description of *Exiguobacterium sibiricum* sp. nov. *Extremophiles* 10, 285–294. doi: 10.1007/s00792-005-0497-5

Rodrigues, D. F., Ivanova, N., He, Z., Huebner, M., Zhou, J., and Tiedje, J. M. (2008). Architecture of thermal adaptation in an *Exiguobacterium sibiricum* strain isolated from 3 million-year-old permafrost: a genome and transcriptome approach. *BMC Genomics* 9:547. doi: 10.1186/1471-2164-9-547

Rodriguez-R, L. M., and Konstantinidis, K. T. (2016). The enveomics collection: a toolbox for specialized analyses of microbial genomes and metagenomes. *PeerJ Prepr.* 4:e1900v1.

Ruvindy, R., White, R. A. III, Neilan, B. A., and Burns, B. P. (2016). Unraveling core microbial metabolisms in the hypersaline microbial mats of Shark Bay using high-throughput metagenomics. *ISMEJ* 10, 183–196. doi: 10.1038/ismej.2015.87

Sancho-Tomás, M., Somogyi, A., Medjoubi, K., Bergamaschi, A., Visscher, P. T., Van Driesschee, E. S. A., et al. (2018). Distribution, redox state and biogeochemical implications of arsenic in present-day microbialites of Laguna Brava, Salar de Atacama. *Chem. Geol.* 490, 13–21. doi: 10.1016/j.chemgeo.2018.04.029

Seiler, C., and Berendonk, U. T. (2012). Heavy metal driven co-selection of antibiotic resistance in soil and water bodies impacted by agriculture and aquaculture. *Front. Microbiol.* 3:399. doi: 10.3389/fmicb.2012.00399

Shao, C., Sun, Y., Wang, N., Yu, H., Zhou, Y., Chen, C., et al. (2013). Changes of proteome components of *Helicobacter pylori* biofilms induced by serum starvation. *Mol. Med. Rep.* 2013, 1761–1766. doi: 10.3892/mmr.2013.1712

Singh, N. K., Raichand, R., Kaur, I., Kaur, C., Pareek, S., and Mayilraj, S. (2013). *Exiguobacterium himgiriensis* sp. nov. a novel member of the genus *Exiguobacterium*, isolated from the Indian Himalayas. *Antonie van Leeuwenhoek* 103, 789–796. doi: 10.1007/s10482-012-9861-5

Sleator, D. R., and Hill, C. (2002). Bacterial osmoadaptation: the role of osmolytes in bacterial stress and virulence. *FEMS Microbiol. Rev.* 26, 49–71. doi: 10.1111/j.1574-6976.2002.tb00598.x

Sorokina, M., Stam, M., Médigue, C., Lespinet, O., and Vallenet, D. (2014). Profiling the orphan enzymes. *Biol. Direct* 9:10. doi: 10.1186/1745-6150-9-10

Stevenson, J. S. (1940). *Mercury Deposits of British Columbia. Bulletin No.5*. Victoria, BC: British Columbia department of mines.

Tang, J., Zhang, Y., Meng, H., Xue, Z., and Ma, J. (2013). Complete genome sequence of *Exiguobacterium* sp. strain MH3, isolated from rhizosphere of Lemna minor. *Genome Announc.* 1:e01059-13. doi: 10.1128/genomeA.01059-13

Tatusova, T., DiCuccio, M., Badretdin, A., Chetvernin, V., Nawrocki, E., Zaslavsky, L., et al. (2016). NCBI prokaryotic genome annotation pipeline. *Nucleic Acids Res.* 44, 6614–6624. doi: 10.1093/nar/gkw569

Trifinopoulos, J., Nguyen, L. T., von Haeseler, A., and Minh, B. Q. (2016). W-IQ-TREE: a fast online phylogenetic tool for maximum likelihood analysis. *Nucleic Acids Res.* 44, W232–W235. doi: 10.1093/nar/gkw256

Tsuzuki, M., Moskvin, O. V., Kuribayashi, M., Sato, K., Retamal, S., Abo, M., et al. (2011). Salt stress-induced changes in the transcriptome, compatible solutes, and membrane lipids in the facultatively phototrophic bacterium *Rhodobacter sphaeroides*. *Appl. Environ. Microbiol.* 77, 7551–7559. doi: 10.1128/AEM.05463-11

Vishnivetskaya, T. A., Chauhan, A., Layton, A. C., Pfiffner, S. M., Huntemann, M., Copeland, A., et al. (2014). Draft genome sequences of 10 strains of the genus *Exiguobacterium*. *Genome Announc.* 2:e01058-14. doi: 10.1128/genomeA.01058-14

Vishnivetskaya, T. A., Kathariou, S., and Tiedje, J. M. (2009). The *Exiguobacterium* genus: biodiversity and biogeography. *Extremophiles* 13, 541–555. doi: 10.1007/s00792-009-0243-5

Vishnivetskaya, T. A., Lucas, S., Copeland, A., Lapidus, A., Glavina del Rio, T., Dalin, E., et al. (2011). Complete genome sequence of the thermophilic Bacterium *Exiguobacterium* sp. AT1b. *J. Bacteriol.* 193, 2880–2881. doi: 10.1128/JB.00303-11

Wada, N., Sakamoto, T., and Matsugo, S. (2013). Multiple roles of photosynthetic and sunscreen pigments in cyanobacteria focusing on the oxidative stress. *Metabolites* 3, 463–483. doi: 10.3390/metabo3020463

White, R. A. III, Chan, A. M., Gavelis, G. S., Leander, B. S., Brady, A. L., Slater, G. F., et al. (2016). Metagenomic analysis suggests modern freshwater microbialites harbor a distinct core microbial community. *Front. Microbiol.* 6:1531. doi: 10.3389/fmicb.2015.01531

White, R. A. III, Gavelis, G. S., Soles, S. A., Gosselin, E., Slater, G. F., Lim, D. S. S., et al. (2018a). The Complete genome and physiological analysis of the microbialite-dwelling *Agrococcus pavilionensis* sp. nov; reveals genetic promiscuity and predicted adaptations to environmental stress. *Front. Microbiol.* 9:2180. doi: 10.3389/fmicb.2018.02180

White, R. A. III, Grassa, C. J., and Suttle, C. A. (2013a). Draft genome sequence of *Exiguobacterium* pavilionensis strain RW-2, with wide thermal, salinity, and pH tolerance, isolated from modern freshwater microbialites. *Genome Announc.* 1:e00597-13. doi: 10.1128/genomeA.00597-13

White, R. A. III, Grassa, C. J., and Suttle, C. A. (2013b). First draft genome sequence from a member of the genus *Agrococcus*, isolated from modern microbialites. *Genome Announc.* 1:e00391-13. doi: 10.1128/genomeA.00391-13

White, R. A. III, Power, I. M., Dipple, G. M., Southam, G., and Suttle, C. A. (2015). Metagenomic analysis reveals that modern microbialites and polar microbial mats have similar taxonomic and functional potential. *Front. Microbiol.* 6:966. doi: 10.3389/fmicb.2015.00966

White, R. W. III, Wong, H. L., Ruvindy, R., Neilan, B. A., and Burns, B. P. (2018b). Viral communities of Shark Bay modern stromatolites. *Front. Microbiol.* 9:1223. doi: 10.3389/fmicb.2018.01223

Wickham, H. (2016). *ggplot2: Elegant Graphics for Data Analysis*. New York, NY: Springer-Verlag.

Wong, H. L., Smith, D.-L., Visscher, P. T., and Burns, B. P. (2015). Niche differentiation of bacterial communities at a millimeter scale in Shark Bay microbial mats. *Sci. Rep.* 5:15607. doi: 10.1038/srep15607

Wong, H. L., Visscher, P. T., White, R. A. III, Smith, D. L., Patterson, M. M., and Burns, B. P. (2017). Dynamics of archaea at fine spatial scales in Shark Bay mat microbiomes. *Sci. Rep.* 7:46160. doi: 10.1038/srep46160

Wong, H. L., White, R. A. III, Visscher, P. T., Charlesworth, J. C., Vázquez-Campos, X., and Burns, B. P. (2018). Disentangling the drivers of functional complexity at the metagenomic level in Shark Bay microbial mat microbiomes. *ISME J.* 12, 2619–2639. doi: 10.1038/s41396-018-0208-8

Yumoto, I., Hishinuma-Narisawa, M., Hirota, K., Shingyo, T., Takebe, F., Nodasaka, Y., et al. (2004). *Exiguobacterium oxidotolerans* sp nov., a novel alkaliphile exhibiting high catalase activity. *Int. J. Syst. Evol. Microbiol.* 54, 2013–2017. doi: 10.1099/ijs.0.63129-0

Conflict of Interest Statement: The authors declare that the research was conducted in the absence of any commercial or financial relationships that could be construed as a potential conflict of interest.

Advantages of publishing in Frontiers

OPEN ACCESS
Articles are free to read for greatest visibility and readership

FAST PUBLICATION
Around 90 days from submission to decision

HIGH QUALITY PEER-REVIEW
Rigorous, collaborative, and constructive peer-review

TRANSPARENT PEER-REVIEW
Editors and reviewers acknowledged by name on published articles

Frontiers
Avenue du Tribunal-Fédéral 34
1005 Lausanne | Switzerland

Visit us: www.frontiersin.org
Contact us: info@frontiersin.org | +41 21 510 17 00

REPRODUCIBILITY OF RESEARCH
Support open data and methods to enhance research reproducibility

DIGITAL PUBLISHING
Articles designed for optimal readership across devices

FOLLOW US
@frontiersin

IMPACT METRICS
Advanced article metrics track visibility across digital media

EXTENSIVE PROMOTION
Marketing and promotion of impactful research

LOOP RESEARCH NETWORK
Our network increases your article's readership